materials

Special Issue Reprint

Alloy Strengthening Mechanisms, Microstructure Control, and Performance Optimization

Edited by
Hongling Zhou and Keqin Feng

mdpi.com/journal/materials

MDPI

Alloy Strengthening Mechanisms, Microstructure Control, and Performance Optimization

Alloy Strengthening Mechanisms, Microstructure Control, and Performance Optimization

Guest Editors

Hongling Zhou
Keqin Feng

MDPI

Basel • Beijing • Wuhan • Barcelona • Belgrade • Novi Sad • Cluj • Manchester

Guest Editors

Hongling Zhou
College of Materials Science and Engineering
Chongqing University
Chongqing
China

Keqin Feng
School of Mechanical Engineering
Sichuan University
Chengdu
China

Editorial Office
MDPI AG
Grosspeteranlage 5
4052 Basel, Switzerland

This is a reprint of the Special Issue, published open access by the journal *Materials* (ISSN 1996-1944), freely accessible at: https://www.mdpi.com/journal/materials/special_issues/37OA12DL88.

For citation purposes, cite each article independently as indicated on the article page online and as indicated below:

Lastname, A.A.; Lastname, B.B. Article Title. *Journal Name* **Year**, *Volume Number*, Page Range.

ISBN 978-3-7258-8715-6 (Hbk)
ISBN 978-3-7258-8716-3 (PDF)
https://doi.org/10.3390/books978-3-7258-8716-3

© 2026 by the authors. Articles in this reprint are Open Access and distributed under the Creative Commons Attribution (CC BY) license. The reprint as a whole is distributed by MDPI under the terms and conditions of the Creative Commons Attribution-NonCommercial-NoDerivs (CC BY-NC-ND) license (https://creativecommons.org/licenses/by-nc-nd/4.0/).

Contents

About the Editors . . . . . **vii**

Hongling Zhou and Keqin Feng
Alloy Strengthening Mechanisms, Microstructure Control, and Performance Optimization
Reprinted from: *Materials* **2025**, *18*, 4808, https://doi.org/10.3390/ma18204808 . . . . . **1**

Kwangmin Choi, Sangjun Lee and Donghyun Bae
Natural and Artificial Aging Effects on the Deformation Behaviors of Al–Mg–Zn Alloy Sheets
Reprinted from: *Materials* **2024**, *17*, 4478, https://doi.org/10.3390/ma17184478 . . . . . **8**

Przemysław Gołasz, Agnieszka Płoska, Viktoriia Korniienko, Kateryna Diedkova, Yuliia Varava, Rafał Zieliński, et al.
Modification of Ti13Nb13Zr Alloy Surface via Plasma Electrolytic Oxidation and Silver Nanoparticles Decorating
Reprinted from: *Materials* **2025**, *18*, 349, https://doi.org/10.3390/ma18020349 . . . . . **24**

Hui Jiang, Junjun Jin, Yu Fang, Guoqing Gou, Wei Lu, Zhiyi Zhang, et al.
Effects of Pre-Deformation in Corrosion Fatigue Crack Growth of Al-Mg-Zn Alloy
Reprinted from: *Materials* **2025**, *18*, 365, https://doi.org/10.3390/ma18020365 . . . . . **39**

Zhijun Ji, Hai Nan, Guirong Li, Shouzuo Guo, Yurong Ye, Hongming Wang and Pengjie Zhou
Synergistic Effects of Deep Cryogenic and Pulsed Magnetic Field Treatments on the Microstructure and Tensile Properties of Aero-TC4 Titanium Alloy
Reprinted from: *Materials* **2025**, *18*, 817, https://doi.org/10.3390/ma18040817 . . . . . **57**

Huimin Li, Junjun Jin, Zhiyi Zhang, Jinpeng Yu, Hairong Sun, Songling Sun, et al.
Mechanical Properties and σ-Phase Precipitation in $FeCoCrNiMo_x$ (x = 0, 0.4, 0.5, 0.8, 1.3) High-Entropy Alloys: Insights from First-Principles Study
Reprinted from: *Materials* **2025**, *18*, 1267, https://doi.org/10.3390/ma18061267 . . . . . **79**

Jianghua Huang, Zeling Zhao, Xiaomin Huang, Tao Liu and Hongchao Ji
Finite Element Simulation and Optimization of Process Parameters for Titanium Chip Crusher
Reprinted from: *Materials* **2025**, *18*, 1894, https://doi.org/10.3390/ma18091894 . . . . . **96**

Dennis Zang, Julia Becker, Ulf Betke, Georg Hasemann, Kateryna Khanchych, Bronislava Gorr and Manja Krüger
Phase Evolution During High-Energy Ball Milling and Annealing of Ti-Doped Mo-V-Si-B Alloys
Reprinted from: *Materials* **2025**, *18*, 2494, https://doi.org/10.3390/ma18112494 . . . . . **113**

Jinwen Cai, Qiaoling Jiang, Keqin Feng and Hongling Zhou
Tailoring Microstructure and Properties of W-Mo-Cu Composites Fabricated via Infiltration Sintering: Effects of Graphene Addition and Skeleton Relative Density
Reprinted from: *Materials* **2025**, *18*, 2539, https://doi.org/10.3390/ma18112539 . . . . . **133**

Ying-Ting Huang, Yu-Wei Yen and Fei-Yi Hung
A Study on Thermally Fatigued Phase Transformation and Bending Fracture Mechanisms of 310S Stainless Steel
Reprinted from: *Materials* **2025**, *18*, 2654, https://doi.org/10.3390/ma18112654 . . . . . **149**

Paweł Jóźwik, Wojciech Polkowski, Andrzej J. Panas and Zbigniew Bojar
Microstructure Evolution of Ni_3Al-Based Intermetallic Alloy Strips After Hot Rolling
Reprinted from: *Materials* **2025**, *18*, 3016, https://doi.org/10.3390/ma18133016 . . . . . **165**

Jan Šmalc, Adam Zaky, Boštjan Markoli and Roman Šturm
Microstructural Stability and High-Temperature Mechanical Behavior of Al–Ni–Zr Alloy Strengthened by $L1_2$-Al_3Zr Precipitates
Reprinted from: *Materials* **2025**, *18*, 3068, https://doi.org/10.3390/ma18133068 . . . . . **181**

Piotr Löschner, Piotr Niesłony and Szymon Kołodziej
Parameter Sensitivity Study of the Johnson–Cook Model in FEM Turning of Ti6Al4V Alloy
Reprinted from: *Materials* **2025**, *18*, 3351, https://doi.org/10.3390/ma18143351 . . . . . **194**

Xuesong Ren, Zuojun Fan, Zhen Jia, Yongping Shen and Huanzhang You
Numerical Simulation Study on Non-Axisymmetric Die-Less Spinning with a Right-Angle Groove in the Tube
Reprinted from: *Materials* **2025**, *18*, 3858, https://doi.org/10.3390/ma18163858 . . . . . **210**

Yaohong Xiao, Hongling Zhou, Pengwei Liu and Lei Chen
Gleeble-Simulated Ultra-Fast Cooling Unlocks Strength–Ductility Synergy in Fully Martensitic Ti-6Al-4V
Reprinted from: *Materials* **2025**, *18*, 4572, https://doi.org/10.3390/ma18194572 . . . . . **227**

About the Editors

Hongling Zhou

Hongling Zhou is an Associate Research Fellow at Chongqing University and a Visiting Scholar at The Pennsylvania State University. Her research focuses on the computational simulation of materials under extreme environments, rapid fabrication of materials assisted by external physical fields, and the design and fabrication of high-performance alloys and ceramics. She has led or participated in several competitive research projects, including projects funded by the National Key Research and Development Program of China and the National Natural Science Foundation of China. She has published more than 50 SCI-indexed papers in academic journals such as *Acta Materialia* and *Additive Manufacturing*, and holds 13 Chinese invention patents. She also serves as a Guest Editor and Editorial Board Member for several materials science journals and as a reviewer for numerous international journals.

Keqin Feng

Keqin Feng is a Professor at Sichuan University. Her primary research interests lie in the synthesis and preparation of metallic materials and metal matrix composites. She has led numerous national-, provincial-, and ministerial-level research projects, including those supported by the National Natural Science Foundation of China, the Scientific Research Foundation for the Returned Overseas Chinese Scholars (Ministry of Education), the China Postdoctoral Science Foundation, the Key Research and Development Program of Sichuan Province, and the Science and Technology Support Program of Sichuan Province, among others. To date, Professor Feng has published over 180 papers in academic journals and holds 12 authorized national invention patents in China.

materials

MDPI

Editorial

Alloy Strengthening Mechanisms, Microstructure Control, and Performance Optimization

Hongling Zhou [1,*] and Keqin Feng [2,*]

[1] College of Materials Science and Engineering, Chongqing University, Chongqing 400044, China
[2] School of Mechanical Engineering, Sichuan University, Chengdu 610065, China
* Correspondence: zhouhongling@cqu.edu.cn (H.Z.); kqfeng@scu.edu.cn (K.F.)

1. Introduction and Scope

Alloys and metal matrix composites (MMCs) are fundamental enablers of technological progress across critical engineering sectors, including aviation, aerospace, marine, automotive, and advanced electronics [1–10]. The rapid evolution of these industries is driving an escalating demand for materials that exhibit superior mechanical properties, lightweight characteristics [11–14], and multifunctional performance, particularly for large-scale, geometrically complex structural components [15–22]. Accordingly, developing high-performance advanced alloys and MMCs has emerged as a pivotal research frontier, holding immense potential for next-generation engineering applications.

Once the primary composition of a material is determined, its key properties—such as density, strength [7,20,23,24], electrical/thermal conductivity [25–28], tensile performance, ductility [29,30], high-temperature stability, and corrosion resistance—are predominantly determined by its microstructure [20,31–33]. Therefore, a deep understanding of the fundamental strengthening mechanisms and the development of effective microstructure control strategies are essential for optimizing the performance of these structural and functional materials.

This Special Issue, entitled "Alloy Strengthening Mechanisms, Microstructure Control, and Performance Optimization", showcases the latest breakthroughs in understanding of strengthening mechanisms, microstructure evolution, and performance enhancement in alloys and MMCs. This Special Issue emphasizes establishing quantitative relationships among processing parameters, microstructure evolution, and mechanical properties. It also highlights the development and application of innovative processing strategies, novel alloy design approaches, and emerging characterization techniques.

By compiling cutting-edge research in this field, this Special Issue aims to provide critical insights to advance the development of next-generation high-performance materials for extreme service environments and advanced engineering applications.

2. Contributions

This Special Issue comprises fourteen peer-reviewed articles, categorized by material systems: five contributions on Ti alloys, four on Al alloys, and five dedicated to other advanced alloys, including Mo alloys, W alloys, Ni_3Al alloys, high-entropy alloys, and stainless steel. Choi et al. [34] investigated the natural aging (NA) and artificial aging (AA) effects on the precipitate formation and the corresponding strengthening and deformation behaviors of Al–Mg–Zn alloys. NA-treated alloys showed ~10% higher elongation at an equivalent strength compared to AA-treated ones, due to their enhanced work-hardening

capacity and narrower precipitate-free zones. NA samples mainly formed GP zones and solute clusters with a coherent interface with the matrix, while AA samples contained incoherent η'/η phases. TEM and EBSD analyses revealed more uniform geometrically necessary dislocations distribution and higher anisotropy in NA-treated sheets, offering guidance for aging process optimization in lightweight applications.

Jiang et al. [35] investigated the effect of pre-deformation on the corrosion fatigue crack propagation (CFCG) of an Al–Mg–Zn alloy in 3.5% NaCl solution. Tensile tests and molecular dynamics simulations showed that higher pre-deformation increased dislocation density and tensile strength by 2.63% (5%) and 10.00% (10%). EBSD and TEM analyses revealed that 5% pre-deformation caused dislocation pile-ups, promoting crack propagation, while 10% led to non-uniform dislocation distribution, enhancing crack resistance.

Šmalc et al. [36] modified the eutectic Al–Ni alloy by adding 0.6 wt.% Zr to enhance its mechanical properties via precipitation strengthening. After T5 heat treatment and aging at 350 °C, the formation of fine, coherent $L1_2$-Al_3Zr precipitates contributed to the increased microhardness by ~60% and doubled the yield strength to 213 MPa room temperature (RT). TEM analysis showed the precipitates maintained relatively good thermal stability after 30 days. However, the strength enhancement was not retained at 300 °C, where the yield strength dropped to 53 MPa. The results suggest that Al–Ni–Zr alloys offer promising room-temperature performance but limited high-temperature strength retention.

Ren et al. [37] investigated non-axisymmetric die-less spinning of 6063-O aluminum alloy tubes with right-angle grooves using finite element simulation and experiments. Multi-pass forming yielded more uniform wall thickness and lower stress than single-pass forming, with stress localized at the groove bottom and strain concentrated at the roller exit. The study demonstrates that optimized roller path design is critical for improving groove quality and process stability.

Gołasz et al. [38] investigated the biocompatibility and antibacterial properties of Ti13Nb13Zr alloys treated by etching, sandblasting, and plasma electrolytic oxidation (PEO), followed by covering in silver nanoparticle (AgNP) suspension. The PEO-treated alloys showed good biocompatibility with human fibroblast cells, promoting cell growth. However, deposited AgNPs exhibited only slight and short-term antibacterial effects against E. coli and S. aureus within the first two hours. The study highlights the need to optimize the concentration of AgNP for the PEO treatment of metal alloys to improve long-term antibacterial performance.

Ji et al. [39] proposed a novel coupled treatment method (PDCT) combining deep cryogenic treatment (DCT) with a high pulsed magnetic field (PMT) to improve the mechanical properties of an as-cast TC4 titanium alloy. The optimized PDCT sample exhibited a tensile strength of 921.4 MPa, elongation of 7.6%, and fracture energy of 5.47×10^7 J/m^3, improved by 4.9%, 28.8%, and 80.5%, respectively, compared to the untreated alloy. The enhanced strength–toughness resulted from combined texture, dislocation, precipitation, and grain refinement strengthening induced by the synergistic effects of DCT and PMT.

Löschner et al. [40] analyzed the influence of Johnson–Cook (JC) material model parameters on FEM simulations of orthogonal turning for Ti6Al4V alloy. Experimental tests of cutting force components, temperature, and chip geometry were used to validate the simulation. Results showed that A, B, and m had the strongest impact on cutting forces, temperature, stress, and chip morphology, while C and n had lesser effects. The study emphasizes the importance of precise parameter calibration to ensure accuracy in modeling machining processes, especially for difficult-to-machine alloys like Ti6Al4V.

Xiao et al. [41] employed a Gleeble thermal simulator to investigate the effect of cooling rate on the microstructure evolution and mechanical behavior of Ti-6Al-4V. Compression

tests revealed that ultra-fast cooling (~7000 °C/s) produces a fully martensitic Ti-6Al-4V structure with enhanced strength and increased fracture strain, which, based on 3D microstructure reconstruction and EVP-FFT crystal plasticity analysis, is attributed to refined α' laths and a higher fraction of high-angle boundaries that promote uniform strain distribution and reduced stress triaxiality. The study highlights extreme-rate martensitic transformation as a potential pathway to overcome the traditional strength–ductility trade-off in Ti-6Al-4V.

Huang et al. [42] analyzed the titanium chip crushing process using finite element simulation to optimize the titanium chip crushing process. Simulation results revealed that increasing the number of roller teeth led to the stresses on the chips changing more smoothly towards the sides and the stresses changing more stably, and also reduced the length of the broken titanium chip. The number of teeth was identified as the most influential parameter, with the optimal conditions being 27 teeth for the crushing roller, a roller speed of 22 r/min, and a cutting edge angle of 90°.

Li et al. [43] investigated the structural stability and mechanical properties of FeCoCrNiMox (x = 0–1.3) high-entropy alloys (HEAs) using first-principles calculations coupled with the special quasi-random structure (SQS) method. It was found that all examined alloys were thermodynamically and dynamically stable except FeCoCrNiMo1.3, and Mo addition increased ductility and anisotropy while slightly reducing strength and stiffness. FeCoCrNiMo0.5 HEA coatings were then fabricated via laser cladding and showed a surface hardness of 437.91 HV0.2.

Zang et al. [44] studied the effect of small Ti additions (2 and 5 at.%) on Mo-40V-9Si-8B alloys prepared via high-energy ball milling and subsequent heat treatment. The Ti-containing alloys formed supersaturated (Mo,V,Ti) solid solutions during milling, which decomposed into (Mo,V,Ti)ss, $(Mo,V,Ti)_3Si$, and $(Mo,V,Ti)_5SiB_2$ phases after heat treatment. Ti additions slightly refined particle size, increased microstrain, and modestly improved microhardness. The results suggest that Ti- and V-modified Mo–Si–B alloys offer potential for high-temperature structural applications.

Cai et al. [45] prepared Cu-coated graphene (Cu@Gr)-reinforced W–Mo–Cu composites via vacuum infiltration sintering at 1300 °C for 1.5 h, and investigated the effects of Cu@Gr content (0.2–1.0 wt.%) and W–Mo skeleton relative density (73–85%). It was found that adding Cu@Gr promoted Mo_2C formation and improved densification. At 0.6 wt.% Cu@Gr, the composite containing 0.6 wt.% Cu@Gr exhibits the highest relative density, thermal conductivity, and electrical conductivity, showing 8%, 64% and 73% increases, respectively, versus Cu@Gr-free samples. Adjusting skeleton density influenced conductivity and hardness, but did not hinder the densification.

Huang et al. [46] investigated the microstructural evolution and mechanical degradation mechanisms of cold-drawn 310S stainless steel under repeated thermal cycling between 900 °C and room temperature. The results revealed that the thermal cycling induced significant lattice distortion, dislocation accumulation, and recrystallization, leading to grain refinement and tensile strength improvement, but also caused subsurface cracking and ductility loss. These findings indicate that even short-term cyclic thermal exposure can markedly accelerate embrittlement.

Jóźwik et al. [47] explored the effects of the temperature and strain rate during the hot rolling process on the microstructural evolution of fine-grained Ni_3Al intermetallic alloy doped with Zr and B. EBSD analysis revealed that dynamic recrystallization initiated at 1100 °C, with recrystallized grain fraction increasing at higher temperatures and strain rates. A non-stationary heat transfer model was developed, and it was found that higher strain rates led to higher material temperatures during deformation.

3. Outlook

This Special Issue of *Materials* has attracted a substantial number of submissions, culminating in the publication of 14 rigorously peer-reviewed, high-quality articles. The collected studies comprehensively showcase the latest advancements in strengthening mechanisms, microstructure control, and performance optimization of alloys and metal matrix composites. They provide critical insights into the interrelationships among processing techniques, microstructural evolution, and material properties. By employing innovative alloy design, advanced processing methods, and cutting-edge multi-dimensional, multi-scale characterization techniques, these works demonstrate effective pathways for enhancing overall material performance. Collectively, they offer valuable guidance for the development of next-generation high-performance materials targeted for critical applications in aerospace, the automotive industry, the energy industry, and advanced electronics.

As Guest Editors, we sincerely appreciate the exceptional contributions from all authors, the rigorous evaluations by the reviewers, and the dedicated support from the editorial team, which were instrumental in ensuring the scientific rigor and impact of this Special Issue.

Funding: This research was funded by the National Natural Science Foundation of China (Grant Nos. 52304380 and 51674171).

Acknowledgments: We extend our heartfelt thanks to all the authors and reviewers whose exceptional efforts made this Special Issue possible. We hope this Special Issue will serve as an informative and valuable reference for ongoing and future research in the field.

Conflicts of Interest: The authors declare no conflicts of interest.

List of Contributions:

1. Choi, K.; Lee, S.; Bae, D. Natural and Artificial Aging Effects on the Deformation Behaviors of Al–Mg–Zn Alloy Sheets. *Materials* **2024**, *17*, 4478. https://doi.org/10.3390/ma17184478.
2. Gołasz, P.; Płoska, A.; Korniienko, V.; Diedkova, K.; Varava, Y.; Zieliński, R.; Pogorielov, M.; Simka, W. Modification of Ti13Nb13Zr Alloy Surface via Plasma Electrolytic Oxidation and Silver Nanoparticles Decorating. *Materials* **2025**, *18*, 349. https://doi.org/10.3390/ma18020349.
3. Jiang, H.; Jin, J.; Fang, Y.; Gou, G.; Lu, W.; Zhang, Z.; Zhou, H.; Sun, H.; Feng, J.; Chen, J.; Fu, Z. Effects of Pre-Deformation in Corrosion Fatigue Crack Growth of Al-Mg-Zn Alloy. *Materials* **2025**, *18*, 365. https://doi.org/10.3390/ma18020365.
4. Ji, Z.; Nan, H.; Li, G.; Guo, S.; Ye, Y.; Wang, H.; Zhou, P. Synergistic Effects of Deep Cryogenic and Pulsed Magnetic Field Treatments on the Microstructure and Tensile Properties of Aero-TC4 Titanium Alloy. *Materials* **2025**, *18*, 817. https://doi.org/10.3390/ma18040817.
5. Li, H.; Jin, J.; Zhang, Z.; Yu, J.; Sun, H.; Sun, S.; Tang, W.; Gou, G. Mechanical Properties and σ-Phase Precipitation in FeCoCrNiMox (x = 0, 0.4, 0.5, 0.8, 1.3) High-Entropy Alloys: Insights from First-Principles Study. *Materials* **2025**, *18*, 1267. https://doi.org/10.3390/ma18061267.
6. Huang, J.; Zhao, Z.; Huang, X.; Liu, T.; Ji, H. Finite Element Simulation and Optimization of Process Parameters for Titanium Chip Crusher. *Materials* **2025**, *18*, 1894. https://doi.org/10.3390/ma18091894.
7. Zang, D.; Becker, J.; Betke, U.; Hasemann, G.; Khanchych, K.; Gorr, B.; Krüger, M. Phase Evolution During High-Energy Ball Milling and Annealing of Ti-Doped Mo-V-Si-B Alloys. *Materials* **2025**, *18*, 2494. https://doi.org/10.3390/ma18112494.

8. Cai, J.; Jiang, Q.; Feng, K.; Zhou, H. Tailoring Microstructure and Properties of W-Mo-Cu Composites Fabricated via Infiltration Sintering: Effects of Graphene Addition and Skeleton Relative Density. *Materials* **2025**, *18*, 2539. https://doi.org/10.3390/ma18112539.
9. Huang, Y.; Yen, Y.; Hung, F. A Study on Thermally Fatigued Phase Transformation and Bending Fracture Mechanisms of 310S Stainless Steel. *Materials* **2025**, *18*, 2654. https://doi.org/10.3390/ma18112654.
10. Jóźwik, P.; Polkowski, W.; Panas, A.; Bojar, Z. Microstructure Evolution of Ni3Al-Based Intermetallic Alloy Strips After Hot Rolling. *Materials* **2025**, *18*, 3016. https://doi.org/10.3390/ma18133016.
11. Šmalc, J.; Zaky, A.; Markoli, B.; Šturm, R. Microstructural Stability and High-Temperature Mechanical Behavior of Al–Ni–Zr Alloy Strengthened by L12-Al3Zr Precipitates. *Materials* **2025**, *18*, 3068. https://doi.org/10.3390/ma18133068.
12. Löschner, P.; Niesłony, P.; Kołodziej, S. Parameter Sensitivity Study of the Johnson–Cook Model in FEM Turning of Ti6Al4V Alloy. *Materials* **2025**, *18*, 3351. https://doi.org/10.3390/ma18143351.
13. Ren, X.; Fan, Z.; Jia, Z.; Shen, Y.; You, H. Numerical Simulation Study on Non-Axisymmetric Die-Less Spinning with a Right-Angle Groove in the Tube. *Materials* **2025**, *18*, 3858. https://doi.org/10.3390/ma18163858.
14. Xiao, Y.; Zhou, H.; Liu, P.; Chen, L. Gleeble-Simulated Ultra-Fast Cooling Unlocks Strength–Ductility Synergy in Fully Martensitic Ti-6Al-4V. *Materials* **2025**, *18*, 4572. https://doi.org/10.3390/ma18194572.

References

1. Fan, Z.H.; Tian, Y.B.; Liu, Z.Q.; Shi, C.; Zhao, Y.G. Investigation of a novel finishing tool in magnetic field assisted finishing for titanium alloy Ti-6Al-4V. *J. Manuf. Process.* **2019**, *43*, 74–82. [CrossRef]
2. Kang, L.M.; Yang, C. A Review on High-Strength Titanium Alloys: Microstructure, Strengthening, and Properties. *Adv. Eng. Mater.* **2019**, *21*, 27. [CrossRef]
3. Fan, Z.H.; Tian, Y.B.; Zhou, Q.; Shi, C. Enhanced magnetic abrasive finishing of Ti-6Al-4V using shear thickening fluids additives. *Precis. Eng.-J. Int. Soc. Precis. Eng. Nanotechnol.* **2020**, *64*, 300–306. [CrossRef]
4. Carvalho, S.R.; Horovistiz, A.; Davim, J.P. The role of roughness parameters in grading the machined surface quality in Ti-alloys. *Proc. Inst. Mech. Eng. Part B-J. Eng. Manuf.* **2024**, *238*, 1013–1029. [CrossRef]
5. Kishore, K.; Sinha, M.K.; Chauhan, S.R. A comprehensive investigation of surface morphology during grinding of Inconel 625 using conventional grinding wheels. *J. Manuf. Process.* **2023**, *97*, 87–99. [CrossRef]
6. Pan, H.C.; Kang, R.; Li, J.R.; Xie, H.B.; Zeng, Z.R.; Huang, Q.Y.; Yang, C.L.; Ren, Y.P.; Qin, G.W. Mechanistic investigation of a low-alloy Mg-Ca-based extrusion alloy with high strength-ductility synergy. *Acta Mater.* **2020**, *186*, 278–290. [CrossRef]
7. Zhang, Z.; Xie, J.S.; Zhang, J.H.; Wu, R.Z.; Wang, J.; Yang, X.S. Ultra-strong and ductile magnesium alloy enabled by ultrafine grains with nano-spacing solute-enriched planar defects. *Int. J. Plast.* **2025**, *189*, 104348. [CrossRef]
8. Zhou, H.L.; Feng, K.Q.; Ke, S.X.; Liu, Y.F. Densification and properties investigation of W-Mo-Cu composites prepared by large current electric field sintering with different technologic parameter. *J. Alloys Compd.* **2018**, *767*, 567–574. [CrossRef]
9. Zhou, H.L.; Feng, K.Q.; Xiao, Y.H.; Liu, Y.F.; Ke, S.X. Pressure effects on a novel W-Mo-Cu alloy by large current electric field sintering: Sintering behavior, microstructure and properties. *J. Alloys Compd.* **2019**, *785*, 965–971. [CrossRef]
10. Zhou, H.L.; Feng, K.Q.; Liu, Y.F. Densification, microstructure, and properties of W-Mo-Cu alloys prepared with nano-sized Cu powders via large electric current sintering. *Adv. Powder Technol.* **2022**, *33*, 103703. [CrossRef]
11. Zhang, L.; Yuan, Q.; Tan, J.; Dong, Q.; Lv, H.; Wang, F.L.; Tang, A.T.; Eckert, J.; Pan, F.S. Enhancing the room-temperature plasticity of magnesium alloys: Mechanisms and strategies. *J. Magnes. Alloys* **2024**, *12*, 4741–4767. [CrossRef]
12. Shah, S.; Liu, M.P.; Khan, A.; Ahmad, F.; Chaudry, U.M.; Khan, M.Y.; Abdullah, M.R.; Xu, S.W.; Peng, Z. Recrystallization aspects and factors affecting their roles in Mg alloys: A comprehensive review. *J. Magnes. Alloys* **2025**, *13*, 1879–1914. [CrossRef]
13. Luo, S.; Li, F.; Bao, F.Y.; Zhang, J.Y.; Wang, H.B. Development and innovations in extrusion process of aluminum and magnesium alloys: A review. *J. Mater. Sci. Technol.* **2025**, *254*, 206–227. [CrossRef]

14. Lee, D.H.; Lee, G.M.; Park, S.H. Difference in extrusion temperature dependences of microstructure and mechanical properties between extruded AZ61 and AZ91 alloys. *J. Magnes. Alloys* **2023**, *11*, 1683–1696. [CrossRef]
15. Zhang, Y.F.; Li, J.Z.; Che, S.H.; Yang, Z.D.; Tian, Y.W. Chemical leveling mechanism and oxide film properties of additively manufactured Ti-6Al-4V alloy. *J. Mater. Sci.* **2019**, *54*, 13753–13766. [CrossRef]
16. Zhang, S.Y.; Yu, Y.C.; Wang, H.; Ren, L.; Yang, K. Study on mechanical behavior of Cu-bearing antibacterial titanium alloy implant. *J. Mech. Behav. Biomed. Mater.* **2022**, *125*, 6. [CrossRef]
17. Zha, M.; Zhang, H.M.; Meng, X.T.; Jia, H.L.; Jin, S.B.; Sha, G.; Wang, H.Y.; Li, Y.J.; Roven, H.J. Stabilizing a severely deformed Al-7Mg alloy with a multimodal grain structure via Mg solute segregation. *J. Mater. Sci. Technol.* **2021**, *89*, 141–149. [CrossRef]
18. Tang, Z.; Xu, W.; Zhao, D.Y.; Zhang, B. Improving the strength and SCC resistance of an Al-5Mg-3Zn alloy with low-angle grain boundary structure. *J. Mater. Sci. Technol.* **2023**, *161*, 63–73.
19. Zhang, H.T.; Zhang, Q.D.; Wang, F.Y.; Guo, C.; Yang, D.H.; Wang, Z.; Tang, X.C.; Li, Z.P.; Nagaumi, H. Influence of Mo on microstructure, mechanical properties and intergranular corrosion properties of Al-Mg-Mn alloys. *J. Alloys Compd.* **2024**, *1007*, 16. [CrossRef]
20. Guo, C.; Wang, H.; Guo, Y.Q.; Chen, Y.F.; Yang, D.H.; Fu, J.Y.; Wu, Z.B.; Zhang, H.T.; Liu, X.A.; Nagaumi, H. Understanding the strengthening mechanism and corrosion behavior of Al-Mg-Zn(-Ag) alloys treated by non-linear heating ageing. *J. Alloys Compd.* **2025**, *1010*, 16. [CrossRef]
21. Tang, Z.C.; Xu, W.; Zhao, D.Y.; Zhang, B. Research Article Enhancing strength and stress corrosion cracking resistance in high-Mg Al-Mg alloys through nanostructuring and controlled annealing. *J. Mater. Sci. Technol.* **2025**, *224*, 19–34. [CrossRef]
22. Yao, C.Y.; Ji, Y.C.; Ding, F.; Wen, J.H.; Qin, W.T.; Xiao, F.L.; Wang, D.; Xiao, K.; Dong, C.F. Revealing the intergranular corrosion mechanism of AA5083 alloys through experiments and atomic-scale computation. *J. Mater. Sci. Technol.* **2025**, *216*, 285–299. [CrossRef]
23. Wang, H.; Zhang, D.; Qiu, C.; Chen, D. Cyclic deformation behavior of a high-strength low-alloy (HSLA) magnesium alloy with heterostructures. *J. Magnes. Alloys* **2024**, *12*, 4610–4621. [CrossRef]
24. Shen, G.W.; Chen, X.L.; Yan, J.; Fan, L.Y.; Yang, Z.; Zhang, J.; Guan, R.G. Effects of heat treatment processes on the mechanical properties, microstructure evolution, and strengthening mechanisms of Al-Mg-Zn-Cu alloy. *J. Mater. Res. Technol.-JmrT* **2023**, *27*, 5380–5388. [CrossRef]
25. Han, Y.; Ma, Z.Y.; Yang, C.C.; Ding, Y.G.; Lu, P.B.; Tan, B.; Zheng, Q.L.; Liu, Z.W. Synchronized Enhancement of Electrical Conductivity and Mechanical Properties of A356 Alloy via Gd Alloying. *Metall. Mater. Trans. A-Phys. Metall. Mater. Sci.* **2025**, *16*. [CrossRef]
26. Lunn, K.F.; Apelian, D. Thermal and Electrical Conductivity of Aluminum Alloys: Fundamentals, structure-property relationships, and pathways to enhance conductivity. *Mater. Sci. Eng. A-Struct. Mater. Prop. Microstruct. Process.* **2025**, *924*, 22. [CrossRef]
27. Liu, Y.X.; Liu, Y.C.; Wang, P.Z.; He, Z.N.; Wang, L.Z.; Akhtar, S.; Lu, Z.D.; Jiao, X.Y.; Ge, S.J.; Zhang, Y.C.; et al. A newly-developed high-pressure die-cast Al-1.5Fe-1Ni alloy with high thermal conductivity: Design, microstructure, and properties. *J. Mater. Sci. Technol.* **2025**, *245*, 130–151. [CrossRef]
28. Zhou, Y.L.; Zhang, X.; Zhong, G.; Zhang, J.C.; Yang, Y.; Kang, D.; Li, H.T.; Jie, W.Q.; Schumacher, P.; Li, J.H. Elucidating thermal conductivity mechanism of Al-9Si based alloys with trace transition elements (Mn, Cr, V). *J. Alloys Compd.* **2022**, *907*, 13. [CrossRef]
29. Zhang, H.F.; Ding, Y.T.; Li, R.M.; Gao, Y.B. Enhanced strength-ductility synergy and activation of non-basal slip in as-extruded Mg-Zn-Ca alloy via heterostructure. *J. Mater. Res. Technol.-JmrT* **2024**, *28*, 1841–1851. [CrossRef]
30. Jin, Z.Z.; Zha, M.; Wang, S.Q.; Wang, S.C.; Wang, C.; Jia, H.L.; Wang, H.Y. Alloying design and microstructural control strategies towards developing Mg alloys with enhanced ductility. *J. Magnes. Alloys* **2022**, *10*, 1191–1206. [CrossRef]
31. Wang, Y.; Gupta, R.K.; Sukiman, N.L.; Zhang, R.; Davies, C.H.J.; Birbilis, N. Influence of alloyed Nd content on the corrosion of an Al-5Mg alloy. *Corros. Sci.* **2013**, *73*, 181–187. [CrossRef]
32. Zha, M.; Li, Y.J.; Mathiesen, R.H.; Bjorge, R.; Roven, H.J. Microstructure evolution and mechanical behavior of a binary Al-7Mg alloy processed by equal-channel angular pressing. *Acta Mater.* **2015**, *84*, 42–54. [CrossRef]
33. Stemper, L.; Mitas, B.; Kremmer, T.; Otterbach, S.; Uggowitzer, P.J.; Pogatscher, S. Age-hardening of high pressure die casting AlMg alloys with Zn and combined Zn and Cu additions. *Mater. Des.* **2019**, *181*, 11. [CrossRef]
34. Choi, K.; Lee, S.; Bae, D. Natural and Artificial Aging Effects on the Deformation Behaviors of Al-Mg-Zn Alloy Sheets. *Materials* **2024**, *17*, 4478. [CrossRef]
35. Jiang, H.; Jin, J.; Fang, Y.; Gou, G.; Lu, W.; Zhang, Z.; Zhou, H.; Sun, H.; Feng, J.; Chen, J.; et al. Effects of Pre-Deformation in Corrosion Fatigue Crack Growth of Al-Mg-Zn Alloy. *Materials* **2025**, *18*, 365. [CrossRef]
36. Šmalc, J.; Zaky, A.; Markoli, B.; Šturm, R. Microstructural Stability and High-Temperature Mechanical Behavior of Al–Ni–Zr Alloy Strengthened by L12-Al3Zr Precipitates. *Materials* **2025**, *18*, 3068. [CrossRef]

37. Ren, X.; Fan, Z.; Jia, Z.; Shen, Y.; You, H. Numerical Simulation Study on Non-Axisymmetric Die-Less Spinning with a Right-Angle Groove in the Tube. *Materials* **2025**, *18*, 3858. [CrossRef]
38. Golasz, P.; Ploska, A.; Korniienko, V.; Diedkova, K.; Varava, Y.; Zielinski, R.; Pogorielov, M.; Simka, W. Modification of Ti13Nb13Zr Alloy Surface via Plasma Electrolytic Oxidation and Silver Nanoparticles Decorating. *Materials* **2025**, *18*, 349. [CrossRef]
39. Ji, Z.; Nan, H.; Li, G.; Guo, S.; Ye, Y.; Wang, H.; Zhou, P. Synergistic Effects of Deep Cryogenic and Pulsed Magnetic Field Treatments on the Microstructure and Tensile Properties of Aero-TC4 Titanium Alloy. *Materials* **2025**, *18*, 817. [CrossRef]
40. Löschner, P.; Niesłony, P.; Kołodziej, S. Parameter Sensitivity Study of the Johnson–Cook Model in FEM Turning of Ti6Al4V Alloy. *Materials* **2025**, *18*, 3351. [CrossRef]
41. Xiao, Y.; Zhou, H.; Liu, P.; Chen, L. Gleeble-Simulated Ultra-Fast Cooling Unlocks Strength–Ductility Synergy in Fully Martensitic Ti-6Al-4V. *Materials* **2025**, *18*, 4572. [CrossRef]
42. Huang, J.; Zhao, Z.; Huang, X.; Liu, T.; Ji, H. Finite Element Simulation and Optimization of Process Parameters for Titanium Chip Crusher. *Materials* **2025**, *18*, 1894. [CrossRef]
43. Li, H.; Jin, J.; Zhang, Z.; Yu, J.; Sun, H.; Sun, S.; Tang, W.; Gou, G. Mechanical Properties and sigma-Phase Precipitation in FeCoCrNiMo(x) (x = 0, 0.4, 0.5, 0.8, 1.3) High-Entropy Alloys: Insights from First-Principles Study. *Materials* **2025**, *18*, 1267. [CrossRef]
44. Zang, D.; Becker, J.; Betke, U.; Hasemann, G.; Khanchych, K.; Gorr, B.; Kruger, M. Phase Evolution During High-Energy Ball Milling and Annealing of Ti-Doped Mo-V-Si-B Alloys. *Materials* **2025**, *18*, 2494. [CrossRef]
45. Cai, J.; Jiang, Q.; Feng, K.; Zhou, H. Tailoring Microstructure and Properties of W-Mo-Cu Composites Fabricated via Infiltration Sintering: Effects of Graphene Addition and Skeleton Relative Density. *Materials* **2025**, *18*, 2539. [CrossRef]
46. Huang, Y.T.; Yen, Y.W.; Hung, F.Y. A Study on Thermally Fatigued Phase Transformation and Bending Fracture Mechanisms of 310S Stainless Steel. *Materials* **2025**, *18*, 2654. [CrossRef]
47. Jóźwik, P.; Polkowski, W.; Panas, A.J.; Bojar, Z. Microstructure Evolution of Ni3Al-Based Intermetallic Alloy Strips After Hot Rolling. *Materials* **2025**, *18*, 3016. [CrossRef]

Disclaimer/Publisher's Note: The statements, opinions and data contained in all publications are solely those of the individual author(s) and contributor(s) and not of MDPI and/or the editor(s). MDPI and/or the editor(s) disclaim responsibility for any injury to people or property resulting from any ideas, methods, instructions or products referred to in the content.

materials

MDPI

Article

Natural and Artificial Aging Effects on the Deformation Behaviors of Al–Mg–Zn Alloy Sheets

Kwangmin Choi [1], Sangjun Lee [1,2] and Donghyun Bae [1,*]

[1] Department of Materials Science and Engineering, Yonsei University, Seoul 03722, Republic of Korea; ckm88wkd@yonsei.ac.kr (K.C.)
[2] Institute of Industrial Science, The University of Tokyo, 4-6-1 Komaba, Meguro 153-8505, Tokyo, Japan
* Correspondence: donghyun@yonsei.ac.kr; Tel.: +82-2-2123-5831

Abstract: This study investigated the effects of aging profiles on the precipitate formation and the corresponding strengthening and deformation behaviors of Al–Mg–Zn alloys. The alloys subjected to natural aging (NA) demonstrated significantly enhanced ductility at equivalent stress levels compared to those subjected to artificial aging (AA). In AA-treated alloys, η' and η-phases with incoherent interfaces were formed, while GP zones and solute clusters were dominantly exhibited in the NA-treated alloy with a coherent interface with the matrix. Due to the change in interface bonding, the dislocation movement and pinning behavior after deformation are varied depending on the aging conditions of Al–Mg–Zn alloy sheet. Thus, the elongation to fracture of the NA alloy sheet was improved compared to that of the AA alloy sheet because of the enhanced work-hardening capacity and the thin precipitate-free zone (PFZ). Deformation textures and dislocation densities varied between NA and AA treatments, as revealed by electron backscatter diffraction (EBSD) and kernel average misorientation (KAM) analysis. The interactions between the precipitates, dislocations, and the PFZ in the AA- and NA-treated alloys were analyzed via transmission electron microscopy (TEM). The insights gained from this research provide a valuable foundation for industrial applications, particularly in sectors demanding lightweight, high-strength materials, where optimizing the aging process can lead to significant performance improvement and cost savings.

Keywords: aluminum alloys; artificial aging; natural aging; precipitates; dislocations; precipitate-free zone

1. Introduction

The demand for high-performance, lightweight aluminum alloys increases rapidly owing to the growing environmental concerns in industries [1–4]. The 7xxx series of Al alloys comprising Al, Mg, Zn, and Cu are promising structural materials with high strength-to-weight ratios because of their exceptional precipitate strengthening. The general precipitation in an Al–Zn–Mg alloy can be described as follows [5]:

Supersaturated solid solution (SSS) → Guinier–Preston (GP) zone (GP I, GP II) → metastable phase η' → equilibrium phase η ($MgZn_2$)

In the initial stage of aging, a GP zone, which has a fully coherent interface with the matrix, is formed from the supersaturated solid solution matrix as a precursor for the nucleation of η'. Two types of precipitates (GP I and GP II) exist in the GP zone. The GP I zone consists of Al–Zn and Zn–Mg on the {001} plane of the aluminum matrix with a fully coherent interface. The GP II zone, however, is treated as a Zn cluster on the {111} plane of the aluminum matrix [6]. The metastable phase η' is the major hardening precipitate responsible for the peak hardening of the Al–Zn–Mg–(Cu) alloy. The stable phase η ($MgZn_2$) is obtained after over-aging [7].

Typically, the mechanical properties of Al–Zn–Mg alloys can be enhanced through artificial aging (AA), which is performed under "elevated temperatures" between 100 and

200 °C for most conventional aluminum alloys [8,9]. The strength of Al alloys is controlled by the type, morphology, and physical characteristics of the precipitates, which in turn depend on the composition and the additional solute elements [4,10]. A high-strength 7000 series aluminum alloy with T-phase ($Mg_{32}(Al, Zn)_{49}$) precipitates was obtained at a high Zn/Mg ratio. Strengthening precipitates can be designed by changing the Zn/Mg ratio, such as T, η′, and η-phases [9]. Zhao et al. [11] obtained Al–Mg alloy sheets with desirable mechanical properties by adding adequate Zn. Hot-rolled Al–9.2Mg–0.5Zn alloy exhibited a higher ultimate tensile strength (UTS, 434 ± 5 MPa), yield strength (YS, 228 ± 2 MPa), and elongation (48 ± 2%) than Al–Mg alloy sheets. Smith and Grant [12] observed that the precipitation rate at low-temperature aging conditions could be increased in the presence of 0.5 wt. % of the Cu element because numerous nucleated GP zones induced considerable strengthening. Liu et al. [13] reported that Ag improved the tensile properties and fracture toughness of novel Al–Mg–Zn alloy sheets by precipitation hardening.

Natural aging (NA) performed at "room temperature" also strengthens the alloy. NA leads to a different type of precipitate from AA, usually requires a long aging time, and achieves a lower hardness level. Liu et al. [14] investigated the formation of solute clusters and GP zones in Al–Mg–Zn alloys during NA. Furthermore, the formation of clusters in long-term natural aging is also defined. Geng et al. [15] studied the effects of Cu atoms on the precipitation and solute clustering during the initial stages of NA. Cu atoms promoted the formation of solute clusters, so a large number of clusters influenced the transformation of T′-phases. Furthermore, the positive effect of NA on the mechanical properties of Al–Mg–Zn alloy was investigated. Zhao et al. [16] explored the influence of a four-stage aging treatment on the strength and elongation of 7000 series of aluminum alloy sheets after AA and NA. Before the re-aging treatment, NA enhanced the tensile strength and elongation of the alloy because of the formation of GP zones.

So far, most research on the aging of Al–Zn–Mg alloys has focused on strategies to enhance their strength or investigations about the formation mechanisms of hardening precipitates. Previously, some researchers tried to develop a ductility-enhanced Al–Mg–Zn alloy. A high-ductility Al–Zn–Mg alloy was obtained from a Zn-modified Al–Mg alloy by enhancing the work hardening [11]. Al–Mg alloy with a moderate Zn content can achieve random grain orientation and effective work hardening, leading to high ductility in hot-rolled samples. Furthermore, Mn and Ag are excellent solute elements because they can promote grain refinement to form a narrow precipitate-free zone (PFZ) in Al–Zn–Mg alloys and enhance ductility [17]. Ogura et al. used Ag-containing intermetallic compounds to stabilize grain structures and accelerate the nucleation of strengthening dispersoids. Although a few studies have investigated the methods to develop high-ductility Al–Mg–Zn alloys using extra solute elements, the specific influence of precipitates on deformation behaviors, such as texture and dislocation interactions, remains unclear. Moreover, the attempts to enhance the ductility of Al–Zn–Mg alloys and define the difference in deformation behavior in artificially and naturally aged alloys have been insufficiently reported.

In this study, the plastic deformation behaviors of Al alloys under AA and NA treatments were investigated to explore the mechanism of strength and ductility enhancement, providing insights into their specific applications. According to the aging conditions, the microstructure of the alloy is varied, and it offers an opportunity to change the dislocation activity. This study also suggests that the presence of precipitates contributes significantly to the mechanical properties with respect to texture and plastic anisotropy, which is a novel perspective to understand the structure–performance relationship of Al alloys.

2. Materials and Methods

Al–Mg–Zn alloys were fabricated using a conventional casting method, an electric resistivity furnace, and a permanent steel mold. Pure Al (purity 3N, Hanjin Metal) was melted at 730 °C under ambient conditions, and then Mg (Purity 4N, Hanjin Metal) and Zn (Purity 4N, Hanjin Metal) were added according to the compositions listed in Table 1. The liquid alloy was held for 30 min to achieve compositional uniformity to the alloy melts, and

the melts were poured into a steel mold. Bar-type ingots were subjected to heat treatment at 500 °C for 12 h for homogenization. The surfaces of the ingots were then mechanically milled to remove surface defects, such as the oxide layer. Subsequently, hot rolling was applied to reduce the thickness of the ingot to 4 mm at a 20% reduction rate. Cold rolling was then performed at a reduction rate of 10–20% to reach a 1.0–1.2 mm thickness. The as-rolled alloy sheet was solution-heat-treated at 500 °C for 15 min to recrystallize the grain and solutionize the alloying element. Subsequently, AA and NA were conducted to enhance the mechanical properties, particularly the strength. AA was performed under 120 °C, and NA was conducted at room temperature (25 °C).

Table 1. Chemical composition of Al–Mg–Zn alloy (wt. %).

	Mg	**Zn**	**Mn**	**Fe**	**Al**
Desired composition	5	4	0.3	-	Bal.
Measured composition	4.85	3.97	0.27	0.08	Bal.

Vickers hardness and uniaxial tension tests were performed on the alloy sheets at regular time intervals. The specimens were artificially and naturally aged, then mechanically polished to remove the oxide layer. Then, the Vickers hardness test was performed with a 200 gf compression load; furthermore, analysis was performed as uniformly as possible. An Instron-type uniaxial tension test machine (RB301, R&B, Daejeon, Korea) with a constant crosshead speed (initial strain rate of 1×10^{-3}/s) was used for the tensile tests at room temperature on a dogbone-type test sample (ASTM E8). Test specimens were prepared along various rolling directions.

The microstructures of the alloys were characterized using electron backscatter diffraction (EBSD, Oxford, UK). EBSD mapping was conducted at 20 kV and 14 mA with a 0.4 μm step size. Furthermore, the AA- and NA-treated alloy precipitates were observed using transmission electron microscopy (TEM, JEM-ARM200F(NEOARM), JEOL, Tokyo, Japan). The specimens were prepared using a focused ion beam (FIB, CrossBeam 350, Zeiss, Oberkochen, Germany).

Thermal analysis was performed using differential scanning calorimetry (DSC; Q100, TA, DE, USA). The heating rate was varied as 5, 10, 15, and 20 °C/min in an Ar gas atmosphere.

3. Results

3.1. Mechanical Properties after AA and NA

The influence of AA and NA treatments on the mechanical properties of Al–Mg–Zn alloy sheets was investigated. Figure 1 presents the evolution of Vickers hardness as a function of aging time. AA (x) and NA (x) indicate the Al–Mg–Zn alloy sheets after AA and NA treatments, respectively, where x is the aging time. As time progressed, the hardness of AA samples generally increased, reaching a maximum at 24 h, as shown in Figure 1a. The increase in hardness was fast at the initial stage of AA and saturated after 12 h. In contrast, NA required a significantly longer time to reach the maximum value than AA, as shown by the dashed line in Figure 1a,b. The hardness of NA (570 d) was still lower than the maximum value of AA. Although the hardening rate at the initial stage was high for NA samples, it remained constantly lower than the AA samples. As indicated by the dashed lines and circles in Figure 1a,b, the 2, 6, and 10 h AA samples had similar hardness values to the 2-, 86-, and 570-day NA samples.

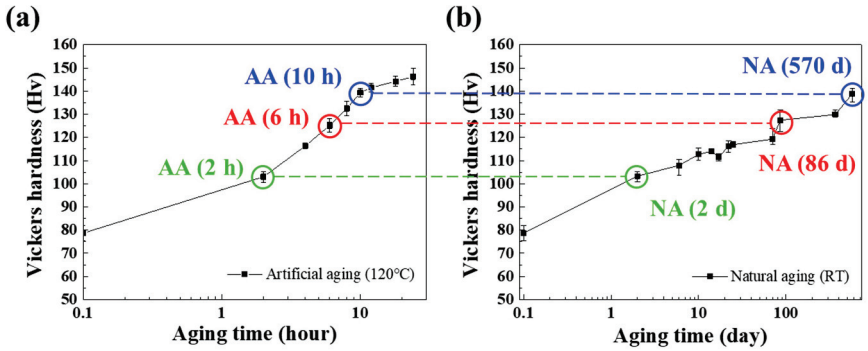


Figure 1. Vickers hardness as a function of aging time in (**a**) AA-treated and (**b**) NA-treated Al alloys.

To investigate the difference in the mechanical properties between AA and NA samples, uniaxial tensile tests were performed on the AA (2 h) and NA (2 d), AA (6 h) and NA (86 d), and AA (10 h) and NA (570 d) parallel to the rolling direction, which showed comparable hardness levels, as marked in Figure 1a,b. As shown in Figure 2a,b with the blue, red, and green dashed lines, the UTSs of AA (2 h), AA (6 h), and AA (10 h) were similar to those of NA (2 d), NA (86 d), and NA (570 d), respectively. The hardness value is calculated by the size of the indenter after the plastic deformation; hence, the Vickers hardness value should be compared with the UTS, which represents the ability to resist deformation. This is a common relationship between Vickers hardness, yield strength, and tensile strength for aluminum alloy [18]. Though the increment trends of YS following the aging time are the same in both AA and NA samples, the value of yield strength is not similar between AA and NA. However, the AA samples showed a higher YS than the NA samples, indicating that the precipitates in the AA and NA samples contributed differently to the YS enhancement. That might have resulted from the dislocation movement during deformation; hence, the relationship between the precipitates and the strengthening behavior will be discussed later in this paper.

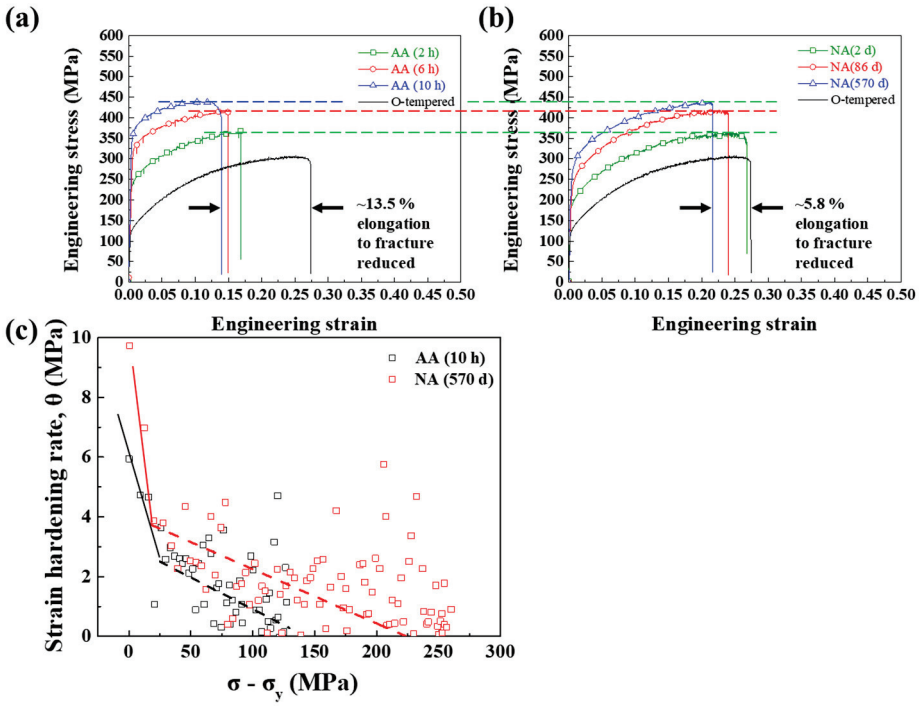


Figure 2. Stress–strain curves of (**a**) AA and (**b**) NA. (**c**) Graphs of instantaneous strain-hardening rate against stress increment for AA (10 h) and NA (570 d).

In contrast to the YS and UTS, the average elongation at the break of AA (~15%) was much lower than that of NA (~25%). Compared with the elongation of the solution-treated (O-tempered) alloy, the strain values decreased by approximately 5.9% and 13.6% for NA and AA, respectively. Typical aging-hardenable alloys showed a decreased ductility when the alloy's strength increased, commonly referred to as the "strength-ductility trade-off phenomenon" [19]. Although the uniaxial tensile tests were performed on AA and NA samples with comparable hardness levels, the ductility decrement ratios of AA and NA were significantly different. The elongation difference between AA and NA was verified by the strain hardening rate as a function of $\sigma - \sigma_y$, which was adopted to confirm the work hardening ability in AA (10 h) and NA (570 d), as shown in Figure 2c. The strain hardening rate (θ) was calculated based on the Kocks–Mecking (KM) plots ($\theta = d\sigma / d\varepsilon$) [20]. The θ value dramatically decreased in the initial stage due to the elastic-to-plastic deformation transition. Then, the θ value decreased continuously until failure. A larger θ value corresponded to uniform elongation and a delay of necking, indicating better ductility [21,22]. As shown in Figure 2c, the strain-hardening rate of NA (570 d) was higher than that of AA (10 h) during the entire plastic deformation process, which was responsible for its greater elongation at break.

3.2. Precipitate Analysis and Microstructure of Al–Mg–Zn Alloy Sheet after AA and NA

Figure 3 shows the DSC curves of Al–Mg–Zn alloy sheets after aging treatment at a heating rate of 10 °C/min. The peaks in the curves indicate an exothermic reaction for the upward peak and an endothermic reaction for the downward peak; hence, the peak temperatures reflect the formation and dissolution of precipitates. Previously, the formation of precipitates in Al–Mg–Zn alloy after artificial aging was sufficiently examined [5–9]. The strengthening precipitates, η′ and η-phases, in peak artificially aged Al–Mg–Zn alloy were formed and distributed. Meanwhile, the main strengthening phases of the naturally aged alloy were not sufficiently discussed because it is hard to discover the clusters and precipitates of naturally aged alloy with microstructure analysis in the initial stage and specific time. Hence, it is necessary to define the dominant precipitates in NA-treated alloy samples using thermal analysis. Some researchers have revealed that the cluster and the GP zone were formed in the temperature range from 50 to 150 °C, and the GP zone was dissolved around 200–250 °C. Furthermore, η′, η, and T-phases could be developed gradually around 250–400 °C [23]. Above 200 °C, the dissolution of GP and clusters occurred with an endothermic peak, and then, η′ and η-phases were formed at the range of 250–300 °C. T-phases, which are stable phases, were formed after over-aging, at over 400 °C. These precipitation processes occurred at similar temperature ranges for naturally aged (NA) samples. At the initial stage, the peaks related to the formation of GP and clusters were observed in the temperature range of 50–150 °C, marked as GP I and GP II in NA (570 d). These thermal analyses indicate that solute clusters and the GP zone can still be formed in NA (570 d) through aging treatment, and the growth of solute clusters and the GP zone also occurred. Then, the GP zone decomposed at 200–230 °C. As seen in the DSC curves in Figure 3, the area, which is related to the formation of the GP zone, decreased according to the natural aging time increasing. The microstructure and compositional condition of NA (2 d) samples were close to the as-quenched (AQ) state; therefore, a large amount of solute clusters and GP zones can be formed. After that, η′-phases developed around 250 °C. From the DSC data, the dominant precipitates in naturally aged samples were composed of solute clusters, GP zones, and η′-phases. Especially, η′-phases might exist in the long-term aged samples, such as NA (86 d) and NA (570 d). The strengthening effect of those precipitates will be discussed.

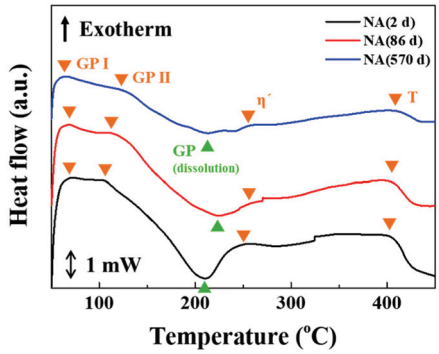


Figure 3. Thermal analysis of NA-treated Al–Mg–Zn alloy sheets using DSC with 10 °C/min heating rate.

The composition of the supersaturated solid solution in the matrix influences the potency of the precipitates in the alloy. From the peak temperature data of DSC analysis, the activation energy of each precipitate can be calculated using the Kissinger method in order to provide a thorough examination of precipitation in the AA- and NA-treated alloy sheets.

Figure 4 shows the raw data of DSC analysis at different heating rates (5, 10, 15, and 20 °C/min), and their scattered points of the peak temperature were plotted. The activation energies of forming (e) GP zones, solute clusters, (f) η′-phases, and (g) η and T-phases in AA (10 h), NA (570 d), and the O-temper sample were calculated using Kissinger's method, which is expressed as follows [24]:

$$\ln\left(\frac{\alpha}{T_p^2}\right) = \left(\frac{-E_a}{R}\right)\left(\frac{1}{T_p}\right) + C \quad (1)$$

where α, T_p, E_a, R, and C represent the heating rate, peak temperature, activation energy, gas constant, and constant number, respectively. The relationship between $\ln\left(\alpha / T_p^2\right)$ and $1/T_p$ allowed for the evaluation of the activation energy using the slope of the linear plot. As shown in Figure 4e,h, the activation energies of the GP and cluster formation for AA (10 h), NA (570 d), and O-temper were 204.26, 74.15, and 53.27 kJ/mol, respectively. The formation of the GP zone and solute clusters was more favorable in the O-temper state than in aged Al–Mg–Zn alloy sheets. Moreover, naturally aged alloy has slightly higher activation energy than O-temper alloy, so the formation peak of the GP zone appears in the DSC data, as shown in Figure 3. Furthermore, it is difficult for AA (10 h) to form GP zones and clusters because of their high formation energies. That result indicates that artificially aged alloy (AA (10 h)) had formed the precipitates using solute atoms, so these alloys include more developed precipitates than other samples. The activation energy for the formation of the η′-phase is evaluated with the same method. As shown in Figure 4f,h, O-tempered and NA (570 d) samples had a similar value of activation energy for the formation of η′-phases. On the other hand, though the activation energy for forming a precipitate decreased, AA (10 h) still had higher activation energy than other samples. The activation energies for forming T and η-phases have comparable values in the AA (10 h), NA (570 d), and O-tempered samples. Notably, the formation of T and η-phases in Al–Mg–Zn alloy sheets occurred in an over-aged state; hence, the initial aging condition did not influence the final aging process. From the thermal analysis of AA (10 h) and NA (570 d)-treated alloy sheets, we can predict the major strengthening precipitates of each aged Al–Mg–Zn alloy sheet. GP zones and solute clusters are still formable in the naturally aged samples; moreover, η′-phases can be formed in NA (570 d). However, the precipitate of AA (10 h) is already formed as stable phases because the formation energy for precipitates is higher than NA (570 d) and O-tempered alloy samples. As a result, these different precipitates could induce different interactions with dislocations, which are generated after plastic deformation; hence, the observation using TEM was conducted.

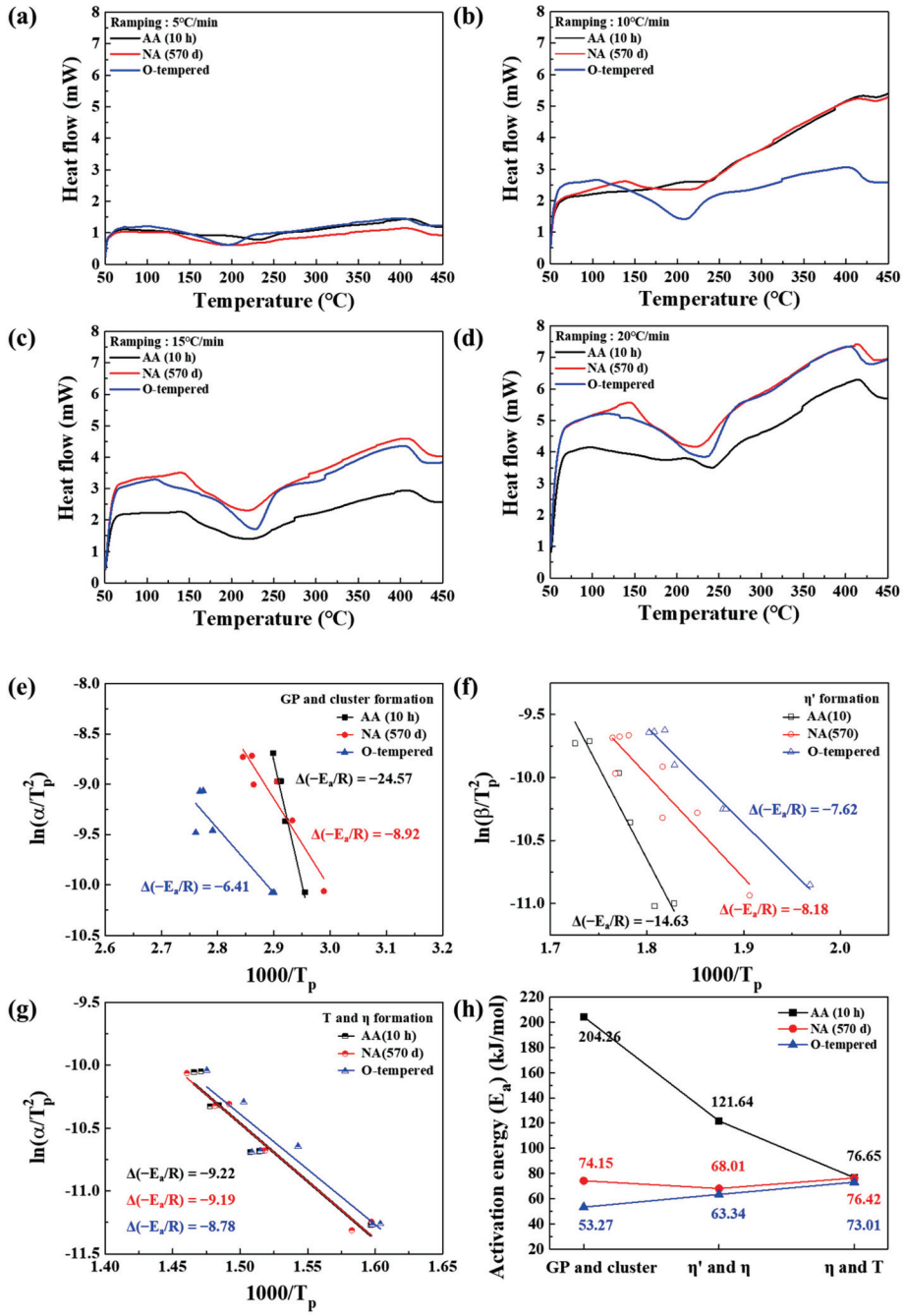


Figure 4. DSC analysis of AA-, NA-treated, and O-tempered Al–Mg–Zn alloy sheets with (**a**) 5, (**b**) 10, (**c**) 15, and (**d**) 20 °C/min heating rate. $\ln(\alpha/(Tp^2))$ is a function of (1000/Tp) of (**e**) GP and solute clusters, (**f**) η′-phases, and (**g**) η and T-phases in AA-, NA-, and O-temper-treated Al–Mg–Zn alloys. (**h**) Activation energy calculated by Kissinger's method.

Figure 5 shows the HRTEM images of 10% deformed AA (10 h) obtained along the (001) zone axis. As mentioned previously, AA (10 h) had a higher dislocation density than NA (570 d). The dislocations generated during deformation tangled, as shown in Figure 5a,c. However, the number of tangled dislocations decreased in the vicinity of grain boundaries, as shown in Figure 5b. The glide of deformation-induced dislocations is hindered by the precipitates in the matrix. As aforementioned in Figures 3 and 4, the major strengthening precipitates of artificially aged Al–Mg–Zn alloy sheets are composed with the η′ and η-phases, and these precipitates are observed with the HRTEM and its corresponding IFFT images, as shown in Figure 5d,e. Moreover, in the FFT pattern, an

extra spot is detected from the selected area C except for the aluminum matrix. Hence, the η′-phase with a semi-coherent interface and the η-phase with an incoherent interface are detected by the IFFT images. Uniformly distributed precipitates with semi-coherent or incoherent interfaces generally prevent the movement of dislocations; hence, dislocations agglomerate with precipitates.

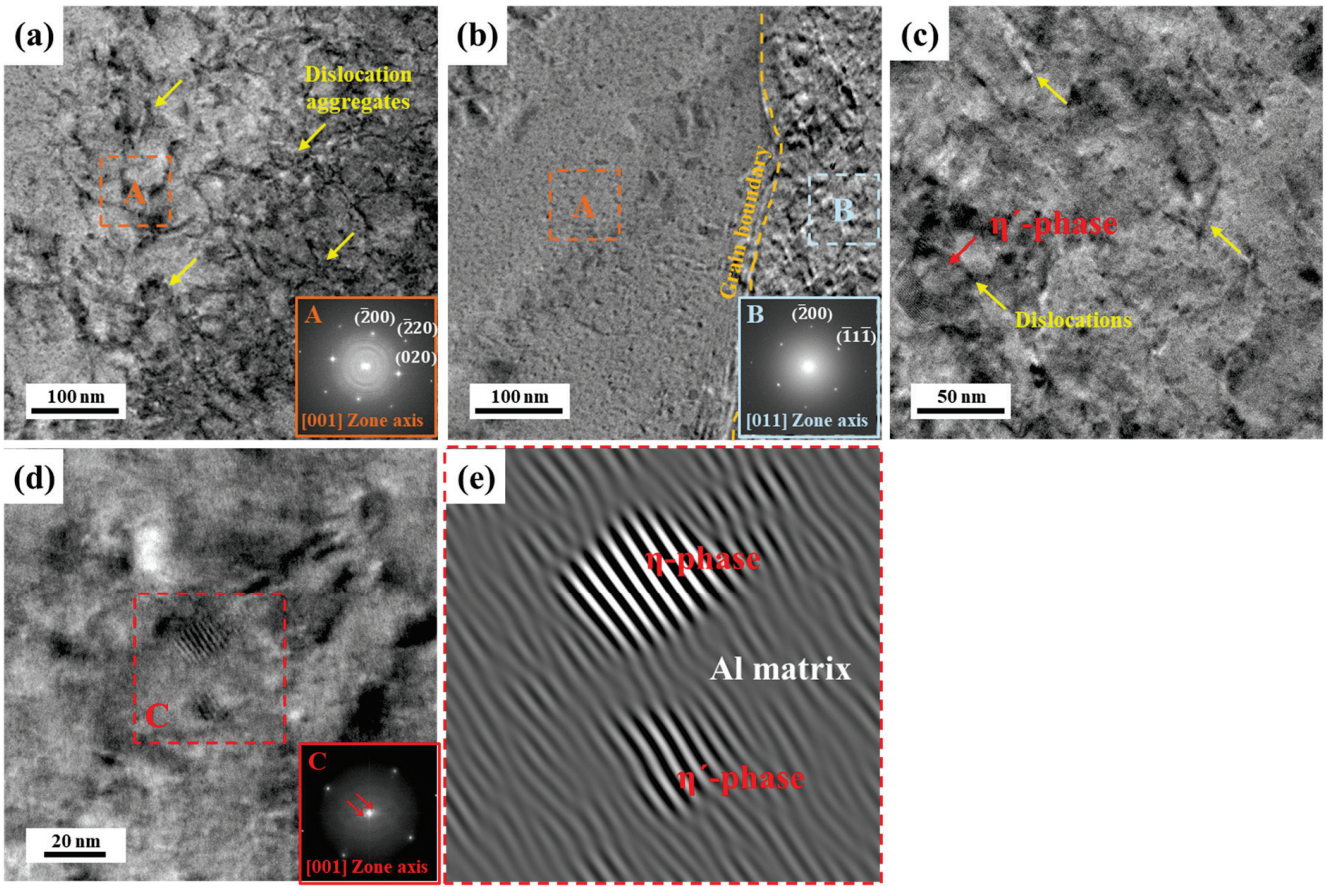


Figure 5. (**a**–**d**) HRTEM images and Fast Fourier Transform (FFT) patterns of AA (10 h) with Al (001) zone axis after 10% tensile deformation. (**e**) The corresponding inverse FFT (IFFT) images of area C with red line in the image (**d**). Yellow arrows indicate the dislocations, and red indicates the precipitates as shown.

In contrast, NA (570 d) has fewer dislocations in the matrix, as shown in Figure 6a–c. Different from AA (10 h), a few dislocations existed near the grain boundaries in NA (570 d), as shown in Figure 6b. Furthermore, the number of tangled or agglomerated dislocations is fewer than the AA (10 h) sample even though those two samples have the same Vickers hardness level; hence, we can estimate that the strengthening precipitates of NA and AA are different. As aforementioned in the thermal analysis, the NA (570 d) sample can have solute clusters, GP zones, and η′-phases. The HRTEM images do not show the distinct precipitate because of its relatively small size and unclear interface with a matrix. Furthermore, the extra spots for precipitates are not defined from the FFT patterns of the selected area, as shown in Figure 6a,c,d at the C area. Solute clusters and GP zones in Al–Mg–Zn alloys have been detected by Zhuang et al. with HRTEM and corresponding IFFT imaging methods [15]. Figure 6d also shows the small clusters in area C, and their corresponding FFT pattern is consistent with the FFT results of the matrix in Figure 6a,c. Furthermore, IFFT images indicate that these small particles have coherent interfaces with the matrix; hence, they could be treated as a GP zone after natural aging. IFFT images in Figure 6e also show the dislocations. The formation of an η′-phase is uncommon in

the early stages of natural aging; however, the NA (570 d) sample experienced a long time to form a η′-phase, and it is defined with the extra spots in the FFT pattern of area D in Figure 6d [25]. The naturally aged NA (570 d) sample has a variety of precipitates to strengthen the alloy; however, the artificially aged AA (10 h) sample is dominantly composed of η′ and η-phases. As a result, the deformation behaviors via the movement of dislocations are varied with the type of aging process because the movement of dislocation during plastic deformation can be affected by precipitates.

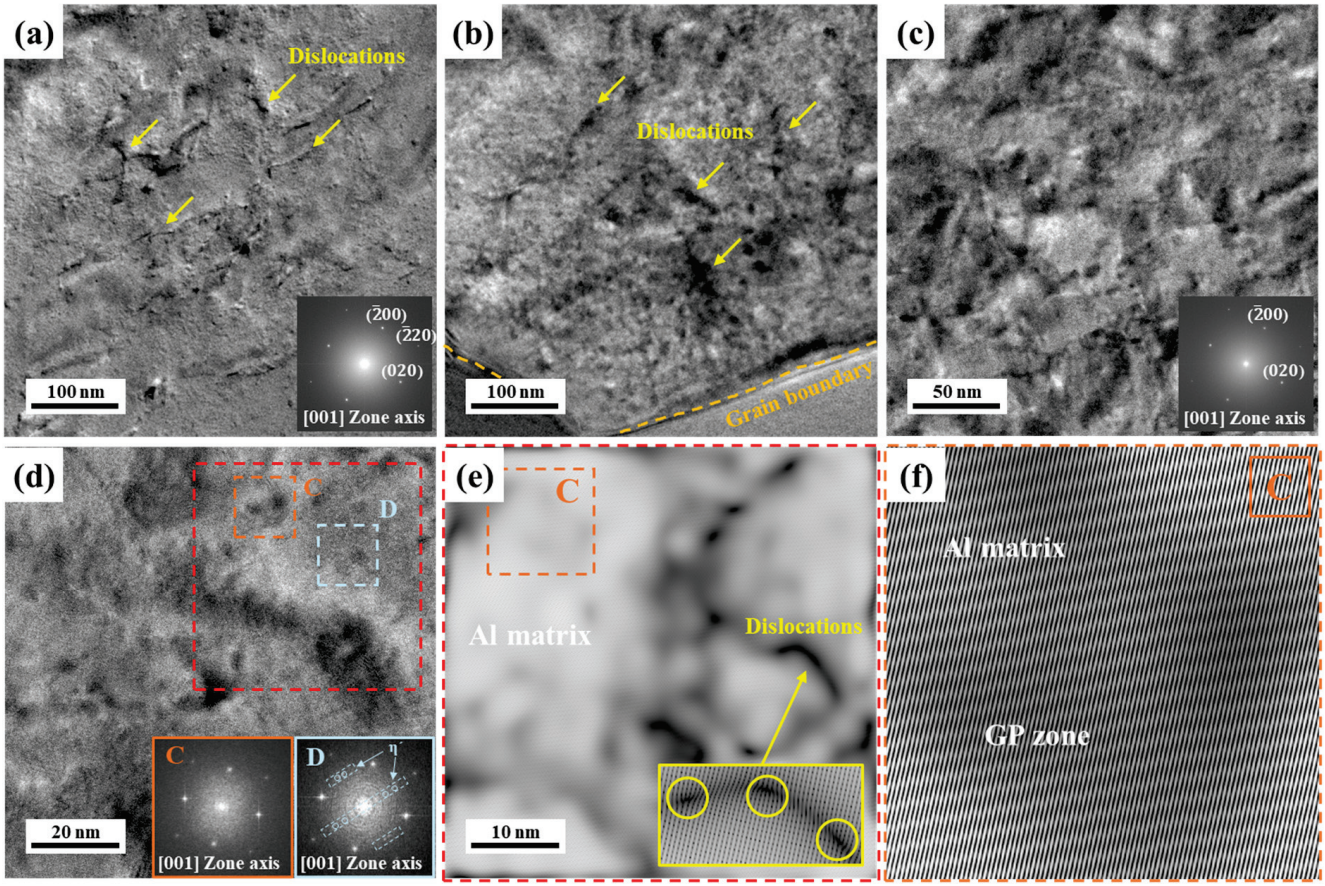


Figure 6. (**a**–**d**) HRTEM images and FFT patterns of NA (570 d) and with Al (001) zone axis after 10% tensile deformation. (**e**,**f**) The corresponding IFFT images of selected area in the image (**d**).

In terms of deformation, the precipitate distributions and dislocation densities were significantly different near the grain boundaries. This is a well-known phenomenon—the precipitate-free zone (PFZ)—developed by the interaction between the diffusion of solute elements and the vacancies at the grain boundaries [26]. Studies on PFZ are beneficial for understanding the effects of aging on the mechanical properties of alloy sheets. A comparison of the microstructures of AA (10 h) and NA (570 d) revealed that the PFZ in AA (10 h) was wider than that in NA (570 d), as shown in Figure 7. The thickness of PFZ is closely related to the mechanical properties of alloys; hence, studies on PFZ are important to understand the effects of precipitation-hardening processes on the mechanical properties of alloy sheets [27–30].

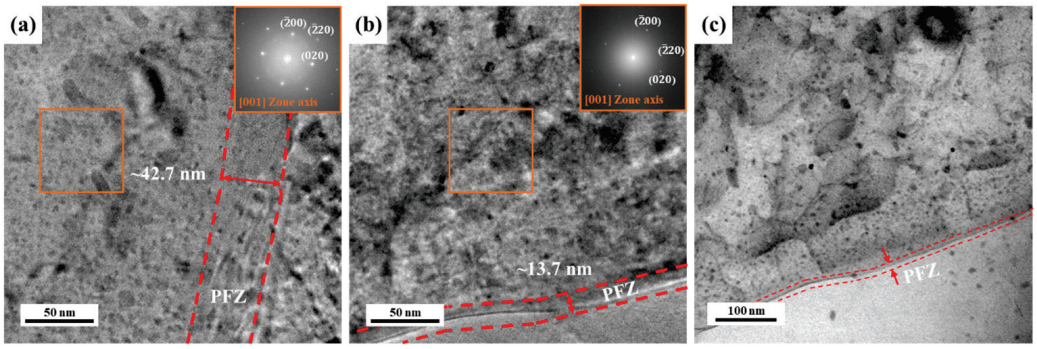


Figure 7. HRTEM images of (**a**) AA (10 h) and (**b**) NA (570 d) at the vicinity of grain boundaries. (**c**) Annular bright field (ABF) images of NA (570 d) with STEM observations.

The PFZ thicknesses in AA (10 h) and NA (570 d) were approximately 42.7 and 13.7 nm, respectively, as shown in Figure 7. AA (10 h) had a wider PFZ area with more distributed precipitates than NA (570 d). Previous studies revealed that the formation of PFZ is affected by the depletion of vacancy and solute atoms in the early and later stages of aging. The width of PFZ is firstly decreased in the early stage of aging and then gradually increased with aging time at 433 K [31]. Hence, the width of PFZ can be changed with the aging condition and diffusion rate. Using plasticity simulations, Kdadyko et al. examined the work hardening scenario in the PFZ area; the local strain was strongly correlated with deformation when perfect PFZ plasticity was assumed [32,33]. Thus, AA (10 h) with a larger PFZ area induced more local strains in the PFZ area owing to the absence of solute elements and precipitation. On the other hand, the work hardening in the PFZ of NA (570 d) showed similar behaviors to those of the bulk alloy samples, which was attributed to its small PFZ area, as shown in Figure 7b,c. NA (570 d) had solute clusters and a GP zone as the strengthening phases, which were difficult to observe in bright-field TEM images. For these reasons, the annular bright field (ABF) STEM image can help define solute clusters using the brightness contrast based on their atomic weight. The atomic weight of Zn is higher than those of Al and Mg, and the uniformly distributed strengthening phases show a darker contrast, as shown in Figure 7c.

Furthermore, the PFZ thickness can affect the localization of the plastic deformation. It is commonly accepted that as the PFZ thickness increases, the restriction from the surrounding grains diminishes, and the localization of plasticity increases. Therefore, the mechanical properties of an aluminum alloy with a PFZ can be expressed by the following equation [34]:

$$\sigma = \sigma_0 + \tau_c \left(\frac{D\varepsilon}{6b}\right)^{\frac{1}{2}} \times \left(1 + \frac{\lambda}{W_0}\right) \quad (2)$$

where σ, σ_0, τ_c, D, ε, b, λ, and W_0 stand for the stress, frictional stress, critical shear stress for cross slip, average grain diameter, strain of sample, Burgers vector, interparticle spacing, and width of PFZ, respectively. The total strain of the specimen is related to the work hardening rate; thus, the hardening rate can be obtained in a differentiated form of Equation (2):

$$\frac{d\sigma}{d\varepsilon} = aW_0^{-1} + b \quad (3)$$

According to this equation, the hardening rate decreases as the thickness of the PFZ increases. The hardening rate of AA (10 h) is lower than that of NA (570 d), as shown in Figure 2c. Furthermore, an increase in PFZ thickness may stimulate the formation of grain boundary precipitates and create voids, which is favorable for fracture propagation along the grain boundaries.

The above observations on Al–Mg–Zn alloy sheets provide insights into designing high-ductility and high-strength alloys with age-condition control. Zhang et al. [20] studied the positive effect of plastic deformation in naturally aged Al–Zn–Mg alloys using

experimental and calculation methods. Solute clusters, formed after long-term NA, can be dissolved at the initial deformation stage because they improve strain hardening ability. Future research should focus on investigating the correlation between precipitation and deformation in these alloy types with the aim of engineering microstructures with enhanced properties.

3.3. Anisotropy Analysis of Al–Mg–Zn Alloy Sheets after AA and NA

Enhanced strain hardening ability and elongation to fracture, associated with delay of necking, could exhibit a reasonable strength and large uniform elongation; hence, NA with a higher strain hardening rate (θ) value could accumulate a larger density of dislocation in the alloy than AA. The characteristics according to the aging condition in mechanical properties are investigated via EBSD methods after 10% tensile deformation. Plastically deformed polycrystalline materials contain dislocations in their matrices, as shown in the TEM images in Figures 5–7. Deformation-induced dislocations can be classified into geometrically necessary dislocations (GNDs) and statistically stored dislocations (SSDs) [35–37]. Generally, GNDs' density is related to microstructure characteristics, such as grain size and texture. The density of the GNDs can be evaluated through EBSD misorientation, which is expressed as follows [38]:

$$\rho_{GNDs} = \frac{\beta \times \varphi}{b \times \Delta x} \tag{4}$$

where β is a constant determined by the type of dislocation boundaries, φ is the average misorientation within a certain distance Δx, and b is the Burgers vector. With the increase in GND density upon deformation, the kernel average misorientation (KAM) value, i.e., θ, also increases, as calculated using Equation (4) [39]. As aforementioned above in TEM observations, GNDs are generated in the internal region of grains; however, it is hard to visualize the distribution of GNDs. Consequently, the distribution of dislocation after plastic deformation was evaluated using a KAM map. Figure 8a–d shows the inverse pole figure EBSD images and KAM maps of AA (10 h) and NA (570 d) after 10% deformation. The dislocation density can be evaluated from the intensity of KAM. The average KAM values of AA (10 h) and NA (570 d) were calculated as approximately 1.78 and 1.25, respectively, using the implemented source of the EBSD analysis program, as shown in Figure 8g. Although the same amount of plastic deformation was applied to the samples, AA (10 h) exhibited a higher dislocation density than NA (570 d). Red and blue arrows indicate the internal and boundary of grains, respectively. In the white circle in the KAM map of AA (10 h), a high density of dislocations is accumulated, as shown in Figure 8a,b. Furthermore, dislocations are accumulated in the internal area of grains, marked as red and blue arrows; hence, the grain boundaries were not revealed clearly. However, the density of GNDs is lower in the NA (570 d) grains than in the AA (10 h) grains, as marked by the white circle in Figure 8c,d. The average density of GND in NA (570 d) is lower than AA; moreover, the partial region has a lower KAM value in the internal grain than the average value, as shown with red and blue arrows in Figure 8c,d. The evaluation of EBSD results shows the same dislocation evaluations as the TEM observations. Notably, the density of GNDs in NA (570 d) was only slightly lower and can be more uniformly distributed in grains than in AA (10 h) at the same strain level; hence, the NA could accumulate more GNDs, contributing to higher elongation. Furthermore, the crystalline order of the plastically deformed Al alloy developed in a favorable texture along the deformation direction. In the rolled Al alloy sheets, Cube, Goss, and P textures developed initially after O-temper treatment [40]. Furthermore, Cube, Goss, and P textures were formed as fibers when the Al alloy was anisotropically deformed. As shown in Figure 8e,f, Cube, P, and rotated-copper textures were mainly developed in the 10%-deformed AA (10 h) sample, whereas only Cube textures were developed in the NA (570 d) sample.

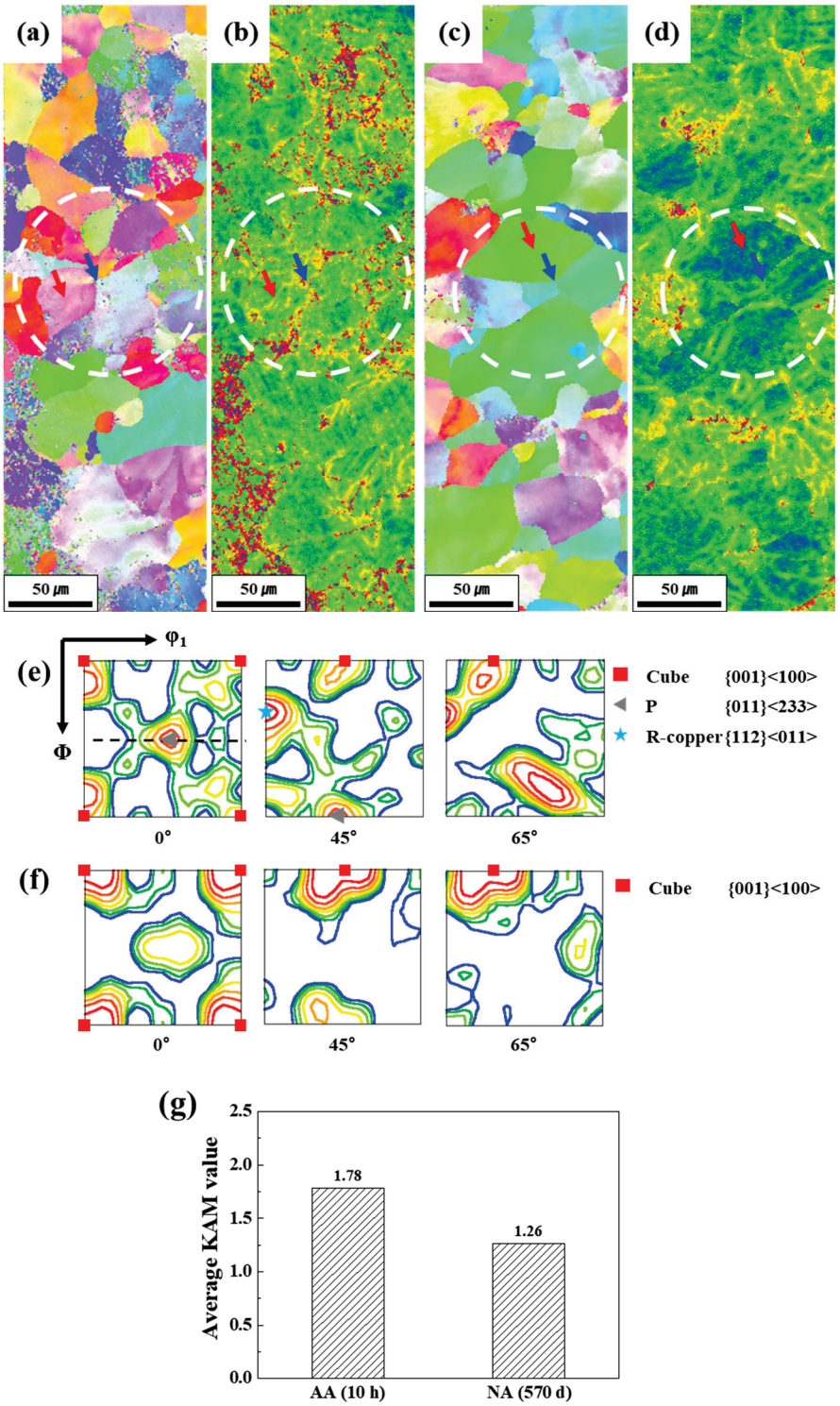


Figure 8. EBSD images and kernel average misorientation (KAM) map of (**a**,**b**) AA (10 h) and (**c**,**d**) NA (570 d) after 10% deformation. The white circle indicates the difference in stress concentration. Texture evaluation with (orientation distribution function) ODF for (**e**) AA (10 h) and (**f**) NA (570 d). (**g**) Graph of the average KAM value of AA (10 h) and NA (570 d). And the red and blue arrows indicate the internal and boundaries of grain.

Based on the above mechanical properties and precipitation analysis, aluminum alloy can exhibit different deformation behaviors depending on the aging temperature. In particular, the generation and accumulation of dislocations in plastic deformation appear nonuniform; hence, the anisotropy in plastic deformation was measured by tensile tests

along the three directions. Figure 9 shows the stress–strain curves obtained for AA (10 h) and NA (570 d) at different angles to the rolling direction: 0° (RD), 45° (ID), and 90° (TD). The results for each sample showed that the YS and UTS of the NA samples were comparable. However, the AA sample tested in the ID direction possessed higher strengths than those tested in the RD and TD directions. The largest difference was observed between the ID and RD. Furthermore, the elongation at break tended to increase in ID and TD compared to RD. The R-value is defined as the ratio between the strain along the thickness and width, suggesting that a lower R-value implies excessive deformation along the thickness direction. As shown in Table 2, the R-value of the ID direction is always higher than other directions; hence, the ID direction can exhibit the highest elongation value. From the results above, though the yield strength of AA has a higher value than those of the NA sample, NA shows better ductility and comparable strength than AA because of the different strengths and elongations required for fracture along the directions [41]. To estimate the anisotropic deformation, the anisotropic coefficient (R) for the AA (10 h) and NA (570 d) samples are listed in Table 2 according to the tensile test direction and following this equation [42]:

$$\mathrm{R} - value = \frac{\frac{\Delta w}{w_i}}{\frac{\Delta \mathrm{t}}{t_i}} \quad (5)$$

where Δw and Δt stand for the change of width and thickness after tensile test. w_i and t_i stand for the initial width and thickness of tensile specimen (ASTM E8). It should be stressed that the anisotropic coefficient, R-value, for an isotropic material is 1; R > 1, which means that the material is resistant to thinning, while R < 1 implies that the material will be reduced more in thickness than in width [42]. The R-value of NA (570 d) has a higher value than the AA (10 h) sample. Notably, AA sheets exhibit significant anisotropy in strength and plasticity compared to NA sheets. These results indicate that the precipitates in Al–Mg–Zn alloy sheets exhibit anisotropy during deformation, depending on the type of precipitates.

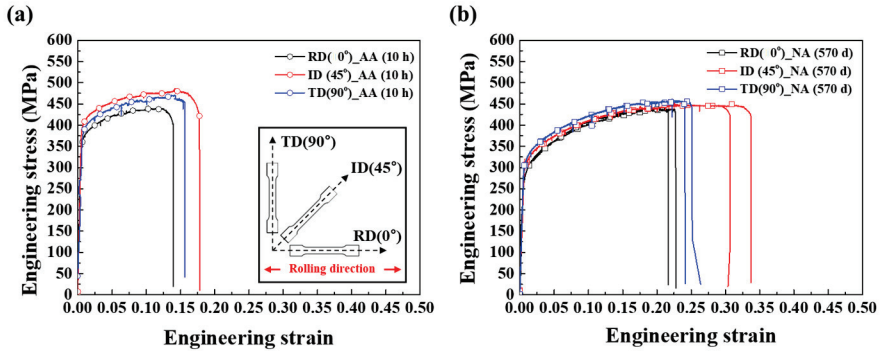


Figure 9. Stress–strain curves of (**a**) AA (10 h) and (**b**) NA (570 d) measured at different angles to the rolling direction (0°, 45°, and 90°).

Table 2. Anisotropic coefficient (R) for AA (10 h) and NA (570 d) according to the tensile test direction.

Aging Condition	Direction	Anisotropic Coefficient (R)
AA (10 h)	0°	0.602
	45°	0.672
	90°	0.619
NA (570 d)	0°	0.778
	45°	0.828
	90°	0.698

4. Conclusions

This study discovered that NA-treated Al–Zn–Mg alloys exhibited better ductility than AA-treated alloys; despite the same strength level, NA-treated samples exhibited about 10% longer elongation at break than their AA-treated counterparts. The capability of dislocation accumulation in the grain interior of the NA samples resulted in a higher strain-hardening rate and, consequently, higher ductility. After deformation at the same stress level, the densities of the GNDs in AA (10 h) and NA (570 d) were only marginally different. Furthermore, NA (570 d) is more favorable to deformation because of a higher anisotropic coefficient than AA (10 h), which contributed to the uniform elongation.

(1) During the aging process, the Vickers hardness of Al–Mg–Zn alloy sheets was increased regardless of aging conditions. In the uniaxial tensile test, however, artificially aged sheets exhibited about 15% elongation to fracture, whereas naturally aged sheets showed about 25% elongation to fracture property.
(2) The analysis of precipitates in AA (10 h) and NA (570 d) samples was performed using the DSC, and their activation energy to form the precipitates were calculated with the Kissinger method. The AA (10 h) sample dominantly had η′ and η-phases as strengthening precipitates; however, NA (570 d) samples had solute cluster, GP, and η′-phases.
(3) TEM observation indicated that the densities of the GNDs in NA (570 d) were lower than AA (10 h); however, they were distributed more uniformly both internal and boundaries of grains. Furthermore, PFZ width varied depending on the aging conditions; hence, NA-treated alloy had a narrower PFZ width than AA-treated alloy.
(4) The NA-treated sheets exhibited notable anisotropy in strength and plasticity with a higher average R-value than their AA-treated counterparts.

Author Contributions: Conceptualization; K.C. and S.L.; Data Curation; K.C., S.L. and D.B.; Investigation; K.C.; Formal analysis; K.C.; writing—original draft preparation; K.C.; writing—review and editing; K.C. and S.L.; supervision; D.B. All authors have read and agreed to the published version of the manuscript.

Funding: This work was supported by the National Research Foundation of Korea (NRF) grant funded by the Ministry of Science and ICT (2021M3H4A1A04092001).

Institutional Review Board Statement: Not applicable.

Informed Consent Statement: Not applicable.

Data Availability Statement: Data are available in a publicly accessible repository.

Conflicts of Interest: The authors declare no conflicts of interest.

References

1. Shin, J.; Kim, T.; Kim, D.; Kim, D.; Kim, K. Castability and mechanical properties of new 7xxx aluminum alloys for automotive chassis/body applications. *J. Alloys Compd.* **2017**, *698*, 577–590. [CrossRef]
2. Kim, H.J.; McMillan, C.; Keoleian, G.A.; Skerlos, S.J. Greenhouse Gas emissions payback for lightweighted vehicles using aluminum and high-strength steel. *J. Ind. Ecol.* **2010**, *14*, 929–946. [CrossRef]
3. Sharma, A.K.; Bhandari, R.; Aherwar, A.; Rimašauskienė, R.; Pinca-Bretotean, C. A study of advancement in application opportunities of aluminum metal matrix composites. *Mater. Today* **2020**, *26*, 2419–2424. [CrossRef]
4. Azarniya, A.; Taheri, A.K.; Taheri, K.K. Recent advances in ageing of 7xxx series aluminum alloys: A physical metallurgy perspective. *J. Alloys Compd.* **2019**, *781*, 945–983. [CrossRef]
5. Embury, J.; Nicholson, R. The nucleation of precipitates: The system Al-Zn-Mg. *Acta Metall.* **1965**, *13*, 403–417. [CrossRef]
6. Sha, G.; Cerezo, A. Early-stage precipitation in Al–Zn–Mg–Cu alloy (7050). *Acta Mater.* **2004**, *52*, 4503–4516. [CrossRef]
7. Zou, Y.; Wu, X.; Tang, S.; Zhu, Q.; Song, H.; Cao, L. Co-precipitation of T′ and η′ phase in Al-Zn-Mg-Cu alloys. *Mater. Charact.* **2020**, *169*, 110610. [CrossRef]
8. Yang, Z.; Banhart, J. Natural and artificial ageing in aluminium alloys–the role of excess vacancies. *Acta Mater.* **2021**, *215*, 117014. [CrossRef]
9. Yang, X.; Chen, J.; Liu, J.; Qin, F.; Xie, J.; Wu, C. A high-strength AlZnMg alloy hardened by the T-phase precipitates. *J. Alloys Compd.* **2014**, *610*, 69–73. [CrossRef]

10. Stemper, L.; Tunes, M.A.; Tosone, R.; Uggowitzer, P.J.; Pogatscher, S. On the potential of aluminum crossover alloys. *Prog. Mater. Sci.* **2022**, *124*, 100873. [CrossRef]
11. Zhao, L.; Yan, H.; Chen, J.; Xia, W.; Su, B.; Song, M.; Li, Z.; Li, X.; Liao, Y. High ductility and strong work-hardening behavior of Zn modified as-hot-rolled Al–Mg sheets. *J. Alloys Compd.* **2021**, *854*, 157079. [CrossRef]
12. Smith, W.; Grant, N. Effects of chromium and copper additions on precipitation in Al− Zn− Mg alloys. *Metall. Trans.* **1971**, *2*, 1333–1340. [CrossRef]
13. Liu, H.; Zhang, Z.; Zhang, D.; Zhang, J. The effect of Ag on the tensile strength and fracture toughness of novel Al-Mg-Zn alloys. *J. Alloys Compd.* **2022**, *908*, 164640. [CrossRef]
14. Liu, J.; Hu, R.; Zheng, J.; Zhang, Y.; Ding, Z.; Liu, W.; Zhu, Y.; Sha, G. Formation of solute nanostructures in an Al–Zn–Mg alloy during long-term natural aging. *J. Alloys Compd.* **2020**, *821*, 153572. [CrossRef]
15. Geng, Y.; Zhang, D.; Zhang, J.; Zhuang, L. Early-stage clustering and precipitation behavior in the age-hardened Al–Mg–Zn (-Cu) alloys. *Mater. Sci. Eng. A* **2022**, *856*, 144015. [CrossRef]
16. Zhao, J.; Liu, Z.; Bai, S.; Zeng, D.; Luo, L.; Wang, J. Effects of natural aging on the formation and strengthening effect of GP zones in a retrogression and re-aged Al–Zn–Mg–Cu alloy. *J. Alloys Compd.* **2020**, *829*, 154469. [CrossRef]
17. Ogura, T.; Otani, T.; Hirose, A.; Sato, T. Improvement of strength and ductility of an Al–Zn–Mg alloy by controlling grain size and precipitate microstructure with Mn and Ag addition. *Mater. Sci. Eng. A* **2013**, *580*, 288–293. [CrossRef]
18. Tiryakioğlu, M.; Robinson, J.; Salazar-Guapuriche, M.; Zhao, Y.; Eason, P. Hardness–strength relationships in the aluminum alloy 7010. *Mater. Sci. Eng. A* **2015**, *631*, 196–200. [CrossRef]
19. Du, J.; Zhang, Z.; Liu, Y.; Shao, Q.; Zhang, A.; Xiong, S.; Liu, F. Strength-ductility trade-off modulated by thermo-kinetic synergy of heat-treatable aluminum alloys. *J. Mater. Sci. Technol.* **2023**, *24*, 7876–7895. [CrossRef]
20. Zhang, P.; Shi, K.; Bian, J.; Zhang, J.; Peng, Y.; Liu, G.; Deschamps, A.; Sun, J. Solute cluster evolution during deformation and high strain hardening capability in naturally aged Al–Zn–Mg alloy. *Acta Mater.* **2021**, *207*, 116682. [CrossRef]
21. Wu, S.; Wang, G.; Wang, Q.; Jia, Y.; Yi, J.; Zhai, Q.; Liu, J.; Sun, B.; Chu, H.; Shen, J. Enhancement of strength-ductility trade-off in a high-entropy alloy through a heterogeneous structure. *Acta Mater.* **2019**, *165*, 444–458. [CrossRef]
22. Kim, S.-H.; Kim, H.; Kim, N.J. Brittle intermetallic compound makes ultrastrong low-density steel with large ductility. *Nature* **2015**, *518*, 77–79. [CrossRef] [PubMed]
23. Jiang, X.; Noble, B.; Hansen, V.; Tafto, J. Influence of zirconium and copper on the early stages of aging in Al-Zn-Mg alloys. *Metall. Mater. Trans. A* **2001**, *32*, 1063–1073. [CrossRef]
24. Kim, I.; Song, M.; Kim, J. Nanocluster formation and two-step aging behavior in Al–Mg–Si (-xCu: X= 0–4 mass%) alloys. *J. Alloys Compd.* **2021**, *857*, 157596. [CrossRef]
25. Deng, Z.; He, H.; Liu, K.; Tao, X.; Shang, Z.; Gong, Z.; Wang, X. The influence of natural aging on the precipitation behavior of the low-alloy content Al-Zn-Mg aluminum alloys during subsequent artificial aging and related mechanisms. *Mater. Sci. Eng. A* **2024**, *891*, 145954. [CrossRef]
26. Chen, M.; Liu, S.; He, K.; Zheng, X.; Jia, G. The effect of precipitate-free zone on mechanical properties in Al-Zn-Mg-Cu aluminum alloy: Strain-induced back stress strengthening. *J. Alloys Compd.* **2023**, *969*, 172426. [CrossRef]
27. Kawabata, T.; Izumi, O. Ductile fracture in the interior of precipitate free zone in an Al-6.0% Zn-2.6% Mg alloy. *Acta Metall.* **1976**, *24*, 817–825. [CrossRef]
28. Dowling, J.M.; Martin, J. The influence of MN additions on the deformation behaviour of an Al Mg Si alloy. *Acta Metall.* **1976**, *24*, 1147–1153. [CrossRef]
29. Vasudevan, A.; Doherty, R. Grain boundary ductile fracture in precipitation hardened aluminum alloys. *Acta Metall.* **1987**, *35*, 1193–1219. [CrossRef]
30. Itoh, G.; Kanno, M.; Hagiwara, T.; Sakamoto, T. Embrittlement in an age-hardened 2091 aluminum alloy by exposure at elevated temperatures below the aging temperature. *Acta Mater.* **1999**, *47*, 3799–3809. [CrossRef]
31. Hirosawa, S.; Oguri, Y.; Ogura, T.; Sato, T. Formation mechanism of precipitate free zones in age-hardenable Al alloys. In Proceedings of the 9th International Conference on Aluminium Alloys, Brisbane, Australia, 2–5 August 2004; pp. 666–671.
32. Khadyko, M.; Marioara, C.D.; Ringdalen, I.G.; Dumoulin, S.; Hopperstad, O.S. Deformation and strain localization in polycrystals with plastically heterogeneous grains. *Int. J. Plast.* **2016**, *86*, 128–150. [CrossRef]
33. Arani, M.M.; Ramesh, N.S.; Wang, X.; Parson, N.; Li, M.; Poole, W. The localization of plastic deformation in the precipitate free zone of an Al-Mg-Si-Mn alloy. *Acta Mater.* **2022**, *231*, 117872. [CrossRef]
34. Abe, M.; Asano, K.; Fujiwara, A. Influence of the precipitate-free zone width on the tensile properties of an Al-6 Wt pct Zn-1.2 Wt pct Mg alloy. *Metall. Trans.* **1973**, *4*, 1499–1505. [CrossRef]
35. Nye, J.F. Some geometrical relations in dislocated crystals. *Acta Metall.* **1953**, *1*, 153–162. [CrossRef]
36. Ashby, M. The deformation of plastically non-homogeneous materials. *Philos. Mag.* **1970**, *21*, 399–424. [CrossRef]
37. Kuhlmann-Wilsdorf, D.; Hansen, N. Geometrically necessary, incidental and subgrain boundaries. *Scr. Metall. Mater.* **1991**, *25*, 1557–1562. [CrossRef]
38. Konijnenberg, P.J.; Zaefferer, S.; Raabe, D. Assessment of geometrically necessary dislocation levels derived by 3D EBSD. *Acta Mater.* **2015**, *99*, 402–414. [CrossRef]
39. Sun, S.; Tian, Y.; Lin, H.; Wang, Z.; Zhang, Z. Revisiting the role of prestrain history in the mechanical properties of ultrafine-grained CoCrFeMnNi high-entropy alloy. *Mater. Sci. Eng. A* **2021**, *801*, 140398. [CrossRef]

40. Sidor, J.; Petrov, R.H.; Kestens, L.A. Deformation, recrystallization and plastic anisotropy of asymmetrically rolled aluminum sheets. *Mater. Sci. Eng. A* **2010**, *528*, 413–424. [CrossRef]
41. Zhang, Y.; Ma, J.; Wang, Q.; Yang, Y.; Zhu, M.; Jia, P.; Duan, Y.; Zhang, Z. Study on anisotropic behavior of 7075 Al alloy after extrusion. *Mater. Res. Express* **2022**, *9*, 026508. [CrossRef]
42. Hosford, W.F.; Caddell, R.M. *Metal Forming: Mechanics and Metallurgy*; Cambridge University Press: Cambridge, UK, 2011.

Disclaimer/Publisher's Note: The statements, opinions and data contained in all publications are solely those of the individual author(s) and contributor(s) and not of MDPI and/or the editor(s). MDPI and/or the editor(s) disclaim responsibility for any injury to people or property resulting from any ideas, methods, instructions or products referred to in the content.

materials

MDPI

Article

Modification of Ti13Nb13Zr Alloy Surface via Plasma Electrolytic Oxidation and Silver Nanoparticles Decorating

Przemysław Gołasz [1,2], Agnieszka Płoska [1], Viktoriia Korniienko [3,4], Kateryna Diedkova [3,4], Yuliia Varava [4], Rafał Zieliński [5], Maksym Pogorielov [1] and Wojciech Simka [1,*]

[1] Department of Inorganic Chemistry, Analytical Chemistry, and Electrochemistry, Faculty of Chemistry, Silesian University of Technology, 44-100 Gliwice, Poland; pg292060@student.polsl.pl (P.G.); agniplo838@student.polsl.pl (A.P.); m.pogorielov@gmail.com (M.P.)
[2] Chemistry Students Research Society, Faculty of Chemistry, Silesian University of Technology, 44-100 Gliwice, Poland
[3] Institute of Atomic Physics and Spectroscopy, University of Latvia, Jelgavas iela 3, LV-1004 Riga, Latvia; v.kornienko@med.sumdu.edu.ua (V.K.); kateryna.diedkova@lu.lv (K.D.)
[4] Biomedical Research Centre, Sumy State University, R-Korsakova Street, 40007 Sumy, Ukraine; yuliia.varava@gmail.com
[5] Stomatologia na Księżym Młynie, 90-365 Łodz, Poland; bkost@op.pl
* Correspondence: wojciech.simka@polsl.pl

Abstract: The dynamically developing field of implantology requires researchers to search for new materials and solutions. In this study, TiNbZr samples were investigated as an alternative for popular, but potentially hazardous TiAl6V4. Samples were etched, sandblasted, subjected to PEO, and covered in AgNP suspension. Simultaneously, SEM images were taken, and the wettability and roughness of the surface were measured. Samples covered in AgNPs were subjected to biological trials. A six-day measurement of human fibroblast proliferation was conducted to assess biocompatibility, and the population of *E. coli* and *S. aureus* was measured over eight hours. Results showed that the TiNbZr PEO surface is biocompatible with human fibroblast cells and promotes growth. However, deposited AgNPs exhibited only slight effectiveness in decreasing bacterial growth over the first two hours. The results suggest that the method of surface preparation is sufficient and might promote osseointegration. On the other hand, more efficient and reliable methods of application of AgNPs should be researched

Keywords: titanium alloy; silver nanoparticles; implant; surface treatment

1. Introduction

The medical industry values titanium and its alloys for their biocompatibility, strength, corrosion resistance, and ability to form a protective TiO_2 oxide layer on an implant. These qualities make titanium implants suitable for use in almost all fields of surgery, ranging from dentistry and plastics to trauma and cardiothoracic interventions. Titanium alloys' Young modulus resembles that of a bone, which makes it an excellent bone replacement material. Many titanium alloys are known for clinical applications, but one of the most commonly used is Ti6Al4V. It exhibits exceptional mechanical strength and high similarity in compression and tension to bones [1,2]. However, it has been demonstrated that the impact of the components of this alloy is unfavorable to human health. Vanadium ions exhibit cytotoxic effects and possibly cause type IV allergies [3,4], and aluminum ions presence might cause bone mineralization issues and were linked to the development

of Alzheimer's disease [4,5]. To research alternatives, the Ti13Nb13Zr alloy was chosen as the investigated material in this study. Studies show that niobium does not exhibit cytotoxic effects on human cells [6]. Its alloys with titanium increase the proliferation of osteoblast cells and exhibit superior cellular response of preosteoclasts compared to vanadium alloys with titanium [7,8]. Zirconium is a well-researched biocompatible metal often used in dentistry as zirconia (zirconium(IV) oxide ZrO_2 [9–11]). H. Michelle Grandin's study shows that binary titanium–zirconium alloys achieve greater osseointegration and biocompatibility compared to pure titanium [12]. The alloy itself was shown to promote the adhesion of human mesenchymal stem cells (MSCs) to the implant surface rather than Ti6Al4V [13].

One of the challenges in implantology is preventing bacterial infections at the implant site. It has been proven that after the successful implantation, the surface of the implant may be covered in a thin, bacterial film, potentially causing infections or inhibiting osseointegration of the implant [14–17]. Those biofilms are proven to be highly resistant to antibiotics [18] and are responsible for in situ infections and also bloodstream infections [19–22]. The resistance to conventional antibiotics has led to extensive research on new methods of preventing the formation of these biofilms. One promising approach is coating implants with bacteriostatic or bactericidal coatings. Essentially, such coatings can be divided into three types—anti-adhesive, contact-killing, and releasing types [23].

Anti-adhesive coatings prevent bacteria from adhering and covering the surface of medical devices with bacterial biofilm [24]. Attachment of the macromolecules to the surface of the implant allows them to alter their physical properties [25–30], and effectively change conditions of the surface of the implant to be hostile toward the bacteria. In essence, those coatings can be described as hydrophilic and hydrophobic. Hydrophilic anti-adhesive coatings prevent bacterial growth by inhibiting bacterial cell adhesion [31], as bacterial cell walls are lipid-based structures that are hydrophobic. Therefore, they are physically repelled by hydrated surfaces. Some commonly used hydrophilic coatings are hyaluronic acid (HA) [32], sodium alginate [33], PEG and its derivatives [34,35], and polyhydroxypropyl methacrylate (PHPMA) [36] to name just a few. However, their mechanism of action was proven to prevent bone cells from migrating and attaching to implants for exactly those same reasons [37] that repel bacteria. On the other hand, hydrophobic surfaces rely on a self-cleaning mechanism, as body fluids wash their surface thoroughly, rinsing off any bacteria attached. Some of the polymers used as hydrophobic antiadhesive coatings are polydimethylsiloxane [38] and fluorinated polymers [39–41]. Also, diamond functional [42] and super anti-wetting nano coatings [43] were developed.

Releasing-type and contact bactericidal coatings are similar in some sense, and they often require special surface preparation to immobilize active particles on the implant. Contact bactericidal coatings contain natural or synthetic particles that are physically or chemically attracted to the surface of the implant. Those particles directly attack the cell membranes of bacteria, not only preventing their adhesion but also killing them [44–47]. Often used antibacterial particles include chitosan [48,49], antimicrobial peptides (AMPSs) [47,50,51], quaternary ammonium compounds (QACs) [52,53], and inorganic bactericidal nanoparticles [54].

Releasing-type antibacterial coatings essentially work as sponges. Antibiotics, anti-inflammatory or antibacterial drugs, or bactericidal molecules are immobilized in highly developed coatings that release them via diffusion, dissolution, or degradation of certain molecules. The coating itself is a carrier that releases particles on the implantation site, preferably on the first day after surgery, as they are most critical in terms of the formation of bacterial biofilm [55–58]. Widely used coatings consist of polymers [59,60] and inorganic

and organic cements [61]. Also, ceramic layers of oxidized metallic material can introduce desired particles to the surface of the implant. Plasma electrolytic oxidation (PEO) is a promising method of surface development. Not only have PEO coatings been described to increase corrosion resistance and hardness of the implant, but they also increase biocompatibility and promote osseointegration [62–66]. Such coatings are highly porous, allowing drugs to migrate out over a fixed amount of time, which is characteristic of the structure of the surface. Therefore, PEO is a simple, yet effective way of preparing implant surfaces, as only one treatment increases bone-implant integration and stability, and it also forms a releasing-type coating. It is possible to introduce antibiotics into those pores [67]; however, such infusion comes with a risk of antibiotic-resistant bacteria development around the implantation site [68,69]. Among various alternative options, metallic ions are a simple and effective source of active particles in releasing-type coatings. They are thermally physically and chemically resistant, and no known bacterial resistance mechanism has been yet discovered. Various ion sources were extensively researched. However, one of the most prominent ones is silver nanoparticles (AgNP). Their incorporation into the coating may effectively inhibit the growth of both Gram-negative Escherichia coli and Gram-positive Staphylococcus aureus, reducing the risk of implant-associated infections [70,71]. Moreover, the use of silver nanoparticles as a coating material offers a very significant advantage over preventive antibiotic therapy after surgery or using implants with immobilized antibiotics and antibacterial drugs on the surface. Silver nanoparticles have been proven to exhibit strong antimicrobial activity against a broad spectrum of bacteria, fungi, and viruses. Second, they have a low tendency to develop resistance, making them effective in the long term [71]. However, it is worth noting that AgNPs are proven to be cytotoxic and are potentially allergenic [72,73]. For the sake of safety, the amount of AgNPs on the implant surface has to be enough to exhibit the bactericidal effects without showing cytotoxicity. In this study, samples of Ti13Nb13Zr were polished, sandblasted, etched in oxalic acid, oxidized in phosphoric acid via plasma electrolytic oxidation, and then coated with silver nanoparticles using silver nanoparticle suspension. A combination of all these surface treatment techniques is in our opinion novel in the literature. Surface images were taken using SEM imaging, roughness and wettability of samples were measured and biological tests were performed to measure the possible cytotoxic effect of the formed silver nanocoating.

2. Materials and Methods

2.1. Preparation of the Samples

In this study, Ti13Nb13Zr alloy samples in the form of 10 mm diameter and 4 mm height disks were used. The preparation process involved polishing each disc with abrasive SiC paper of 320 and 800 grit size. Subsequently, they were sandblasted using Al_2O_3 with an 80-grit size until a uniform and matte surface finish was achieved. Following this, the samples underwent rinsing in distilled water and degreasing in a mixture of distilled water with detergent and isopropanol for three minutes each using an ultrasonic bath.

2.2. Processing the Samples

The samples were etched using a solution consisting of 10% (*w*/*w*) oxalic acid in distilled water at a temperature of 100 °C in a water bath for 70 min. Following the etching process, the samples were rinsed in distilled water for 3 min. Subsequently, plasma electrolytic oxidation was carried out in a controlled-temperature electrolyzer with a 1 M H_3PO_4 solution at 10 °C. The PEO process was performed in two stages using a DC power supply (Kiksui, Sapporo, Japan). First, the process occurred under galvanostatic conditions of current density (100 mA/cm^2) at a limiting voltage (250, 275, 300, 325 V). After the

limiting potential was reached, the process continued under potentiostatic conditions of the limiting voltage. The voltage of the PEO process for the further investigated samples was determined by analysis of SEM images (Phenom Pro-X, 15 kV) of samples processed at voltages of 250, 275, 300, and 325 V. Based on this analysis, it was determined that further investigations would be carried out under constant voltage of 250 V. The PEO of these samples was performed as mentioned above, with 100 mA/cm^2 current density in the galvanostatic part, and at 250 V at the potentiostatic part. Finally, after completion of the PEO treatment, distilled water was used to rinse the disks, and they were left to dry.

Silver nanoparticles solution (3 g/L suspended in PVP—Polyvinylpyrrolidone) (NanoWave, Warsaw, Poland) was used to prepare the solutions (0.5, 0.25, and 0.125 g/L) by diluting it with distilled water. Prepared, oxidized, and dried samples were divided into three groups. Then, 20 µL of solutions of the silver nanoparticles were applied accordingly on the samples using the automatic pipette and then were left to dry. The samples labels were shown in Table 1.

Table 1. Explanation of labeling of samples and treatments that have been conducted.

Label	Polished	Sandblasted	Acid-Etched	PEO	Silver Suspension [g/L]		
					0.125	0.25	0.5
G	×						
GS	×	×					
GSE	×	×	×				
GSE-A	×	×	×	×			
GSEA Ag 0.125	×	×	×	×	×		
GSEA Ag 0.25	×	×	×	×		×	
GSEA Ag 0.25	×	×	×	×			×

2.3. Surface Characteristics

The samples were investigated using the Phenom Pro-X with an applied voltage of 15 kV. SEM images were taken, and 3D images were generated for the polished, sandblasted, etched, oxidized, and treated with AgNP suspension samples. The sample's average arithmetical roughness of a surface (Sa) was measured using the Phenom Pro-X (λs: 200 nm, λc: 198.61 µm). Also, the EDX analysis of the atomic composition of the investigated samples was conducted. Furthermore, the wettability of the samples was determined using a goniometer (DataPhysics, OCA 15EC, Filderstadt, Germany) by measuring contact angle (CA). Then, 0.5 µL of water was dropped on the samples, and the CA between the disk surface and a water droplet was measured. Each sample's CA was measured five times from the left and right sides of the water droplet, and the mean value of those measurements was calculated. Also, standard deviations of the measured CAs were obtained.

2.4. Biocompatibility and Biological Tests

Biocompatibility test of the samples was performed on human dermal fibroblasts (HDF) (Pharmacy program research group, Medical Faculty of the Latvian University) with the 7th passage (P7). The Institute of Experimental and Clinical Medicine Ethics Committee, University of Latvia, approved the use of primary cells from frozen primary cell stock-No. 71-35/17. The materials were sterilized by autoclaving for 15 min at a pressure of 102.6 kPa and a temperature of 121 °C. Dermal fibroblasts were thawed and cultured according to the Sigma-Aldrich protocol [74]. Cells were seeded onto culture flasks at a density of 5000 cells/cm^2 under standard conditions of 37 °C, 5% CO_2, with medium changes every 2–3 days. The cell culture medium containing Dulbecco's modified Eagle's medium/nutrient mixture F-12 (DMEM/F-12 3:1 v/v), L-glutamine, antibiotics

(penicillin, streptomycin, and amphotericin B), and 10% fetal bovine serum. All cell culture reagents were purchased from Sigma-Aldrich, St. Louis, MO, USA. The sterilized samples were placed in a 24-well plate and cells were seeded on the surface of samples at a density of 10,000 cells/cm^2. As a positive control, we used wells with cells without samples, and as a negative control, we used wells with medium without cells and samples. The Alamar blue assay was utilized to evaluate cell adhesion and growth. After 24 h, this colorimetric test measured cell adhesion. It also assessed cell proliferation on days 4 and 6. An amount, accounting for 10% of the entire volume, of Alamar blue (procured from Sigma-Aldrich, St. Louis, MO, USA) was added to each well, including the negative and positive control wells. The plates were then incubated for 8 h at 37 °C. Absorbance readings were taken at 570 and 600 nm wavelengths using a Tecan Infinite M200 Pro microplate reader (from Tecan Trading AG, Männedorf, Switzerland). Cell quantification occurred at intervals of 1, 4, and 6 days. Triplicate samples were prepared for each condition.

After six days of cultivation, the samples underwent a two-step washing process with PBS, then fixation for 10 min using a 3.5% formaldehyde solution from Sigma-Aldrich. Post-fixation, the cells were permeabilized to enhance staining results via a solution of 1% BSA and 0.1% Triton X-100, diluted in PBS. The cell cytoskeleton was stained with ActinRed 555 from Thermo Scientific, Waltham, MA, USA, while the dermal fibroblasts' nuclei were stained using Hoechst 33342, also from Thermo Scientific, Waltham, MA, USA, diluted 1:1000. Subsequently, all samples underwent analysis utilizing a Nikon Eclipse TI Fluorescence Microscope, Tokyo, Japan, in the DAPI and TRITC channels.

Staphylococcus aureus (*S. aureus*, ATCC 25923) and *Escherichia coli* (*E. coli*, ATCC 25922) underwent 24 h cultivation on nutrient agar. Following this, overnight culture suspensions were blended with nutrient broth medium, adjusting the microorganism in the initial concentration of bacterial cells 1×10^6 CFU/mL (colony-forming units per milliliter).

The Ti13Nb13Zr alloy samples, including those untreated, treated with the PEO process, and coated with AgNPs at concentrations of 0.125, 0.25, and 0.50 g/L, were submerged in a bacterial suspension. They were then horizontally incubated with 2.0 mL of the bacterial suspension in static conditions in a 24-well plate at 37 °C for 2, 4, 6, and 8 h. Subsequently, the disks underwent three washes with sterile sodium chloride solution to eliminate non-adherent cells. An ultrasonic bath (EMAG Ultrasonic cleaner Emmi-20 HC, EMAG AG, Mörfelden-Walldorf, Germany) was then used to sonicate the samples in tubes containing 1.0 mL of sterile saline solution for 1 min to remove bacteria adhered to the specimen surfaces. Following this step, 10 µL aliquots of saline solution were inoculated onto nutrient agar plates using the streak plate technique to quantify the bacterial count after 24 h of incubation at 37 °C.

3. Results

The following samples—G, GS, GSE, and GSE-A (250 V)—were investigated under an SEM microscope, and corresponding images of their surfaces were collected in Figure 1. In the G, GS, and GSE samples, abrasive grains remaining from the grinding and sandblasting processes are visible. GSE exhibits the propagation of the surface profile of the developed GS. The atrophy of grinding marks and the development of the surface in the GS samples are also evident in the GSE. The 250 V PEO-treated sample (GSE-A) surface exhibits a similar height profile and 3D structure to GSE, however, after the oxidation, the surface has been covered in regular, oval-shaped pits (Figure 1).

SEM images of the PEO-treated samples were taken, analyzed, and collected as in Figure 2. From these images, there is a visible trend, whereby with the increase in voltage, the size of obtained pores in the ceramic, oxide layer increases. As the voltage increases,

more uniformly structured surfaces are being formed. The extent of the arrangement of the chaotic pores increases with the increase in voltage—for samples treated with 275 V, it is visible that small pores formed on the uniform surface are arranged in an array following grinding marks from the polishing step. A vague geometric pattern was found for samples oxidized in 300 V. The surface of the sample oxidized with 325 V had no geometric pattern of the pit formation and the size of the pores was the greatest of all investigated samples. The surface topography of samples anodized in 250 V was found to propagate the imperfections and random defects caused by the sandblasting process; therefore, it was concluded that this voltage would be applied to the rest of the samples.

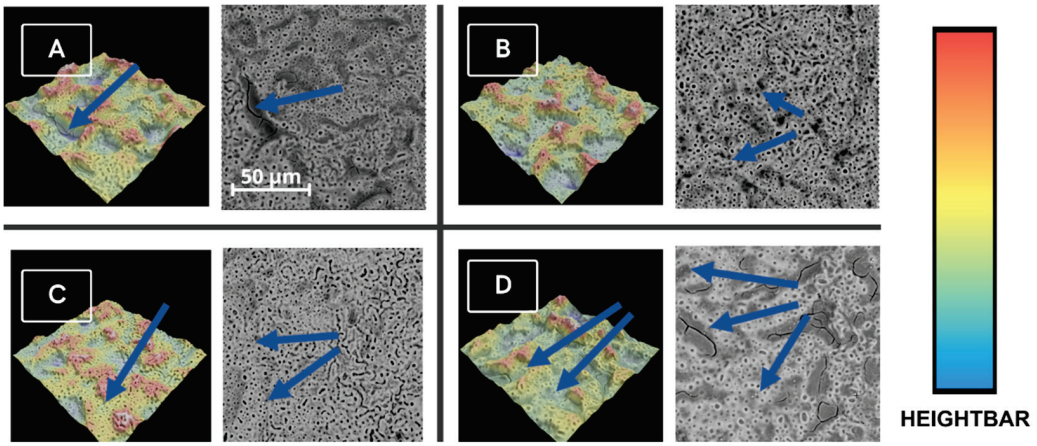


Figure 1. SEM images with corresponding 3D generated images of (**A**)—G sample; (**B**)—GS sample; (**C**)—GSE sample; (**D**)—GSE-A sample. Blue arrows point on the spots with the abrasive SiC material stuck on the surface of samples. The magnification of images is ×2000.

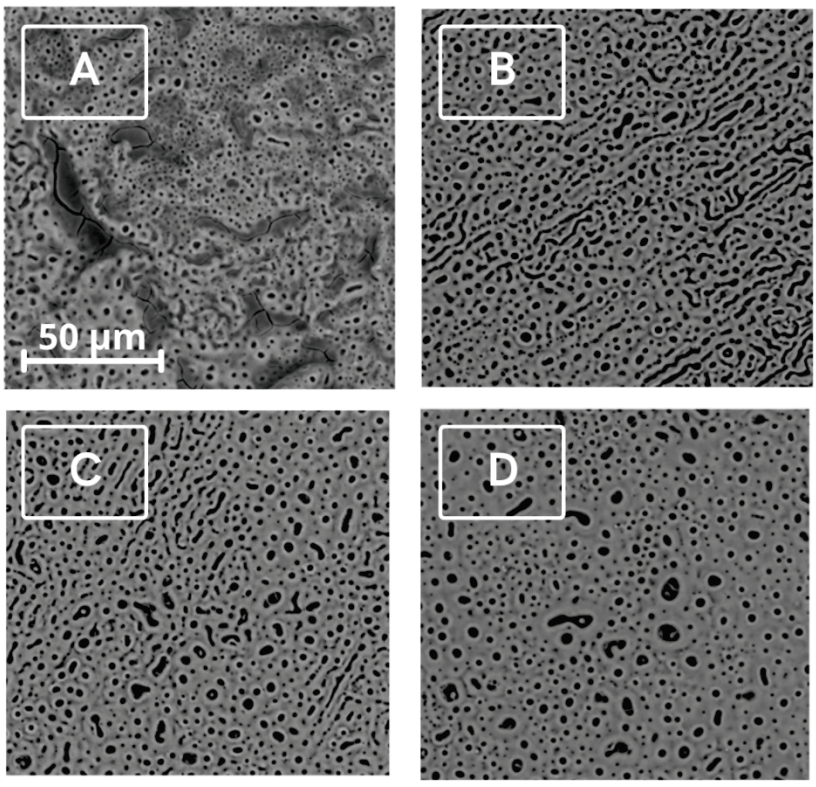


Figure 2. SEM images of the PEO-treated samples in 1M H_3PO_4: (**A**)—250 V; (**B**)—275 V; (**C**)—300 V; and (**D**)—325 V. The magnification of images is ×2000.

Samples treated with a suspension of nanoparticles visually differ from the GSE-A sample (Figure 3). Visible small pores at the lowest points of the PEO sample disappear with the increasing concentration of the silver suspension. The quantity of silver nanoparticles and larger conglomerates visible on the surface of the samples increases with the increase in the concentration of silver nanoparticles. In the sample treated with a 0.5 g/L solution, complete sealing of the lowest localized pores of the coating is observed, which probably cracked during the sample drying process. In all samples, the pores of the structures visibly decrease in depth and size with the increasing concentration of the suspension, suggesting that more silver is deposited on the ceramic coating of the alloy.

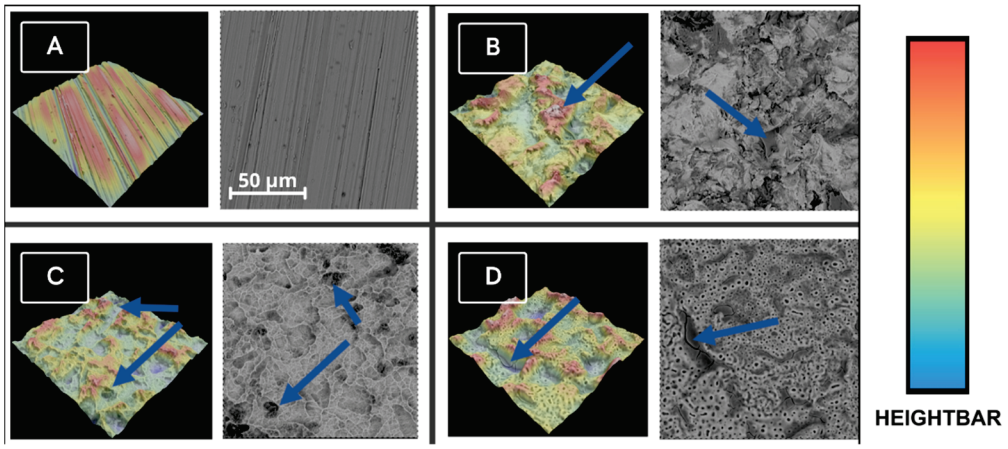


Figure 3. SEM images and according to 3D images of samples, where (**A**)—GSE-A sample with blue arrow showing cracked surface of the sample; (**B**)—TnZ GSEA Ag 0.125 sample; (**C**)—TnZ GSEA Ag 0.25; and (**D**)—TnZ GSEA Ag 0.5 sample. Blue arrows are pointing to the visible AgNP on (**B**–**D**).

Surface roughness measurements show that sandblasting greatly increases surface roughness compared to polished samples. According to data collected in Table 2, etching in oxalic acid did not affect the roughness of the surface significantly. However, PEO treatment in 1 M H_3PO_4 in 250 V increased the arithmetical mean value by 1.30 µm. The deposition of AgNPs on the surface of GSE-A did not affect surface roughness significantly.

Table 2. EDX analysis—average weight percentage composition [*w*/*w*%] of investigated samples and their standard deviations.

	0.5	**0.25**	**0.125**	**PEO**
Element Symbol	**%Weight (Stand. Deviation) [*w*/*w*%]**			
O	46.59 (2.54)	49.48 (4.23)	43.93 (2.24)	51.96 (1.92)
Ti	22.67 (1.26)	21.99 (2.42)	29.02 (5.62)	22.58 (2.53)
Nb	2.54 (0.34)	3.13 (0.54)	2.48 (0.12)	3.82 (0.68)
Zr	10.45 (0.92)	11.29 (1.45)	12.85 (1.12)	14.12 (2.55)
P	6.74 (1.02)	6.26 (0.74)	7.68 (1.23)	7.52 (0.41)
Ag	11.01 (1.67)	7.85 (1.21)	4.04 (0.22)	

The energy-dispersive X-ray spectroscopy (EDX) provided a qualitative analysis of elements present on the surface of the investigated samples. Obtained EDX spectra were gathered in Figure 4 below. Nanocoated samples treated with silver suspension had silver atoms detected, in addition to the elemental components of the alloy and the elements incorporated in the oxide layer. Data presented in Table 2 show that with the increase in AgNP concentration in the suspension, the amount of silver deposited on the surface

increases. All the samples contain incorporated phosphorus and high oxygen content due to the PEO process.

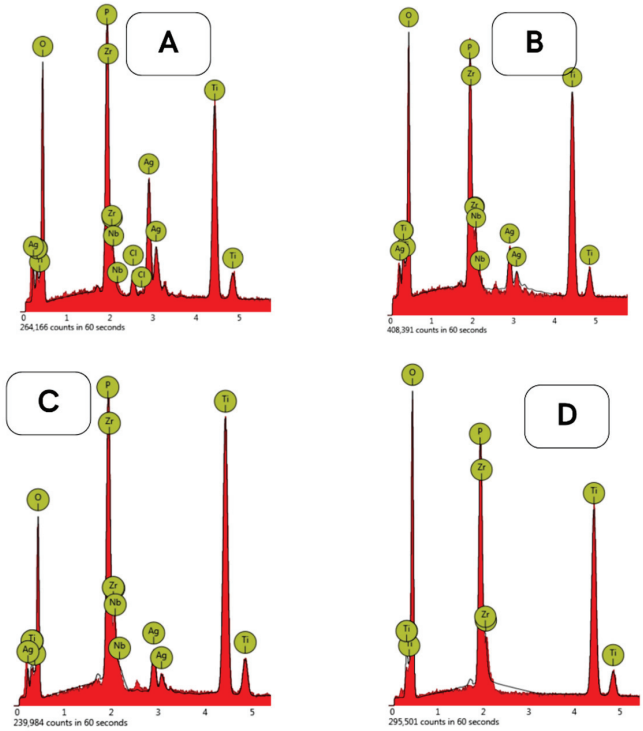


Figure 4. EDX analysis graphs of the samples where (**A**)—GSEA-0.5Ag sample; (**B**)—GSEA-0.25 Ag sample; (**C**)—GSEA-0.125 Ag sample; and (**D**)—GSE-A sample.

Results presented in Table 3 show that the polished surface exhibits the highest hydrophilicity having the smallest contact angle. Water droplets spread on its surface almost instantly. The sandblasted surface exhibits the most hydrophobic properties since the obtained contact angle for it is the highest. Acid etching decreased the value of contact angle, possibly by smoothing the surface and increasing the size of cavities and pores, allowing water to flow into them. The PEO surface shows an increase in the contact angle. There is no clear dependence between the CA value and the concentration of the silver nanoparticle suspension used. The surface with a silver concentration of 0.5 g/L exhibits the highest hydrophobicity among the nanocoated samples, while the surface with a silver content of 0.125 g/L shows the lowest.

Table 3. Average contact angle and roughness of the surface of the samples.

Label of Sample	Average Contact Angle [°]	Sa [µm]
G	26.3 ± 6.9	1.87 ± 0.13
GS	93.4 ± 3.7	3.18 ± 0.21
GSE	41.2 ± 4.1	3.31 ± 0.26
GSE-A	55.2 ± 2.2	4.61 ± 0.19
TnZ GSEA Ag 0.125	34.4 ± 3.0	4.51 ± 0.54
TnZ GSEA Ag 0.25	46.6 ± 4.9	4.51 ± 0.23
TnZ GSEA Ag 0.5	30.9 ± 3.3	4.39 ± 0.18

The data presented in Figure 5 indicate that the application of orthophosphoric acid to plasma-electrolyte-treated Ti13Nb13Zr alloy does not influence implant biocompatibility. At the same time, the novel coating did not influence fibroblast proliferation compared to the untreated surface. However, the addition of AgNPs at varying concentrations slightly

influences biocompatibility, as compared to the untreated control samples. Notably, the lowest observed cytotoxicity correlates with the minimal AgNP concentration of 0.125 g/L. After a four-day incubation period, there was no significant difference in adhesion and proliferation among all sample groups.

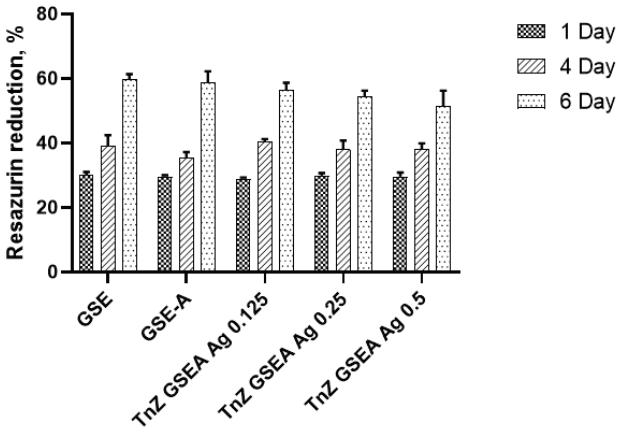


Figure 5. Resazurin reduction assay data on human dermal fibroblast proliferation during the 6-day experiment on different TnZ samples.

Furthermore, upon a six-day incubation of the cells on the Ti13Nb13Zr alloy samples, fluorescence microscopy was employed to examine cell morphology. Here, the filamentous actin was highlighted with Rhodamine Phalloidin, emitting a red fluorescence, while the nuclei were counterstained with Hoechst, emitting a blue fluorescence, as showcased in Figure 6. The resulting images reveal an elongated cytoskeleton structure in the human dermal fibroblasts with oval-shaped nuclei, indicating typical morphology. A uniform distribution of fibroblasts was observed across both the control and nanoparticle-modified samples, suggesting that the surface modifications did not adversely affect the fibroblast distribution.

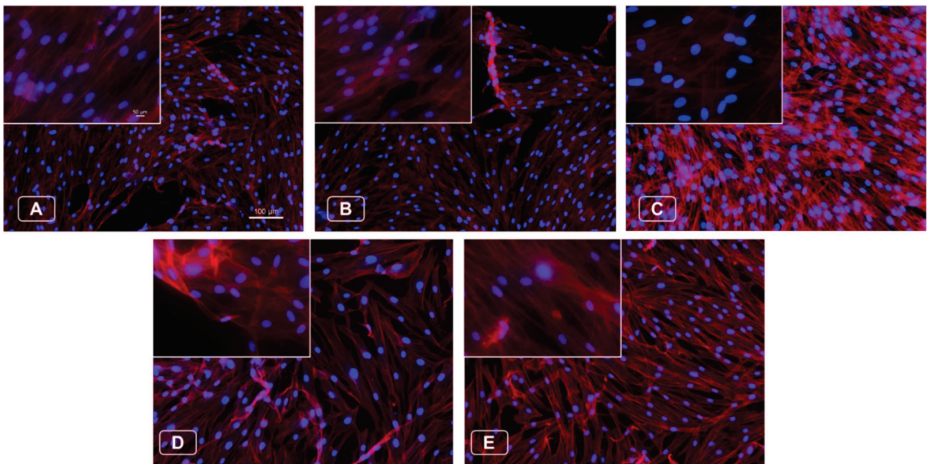


Figure 6. Fluorescent images of nuclei (blue) and cytoskeleton staining (red) on the 6th day of dermal fibroblasts on the samples, where (**A**)—TnZ G-S-E, (**B**)—TnZ G-S-E-A, (**C**)—TnZ G-S-E Ag 0.125 μg/mL, (**D**)—TnZ G-S-E-A Ag 0.25 μg/mL, (**E**)—TnZ G-S-E-A Ag 0.5 μg/mL. The magnification of the main images is ×100 (scale bar = 100 μm), and on the insets ×400 (scale bar = 50 μm).

The initial seeded concentration of 10^6 CFU/mL was used. There was a slight reduction in the *E. coli* population within the first 2–4 h of incubation, with a 2.9–4 Log10 CFU/mL decrease for samples containing 0.25 g/dm^3 and 0.50 g/dm^3. However, after 4–8 h of incubation, there was a concerning increase in the *E. coli* population, reaching up to 8 Log10 CFU/mL. This suggests that the AgNPs might lose effectiveness over time due to detachment from the alloy surface, reducing their availability to interact with bacteria (Figure 7).

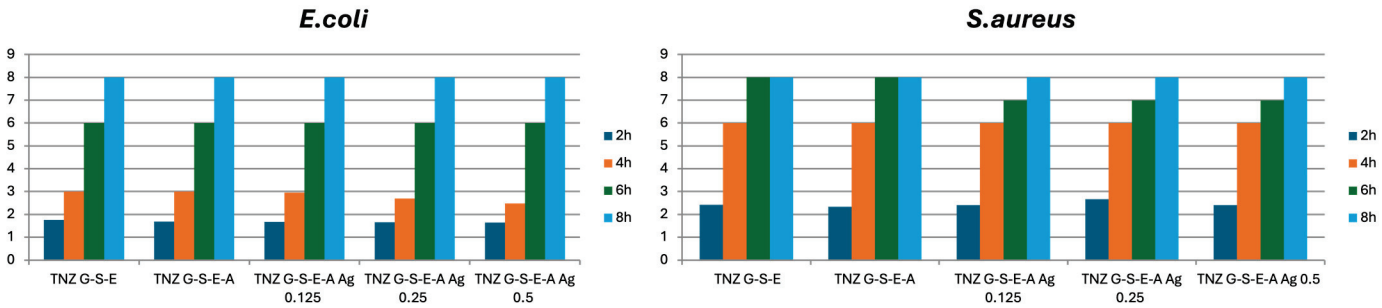


Figure 7. Time-dependent antibacterial effects on *E. coli* and *S. aureus* bacterial strain.

The same effect was observed in the case of *S. aureus* (Figure 7).

4. Discussion

The presented research indicates that the proposed method of dropwise application of an AgNP suspension may prove to be a useful method of achieving bactericidal releasing-type coatings on the surfaces of PEO-H_3PO_4 implants. The acid-etched sample surfaces are similar in terms of topography, roughness, and wettability to the SLA surfaces of the titanium implants, which are proven to promote osseointegration and speed up the recovery period. It is clear that sandblasting and etching in oxalic acid developed and increased the surface area of samples. Scanning electron microscope images provide evidence that an AgNP suspension deposits onto the sample surface, as also supported by atomic composition studies using the EDX method. The conducted experiments demonstrate that plasma electrolytic oxidation is an effective tool for both preparing the sample surface through additional cleaning from abrasive materials and residues from etching and enabling the deposition of silver nanoparticles into the created pores. Plasma electrolytic oxidation of titanium and its alloys in acidic conditions forms a biocompatible layer of anatase, which is an α phase of titanium oxide. SEM images show that increasing the concentration of silver in the suspension increases the amount deposited on the sample surfaces. However, the use of a suspension with a concentration of 0.5 g/L resulted in flooding the lower layers of the surface and covering the pores. Contact angle analysis provides information about the wettability of samples, which is higher for samples with silver nanocoating compared to the PEO sample. Achieved coatings may be described as hydrophilic, and may have similar properties to anti-adhesive self-assembling polymer coatings in terms of bacteriostatic properties. Most hydrophobic properties were observed for samples just sandblasted and acid-etched, where PEO treatment effectively decreased the contact angle, indicating an increase in hydrophilicity.

Several studies demonstrated the antibacterial, anti-adhesive effects of nanosilver-doped titanium implants [75–77]. The mechanism of silver nanoparticle action involves the release of ions, leading to degradation of the peptidoglycan component of the cell wall, inhibition of protein synthesis, and interaction with DNA, ultimately resulting in bacterial cell death [78]. In our previous research, applied AgNPs exhibited a variable

degree of effectiveness in disrupting the biofilms of all tested Gram-negative microbes, including *A. baumannii*, *P. aeruginosa*, *K. pneumonia*, and *Enterobacter* spp. [79]. Incorporating AgNPs into the PEO coating led to the release of silver during immersion tests, enhancing antibacterial properties and exhibiting activity against *S. aureus* through continuous Ag+ ion release [80]. It has been demonstrated that AgNPs incorporated into PEO coatings can decrease *S. aureus* bacterial cell amounts on the surfaces of Ti alloys at the 2 h and 4 h time points of the test [81]. However, Gram-positive bacteria tend to be more resistant to AgNPs due to differences in cell wall structure [82].

5. Summary

This study shows that PEO-treated Ti13Nb13Zr alloy offers a high degree of biocompatibility with human fibroblast cells. The surface treatment consisting of sandblasting, etching, and plasma electrolytic oxidation formed an oxide, ceramic layer that promotes the growth of human cells. On the other hand, the results suggest that while AgNPs exhibit promising initial bactericidal effects against *E. coli* and *S. aureus*, they may not be sustainable in the long term. Otherwise, dose-dependent efficacy was not admitted in applied concentrations of nanoparticles. In conclusion, our study underscores the necessity for additional research aimed at determining the optimal concentration of silver nanoparticles for the Plasma Electrolytic Oxidation (PEO) treatment of metal alloys. By refining this parameter, we can potentially enhance the efficacy and performance of PEO treatments, paving the way for improved antibacterial surface properties.

Author Contributions: Conceptualization, M.P. and W.S.; methodology, M.P. and W.S.; software, P.G.; formal analysis, M.P. and R.Z.; investigation, A.P., Y.V. and P.G.; resources, K.D.; data curation, K.D. and V.K.; writing—original draft preparation, A.P., P.G. and W.S.; writing—review and editing, P.G. and W.S.; supervision, R.Z. and W.S. project administration, W.S. All authors have read and agreed to the published version of the manuscript.

Funding: This research received no external funding.

Institutional Review Board Statement: Not applicable.

Informed Consent Statement: Not applicable.

Data Availability Statement: Data are available on request.

Conflicts of Interest: The authors declare no conflicts of interest.

References

1. Niinomi, M. Mechanical Biocompatibilities of Titanium Alloys for Biomedical Applications. *J. Mech. Behav. Biomed. Mater.* **2008**, *1*, 30–42. [CrossRef] [PubMed]
2. Elias, C.N.; Fernandes, D.J.; De Souza, F.M.; Monteiro, E.D.S.; De Biasi, R.S. Mechanical and Clinical Properties of Titanium and Titanium-Based Alloys (Ti G2, Ti G4 Cold Worked Nanostructured and Ti G5) for Biomedical Applications. *J. Mater. Res. Technol.* **2019**, *8*, 1060–1069. [CrossRef]
3. Thyssen, J.P.; Jakobsen, S.S.; Engkilde, K.; Johansen, J.D.; Søballe, K.; Menné, T. The Association between Metal Allergy, Total Hip Arthroplasty, and Revision. *Acta Orthop.* **2009**, *80*, 646–652. [CrossRef] [PubMed]
4. Lugowski, S.; Smith, D.C.; McHugh, A.; Van Loon, J.C. Release of Metal Ions from Dental Implant Materialsin Vivo: Determination of Al, Co, Cr, Mo, Ni, V, and Ti in Organ Tissue. *J. Biomed. Mater. Res.* **1991**, *25*, 1443–1458. [CrossRef] [PubMed]
5. Klein, G.L. Aluminum Toxicity to Bone: A Multisystem Effect? *Osteoporos. Sarcopenia* **2019**, *5*, 2–5. [CrossRef]
6. Dsouki, N.A.; De Lima, M.P.; Corazzini, R.; Gascón, T.M.; Azzalis, L.A.; Junqueira, V.B.C.; Feder, D.; Fonseca, F.L.A. Cytotoxic, Hematologic and Histologic Effects of Niobium Pentoxide in Swiss Mice. *J. Mater. Sci. Mater. Med.* **2014**, *25*, 1301–1305. [CrossRef] [PubMed]
7. Challa, V.S.A.; Mali, S.A.; Misra, R.D.K. Reduced Toxicity and Superior Cellular Response of Preosteoblasts to Ti-6Al-7Nb Alloy and Comparison with Ti-6Al-4V. *J. Biomed. Mater. Res. Part A* **2013**, *101*, 2083–2089. [CrossRef] [PubMed]

8. Olivares-Navarrete, R.; Olaya, J.J.; Ramírez, C.; Rodil, S.E. Biocompatibility of Niobium Coatings. *Coatings* **2011**, *1*, 72–87. [CrossRef]
9. Lin, H.; Yin, C.; Mo, A. Zirconia Based Dental Biomaterials: Structure, Mechanical Properties, Biocompatibility, Surface Modification, and Applications as Implant. *Front. Dent. Med.* **2021**, *2*, 689198. [CrossRef]
10. Apratim, A.; Eachempati, P.; Salian, K.K.K.; Singh, V.P.; Chhabra, S.; Shah, S. Zirconia in Dental Implantology: A Review. *J. Int. Soc. Prev. Community Dent.* **2015**, *5*, 147–156. [CrossRef] [PubMed]
11. Da Hora Sales, P.H.; Barros, A.W.P.; De Oliveira-Neto, O.B.; De Lima, F.J.C.; De Albuquerque Tavares Carvalho, A.; Leão, J.C. Do Zirconia Dental Implants Present Better Clinical Results than Titanium Dental Implants? A Systematic Review and Meta-Analysis. *J. Stomatol. Oral Maxillofac. Surg.* **2023**, *124*, 101324. [CrossRef]
12. Grandin, H.M.; Berner, S.; Dard, M. A Review of Titanium Zirconium (TIZR) Alloys for Use in Endosseous Dental Implants. *Materials* **2012**, *5*, 1348–1360. [CrossRef]
13. Bigi, A.; Fini, M.; Bracci, B.; Boanini, E.; Torricelli, P.; Giavaresi, G.; Aldini, N.N.; Facchini, A.; Sbaiz, F.; Giardino, R. The Response of Bone to Nanocrystalline Hydroxyapatite-Coated Ti13Nb11Zr Alloy in an Animal Model. *Biomaterials* **2008**, *29*, 1730–1736. [CrossRef]
14. Antoniac, I.V. *Handbook of Bioceramics and Biocomposites*; Springer: Berlin/Heidelberg, Germany, 2016.
15. Bjarnsholt, T. The Role of Bacterial Biofilms in Chronic Infections. *APMIS* **2013**, *121*, 1–58. [CrossRef] [PubMed]
16. Gupta, P.; Sarkar, S.; Das, B.; Bhattacharjee, S.; Tribedi, P. Biofilm, Pathogenesis and Prevention—A Journey to Break the Wall: A Review. *Arch. Microbiol.* **2015**, *198*, 1–15. [CrossRef] [PubMed]
17. Bjarnsholt, T.; Jensen, P.Ø.; Moser, C.; Høiby, N. *Biofilm Infections*; Springer: Berlin/Heidelberg, Germany, 2014.
18. Paharik, A.E.; Horswill, A.R. The Staphylococcal Biofilm: Adhesins, Regulation, and Host Response. *Microbiol. Spectr.* **2016**, *4*, 529–566. [CrossRef] [PubMed]
19. Zaborowska, M.; Tillander, J.; Brånemark, R.; Hagberg, L.; Thomsen, P.; Trobos, M. Biofilm Formation and Antimicrobial Susceptibility of Staphylococci and Enterococci from Osteomyelitis Associated with Percutaneous Orthopaedic Implants. *J. Biomed. Mater. Res. Part B Appl. Biomater.* **2016**, *105*, 2630–2640. [CrossRef] [PubMed]
20. Khan, M.S.; Rehman, S.U.; Ali, M.A.; Sultan, B.; Sultan, S. Infection in Orthopedic Implant Surgery, Its Risk Factors and Outcome. *J. Ayub Med. Coll. Abbottabad* **2008**, *20*, 23–25. [PubMed]
21. De Oliveira, W.F.; Silva, P.M.S.; Silva, R.C.S.; Silva, G.M.M.; Machado, G.; Coelho, L.C.B.B.; Correia, M.T.S. Staphylococcus Aureus and Staphylococcus Epidermidis Infections on Implants. *J. Hosp. Infect.* **2018**, *98*, 111–117. [CrossRef] [PubMed]
22. Zheng, Y.; He, L.; Asiamah, T.K.; Otto, M. Colonization of Medical Devices by Staphylococci. *Environ. Microbiol.* **2018**, *20*, 3141–3153. [CrossRef] [PubMed]
23. Cloutier, M.; Mantovani, D.; Rosei, F. Antibacterial Coatings: Challenges, Perspectives, and Opportunities. *Trends Biotechnol.* **2015**, *33*, 637–652. [CrossRef] [PubMed]
24. Banerjee, I.; Pangule, R.C.; Kane, R.S. Antifouling Coatings: Recent Developments in the Design of Surfaces That Prevent Fouling by Proteins, Bacteria, and Marine Organisms. *Adv. Mater.* **2010**, *23*, 690–718. [CrossRef] [PubMed]
25. Lu, G.; Tian, S.; Li, J.; Xu, Y.; Shuan, L.; Pu, J. Fabrication of Bio-Based Amphiphilic Hydrogel Coating with Excellent Antifouling and Mechanical Properties. *Chem. Eng. J.* **2021**, *409*, 128134. [CrossRef]
26. Maan, A.M.C.; Hofman, A.H.; De Vos, W.M.; Kamperman, M. Recent Developments and Practical Feasibility of Polymer-Based Antifouling Coatings. *Adv. Funct. Mater.* **2020**, *30*, 2000936–2000966. [CrossRef]
27. Page, K.; Wilson, M.; Parkin, I.P. Antimicrobial Surfaces and Their Potential in Reducing the Role of the Inanimate Environment in the Incidence of Hospital-Acquired Infections. *J. Mater. Chem.* **2009**, *19*, 3819–3831. [CrossRef]
28. Cao, Z.; Jiang, S. Super-Hydrophilic Zwitterionic Poly(Carboxybetaine) and Amphiphilic Non-Ionic Poly(Ethylene Glycol) for Stealth Nanoparticles. *Nano Today* **2012**, *7*, 404–413. [CrossRef]
29. Valotteau, C.; Calers, C.; Casale, S.; Berton, J.; Stevens, C.V.; Babonneau, F.; Pradier, C.; Humblot, V.; Baccile, N. Biocidal Properties of a Glycosylated Surface: Sophorolipids on AU(111). *ACS Appl. Mater. Interfaces* **2015**, *7*, 18086–18095. [CrossRef] [PubMed]
30. Li, M.; Mitra, D.; Kang, E.; Lau, T.; Chiong, E.; Neoh, K.G. Thiol-Ol Chemistry for Grafting of Natural Polymers to Form Highly Stable and Efficacious Antibacterial Coatings. *ACS Appl. Mater. Interfaces* **2017**, *9*, 1847–1857. [CrossRef] [PubMed]
31. Romanò, C.L.; Scarponi, S.; Gallazzi, E.; Romanò, D.; Drago, L. Antibacterial Coating of Implants in Orthopaedics and Trauma: A Classification Proposal in an Evolving Panorama. *J. Orthop. Surg. Res.* **2015**, *10*, 157–158. [CrossRef]
32. Palumbo, F.S.; Volpe, A.B.; Cusimano, M.G.; Pitarresi, G.; Giammona, G.; Schillaci, D. A Polycarboxylic/Amino Functionalized Hyaluronic Acid Derivative for the Production of pH Sensible Hydrogels in the Prevention of Bacterial Adhesion on Biomedical Surfaces. *Int. J. Pharm.* **2015**, *478*, 70–77. [CrossRef] [PubMed]
33. Alves, D.; Sileika, T.S.; Messersmith, P.B.; Pereira, M.O. Polydopamine-Mediated Immobilization of Alginate Lyase to PreventP. aeruginosaAdhesion. *Macromol. Biosci.* **2016**, *16*, 1301–1310. [CrossRef]

34. Shang, D.; Sun, X.; Shen, X.; Hang, J.; Jin, L.; Shi, L. Effects of PEG-TMS on the Stability and Antifouling Performances of Hydrocarbon-Modified Amphiphilic Xerogel Coatings. *Prog. Org. Coat.* **2018**, *121*, 142–150. [CrossRef]
35. Zhou, Z.; Calabrese, D.; Taylor, W.C.; Finlay, J.A.; Callow, M.E.; Callow, J.A.; Fischer, D.A.; Krämer, E.J.; Ober, C.K. Amphiphilic Triblock Copolymers with PEGylated Hydrocarbon Structures as Environmentally Friendly Marine Antifouling and Fouling-Release Coatings. *Biofouling* **2014**, *30*, 589–604. [CrossRef]
36. Zhao, C.; Li, L.; Zheng, J. Achieving Highly Effective Nonfouling Performance for Surface-Grafted Poly(HPMA) via Atom-Transfer Radical Polymerization. *Langmuir* **2010**, *26*, 17375–17382. [CrossRef]
37. Neoh, K.G.; Hu, X.; Zheng, D.; Kang, E. Balancing Osteoblast Functions and Bacterial Adhesion on Functionalized Titanium Surfaces. *Biomaterials* **2012**, *33*, 2813–2822. [CrossRef] [PubMed]
38. Zheng, W.; Jia, Y.; Chen, W.; Wang, G.; Guo, X.; Jiang, X. Universal Coating from Electrostatic Self-Assembly to Prevent Multidrug-Resistant Bacterial Colonization on Medical Devices and Solid Surfaces. *ACS Appl. Mater. Interfaces* **2017**, *9*, 21181–21189. [CrossRef]
39. Wang, J.; Sun, J.; Zhou, J.; Jin, K.; Fang, Q. Fluorinated and Thermo-Cross-Linked Polyhedral Oligomeric Silsesquioxanes: New Organic–Inorganic Hybrid Materials for High-Performance Dielectric Application. *ACS Appl. Mater. Interfaces* **2017**, *9*, 12782–12790. [CrossRef]
40. Wang, Z.; Zuilhof, H. Self-Healing Superhydrophobic Fluoropolymer Brushes as Highly Protein-Repellent Coatings. *Langmuir* **2016**, *32*, 6310–6318. [CrossRef]
41. Xu, X.; Shao, Y.; Wang, W.; Zhu, L.; Líu, H.; Shen, Y. Fluorinated Polyhedral Oligomeric Silsesquioxanes End-Capped Poly(Ethylene Oxide) Giant Surfactants: Precise Synthesis and Interfacial Behaviors. *Polymer* **2020**, *186*, 122055. [CrossRef]
42. Wang, T.; Huang, L.; Liu, Y.; Li, X.; Liu, C.; Handschuh-Wang, S.; Yang, X.; Zhao, Y.; Tang, Y. Robust Biomimetic Hierarchical Diamond Architecture with a Self-Cleaning, Antibacterial, and Antibiofouling Surface. *ACS Appl. Mater. Interfaces* **2020**, *12*, 24432–24441. [CrossRef] [PubMed]
43. Pan, S.; Guo, R.; Björnmalm, M.; Richardson, J.J.; Li, L.; Peng, C.; Bertleff-Zieschang, N.; Jiang, J.; Caruso, F. Coatings Super-Repellent to Ultralow Surface Tension Liquids. *Nat. Mater.* **2018**, *17*, 1040–1047. [CrossRef] [PubMed]
44. Kugel, A.; Stafslien, S.J.; Chisholm, B.J. Antimicrobial Coatings Produced by "Tethering" Biocides to the Coating Matrix: A Comprehensive Review. *Prog. Org. Coat.* **2011**, *72*, 222–252. [CrossRef]
45. Sukhorukova, N.W.; Sheveyko, A.N.; Kiryukhantsev-Korneev, P.V.; Zhitnyak, I.Y.; Gloushankova, N.A.; Denisenko, E.A.; Filippovich, S.Y.; Ignatov, S.G.; Shtansky, D.V. Toward Bioactive yet Antibacterial Surfaces. *Colloids Surf. B Biointerfaces* **2015**, *135*, 158–165. [CrossRef]
46. Yuan, X.; Ouyang, L.; Luo, Y.; Sun, Z.; Yang, C.; Wang, J.; Liu, X.; Zhang, X. Multifunctional Sulfonated Polyetheretherketone Coating with Beta-Defensin-14 for Yielding Durable and Broad-Spectrum Antibacterial Activity and Osseointegration. *Acta Biomater.* **2019**, *86*, 323–337. [CrossRef]
47. Costa, F.; Carvalho, I.F.; Montelaro, R.C.; Gomes, P.; Martins, M.C.L. Covalent Immobilization of Antimicrobial Peptides (AMPs) onto Biomaterial Surfaces. *Acta Biomater.* **2011**, *7*, 1431–1440. [CrossRef]
48. Hu, X.; Neoh, K.G.; Shi, Z.; Kang, E.; Poh, C.; Wang, W. An in Vitro Assessment of Titanium Functionalized with Polysaccharides Conjugated with Vascular Endothelial Growth Factor for Enhanced Osseointegration and Inhibition of Bacterial Adhesion. *Biomaterials* **2010**, *31*, 8854–8863. [CrossRef]
49. Peng, Z.; Tu, B.; Yan, X.; Du, L.; Wang, L.; Guo, S.; Tang, T. Quaternized Chitosan Inhibits ICAA Transcription and Biofilm Formation by Staphylococcus on a Titanium Surface. *Antimicrob. Agents Chemother.* **2011**, *55*, 860–866. [CrossRef] [PubMed]
50. Melo, M.N.; Ferré, R.; Castanho, M.A.R.B. Antimicrobial Peptides: Linking Partition, Activity and High Membrane-Bound Concentrations. *Nat. Rev. Microbiol.* **2009**, *7*, 245–250. [CrossRef] [PubMed]
51. Carratalá, J.V.; Serna, N.; Villaverde, A.; Vázquez, E.; Ferrer-Miralles, N. Nanostructured Antimicrobial Peptides: The Last Push towards Clinics. *Biotechnol. Adv.* **2020**, *44*, 107603. [CrossRef]
52. Jiao, Y.; Niu, L.N.; Ma, S.; Li, J.; Tay, F.R.; Chen, J.H. Quaternary Ammonium-Based Biomedical Materials: State-of-the-Art, Toxicological Aspects and Antimicrobial Resistance. *Prog. Polym. Sci.* **2017**, *71*, 53–90. [CrossRef] [PubMed]
53. Cheng, L.; Zhang, K.; Zhang, N.; Melo, M.A.S.; Weir, M.D.; Zhou, X.; Bai, Y.; Reynolds, M.A.; Xu, H.H.K. Developing a New Generation of Antimicrobial and Bioactive Dental Resins. *J. Dent. Res.* **2017**, *96*, 855–863. [CrossRef]
54. Natan, M.; Edin, F.; Perkas, N.; Yacobi, G.; Perelshtein, I.; Segal, E.; Homsy, A.; Laux, E.; Keppner, H.; Rask-Andersen, H.; et al. Two Are Better than One: Combining ZnO and MgF2Nanoparticles ReducesStreptococcus pneumoniaeandStaphylococcus aureusBiofilm Formation on Cochlear Implants. *Adv. Funct. Mater.* **2016**, *26*, 2473–2481. [CrossRef]
55. Xiong, M.; Bao, Y.; Yang, X.; Zhu, Y.; Wang, J. Delivery of Antibiotics with Polymeric Particles. *Adv. Drug Deliv. Rev.* **2014**, *78*, 63–76. [CrossRef] [PubMed]

56. Castelletto, V.; Edwards-Gayle, C.J.C.; Hamley, I.W.; Barrett, G.; Seitsonen, J.; Ruokolainen, J. Peptide-Stabilized Emulsions and Gels from an Arginine-Rich Surfactant-like Peptide with Antimicrobial Activity. *ACS Appl. Mater. Interfaces* **2019**, *11*, 9893–9903. [CrossRef] [PubMed]
57. Sadrearhami, Z.; Nguyen, T.; Namivandi-Zangeneh, R.; Jung, K.; Wong, E.H.H.; Boyer, C. Recent Advances in Nitric Oxide Delivery for Antimicrobial Applications Using Polymer-Based Systems. *J. Mater. Chem. B* **2018**, *6*, 2945–2959. [CrossRef]
58. Tang, S.; Zheng, J. Antibacterial Activity of Silver Nanoparticles: Structural Effects. *Adv. Healthc. Mater.* **2018**, *7*, 1701503. [CrossRef]
59. Guillaume, O.; Garric, X.; Lavigne, J.; Van Den Berghe, H.; Coudane, J. Multilayer, Degradable Coating as a Carrier for the Sustained Release of Antibiotics: Preparation and Antimicrobial Efficacy in Vitro. *J. Control. Release* **2012**, *162*, 492–501. [CrossRef] [PubMed]
60. Tang, Y.; Zhao, Y.; Wang, H.; Gao, Y.; Liu, X.; Wang, X.; Lin, T. Layer-by-layer Assembly of Antibacterial Coating on Interbonded 3D Fibrous Scaffolds and Its Cytocompatibility Assessment. *J. Biomed. Mater. Res. Part A* **2012**, *100*, 2071–2078. [CrossRef]
61. Liu, D.; Cui, C.; Chen, W.; Shi, J.; Li, B.; Chen, S. Biodegradable Cements for Bone Regeneration. *J. Funct. Biomater.* **2023**, *14*, 134. [CrossRef] [PubMed]
62. Fazel, M.; Salimijazi, H.; Golozar, M.A.; Jazi, G. A Comparison of Corrosion, Tribocorrosion and Electrochemical Impedance Properties of Pure Ti and Ti6Al4V Alloy Treated by Micro-Arc Oxidation Process. *Appl. Surf. Sci.* **2015**, *324*, 751–756. [CrossRef]
63. Fan, X.; Feng, B.; Di, Y.; Li, X.; Duan, K.; Wang, J.; Weng, J. Preparation of Bioactive TiO Film on Porous Titanium by Micro-Arc Oxidation. *Appl. Surf. Sci.* **2012**, *258*, 7584–7588. [CrossRef]
64. Yetim, A.F. Investigation of Wear Behavior of Titanium Oxide Films, Produced by Anodic Oxidation, on Commercially Pure Titanium in Vacuum Conditions. *Surf. Coat. Technol.* **2010**, *205*, 1757–1763. [CrossRef]
65. Xie, L.; Yin, G.; Yan, D.; Liao, X.; Huang, Z.; Yao, Y.; Kang, Y.; Liu, Y. Structure, Morphology and Fibroblasts Adhesion of Surface-Porous Titanium via Anodic Oxidation. *J. Mater. Sci. Mater. Med.* **2009**, *21*, 259–266. [CrossRef]
66. Chrzanowski, W. Corrosion Study of Ti6Al7Nb Alloy after Thermal, Anodic and Alkali Surface Treatments. *J. Achiev. Mater. Manuf. Eng.* **2008**, *31*, 203–211.
67. Antoci, V.; Adams, C.S.; Parvızı, J.; Davidson, H.M.; Composto, R.J.; Freeman, T.A.; Wickstrom, E.; Ducheyne, P.; Jungkind, D.; Shapiro, I.M.; et al. The Inhibition of Staphylococcus Epidermidis Biofilm Formation by Vancomycin-Modified Titanium Alloy and Implications for the Treatment of Periprosthetic Infection. *Biomaterials* **2008**, *29*, 4684–4690. [CrossRef] [PubMed]
68. Tshibangu-Kabamba, E.; Yamaoka, Y. Helicobacter Pylori Infection and Antibiotic Resistance—From Biology to Clinical Implications. *Nat. Rev. Gastroenterol. Hepatol.* **2021**, *18*, 613–629. [CrossRef]
69. Rossi, E.; La Rosa, R.; Bartell, J.A.; Marvig, R.L.; Haagensen, J.A.J.; Sommer, L.M.M.; Molin, S.; Johansen, H.K. Pseudomonas Aeruginosa Adaptation and Evolution in Patients with Cystic Fibrosis. *Nat. Rev. Microbiol.* **2020**, *19*, 331–342. [CrossRef]
70. Tian, X.; Jiang, X.; Welch, C.; Croley, T.R.; Wong, T.-Y.; Chen, C.; Fan, S.; Chong, Y.; Li, R.; Ge, C.; et al. Bactericidal Effects of Silver Nanoparticles on Lactobacilli and the Underlying Mechanism. *ACS Appl. Mater. Interfaces* **2018**, *10*, 8443–8450. [CrossRef] [PubMed]
71. Xie, K.; Zhou, Z.; Yu, G.; Wang, L.; Li, G.; Zhao, S.; Liu, X.; Li, J.; Jiang, W.; Wu, S.L.; et al. Long-Term Prevention of Bacterial Infection and Enhanced Osteoinductivity of a Hybrid Coating with Selective Silver Toxicity. *Adv. Healthc. Mater.* **2019**, *8*, 1801465–1801477. [CrossRef]
72. Fischer, H.D.; Chan, W.C.W. Nanotoxicity: The Growing Need for in Vivo Study. *Curr. Opin. Biotechnol.* **2007**, *18*, 565–571. [CrossRef]
73. Zhang, K.; Lui, V.C.H.; Chen, Y.; Lok, C.N.; Wong, K.K. Delayed Application of Silver Nanoparticles Reveals the Role of Early Inflammation in Burn Wound Healing. *Sci. Rep.* **2020**, *10*, 6338. [CrossRef] [PubMed]
74. Sigma-Aldrich Co., Ltd. *Fundamental Techniques in Cell Culture 3*; Sigma Aldrich: St. Louis, MO, USA, 2016; p. 80.
75. Necula, B.S.; Apachitei, I.; Tichelaar, F.D.; Fratila-Apachitei, L.E.; Duszczyk, J. An electron microscopical study on the growth of TiO2–Ag antibacterial coatings on Ti6Al7Nb biomedical alloy. *Acta Biomater.* **2011**, *7*, 2751–2757. [CrossRef] [PubMed]
76. Necula, B.S.; Van Leeuwen, J.P.T.M.; Fratila-Apachitei, L.E.; Zaat, S.A.J.; Apachitei, I.; Duszczyk, J. In vitro cytotoxicity evaluation of porous TiO2–Ag antibacterial coatings for human fetal osteoblasts. *Acta Biomater.* **2012**, *8*, 4191–4197. [CrossRef]
77. Pokrowiecki, R.; Zaręba, T.; Szaraniec, B.; Pałka, K.; Mielczarek, A.; Menaszek, E.; Tyski, S. In vitro studies of nanosilver-doped titanium implants for oral and maxillofacial surgery. *Int. J. Nanomed.* **2017**, *12*, 4285–4297. [CrossRef] [PubMed]
78. Brennan, S.; Fhóghlú, C.N.; Devitt, B.M.; O'Mahony, F.J.; Brabazon, D.; Walsh, A.M. Silver nanoparticles and their orthopaedic applications. *Bone Jt. J.* **2015**, *97*, 582–589. [CrossRef]
79. Holubnycha, V.M.; Husak, Y.; Korniienko, V.; Bolshanina, S.; Tveresovska, O.; Myronov, P.; Holubnycha, M.; Butsyk, A.; Borén, T.; Banasiuk, R.; et al. Antimicrobial Activity of Two Different Types of Silver Nanoparticles against Wide Range of Pathogenic Bacteria. *Nanomaterials* **2024**, *14*, 137. [CrossRef]

80. Husak, Y.; Olszaniecki, J.; Pykacz, J.; Ossowska, A.; Blacha-Grzechnik, A.; Waloszczyk, N.; Babilas, D.; Korniienko, V.; Varava, Y.; Diedkova, K.; et al. Influence of silver nanoparticles addition on antibacterial properties of PEO coatings formed on magnesium. *Appl. Surf. Sci.* **2024**, *654*, 159387. [CrossRef]
81. Oleshko, O.; Liubchak, I.; Husak, Y.; Korniienko, V.; Yusupova, A.; Oleshko, T.; Banasiuk, R.; Szkodo, M.; Matros-Taranets, I.; Kazek-Kęsik, A.; et al. In vitro biological characterization of Silver-Doped anodic oxide coating on titanium. *Materials* **2020**, *13*, 4359. [CrossRef]
82. Rai, M.; Deshmukh, S.; Ingle, A.P.; Gade, A. Silver nanoparticles: The powerful nanoweapon against multidrug-resistant bacteria. *J. Appl. Microbiol.* **2012**, *112*, 841–852. [CrossRef] [PubMed]

Disclaimer/Publisher's Note: The statements, opinions and data contained in all publications are solely those of the individual author(s) and contributor(s) and not of MDPI and/or the editor(s). MDPI and/or the editor(s) disclaim responsibility for any injury to people or property resulting from any ideas, methods, instructions or products referred to in the content.

materials

MDPI

Article

Effects of Pre-Deformation in Corrosion Fatigue Crack Growth of Al-Mg-Zn Alloy

Hui Jiang [1], Junjun Jin [2,3], Yu Fang [1], Guoqing Gou [3,*], Wei Lu [3], Zhiyi Zhang [4], Hongmei Zhou [5], Hairong Sun [6], Jikui Feng [7], Jia Chen [1,*] and Zhenghong Fu [2,8]

1 School of Mechanical Engineering, Chengdu Industry and Trade College, Chengdu 610031, China; jianghui@cdgmxy.edu.cn (H.J.); fangyu@cdgmxy.edu.cn (Y.F.)
2 State Key Laboratory of Precision Manufacturing for Extreme Service Performance, Central South University, Changsha 410083, China; jinjun2358@163.com (J.J.); fuzhenghong@swjtu.edu.cn (Z.F.)
3 Key Laboratory of Advanced Technologies of Materials, Ministry of Education, School of Materials Science and Engineering, Southwest Jiaotong University, Chengdu 610031, China; swjtuluwei@163.com
4 CRRC Qingdao Sifang Co., Ltd., Qingdao 266111, China; zhangzhiyi@cqsf.com
5 School of Materials and Environmental Engineering, Chengdu Technological University, Chengdu 610031, China; angriy@163.com
6 Sichuan Special Equipment Inspection Institute, Chengdu 610031, China; shr-19@163.com
7 Hubei Aerospace Flight Vehicle Institute, Wuhan 430000, China; 18327030324@139.com
8 Applied Mechanics and Structure Safety Key Laboratory of Sichuan Province, School of Mechanics and Aerospace Engineering, Southwest Jiaotong University, Chengdu 610031, China
* Correspondence: gouguoqing@swjtu.edu.cn (G.G.); chenjia@cdgmxy.edu.cn (J.C.)

Abstract: This study investigated the effect of pre-deformation on the corrosion fatigue crack propagation (CFCG) of Al-Mg-Zn alloy in a corrosive environment. Tensile tests at different pre-deformation levels and molecular dynamics simulations analyzed changes in dislocation density. Corrosion fatigue experiments were conducted in a 3.5% NaCl solution at room temperature, and crack propagation morphology was characterized using electron backscatter diffraction (EBSD), scanning electron microscopy (SEM), and transmission electron microscopy (TEM). The results showed that tensile strength increased by 2.63% and 10.00% for 5% and 10% pre-deformation, respectively. The crack propagation threshold values were L_2 (6.36 MPa·$m^{1/2}$) > L_0 (6.05 MPa·$m^{1/2}$) > L_1 (5.13 MPa·$m^{1/2}$), attributed to increased dislocation density and material strength. At 5% pre-deformation, dislocation pile-ups created stress concentrations that facilitated crack propagation. In contrast, the non-uniform dislocation distribution at 10% pre-deformation enhanced both material strength and resistance to crack growth.

Keywords: Al-Mg-Zn alloy; pre-deformation; corrosion fatigue; cracking path; dislocation density

1. Introduction

Al-Mg-Zn alloy is widely used in high-speed trains for its high strength-to-density ratio and good fatigue resistance. It is 35% lighter than traditional materials like stainless steel and weathering steel, allowing for increased load capacity and reduced energy consumption under the same traction conditions [1–3]. A dense oxide layer is readily formed on the surface of the alloy, which prevents oxidative corrosion. Youhong Peng et al. revealed the characteristics of sustained load crack growth in Al-Zn-Mg-Cu aluminum alloys in a saline environment [4]. Melika Jalali et al. studied how ARB (Accumulated Roll Bonding) as a severe plastic deformation technique alters the microstructure and corrosion

resistance of this alloy. The results indicated that, due to the higher dislocation density, an increased number of ARB cycles initially leads to a decrease in corrosion resistance [5]. Fatigue refers to the fracture phenomenon caused by an accumulation of pre-deformation in metals and their structural parts under the action of long-term loads. The damage caused by fatigue fracture accounts for more than 80% of total operation failures. Lingjian Meng et al. found that flaky α fracture releases a greater local stress concentration during low-temperature pre-stretching, thereby maintaining the high work hardening capacity of the alloy [6]. The corrosion fatigue of metallic materials is a form of corrosion–plastic failure under the influence of alternating loads and corrosive environments. This involves a process of mutual promotion of corrosion and fatigue damage [7–11]. The operating conditions of high-speed trains necessitate exposure to complex and diverse conditions, such as humidity, marine atmospheres, and industrial pollution environments. Corrosive media such as Cl^- and $NO_3{}^-$ in a humid environment will affect aluminum alloy materials and aluminum alloys, notably welded joints, which can experience corrosion damage. In addition, the aluminum alloy body of high-speed trains and the associated welded structural parts are subject to a constant load and alternating cyclic loads over extended periods. Therefore, the service reliability of the aluminum alloy body and the welded structural parts is a critical guarantee for the safe operation of high-speed trains [12–14].

During actual operation, the cover plate made of Al-Mg-Zn alloy in key components of high-speed trains is responsible for withstanding both the cyclic load and the dead weight of the corbel. Consequently, the Al-Mg-Zn Alloy cover plate will exhibit a certain degree of pre-deformation during operation and service. Pre-deformation has a significant impact on the crack propagation behavior of aluminum alloys. Through pre-deformation, the grain structure of aluminum alloys can be refined, and the degree of bending and twisting of grain boundaries increases, thereby enhancing the material's strength and toughness and inhibiting crack propagation. At the same time, pre-deformation also alters the residual stress distribution of aluminum alloys. If pre-deformation introduces stress concentration areas, it may accelerate crack propagation. Additionally, pre-deformation increases the dislocation density of aluminum alloys. A moderate dislocation density can enhance the material's strength and toughness [15], suppressing crack propagation, but excessive dislocation density may lead to easier crack propagation. Therefore, in the design and application of aluminum alloy materials, it is necessary to comprehensively consider the influence of pre-deformation on crack propagation behavior to improve the material's resistance to crack propagation, However, there is still insufficient research on the fatigue behavior and corrosion effects of aluminum–magnesium–zinc alloys under pre-deformation conditions, especially regarding the long-term durability of aluminum alloys in high-humidity environments and marine climates, where relevant literature is scarce. Therefore, this study aims to fill this research gap by systematically analyzing the impact of pre-deformation on the fatigue and corrosion performance of aluminum alloys, providing a theoretical foundation for the optimization design and application of aluminum alloy materials in future high-speed trains.

This study aims to investigate the corrosion fatigue crack propagation (CFCG) behavior of Al-Mg-Zn alloy aluminum alloys under different levels of pre-deformation. Microscopic analysis of the aluminum alloy's microstructure, residual stress, crack orientation, and fracture morphology was conducted using optical microscopy, electron backscatter diffraction (EBSD), scanning electron microscopy (SEM), and transmission electron microscopy (TEM). Furthermore, molecular dynamics simulation methods were employed to explore the changes in dislocation density resulting from different levels of

pre-deformation, which to some extent explains the differences in corrosion fatigue crack propagation rates and mechanisms under different plastic damage conditions.

2. Materials and Methods

2.1. Materials and Mechanical Properties

In this study, Al-Mg-Zn alloy was used as the research object. The composition is given in Table 1. The Al-Mg-Zn Alloy sheet was processed into standard tensile specimens by wire cutting, according to the standard tensile specimen size in Figure 1. The sample thickness was 10 mm.

Table 1. Al-Mg-Zn alloy composition (wt.%).

Material	Zn	Mg	Cu	Mn	Si	Ti	Cr	Fe	Al
Al-Mg-Zn alloy	4.0~5.0	1.0~1.8	0.10	0.20~0.70	0.35	0.01~0.06	0.06~0.20	0.40	Bal.

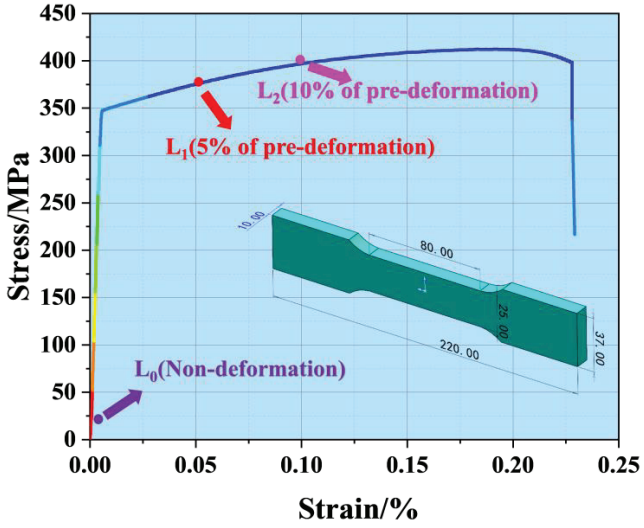


Figure 1. Stress–strain curve of Al-Mg-Zn Alloy base metal.

The stress–strain curve for the Al-Mg-Zn alloy is illustrated in Figure 1. In this study, we prepared three distinct groups of samples: Group L_0 (non-deformation), Group L_1 (5% pre-deformation), and Group L_2 (10% pre-deformation). Each sample was machined to standardized dimensions and mounted on a DNS300 tensile testing machine (Changchun Machinery Research Institute, Changchun, China). During the pre-deformation process, tensile loads were applied to the L_1 and L_2 samples until strains of 5% and 10% were achieved, respectively. An extensometer continuously monitored the strain, and each sample was held under the applied load for 10 min to ensure consistent sample deformation. After this period, the samples were unloaded and prepared for further mechanical testing to evaluate the effects of pre-deformation on their stress–strain behavior.

Figure 2a and b illustrate the improved unilateral notch specimen (improved Single edged notched tension, (SENT) specimen) and the sampling position of the CFCG. The specimen was provided with an extensometer slot above the notch to facilitate a fixed extensometer. The size of the improved SENT sample is shown in Figure 2c, and the crack expansion device is given in Figure 2d. Samples were taken from the three groups: L_0, L_1, and L_2. The crack length data were collected in real time using a computer program interfaced with the extensometer. The computer program was written in Visual Basic (VB)

language, the electronic extender adopted model Y5/2.5 for data acquisition, the extender range was 5 mm, and the measuring range was 2.5 mm.

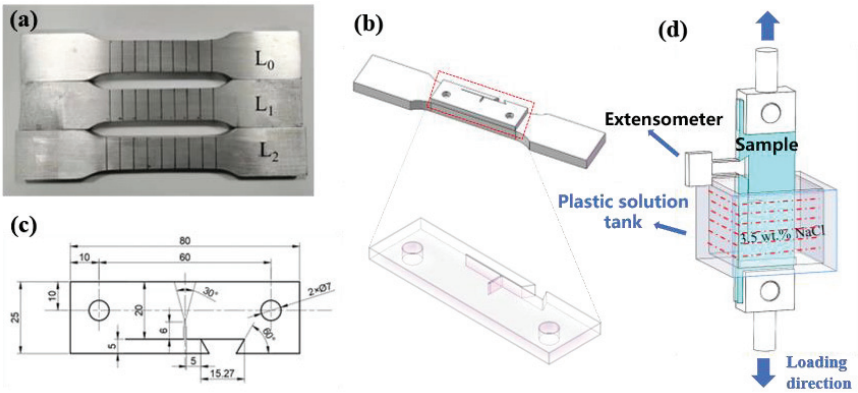


Figure 2. Pre-deformation of CFCG: (**a**) tensile specimen with different degrees of pre-deformation; (**b**) schematic diagram of the sampling position of the crack growth sample; (**c**) the size of the crack growth sample; and (**d**) schematic diagram of the crack growth device.

2.2. Microstructure

The metallographic samples were treated with sandpaper of different grit sizes (180–2000), and then polished on a polishing machine until there were no detectable surface scratches. After polishing, the samples were cleaned with alcohol and then treated with acid (2% HF, 3% HCL, 5% HNO_3, and 90% H_2O). An optical microscope (OM) (model of equipment: Zeiss−A1M, Carl Zeiss AG, Oberkochen, Germany,) and scanning electron microscope (SEM) ((model of equipment: JSM−6490LV, JEOL, Tokyo, Japan) were used to observe the fracture of the corrosion fatigue crack growth sample. The element types and product components were then analyzed. Using electron back-scattered diffraction (EBSD) (model of equipment: NordlysNano, Oxford Instruments, Oxford, UK), the distribution of secondary phases and grain boundaries was investigated analytically. All samples were then electropolished in an electrolyte consisting of 10% roach acid and 90% ethanol. The electropolishing process was run at 25 V for a polishing time of 40 s. The distribution of dislocations and strengthening phases under different pre-deformations was investigated using an FEI Tecnai 20 TEM (model of equipment: Thermo Fisher Scientific, Hillsboro, OR, USA).

2.3. Molecular Dynamics Simulation

In order to probe possible microstructural changes under different degrees of pre-deformation, the molecular dynamics simulation software package LAMMPS (Large-scale Atomic/Molecular Massively Parallel Simulator: LAMMPS 3 Mar 2020) [16] developed by Sandia National Laboratory was used for simulation calculation. The data processing software used was the Open Visualization Tool (Ovito-3.11.3—OVITO), developed by Alexander Stukowski of Darmstadt University of Technology [17]. This visualization and analysis software for atomic and particle simulation data enables valuable insight into material phenomena and physical processes. The Voronoi algorithm and MEAM [18] (Modified Embed Atom Method) were employed to establish and calculate the tensile test of the polycrystalline model of Mg-Al alloy.

In order to facilitate modeling and calculations, we have neglected the influence of other trace elements. Figure 3 shows the simplified molecular dynamics tensile model of the Al-Mg-Zn alloy. The model represents a polycrystalline Al-Mg-Zn aluminum alloy of constant size (200 nm × 100 nm × 200 nm), where the lattice constant of Al atoms is

"a = 4.05". The model contains 240,877 atoms and 20 grains. The composition of the alloy is Al (wt%): Zn (wt%): Mg (wt%) = 94%: 4.6%: 1.4%. The X, Y, and Z coordinates correspond to the [100], [010], and [001] crystallographic directions.

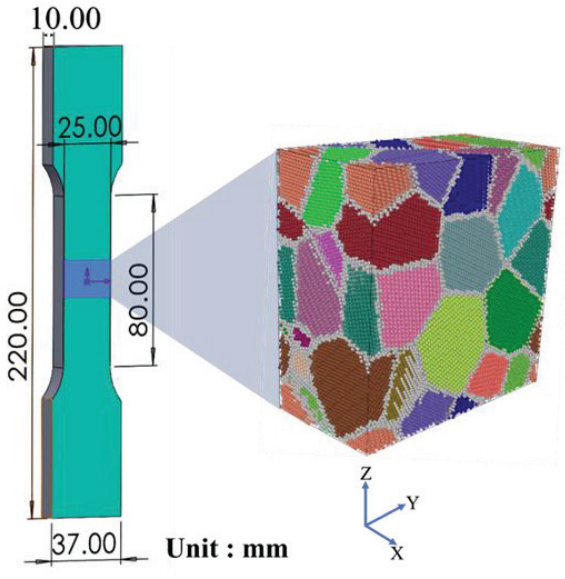


Figure 3. Molecular dynamic tensile model of Al-Zn-Mg alloy.

Following model establishment and relaxation, a tensile load in the [0 0 1] direction was applied to the alloy system to assess the motion of atoms and the relationship between stress and strain during the entire stretching process. The temperature of the system was set at 300 K, and the X, Y, and Z directions are all periodic boundary conditions. A time step of 0.001 ps was used for the simulation, a strain rate of 0.001 was applied, and the system was simulated using isothermal and isobaric ensemble (NPT) relaxation for 50,000 steps; the atoms were recorded every 100 steps during stretching. Analysis of crystal defects employed Common Neighbor Analysis (CNA) [19]. The deformation mechanism of the polycrystalline Al-Mg-Zn aluminum alloy was monitored and analyzed by dislocation analysis (DXA).

2.4. Corrosion Fatigue Crack Propagation

The CFCG test was carried out on a vertical fatigue testing machine (Changchun Qianbang Testing Equipment Co., Ltd., Changchun, China). A 3.5 wt.% NaCl solution was used to simulate the corrosive effect of seawater, and the fatigue crack length was measured by the flexibility method; measurement accuracy was not less than 0.01 mm. The measurement gap opening displacement was calibrated according to the GB/T 12160-2002 [20] standard. The maximum axial loading force was 3.5 KN, the frequency 0.5 Hz, the waveform a sine wave, and the stress ratio = 0.1. According to the GB/T 2012.2-2006 standard [21], the sample was pre-cracked, with the length of the pre-crack being approximately 2 mm. During the test, the number of cycles (N) and the crack length (a) were collected in real time, applying GB/T 6398-2017 [22]. "Fatigue of Metal Materials", the seven-point incremental polynomial data processing method, was adopted, with the method specified in the "Crack Growth Rate Test Method". The data were processed by a Visual Basic (VB) programming program (Visual Basic 15.5), where the CFCG behavior can be described by the relationship between the crack growth rate (da/dN) and the range of the stress intensity (factor K).

$$\Delta K = \frac{\Delta P}{B\sqrt{W}} \times \frac{2+\alpha}{(1-\alpha)^{3/2}} \times \left(0.886 + 4.64\alpha - 13.32\alpha^2 + 14.72\alpha^3 - 5.6\alpha^4\right) \quad (1)$$

$$\frac{da}{dN} = C(\Delta K)^{2} \quad (2)$$

In this relationship, $\alpha = a/W$, where a represents the crack length, W is the sample width, B is the sample thickness, ΔP is the load amplitude, N is the number of stress cycles, C and m are constants related to the material, and ΔK is the stress intensity factor variation range.

3. Results and Discussion

3.1. Microstructure and Mechanical Properties

The three-direction microstructure of Al-MgZn Alloy is shown in Figure 4a. The directions are rolling (L), long transverse (T) and thickness (S), respectively. The grains in the L-T plane are uniformly arranged, and pre-deformation is negligible. The grains in the L-S plane are "flattened", and the grains show obvious fibrous features along the rolling direction.

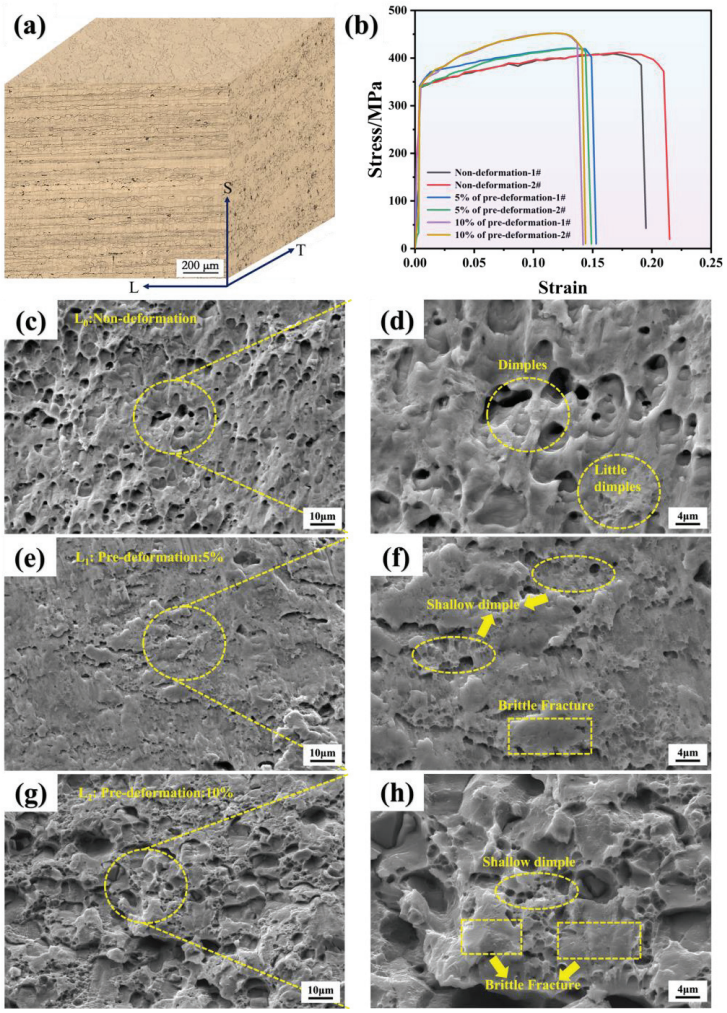


Figure 4. (**a**) Optical microscope image of Al-Mg-Zn alloy: orientation: rolled (L), long transverse (T), and thickness (S). (**b**) Tensile strength of Al-Mg-Zn Alloy after pre-deformation. (**c**,**d**) Tensile fracture of non-deformation. (**e**,**f**) Tensile fracture of 5% of pre-deformation. (**g**,**h**) Tensile fracture of 10% of pre-deformation.

In addition, the Al matrix is dispersed with fine $MgZn_2$ secondary phases. Figure 4b shows the tensile curves of two sets of parallel samples of Al-Mg-Zn alloy under different pre-deformation levels. After pre-deformation, the overall tensile strength increases; the average tensile strength of L_0 is 410 MPa, L_1 is 421 MPa, and L_2 is 451 MPa. It can be seen that, compared to the unstrained condition, the tensile strength increased by 2.63% and 10.00% with pre-deformation of 5% and 10%, respectively. As the pre-deformation level increases, the material's tensile strength increases. This is because pre-deformation can introduce grain boundaries and dislocations, thereby increasing the material's dislocation density, enhancing the grain boundary strengthening effect, and improving the material's tensile strength [23,24].

At the same time, as the pre-deformation level increases, the tensile fracture of the material also exhibits different characteristics. In the unstrained condition, the dimples are deep, indicating good toughness of the material. However, when the pre-deformation level reaches 5% and 10%, the dimples become shallower, and even disappear, with localized areas of smooth surfaces and a certain degree of brittle fracture on the fracture surface. This indicates that the strength of the material increases after pre-deformation, while the plastic toughness decreases. This is bound to have an impact on the fatigue crack propagation of the material in a corrosive environment.

3.2. Molecular Dynamics Calculation Results

As shown in Figure 5, the atomic structure diagram of the stretched [001] crystal direction clearly shows the rotation of the grains and the occurrence of defects such as slip and vacancies in local areas. The greater the pre-deformation, the more pronounced these changes become. Further analysis of the microstructure under different pre-deformation levels reveals that the white disordered atomic regions gradually increase with pre-deformation, leading to an increase in atomic spacing and enhanced atomic disturbance behavior. A large number of disordered atoms in this area release stress, making the proliferation of dislocations relatively easy. By observing the distribution of dislocations, it can be found that as the pre-deformation level increases, dislocations continue to proliferate [25].

Using the Dislocation Extraction Algorithm (DXA) to analyze the internal dislocation situation in different pre-deformation models, the color scheme indicates unknown dislocations in red, 1/2<1 1 0> (perfect) dislocations in blue, 1/6<1 1 2> (Shockley) dislocations in green, and 1/3<1 1 1> (Frank) dislocations in cyan. In the undeformed model, a small number of dislocations appear, mainly dominated by 1/2 (perfect) dislocations. When the pre-deformation reaches 5%, the number of dislocations sharply increases, mainly consisting of 1/2<1 1 0> (perfect) and 1/6<1 1 2> (Shockley) dislocations, with 1/2<1 1 0> (perfect) dislocations playing a dominant role in deformation, while other types of dislocations have relatively smaller line lengths. As the pre-deformation continues to increase to 10%, the number of dislocations continues to increase, with 1/6<1 1 2> (Shockley) dislocations becoming the primary form, playing a dominant role in deformation.

Dislocation density is the ratio of dislocation lines to volume [26]. Figure 6 illustrates the relationship between dislocation density and strain under various pre-deformation levels, highlighting the significance of dislocation density, which is defined as the ratio of dislocation lines to volume. As pre-deformation increases, dislocations accumulate, enhancing elastic interactions between them that raise the resistance to dislocation slip and, consequently, the material's tensile strength, consistent with the tensile test results. However, the non-uniform distribution of dislocations can lead to dislocation pile-ups, causing stress concentration, which may promote the propagation of fatigue cracks. This

emphasizes the importance of understanding both the accumulation and distribution of dislocations in optimizing material performance [27,28].

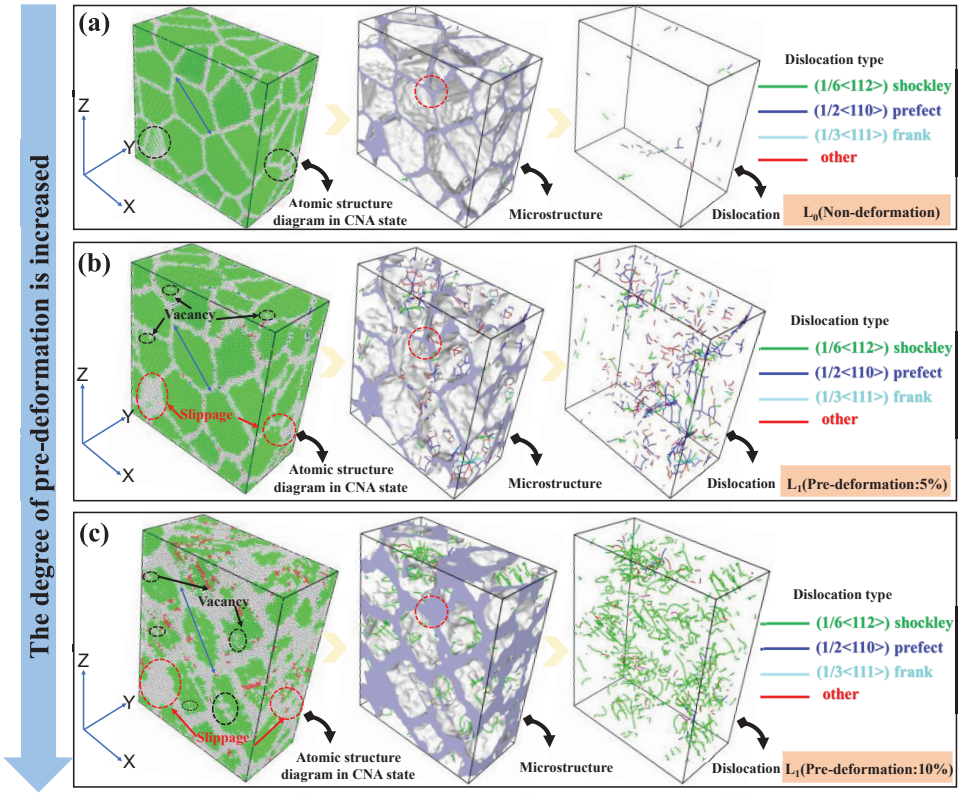


Figure 5. Variation trend of the number of crystal slips, vacancies, and dislocations under different pre-deformation degrees along the crystal direction of [001]: (**a**) Tensile fracture of non-deformation. (**b**) Tensile fracture of 5% of pre-deformation. (**c**) Tensile fracture of 10% of pre-deformation.

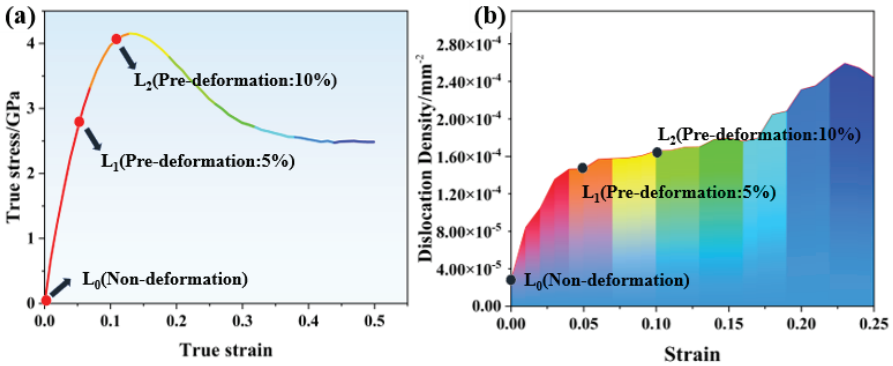


Figure 6. (**a**) Tensile stress–strain curves of Al-Mg-Zn alloy and (**b**) dislocation densities under different degrees of pre-deformation.

From a comprehensive comparison of dislocation density and type, it can be observed that when pre-deformation reaches a certain level, dislocations accumulate, and the elastic interaction between dislocations increases the resistance to dislocation slip, thereby increasing the material's tensile strength, consistent with the results of tensile tests [29,30]. However, it is worth noting that the uneven distribution of dislocations can also lead to dislocation pile-ups, causing stress concentration, which to some extent promotes the propagation of fatigue cracks [31].

3.3. Corrosion Fatigue Crack Growth Rate Curve

Figure 7 shows the crack propagation rate curves of Al-Mg-Zn alloy under different pre-deformation levels in a 3.5 wt.% NaCl solution. Table 2 presents the fitting results of the Paris formula. By comparing the crack propagation rate curves of Al-Mg-Zn alloy under different pre-deformation levels in a 3.5 wt.% NaCl solution environment, it can be observed that the difference in pre-deformation levels leads to differences in crack propagation threshold values. The crack propagation threshold values under three pre-deformation states are in the following order from highest to lowest: L2 (6.36 MPa·m$^{1/2}$) > L0 (6.05 MPa·m$^{1/2}$) > L1 (5.13 MPa·m$^{1/2}$). A lower threshold value indicates easier crack propagation. This is attributed to the change in the internal structure and microstructure of the material due to pre-deformation under external stress. The crack propagation threshold value is lowest for 5% pre-deformation, resulting in the fastest crack propagation rate. The threshold value is highest for 10% pre-deformation, leading to the lowest propagation rate, while the threshold value and propagation rate for no pre-deformation tend to be in between.

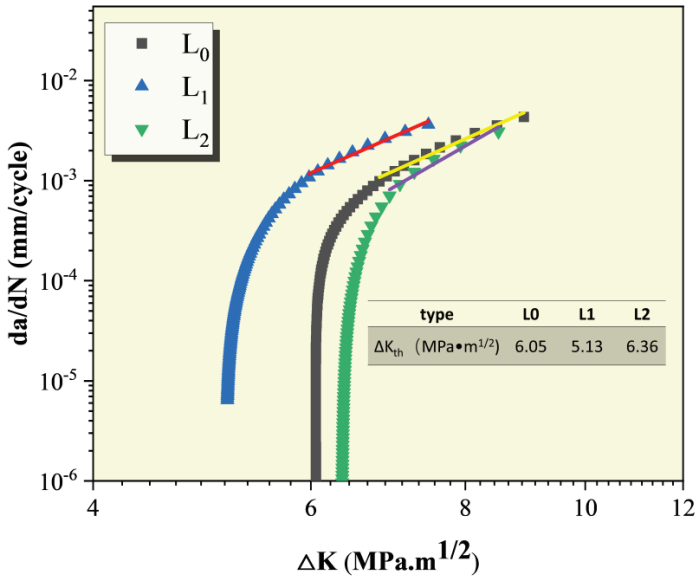


Figure 7. CFCG rate curve of Al-Mg-Zn Alloy after pre-deformation.

Table 2. Paris formula fitting results.

Degree of Pre-Deformation	Constant C	Constant m	Paris Formula
L_0 (non-deformation)	7.09×10^{-8}	5.43	$da/dN = 7.09 \times 10^{-8}(\Delta K)^{5.43}$
L_1 (5% pre-deformation)	2.66×10^{-8}	5.23	$da/dN = 2.66 \times 10^{-8}(\Delta K)^{5.23}$
L_2 (10% pre-deformation)	8.41×10^{-10}	7.11	$da/dN = 8.41 \times 10^{-10}(\Delta K)^{7.11}$

The reason for these results is that pre-deformation increases the density of internal dislocations in the material, leading to enhanced grain boundary strengthening effects and an increase in material strength, which to some extent inhibits crack propagation. However, pre-deformation may also cause dislocation pile-ups, resulting in significant stress concentration, making crack propagation easier in regions with higher stress under fatigue loading. Combining the results of tensile tests and the evolution of dislocations during pre-deformation through molecular dynamics simulations, it can be concluded that the distribution of dislocations is non-uniform under 5% pre-deformation, leading to stress concentration, while the density of dislocations is increased under 10% pre-deformation,

but the distribution is more uniform, increasing the material strength and also raising the threshold value for crack propagation, hindering crack propagation. The threshold value for no pre-deformation lies between the two. This indicates that while pre-deformation enhances the material's strength, it also leads to a decrease in fatigue performance, highlighting the critical importance of selecting an appropriate pre-deformation level.

3.4. Corrosion Fatigue Crack Propagation Path

To further clarify the differences in the CFCG rates, an analysis of the characteristics of the crack propagation paths was conducted. Figure 8 displays macroscopic photographs of the cracks in Al-Mg-Zn alloy under different pre-deformation levels. As shown in Figure 8a, the crack under no pre-deformation exhibits a typical "Z"-shaped path, with an angle of approximately 40° with the horizontal direction. Additionally, there are micro-cracks parallel or perpendicular to the main crack direction. The crack path under 5% pre-deformation (Figure 8b) is relatively straight, with the crack propagation direction at an angle of around 24° with the horizontal direction. Compared to no pre-deformation, there are more secondary cracks at certain angles to the main crack. The crack path under 10% pre-deformation (Figure 8c) is more similar to the unstrained condition (Figure 8a), with the crack propagation direction at an angle of approximately 60° with the horizontal direction. The results indicate significant differences in the crack propagation paths under different pre-deformation levels. The crack path under 5% pre-deformation is straighter, smoother, and has the smallest angle with the horizontal direction, with the highest number of secondary cracks. This suggests that the embrittlement of the crack tip region is more pronounced at 5% pre-deformation, resulting in a lower crack propagation threshold value and a faster propagation rate, corresponding to the crack propagation rate curve (Figure 7).

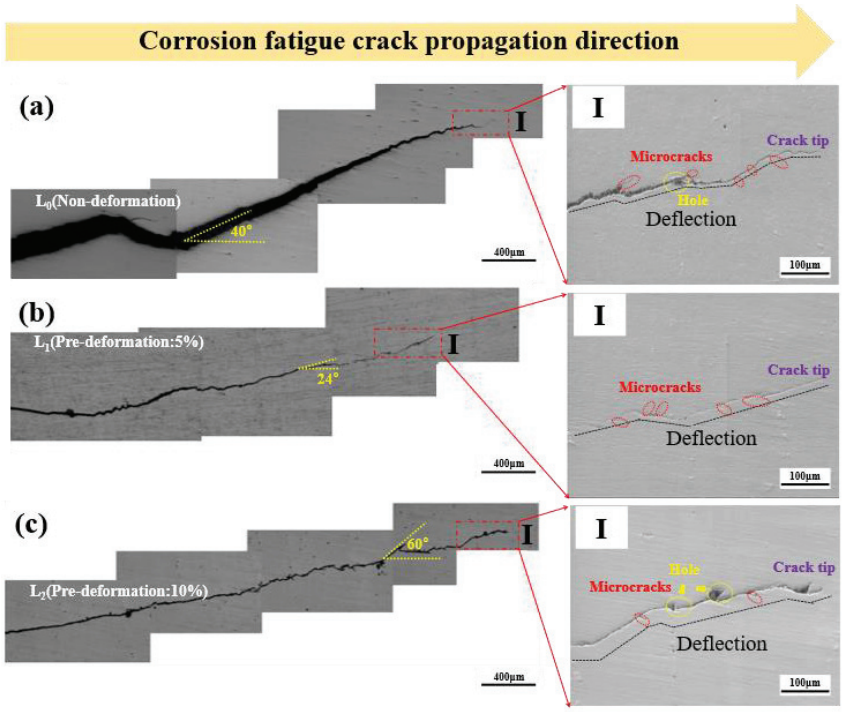


Figure 8. Corrosion fatigue crack propagation path of Al-Mg-Zn Alloy with different degrees of pre-deformation: (**a**) non-deformation L_0, (**b**) pre-deformation L_1, and (**c**) pre-deformation L_2.

Using scanning electron microscopy combined with EBSD, further analysis of the crack tip CFCG path and microstructural changes was conducted (Figure 9). The IPF

maps of the crack tips of the non-deformation sample L0 and pre-deformation samples L1 (5%) and L2 (10%) are shown in Figure 9a,c,e, respectively. The analysis indicates that the corrosion fatigue cracks in all three conditions exhibit a mixed mode of transgranular and intergranular crack propagation during the expansion process, with transgranular propagation being predominant. The distribution of grain boundaries at the crack tip is shown in Figure 9b,d,f, where high-angle grain boundaries are represented in black and low-angle grain boundaries are represented in green. With the increase in pre-deformation level, the number of high-angle grain boundaries decreases. This is due to the deformation and slip of grain boundaries caused by plastic deformation, leading to changes in the shape and position of the grain boundaries [23]. Additionally, a large number of subgrains form, and due to the small orientation differences between adjacent subgrains, it is difficult to distinguish them by color. Furthermore, in the strain region, the deformation reduces the orientation differences of the grain boundaries, making the grain boundaries less distinct. From the perspective of crack morphology, there is significant crack deflection in the crack path with 10% pre-deformation, which to some extent impedes the crack propagation.

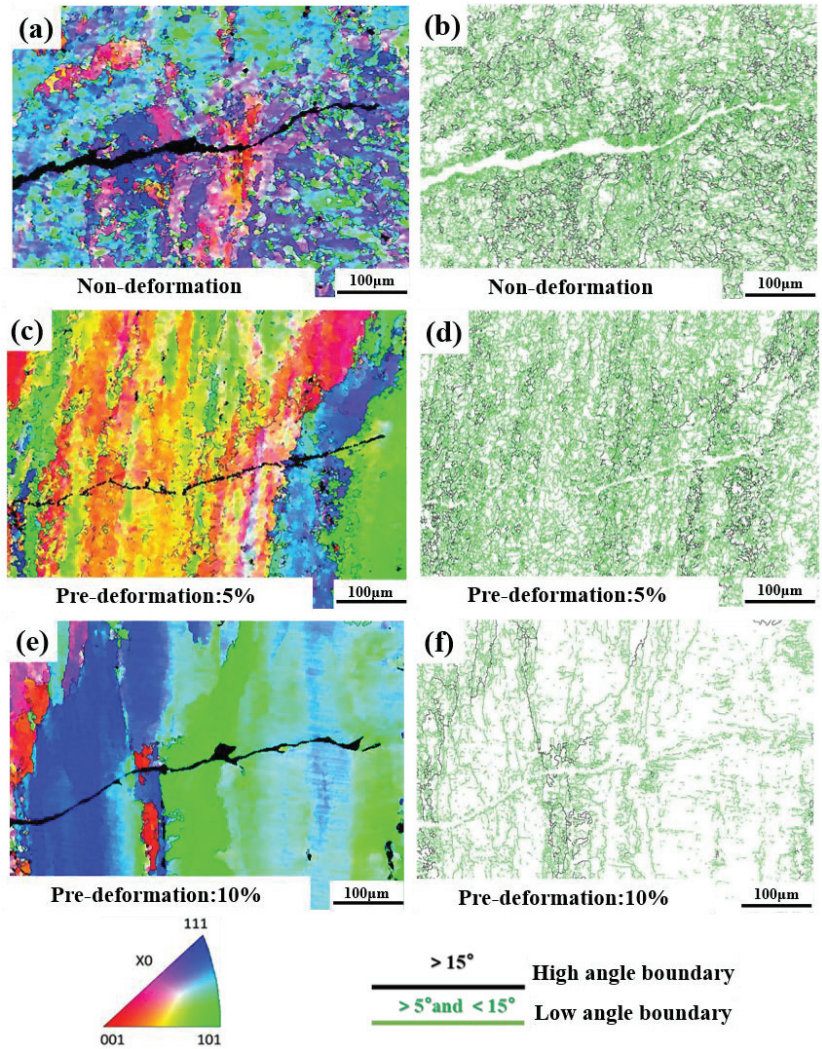


Figure 9. EBSD images of Al-Mg-Zn Alloy with different degrees of pre-deformation: (**a**) IPF maps of non-deformation, (**b**) grain boundary of non-deformation, (**c**) IPF maps of pre-deformation: 5%, (**d**) grain boundary of pre-deformation: 5%, (**e**) IPF maps of pre-deformation: 10%, and (**f**) grain boundary of pre-deformation: 10%.

The Kernel Average Misorientation (KAM) images (Figure 10a,c,e) represent the degree of plastic deformation at the crack tip, with green indicating irregular residual strain. It can be seen that the distribution of residual strain near the crack tip is consistent with the distribution of small-angle grain boundaries. During the process of corrosion fatigue crack propagation, significant plastic deformation occurs near the crack. Compared to no deformation and 5% pre-deformation, the residual strain at the crack tip is smaller and the plastic deformation is more uniform with 10% pre-deformation. The Schmid factor represents the ease of activation of slip systems and is used to evaluate the plastic deformation ability of single-crystal grains. The Schmid factor map at the crack tip position is shown in Figure 10b,d,f. A larger Schmid factor indicates a soft orientation in the material structure, which is conducive to crack propagation. When the Schmid factor is smaller, it is difficult for the material to undergo slip, indicating a hard orientation in the structure. The Schmid factor is larger when the pre-deformation is 5%, leading to a faster crack propagation rate, which is consistent with the distribution trend of the crack propagation threshold and crack propagation rate [32,33].

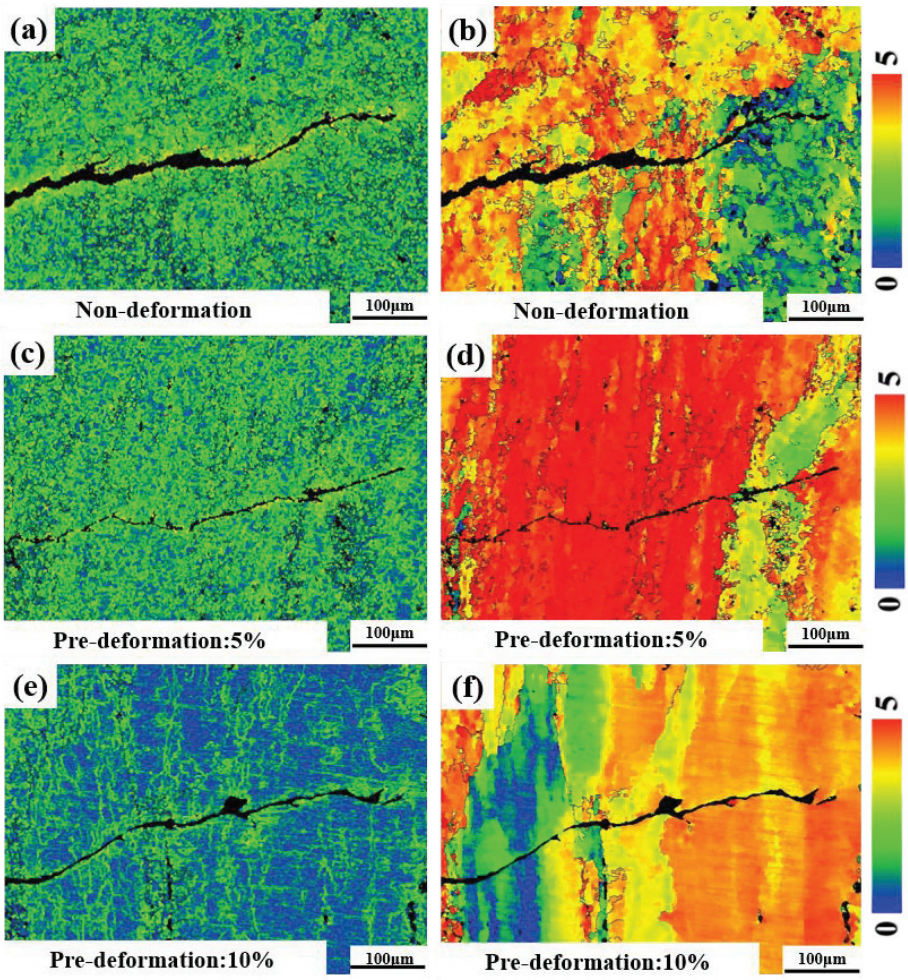


Figure 10. EBSD images of Al-Mg-Zn Alloy with different degrees of pre-deformation: (**a**) KAM maps of non-deformation, (**b**) Schmid factor map of non-deformation, (**c**) KAM maps of pre-deformation: 5%, (**d**) Schmid factor map of pre-deformation: 5%, (**e**) KAM maps of pre-deformation:10%, and (**f**) Schmid factor map of pre-deformation: 10%.

Figure 11 shows TEM images of the near-fracture region of Al-Mg-Zn alloy with different pre-deformation during corrosion fatigue. As shown in Figure 11a, the alloy

under no deformation has a low dislocation density, with a large amount of $MgZn_2$ (η phase) distributed at grain boundaries and within the grains. From Figure 11b, it can be observed that when the pre-deformation is 5%, the dislocation density of the alloy significantly increases, and the distribution of dislocations becomes uneven [34]. Local accumulation of dislocations forms dislocation walls in the matrix, surrounded by the η phase, creating stress concentration areas and increasing the risk of cracking. In Figure 11c, when the pre-deformation increases to 10%, although the dislocation density continues to increase, the distribution of dislocations becomes more uniform, to some extent reducing the stress concentration and improving the material's deformation ability [35]. This is consistent with the trend in dislocation distribution during tensile deformation in molecular dynamics simulations.

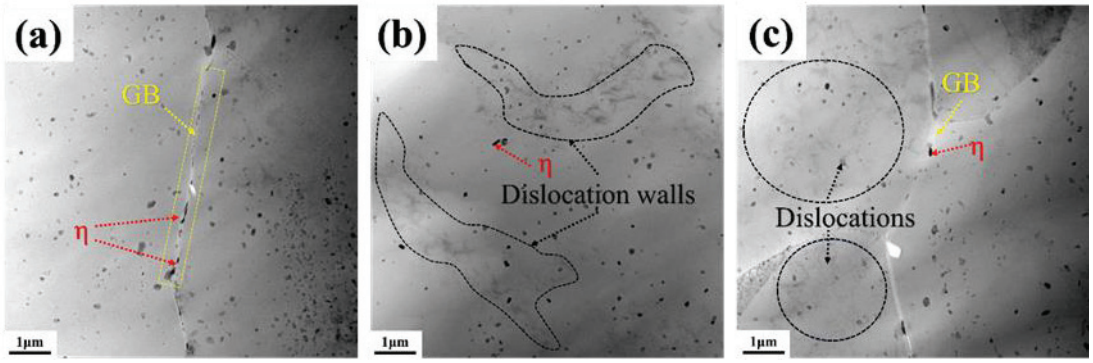


Figure 11. TEM images of the corrosion fatigue near fracture zone of Al-Mg-Zn alloy with different deformation: (**a**) no deformation; (**b**) 5% pre-deformation; and (**c**) 10% pre-deformation.

3.5. Fractography

Figure 12 shows the micro-fractures associated with the CFCG of Al-Mg-Zn alloy under different degrees of pre-deformation. It can be seen that the fracture morphologies are quite distinct. Compared with no deformation L0 (Figure 12a,b), the specimens after pre-deformation, L_1 (Figure 12c,d) and L_2 (Figure 12e,f), exhibit a relatively flat corrosion fatigue fracture. We can attribute this response to the increase in the strength of the pre-deformation samples, the decrease in plasticity, and the alteration to the material structure. Moreover, a large number of holes left by the detachment of the second phase can be seen on the fracture, with many secondary cracks along the direction of fatigue crack propagation for pre-deformation: 5%. Clear secondary cracks can be seen in the fracture with 5% pre-deformation, which will lead to local stress concentration at the crack tip and accelerate the process of crack propagation, which is consistent with the trend in the threshold value and rate of crack propagation. Higher-magnification analysis allowed a more detailed consideration of fracture morphology. Fatigue striations are relatively blurred, but striations with different spacings can still be seen locally. The spacing for sample L_0 is about 0.8 μm, whereas that for L_1 and L_2 is, respectively, 1.5 μm and 1.1 μm. The fatigue striation spacing reflects the force crack growth rate to a certain extent, and the spacing for L1 is the largest. In addition, the crack growth rate test has also shown that the crack growth rate of L1 is highest. Undulating bright bands are a feature of L_1 SEM images, which may be caused by damage to the crack tip. This indicates that a certain degree of pre-deformation can enhance the anti-corrosion response, but excessive pre-deformation inhibits this effect in terms of fatigue performance [36].

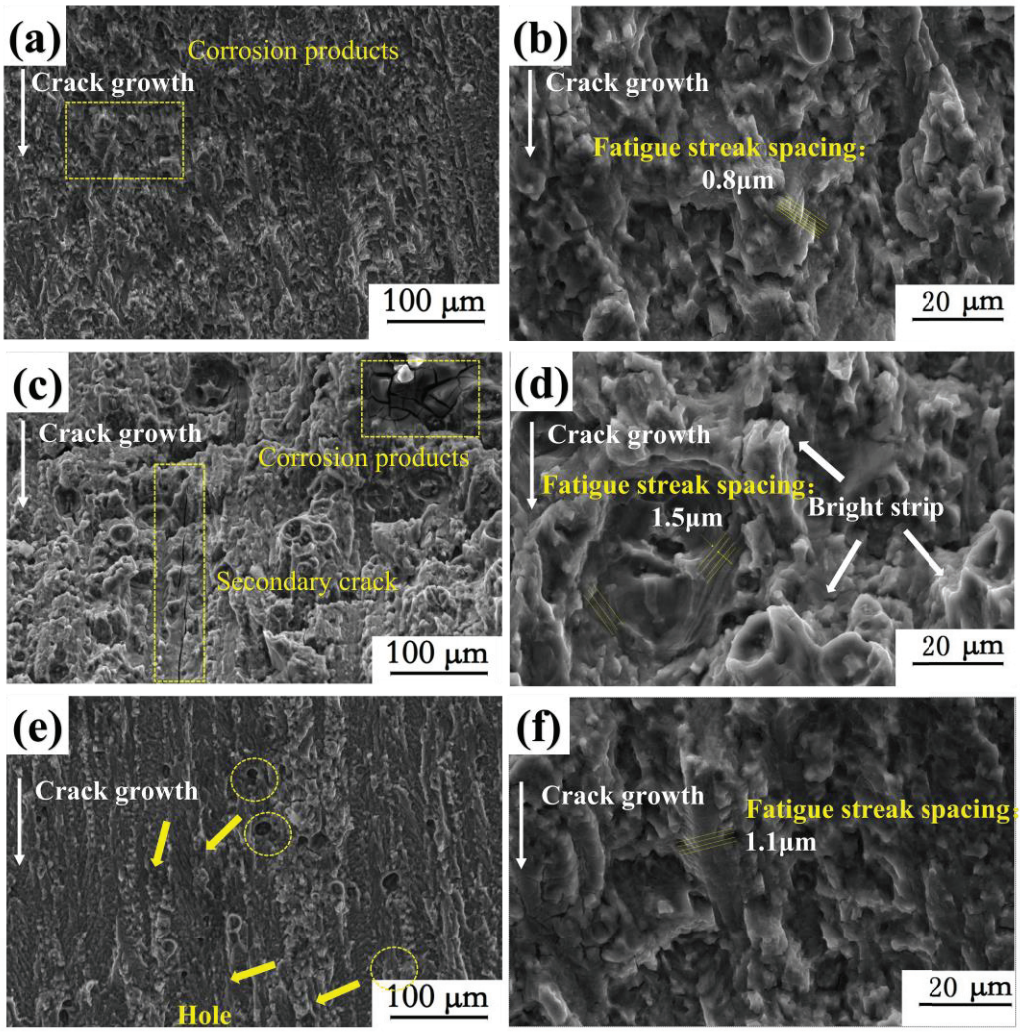


Figure 12. Micromorphology of corrosion fatigue crack propagation fracture of samples with different degrees of pre-deformation in 3.5 wt.% NaCl solution. (**a**,**b**) L_0: non-deformation; (**c**,**d**) L_1: 5% pre-deformation; and (**e**,**f**) L_2: 10% pre-deformation.

3.6. Mechanism Analysis

The pre-deformation of Al-Mg-Zn alloy affects its corrosion fatigue crack propagation behavior. The microstructure of Al-Mg-Zn alloy after pre-deformation changes due to the deformation of the material. The aluminum alloy structure is more chaotic and grain deformation is significant, hampering the resistance of the material to crack growth. Such pre-deformation will lead to a reduction in the corrosion fatigue crack growth threshold for Al-Mg-Zn alloy. Greater pre-deformation results in work hardening, which serves to increase material tensile strength, which is manifested as an increase in the CFCG threshold and a decrease in the crack growth rate [37]. Tibor Berecz [38] studied the pre-deformation behavior of 6082 aluminum alloy and found that the dislocation density increased significantly with an increase in the degree of pre-deformation deformation. The elastic interaction increases the resistance to dislocation sliding, which eventually leads to a significant increase in tensile strength, so the CFCG threshold of 10% pre-deformation increases. Wang [39] studied the microstructure and tensile properties of industrially prepared 7050 aluminum alloy plates. Their results showed that the grain size distribution in the aluminum alloy was not uniform, and some grains exhibited coarseness, which can lead to uneven deformation during the pre-deformation process. Chen [40] studied the

torsional thermal deformation behavior of 7A04 aluminum alloy. They reported differences in grain shape in different regions (equiaxed, elliptical, and fibrillar) due to deformation, resulting in different properties with pre-deformation. This can also be seen in our 3D metallographic analysis, given in Figure 4a. Yang [41] examined the effect of different strain rates on recrystallization and flow stress in 7085 aluminum alloy during hot compression, and found that high strain rates promote the formation of a grain boundary structures. Jian-Liang [42] used the K-M dislocation density model to quantitatively assess the dislocation density of 7A85 aluminum alloy during hot deformation. The parameters in the model were determined by the stress–true strain curve obtained from hot compression experiments. Their two-stage K-M dislocation density model [42–45] considered that some dislocations transformed into dislocation cells or sub-crystals, which retained a high dislocation density. Their work established that an increase in plasticity was accompanied by an increased dislocation density, but the dislocation density inside the original crystal was ignored.

Based on the current research results, the influence of pre-deformation on the mechanism of corrosion fatigue crack propagation has not been studied. We conducted an in-depth analysis of the tensile strength and fracture surfaces of Al-Mg-Zn alloy under different pre-deformation levels, and elucidated the role of pre-deformation in the fracture mechanism. Additionally, molecular dynamics simulations were used to analyze the formation process of defects such as dislocations and vacancies under different pre-deformation levels, and the variation in dislocation density under pre-deformation conditions. Based on these research results, corrosion fatigue crack propagation tests were conducted to obtain the crack propagation threshold and rate under different pre-deformation levels. Combined with characterization methods such as EBSD, SEM, and TEM, the characteristics along the crack propagation path, fracture morphology, and the variation of dislocation density near the crack tip were analyzed. As shown in Figure 13, compared to the experiments with non-deformation and 10% pre-deformation, the threshold value is lowest and the crack propagation rate is fastest with 5% pre-deformation. This is mainly due to the increase in dislocation density and material strength caused by pre-deformation. However, under 5% pre-deformation, the accumulation of dislocations forms dislocation walls, resulting in significant stress concentration, making it easier for the crack to propagate along the stress concentration areas. On the other hand, under 10% pre-deformation, the distribution of dislocations is more uneven, increasing the material strength while also increasing the resistance to crack propagation [46,47].

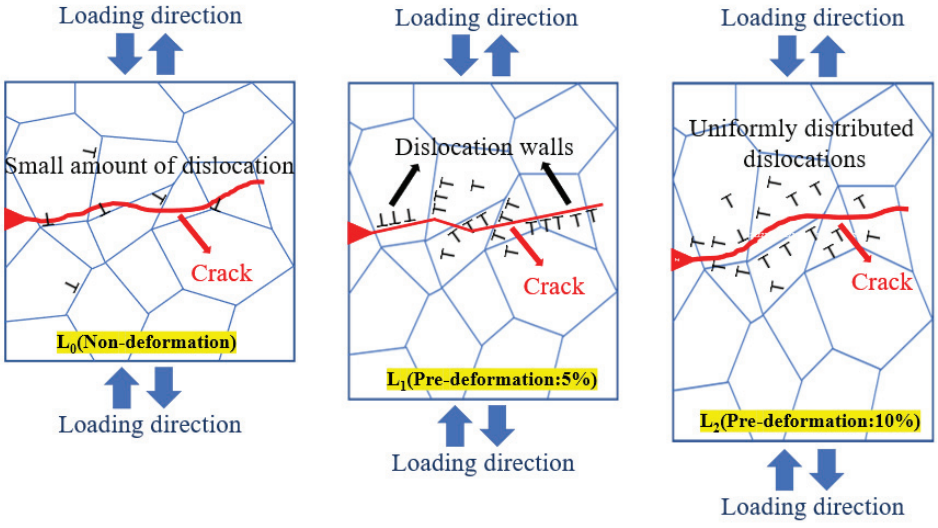


Figure 13. Crack propagation paths under different degrees of dislocation density.

4. Conclusions

This study examines the impact of pre-deformation on the corrosion fatigue crack propagation (CFCG) of Al-Mg-Zn alloy in a corrosive environment. Through tensile tests and molecular dynamics simulations, we assessed how varying pre-deformation levels affected dislocation density and ultimately influenced the alloy's mechanical properties and crack propagation behavior in a 3.5% NaCl solution.

1. Enhanced Tensile Strength: The results show that pre-deformation improves the tensile strength of Al-Mg-Zn alloy, with increases of 2.63% and 10.00% at 5% and 10% pre-deformation, respectively, compared to the unstrained condition.
2. Influence on Crack Propagation: Corrosion fatigue crack propagation is significantly affected by pre-deformation, with thresholds varying as L2 (6.36 $MPa \cdot m^{1/2}$) > L0 (6.05 $MPa \cdot m^{1/2}$) > L1 (5.13 $MPa \cdot m^{1/2}$). Higher dislocation densities at 10% pre-deformation enhance resistance to crack propagation.
3. Molecular dynamics simulations showed that as the pre-deformation level increased, the dislocation density also increased, consistent with the results of the tensile tests. However, the uneven distribution of dislocations also led to stress concentration, which to some extent promoted the propagation of corrosion fatigue cracks.

Author Contributions: H.J.: Methodology, funding acquisition, project administration, and writing—review and editing. Y.F.: data curation and writing—original draft. G.G.: methodology, funding acquisition, and project administration. J.J.: conceptualization, investigation, validation, writing—original draft, and writing—review and editing. J.C.: data curation, writing—original draft, and writing—review and editing. W.L.: writing—review and editing and data curation. Z.Z.: project administration and supervision. H.Z.: data curation. H.S.: data curation. J.F.: data curation. Z.F.: data curation. All authors have read and agreed to the published version of the manuscript.

Funding: Fund Project: "Research on rapid scanning and health Assessment Technology of spherical Tank stress based on electromagnetic Ultrasound" scientific research project of the State Market Supervision Administration in 2023, project No. 2023MK054; Key Research and Development Plan of Sichuan Province [25GJHZ0239]; Open Research Fund of State Key Laboratory of Precision Manufacturing for Extreme Service Performance, Central South University [Kfkt2022-03]; Natural Science Foundation of Sichuan province in China [2023NSFSC1302].

Institutional Review Board Statement: Not applicable.

Informed Consent Statement: Not applicable.

Data Availability Statement: The original contributions presented in this study are included in the article. Further inquiries can be directed to the corresponding authors.

Conflicts of Interest: Author Zhiyi Zhang was employed by the company CRRC Qingdao Sifang Co., Ltd. The remaining authors declare that the research was conducted in the absence of any commercial or financial relationships that could be construed as a potential conflict of interest.

References

1. Chen, L.; Yuan, S.; Kong, D.; Zhao, G.; Zhang, C. Influence of aging treatment on the microstructure, mechanical properties and anisotropy of hot extruded Al-Mg-Si plate. *Mater. Des.* **2019**, *182*, 107999. [CrossRef]
2. Liu, X.S.; Zhang, L.; Wang, L.S.; Wu, S.H.; Fang, H.Y. Fatigue behavior and life prediction of A7N01 aluminium alloy welded joint. *Trans. Nonferrous Met. Soc. China* **2012**, *22*, 2930–2936. [CrossRef]
3. Ana, J.; Chena, J.; Goua, G.; Qina, C.; Chena, H.; Lic, P.; Lid, Z. Research on Corrosion Fatigue Crack Propagation Behavior of Welded Joints of A7N01P-T4 Aluminum Alloys. *J. Corros. Sci. Eng.* **2016**, *19*, 1–14.
4. Peng, Y.; Li, D.; Wu, H.; Miao, K.; Liu, C.; Wang, L.; Liu, W.; Xu, C.; Geng, L.; Wu, P.; et al. Insights into the deformation mechanisms of an Al1Mg0.4Si alloy at cryogenic temperature: An integration of experiments and crystal plasticity modeling. *J. Mater. Sci. Technol.* **2024**, *200*, 69–82. [CrossRef]

5. Jalali, M.; Jafarian, H.R.; Shanaghi, A.; Eivani, A.R. On the microstructure and corrosion behavior of Fe-28.5Ni steel subjected to severe plastic deformation. *J. Mater. Res. Technol.* **2025**, *34*, 90–99. [CrossRef]
6. Meng, L.; Zhao, Z.; Lin, P.; Jiang, Z.; Zhao, J. Achieving enhanced strength-ductility synergy in heterogeneous equiaxed structured Ti-6Al-4V alloy sheets by cryogenic pre-stretching. *Mater. Des.* **2025**, *249*, 113563. [CrossRef]
7. Cavalcante, T.R.F.; Pereira, G.S.; Koga, G.Y.; Bolfarini, C.; Filho, W.W.B.; Avila, J.A. Fatigue crack propagation of aeronautic AA7050-T7451 and AA2050-T84 aluminum alloys in air and saline environments. *Int. J. Fatigue* **2022**, *154*, 106519. [CrossRef]
8. Young, G.A.; Scully, J.R. The effects of test temperature, temper, and alloyed copper on the hydrogen-controlled crack growth rate of an Al-Zn-Mg-(Cu) alloy. *Metall. Mater. Trans. A* **2002**, *33*, 101–115. [CrossRef]
9. Horner, D.A.; Connolly, B.J.; Zhou, S.; Crocker, L.; Turnbull, A. Novel images of the evolution of stress corrosion cracks from corrosion pits. *Corros. Sci.* **2011**, *53*, 3466–3485. [CrossRef]
10. Holroyd, N.; Scamans, G.M. Crack Propagation During Sustained-Load Cracking of Al-Zn-Mg-Cu Aluminum Alloys Exposed to Moist Air or Distilled Water. *Metall. Mater. Trans. A* **2011**, *42*, 3979–3998. [CrossRef]
11. Thirumalaikumarasamy, D.; Shanmugam, K.; Balasubramanian, V. Influence of chloride ion concentration on immersion corrosion behaviour of plasma sprayed alumina coatings on AZ31B magnesium alloy. *J. Magnes. Alloys* **2014**, *2*, 325–334. [CrossRef]
12. Qi, X.; Song, R.; Qi, W.; Jin, J.; Wang, C.; Li, H.; Sun, B. Correspondence between Susceptibility to SCC of 7050 Aluminum Alloy and Passive Film-induced Stress at Various pH Values. *J. Cent. South Univ.* **2017**, *32*, 173–178. [CrossRef]
13. Shah, S.R.; Pryce, I.L.; John, T.S.; Greer, J.M. Effect of Environmental Corrosion on Fatigue Crack Growth Morphology: A Detailed Investigation of the Boundary between Fatigue and Corrosion Control Regimes. *Adv. Mater. Res.* **2014**, *891*, 278–285. [CrossRef]
14. Borchers, T.E.; McAllister, D.P.; Zhang, W. Macroscopic segregation and stress corrosion cracking in 7xxx series aluminum alloy arc welds. *Metall. Mater. Trans. A* **2015**, *46*, 1827–1833. [CrossRef]
15. Ma, A.; Roters, F.; Raabe, D. A dislocation density based constitutive law for BCC materials in crystal plasticity FEM. *Comp. Mater. Sci.* **2007**, *39*, 91–95. [CrossRef]
16. Jung, S.; Kwon, Y.; Lee, C.S.; Lee, B. Influence of hydrogen on the grain boundary crack propagation in bcc iron: A molecular dynamics simulation. *Comp. Mater. Sci.* **2018**, *149*, 424–434. [CrossRef]
17. Terentyev, D.; Zhurkin, E.E.; Bonny, G. Emission of full and partial dislocations from a crack in BCC and FCC metals: An atomistic study. *Comp. Mater. Sci.* **2012**, *55*, 313–321. [CrossRef]
18. Baskes, M.I. Modified embedded-atom potentials for cubic materials and impurities. *Phys. Rev. B* **1992**, *46*, 2727. [CrossRef]
19. Feng, Q.; Song, X.; Xie, H.; Wang, H.; Liu, X.; Yin, F. Deformation and plastic coordination in WC-Co composite—Molecular dynamics simulation of nanoindentation. *Mater. Des.* **2017**, *120*, 193–203. [CrossRef]
20. *GB/T 12160-2002*; Calibration of Extensometers for Uniaxial Tests, National Standard of China. Standardization Administration of China: Beijing, China, 2002.
21. *GB/T 20120.2-2006*; Corrosion of Metals and Alloys—Corrosion Fatigue Test—Part 2: Crack Propagation Test on Pre-Cracked Specimens, National Standard of China. Standardization Administration of China: Beijing, China, 2006.
22. *GB/T 6398-2017*; Metallic Materials-Fatigue Test-Fatigue Crack Growth Method, National Standard of China. Standardization Administration of China: Beijing, China, 2017.
23. Lu, D.; Lin, B.; Liu, T.; Deng, S.; Guo, Y.; Li, J.; Liu, D. Effect of grain structure on fatigue crack propagation behavior of Al-Cu-Li alloys. *J. Mater. Sci. Technol.* **2023**, *148*, 75–89. [CrossRef]
24. Tian, N.; Feng, Z.; Shi, X.; Wang, W.; Liu, K.; Zhao, G.; Qin, G. Effects of Pre-Tensile Deformation on the Fatigue Fracture Behavior of Annealed 7005 Aluminum Alloy Plate. *Materials* **2022**, *15*, 623. [CrossRef] [PubMed]
25. Yakovtseva, O.; Sitkina, M.; Mosleh, A.O.; Mikhaylovskaya, A. High Strain Rate Superplasticity in Al-Zn-Mg-Based Alloy: Microstructural Design, Deformation Behavior, and Modeling. *Materials* **2020**, *13*, 2098. [CrossRef] [PubMed]
26. Cheng, X.; Furukawa, M.; Horita, Z.; Langdon, T.G. Producing Superplastic Ultrafine-Grained Aluminum Alloys through Severe Plastic Deformation. In *Materials Science Forum*; Trans Tech Publications Ltd.: St. Margrethen, Switzerland, 2004; pp. 403–410.
27. Wang, Y.; Li, Y.; Yu, W.; Tang, H.; Wang, H.; Xu, G.; Wang, Z. Effect of a special thermo-mechanical treatment process on microstructure and properties of 7185 alloy. *J. Alloys Compd.* **2023**, *935*, 168072. [CrossRef]
28. Ramesh, S.; Anne, G.; Naik, G.M.; Jagadeesh, C.; Nayaka, H.S. Microstructural and mechanical characterisation of Al-Zn-Mg-Cu alloy processed by multi-directional cryo-forging. *Mater. Today Proc.* **2021**, *46*, 5752–5756. [CrossRef]
29. Liu, X.; You, X.; Liu, Z.; Nie, J.; Zhuang, Z. Molecular dynamical investigation on plastic behavior of Cu(100) twist-grain boundary under uniaxial tension. *Acta Phys. Sin.* **2009**, *58*, 1849–1856.
30. Ouyang, D.; Mao, R.; Zhang, L.; Liang, S.; Song, J. Study on the tensile properties of Al-Zn-Mg alloy based on molecular dynamics. *Eng. Fail. Anal.* **2024**, *155*, 107752. [CrossRef]
31. Yu, C.; Feng, Y.; Wang, L.; Fu, J.; Kang, F.; Zhao, S.; Guo, E.; Ma, B. Effect of pre-stretching deformation treatment process on microstructure and mechanical properties of Al-Cu-Mg alloy. *Mater. Today Commun.* **2022**, *31*, 103368. [CrossRef]

32. Briffod, F.; Bleuset, A.; Shiraiwa, T.; Enoki, M. Effect of crystallographic orientation and geometrical compatibility on fatigue crack initiation and propagation in rolled Ti-6Al-4V alloy. *Acta Mater.* **2019**, *177*, 56–67. [CrossRef]
33. Wang, W.; Wu, H.; Sun, Y.; Yan, J.; Zhang, L.; Zhang, S.; Ni, J.; Song, Y.; Zhang, X. Local intragranular misorientation accelerates corrosion in biodegradable Mg. *Acta Biomater.* **2020**, *101*, 575–585. [CrossRef]
34. Safyari, M.; Khossossi, N.; Meisel, T.; Dey, P.; Prohaska, T.; Moshtaghi, M. New insights into hydrogen trapping and embrittlement in high strength aluminum alloys. *Corros. Sci.* **2023**, *223*, 111453. [CrossRef]
35. Xiang, S.; Mo, W.; Ouyang, Z.; Deng, P.; Tan, H.; Luo, B.; Bai, Z. Effects of pre-deformation on microstructure, mechanical properties and corrosion performance of an Al-Cu-Mg-Ag alloys. *J. Alloys Compd.* **2024**, *987*, 174222. [CrossRef]
36. Chen, Y.Q.; Zhang, H.; Pan, S.P.; Song, Y.F.; Liu, X.; Liu, W.H. Effects of service environment and pre-deformation on the fatigue behaviour of 2524 aluminium alloy. *Arch. Civ. Mech. Eng.* **2019**, *20*, 5. [CrossRef]
37. Mikhaylovskaya, A.V.; Yakovtseva, O.A.; Sitkina, M.N.; Kotov, A.D. Grain-boundary and intragranular deformation in ultrafine-grained aluminum-based alloy at high strain rate. *Mater. Lett.* **2020**, *276*, 128242. [CrossRef]
38. Berecz, T.; Jenei, P.; Csóré, A.; Lábár, J.; Gubicza, J.; Szabó, P.J. Determination of dislocation density by electron backscatter diffraction and X-ray line profile analysis in ferrous lath martensite. *Mater. Charact.* **2016**, *113*, 117–124. [CrossRef]
39. Shengyu, W.; Zhu, X.; Zheng, W.; Zhou, L.I.; Ziqian, Z. Microstructure and tensile properties of industrially prepared 7050 aluminum alloy thick plate. *Nonferrous Met. Sci. Eng.* **2017**, *8*, 48–53.
40. Chen, Y.J.; Yang, Y.B.; Zhang, Z.M.; Wang, Q. Hot torsional deformation behavior of 7A04 aluminum alloy, Suxing Gongcheng Xuebao. *J. Plast. Eng.* **2018**, *25*, 167–174.
41. Yang, Q.; Deng, Z.; Zhang, Z.; Liu, Q.; Jia, Z.; Huang, G. Effects of strain rate on flow stress behavior and dynamic recrystallization mechanism of Al-Zn-Mg-Cu aluminum alloy during hot deformation. *Mater. Sci. Eng. A* **2016**, *662*, 204–213. [CrossRef]
42. Hu, J.L.; Wu, X.J.; Bo, H.; Jiao, Z.T.; Huang, S.Q.; Jin, M. Dislocation density model and microstructure of 7A85 aluminum alloy during thermal deformation. *J. Cent. South. Univ.* **2021**, *28*, 2999–3007. [CrossRef]
43. Chen, S.; Chen, K.; Peng, G.; Chen, X.; Ceng, Q. Effect of heat treatment on hot deformation behavior and microstructure evolution of 7085 aluminum alloy. *J. Alloys Compd.* **2012**, *537*, 338–345. [CrossRef]
44. Hallberg, H.; Chamanfar, A.; Nanninga, N.E. A constitutive model for the flow stress behavior and microstructure evolution in aluminum alloys under hot working conditions—With application to AA6099. *Appl. Math. Model.* **2020**, *81*, 253–262. [CrossRef]
45. Wu, H.; Wen, S.P.; Huang, H.; Wu, X.L.; Gao, K.Y.; Wang, W.; Nie, Z.R. Hot deformation behavior and constitutive equation of a new type Al–Zn–Mg–Er–Zr alloy during isothermal compression. *Mater. Sci. Eng. A* **2016**, *651*, 415–424. [CrossRef]
46. Schwarzenböck, E.; Ollivier, E.; Garner, A.; Cassell, A.; Hack, T.; Barrett, Z.; Engel, C.; Burnett, T.L.; Holroyd, N.H.; Robson, J.D. Environmental cracking performance of new generation thick plate 7000-T7x series alloys in humid air. *Corros. Sci.* **2020**, *171*, 108701. [CrossRef]
47. Hornbogen, E.; Gahr, K. Microstructure and Fatigue Crack Growth in a γ-Fe-Ni-Al Alloy. *Acta Metall.* **1976**, *24*, 581–592. [CrossRef]

Disclaimer/Publisher's Note: The statements, opinions and data contained in all publications are solely those of the individual author(s) and contributor(s) and not of MDPI and/or the editor(s). MDPI and/or the editor(s) disclaim responsibility for any injury to people or property resulting from any ideas, methods, instructions or products referred to in the content.

materials

MDPI

Article

Synergistic Effects of Deep Cryogenic and Pulsed Magnetic Field Treatments on the Microstructure and Tensile Properties of Aero-TC4 Titanium Alloy

Zhijun Ji [1,2,*], Hai Nan [1,2], Guirong Li [3,*], Shouzuo Guo [3], Yurong Ye [3], Hongming Wang [3] and Pengjie Zhou [4]

[1] AECC Beijing Institute of Aeronautical Materials, Beijing 100095, China
[2] Advanced Titanium Alloy Precision Forming Technology, Beijing 100094, China
[3] School of Materials Science & Engineering, Jiangsu University, Zhenjiang 212013, China
[4] School of Materials Science & Engineering, Jiangsu University of Science and Technology, Zhenjiang 212003, China
* Correspondence: jzjbiam@sina.com (Z.J.); liguirong@ujs.edu.cn (G.L.)

Abstract: A novel coupled processing method (PDCT) that associated deep cryogenic treatment (DCT) with a high pulsed magnetic field (PMT) was investigated to improve the performance of an as-cast TC4 aero-titanium alloy. Through XRD, SEM, TEM, EBSD, and a properties test, its microstructure and tensile properties and their relationship were investigated. The results show that in comparison with the untreated samples, in the PDCT alloys, the amount of nano-sized precipitates and dislocation density are increased, and this phenomenon is characterized by their combed dislocation morphology. The grain sizes are refined and rounded, and the deformed grains are enhanced, together with the enhancement of low-angle grain boundaries in grains and the transformation from the β phase to the α phase. The (112) crystal orientation is apparently strengthened. The tensile strength, elongation, and fracture energy of the optimized PDCT sample are 921.4 MPa, 7.6% and 5.47 × 10^7 J/m^3, which increased by 4.9%, 28.8% and 80.5% compared with the untreated sample, respectively. The tensile fracture exhibits rheological deformation along the phase boundaries. The strength–toughness mechanisms are mainly attributed to the texture, precipitation, dislocation and fine grain strengthening, which stem from the cold contraction and lattice distortion of DCT and the main magneto-plasticity effect of PMT, together with their coupling effects.

Keywords: aero-titanium alloy; deep cryogenic treatment (DCT); pulsed magnetic field (PMF); microstructures and properties

1. Introduction

The ZTC4 (as-cast Ti-6Al-4V) titanium alloy studied in this paper is an α + β type duplex titanium alloy. It has medium strength and good comprehensive properties and is the most widely used titanium alloy in aircraft [1–4]. It can be processed into plates, bars and forgings and can also be processed and prepared into castings with complex sizes by precision casting. It is widely used in aircraft and engines, such as casings and mounts in aircraft engine, as well as frames, beams and joints in aircraft, and can reduce the weight of these objects by about 30% when replacing steel.

However, there are several problems in casting using this titanium alloy at present. The first reason is that during the solidification and cooling process of the casting, casting stress

will inevitably be generated because of the different cooling rates of each part, the shrinkage resistance, and the volume change caused by the structural transformation [5]. If the casting stress is not relieved, it will remain in the casting as residual stress. Excessive residual stress in castings will cause the deformation of parts in the process of placement, operation, processing, and utilization and a serious reduction in dimensional accuracy, which will then result in cracking [6]. Secondly, the high temperature in the casting process causes coarse grains and other defects, which deteriorate the strength and toughness of the material [7]. Thirdly, as a medium-strength titanium alloy, ZTC4 titanium alloy has many advantages, such as high specific strength, good corrosion resistance, and good stability under low- and high-temperature conditions [8–11]. However, with the continuously increasing demand for titanium alloys in various high-end manufacturing industries, traditional titanium alloys appear to be a little behind. Therefore, it is necessary to explore a new method of reducing residual stress, promoting grain refinement, and improving the strength and toughness of the ZTC4 alloy to meet gradually growing needs.

Deep cryogenic treatment (DCT) is a kind of solid-state material treatment method in which the sample is placed in a low-temperature field below −150 °C, generally using liquid nitrogen as a low-temperature medium, and the microstructures and properties of the material are improved by adjusting the parameters, such as processing temperature (*T*), treatment time (*t*), cooling rate (*V*), and number of thermal cycles (*N*). At present, besides its specific utilization in chemistry and food storage [12,13], DCT has been applied to improve the properties of ferrous metals and various non-ferrous metals [14]. Li H et al. found that a large number of tiny secondary carbides were precipitated from high-vanadium steel after DCT, and the hardness, impact toughness, and abrasive resistance of the sample were improved [15]. Liu et al. found that the plasticity of HEAp/Al (a high-entropy alloy particle-reinforced Al matrix) composites after DCT for 36 h was greatly improved, and the crack propagation changed from unidirectional to bidirectional [16]. Li et al. argued that low-temperature treatment (DCT) was an effective method of improving the wear resistance and tensile properties of CoCrFeMnNi and reducing its residual stress [17]. Gu et al. studied the effect of DCT on the mechanical properties of a Ti-6Al-4V alloy for biomedical applications. The results show that the Vickers hardness of Ti-6Al-4V increased slightly with the decrease in temperature and increased significantly with the increase in immersion time at −196 °C. It was found that DCT reduced the friction coefficient of Ti-6Al-4V alloy under a 50 N load. In addition, the lower the temperature and the longer the immersion time during DCT, the smaller the friction coefficient will be [18]. Gu et al. also studied DCT alone and DCT followed by aging treatment and found that both could significantly improve the plasticity of a Ti-6Al-4V alloy. After DCT and aging treatment at 650 °C, the ductility of the alloy increased by about 22.7% [19]. M.C. Zang et al. studied the low-temperature tensile properties and deformation behavior of the metastable beta titanium alloy Ti-15Mo-2Al, which has ultra-high tensile strength and intergranular fractures caused by a strong stress concentration at the grain boundary during tension [20]. The studies of the above researchers all found that DCT played a positive role in improving the properties of the alloy.

In recent years, the pulsed magnetic field (PMF) has been introduced into the manufacturing of many new substances [21,22] or to improve material quality [23]. In particular, applying PMF to different alloys can improve the microstructure uniformity of the material, promote dislocation slip, and reduce residual stress [24]. Wang et al. reported that the application of external PMF led to the magneto-plasticity phenomenon of alloyed steel. The rotation of the magnetic domain led to the movement of the magnetic domain wall, disrupting the original balance between the region containing the magnetic domain; the grain was broken, and the change in the internal stress of the grains changed the residual stress in the material [25]. G.R. Li reported that the high-intensity pulsed magnetic field treat-

ment changed the electron spin state between dislocations and obstacles in TiAl-4822 alloy, weakened the pinning effect of obstacles on dislocations, facilitated dislocation movement, and improved the plasticity of materials [26].

In the process of material processing and preparation, it is found that the effect of associated treatment is sometimes more effective than the single treatment [27,28]. Currently, numerous studies have been conducted on the application of single cryogenic treatment and magnetic field treatment in materials science, and the theoretical study of their respective mechanisms has gradually advanced. However, only a few studies have been conducted on an associated treatment method which combines cryogenic treatment with magnetic field treatment. Akhbarizadeh et al. [29] reported that the DCT of tool steels under the action of a static magnetic field changed the distribution of carbides and improved mechanical properties.

In this study, the effects of cryogenic treatment and a high pulsed magnetic field on the microstructure and mechanical properties of the ZTC4 titanium alloy were investigated. This study aimed to optimize the technical parameters of physical field modification treatment and establish the internal relationship between different physical fields, experimental parameters, alloy microstructures, and the mechanical properties of alloys. Additionally, it aimed to explore the optimization mechanism of new technology for the synchronous improvement of strength and toughness.

2. Experimental and Procedures

2.1. Materials

The original sample of ZTC4 titanium alloy used in the experiment was obtained from the Beijing Institute of Aeronautical Materials, Beijing, China. It was cast in a vacuum consumable electrode arc furnace after melting twice. Table 1 shows the components of the ZTC4 titanium alloy. The casting was treated using a hot isostatic pressing technique by maintaining it at 920 °C for 2.5 h in a 120 MPa argon condition before being cooled to below 300 °C with the furnace in order to eliminate the casting stress and accomplish annealing.

Table 1. Components of the ZTC4 titanium alloy (wt.%).

Element	Ti	Al	V	Fe	Si	C	N	H	O
	Base	5.5~6.8	3.5~4.5	0.30	0.15	0.10	0.05	0.015	0.20

To test the mechanical properties of the ZTC4 titanium alloy, the material was processed into a standard tensile specimen through precise wire cutting (Figure 1).

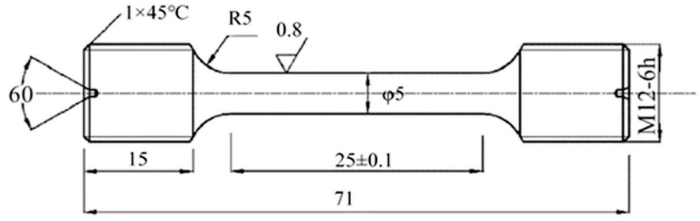


Figure 1. Schematic diagram of the tensile sample (unit: mm).

2.2. Experiment Procedure

To explore the effects of deep cryogenic treatment (DCT) and pulsed magnetic field treatment (PMT) on the mechanical properties and microstructure of ZTC4 titanium alloy, three different modification methods of ZTC4 titanium alloy were designed, as follows.

(1) Deep cryogenic treatment

The liquid DCT method was adopted, which involved direct immersion in liquid nitrogen to maintain the temperature. The used YDS-30-125 liquid nitrogen tank was produced by China Yuxin Aviation Cryogenic Container Co., Ltd., which is located in Xinxiang City, China. The experimental scheme is shown in Table 2. The samples were named according to the cryogenic treatment time (unit: hours) as untreated, DCT12, DCT24, DCT36, and DCT48. The effect of different cryogenic times on microstructure evolution and mechanical properties was investigated to determine the optimized cryogenic treatment time. The cryogenic time was selected based on previous studies [28]. During DCT processing, the ambient temperature was controlled at 25 °C through an air conditioner.

Table 2. Scheme for DCT experiments using ZTC4 titanium alloy.

Specimens	Cryogenic Temperature *T* (°C)	Cryogenic Time *t* (h)
DCT12	−196	12
DCT24	−196	24
DCT36	−196	36
DCT48	−196	48

(2) Pulsed magnetic treatment

Pulsed magnetic treatment involved placing the sample in the magnetic field coil and uniformly performing the magnetic field treatment on the sample, as shown in Figure 2. The magnetic field generator was produced by the Nanjing Advance Magnetic Components Co., Ltd., which is located in Nanjing City, China, and its type is HSK-H2060. The two most important parameters of the PMF are magnetic induction intensity (*B*) and pulse number (*N*). The differences in *B*, which lead to the deviations in pulse interval, make the characterization of the effective action time of the pulsed magnetic field challenging when using continuous time. Thus, in this experiment, *N* was used to characterize the effective action time of the magnetic field.

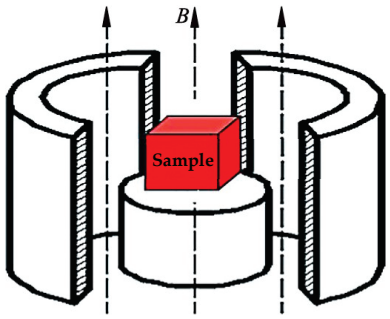


Figure 2. Schematic of the PMT apparatus.

The PMT experiment comprised two parts (Table 3); the first was to set N = 30 (in accordance with the previous optimization results). Then, B was adjusted from 2 T to 5 T, and the corresponding sample numbers were PMT2, PMT3, PMT4, and PMT5. When $B = B^*$, the effects of different magnetic field pulse numbers N (10, 20, 30 and 40) on the mechanical properties of ZTC4 titanium alloy were investigated, and the optimal pulse numbers N^* were obtained by naming the samples PMT10, PMT20, PMT30, and PMT40. Finally, according to the above two parts of the experimental results, the optimal pulse magnetic field parameters were determined. The parameters of pulse magnetic field treatment were selected according to previous studies [26]. During the PMT processing,

the input current and voltage were monitored and controlled at an exact value so as to ensure the accuracy of *B*.

Table 3. Scheme for PMT experiment.

Samples	Magnetic Induction Intensity *B* (T)	Pulses Counts *N*
Untreated	0	0
PMT2	2	30
PMT3	3	30
PMT4	4	30
PMT5	5	30
PMT20	3	20
PMT30	3	30
PMT40	3	40

(3) PDCT treatment

Building on the results of the previous two studies, the two treatment methods were combined, resulting in PDCT. This involved two steps; at first, the titanium alloy was immersed in the liquid nitrogen for the set soaking times of 12 h, 24 h, 36 h and 48 h. Afterwards, the alloy was removed and exposed to the room-temperature environment. Then, the sample at room temperature was treated with a PMF with B = 3 T, N = 30. This treatment aimed to investigate the modification effect of associated cryogenic deep treatment and magnetic field treatment on the microstructure and properties of ZTC4 titanium alloy, optimize experimental parameters, and analyze the modification mechanism under the PDCT condition.

2.3. Detection Method

An X-ray diffractometer (BRUKER D8 ADVANCE, Bruker, Germany) was used to analyze the phase, and the dislocation density was observed and calculated. The ranges of diffraction angle and scanning speed were set to 20–90°and 5°/min. Field emission scanning electron microscopy (FEI NovaNano 450, Hillsboro, OR, USA), transmission electron microscopy (JEM-2100, Akishima City, Tokyo, Japan), and an electron backscatter diffraction (EBSD) system composed of S3400 field emission scanning electron microscopy (SEM, Tokyo, Japan) and an Oxford prober (London, UK) were used to examine the microstructure evolution of the material before and after treatment, including the changes in grain size, dislocation morphology, phase evolution, and texture. The FEI NovaNano450 SEM had a resolution of 1 nm and an operated acceleration voltage of 10 kV, and the resolution and acceleration voltage of the JEM-2100 transmission electron microscopy (TEM) were 0.1 nm and 250 kV, respectively. The main parameters of EBSD were as follows: a working distance of 30 mm, an acceleration voltage of 3 kV, a beam current of 90 pA, a spatial resolution of 0.05 μm, and an angular resolution of 0.05°. MDI JADE6.5, Digital Micrograph 1.6, and OIM analysis software 8.6 were used to analyze the images or data from X-ray diffraction (XRD), TEM, and EBSD, respectively. The tensile properties of the samples were tested at room temperature using a DDL100 electronic universal testing machine(Changchun Institute of Mechanical Science Co., Ltd., Changchun City, China), and the tensile rate was 1 mm/min.

3. Results and Discussion

3.1. Performances of DCT and PMT Alloys

Table 4 shows the effect of cryogenic soaking time on the tensile properties of the ZTC4 titanium alloy, and the optimized parameter for liquid cryogenic treatment was ascertained to be 36 h.

Table 4. Tensile properties of the DCT-ed ZTC4 titanium alloy using different cryogenic times.

Samples	Cryogenic Temperature (°C)	Cryogenic Time (h)	Tensile Strength, σ_b (MPa)	Elongation, δ (%)	Remarks
Untreated	Room temperature	0	878.3	5.9	
DCT12	−196 °C	12	859.2	7.3	
DCT24	−196 °C	24	893.2	7.5	
DCT36	−196 °C	36	916.5	7.5	Best
DCT48	−196 °C	48	875.9	6.8	

Table 5 shows the tensile properties of the ZTC4 titanium alloy subject to PMT at different *B* and *N* values. The PMT caused various degrees of change in the samples compared with the untreated samples. PMT proved able to achieve simultaneous improvement in strength and toughness, with a more significant effect in the *B* = 3 T, *N* = 30 samples. The ultimate tensile strength and elongation of the sample were 912.5 MPa and 7.3%, showing an increase of 3.9% and 23.7%, respectively, compared with the untreated sample. Therefore, *B* = 3 T and *N* = 30 were the optimal parameters for PMT processing.

Table 5. Mechanical properties of the PMT-ed ZTC4 titanium alloy.

Samples	Magnetic Induction Intensity, *B* (T)	Pulse Count *N*	Tensile Strength, σ_b (MPa)	Elongation, δ (%)	Remarks
Untreated	/	/	878.3	5.9	
PMT2	2	30	901.6	6.6	
PMT3	3	30	912.5	7.3	Best *B*
PMT4	4	30	910.4	7.1	
PMT5	5	30	897.1	6.9	
PMT20	3	20	901.9	7.2	
PMT30	3	30	912.5	7.3	Best *N*
PMT40	3	40	899.3	6.9	

3.2. Microstructure and Performance of PDCT Alloys

The collaborative processing method was as follows. DCT was processed for 12 h, 24 h, 36 h and 48 h; then, PMF processing with *N* = 30 and *B* = 3 T was performed. The collaborative processing method was abbreviated to PDCT12, PDCT24, PDCT36 and PDCT48 for each sample.

Figure 3 shows the SEM microstructure (8000×) of PDCT alloys with different DCT times. As shown in Figure 3a, the untreated ZTC4 alloy mainly consisted of a long-stripe α phase with a black color and a needle-like β phase with a white color. No noticeable precipitates were observed in the α phase, and the orientation of the β phase was chaotic.

In the PDCT12 sample (Figure 3b), the grains exhibited orientation characteristics, and small nanoscale precipitates were observed in the α phase. The β phases of PDCT24 and PDCT36 samples exhibited sheet-like morphology, and their height gradually increased along the vertical direction, thus preventing crack propagation under external tensile stress, which was more evident, as shown in Figure 3d. Meanwhile, numerous nanometer precipitates were observed among α phase in the PDCT36 sample. In contrast, the orientation of PDCT48 (Figure 3e) was pronounced, but the small precipitates were not clearly visible. This phenomenon indicates that prolonged DCT is not beneficial for the precipitation process due to stable energy and stress conditions.

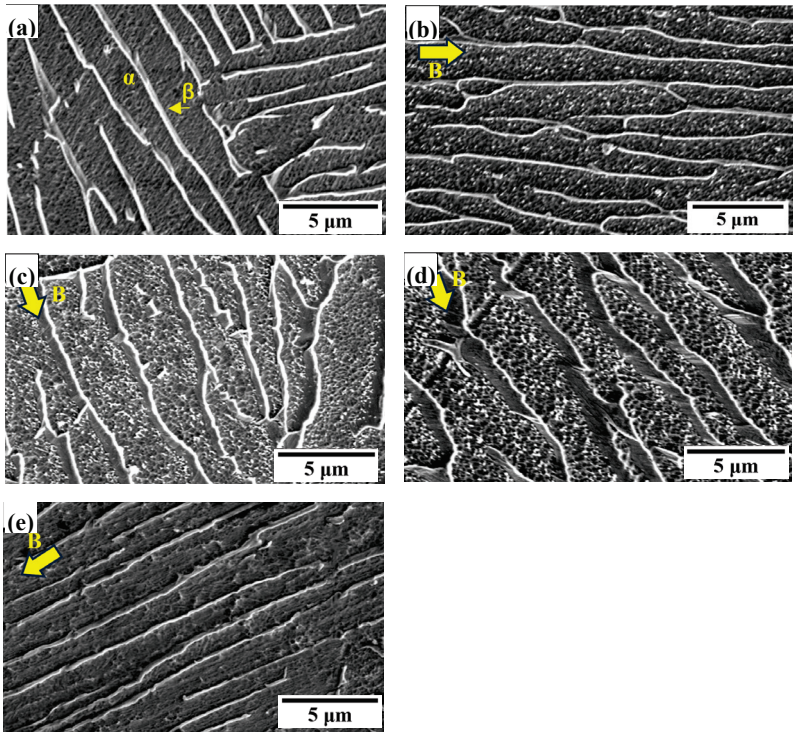


Figure 3. SEM images of PDCT samples with different cryogenic times (8000×). (**a**) Untreated sample; (**b**) PDCT12; (**c**) PDCT24; (**d**) PDCT36; and (**e**) PDCT48.

Generally, the microstructure of PDCT alloys exhibited the following typical characteristics: first, the number of nano-scale precipitates among the α phase in the PDCT12, PDCT24 (Figure 3c), and PDCT36 samples significantly increased. Second, the morphology of the coarse elongated α phase exhibited the orientation characteristics along the magnetic field direction, as represented by the yellow arrows. Third, the height of the β-phase increased along the vertical direction, which was more pronounced in the optimized PDCT36 sample.

Table 6 shows the comprehensive mechanical properties of the PDCT alloy with different cryogenic times. To ensure the reliability and accuracy of properties, three samples were prepared and processed in the same conditions, resulting in three PDCT12 samples with three corresponding tensile properties. The average property value and standard deviations were calculated based on the three samples.

Table 6. Mechanical properties of PDCT samples with different cryogenic times.

Samples	Tensile Strength (MPa)	Standard Deviations (SD) of Tensile Strength (MPa)	Elongation (%)	SD of Elongation	Fracture Energy (J/m^3)	SD of Fracture Energy (J/m^3)
Untreated	878.3	2.1	5.9	0.3	3.03×10^7	0.09×10^7
PDCT12	884.4	1.7	7.6	0.1	4.91×10^7	0.11×10^7
PDCT24	910.5	1.6	7.4	0.1	4.81×10^7	0.08×10^7
PDCT36	921.4	1.7	7.6	0.2	5.47×10^7	0.12×10^7
PDCT48	886.1	2.0	6.7	0.1	3.93×10^7	0.11×10^7
Average of PDCT samples (AVE)	900.6	/	7.3	/	4.78×10^7	/
AVE vs. Untreated	Increase of 2.5%	/	Increase of 23.7%	/	/	Increase of 57.8%

Figure 4a shows the tensile stress–strain curve, and Figure 4b,c show the changes in tensile strength, elongation and fracture energy. Notably, the tensile strength and elongation of PDCT36 were 921.4 MPa and 7.6%, which were 4.9% and 28.8% higher than those of the

untreated sample, respectively. The mechanical properties were also superior to those of optimized DCT (soaking for 36 h) or PMF (B = 3 T, N = 30) samples.

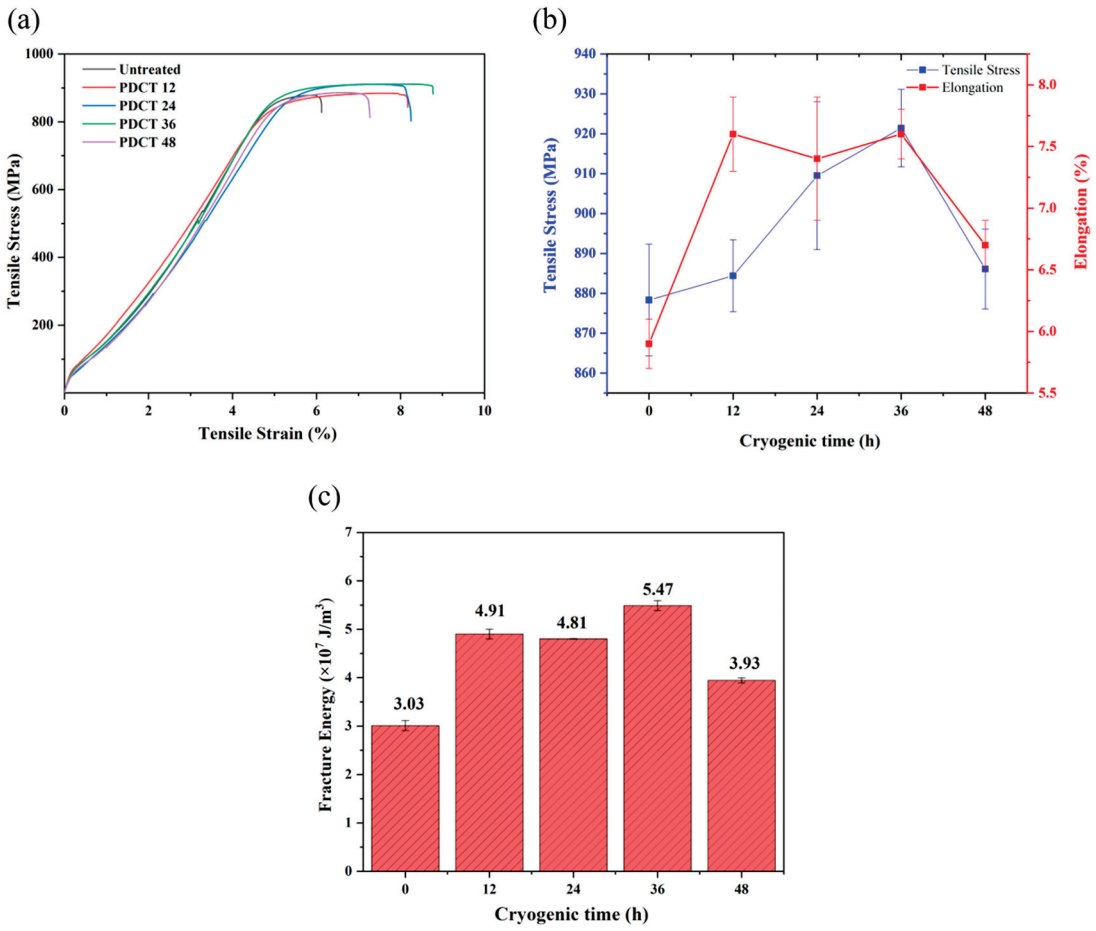


Figure 4. Mechanical properties of PDCT alloy with different cryogenic times. (**a**) Stress–strain curve; (**b**) tensile strength and elongation; and (**c**) fracture energy.

The analysis of the PDCT effect revealed that all the tensile strengths of four PDCT alloys were higher than that of the untreated sample. When the processing time increased from 0 h to 36 h, the tensile strength increased, reached a maximum value at 36 h, and decreased after 48 h. Regarding the change in fracture absorption energy, all the PDCT alloys of fracture absorption energy were superior to that of the untreated sample on the whole. The PDCT36 sample had the highest value of 5.47 × 10^7 J/m^3, which was 81% more than that of the untreated sample.

The Schmid factor was introduced to investigate the strength characteristic. Figure 5 shows the change and distribution statistics of the Schmid factor before and after PDCT. Figure 5a,c show the distributions of Schmid factors before and after PDCT. The whole Schmid factor of the untreated sample was generally large, with values above 0.3 in most areas. In contrast, the Schmid factor decreased significantly after PDCT processing. According to the statistical results in Figure 5b,d, the Schmid factor of the untreated sample was 0.3465, mainly distributed in the range of 0.35–0.5. The average Schmid factor of PDCT36 was 0.3141 and mainly distributed in the range of 0.3–0.4.

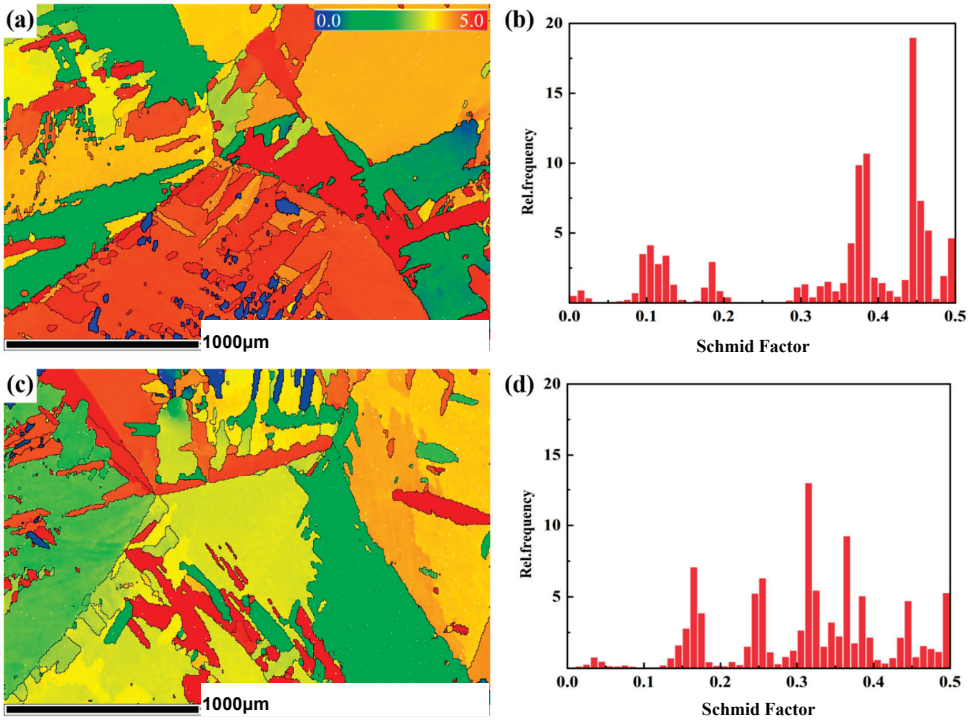


Figure 5. Schmid factor (SF) distribution before and after PDCT: (**a**) SF distribution before PDCT; (**b**) distribution histogram before PDCT; (**c**) SF distribution after PDCT; and (**d**) distribution histogram after PDCT.

The relationship between the Schmid factor and critical shear stress τ_c can be expressed as in Equation (1).

$$\tau_c = \frac{F}{A}\cos\lambda \cdot \cos\varphi \quad (1)$$

where φ represents the angle between the axial stress (F) and the normal of the glide plane whose square is A, and λ stands for the angle between the force axis and the glide direction. The Schmid factor is defined as $\cos\lambda \cdot \cos\varphi$. Because the critical shear stress τ_c is an inherent property of the material, the magnitude of the Schmid factor $\cos\lambda \cdot \cos\varphi$ will affect the magnitude of the axial stress (F). When the shear stress along the slip direction reaches the critical value, the slip occurs between crystal planes, corresponding to the macroscopic yield limit.

Figure 6 shows the tensile fracture of the PDCT sample under SEM. Compared with the untreated sample in Figure 6a, the PDCT sample had noticeable dimples, which are represented by red dashed lines in Figure 6b,d. Figure 6c,d show the rheological characteristics (yellow dashed lines) in the PDCT samples. The fracture surface of PDCT enhanced the toughness and rheological properties of the alloy and supported the performance characteristics in terms of strength and toughness.

In contrast to brittle fracture, ductile fracture was characterized by several features: large energy absorption before actual fracture, large deformation at a certain strain rate, rheological characteristics of metal elongation before fracture, and ductile dimples. According to the characteristics of the elongated microstructure in Figure 6, the alloy deformed along the nano-scaled elongated phase and the phase interface under the action of external forces. The rheological deformation occurred along the phase boundary before reaching the fracture limit. The analysis results showed that as the temperature and cryogenic time decrease and increase, respectively, the lattice distortion will be intensified, and the

growth of the precipitated phase will lead to the failure of the fracture originating from the grain interior.

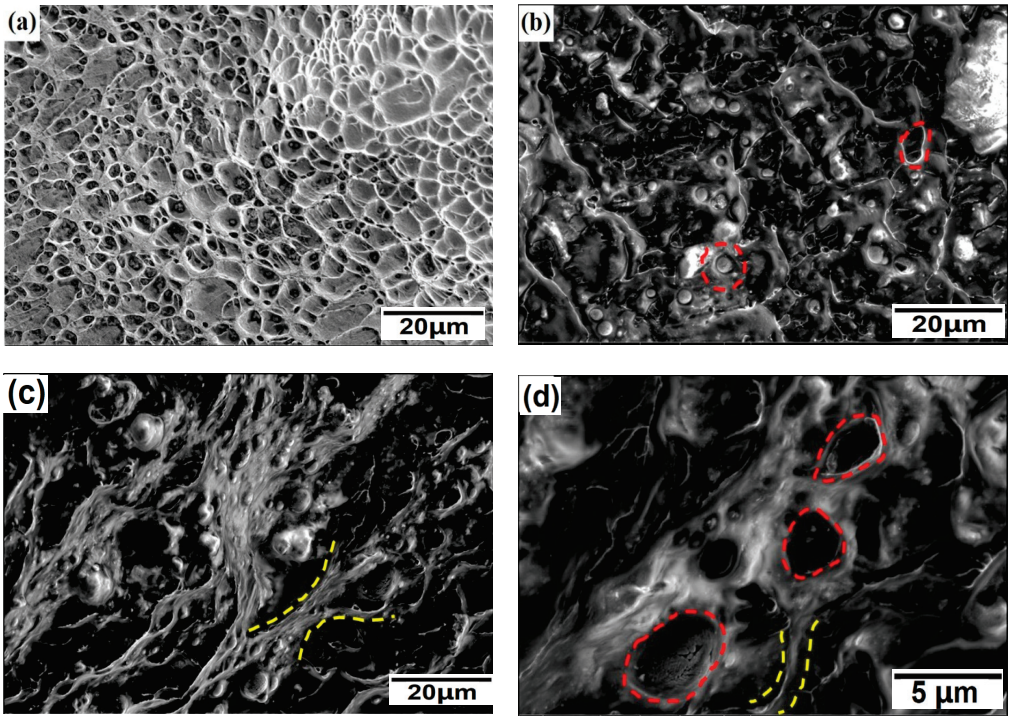


Figure 6. The morphology of the fracture surface for untreated and PDCT samples. (**a**) Untreated sample; (**b**) dimples in PDCT36; (**c**) rheology in PDCT36; and (**d**) magnified dimples and rheology in PDCT36.

3.3. Mechanism Analysis

3.3.1. Structure and Texture

Figure 7 shows the X-ray diffraction pattern of the ZTC4 titanium alloy treated by PDCT with different cryogenic times. The peak intensity (*I*) before and after PDCT is shown in Table 7.

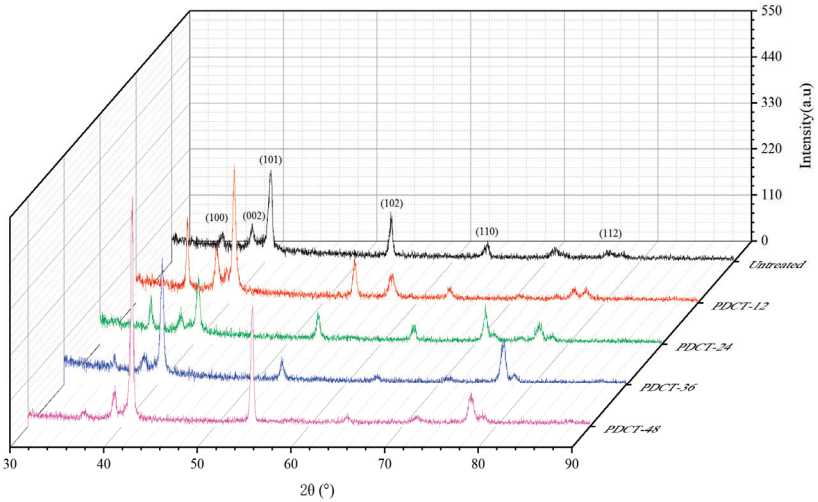


Figure 7. Effect of cryogenic time on the XRD diagram of the PDCT alloy.

Table 7. The relative peak intensities (*I*) of the main strong peaks before and after PDCT.

I (%)	(100)	(002)	(101)	(102)	(112)
Untreated	17.2	25.9	100.0 *	48.9	8.0
PDCT12	58.6	30.2	100.0	32.1	7.1
PDCT24	62.6	27.0	100.0	49.6	32.2
PDCT36	10.7	11.9	100.0	17.7	37.4
PDCT48	2.1	6.6	100.0	33.3	7.1

Note: * The intensity of the strongest (101) peak is set to 100%. The peak intensities of other peaks are calculated on the basis of this and are therefore named relative peaks.

The grain orientations of the PDCT alloys significantly changed apparently. The three strongest peaks of the untreated sample corresponded to the (002), (101), and (102) diffraction peaks, among which (101) was the main peak. The three strongest diffraction peaks of PDCT12 and PDCT24 were (100), (101) and (102), respectively. For the PDCT36 and PDCT48 samples, the three strongest diffraction peaks were transferred to the (101), (102) and (112) crystal planes, and the overall intensity significantly decreased.

The texture coefficient was used to analyze the grain orientation change and grain rotation effect. The formula for calculating the texture coefficient of each diffraction intensity peak can be calculated through Equation (2).

$$T_C(hkl) = \frac{I_i(hkl)/I_0(hkl)}{\sum_{i=1}^{n}[I_i(hkl)/I_0(hkl)]} \times 100\% \quad (2)$$

where T_C (*hkl*) represents the texture coefficient; I_i(*hkl*) is the actual measurement of the peak intensity; I_0(*hkl*) is the peak intensity of the standard crystal face in the PDF card; and *n* represents the number of diffraction peaks. The calculated results are shown in Table 8.

Table 8. The T_C (*hkl*) of main crystal planes for PDCT alloys with different cryogenic times (unit: %).

Samples	T_C (100)	T_C (002)	T_C (101)	T_C (102)	T_C (112)
PDCT12	45.87	16.38	14.05	9.22	12.47
PDCT24	33.95	9.72	9.33	9.46	37.54
PDCT36	8.74	6.45	14.05	5.08	65.67
PDCT48	4.15	8.65	33.95	23.12	30.13
Untreated	47.64	13.68	18.03	10.98	12.31
Average of PDCT samples (AVE)	23.67	10.31	17.85	11.72	36.45
AVE. vs. Untreated	Decrease of 48.1%	Decrease of 11.8%	Almost unchanged	Almost unchanged	Increase of 196.1%

The texture coefficient of PDCT samples changed with different cryogenic times. First, the T_C (*hkl*) of the (100) crystal surface of the ZTC4 sample continued to decrease. The average texture coefficient of four PDCT samples significantly decreased by 48.1% in comparison to the untreated sample. The average texture coefficient of (002) crystal was 11.8% lower than that of the untreated sample. Secondly, the average texture coefficients of the (101) and (102) crystal plane slightly changed. Third, the (112) texture coefficient gradually increased with the processing time and reached a maximum in the PDCT36 sample. Overall, the PDCT weakened the grain orientation in the direction of (100) and (002) but strengthened the grain orientation in the direction of (112), indicating that PDCT treatment promoted grain rotation and orientation, causing some of the grains in the direction of (100) and (002) to be deflected to the direction of (112).

To reveal the effect of PDCT on the texture characteristic, the pole and inverse pole figures were tested, as shown in Figure 8. The result revealed the pole figures and inverse

pole figures before and after PDCT. High pole density texture caused mechanical anisotropy in the performance of samples because there was a high-density texture in the alloy; thus, the ease of achieving the slip systems required for the initiation of deformation in a certain direction during plastic deformation was different. As a result, differences were observed in the strength and plasticity of the alloy in various directions.

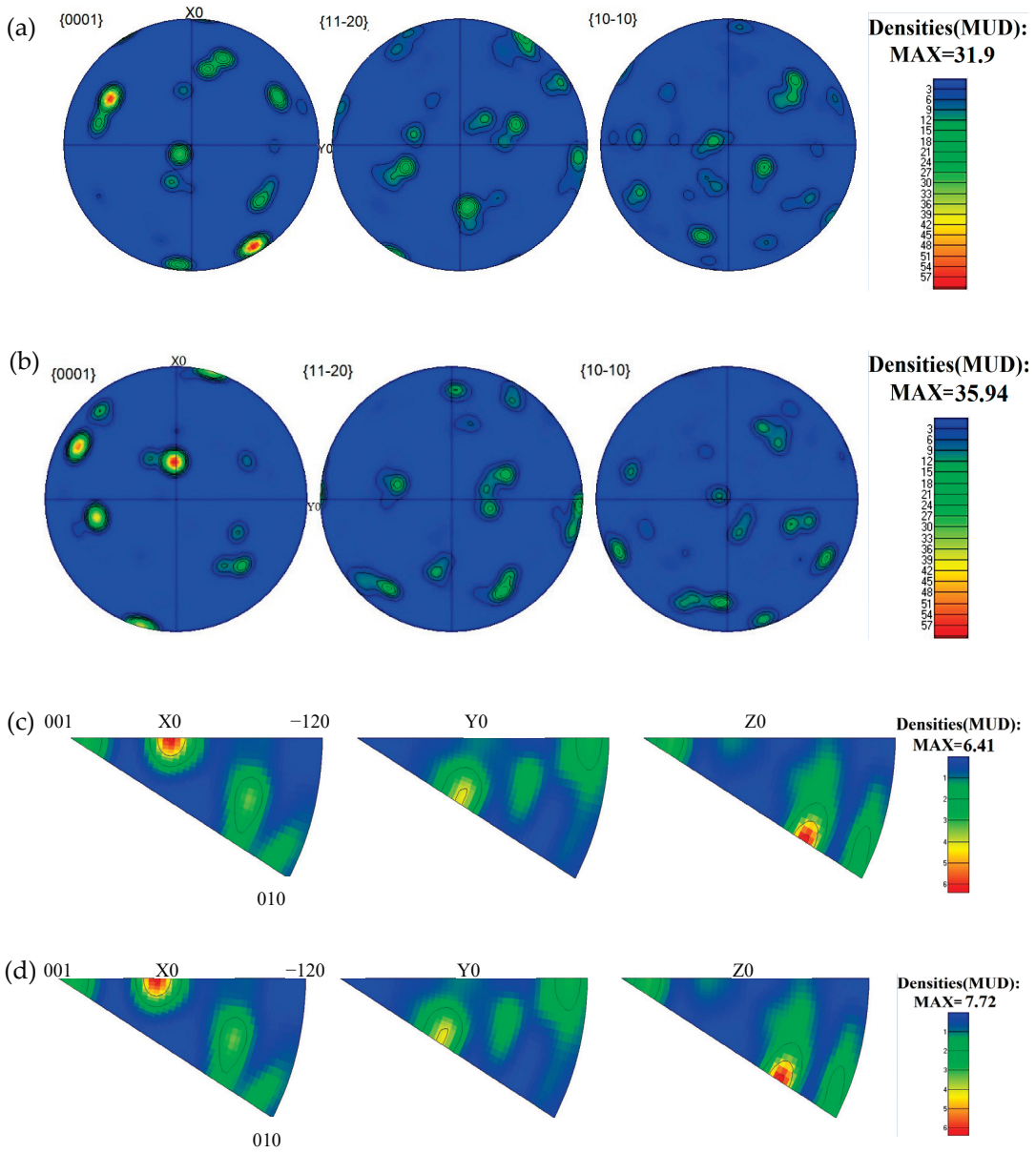


Figure 8. Polar figures of untreated and PDCT samples. (**a**) Polar plot of untreated sample. (**b**) Polar plot of PDCT36 sample. (**c**) Inverse polar plot of untreated sample. (**d**) Inverse polar plot of PDCT36 sample.

In the pole figures (Figure 8a), the highest strength of the untreated sample was 31.90. After the sample was subjected to PDCT (Figure 8b), the highest strength was 35.94. The plate texture orientation was insignificant. In the inverse pole figure, the PDCT-ed ZTC4 titanium alloy shifted towards (010) in the X0 direction, and the highest strength of the untreated sample's inverse pole figure was 6.41 (Figure 8c), while after the sample was subjected to PDCT, the highest strength was 7.72 (Figure 8d). The more significant the maximum value of pole density strength, the more pronounced the preferred crystal

orientations. The (001) and (−120) directions of some grains in the untreated sample were parallel to the X0 direction of the sample coordinate system, and after PDCT, they shifted towards the (001) and (010) directions. The preferred orientations appeared in these two directions.

3.3.2. Dislocation Strengthening

Firstly, the morphology of dislocation was focused. Figure 9 shows the dislocation morphology and characteristic phases in the untreated and PDCT samples. Dislocation lines in the untreated sample were few and irregular, which was revealed by the red dotted line (Figure 9a). After PDCT, the dislocation lines in the sample significantly increased, indicating the enhancement of dislocation density (Figure 9b). The high-density dislocation area can act as an obstacle for grains to slip. The dislocation lines in local areas were regular, as shown in Figure 9b,c. These regular lines are a typical structural feature of alloys treated with pulsed magnetic fields, which enhance the mobility of dislocations and the ability to overcome obstacles, thus improving plastic deformation ability.

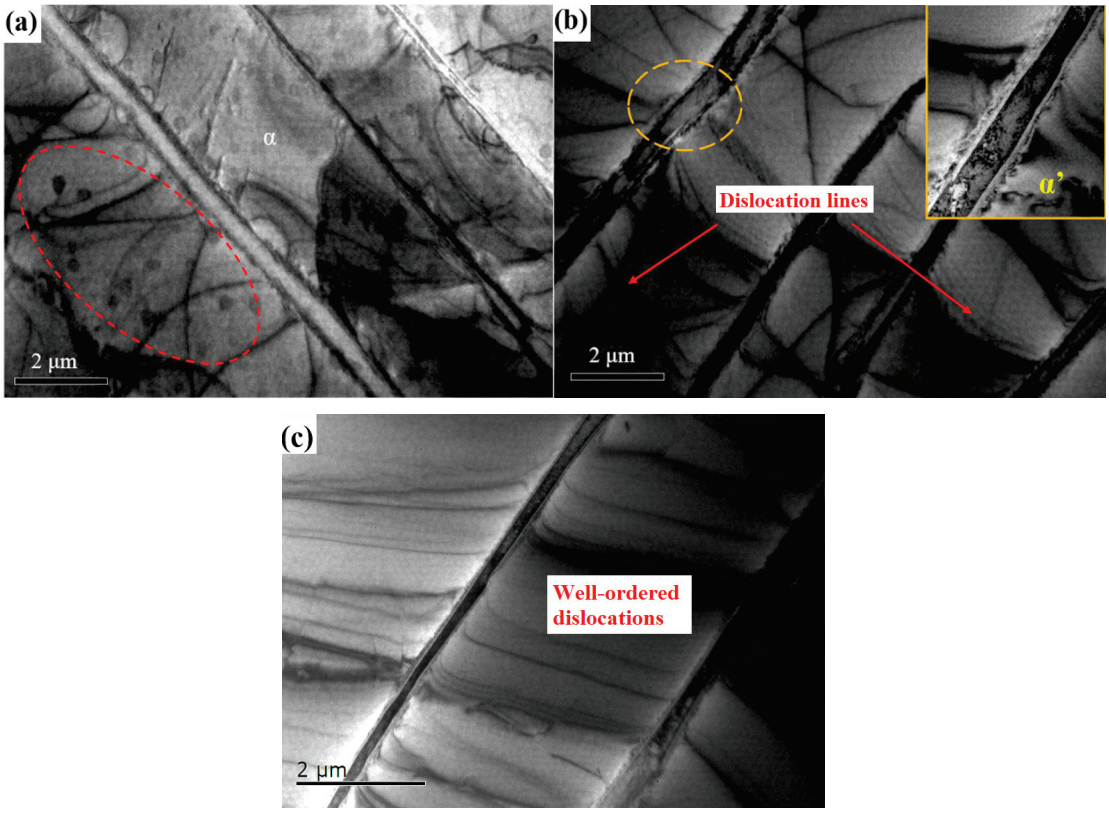


Figure 9. Dislocation characteristic of samples in untreated and PDCT samples. (**a**) Untreated sample; (**b**) proliferative dislocation lines in PDCT36; (**c**) well-ordered dislocations in PDCT36.

Then, the full width at half maximum (FWHM, short writing L) was introduced to quantificationally characterize the dislocation density. Table 9 shows the L values of alloy before and after PDCT treatment. The values in Lines 2–6 are the original data. Combined with the preferred orientation index T_C (hkl) (Table 8), the average FWHM value of the alloy (L_{ave}) can be calculated using Equation (3):

$$L_{ave} = \Sigma L(hkl) \cdot T_c(hkl) \quad (3)$$

As the cryogenic time increased, the dislocation density initially increased and then decreased. The inflection point was 36 h of cryogenic time. The L_{ave} of ZTC4 peaked at PDCT36, indicating the enhancement of dislocation density.

Table 9. The FWHM of alloy before and after PDCT treatment.

Samples	*L*(100)	*L*(002)	*L*(101)	*L*(102)	*L*(112)	L_{ave}
Untreated	0.34	0.39	0.41	0.39	0.45	1.98
PDCT12	0.27	0.38	0.35	0.43	0.56	1.98
PDCT24	0.27	0.39	0.39	0.46	0.54	2.04
PDCT36	0.39	0.42	0.38	0.42	0.49	2.11
PDCT48	0.43	0.38	0.30	0.33	0.53	1.97

The PDCT processing significantly increased the dislocation density. During the PDCT process, the cast TC4 titanium alloy with a surface area of 1 cm^2 was subjected to approximately two tons of pressure. The enormous internal stress distorted the crystal lattice and induced dislocations. At the same time, due to the entanglement and pinning of these dislocations, the strength and toughness of the titanium alloy were improved.

Due to the important effects of the geometrically necessary dislocation (GND), the density (ρ^{GND}) of the alloy was calculated based on EBSD results. A certain conversion relationship was observed between the average local orientation difference (KAM_{av}) and the geometrically necessary dislocation density (ρ^{GND}), as expressed in Equation (4) [30].

$$\rho^{GND} = \frac{2KAM_{av}}{\mu b} \tag{4}$$

where "μ" is the scanning step size, "b" represents the Burgers vector, and the *KAM* means the local orientation difference. The average *KAM* (KAM_{av}) can reflect the degree of plastic deformation uniformity, with a higher value indicating greater plastic deformation or higher defect density. Equation (4) can be used to calculate the relative magnitude of geometric dislocation density to determine the stress level during the deformation process.

Figure 10 reveals the *KAM* diagram and distribution histogram before and after PDCT. Figure 10a,c show the *KAM* distribution maps, where the blue regions represent areas with low local orientation differences and the green regions represent areas with high local orientation differences. Zhang reported that the accumulation of geometrically necessary dislocations at grain boundaries was due to the uneven micro-strain [31].

The greater the difference in local orientation, the higher the cumulative degree of local deformation within the material, resulting in a larger amount of stored deformation energy and a higher geometric density of dislocations (ρ^{GND}). After the samples were subjected to PDCT, regions with high local orientation differences exhibited a greater overlap with small-angle grain boundaries, providing further evidence for an increase in dislocation density within these localized areas (i.e., dislocation pile-up zones).

Figure 10b,d present the statistical results of the average local orientation difference for the untreated and PDCT samples. Most KAM_{av} values for both samples fall within the range of 0°–1°. The KAM_{av} of the untreated sample was 0.6087 and decreased to 0.4619 in PDCT36. Although the KAM_{av} of the PDCT36 sample decreased, some local areas had high *KAM* values, represented by a bright green color, as shown in Figure 10c. This phenomenon, marked by the concentration of local orientation difference, corresponds to an increase in the geometric density of dislocations within certain regions.

The grain orientation spread (GOS) of the cross-section of untreated and PDCT samples was studied, as shown in Figure 11. The GOS diagram is regarded as a measurement of

dislocation density and strain in a single grain. Its average value is a quantitative estimate of the orientation deviation within the grain, mainly reflecting some grains with large deformation. The color bar is displayed in the upper right location of Figure 11a. The region with a small GOS indicates a more uniform strain distribution, while a large GOS represents a higher dislocation density, which may be caused by dislocation plugging. The red part in the upper right corner of Figure 11b shows the region with the highest GOS value compared with other grains, which is close to 5.0. This value shows that the average orientation difference in this grain is large, indicating a higher dislocation density and higher strain.

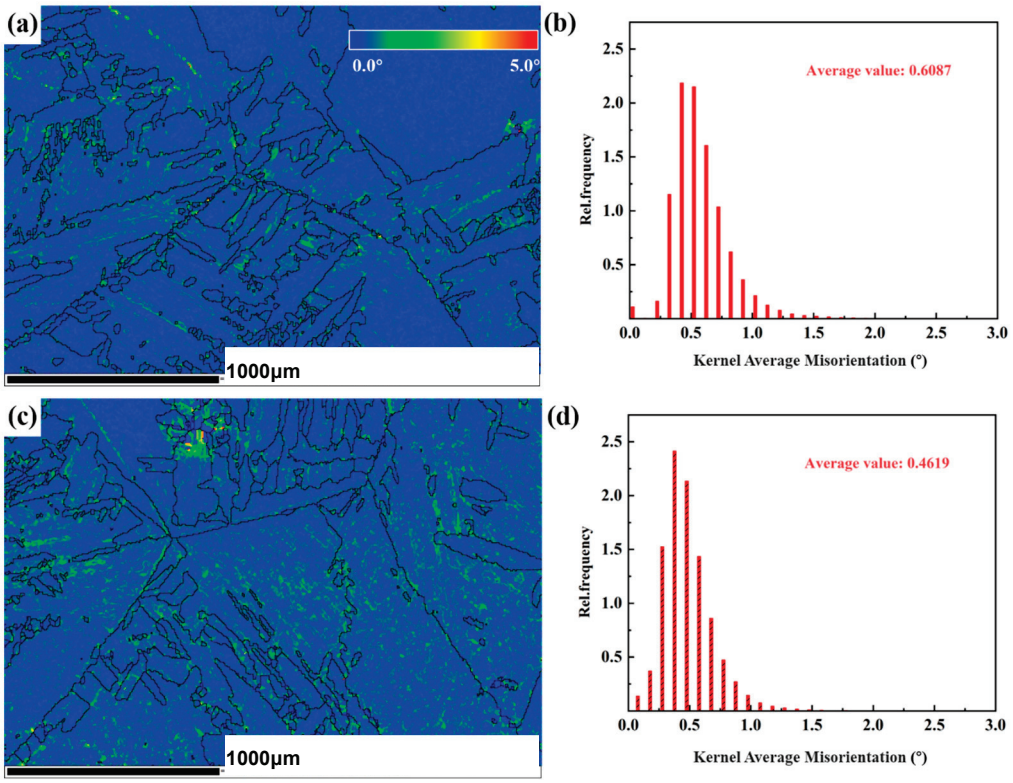


Figure 10. *KAM* diagram and distribution histogram before and after PDCT. (**a**) *KAM* of the untreated sample; (**b**) *KAM* distribution of the untreated sample; (**c**) *KAM* of PDCT36; and (**d**) *KAM* distribution of PDCT36.

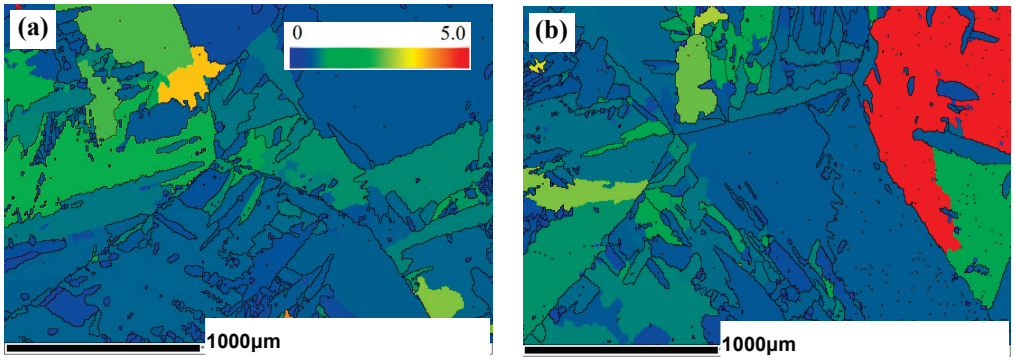


Figure 11. GOS before and after PDCT. (**a**) Untreated; (**b**) PDCT36.

The high-resolution TEM used to examine the dislocation characteristic in typical samples. Figure 12 shows the high-resolution IFFT (inverse fast Fourier transform) images

of the untreated and PDCT samples. The T symbols refer to the dislocation location. The yellow dotted line in Figure 12c meant an apparent deforming line. The corresponding average lattice spacings were 0.2494 nm and 0.2017 nm, respectively. The decrease in the lattice spacing implies a stronger interaction between atoms or ions in the crystal, which improves physical properties.

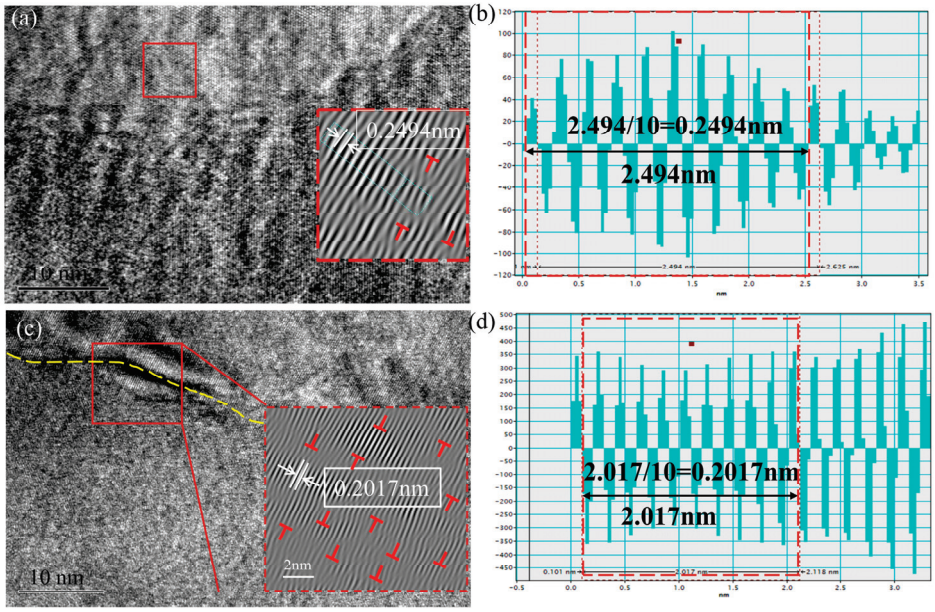


Figure 12. IFFT images of high-resolution and lattice spacing of untreated and PDCT samples; (**a**) high-resolution image of untreated sample; (**b**) lattice spacing of untreated sample; (**c**) high-resolution image of PDCT36 sample; (**d**) lattice spacing of PDCT36 sample.

3.3.3. Precipitation Strengthening

As shown in Figure 13, some secondary phases appeared along the phase interface between α and β in the PDCT sample. The α'secondary phase appeared at the β edge, demonstrating the transition from β to α. Therefore, the α lath was thickened after PDCT, which was also considered to be the result of the incomplete phase transition promoted by PDCT. The secondary α′ phase was short and rod-like at the micro and nanoscale (as shown by the yellow lines in Figure 9b). As shown in Figure 9a, there were a few second precipitates in the untreated sample.

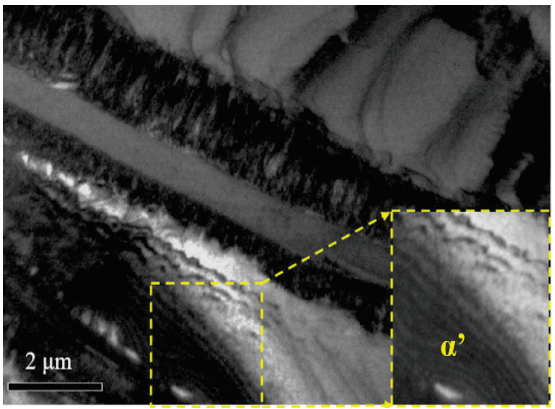


Figure 13. Precipitations in the PDCT alloy.

Because the secondary α′ phase mainly appeared at the grain boundary, the types and orientations of the grain boundaries of the untreated and PDCT samples were investigated, as shown in Figure 14. The black lines represent high-angle grain boundaries (HAGBs), while the green lines represent low-angle grain boundaries (LAGBs) whose misorientation angle (MA) is less than 10°. The black HAGBs were the main component in the two typical samples. In the untreated sample, the green LAGBs were initially preferentially distributed at the grain boundaries (Figure 14a).

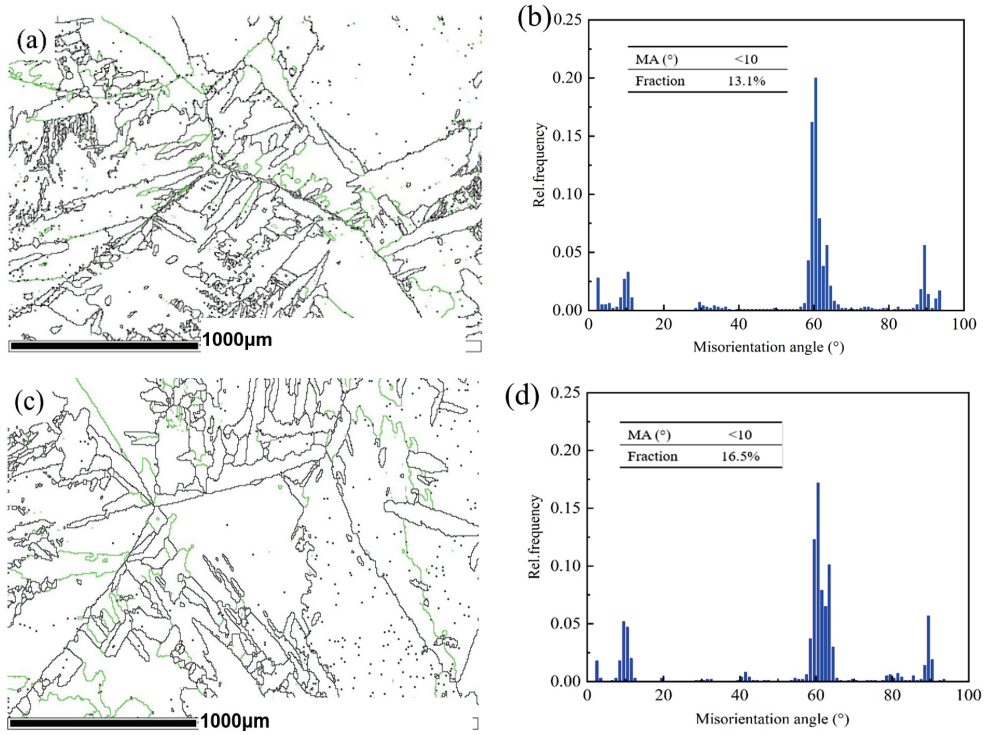


Figure 14. Type and orientations of grain boundaries (GB) in untreated and PDCT36 samples: (**a**) GB type of untreated sample; (**b**) GB orientations of untreated sample; (**c**) GB type of PDCT36 sample; (**d**) GB orientations of PDCT36 sample.

As shown in Figure 14b,d, the percentage of LAGBs in the untreated sample was 13.1%, while the percentage of those in PDCT36 increased to 16.5%. SEM microstructure analysis revealed that the phase transformation occurred from the β phase to the α′ phase in some locations where the grain boundaries were less than 10° during the PDCT. The driving energy of phase transformation in the LAGB area was the energy stored in the internally accumulated dislocations. In addition, because of the Burgers orientation relationship between the β and α phases, a single β phase can be transformed into twelve different α variants [32]. This transformation means that various selections will occur during the PDCT process, resulting in the precipitation of many secondary α′ phases with small-angle grain boundaries on both sides of the α and β grain boundaries.

3.3.4. Fine Grain Strengthening

We initially focus on the grain type in typical TC4 titanium alloys (Figure 15). As shown in Figure 15a,b, the blue, yellow, and red regions represent recrystallized grains, sub-grains, and deformed grains, respectively. Figure 15c,d show the proportion of different grains. After PDCT treatment for 36 h, the recrystallized grains of the samples were reduced from 12.5% to 4.9% and transformed into sub-grains (increasing from 85.8% to 88.5%) or deformed crystals (increasing from 1.3% to 6.6%). The percentage of sub-grains

and deformed grains increased by 2.7% and 5.3% in PDCT36 compared with the untreated sample. This phenomenon indicates that PDCT treatment promotes the nucleation and growth of sub-grain structures, mainly through aggregation at grain boundaries or phase boundaries, transforming into small-sized sub-grains driven by high-density dislocation.

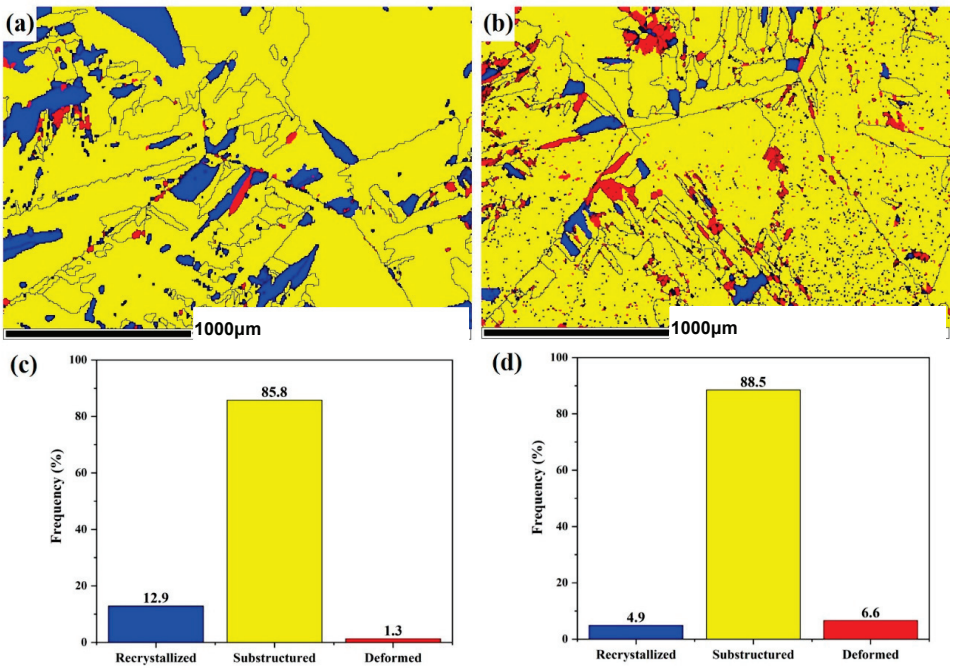


Figure 15. Comparison of grain morphology and type changes before and after PDCT. (**a**) Grain morphology of untreated sample; (**b**) grain morphology of PDCT36 sample; (**c**) grain type of untreated sample; (**d**) grain type of PDCT36 sample.

The enhancement of deformed grains indicates that the microplastic deformation of ZTC4 alloy samples is induced under the cryogenic condition and PMF. Liu et al. used the Volterra dislocation model of the continuum to calculate the strain energy of edge dislocation under the influence of the external magnetic field by applying elastic theory and electrodynamics theories. The results showed that the strain energy of paramagnetic edge dislocation increased with an increase in magnetic field [33]. The increase in dislocation energy affected the dislocation unpinning, resulting in plastic deformation. The growth of deformed grains indicated that the PDCT sample was subjected to micro-plastic deformation, and some deformed grains reached detectable size, indicating that the PDCT alloy exhibited a significant "magneto-plastic" effect. Due to the other causes of plastic deformation, the magneto-plastic effect varied with crystal orientation. The magnetic field reduced the micro-strain around dislocation lines, which was induced by the cold contraction stress field, making dislocations easier to move. This process increased the slip line spacing and the complete deformation of the alloy [34,35].

We now focus on the distribution of grain size before and after PDCT (Figure 16). After the sample was subjected to PDCT, the average grain size decreased from 58.84 μm to 56.01 μm. The general trend of grain size reduction shifted from the columnar distribution to the left, and the number of grains larger than 100 μm in diameter significantly decreased. When the grain size was smaller, the grain boundary area became larger. Nucleation at grain boundaries was more likely to occur during solid-phase transformation because of the high energy of the grain boundaries and the significant activity of atoms. The increase in the number of grain boundaries with the refinement of grains enhanced the nucleation

rate, facilitating the generation of the precipitated phase to a certain extent. The overall grain size refinement means the simultaneous improvement of strength and toughness at the macro level.

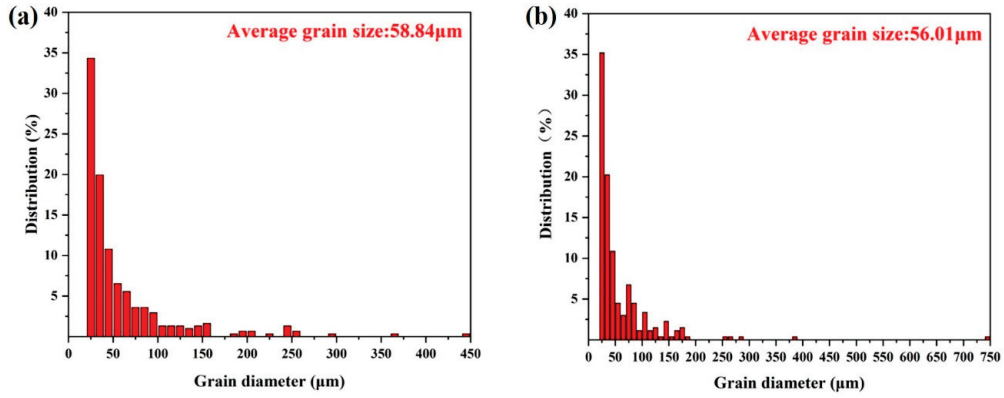


Figure 16. Grain size distribution before and after PDCT: (**a**) untreated sample; (**b**) PDCT36 sample.

3.3.5. Discussion

Overall, the combination of cryogenic treatment and magnetic field treatment effectively improved the tensile properties. The main factors contributing to the strengthening and toughening mechanism are summarized as follows: (1) optimized morphology of α and β phase; (2) preferred grain orientation along (112); (3) high-density dislocation and compact lattice spacing; (4) nano-sized and uniformly distributed precipitates; and (5) dominant sub-grains and deformed grains together with grain refinement. Table 10 summarizes the main microstructural characteristics and performance of the untreated and optimized PDCT36. The corresponding strengthening and toughening mechanism can be found in the right column.

Table 10. Summary and comparison of main microstructural characteristics and performance.

Items	Untreated	PDCT36	Mechanism
Precipitates within the α phase	none	Massive nano-sized precipitates	Precipitation strengthening
α morphology	Random	Complete and orientated	α phase strengthening
β morphology	Striped	Vertical preference growing	β phase strengthening
Grain type	More recrystallized grains	Sub-grains and deformed grains increase	Fine-grain strengthening
Grain size	58.84 μm	56.00 μm	Fine-grain strengthening
Grain boundary	HGAB occupies	LGAB occupies	Dislocation strengthening Precipitation strengthening
Dislocation density	Low	High	Dislocation strengthening
KAM	0.61	0.46	Decrease in average while increase in local areas
Lattice spacing	2.494 nm	2.017 nm	Fine-grain strengthening
Texture	Orientated planes are (100) and (002)	Orientated planes are (112)	Texture strengthening
Schmid factor	0.3465	0.3141	Yield strength increases
Residual stress	−577 MPa	−480.3 MPa	Stability increase

The combined effects of cryogenic treatment and PMF are analyzed as follows.

First, the cryogenic treatment resulted in cold shrinkage stress and lattice distortion. The changes in the grain accelerated the moving ability of dislocation, leading to dislocation plugging and increased dislocation density. Under the continuous effect of cold shrinkage force, the dislocation moved in the polycrystal, and the grain near the grain boundary increased the slip resistance due to differences in local orientation. As a result, dislocation movement was hindered, making it difficult for dislocations to cross grain boundaries, leading to their accumulation at the boundaries. The high-density dislocation formed entanglements, increasing strength through the dislocation-strengthening mechanism.

After cryogenic treatment, the dislocations that accumulated at grain boundaries formed a dislocation wall. In the subsequent magnetic field treatment, the magnetic field facilitated the release of stress that improved the transformation of recrystallized grains existing in the as-cast alloy. At this point, the dislocation at the grain boundary began to diffuse at a high speed. Some unstable dislocations were released during the diffusion process, rearranging to form a large angle orientation, that is, forming a small sub-structured grain. Figure 15b shows some fine grains. As shown in Figure 15d, the percentage of sub-structured grains increased from 85.8% in the untreated sample to 88.5% in the PDCT sample. The whole grain size reduced from 58.84 μm to 56.00 μm. According to the Hall–Petch equation, the refined grains imparted higher strength to the material [36]. The grain refinement significantly reduced the impurity content of unit grain boundary area segregation. Meanwhile, during the process of magnetic field treatment, the magnetic field reduced stress concentration, which facilitated the precipitation of the nanoscale secondary alpha phase [37].

4. Conclusions

In this study, a novel coupled processing method combining deep cryogenic treatment (DCT) and high PMT was used to enhance TC4 titanium alloys. The mechanism of microstructure and performance improvement was analyzed. The following findings were obtained.

(1) The tensile strength, elongation and fracture absorption energy of the optimized PDCT sample were 921.4 MPa, 7.6%, and 5.47 $\times$ 10^7 J/m^3, respectively, showing increases of 4.9%, 28.8% and 80.5% compared with the untreated sample. The tensile fracture exhibited rheological deformation along the phase boundaries.

(2) The grain orientation of the PDCT alloy significantly changed, thus exhibiting different textural characteristics, and some grains in the direction of (002) and (100) were deflected to the direction of (112). The polar density and intensity in the polar and inverse polar diagrams of the treated samples were higher than those of the untreated samples, indicating that the PDCT increased the preferred orientation characteristics of the crystals. In this case, PDCT acted as the texture strengthener.

(3) The cryogenic treatment improved the dislocation density and formed a dislocation wall at the grain boundary due to the cold shrinkage force. The PMF facilitated the dislocation rearrangement and improved the moving ability of the dislocation, making PMF the dislocation strengthener.

(4) The secondary nano α' phase with a width of >100 nm appeared at the edge of the β phase. The proportion of grain boundary with small angle increased from 13.6% to 16.5%, which facilitated the transformation of β to the α and α' phases. In the PDCT sample, the long-strip β phase had good grain connectivity and exhibited orientation characteristics along the magnetic field direction, thus increasing verti-

cal β phase height. This phenomenon indicates that PDCT acts to strengthen the precipitated phase.

(5) PDCT facilitated the transformation of recrystallized grains into sub-crystalline and deformed grains. Meanwhile, the average grain size decreased due to the generation of nanoscale sub-crystalline grains. PDCT decreased the lattice spacing and increased the interatomic forces. Thus, it acted to strengthen the refined crystals.

Author Contributions: Conceptualization, Z.J., H.N. and G.L.; methodology, G.L., Y.Y. and P.Z.; formal analysis, S.G. and Y.Y.; investigation, Z.J. and G.L.; resources, H.W. and P.Z.; data curation, G.L. and Y.Y.; writing—original draft preparation, Y.Y. and H.W.; writing—review and editing, Z.J., G.L. and S.G.; visualization, S.G.; supervision, H.N.; project administration, G.L.; funding acquisition, S.G. All authors have read and agreed to the published version of the manuscript.

Funding: This work was financially supported by the Postgraduate Research & Practice Innovation Program of Jiangsu Province (KYCX23_3716).

Institutional Review Board Statement: The study was approved by the Aero Engine Corporation of China Beijing Institute of Aeronautical Materials, Advanced Titanium Alloy Precision Forming Technology, Jiangsu University and Jiangsu University of Science and Technology.

Informed Consent Statement: Informed consent was obtained from all subjects involved in the study.

Data Availability Statement: The data presented in this study are available on request from the authors due to privacy.

Conflicts of Interest: Authors Zhijun Ji and Hai Nan were employed by the company AECC Beijing Institute of Aeronautical Materials. The remaining authors declare that the research was conducted in the absence of any commercial or financial relationships that could be construed as a potential conflict of interest.

References

1. Ma, R.; Zhang, X.F. Improvement of mechanical properties and microstructural refining of cast titanium alloys by coupling of electro-pulsing and temporary alloying element hydrogen. *Mater. Sci. Eng. A* **2022**, *858*, 144176. [CrossRef]
2. Zhao, Q.Y.; Sun, Q.Y.; Xin, S.W. High-strength titanium alloys for aerospace engineering applications: A review on melting-forging process. *Mater. Sci. Eng. A* **2022**, *845*, 143260. [CrossRef]
3. Wang, M.S.; Wang, Y.F.; He, Q. A strong and ductile pure titanium. *Mater. Sci. Eng. A* **2022**, *833*, 142534. [CrossRef]
4. Banerjee, D.; Williams, J.C. Perspectives on titanium science and technology. *Acta Mater.* **2013**, *61*, 844–879. [CrossRef]
5. Withers, P.J. Residual stress and its role in failure. *Rep. Prog. Phys.* **2007**, *70*, 2211. [CrossRef]
6. Carrera, E.; Rodriguez, A.; Silva, J.T. Study of residual stresses in complex aluminum castings. *Inter. J. Cast Metals Res.* **2012**, *25*, 264–269. [CrossRef]
7. Yang, Z.Y.; Liu, H.W.; Cui, Z.S. Refinement mechanism of centimeter-grade coarse grains in as-cast Ti2AlNb-based alloy during multi-directional forging. *Mater. Des.* **2023**, *225*, 111508. [CrossRef]
8. Jin, H.X.; Wei, K.X.; Li, J.M. Research progress of titanium alloys for aviation. *Chi. J. Nonferrous Met.* **2023**, *25*, 280–292.
9. Li, G.R.; Zhang, J.J.; Liu, C.X. Microstructure and property alterations and toughening mechanism of cast TC4 alloy by solid state treatment with low-density DC electric field. *J. Mater. Res. Technol.* **2024**, *33*, 9862–9875. [CrossRef]
10. Pathania, A.; Kumar, S.A.; Nagesha, B.K. Reclamation of titanium alloy-based aerospace parts using laser-based metal deposition methodology. *Mater. Today Proc.* **2021**, *45*, 4886–4892. [CrossRef]
11. Thomas, M.; Jackson, M. The role of temperature and alloy chemistry on subsurface deformation mechanisms during shot peening of titanium alloys. *Scripta Mater.* **2012**, *66*, 1065–1068. [CrossRef]
12. Li, P.P.; Sun, L.G.; Wang, J.K. Effects of combined ultrasound and low-temperature short-time heating pretreatment on proteases inactivation and textural quality of meat of yellow-feathered chickens. *Food Chem.* **2021**, *355*, 129645. [CrossRef] [PubMed]
13. Guo, L.N.; Hong, C.; Wang, W.J. Evaluation of low-temperature ultrasonic marination of pork meat at various frequencies on physicochemical properties, myoglobin levels, and volatile compounds. *Meat Sci.* **2024**, *217*, 109606. [CrossRef] [PubMed]

14. Li, H.G.; Huang, Y.J.; Zhao, W.J. Overcoming the strength-ductility trade-off in an additively manufactured CoCrFeMnNi high entropy alloy via deep cryogenic treatment. *Addit. Manuf.* **2022**, *50*, 102546. [CrossRef]
15. Li, H.; Tong, W.; Cui, J. The influence of deep cryogenic treatment on the properties of high-vanadium alloy Steel. *Mater. Sci. Eng. A* **2016**, *662*, 356–362. [CrossRef]
16. Liu, J.Q.; Wang, H.M.; Huang, Z.H.; Ma, Z.H. Enhanced strength-ductility synergy of aging treated (FeCoNi1.5CrCu)p/2024Al composite. *J. Alloys Compd.* **2022**, *929*, 167372. [CrossRef]
17. Li, H.G.; Zhao, W.J.; Chen, T.; Huang, Y.J. Beneficial effects of deep cryogenic treatment on mechanical properties of additively manufactured high entropy alloy: Cyclic vs single cryogenic cooling. *J. Mater. Sci. Technol.* **2022**, *115*, 40–51. [CrossRef]
18. Gu, K.X.; Zhao, B.; Wang, Z.J. Microstructure evolution in metastable β titanium alloy subjected to deep cryogenic treatment. *Mater. Sci. Eng. A* **2018**, *723*, 157–164. [CrossRef]
19. Gu, K.X.; Zhang, H.; Zhao, B. Effect of cryogenic treatment and aging treatment on the tensile properties and microstructure of Ti–6Al–4V alloy. *Mater. Sci. Eng. A* **2013**, *584*, 170–176. [CrossRef]
20. Zang, M.C.; Niu, H.Z.; Zhang, H.R. Cryogenic tensile properties and deformation behavior of a superhigh strength metastable beta titanium alloy Ti-15Mo-2Al. *Mater. Sci. Eng. A* **2021**, *817*, 141344. [CrossRef]
21. Xu, J.; Wang, B.; Wang, Y. Electromagnetic fields assisted blanching-Effect on the dielectric and physicochemical properties of cabbage. *J. Food Pro. Eng.* **2019**, *42*, 12888. [CrossRef]
22. Qian, J.; Zhou, C.; Ma, H. Biological effect and inactivation mechanism of bacillus subtilis exposed to pulsed magnetic field: Morphology, membrane permeability and intracellular contents. *Food Biophys.* **2016**, *11*, 429–435. [CrossRef]
23. Lin, L.; Wang, X.; Cui, H. Synergistic efficacy of pulsed magnetic fields and Litseacubeba essential oil treatment against Escherichia coli O157:H7 in vegetable juices. *Food Control* **2019**, *106*, 106686. [CrossRef]
24. Shao, Q.; Wang, G.; Wang, H. Improvement in uniformity of alloy steel by pulsed magnetic field treatment. *Mater. Sci. Eng. A* **2021**, *799*, 140143. [CrossRef]
25. Wang, Y.; Xing, Z.G.; Huang, Y.F. Effect of pulse magnetic field treatment on the hardness of 20Cr2Ni4A steel. *J. Magn. Magn. Matet.* **2021**, *538*, 168248. [CrossRef]
26. Li, G.R.; Zhao, B.W.; Wang, H.M. Microstructure and properties of TiAl-4822 alloy subject to the solid-state treatment with pulsed magnetic field. *Mater. Charact.* **2024**, *211*, 113919. [CrossRef]
27. Li, K.; Ma, H.; Li, S. Numerical simulation of three physical fields in counter-current ultrasound. *J. Food Process Eng.* **2024**, *47*, 14676. [CrossRef]
28. Li, G.R.; Zhang, Z.B.; Wang, H.M.; Cao, Z.L.; Liu, J.Q.; Zhou, Z.C. Modiffcation of $FeCoNi_{1.5}CrCu_P$/2024Al composites subject to improved aging treatments with cryogenic and magnetic field. *J. Alloys Comp.* **2023**, *967*, 17176. [CrossRef]
29. Akhbarizadeh, A.; Amini, K.; Javadpour, S. Effect of simultaneous magnetic field and deep cryogenic heat treatment on the microstructure of 1.2080 tool steel. *Mater. Des.* **2012**, *35*, 484–490. [CrossRef]
30. Su, W.X.; Wang, H.M.; Li, G.R.; Zhang, Y.F. Evolution of microstructure and mechanical properties of aluminum matrix composites reinforced with dual-phase heterostructures. *Mater. Sci. Eng. A* **2024**, *901*, 146500. [CrossRef]
31. Zhang, Z.; Zhang, J.H.; Wang, W.K. Unveiling the deformation mechanism of highly deformable magnesium alloy with heterogeneous grains. *Scripta Mater.* **2022**, *221*, 114963. [CrossRef]
32. Lu, S.L.; Todaro, C.J.; Sun, Y.Y. Variant selection in additively manufactured alpha-beta titanium alloys. *J. Mater. Sci. Technol.* **2022**, *113*, 14–21. [CrossRef]
33. Liu, Z.L.; Fan, T.Y.; Hu, H.Y. Possible mechanism of plasticity influenced by magnetic field. *Chinese Phys. Lett.* **2006**, *23*, 175–177.
34. Liao, Z.; Qin, Y.; Yang, Y. Enhanced service life of nickel-based alloy die for copper extrusion by pulsed magnetic field. *J. Manuf. Process* **2022**, *81*, 798–806. [CrossRef]
35. Dong, K.; Wang, H.M.; Li, G.R. Microstructure and properties of $FeCoNi_{1.5}CuB_{0.5}Y_{0.2}$ high-entropy alloy subject to high magnetic field treatment. *Intermetallics* **2024**, *169*, 108278. [CrossRef]
36. Wang, H.M.; Su, W.X.; Liu, J.Q. Microstructure and properties of FeCoNiCrMn and Al_2O_3 hybrid particle-reinforced aluminum matrix composites fabricated by microwave sintering. *J. Mater. Res. Technol.* **2023**, *24*, 8618–8634. [CrossRef]
37. Xiong, M.; Li, G.R.; Wang, H.M. Influence of pulsed magnetic field processing on the microstructure and mechanical properties of TC27 titanium alloy. *Mater. Lett.* **2024**, *372*, 137092. [CrossRef]

Disclaimer/Publisher's Note: The statements, opinions and data contained in all publications are solely those of the individual author(s) and contributor(s) and not of MDPI and/or the editor(s). MDPI and/or the editor(s) disclaim responsibility for any injury to people or property resulting from any ideas, methods, instructions or products referred to in the content.

materials

MDPI

Article

Mechanical Properties and σ-Phase Precipitation in $FeCoCrNiMo_x$ (x = 0, 0.4, 0.5, 0.8, 1.3) High-Entropy Alloys: Insights from First-Principles Study

Huimin Li [1], Junjun Jin [1], Zhiyi Zhang [2], Jinpeng Yu [3], Hairong Sun [4], Songling Sun [5], Weijie Tang [6] and Guoqing Gou [1,*]

[1] Key Laboratory of Advanced Technologies of Materials, Ministry of Education, School of Materials Science and Engineering, Southwest Jiaotong University, Chengdu 610031, China; swjt_lhm@163.com (H.L.); jinjunjun@my.swjtu.edu.cn (J.J.)
[2] CRRC Qingdao Sifang Co., Ltd., Qingdao 266111, China; zhangzhiyi@cqsf.com
[3] School of Computer Engineering, Chengdu Technological University, Chengdu 610031, China; jxsj01330@163.com
[4] Chengdu Metro Operation Co., Ltd., Chengdu 610058, China; shr-19@163.com
[5] Sichuan Special Equipment Inspection Institute, Chengdu 610031, China; cdtj_sunsl@chengdu.gov.cn
[6] Industrial Center, Shenzhen Polytechnic University, Shenzhen 518055, China; tangweijie@szpt.edu.cn
* Correspondence: gouguoqing1001@163.com

Abstract: High-entropy alloys (HEAs) have garnered significant global interest due to their outstanding properties. This study investigates the structural stability and mechanical properties of $FeCoCrNiMo_x$ (x = 0, 0.4, 0.5, 0.8, 1.3) HEAs using a first-principles approach coupled with the special quasi-random structure (SQS) method. Of the alloys examined, all except $FeCoCrNiMo_{1.3}$ were found to be thermodynamically and dynamically stable. Elasticity calculations revealed that molybdenum improves the ductility and anisotropy of the alloys, though with a slight decrease in strength and stiffness, as confirmed by electronic structure analysis. Defect-free $FeCoCrNiMo_{0.5}$ HEAs coatings were then prepared using laser cladding and characterized for their microstructure and hardness. The coating exhibited a transition from columnar crystals at the bottom to equiaxed crystals at the surface, forming a honeycomb-like structure. Inside the crystal cells, high-density dislocations and σ-phase were observed. Elasticity calculations of the σ-phase confirmed its high hardness, low ductility, and classification as a brittle, hard phase.

Keywords: high-entropy alloys; first-principles calculations; special quasi-random structure; microstructure; mechanical properties

1. Introduction

High-entropy alloys (HEAs), a novel material class born under a new design paradigm, have fundamentally redefined traditional alloy design principles [1]. In the conventional design framework, the introduction of alloying elements often leads to the formation of multiphase, complex intermetallic compounds. However, multicomponent alloys, characterized by high conformational entropy, tend to reduce Gibbs free energy, thereby favoring the formation of simple solid solutions over complex structures [1–3]. This unique behavior has attracted significant attention from researchers worldwide, driven by the exceptional properties of HEAs, such as wear resistance, corrosion resistance, and high strength [4–8].

Among FeCoCrNi-based high-entropy alloys (HEAs), various compositions have shown promising properties for structural applications. For instance, FeCoCrNiMn alloy demonstrates excellent wear resistance [9], while FeCoCrNiCuAl exhibits strong oxidation resistance [4]. The FeCoCrNiMnAl alloy offers high-temperature wear resistance [10], and FeCoCrNiCu alloy provides good dislocation storage capacity as well as high ductility and toughness [11]. Additionally, $FeCoCrNiAl_{0.5}Ti_{0.5}$ alloy is noted for its strong corrosion resistance [12].

Molybdenum (Mo), as an alloying element, has been extensively studied for its ability to enhance the mechanical and corrosion-resistant properties of conventional alloys. Dai et al. [13] reported that in $FeCoCrNiMo_x$ alloys, Mo content as low as 0.3% led to the formation of precipitates, which increased at higher Mo content, enhancing the protective nature of the passive film and improving corrosion resistance. Furthermore, Zhao [14] demonstrated that increasing Mo content in $FeCoCrNiMnMo_x$ alloys led to a transition from a face-centered cubic (FCC) phase to a mixed FCC and body-centered cubic (BCC) phase, significantly improving hardness and reducing the coefficient of friction, thereby enhancing damage tolerance. The effect of Mo content on HEA properties was further exemplified by Gu et al. [15], who found that varying Mo content in $Ni_{1.5}CrFeTi_2B_{0.5}Mo_x$ HEAs altered the coating structure from a single BCC phase to a dual-phase BCC + FCC structure, improving corrosion resistance in simulated saturated brine mud solutions. Liang [16] designed $(FeCoNi)_{(88-x)}(AlTi)_{12}Mo_x$ (x = 0.5, 1.0, 1.5) HEAs with simple FCC solid solutions, identifying that the Mo1.0 alloy exhibited the best mechanical properties, with yield strength, tensile strength, and elongation reaching 980 MPa, 1260 MPa, and 34.5%, respectively. Additionally, based on valuable research on HEAs, Mo can combine with other elements in the coating to form hard and brittle intermetallic compounds, thereby enhancing the material's strength and hardness. For instance, Mo and Cr can form the σ phase, which has a body-centered tetragonal structure. These σ phases are dispersed throughout the material, resulting in a precipitation strengthening effect [17].

However, the role of molybdenum in FeCoCrNi-based high-entropy alloys (HEAs) remains underexplored, particularly in optimizing molybdenum content to balance mechanical strength, ductility, and thermal stability. While earlier studies have focused on molybdenum-induced phase transitions and hardness improvements, there is still a lack of detailed understanding regarding the relationship between molybdenum content, microstructure, mechanical properties, and electronic structure in HEAs. Most existing research, both experimental and computational, has concentrated on molybdenum contents up to 0.3 [18,19], with limited exploration of higher molybdenum fractions (e.g., 0.4, 0.5, etc.). The effects of these higher concentrations, particularly in combination with other elements, remain largely unexplored. Therefore, this paper presents a comprehensive study of $FeCoCrNiMo_x$ (x = 0.0, 0.4, 0.5, 0.8, 1.3) alloys using first-principles methods based on density functional theory (DFT), investigating the effect of varying molybdenum content on the structural stability, mechanical properties, and electronic structure of $FeCoCrNiMo_x$ HEAs. Additionally, based on the results of first-principles calculations, a $FeCoCrNiMo_{0.5}$ coating was fabricated using laser cladding, and its microstructure and mechanical properties were characterized. This study contributes to the growing body of knowledge on HEAs and highlights the potential of molybdenum-doped FeCoCrNi-based alloys for engineering applications that demand high strength and thermal stability.

2. Methods

2.1. Computational Details

To compute the elastic constants of $FeCoCrNiMo_x$ HEAs using the first-principles approach, we employed the Monte Carlo SQS method [20] to generate a symmetrically ideal FCC lattice with site occupancies for the $FeCoCrNiMo_x$ (x = 0, 0.4, 0.5, 0.8, 1.3) HEAs model. The FCC structure is determined by the atomic radius difference (δ) and valence electron concentration (VEC) in Table 1. When the atomic radius difference is less than 6.6%, and the valence electron concentration is greater than 8, the structure of high-entropy alloys mainly consists of the FCC structure. To accommodate our computational resources, we adopted a compromise solution by constructing a 2 × 2 × 3 supercell with FCC structure, each containing 48 atoms, and the SQS model for each component is illustrated in Figure 1.

Table 1. The calculation results of δ and VEC in this system.

	δ%	VEC
$FeCoCrNiMo_0$	5.54	8.2500
$FeCoCrNiMo_{0.4}$	5.41	8.0625
$FeCoCrNiMo_{0.5}$	5.39	8.0624
$FeCoCrNiMo_{0.8}$	5.27	7.8749
$FeCoCrNiMo_{1.3}$	5.13	7.6875

When $\delta \leq 6.6\%$, it is beneficial to form a single solid solution; when VEC ≥ 8, it tends to form FCC structure phase [21].

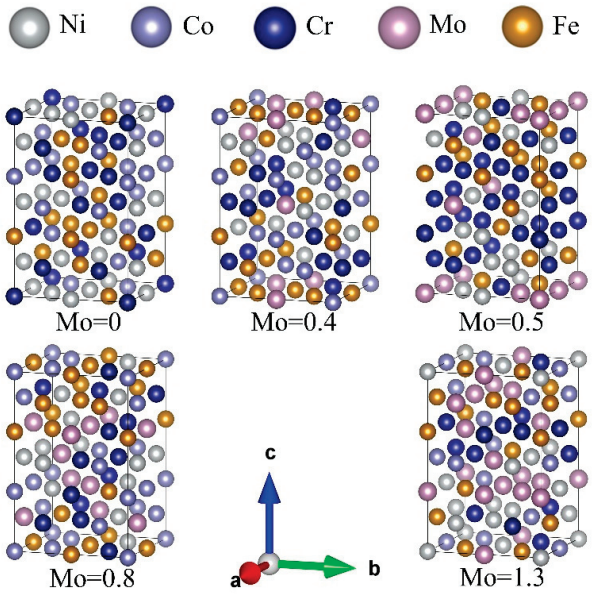


Figure 1. The 2 × 2 × 3 SQS supercell for different Mo elemental contents.

All first-principles computational methods based on density functional theory utilize the generalized gradient approximation (GGA) of the Perdew–Burke–Ernzerhof (PBE) generalization as the exchange-correlation functional for self-consistent calculations [22]. To ensure computation accuracy, we conducted a rigorous convergence test by computing Brillouin zone integrals. The convergence criteria were set as follows: stress less than 0.01 GPa, force tolerance less than 0.005 eV/Å, maximum displacement less than 0.0003 Å, and total energy change less than 3×10^{-6} eV/atom. After the convergence test, a final plane wave energy cutoff of 500 eV and a 3 × 3 × 2 k-point mesh were selected to calculate the elastic constants of the HEA. The energy variation with increasing cutoff energy and k-points was less than 1 meV/atom. Before calculating the elastic constants,

all structures were optimized and energetically computed using the CASTEP software (Version 2019). The equilibrium lattice constant of the FeCoCrNi HEA after structural optimization was 3.507 Å, which aligns well with previous calculations and experimental data (a = 3.568 Å [14], a = 3.540 Å [23]), with an error of less than 2%. This suggests the reliability of our calculations. The dynamic stability of $FeCoCrNiMo_x$ HEAs was examined by the phonon dispersion curves. The elastic stiffness constants were then calculated using the stress–strain method [24], and the associated mechanical properties were determined.

2.2. Experimental Method

Based on the calculations, the composition at x = 0.5 optimizes the balance between strength and ductility, and therefore, the FeCoCrNiMo0.5 coatings were prepared by laser deposition. This study used quenched and tempered EA4T axle steel as the base material. The coating material, $FeCoCrNiMo_{0.5}$ HEAs powder, was produced through vacuum atomization. Before laser cladding, the powder was dried in an oven at 120 °C for 2 h to enhance its flowability. The $FeCoCrNiMo_{0.5}$ HEAs coating was applied using the laser cladding method with the following parameters: laser power of 1800 W, scanning speed of 300 mm/min, spot diameter of 5 mm, powder feeding speed of 2 r/min, and a lap rate of 50%. Specimens were cut perpendicular to the coating using a linear cutting method. The specimens for microstructural analysis were ground using 400 to 2000 grit silicon carbide paper, polished with 1 μm diamond powder, and electrolytically etched with a 5% oxalic acid solution. The coating microstructure was examined using electron microscopy, X-ray diffraction, scanning electron microscopy, and electron channel contrast imaging (ECCI). The compositional distribution was analyzed using energy dispersive spectroscopy (EDS). A JMHVS-1000AT digital microhardness tester (Aolong Company, Shanghai, China) was used to measure the microhardness of the coating and substrate. The test parameters were as follows: a loading force of 1.96 N, a holding time of 15 s, and test areas including the coating, bonding zone, heat-affected zone, and substrate. To visualize the hardness variations across different areas of the cladding specimen, tests were performed at equal intervals from the coating to the substrate, with a 0.2 mm spacing between each test point. In this study, residual stresses across different areas of the coating cross-section were measured using a μ-X360s X-ray residual stress analyzer (Pulstec Company, Shizuoka, Japan). The cosα method was employed for stress calculation, utilizing diffraction data collected from the diffraction ring (normal strain in the direction of the Debye ring circumference angle) using a two-dimensional detector. The analysis employed a Cr target; the diameter of the collimating tube was 1 mm, power setting at 30 kV·1 mA, with a zero stress iron powder calibration. Following a single incident at a single angle, a complete Debye ring was obtained, where the difference between the Debye ring without stress and the deformed Debye ring under stress facilitated calculation of the change of interplanar spacing under stress and the corresponding stress. This approach provided information on full residual stress. The KEYSIGHT G200 Nano Indenter (Santa Rosa, CA, USA) was used to conduct nanoindentation tests on the coatings, using a diamond Berkovich indenter and controlling the indentation-depth mode. The specific test parameters were set as follows: maximum indentation depth of 500 nm, loading strain rate of 1 mN/s, holding time of 10 s to reach the maximum indentation depth, and then unloading.

3. Results and Discussion

3.1. First-Principles Calculation

3.1.1. Thermodynamic and Dynamic Stability Analysis

To investigate the structural characteristics of $FeCoCrNiMo_x$ HEAs, we first calculated the formation enthalpies of four alloys to determine their thermodynamic stability [25]. The formation enthalpy serves as a key indicator of the thermodynamic stability of HEAs,

representing the enthalpy change when 1 mol of the substance is formed from its constituent elements in their standard states. This process involves the rearrangement of atoms and the formation of new chemical bonds, leading to changes in bond energy, van der Waals forces, and electrostatic energy, which collectively result in a change in the system's total enthalpy. The formula for calculating the formation enthalpy (ΔH_f) is as follows:

$$\Delta H_f = \frac{1}{x+y+z+m+n}[E_{FeCoCrNiMo_x} - (xE_{Fe} + yE_{Co} + zE_{Cr} + mE_{Ni} + nE_{Mo})] \quad (1)$$

where $E_{FeCoCrNiMox}$ is the total energy of $FeCoCrNiMo_x$ models. E(Fe), E(Co), E(Cr), E(Ni), and E(Mo) represent the total energies of Fe, Co, Cr, Ni, and Mo, respectively, while x + y + z + m + n corresponds to the total number of atoms in the model. The energies of $FeCoCrNiMo_x$ were calculated using first-principles density-functional theory (DFT). These calculations were performed with the CASTEP software for each alloy model. Structural optimization was carried out to minimize atomic forces, ensuring accurate ground-state energy representations for each component. For the five pure metals (Fe, Co, Cr, Ni, and Mo), we considered their respective crystal structures—FCC for Ni, Cr, and Co and BCC for Fe and Mo—and modeled them separately. The energy calculations for these pure metals followed the same approach used for the $FeCoCrNiMo_x$ alloy. A negative formation enthalpy indicates thermodynamic stability, and the more negative the formation enthalpy, the easier the formation process and the more stable the phase. Figure 2a shows the formation enthalpies of the five alloys. Except for the alloy with a Mo content of 1.3, the formation enthalpies of the other four alloys are negative. The alloy without molybdenum exhibited the lowest enthalpy of formation, approximately -0.08 eV/atom, which corresponds well with the calculation by Hayun et al. (-0.036 ± 0.01 eV/atom) [26]. As the molybdenum content increases, the thermodynamic stability gradually decreases, which is consistent with the findings of Cichocki et al. [19].

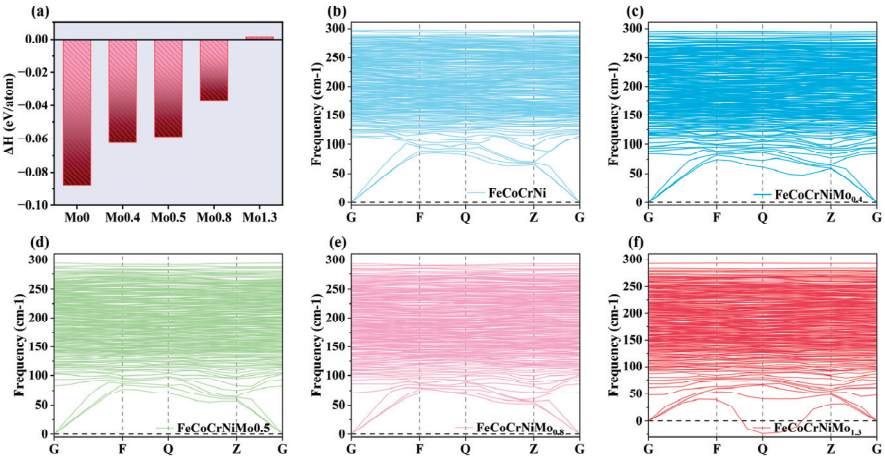


Figure 2. (**a**) Formation enthalpy; (**b**–**f**) phonon dispersion curves: (**b**) FeCoCrNi; (**c**) $FeCoCrNiMo_{0.4}$; (**d**) $FeCoCrNiMo_{0.5}$; (**e**) $FeCoCrNiMo_{0.8}$; (**f**) $FeCoCrNiMo_{1.3}$.

To further determine the stability of the five alloys, we also calculated the phonon dispersion curves to assess their dynamic stability. Dynamic stability is determined by the characteristics of the phonon frequencies; if all frequencies in the phonon dispersion curve are positive, the phase is considered dynamically stable [27,28]. Conversely, the presence of imaginary phonon frequencies indicates dynamic instability. The phonon dispersion curves for the four alloys are shown in Figure 2b–f. The results indicate that $FeCoCrNiMo_{1.3}$ exhibits imaginary phonon frequencies, suggesting dynamic instability,

whereas the phonon frequencies for the other four alloys are all positive, indicating the presence of dynamic stability. In summary, combining these results with the formation enthalpy analysis, we conclude that $FeCoCrNiMo_{1.3}$ cannot stably exist. This can be attributed to the higher concentration of Mo in the alloy, which could disrupt the ideal atomic arrangement required for stability in high-entropy alloys (HEAs). The large atomic size difference between Mo and the other elements may also contribute to lattice distortions, leading to higher enthalpy. Therefore, it is not further discussed in this paper.

3.1.2. Effect of Mo Content on Mechanical Properties

For the structurally optimized model, the elastic constants C_{ij} of the alloys, as calculated by the stress–strain method of generalized Hooke's law [29,30], can be used to assess their mechanical properties. According to Born–Huang theory, for face-centered cubic crystals, the mechanical stability is determined by the following conditions [31]:

$$C_{11} > 0, C_{44} > 0, C_{11} - C_{12} > 0, C_{11} + 2C_{12} > 0 \quad (2)$$

In Figure 3a, it is observed that all compositions of HEAs satisfy the mechanical stability conditions. Notably, C_{11} and C_{44} demonstrated a significant decrease with increasing Mo content, while C_{12} slightly increased. C_{11} represents the linear compressive response in the a-axis, and C_{44}, which is related to its shear behavior, is the key parameter affecting the hardness. Thus, the addition of Mo elemental content in the alloy decreased the compressive resistance and hardness of the alloy.

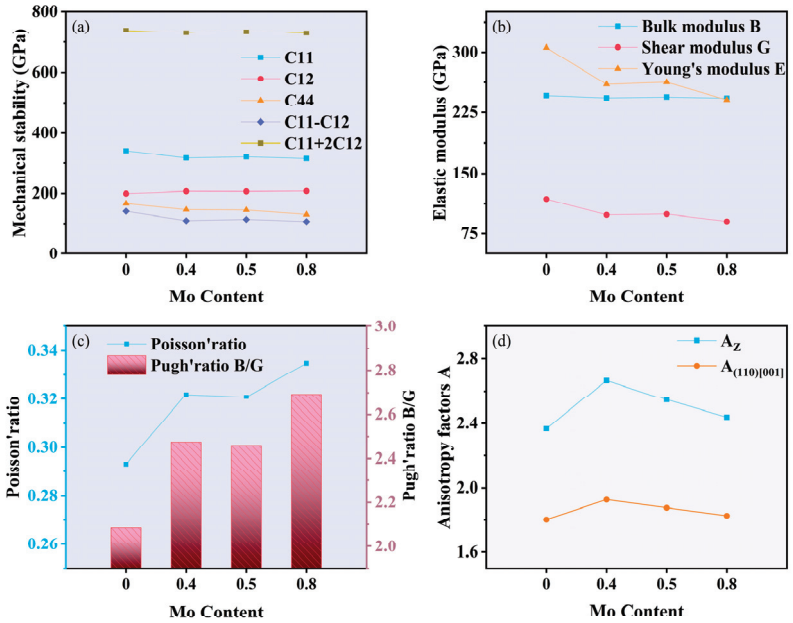


Figure 3. Mechanical properties at different Mo contents: (**a**) variation of elastic constants with Mo content; (**b**,**c**) variation of mechanical properties with Mo content; (**d**) variation of anisotropy with Mo content.

Based on the results of the elastic constants, the elastic properties of HEAs, including bulk modulus, shear modulus, Young's modulus, and Poisson's ratio, can be determined using the Voigt–Reuss–Hill approximation [32]. Since the Voigt and Reuss approximations denote the maximum and minimum limits of the polycrystalline elastic modulus, respectively, the bulk

modulus B and shear modulus G can be expressed as the Voigt and Reuss averages between them. For the cubic phase, B and G can be given by the following equations [33]:

$$B = \frac{1}{3}(C_{11} + 2C_{12}) \tag{3}$$

$$G = \frac{1}{2}(G_V + G_R) \tag{4}$$

where Voigt shear modulus $G_V = (C_{11} - C_{12} + 3C_{44})/5$, and Reuss shear modulus $G_R = 5(C_{11} - C_{12})C_{44}/[4C_{44} + 3(C_{11} - C_{12})]$.

In addition, Young's modulus and Poisson's ratio can be obtained from B and G [34]:

$$E = \frac{9BG}{3B + G} \tag{5}$$

$$V = \frac{(3B - 2G)}{2(38 + G)} \tag{6}$$

The calculated elastic properties of the four alloys are shown in Figure 3b,c. The bulk modulus B of the alloy is usually proportional to the cohesive energy of the material, which represents the resistance of the material to bond fracture. The shear modulus G and Young's modulus E represent the resistance of the material to shear deformation and the stiffness of the material [35], respectively, and can be used to assess the mechanical hardness of the alloy in the annealed state. Meanwhile, the Poisson's ratio can be used to assess the degree of covalent bonding and to predict its ductility or brittleness. When the Poisson's ratio is greater than 0.26, the material is more ductile [36]. In addition, the ratio of bulk modulus to shear modulus (B/G) is also closely related to the ductility of the alloy. When the ratio is greater than 1.75, it means that the material is more ductile [37]. From the calculation results, it can be seen that both the shear modulus and Young's modulus decreased with the increase in Mo content, while Poisson's ratio and B/G showed the opposite trend. Poisson's ratio was greater than 0.26, and B/G was greater than 1.75, and the bulk modulus was basically unchanged. These results indicate that the addition of Mo element improved the ductility of the alloy but at the same time reduced its shear resistance as well as its stiffness.

Typically, applications of crystalline materials are significantly affected by mechanical anisotropy. The elastic anisotropy of a material is assessed by means of an anisotropy factor A, which is also used to study the mechanical properties of anisotropic materials, where A = 1 indicates isotropy and otherwise anisotropy. The magnitude of A determines the degree of anisotropy, and the greater the deviation of A from 1, the more anisotropic the material is. Based on the elasticity constant C_{ij} for cubic crystals, we calculated the Zener anisotropy ratio A_Z and the anisotropy factor $A_{(110)[001]}$ by means of Equations (6) and (7), where the Zener ratio A_Z denotes the ratio of the shear moduli between the (100) and [110] crystal planes, which can be used to characterize the degree of anisotropy of the material:

$$A_Z = \frac{2C_{44}}{C_{11} - C_{12}} \tag{7}$$

$$A_{(110)[001]} = \frac{C_{44}(C^{'} + 2C_{12} + C_{11})}{C_{11}C^{'} - C_{12}^2} \tag{8}$$

where $C^{'} = C_{44} + (C_{11} + C_{12})/2$. $A_{(110)[001]}$ denotes the anisotropy factor in the (110) [001] direction. By using the above equations, we calculated the Zener ratios A_Z and anisotropy

factors A $_{(110)\,[001]}$ for the four alloys, and the results are shown in Figure 3d, and the detailed values are presented in Table 2. The Zener ratio AZ and anisotropy factor A $_{(110)\,[001]}$ of all the alloys were not equal to 1, which indicates that the HEAs of all four compositions are anisotropic materials. The Zener ratio AZ and anisotropy factor A $_{(110)\,[001]}$ showed the same increasing trend with increasing Mo content.

In order to examine the anisotropic properties of the four alloys, the three-dimensional surfaces representing the Bulk modulus, Young's modulus, shear modulus, and Poisson's ratio were further analyzed. An alloy demonstrates isotropy when its three-dimensional surface manifests as a sphere; otherwise, it displays anisotropic behavior. Greater deviation of the 3D surface from a sphere signifies higher levels of anisotropy. Figure 4 depicts the three-dimensional surfaces of the bulk modulus B, Young's modulus E, shear modulus G, and Poisson's ratio V, respectively. Inspection of Figure 4a reveals that the 3D surfaces representing the bulk modulus of the four alloys conform to standard spherical shapes, indicating isotropic behavior. However, in Figure 4b–d, the shapes of the surfaces representing Young's modulus, shear modulus, and Poisson's ratio for the four alloys deviate significantly from that of a standard sphere, suggesting pronounced anisotropy. The color of a three-dimensional surface corresponds to the magnitude of its modulus, while its curvature indicates the extent of anisotropy. Young's modulus surfaces for all alloys exhibit eight corners, whereas the shear modulus and Poisson's ratio surfaces possess six corners. Furthermore, the maximum values of Young's modulus align with the <111> direction, whereas for shear modulus and Poisson's ratio, they align with the <100> direction. This alignment suggests that the alloys are more resistant to longitudinal deformation along the <111> direction and transverse deformation along the <100> direction.

Table 2. Elastic constants and properties of σ phase.

	Elastic Properties						Elastic Constants		
	B	**E**	**G**	**H**	**V**	**B/G**	**C11**	**C12**	**C44**
Σ phase	113.1	239.9	104.7	22.7	0.15	1.1	240.9	49.1	110.9

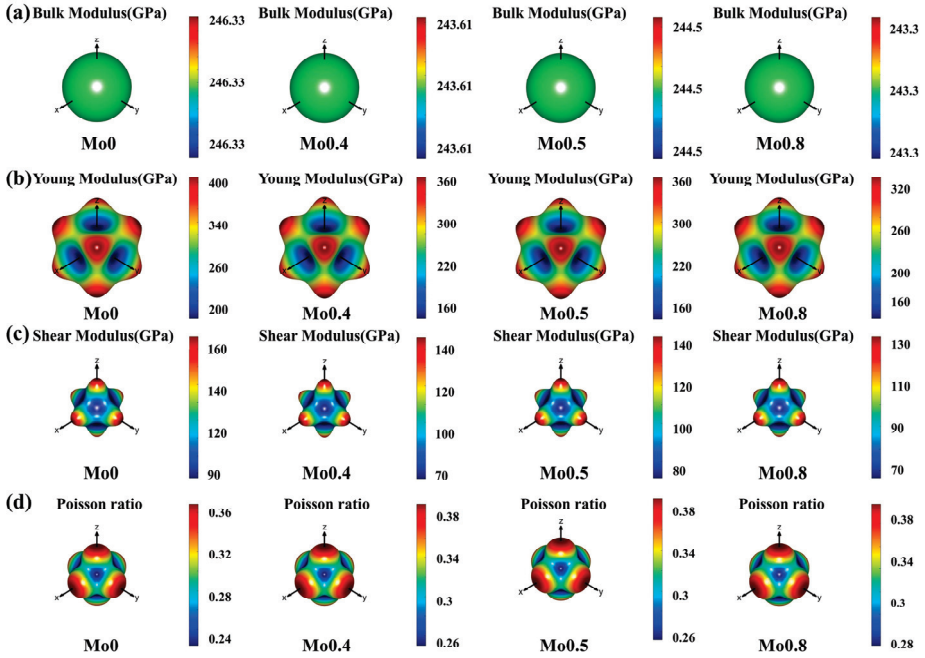


Figure 4. Three-dimensional surface plot: (**a**) Bulk modulus; (**b**) Young's modulus; (**c**) shear modulus; (**d**) Poisson's ratio.

3.1.3. Effect of Mo Content on Electronic Structure

The electronic structure significantly influences the stability and mechanical properties of materials. To elucidate the relationship between the mechanical properties of $FeCoCrNiMo_x$ high-entropy alloys (HEAs) and Mo elements from an electronic perspective, we analyzed changes in the density of states (DOS) resulting from the introduction of Mo elements, as depicted in Figure 5a–d. The position of the Fermi energy level is denoted by the green dashed line. Figure 5a illustrates the total density of states (TDOS), indicating the metallic nature of $FeCoCrNiMo_x$ with a non-zero density at the Fermi energy level. As Mo content increases, the TDOS at lower energy levels diminishes, with peak positions shifting towards higher energy levels, signifying a gradual reduction in the alloy's structural stability [38]. Simultaneously, the depth of the pseudo-energy gap near the Fermi energy levels in the TDOS decreases with increasing Mo content, implying a weakening of atomic covalency and consequent reduction in mechanical properties [39,40].

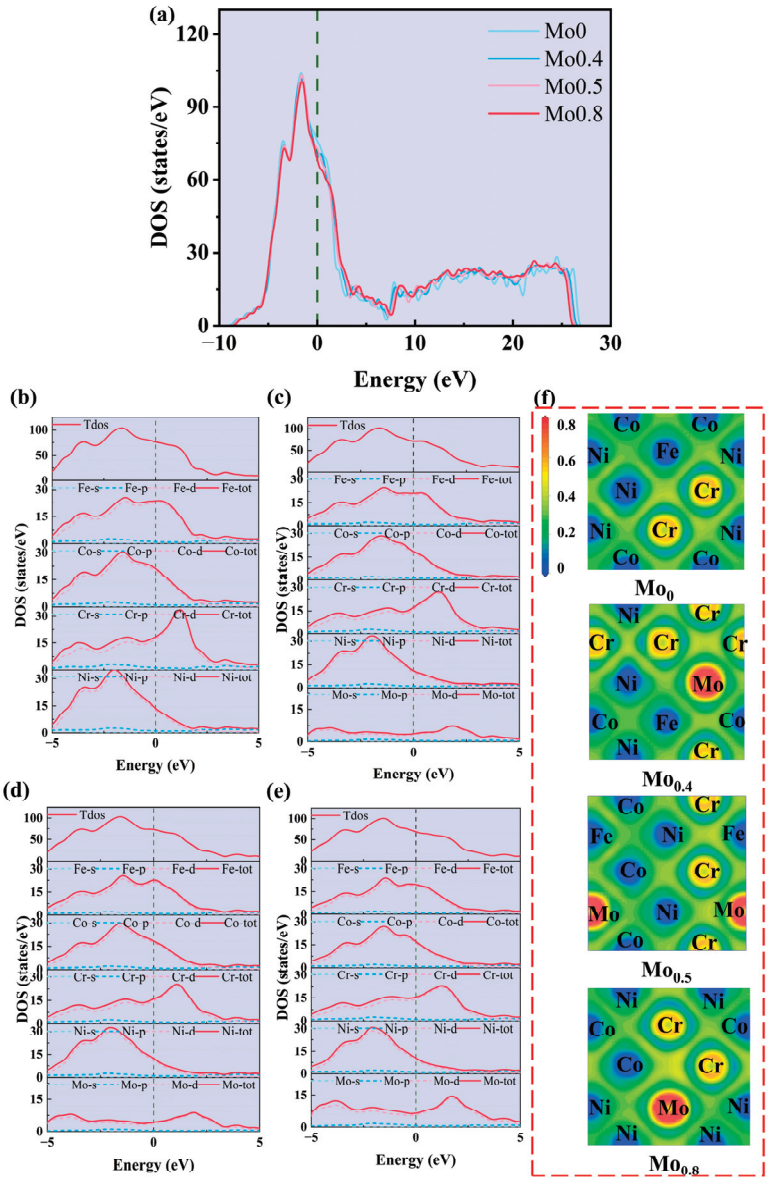


Figure 5. (**a**) Total density of states of $FeCoCrNiMo_x$; (**b**–**d**) partial density of states of $FeCoCrNiMo_x$: (**b**) Mo_0, (**c**) $Mo_{0.4}$, (**d**) $Mo_{0.5}$ and (**e**) $Mo_{0.8}$. (**f**) Contour plots of ELF on the (1 0 0) plane of $FeCoCrNiMo_x$.

Furthermore, as depicted in Figure 5b–d, analysis of the partial density of states (PDOS) for each metallic element reveals a notable hybridization of electronic states within the −5–5 eV range. Particularly, the d orbitals of each element predominantly contribute to these electronic states, with the electron occupation of these d-orbitals significantly impacting the materials' mechanical properties [41]. The height of the DOS peak of Mo notably escalates with increasing Mo content, particularly for the first peak above the Fermi energy level, albeit consistently lower than peaks of other elements. The diminished hybridization strength between Mo's d orbitals and those of other elements results in the formation of covalent bonds with reduced strength compared to bonds involving other elements. The weaker covalent bonding could make the material more prone to brittle fracture, especially under tensile stress or high strain rates. This is because materials with weaker covalent bonds generally exhibit lower resistance to crack propagation. Consequently, the system's mechanical properties exhibit a decline with increasing Mo content.

To explore the correlation between electronic structure and mechanical properties in alloys, electronic localization functions (ELF) were computed for alloys with varying compositions. ELF offer both quantitative and visual insights into the chemical environment of a compound. For instance, an ELF value of 0.5 signifies metallic bonding properties, while a value of 1 indicates full covalent bonding. Figure 5e illustrates the ELF plot of $FeCoCrNiMo_x$. In the FeCoCrNi HEA, the electron cloud is uniformly distributed around Fe, Co, and Ni, exhibiting similar electronegativities and an ELF value of approximately 0.35, indicating typical metallic bonding. Conversely, a charge depletion region (depicted in light blue) surrounds Mo and Cr atoms due to their lower valence electron counts, leading to electron expulsion from their surroundings. This phenomenon weakens the bonds between Cr/Mo and their nearest neighboring atoms. Consequently, as Mo content increases, interlayer bonds become more susceptible to breakage, rendering Mo-containing alloys more prone to slip, thereby diminishing their mechanical properties.

3.2. Microstructure and Microhardness

Figure 6 presents the X-ray diffraction results of $FeCoCrNiMo_x$ HEA. First-principles-calculated XRD patterns of the four high-entropy alloys revealed a dual-phase structure dominated by face-centered cubic (FCC) phases with minor σ-phase contributions. By comparing the positions of the diffraction peaks, it can be observed that the diffraction peaks as a whole show a slight leftward shift with the addition of Mo element. This suggests that the introduction of Mo element leads to significant lattice distortion, causing the lattice constant to increase with its content. Similar to the results of first-principles calculations, the phase structure of the $FeCoCrNiMo_{0.5}$ coating mainly consists of the FCC phase and the σ phase, which is the same as that observed by Zhao et al. [42]. The addition of Mo promotes the formation of sigma phase but did not change the crystal structure (FCC). The σ-phase formation is primarily due to molybdenum's relatively low enthalpy of mixing with other elements, making it prone to combining with them. The addition of molybdenum enhances the tendency for intermetallic compound formation, and the segregation of Mo and Cr promotes the formation of the σ phase [43]. Molybdenum's low enthalpy of formation with metals like Fe, Ni, and Co favors the energetically favorable mixing of these metals into a solid solution. Despite molybdenum's larger atomic radius and higher melting point, these thermodynamic properties—especially the favorable interactions with other alloying elements—overcome size differences and promote its solubility in the HEA system. Furthermore, the high configurational entropy resulting from the near-equal mixing of multiple elements stabilizes phases like FCC solid solutions and complex intermetallics. This entropy effect counteracts the tendency of immiscible elements to phase separate.

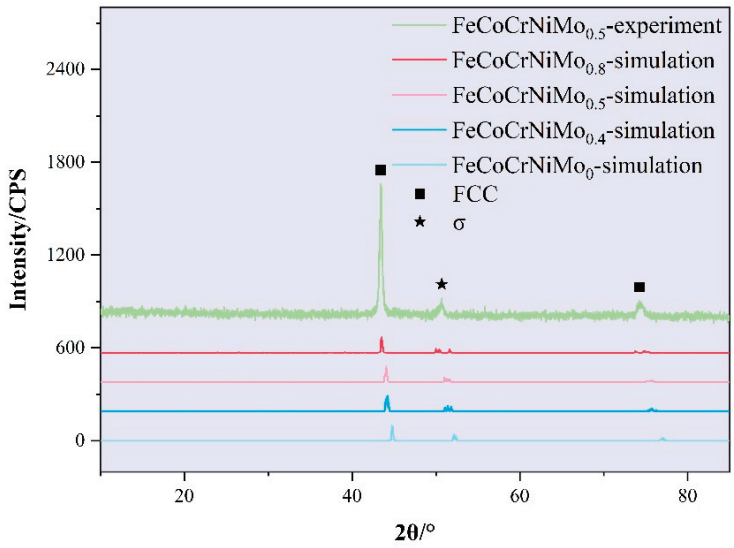


Figure 6. X-ray diffraction results of $FeCoCrNiMo_x$ HEA.

Figure 7a–f display secondary electron images and EDS mappings of $FeCoCrNiMo_{0.5}$ HEA coating. The images reveal a defect-free and crack-free surface, with uniform distribution of the five elements—Fe, Co, Cr, Ni, and Mo—across the coating. No signs of elemental segregation are observed. Figure 7g–i illustrate the coating's microstructure at the surface, middle, and interface. The surface consists primarily of equiaxed crystals, while the middle includes both equiaxed and columnar crystals. The bottom is characterized by columnar crystals. Overall, the coating transitions from columnar to equiaxed crystals, forming a honeycomb-like structure [43]. The formation of columnar grains near the substrate and equiaxed grains at the surface leads to differences in thermal expansion, which can induce internal stresses upon cooling. This phenomenon, commonly observed in coatings produced by rapid cooling techniques such as laser cladding and welding, may adversely affect mechanical properties, particularly fatigue resistance, and could lead to cracking under mechanical loading. To investigate the distribution of these residual stresses, tests were conducted on different regions of the coating, as shown in Figure 7l. The results demonstrate that the surface of the coating experiences residual compressive stress due to rapid cooling, which restricts thermal contraction. The middle region shows minimal residual tensile stress, while the bottom exhibits significant residual tensile stress. This is attributed to the large mismatch in the thermal expansion coefficients and the growth direction of columnar crystals between the coating and the substrate. Additionally, phase expansion of the substrate induces a reverse constraint on the coating, resulting in high residual tensile stress at the bottom, which progressively decreases towards the heat-affected zone. Figure 7j,k present electron channeling contrast imaging (ECCI) at the coating surface and interface. The images reveal closely aligned crystal cells and white precipitates. A high density of dislocations is present within the crystal cells, while the white precipitates, identified as Mo-rich σ phase (Cr_2Mo_3), are located at grain boundaries and within the cells [44–46]. The combination of these dislocations and the precipitated σ phase are the key for the increase in the hardness of the coating [17]. Additionally, black particles, primarily Cr_2O_3 oxides, are found at grain boundaries and within the grains. These oxides form during the laser cladding process.

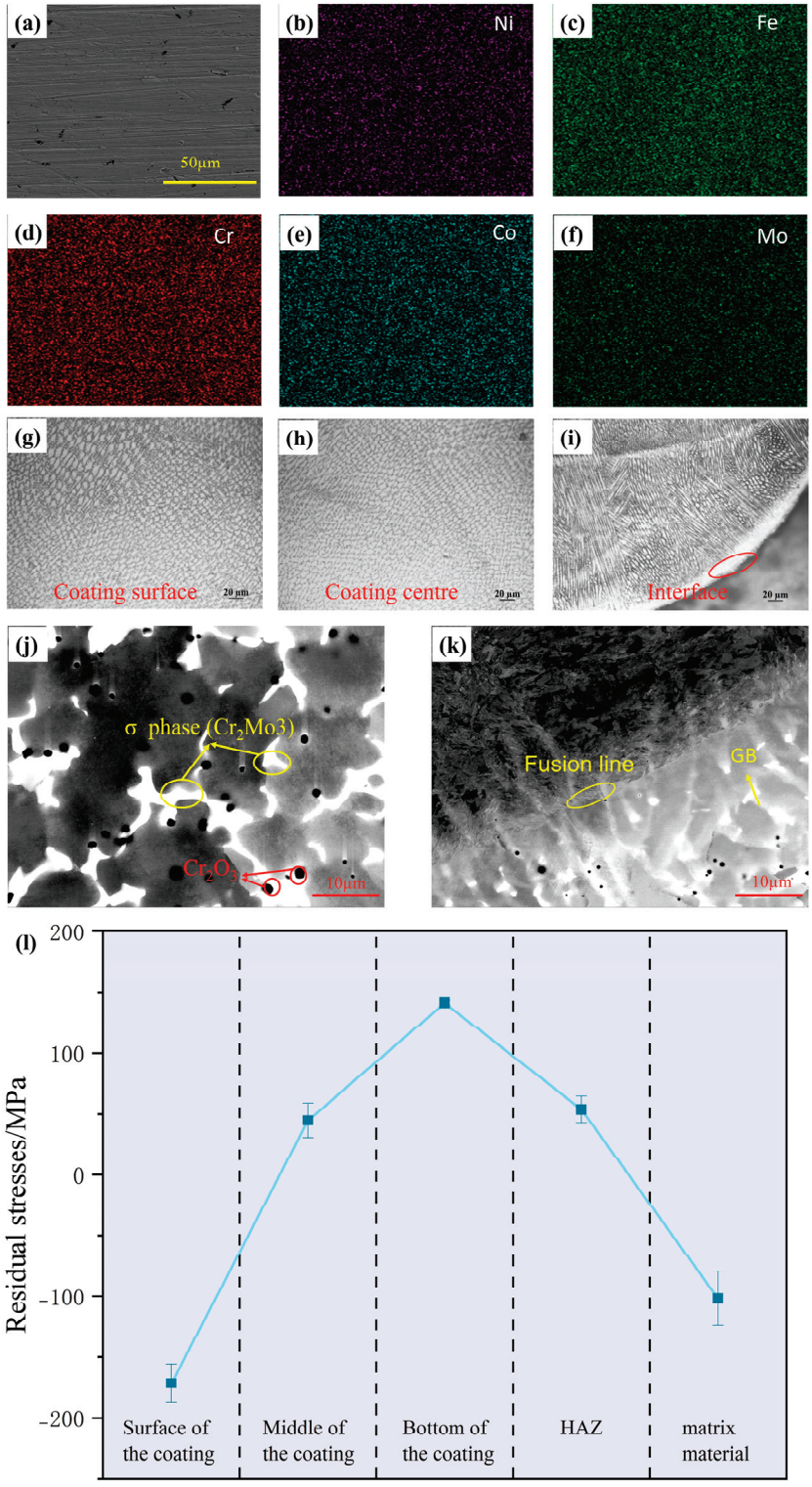


Figure 7. Microstructure of $FeCoCrNiMo_{0.5}$ HEA coating: (**a**–**f**) secondary electron images and EDS mappings of coating; (**g**–**i**) coating's microstructure at the surface, middle, and interface; (**j**,**k**) electron channeling contrast imaging (ECCI) at the coating surface and interface; (**l**) residual stress distribution in coatings.

The indentation and hardness values across the cross-section of the $FeCoCrNiMo_{0.5}$ HEA are shown in Figure 8a. The hardness increases progressively from the substrate

to the coating, forming a clear gradient. The microhardness distribution diagrams of the substrate, cladding layer, and heat-affected zone show that the EA4T steel substrate retains its original material properties, with an average hardness of 218.9 $HV_{0.2}$. The heat-affected zone is relatively narrow, and its hardness varies significantly. Near the interface, the hardness is close to that of the coating, but as the distance from the interface increases, the hardness gradually decreases, approaching the substrate's value. The microhardness in the heat-affected zone, compared to the substrate, is largely influenced by thermal cycling. The formation of residual austenite also contributes to the hardness increase. The maximum hardness of the coating is 437.91 $HV_{0.2}$, with the surface being significantly harder than the bottom. This hardness variation is primarily due to differences in microstructure: the surface consists of fine equiaxed crystals, while the bottom is mainly made up of coarse columnar crystals. Figure 8b shows typical indentation load–depth curves of the $FeCoCrNiMo_{0.5}$ HEA. The average Young's modulus and hardness of the alloy are 250.6 and 5.3 GPa, respectively. The value of Young's modulus measured by the nanoindentation has a good correspondence with the previous first-principle calculation (262.8 GPa), with an error of about 4.9%. This also verifies the accuracy of our calculation results from the side.

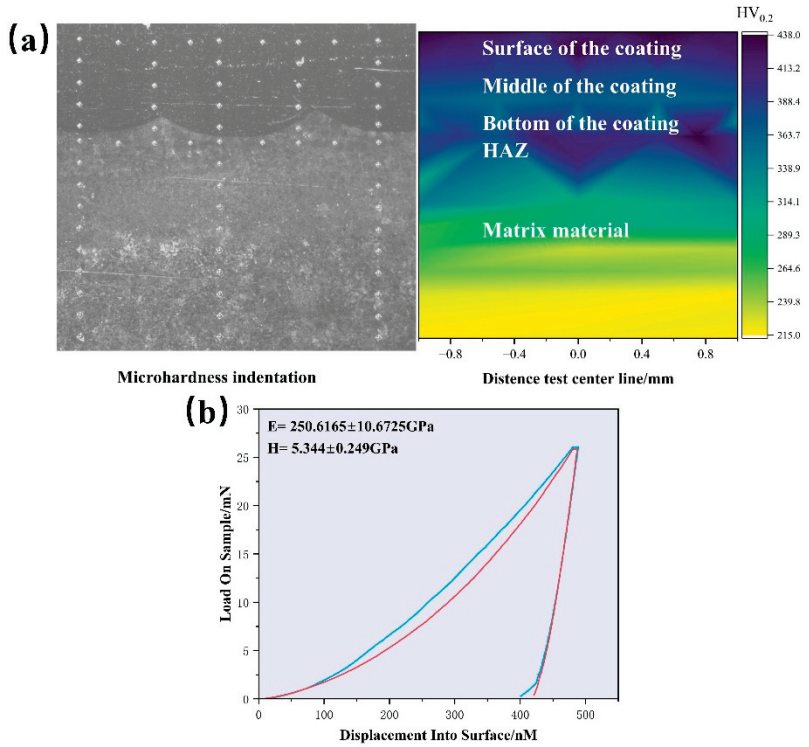


Figure 8. Mechanical properties of FeCoCrNiMo0.5 HEA coating: (**a**) Vickers hardness indentation and hardness values of coating cross-sections; (**b**) nanoindentation results for coating.

3.3. Elastic Properties of σ Phase

Section 3.2 highlights the significant presence of the σ phase in the coating, which greatly impacts the mechanical properties of $FeCoCrNiMo_{0.5}$ HEA. Therefore, it is essential to investigate the elastic properties of the σ phase to understand its influence on the alloy's overall behavior. The σ phase is primarily composed of Cr_2Mo_3, which has a cubic structure. To analyze it, a crystal structure model of Cr_2Mo_3 was created, as illustrated in Figure 9. After optimizing the structure, the elastic properties were calculated using the stress–strain method based on first-principles calculations.

The mechanical stability conditions for the cubic crystal system, as defined by the Born–Huang theory, are given in Equation (2). Table 2 shows that the elastic constants of the σ phase meet the mechanical stability criteria, confirming that the phase is structurally stable. Elastic property calculations indicate that the bulk modulus (B) and shear modulus (G) are low compared to the FCC phase, with a Poisson's ratio below 0.26 and a B/G ratio less than 1.75. This suggests that the σ phase has weak shear resistance and low ductility, making it an entirely brittle phase. Using Chen et al.'s hardness prediction formula [47], the hardness of the σ phase was calculated to be approximately 22.7 GPa, which corresponds to a Vickers hardness of about 2300 HV. This value is significantly higher than that of conventional alloys. Therefore, the σ phase, formed due to the addition of Mo, is a brittle and hard phase that significantly alters the coating's properties and enhances its hardness. Moderate amounts of the σ phase can significantly enhance the hardness of the alloy, whereas excessive precipitation of the σ phase leads to increased brittleness [48].

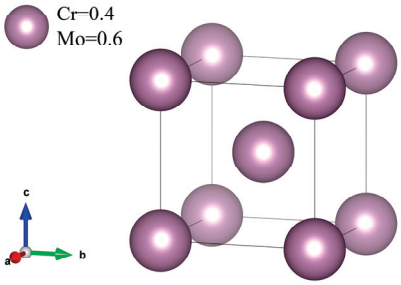


Figure 9. Model structure of the σ phase.

To mitigate the brittleness while maintaining the hardness benefits of the σ phase, strategies such as heat treatment (e.g., annealing) or compositional adjustments can be considered. Heat treatment may modify the distribution and morphology of the σ phase, potentially reducing its negative impact on ductility. For example, the formation of the σ phase can be suppressed by controlling the cooling rate and introducing an annealing step, which enhances the ductility of the alloy without significantly reducing the hardness [49]. Additionally, compositional adjustments, such as reducing Mo content or adding stabilizing elements like Ti, can suppress σ-phase formation or modify its morphology [48].

4. Conclusions

This study investigated the mechanical properties and electronic structure of $FeCoCrNiMo_x$ HEAs using first-principles calculations based on density functional theory. Additionally, $FeCoCrNiMo_{0.5}$ HEAs coatings were prepared on EA4T steel using the laser cladding method, and their microstructure and microhardness were characterized. The main conclusions of the study are as follows:

(1) The addition of molybdenum increases the ductility and anisotropy of the $FeCoCrNiMo_x$ HEAs FCC phase, though it slightly reduces strength and stiffness, as confirmed by electronic structure calculations. As the Mo content increases, lattice distortion in the coating becomes more pronounced, with a corresponding leftward shift in the diffraction peak. The Young's modulus measured by nanoindentation closely aligns with first-principles calculations, showing a deviation of approximately 4.9%;

(2) The $FeCoCrNiMo_{0.5}$ HEAs coatings exhibit a transition from columnar crystals at the bottom to equiaxed crystals at the surface. The surface hardness reaches 437.91 $HV_{0.2}$, while the bottom shows slightly lower hardness. Residual stress tests show that the coating surface experiences residual compressive stress due to rapid cooling,

while the bottom exhibits significant residual tensile stress. This is attributed to the thermal expansion coefficient mismatch and the directional growth of columnar crystals between the coating and substrate. Furthermore, a large number of σ phases were precipitated in the coating due to the deviation of Cr and Mo elements;

(3) The elastic properties of the σ phase were calculated using the stress–strain method, showing low bulk modulus, shear modulus, and Poisson's ratio. Its hardness is 22.7 GPa, classifying it as a brittle, hard phase. The presence of the σ phase alters the coating's properties, contributing to its increased hardness.

Author Contributions: G.G., methodology, funding acquisition, project administration, and writing—review and editing; H.L., conceptualization, investigation, validation, writing—original draft, and writing—review and editing; J.J., data curation, writing—original draft, and writing—review and editing; Z.Z., project administration and supervision; J.Y., data curation; H.S., data curation; S.S., data curation; W.T., data curation. All authors have read and agreed to the published version of the manuscript.

Funding: "Research on rapid scanning and health Assessment Technology of spherical Tank stress based on electromagnetic Ultrasound" scientific research project of State Market Supervision Administration in 2023, project No. 2023MK054; Key Research and Development Plan of Sichuan Province [25GJHZ0239].

Institutional Review Board Statement: Not applicable.

Informed Consent Statement: Not applicable.

Data Availability Statement: The original contributions presented in this study are included in the article. Further inquiries can be directed to the corresponding author.

Conflicts of Interest: Author Zhiyi Zhang was employed by the CRRC Qingdao Sifang Co., Ltd. Author Hairong Sun was employed by the Chengdu Metro Operation Co., Ltd. The remaining authors declare that the research was conducted in the absence of any commercial or financial relationships that could be construed as a potential conflict of interest.

References

1. Alaneme, K.K.; Bodunrin, M.O.; Oke, S.R. Processing, alloy composition and phase transition effect on the mechanical and corrosion properties of high entropy alloys: A review. *J. Mater. Res. Technol.* **2016**, *5*, 384–393. [CrossRef]
2. Sheng, H.F.; Gong, M.; Peng, L.M. Microstructural characterization and mechanical properties of an $Al_{0.5}CoCrFeCuNi$ high-entropy alloy in as-cast and heat-treated/quenched conditions. *Mater. Sci. Eng. A* **2013**, *567*, 14–20. [CrossRef]
3. Tsao, L.C.; Chen, C.S.; Chu, C.P. Age hardening reaction of the $Al_{0.3}CrFe_{1.5}MnNi_{0.5}$ high entropy alloy. *Mater. Des.* **2012**, *36*, 854–858. [CrossRef]
4. George, E.P.; Curtin, W.A.; Tasan, C.C. High entropy alloys: A focused review of mechanical properties and deformation mechanisms. *Acta Mater.* **2020**, *188*, 435–474. [CrossRef]
5. Giwa, A.M.; Aitken, Z.H.; Liaw, P.K.; Zhang, Y.-W.; Greer, J.R. Effect of temperature on small-scale deformation of individual face-centered-cubic and body-centered-cubic phases of an $Al_{0.7}CoCrFeNi$ high-entropy alloy. *Mater. Des.* **2020**, *191*, 10611. [CrossRef]
6. Lu, C.-W.; Lu, Y.-S.; Lai, Z.-H.; Yen, H.-W.; Lee, Y.-L. Comparative corrosion behavior of $Fe_{50}Mn_{30}Co_{10}Cr_{10}$ dual-phase high-entropy alloy and CoCrFeMnNi high-entropy alloy in 3.5 wt% NaCl solution. *J. Alloys Compd.* **2020**, *842*, 155824. [CrossRef]
7. Zhu, Z.; Yan, S.; Chen, H.; Gou, G. Unprecedented combination of strength and ductility in laser welded NiCoCr medium entropy alloy joints. *Mater. Sci. Eng. A* **2021**, *803*, 140501. [CrossRef]
8. Minouei, H.; Kheradmandfard, M.; Rizi, M.S.; Jalaly, M.; Kim, D.-E.; Hong, S.I. Formation mechanism of high-entropy spinel thin film and its mechanical and magnetic properties: Linking high-entropy alloy to high-entropy ceramic. *Appl. Surf. Sci.* **2022**, *576*, 151719. [CrossRef]
9. Yang, C.-M.; Liu, X.-B.; Zhu, Z.-X.; Zhou, A.; Zhou, H.-B.; Zhang, S.-H. Study of tribological property of laser-cladded FeCoCrNiMnx high-entropy alloy coatings via experiment and molecular dynamics simulation. *Tribol. Int.* **2024**, *191*, 109106. [CrossRef]

10. Cui, Y.; Shen, J.Q.; Geng, K.P.; Hu, S.S. Fabrication of FeCoCrNiMnAl$_{0.5}$-FeCoCrNiMnAl gradient HEA coating by laser cladding technique. *Surf. Coat. Technol.* **2021**, *412*, 127077. [CrossRef]
11. Chen, D.; Guan, Y.J.; Jin, G.; Cui, X.F.; Liu, E.B.; Feng, L.T.; Li, X.Y. In-situ synthesis of a FeCoCrNiCu/FeCoCrNiAl composite high entropy alloy coating by laser cladding. *Surf. Coat. Technol.* **2023**, *461*, 129447. [CrossRef]
12. Guo, Y.F.; Zhu, J.Q.; Cao, J.J.; Qiu, Z.G.; Chang, C.; Yan, X.C.; Yin, S.; Liu, M. Pitting corrosion mechanism of BCC+FCC dual-phase structured laser cladding FeCoCrNiAl$_{0.5}$Ti$_{0.5}$ HEAs coating. *J. Alloys Compd.* **2024**, *980*, 173643. [CrossRef]
13. Dai, C.; Zhao, T.; Du, C.; Liu, Z.; Zhang, D. Effect of molybdenum content on the microstructure and corrosion behavior of FeCoCrNiMo$_x$ high-entropy alloys. *J. Mater. Sci. Technol.* **2020**, *46*, 64–73. [CrossRef]
14. Zhao, Y.; Zhang, X.; Quan, H.; Chen, Y.; Wang, S.; Zhang, S. Effect of Mo addition on structures and properties of FeCoNiCrMn high entropy alloy film by direct current magnetron sputtering. *J. Alloys Compd.* **2022**, *895*, 162709. [CrossRef]
15. Gu, Z.; Peng, W.; Guo, W.; Zhang, Y.; Hou, J.; He, Q.; Zhao, K.; Xi, S. Design and characterization on microstructure evolution and properties of laser-cladding Ni$_{1.5}$CrFeTi$_2$B$_{0.5}$Mo$_x$ high-entropy alloy coatings. *Surf. Coat. Technol.* **2021**, *408*, 126793. [CrossRef]
16. Liang, C.; Wang, C.; Zhang, K.; Tan, H.; Liang, M.; Xie, Y.; Liu, W.; Yang, J.; Zhou, S. Mechanical and tribological properties of (FeCoNi)$_{88-x}$(AlTi)$_{12}$Mo$_x$ high-entropy alloys. *Int. J. Refract. Met. Hard Mater.* **2022**, *105*, 105845. [CrossRef]
17. Li, Y.T.; Fu, H.G.; Wang, K.M.; Yang, X.J.; Zong, B.; Lin, J. Effect of Mo addition on microstructure and wear resistance of laser clad AlCoCrFeNi-TiC composite coatings. *Appl. Surf. Sci.* **2023**, *623*, 157071. [CrossRef]
18. Wu, H.; Zhang, S.; Wang, Z.Y.; Zhang, C.H.; Chen, H.T.; Chen, J. New studies on wear and corrosion behavior of laser cladding FeNiCoCrMo$_x$ high entropy alloy coating: The role of Mo. *Int. J. Refract. Met. Hard Mater.* **2022**, *102*, 105721. [CrossRef]
19. Cichocki, K.; Bała, P.; Kozieł, T.; Cios, G.; Schell, N.; Muszka, K. Effect of Mo on Phase Stability and Properties in FeMnNiCo High-Entropy Alloys. *Metall. Mater. Trans. A* **2022**, *53*, 1749–1760. [CrossRef]
20. van de Walle, A.; Tiwary, P.; de Jong, M.; Olmsted, D.L.; Asta, M.; Dick, A.; Shin, D.; Wang, Y.; Chen, L.-Q.; Liu, Z.-K. Efficient stochastic generation of special quasirandom structures. *Calphad* **2013**, *42*, 13–18. [CrossRef]
21. Lin, S.Y.; Yao, Y.; Yao, Z.P.; Liu, Y.; Liu, Y.Y.; Zhang, P.; Qin, W.; Wu, X.H. Construction of FeCrVTiMo$_X$ high-entropy alloys with enhanced mechanical properties based on electronegativity difference regulation strategy. *J. Alloys Compd.* **2023**, *957*, 10. [CrossRef]
22. Boudiaf, K.; Bouhemadou, A.; Al-Douri, Y.; Khenata, R.; Bin-Omran, S.; Guechi, N. Electronic and thermoelectric properties of the layered BaFAgCh (Ch = S, Se and Te): First-principles study. *J. Alloys Compd.* **2018**, *759*, 32–43. [CrossRef]
23. Zaddach, A.J.; Niu, C.; Koch, C.C.; Irving, D.L. Mechanical Properties and Stacking Fault Energies of NiFeCrCoMn High-Entropy Alloy. *JOM* **2013**, *65*, 1780–1789. [CrossRef]
24. Li, Y.; Gao, Y.; Xiao, B.; Min, T.; Yang, Y.; Ma, S.; Yi, D. The electronic, mechanical properties and theoretical hardness of chromium carbides by first-principles calculations. *J. Alloys Compd.* **2011**, *509*, 5242–5249. [CrossRef]
25. Gu, Q.; Wang, Y.; Leng, E.G.; Huang, Y.H.; Jin, N. First-principles study of the stability and mechanical properties for binary Mo–Re alloys. *Phys. B Condens. Matter* **2024**, *693*, 416401. [CrossRef]
26. Hayun, S.; Lilova, K.; Salhov, S.; Navrotsky, A. Enthalpies of formation of high entropy and multicomponent alloys using oxide melt solution calorimetry. *Intermetallics* **2020**, *125*, 106897. [CrossRef]
27. Pan, Y. First-principles investigation of the new phases and electrochemical properties of MoSi2 as the electrode materials of lithium ion battery. *J. Alloys Compd.* **2019**, *779*, 813–820. [CrossRef]
28. Pan, Y.; Mao, P.Y.; Jiang, H.; Wan, Y.Y.; Guan, W.M. Insight into the effect of Mo and Re on mechanical and thermodynamic properties of $NbSi_2$ based silicide. *Ceram. Int.* **2017**, *43*, 5274–5282. [CrossRef]
29. Zhang, X.; Dong, T.; Ma, H.; Yu, H.; Li, X.; Wang, F. Insight into the vacancy effects on mechanical and electronic properties of V5Si3 silicides from first-principles calculations. *J. Mol. Graph. Model.* **2020**, *98*, 107600. [CrossRef]
30. Tan, Y.; Ma, L.; Wang, Y.; Zhou, W.; Wang, X.; Guo, F. Pressure dependence of mechanical and thermodynamic properties of Al2Si4Sr3: A first-principles study. *Comput. Theor. Chem.* **2023**, *1230*, 114400. [CrossRef]
31. Güler, E.; Güler, M.; Uğur, G.; Uğur, Ş. A first-principles study for the elastic and mechanical properties of Ti64, Ti6242 and Ti6246 alloys. *Eur. Phys. J. B* **2021**, *94*, 222. [CrossRef]
32. Wang, X.; Li, X.; Xie, H.; Fan, T.; Zhang, L.; Li, K.; Cao, Y.; Yang, X.; Liu, B.; Bai, P. Effects of Al and La elements on mechanical properties of CoNiFe$_{0.6}$Cr$_{0.6}$ high-entropy alloys: A first-principles study. *J. Mater. Res. Technol.* **2023**, *23*, 1130–1140. [CrossRef]
33. Duan, Y.H.; Sun, Y.; Guo, Z.Z.; Peng, M.J.; Zhu, P.X.; He, J.H. Elastic constants of AlB2-type compounds from first-principles calculations. *Comput. Mater. Sci.* **2012**, *51*, 112–116. [CrossRef]
34. Bi, X.; Hu, X.; Jiang, X.; Li, Q. Effect of Cu additions on mechanical properties of Ni3Sn4-based intermetallic compounds: First-principles calculations and nano-indentation measurements. *Vacuum* **2019**, *164*, 7–14. [CrossRef]

35. Wan, Y.; Zeng, Y.; Qian, X.; Yang, Q.; Sun, K.; Zhang, Y.; Shang, X.; Quan, G.; Jiang, B. First-principles calculations of structural, elastic and electronic properties of second phases and solid solutions in Ti–Al–V alloys. *Phys. B Condens. Matter* **2020**, *591*, 412241. [CrossRef]
36. Liu, S.; Zhang, S.; Liu, S.; Li, D.; Li, Y.; Wang, S. Phase stability, mechanical properties and melting points of high-entropy quaternary metal carbides from first-principles. *J. Eur. Ceram. Soc.* **2021**, *41*, 6267–6274. [CrossRef]
37. Pu, D.L.; Pan, Y. Influence of high pressure on the structure, hardness and brittle-to-ductile transition of $NbSi_2$ ceramics. *Ceram. Int.* **2021**, *47*, 2311–2318. [CrossRef]
38. Shao, L.; Xu, C.-R.; Ding, N.; Chen, X.-T.; Duan, J.-M.; Tang, B.-Y. The intrinsic mechanical properties of NbTaTiZr and the influence of alloying elements Mo and W: A first-principles study. *J. Alloys Compd.* **2022**, *911*, 165109. [CrossRef]
39. Wang, Y.; He, J.; Yan, M.; Li, C.; Wang, L.; Zhou, Y. First-principles study of NiAl alloyed with rare earth element Ce. *J. Mater. Sci. Technol.* **2011**, *27*, 719–724. [CrossRef]
40. Ma, Z.N.; Jiang, M.; Wang, L. First-principles study of electronic structures and phase stabilities of ternary intermetallic compounds in the Mg-Y-Zn alloys. *Acta Phys. Sin.* **2015**, *64*, 187102. [CrossRef]
41. Xiao, Z.P.; Zhang, L.Q.; Guo, Z.Q. Ab initio investigation of phase stability, thermo-physical and mechanical properties of $(Mo_{0.2}Cr_{0.2}Ta_{0.2}Nb_{0.2}X_{0.2})Si_2$ (X = W, V) high-entropy refractory metal silicides. *Comput. Mater. Sci.* **2022**, *203*, 111116. [CrossRef]
42. Zhao, W.; Li, Z.; Song, C.; Wang, M.; Xiao, G.; Zhang, H.; Li, X.; Yu, K.; Xu, L. Al and Mo synergistic enhancement of CoCrFeNi high-entropy alloy laser cladding layer. *J. Mater. Res. Technol.* **2024**, *28*, 2572–2581. [CrossRef]
43. Sun, Y.; Gao, J.; Wang, K.N.; Song, Q.; Cui, H.Z.; Li, W.S.; Wang, C.M. The effect of multi-element alloying on the structure and properties of laser cladding nickel-based coatings. *Surf. Coat. Technol.* **2023**, *454*, 129174. [CrossRef]
44. Jin, J.J.; Chen, B.; Zhang, Z.Y.; Wu, Y.B.; Luo, Z.Y.; Gou, G.Q.; Chen, W.J. Effects of Mo content on the microstructure and mechanical properties of laser cladded $FeCoCrNiMo_x$ (x = 0.2, 0.5) high-entropy alloy coatings. *Surf. Coat. Technol.* **2024**, *482*, 130697. [CrossRef]
45. Liu, P.; Hu, J.Y.; Sun, S.Y.; Feng, K.Y.; Zhang, Y.B.; Cao, M.Q. Microstructural evolution and phase transformation of Inconel 718 alloys fabricated by selective laser melting under different heat treatment. *J. Manuf. Process.* **2019**, *39*, 226–232. [CrossRef]
46. Huang, L.; Cao, Y.; Li, G.H.; Wang, Y.F. Microstructure characteristics and mechanical behaviour of a selective laser melted Inconel 718 alloy. *J. Mater. Res. Technol.* **2020**, *9*, 2440–2454. [CrossRef]
47. Chen, X.-Q.; Niu, H.; Li, D.; Li, Y. Modeling hardness of polycrystalline materials and bulk metallic glasses. *Intermetallics* **2011**, *19*, 1275–1281. [CrossRef]
48. Liu, Y.; Xie, Y.; Cui, S.; Yi, Y.; Xing, X.; Wang, X.; Li, W. Effect of Mo Element on the Mechanical Properties and Tribological Responses of $CoCrFeNiMo_x$ High-Entropy Alloys. *Metals* **2021**, *11*, 486. [CrossRef]
49. Bae, J.W.; Park, J.M.; Moon, J.; Choi, W.M.; Lee, B.-J.; Kim, H.S. Effect of μ-precipitates on the microstructure and mechanical properties of non-equiatomic CoCrFeNiMo medium-entropy alloys. *J. Alloys Compd.* **2019**, *781*, 75–83. [CrossRef]

Disclaimer/Publisher's Note: The statements, opinions and data contained in all publications are solely those of the individual author(s) and contributor(s) and not of MDPI and/or the editor(s). MDPI and/or the editor(s) disclaim responsibility for any injury to people or property resulting from any ideas, methods, instructions or products referred to in the content.

materials

MDPI

Article

Finite Element Simulation and Optimization of Process Parameters for Titanium Chip Crusher

Jianghua Huang [1], Zeling Zhao [2,*], Xiaomin Huang [3], Tao Liu [4] and Hongchao Ji [3,*]

[1] School of Mechanical and Energy Engineering, Zhejiang University of Science and Technology, Hangzhou 310023, China; huangjianghua@zust.edu.cn
[2] College of Mechanical & Energy Engineering, Beijing University of Technology, Beijing 100124, China
[3] College of Mechanical Engineering, North China University of Science and Technology, Tangshan 063210, China; xmhuang@ncst.edu.cn
[4] China MCC 22 Group Corporation Ltd., Tangshan 063035, China; mccliutao@163.com
* Correspondence: zhaozeling@163.com (Z.Z.); jihongchao@ncst.edu.cn (H.J.); Tel.: +86-0315-8805-440 (H.J.)

Abstract: Titanium alloy has been widely used in aerospace, military, and national defense, and other high-tech fields due to its advantages of light weight, high specific strength, excellent corrosion resistance, excellent heat resistance, and good low-temperature performance. In the turning of titanium alloys, a significant quantity of continuous chips with poor breakability is generated. Recycling these titanium chips can effectively reduce raw material costs and minimize environmental impacts, as it decreases the dependency on primary titanium sources. The titanium chip crushing process is an indispensable part of the titanium chip recovery process, and the double-teeth roll crushing process is the most commonly used metal crushing process. Finite element simulation is an efficient, time-saving, and resource-saving method to optimize the titanium chip crushing process. In this paper, the stress change in the process of titanium chip crushing is analyzed by finite element simulation, and the influence of the number of cutter roller teeth and the speed of the cutter roller on the crushing effect of the titanium chip is analyzed. The optimal process parameters of the titanium chip crusher were obtained by response surface optimization, and the accuracy of the finite element simulation was verified by experiments, which provided a theoretical and practical basis for optimizing the titanium chip crushing process.

Keywords: TC4; titanium chips; Johnson–Cook constitutive model; double-teeth roll crushing process; finite element simulation

1. Introduction

With the development of science and technology, the requirements for materials, especially metal materials, are increasing in various industrial fields. Titanium alloy is widely used in aerospace, military defense, and other high-tech fields because of its light mass, high specific strength, good corrosion resistance, high thermal strength, and good low-temperature performance [1–3]. The main components of titanium alloy are α-phase, β-phase, and α + β phase titanium alloy, and the two-phase titanium alloy is most widely used. The α + β phase titanium alloy has good comprehensive performance and a stable structure. TC4 is a typical two-phase titanium alloy [4–6]. Due to the unique processing characteristics of a titanium alloy, a large number of chips will be produced in the turning process. How to

recycle these titanium alloy chips and reduce the costs of titanium production has become an important research direction in the titanium processing industry.

The metal crushing process is an indispensable part of the metal recovery process. Double-tooth roller crushers have been widely used because of their simple structure, reliable work, and low costs [7]. However, most of the twin-tooth roller crushers are developed for ore, and there are few studies on ductile metal crushing processes with low hardness such as titanium chips [8–11]. Ordinary ore crusher work is to rely on the adjacent two teeth of the ore impact extrusion crushing, and the state of titanium chip crushing is different; titanium chip crushing needs to form a shear mouth between the teeth roller, using the shear force to break the titanium chip [12,13].

In previous times, numerous researchers have delved into the study of crushers and their associated crushing processes. André et al. [14] used a discrete element model to simulate the crushing of mixed materials containing hard and soft materials in a cone crusher. The results show that the crusher output will not decrease with the proportion of ductile materials. Neto et al. [15] developed a discrete-event simulation model to improve the performance of a steel production line and applied the model to a steel production line, showing that it could significantly improve the efficiency of the line. Kwon et al. [10] established a crushing-agglomeration combination model to characterize the particle characteristics of the double-teeth roller crusher and predict the particle size distribution of the crusher products. This model can represent the decrease and increase in the complex particle size in the process. The experimental parameters were used to predict the particle size distribution of the products with distributed particle size feed, and the results were compared to the experimental results, which were in good agreement. This indicates that this model can better predict the product size distribution. Lieberwirth et al. [16] studied the load variation law of the double-teethed roller crusher under extreme conditions. Considering the fact that a large amount of energy is stored in the flywheel and the mass of the floating roller of the maximum machine is too large, suggesting that any unexpected dynamic behavior may raise issues of safe operation, and obtained the crushing force dynamics results under extreme conditions, as well as the influence of the particle size distribution of related products and the mineral structure of various rocks on the clamping behavior. Marcus Johansson et al. [17] established the time dynamic response model of a high-pressure roller mill and studied the dynamic response of hydraulic system damping, feed particle size change, ore hardness, and crusher-to-roller speed change. The model is suitable for high-fidelity analysis and shows the potential of predicting the performance of a crusher in process simulation, with an average error of about 10%.

Finite element simulation is an effective way to study the titanium chip crushing process and can effectively reduce research costs through finite element simulation [18–22]. ABAQUS has a huge database and a powerful three-dimensional modeling function; it can also import the built model directly into the software. Its rich material attribute table can directly give the model material and analyze its properties [23].

A reasonable intrinsic constitutive model is a prerequisite for accurate finite element simulation results. Over the years, many researchers have investigated the deformation properties of materials under different loading conditions and modified many constitutive models to describe the flow behavior. These models can be divided into the following three categories: empirical model, semi-empirical model, and physical-based model [24–26]. For example, the Johnson–Cook model, the Zerilli-Armstrong model, the Steinberg-Guinan model, and the Cowper-Symonds model [27–30]. Among them, the Johnson–Cook constitutive model has been widely used because it involves fewer material constants and

can be directly applied to a variety of finite element software, especially for predicting the mechanical properties of materials under different conditions [31–34].

In this paper, SolidWorks 2017 software is used to model the double-tooth roller crusher, and a multi-group crushing tooth roller model based on different tooth numbers is established. Then the model is imported into ABAQUS for simulation. The effects of different numbers of cutter teeth, different rotational speeds, and different tip angles on the crushing of titanium chips were considered. Through finite element simulation, the stress change during the crushing process of titanium chips was analyzed, and the influence of the number of cutter roller teeth and the speed of the cutter roller on the crushing effect of titanium chips was analyzed. The optimal process parameters of the titanium chip crusher were obtained by response surface optimization, and the accuracy of the finite element simulation was verified by experiments, which provided a theoretical and practical basis for optimizing the titanium chip crushing process.

2. Model and Simulation of Titanium Chip Crushing Process

2.1. Selection of Cutter Tooth Profile Structure of Double-Toothed Roll Crusher

When the double-toothed roll crusher is working, the installation of different types of crushing teeth will directly affect the crushing effect of the processed materials and the energy consumption during processing and will also affect the output of the crusher and the service life of the cutter teeth. Therefore, it is necessary to conduct a comprehensive analysis of the common broken tooth structure in the market. The crushing behavior of different cutter tooth structures on the material during operation is different, including shearing, extrusion, collision, and puncture. Considering the characteristics of low stiffness and good toughness of titanium chip material, a cutter tooth structure suitable for titanium chip crushing is designed.

There are many factors affecting the design of the tooth structure of the double-toothed roll crusher, especially for the particle size distribution of the product and the material properties of the processed materials. Therefore, considering the material properties of titanium chips and the requirements for their processing granularity, a broken tooth with simple structure is proposed. Although it only involves the basic shape parameters of the broken tooth, it can generally describe the shape of the broken tooth and provide a good basis for further optimization design of the tooth shape. As shown in Figure 1, the tooth structure of the tooth plate crushing tooth for titanium chips is shown.

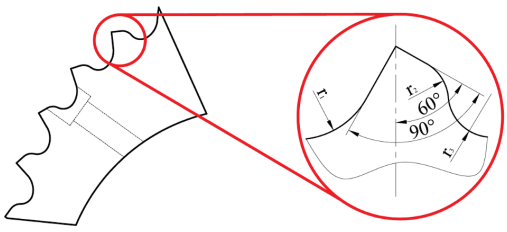


Figure 1. Schematic diagram of tooth plate and crusher tooth structure.

In order to study the influence of different cutter tooth shapes on the stress of titanium chips when the crusher is working, 60°, 75°, and 90° are selected as the cutter tip angles to model the cutter. Figure 2 is a schematic diagram of broken teeth with different tip angles. Among them, (a) corresponds to a cutting-edge angle of 60°, (b) to 75°, and (c) to 90°.

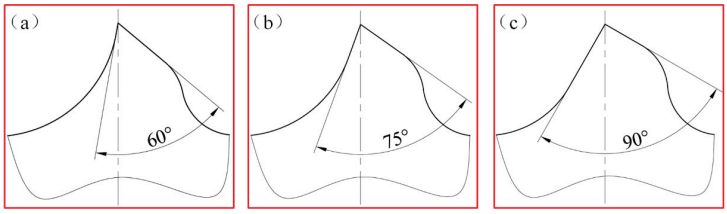


Figure 2. Schematic diagram of crusher teeth with different cutting edge angles. (**a**) 60° blade angle. (**b**) 75° blade angle. (**c**) 90° blade angle.

2.2. Model of Titanium Chip Crushing Teeth Roller

The establishment of a geometric model is the basis of finite element analysis, and the establishment of an accurate 3D model can improve the accuracy of simulation results [35]. Therefore, how to establish the 3D model efficiently and accurately is particularly critical. If the 3D model is too complex, it will bring considerable difficulties to the later finite element analysis. So, it is necessary to make a reasonable simplification of the 3D model of the titanium chip crushing roll.

Figure 3 is the overall model of the double-teethed roll titanium sheet crusher. The broken teeth plate is fixed on the broken teeth roller by bolts. To facilitate the later finite element software to mesh the broken teeth roller and save the simulation calculation time, only a part of the broken teeth roller is taken to establish the simulation model.

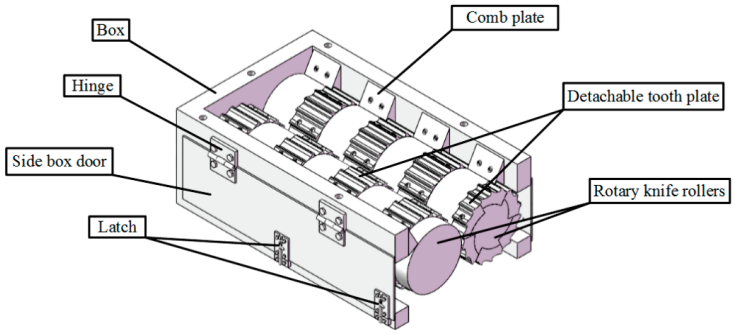


Figure 3. Double-teethed roller titanium chip crusher.

To explore the influence of different tooth numbers on the crushing effect of titanium chips, SolidWorks 2017 software was used to model the crushing knife roller, and 18, 23, 27, and 32 tooth numbers were used for the model. Then it is imported into the finite element software ABAQUS 2020 for calculation.

To study the effect of different rotational speeds on titanium chip crushing, different simulation groups were established at different rotational speeds of 18 rpm, 22 rpm, 26 rpm, and 30 rpm.

2.3. Simulation of Titanium Chip Breaking Process

To greatly reduce the calculation time and amount of calculation of the titanium chips crushing simulation, the established model should be simplified as much as possible on the premise of improving the accuracy of simulation calculation results. So, to more effectively apply the finite element analysis of the titanium chip crushing process, in this paper, the following settings were used:

(1) The ambient temperature is always 25 °C.
(2) The cutter is a sharp, rigid body, and it only rotates.
(3) The processed work-piece material is isotropic.

(4) All the chemical changes due to temperature changes during the crushing of titanium chips are not considered.
(5) The titanium chip material transition temperature is set at 25 °C.

Since the hardness of the tool material is much higher than that of the titanium chip, the elastic modulus of the tool material is large compared to that of the titanium chip material. When the titanium chip is broken, the titanium chip will have large plastic deformation, and the deformation of the tool can be completely ignored. Therefore, in this paper, the tool is set as a rigid body [36].

The most important step in the process of establishing the finite element model is to divide the finite element mesh. Many factors should be considered when meshing because the calculation accuracy and calculation scale of the simulation model are limited by the number and shape of the mesh [37].

Usually, two specific parameters are used to determine the number of meshes. One parameter is the number of elements divided by the selected solid surface, and the other parameter is the mesh density control parameter. Through the trade-off between these two parameters, the accurate division of finite element meshes is finally achieved.

In finite element simulation analysis software, the commonly used mesh elements mainly include the following two types: mixed tetrahedral elements and eight-node hexahedral elements [38]. The mesh generation of mixed tetrahedral elements is relatively easy because its geometric characteristics are linear. However, the mesh division of eight-node hexahedral elements is more difficult, but it is suitable for deformation analysis and heat conduction analysis.

In the process of finite element simulation analysis, sometimes the analysis is terminated due to some extreme phenomena, which are mainly due to the serious deformation of the element mesh. This phenomenon will seriously affect the accuracy of simulation results and even lead to the termination of the analysis process. To solve this phenomenon, the grid should be re-divided, that is, the abnormal grid should be divided.

Finite element software enables automatic mesh re-division to deal with mesh distortions [39]. Figure 4a shows the model of the rotating cutter roller after tetrahedral meshing by finite element software. The model is a rigid body, shell element. Figure 4b is the titanium chip model after meshing using a hexahedral mesh solid model.

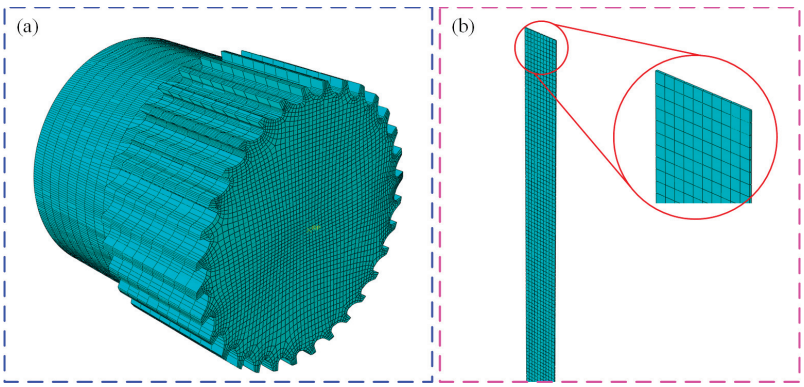


Figure 4. Meshing division for the knife roll and titanium chips. (**a**) Broken knife roller model (**b**) Titanium chip model.

A prerequisite for the accuracy of the crushing process in titanium chip crushing simulation is to obtain an accurate material model. The TC4 titanium alloy was selected as the titanium chips material. In finite element software, the following parameters need to be set: material density, elastic modulus, conductivity, Poisson's ratio, inelastic heat

share, expansion coefficient, specific heat capacity, Johnson–Cook damage coefficient, and Johnson–Cook constitutive parameters. See Tables 1 and 2 for the properties of titanium chip materials. Among them, the Johnson–Cook constitutive model setting parameters can be obtained by reference [40].

Table 1. Johnson–Cook model setting parameters.

Parameter	*A* (MPa)	*B* (MPa)	*n*	*C*	*m*	Melt Temperature (°C)	Transition Temperature (°C)
TC4	1003.132	1003.510	0.663	0.0137	1	1605	25

Table 2. Property parameters of TC4 titanium alloy material.

Parameter	Density	Elastic Modulus	Conductivity	Poisson's Ratio	Inelastic Heat Share	Expansion Coefficient	Specific Heat Capacity
TC4	4.43×10^{-9}	108,000	6.8	0.33	0.9	9.0×10^{-6}	520,000

Material density: t/mm^3, elastic modulus: MPa, conductivity: W/(m·K), expansion coefficient: 1/°C, and specific heat capacity: J/(kg·°C).

The Johnson–Cook failure model parameters d1, d2, d3, d4, and d5 of TC4 titanium alloy can be obtained by referring to the literature [40]. Table 3 shows the Johnson–Cook damage parameters used in finite element software.

Table 3. Johnson–Cook damage parameters.

d1	d2	d3	d4	d5	Melting Point °C	Transition Temperature °C	Reference Strain Rate
−0.197	2.332	3.138	0.034	3.87	1605	25	0.001

The built model is imported into finite element software, given titanium chip material, and the model is assembled. Through the interaction between the titanium chip and the crushing roller, the load was applied to the model, and the finite element model was established and solved.

3. Results and Discussion

3.1. Processing of Simulation Results

In the cutting process, when the tool is in contact with the titanium chip, the titanium chip first undergoes elastic deformation. With the rotation of the knife roller, the teeth on the knife roller continuously interact with the titanium chips for the shearing operation. With this continuous meshing and the shearing process, the accumulated stress on the titanium chips gradually increases, resulting in plastic deformation of the titanium chips. Finally, after the stress reaches a certain degree, the titanium chips break.

The crushing process of titanium scraps can be divided into two stages. The first stage is the initial stage, during which the titanium scraps just begin to contact the crushing roller teeth, and the stress on the titanium scraps gradually increases. However, the contact position between the titanium chips and cutter teeth remains in the elastic deformation stage, with no yield or plastic deformation occurring, as illustrated in Figure 5a; With the continuous action of external load, the stress concentration at the contact position gradually increased, the titanium chip was continuously compressed, and yielding and plastic deformation occurred, as shown in Figure 5b. The second stage is the fracture stage

of titanium chips. Under the continuous shear extrusion of the crushing roller, the titanium chips are sheared, and the plastic deformation zone is continuously thinning until the crushing teeth are fully engaged with another crushing roller. At this time, the titanium chips are completely fractured, and the stress at the fracture position of the titanium chips reaches the maximum, as shown in Figure 5c. The unit is continuously removed during the fracture of the titanium chips, and the two sections are gradually separated while the stress on the chip gradually becomes less, as shown in Figure 5d.

Ten nodes were selected from each side of the center of the titanium chip fracture position, and the distance between each two nodes was set to 0.5 mm. According to these nodes, the respective stress values are calculated, and the point-line diagram is drawn (as shown in Figure 6). Figure 6 shows the stress distribution of the nodes at the fracture of titanium chips in the four stages of a-d in Figure 5. It can be seen from the point-line diagram that when the cutter teeth contacted the titanium chip at the beginning, the stress fluctuation of the titanium chip was small. With the continuous effect of external load, when the plastic deformation of the titanium chip began to occur, as shown in Figure 5b, the stress of the contact point increased rapidly, and the stress on both sides of the central point decreased with the increase in distance. It can be seen from curves c and d that when the titanium chip is broken, the stress of the cut titanium chip decreases. At the initial fracture time, the remaining titanium chip exhibits a stress peak. The maximum stress on the titanium chips decreases over time, and the stress on each node diminishes with increasing distance.

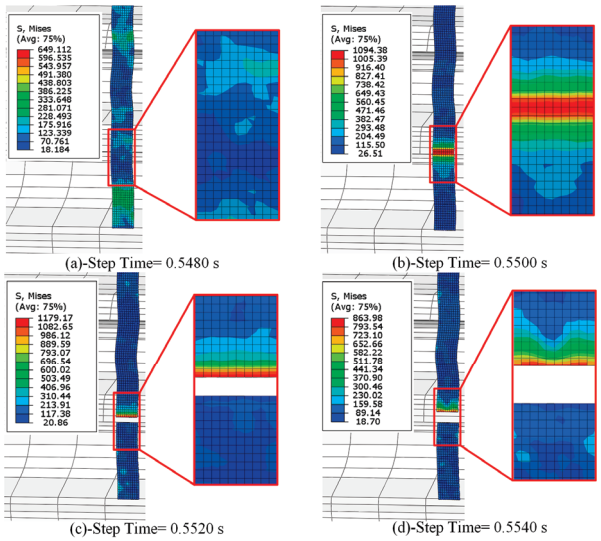


Figure 5. Stress cloud chart of the titanium chip fracture process. (**a**) elastic deformation. (**b**) plastic deformation. (**c**) break. (**d**) break.

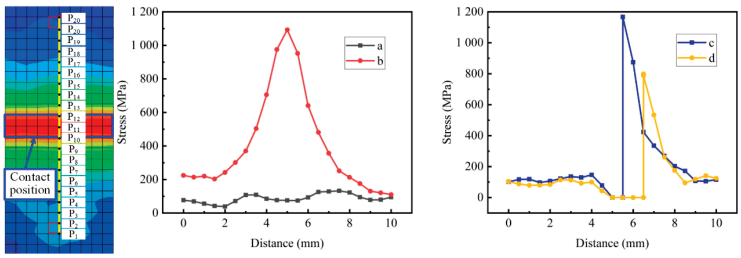


Figure 6. Distance–stress curve of the titanium chip fracture process.

The simulation experiment was carried out on the titanium chip crushing process under different tooth numbers of cutter rolls and different crushing roll speeds. At the same moment (the initial moment of plastic deformation), 10 nodes were selected from the contact position of the cutter teeth and the titanium chip to both sides, and the stress of each node was extracted. The distance–stress curve is shown in Figure 7. It is found from the figure that the distance–stress curves under different tooth numbers of cutter rolls are very similar. It is found from the curve that when the plastic deformation of the titanium chip begins, the stress at the contact position between the titanium chip and a cutter tooth increases, and the stress at each node decreases with the increase in distance.

It can be seen from Figure 7b that the stress fluctuation of titanium chips on both sides of the contact position of different tooth numbers is larger. The stress change in titanium chips increases with the increase in teeth number, and the curve changing to both sides is smoother, and the stress change is more stable.

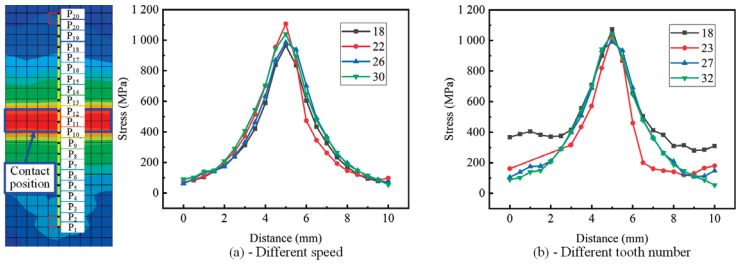


Figure 7. Stress distribution of titanium chips under different tooth numbers and rotational speeds. (**a**) Different speed. (**b**) Different number of teeth.

The four figures in Figure 8 correspond to the four curves in Figure 7b. It can be seen that due to the different number of teeth, the teeth profile structure is also different, which leads to the different contact areas between the teeth roller and the titanium chip. Due to the large angle of the blade, some tooth rollers not only contact with the titanium chips at the tip of the tooth, but also contact with the titanium chips at other positions. This means that in addition to the force at the tip of the tooth, the titanium chip will also be subjected to the force of other parts, resulting in a large stress fluctuation on both sides of the contact point.

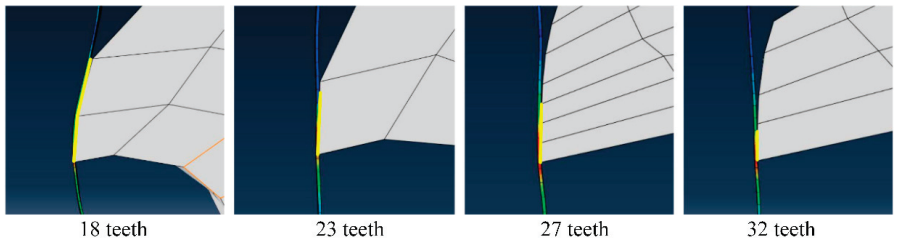


Figure 8. Contact position of titanium chip and roller teeth.

As shown in Figure 9, the equivalent plastic strain cloud chart of the titanium chip crushing process at 32 teeth and a rotating speed of 30 rpm is shown. Figure 9a–d correspond to Figure 5a–d, respectively. It can be seen from Figure 9a that when Step Time = 0.548, there is no change in the strain cloud chart. This is because the initial contact between the titanium chip and the crushing roller teeth is at this time. The stress change in the titanium chip at this time is small. At this time, the titanium chip is in the elastic change stage, and no plastic strain occurs.

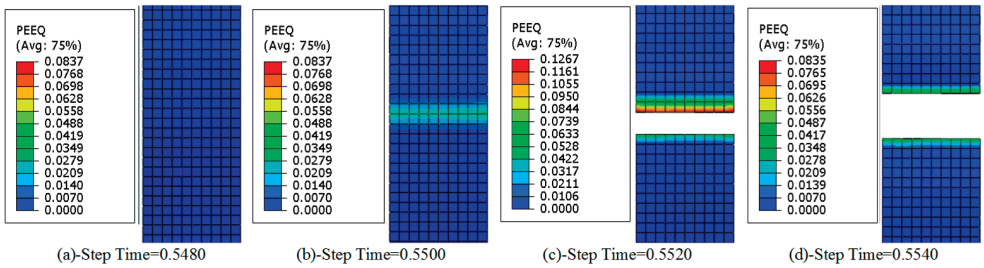


Figure 9. Equivalent plastic strain during titanium chip breaking. (**a**) elastic deformation. (**b**) plastic deformation. (**c**) break. (**d**) break.

Figure 9b under the shearing action of crushing roller teeth, plastic deformation of titanium chips begins due to the increase in stress. Figure 9c shows that the titanium chip has been broken and fractured at this time. The plastic deformation at the fracture site is the largest, and the degree of plastic deformation decreases with the distance to both sides. After the crushing, the stress of the titanium chip is gradually smaller, and the plastic deformation is also reduced, as shown in Figure 9d.

Figure 10a shows the peak value statistics of the equivalent plastic strain of the titanium chip in the process of the titanium chip crushing under different rotational speeds with the same number of teeth (32 teeth). It can be seen that the peak strain difference at different speeds is small and there is no obvious fluctuation. Figure 10b shows the peak value statistics of the equivalent plastic strain of the titanium chip in the process of the titanium chip crushing under the same rotational speed (30 rpm) and different tooth numbers. It can be seen that when the tooth number of the crushing roller is 18, the peak strain is the largest, followed by 20 to 32.

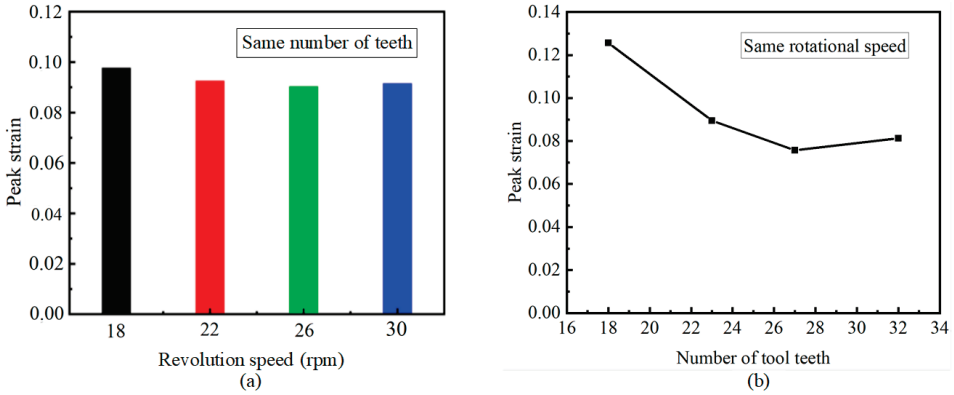


Figure 10. Peak statistics of equivalent plastic strain under different conditions. (**a**) The peak value of equivalent plastic strain at different rotational speeds with the same number of teeth. (**b**) The peak value of equivalent plastic strain under the same rotational speed and different number of teeth.

Four simulation models are established with 18 teeth, 23 teeth, 27 teeth, and 32 teeth at the same rotational speed. The broken models are measured and counted, and the results are shown in Table 4.

Through the simulation of the titanium chip crushing process, it is found that the initial contact position between the titanium chip and the crushing roller is different in the four groups. Thus, shorter titanium chips were obtained, respectively, 0.5 mm, 2.4 mm, 5 mm, and 7 mm.

Table 4. Finite element prediction of the effect of different numbers of crushing teeth on the crushing effect of titanium chips.

Teeth Number	Length of Titanium Chip After Breaking/mm					
18	0.5	18	19.5	39	49	-
20	2.4	7	28.5	33.5	-	-
27	5	7	12	17	19	20
32	5	12	18	19	23.5	17

As shown in Figure 11, the contact position between the initial tool and the titanium chip is found. It is found that the length of such titanium chips varies greatly, so it cannot be included in the analysis of the crushing effect of titanium chips.

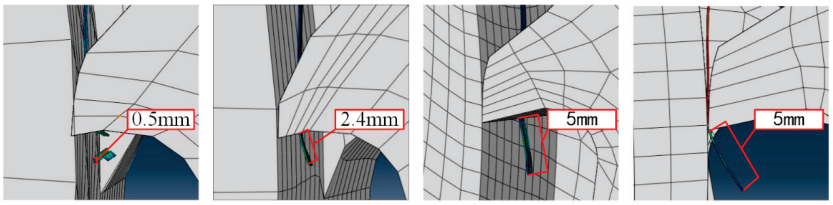


Figure 11. Initial contact position between the tool and a titanium chip.

Under the condition of the same tooth number, the simulation analysis of different crushing roller speed crushing models is carried out. Statistical analysis of the simulation results is shown in Tables 5–8.

Table 5. Finite element prediction of the effect of different roller speeds on titanium chip crushing (18 teeth).

Knife Roller Speed/rpm	Length of Titanium Chip After Breaking/mm						
18	5.5	27	31	6	-	-	-
22	13	32	27.5	21.5	-	-	-
26	6.5	25	27	28.5	-	-	-
30	24	28	26	27	10	-	-

Table 6. Finite element prediction of the effect of different roller speeds on titanium chip crushing (23 teeth).

Knife Roller Speed/rpm	Length of Titanium Chip After Breaking/mm						
18	23.5	29.5	30	-	-	-	-
22	4.5	27	29	27	-	-	-
26	0.5	33	28	31	27	-	-
30	0.5	25	30	31	27	-	-

Table 7. Finite element prediction of the effect of different roller speeds on titanium chip crushing (27 teeth).

Knife Roller Speed/rpm	Length of Titanium Chip After Breaking/mm						
18	9	18.5	19.5	19.5	-	-	-
22	18.5	19	18.5	19.5	18.5	17.5	-
26	18.5	19.5	19.5	19	18	14.5	-
30	1.5	18.5	18	17.5	18	19.5	16.5

Table 8. Finite element prediction of the effect of different roller speeds on titanium chip crushing (32 teeth).

Knife Roller Speed/rpm	Length of Titanium Chip After Breaking/mm							
18	5	15.5	14.5	17	16.5	-	-	-
22	2	16.5	15.5	16	15.5	16	-	-
26	1.5	16.5	16.5	16	16	16	17	8
30	1.5	16	15.5	17	16.5	16	17	7.5

It is also found that due to the different initial contact positions between the tool and the titanium chip, the shorter titanium chips are produced at the beginning, and similarly, shorter titanium chips are produced after the titanium chip is broken. The crushing length of such titanium chips is not stable, which cannot be used as a basis for analyzing the crushing effect of titanium chips.

3.2. Effect of Different Model Parameters on Titanium Chip Crushing

The above simulation results were processed to remove the obvious deviation results, and the remaining values were averaged, and the point-line diagram was drawn. Figures 12a and 12b, respectively, show the influences of different tooth numbers and different crushing roll speeds on the titanium chip crushing effect.

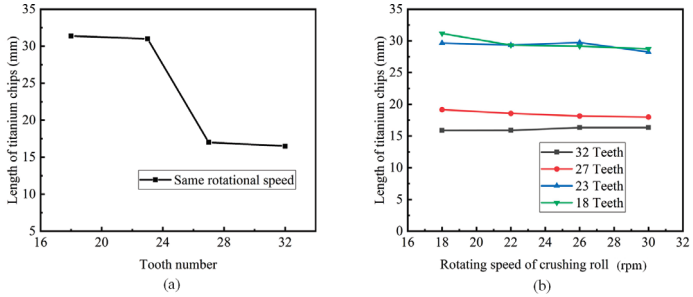


Figure 12. The influence of tooth number and rotational speed on the crushing effect of titanium chips. (**a**) The influence of tooth number on the crushing effect of titanium chips. (**b**) The effect of rotational speed on the crushing effect of titanium chips.

It can be seen from Figure 12a that with the increase in the number of crushing roller teeth, the crushing effect of titanium chips gradually becomes better, and the length of titanium chips after the crushing becomes shorter. It can obviously be found that with the increase in the number of teeth, the length of titanium chips after crushing changes more obviously. When the model was established, it was assumed that the top circle and the teeth and root circle of all crushing rollers were identical. Consequently, as the number of teeth increases, the distance between the adjacent teeth decreases. This implies that the length of crushed titanium chips diminishes with a reduced tooth distance, resulting in a more effective crushing effect.

It can be considered that the length of crushed titanium chips decreases as the distance between the two teeth decreases and the crushing effect becomes increasingly effective.

As can be seen from Figure 12b, when the number of crushing roller teeth is constant, the speed of the crushing roller has negligible impact on the length of titanium chips after crushing. When the rotational speed varies for each tooth number model, the length of the crushed titanium chips does not change significantly, suggesting that the rotational speed has little influence on the crushing effect of titanium chips.

4. Parameter Optimization of Double-Teethed Roll Crusher Based on Response Surface Method

In the process of titanium scrap crushing production, there are many factors that affect the crushing effect of titanium scraps. Among them, the number of teeth of the rotating cutter roller, the rotation speed of the cutter roller during the processing, and the angle of the tip of the broken teeth are directly related to the crushing effect of titanium scraps. The response surface optimization test is combined with the finite element simulation test. The number of teeth of the cutter roller, the speed of the cutter roller, and the angle of the tool tip are the influencing factors of the test. The average value of the broken length of the titanium scraps after crushing is used as the response value. By establishing the regression curve between the test factors and the response value, the influence of the test factors on the response value was analyzed.

The BBD experimental design method was used in this titanium chip crushing test. There are three factor values, and the actual values are presented in the design table. The experimental design scheme is shown in Table 9. In the test table, the fourth group, the sixth group, the tenth group, the fourteenth group, and the fifteenth group were the central group. To reduce the test error, the central group was repeated five times. In this response surface test, the number of teeth of the crusher was 22 to 30, the speed of the crushing teeth roller was 22 rpm to 30 rpm, and the angle between the crushing teeth was 60° to 90°. Based on these, the finite element simulation test parameters of the double-teethed roller crusher are determined as shown in Table 9.

The simulation calculation is carried out according to the test scheme. The Box-Behnken response surface quadratic nonlinear model was established, and the variance analysis and significance test were carried out. The model determination coefficient is R2 = 0.9915, and the coefficient of variation is C.V = 2.88%. Table 10 shows the variance analysis of the crushing length of titanium chips. P and F are two important measurement parameters in the table. The p value is an index to measure the difference between the control group and the experimental group. When the p value is less than 0.1, the difference between the two groups is very significant. The larger the F value, the higher the significance of the selected model. From Table 10, one can see that the F value of the selected quadratic nonlinear model is 35.29. According to the previous description, the larger the F value, the more significant the model is. According to $p < 0.0001$, the probability that the accuracy of the model is affected by error is low. The F value of the first term A is 148.78, and the p value is less than 0.0001, indicating that the number of teeth has a significant effect on the response value.

Table 9. Test design scheme.

Numbering	Experimental Factors			Response Target
	A: Teeth Number	*B*: Revolution Speed/rpm	*C*: Angle/°	*f*: Average Length of Titanium Chips/mm
1	26	30	90	17.8
2	22	22	75	27
3	30	30	75	16.3
4	26	26	75	18.2
5	30	26	60	17
6	26	26	75	18.2
7	30	26	90	16.3
8	26	22	60	18.6
9	30	22	75	15.9
10	26	26	75	18.2
11	26	30	60	18.1
12	26	22	90	18.4
13	22	30	75	26.3
14	26	26	75	18.2
15	26	26	75	18.2
16	22	26	60	27
17	22	26	90	26.8

The regression equation with the average length of titanium chips after crushing as the response index is obtained by fitting:

$$f = 0.2102A^2 - 0.0117B^2 + 0.0009C^2 + 0.0172AB - 0.0020AC - 0.0004BC - 12.5187A + 0.1500B - 0.0883C + 200.2125 \quad (1)$$

Figure 13 shows the response surface model of the mean length of titanium chips after the crushing. From the figure, it can be seen that the number of teeth of the crushing roller is the most significant factor affecting the crushing length of titanium chips, among all the design parameters, and the length of titanium chips after crushing decreases with the increase in the number of teeth, but the length of titanium chips is not sensitive to the change in the speed of the crushing roller and the angle of the tool tip.

Table 10. Variance analysis of titanium chip length.

Type	Sum of Squares	Degree of Freedom	Mean Square Deviation	F	*p*	
Model	163.92	9	18.21	35.29	<0.0001	Significant
A	148.78	1	148.78	288.30	<0.0001	-
B	2.65	1	2.65	0.61	0.44	-
C	3.78	1	3.78	7.33	0.0303	-
AB	1	1	1	1.94	0.2065	-
AC	1.56	1	1.56	3.03	0.1254	-
BC	0.25	1	0.25	0.48	0.5089	-
A^2	5.69	1	5.69	11.03	0.0128	-
B^2	0.35	1	0.35	0.67	0.4386	-
C^2	1.85	1	1.85	3.58	0.1003	-
Residual error	3.61	7	0.52	-	-	-
Misfit term	0.31	3	0.11	0.13	0.9397	Non-significant
Pure differences	3.3	4	0.82	-	-	-
Summation	167.53	16	-	-	-	-

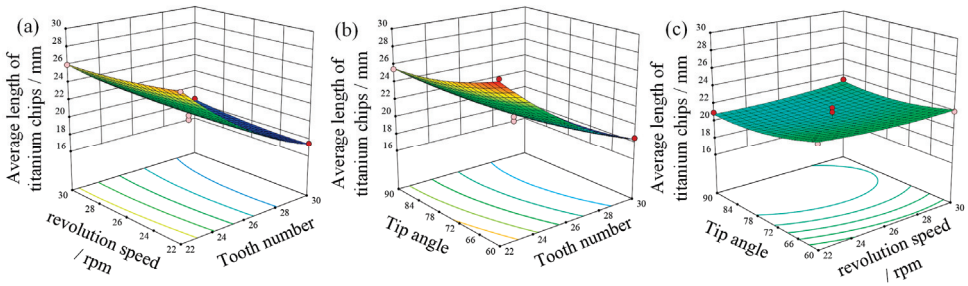


Figure 13. Response surface diagram of the average length of titanium chips after crushing. (**a**) Rotation speed and number of teeth. (**b**) Angle and number of teeth. (**c**) Angle and rotation speed.

Taking the length of broken titanium chips as 20 mm as the optimization goal, the obtained regression equation is optimized. The mathematical model established according to the actual situation is as follows:

$$Y = \min f(A, B, C) \quad (2)$$

After the calculation, the optimal solution of each parameter is A = 27.25, B = 22 rpm, and C = 90°; since the parameter A is the number of crushing teeth of the crusher, it must be an integer, so the optimal parameter A = 26 of the crusher is selected by the nearest principle. The optimized design parameters of the crusher were used to model the crushing teeth roller of the double-teethed roller crusher, and the finite element simulation was carried out. The average value of the simulation results was statistically averaged. The average length of the titanium chips after the crushing was 22.88 mm, and the error with

the response surface optimization target was 0.055, which further verified the accuracy of the optimization results.

5. Experiment

Figure 14 shows a small double-tooth roller crusher with 26 teeth, including a motor, switch, feed inlet, knife roll, and comb plate. The TC4 titanium alloy chips were crushed by double teeth roller crusher, and the working speed of the crushing test machine was 18 rpm.

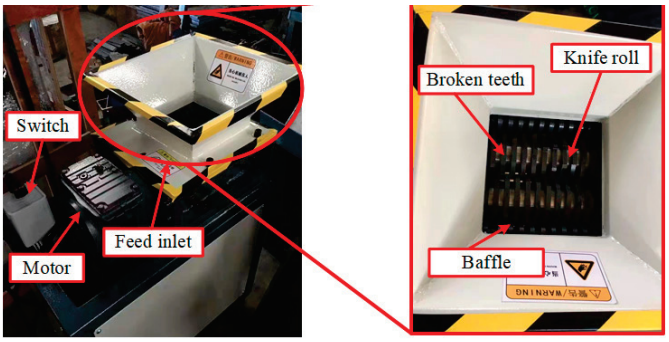


Figure 14. Double-tooth roller crusher for experiment.

Figure 15 shows the broken titanium chips. The test results show that titanium chips can break well.

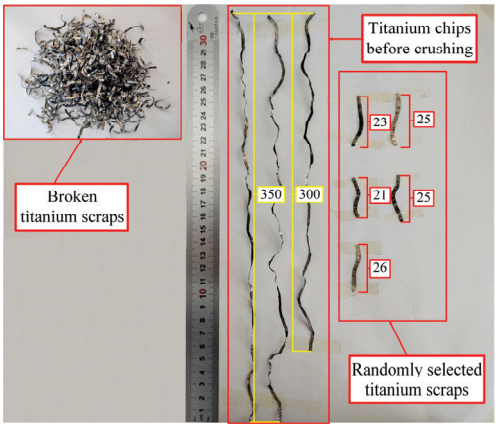


Figure 15. Length comparison of titanium chips before and after crushing.

Figure 15 presents the length comparison of titanium chips before and after the crushing process. As illustrated in the figure, the length of titanium chips prior to crushing surpasses 300 mm, with some reaching approximately 350 mm. Conversely, the length of the crushed titanium chips is about 25 mm. The experimental results are in excellent accordance with the finite element simulation results, thereby providing a solid foundation for the simulation.

6. Conclusions

Taking the TC4 titanium alloy ribbon-cutting chips (titanium chips) as the processing object, the double-tooth roller crusher model was established. Through the finite element crushing simulation, the influence of different broken roller tooth numbers and different broken roller speeds on the titanium chip crushing effect was systematically studied. The following conclusions can be drawn:

(1) Through the finite element simulation experiment, the stress change in the process of titanium chip breaking is obtained, and the stress change cloud diagram of the titanium chip from the initial contact position to the end of complete fracture is obtained. The stresses on the titanium chips in the simulation experiments with different numbers of teeth and different speeds were compared and analyzed, and it was found that as the number of teeth increased, the stresses on the chips changed more smoothly towards the sides and the stresses changed more stably.

(2) The influence of the number of crushing roller teeth and the speed of the crushing roller on the crushing effect of titanium chips was predicted by finite element simulation. The results show that with the increase in the number of teeth of the crushing roller cutter, the length of the broken titanium chip decreases gradually, and with the increase in the number of teeth, the crushing effect is more obvious. With the increase in the rotational speed of the knife roller, the processing speed of titanium chips becomes higher. That is, the number of cutter teeth has great influence on the length (particle size) of the titanium chip after the crushing, and the rotational speed of the cutter roller has little influence on the crushing particle size but has great influence on the working efficiency of titanium chip crushing.

(3) With the production of titanium chip crushing and the particle size of titanium chip after the crushing as the processing objectives, the number of cutter teeth and the rotational speed of the cutter roller can be adjusted to select the appropriate tool parameters and then provide the processing efficiency.

(4) The experimental design for optimizing the design parameters of the double-tooth roller crusher using response surface methodology revealed that the number of crushing roller teeth is the most significant factor affecting the titanium chip fragmentation length among all design parameters. Furthermore, the length of the crushed titanium chips decreases with an increase in the number of teeth, while the chip length is insensitive to changes in the crusher roller speed and cutting edge angle. The optimal design parameters for the crusher were determined to be 27 teeth for the crushing roller, a roller speed of 22 r/min, and a cutting edge angle of 90°.

Author Contributions: J.H.: writing—original draft, investigation; Z.Z.: writing—review and editing, investigation, methodology, conceptualization; X.H.: investigation, writing—review and editing; T.L.: validation, conceptualization; H.J.: methodology, writing—review and editing; project administration, conceptualization. All authors have read and agreed to the published version of the manuscript.

Funding: This study was funded by the 2022 Graduate Research and Innovation Fund of Zhejiang University of Science and Technology (0101320464), and the Tangshan talent foundation innovation team (20130204D).

Institutional Review Board Statement: The authors claim that there are no ethical issues involved in this research.

Informed Consent Statement: All of the authors consented to participate in this research and contributed to the research. All of the authors consent to publication of the research.

Data Availability Statement: The original contributions presented in this study are included in this article. Further inquiries can be directed to the corresponding author.

Conflicts of Interest: Author Tao Liu was employed by the company China MCC 22 Group Corporation Ltd. The remaining authors declare that the research was conducted in the absence of any commercial or financial relationships that could be construed as a potential conflict of interest.

References

1. Gökelma, M.; Celik, D.; Tazegul, O.; Cimenoglu, H.; Friedrich, B. Characteristics of Ti6AL4V Powders Recycled from Turnings Via the HDH Technique. *Metals* **2018**, *8*, 336. [CrossRef]
2. Cheng, W.; Outeiro, J.; Costes, J.; M'Saoubi, R.; Karaouni, H.; Astakhov, V. A Constitutive Model for Ti6Al4V Considering the State of Stress and Strain Rate Effects. *Mech. Mater.* **2019**, *137*, 103103. [CrossRef]
3. Gloria, A.; Montanari, R.; Richetta, M.; Varone, A. Alloys for Aeronautic Applications: State of the Art and Perspectives. *Metals* **2019**, *9*, 662. [CrossRef]
4. Jin, H.X.; Wei, K.X.; Li, J.M.; Zhou, J.Y.; Peng, W.J. Research Development of Titanium Alloy in Aerospace Industry. *Chin. J. Nonferrous Met.* **2015**, *25*, 280–292.
5. Ji, H.; Peng, Z.; Huang, X.; Wang, B.; Xiao, W.; Wang, S. Characterization of the Microstructures and Dynamic Recrystallization Behavior of Ti-6Al-4V Titanium Alloy through Experiments and Simulations. *J. Mater. Eng. Perform.* **2021**, *30*, 8257–8275. [CrossRef]
6. Peng, Z.; Ji, H.; Huang, X.; Wang, B.; Xiao, W.; Wang, S. Numerical Analysis and Parameter Optimization of Wear Characteristics of Titanium Alloy Cross Wedge Rolling Die. *Metals* **2021**, *11*, 1998. [CrossRef]
7. Jiang, T.; Ye, W.H.; Li, J.X. Simulation Analysis of Scrap Metal Crusher's Crushing Performance Based on ANSYS/LS-DYNA. *Mach. Build. Autom.* **2017**, *6*, 107–109+117.
8. Tosun, A.; Konak, G. Development of a Model Estimating Energy Consumption Values of Primary and Secondary Crushers. *Arab. J. Geosci.* **2015**, *8*, 1133–1144. [CrossRef]
9. Li, Y.; Zhao, L.; Hu, E.; Yang, K.; He, J.; Jiang, H.; Hou, Q. Laboratory-Scale Validation of a DEM Model of a Toothed Double-Roll Crusher and Numerical Studies. *Powder Technol.* **2019**, *356*, 60–72. [CrossRef]
10. Kwon, J.; Cho, H.; Mun, M.; Kim, K. Modeling of Coal Breakage in a Double-Roll Crusher Considering the Reagglomeration Phenomena. *Powder Technol.* **2012**, *232*, 113–123. [CrossRef]
11. Di, Z.; Yang, F.; Cao, Y.; Zhang, P.; Zhang, K.; Cheng, F. Optimization of Particle Size Distribution in Circulating Fluidized Beds Via Adjustment of Crushers and Tuning Parameters of Two-Toothed Roll Crusher. *Powder Technol.* **2019**, *352*, 151–158. [CrossRef]
12. Rasyid, M.A.; Aslam, A.; Rafiei, A.; Hassani, F.; Sasmito, A.P. Application of Instantaneous Power Draw Analysis to Investigate the Impact of Microwave Heating on Kimberlite Ore Crushing. *Appl. Energy* **2023**, *352*, 121900. [CrossRef]
13. Chen, Z.; Wang, G.; Xue, D.; Cui, D. Simulation and Optimization of Crushing Chamber of Gyratory Crusher Based on the DEM and GA. *Powder Technol.* **2021**, *384*, 36–50. [CrossRef]
14. André, F.P.; Tavares, L.M. Simulating a Laboratory-Scale Cone Crusher in DEM Using Polyhedral Particles. *Powder Technol.* **2020**, *372*, 362–371. [CrossRef]
15. Neto, W.A.F.; Cavalcante, C.A.; Santos, A.C.; Araújo, L.H.; Alberti, A.R.; Lima, H.B. An Inspection Policy for Shredder Equipment Used in Steel Production Lines Considering Buffer Level and Operating Time. *J. Manuf. Syst.* **2021**, *60*, 640–651. [CrossRef]
16. Lieberwirth, H.; Hillmann, P.; Hesse, M. Dynamics in Double Roll Crushers. *Miner. Eng.* **2017**, *103*, 60–66. [CrossRef]
17. Johansson, M.; Evertsson, M. A Time Dynamic Model of a High Pressure Grinding Rolls Crusher. *Miner. Eng.* **2019**, *132*, 27–38. [CrossRef]
18. Jantarasricha, T.; Chongbunwatana, K.; Panich, S. Comparative Study of Fracture Criteria through Bona Fide Experimental–Numerical Examinations on AA2024-T3. *Int. J. Adv. Manuf. Technol.* **2022**, *119*, 7685–7710. [CrossRef]
19. Lv, M.; Li, A.; Ge, D.; Zhang, R. Step-Dependent Grain Refinement and Micro-Harness Evolution During Chip Formation Process in Orthogonal Cutting of Titanium Alloy Ti-6Al-4V. *Int. J. Adv. Manuf. Technol.* **2022**, *119*, 4219–4236. [CrossRef]
20. Shi, Y.; Li, H.; Wang, W.; Hou, C. A Fiber Model Based on Secondary Development of Abaqus for Elastic–Plastic Analysis. *Int. J. Steel Struct.* **2018**, *18*, 1560–1576. [CrossRef]
21. Wu, H.B.; Zhang, S.J. 3D FEM Simulation of Milling Process for Titanium Alloy Ti6Al4V. *Int. J. Adv. Manuf. Technol.* **2014**, *71*, 1319–1326. [CrossRef]
22. Li, X.; Wang, Y.; Guo, K.; Miao, L. Simulation Analysis of Cutting Process for Inconel718 Nickel-Based Superalloy. *Int. J. Adv. Manuf. Technol.* **2021**, *114*, 2721–2738. [CrossRef]
23. Xu, Z.; Peng, L.; Jain, M.K.; Anderson, D.; Carsley, J. Local and Global Tensile Deformation Behavior of AA7075 Sheet Material at 673OK and Different Strain Rates. *Int. J. Mech. Sci.* **2021**, *195*, 106241. [CrossRef]
24. Zhang, D.; Shangguan, Q.; Xie, C.; Liu, F. A Modified Johnson–Cook Model of Dynamic Tensile Behaviors for 7075-T6 Aluminum Alloy. *J. Alloys Compd.* **2015**, *619*, 186–194. [CrossRef]
25. Jia, Z.; Guan, B.; Zang, Y.; Wang, Y.; Mu, L. Modified Johnson-Cook Model of Aluminum Alloy 6016-T6 Sheets at Low Dynamic Strain Rates. *Mater. Sci. Eng. A* **2021**, *820*, 141565. [CrossRef]
26. Zhu, S.; Liu, J.; Deng, X. Modification of Strain Rate Strengthening Coefficient for Johnson-Cook Constitutive Model of Ti6Al4V Alloy. *Mater. Today Commun.* **2021**, *26*, 102016. [CrossRef]

27. Johnson, G.R. A Constitutive Model and Data for Metals Subjected to Large Strains, High Strain Rates and High Temperatures. In Proceedings of the 7th International Symposium on Ballistics, The Hague, The Netherlands, 19–21 April 1983.
28. Zerilli, F.J.; Armstrong, R.W. Dislocation-Mechanics-Based Constitutive Relations for Material Dynamics Calculations. *J. Appl. Phys.* **1987**, *61*, 1816–1825. [CrossRef]
29. Steinberg, D.J.; Cochran, S.G.; Guinan, M.W. A Constitutive Model for Metals Applicable at High-Strain Rate. *J. Appl. Phys.* **1980**, *51*, 1498. [CrossRef]
30. Cowper, G.R.; Symonds, P.S. *Strain Hardening and Strain Rate Effects in the Impact Loading of Cantilever Beams*; Brown University: Providence, RI, USA, 1952.
31. Khawarizmi, R.M.; Lu, J.; Nguyen, D.S.; Bieler, T.R.; Kwon, P. The Effect of Ti-6Al-4V Microstructure, Cutting Speed, and Adiabatic Heating on Segmented Chip Formation and Tool Life. *JOM* **2022**, *74*, 526–534. [CrossRef]
32. Xie, S.; Zhou, H. Impact Characteristics of a Composite Energy Absorbing Bearing Structure for Railway Vehicles. *Compos. Part B Eng.* **2014**, *67*, 455–463. [CrossRef]
33. Wan, Y.; Zhang, F.; Gu, B.; Sun, B.; Wang, Y. Predicting Dynamic in-Plane Compressive Properties of Multi-Axial Multi-Layer Warp-Knitted Composites with a Meso-Model. *Compos. Part B Eng.* **2015**, *77*, 278–290. [CrossRef]
34. Rasaee, S.; Mirzaei, A.H.; Almasi, D. Constitutive Modelling of Al7075 Using the Johnson–Cook Model. *Bull. Mat. Sci.* **2020**, *43*, 23. [CrossRef]
35. Wang, B.; Wang, G.; Wang, H.; Ding, Y.; Chen, T. Comparison of Breakage Behavior Between the Sieving Crusher and Ordinary Teeth Roll Crushers. *Energy Sources Part A Recovery Util. Environ. Eff.* **2019**, *41*, 252–259. [CrossRef]
36. Li, J.; Huang, Z.; Liu, G.; An, Q.; Chen, M. An Experimental and Finite Element Investigation of Chip Separation Criteria in Metal Cutting Process. *Int. J. Adv. Manuf. Technol.* **2021**, *116*, 3877–3889. [CrossRef]
37. Cheng, W.; Outeiro, J.C. Modelling Orthogonal Cutting of Ti-6Al-4 V Titanium Alloy Using a Constitutive Model Considering the State of Stress. *Int. J. Adv. Manuf. Technol.* **2022**, *119*, 4329–4347. [CrossRef]
38. Ye, Z.; Lv, D.; Wang, Y. Design of Chip Breaker and Study on Cutting Performance in Reaming 7050 Aluminum Alloy. *Int. J. Adv. Manuf. Technol.* **2021**, *116*, 159–173. [CrossRef]
39. Yan, L.; Guan, L.; Wang, D.; Xiang, D. Application and Prospect of Wear Simulation Based on ABAQUS: A Review. *Lubricants* **2024**, *12*, 57. [CrossRef]
40. Zhao, Z.; Ji, H.; Zhong, Y.; Han, C.; Tang, X. Mechanical Properties and Fracture Behavior of a TC4 Titanium Alloy Sheet. *Materials* **2022**, *15*, 8589. [CrossRef]

Disclaimer/Publisher's Note: The statements, opinions and data contained in all publications are solely those of the individual author(s) and contributor(s) and not of MDPI and/or the editor(s). MDPI and/or the editor(s) disclaim responsibility for any injury to people or property resulting from any ideas, methods, instructions or products referred to in the content.

materials

MDPI

Article

Phase Evolution During High-Energy Ball Milling and Annealing of Ti-Doped Mo-V-Si-B Alloys

Dennis Zang [1,*], Julia Becker [1], Ulf Betke [1], Georg Hasemann [1], Kateryna Khanchych [2], Bronislava Gorr [2] and Manja Krüger [1]

[1] Institute of Materials, Technologies and Mechanics (IWTM), Otto-von-Guericke University Magdeburg, Universitätsplatz 2, 39106 Magdeburg, Germany
[2] Institute for Applied Materials (IAM), Karlsruhe Institute of Technology (KIT), Kaiserstraße 12, 76131 Karlsruhe, Germany
* Correspondence: dennis.zang@ovgu.de

Abstract: Refractory metal-based Mo-Si-B alloys have long been considered the most promising candidates for replacing nickel-based superalloys in the aerospace and energy sector due to their outstanding mechanical properties and good oxidation of the Mo-silicide phases. In general, the addition of vanadium to Mo-Si-B alloys leads to a significant density reduction, while small amounts of titanium provide additional strengthening without changing the phase evolution within the Mo_{ss}-Mo_3Si-Mo_5SiB_2 phase field. In this work, high-energy ball milling studies on Mo-40V-9Si-8B, substituting both molybdenum and vanadium with 2 and 5 at. % Ti in all constituents, were performed to evaluate the potential milling parameters and investigate the effects of Ti doping on the milling characteristics and phase formation of these multicomponent alloys. After different milling durations, the powders were analysed with regard to their microstructure, particle size, oxygen concentration and microhardness. After heat treatment, the silicide phases $(Mo,V)_3Si$ and $(Mo,V)_5SiB_2$ precipitated homogeneously within a (Mo,V) solid solution matrix phase. Thermodynamic phase calculations using the CALPHAD method showed good agreement with the experimental phase compositions after annealing, confirming the stability of the observed microstructure.

Keywords: Mo-Si-B; mechanical alloying; lattice parameter; microstructure; heat treatment

1. Introduction

The potential for improving nickel-based superalloys, currently used in jet engines and power plants, is severely limited due to their comparatively low melting temperature [1]. Therefore, molybdenum–silicide alloys, which not only satisfy requirements like high melting temperature and acceptable density but also exhibit appropriate oxidation and creep resistance, have increasingly come into scientific and industrial focus during the last few decades [1,2]. Promising candidates for replacing nickel-based superalloys in the aerospace and energy sector are multiphase Mo-Si-B alloys, pioneered by Berczik [3,4].

It is well known that Mo-Si-B alloys with a continuous α-Mo matrix (Mo_{ss}) and embedded, homogeneously distributed silicide phases (Mo_3Si and Mo_5SiB_2) provide the best combination of mechanical properties and oxidation resistance [5–8]. Such a microstructure can be realized via mechanical alloying (MA) and subsequent sintering and/or different methods for powder compaction. Mechanical alloying is a solid-state process in which a very homogeneous and fine microstructure can be produced using high-energy ball milling,

which might lead to non-equilibrium states [9]. The principle is essentially based on repeated fracture and cold-welding processes of the individual powder particles [10]. The progress of mechanical alloying of powders primarily depends on the chosen milling parameters, especially the milling duration and the rotational speed. Krüger et al. [8] showed that a treatment of at least 20 h in a planetary ball mill PM400 with 200 rpm is necessary for Mo-Si-B alloys to achieve the above-mentioned type of microstructure during subsequent heat treatment. Likewise, some characteristic powder parameters change with milling time, such as lattice parameter, microstrain, particle size and microhardness [8,11–13]. These parameters dictate the milling progress, and they have a significant impact on the microstructure of the powders and the consolidated bulk material.

One disadvantage of Mo-rich Mo-Si-B alloys is their high density [2]. An interesting approach for reducing alloy density is to add lighter elements compared to Mo like Al, Cr, Ti and V. However, it was shown that larger amounts of Al, Cr and Ti in Mo-Si-B alloys lead to a reduction in the Mo solid solution fraction [14–16]. Becker et al. [17] were able to show that the addition of 40 at. % V to powder metallurgically processed (PM) Mo-9Si-8B alloys leads to a density reduction of approximately 17%. This phenomenon is directly related to the high solubility of V in Mo and the respective Mo-silicides, while V has only a minor influence on the phase fractions of the Mo_{ss}-Mo_3Si-Mo_5SiB_2 phase field. Apart from this, the addition of V significantly affects the mechanical properties of Mo-Si-B alloys.

Becker et al. [18] obtained slightly higher hardness values after the addition of 5 at. % V to Mo, which was attributed to the relatively weak lattice distortion caused by the vanadium atoms. In addition, the PM alloy Mo-40V-9Si-8B exhibits comparatively high room-temperature fracture toughness values of approximately 13.3 MPa $\sqrt{m}$, although these alloys have significantly higher oxygen concentrations due to the oxygen-contaminated V raw powder and the high affinity of V for oxygen [17]. It must be noted that Mo tends to significantly embrittle when oxygen is dissolved in the crystal lattice, even at low concentrations of around 10 ppm [19]. Although the brittle silicide phases in Mo-40V-9Si-8B and Mo-9Si-8B are similarly distributed, the addition of V results in a higher fracture toughness, which is due to both the slightly increased volume fraction of the tough Mo_{ss} phase and its size [7,17]. Unfortunately, the addition of high V concentrations to Mo-Si-B alloys also has an impact on the high-temperature mechanical properties, leading to a reduction in high-temperature compressive strength and creep resistance, as shown in [17].

Another promising alloying element in Mo-Si-B alloys is Ti, which will also reduce alloy density and at the same time has the potential to additionally strengthen the material via solid solution strengthening and second-phase or particle strengthening. Mo-Si-B alloys with Ti additions above 20 at. % are already well studied [20–22], with high Ti concentrations leading to the formation of the $(Mo,Ti)_5Si_3$ phase instead of the Mo_3Si phase.

However, there is less information about the influence of low Ti concentrations (up to 5 at. %) in these materials. Inoue et al. [23] found that doping Mo with 1.0 and 1.5 mass% Ti, which were carburized via two-step heat treatment, leads to an improvement in hardness as a result of solid solution hardening. A similar conclusion was drawn by Becker et al. [18], who showed that the hardness of arc-melted Mo-5Ti is significantly higher compared to pure Mo due to solid solution hardening. According to Fan et al. [24], small amounts of Ti are sufficient to increase the tensile strength of pure Mo, since Ti forms a solid solution with Mo in a large solubility range up to 100 at. %, while at lower temperatures, the BCC solid solution will transfer to an HCP solid solution at higher Ti concentrations according to the phase diagram shown in [25]. In this context, it was shown that the addition of TiH_2

to Mo powders during mechanical alloying has a higher impact on the tensile strength than the addition of pure Ti.

These observations align with more recent studies which also highlight the beneficial role of low Ti concentrations in Mo-based alloys. Hu et al. [26] demonstrated that even small amounts of Ti (0.5 wt.%) can significantly refine the grain size in pure Mo, enhance densification during sintering, and reduce oxygen impurity levels through the in situ formation of fine TiO_2 or Ti_8O_{15} particles. These oxide particles also act as effective grain boundary pinners, contributing to improved mechanical properties. Similarly, Choi et al. [27] reported that Ti additions in Mo-Si-B alloys led to partial solid solution formation within the Mo matrix and promoted the formation of intergranular TiO_2, which influences fracture behaviour. Despite a moderate decrease in toughness, titanium proved effective in refining the microstructure and reducing oxygen levels, underlining its functional relevance even at minor concentrations.

While elemental Ti has shown these beneficial effects, TiH_2 is considered even more suitable for powder-based processing routes, as its brittle nature promotes homogeneous dispersion within the Mo matrix during milling. During subsequent heat treatment, the hydrogen volatilizes and a Mo-Ti solid solution forms. The addition of TiH_2 accelerates solid solution formation, since the smaller particle size of this compound reduces the diffusion paths of the decomposed Ti [24]. In addition, the H_2 of the decomposed TiH_2 can react with oxygen dissolved in the alloy to form H_2O, which is then evaporated in the atmosphere. This reaction can effectively lower the oxygen concentration in the alloy [28]. Simultaneously, the gettering of oxygen is achieved by Ti at temperatures higher than 700 °C, reducing the free oxygen concentration in the material by forming Ti oxides, and is no longer reactively available in this form [29].

While previous studies have extensively addressed the mechanical alloying of Mo-Si-B alloys with vanadium as a major alloying element [17] and others have focused on high Ti contents (>20 at. %) leading to the formation of $(Mo,Ti)_5Si_3$ phases [20–22], the effects of small Ti additions ($\leq$5 at. %) in combination with V remain largely unexplored. This study therefore introduces a novel alloying approach by combining Ti and V via TiH_2-assisted mechanical alloying, with particular emphasis on phase evolution, particle size behaviour and oxygen uptake. The results are benchmarked against undoped and solely V-doped reference systems to systematically evaluate the influence of minor Ti additions.

2. Material and Methods

Elemental powders of Mo, V, Si, B and TiH_2 of 99.95%, 99.5%, 99.5%, 98% and 99.5% purity, respectively, were used to produce different Mo-V-Si-B(-Ti) alloys via a multi-step powder metallurgical process. The elemental powders had different average particle sizes of 4 µm (Mo), 38 µm (B) and 44 µm (V, Si, TiH_2). Mechanical alloying was carried out in a planetary ball mill (Retsch® PM 100, Retsch, Haan, Germany) with a powder-to-ball weight ratio of 1:13 and a rotational speed of 300 rpm. Weighing, mixing and powder removal (after 1, 2, 5, 10 and 20 h of milling) were performed in a glovebox under protective argon atmosphere in order to keep the oxygen concentration in the powders as low as possible. In this study, stainless steel vials and balls (d = 10 mm) were used. In the first step, a milling study for the Mo-40V-9Si-8B alloy was carried out. In the second step, 2 at. % and 5 at. % Ti was added to this alloy composition to vary either the Mo or V concentrations (Mo-40V-9Si-8B-2Ti, Mo-40V-9Si-8B-5Ti, Mo-38V-9Si-8B-2Ti and Mo-35V-9Si-8B-5Ti). The mechanically alloyed powders obtained from the five milling studies were then characterized as a function of milling time.

The powders, finally milled for 20 h, were subjected to heat treatment under vacuum at 1400 °C for 1 h using a tube furnace (HTM Reetz LORA 1700-80-330-1, HTM Reetz GmbH, Berlin, Germany) and characterized as described above. Field-assisted sintering (FAST) of the mechanically alloyed powders was carried out in a hot press HP D (FCT System GmbH, Frankenblick, Germany) at the Karlsruher Institute of Technology (KIT). For the process, a heating rate of 100 K/min and a holding time of 15 min at 1100 °C and 1500 °C were chosen. The sintering process was performed under vacuum (<10 bar) and a uniaxial pressure of 50 MPa.

The quantitative phase analysis of the mechanically alloyed powders was performed with powder X-ray diffraction (XRD) using a D8 Discover X-ray diffractometer with Bragg–Brentano reflection geometry (Bruker-AXS GmbH, Karlsruhe, Germany). The diffractometer was equipped with an Eiger2 detector operating in 1D mode, as well as a 0.6 mm fixed divergence slit and 2.5° primary and secondary soller slits as optical components. The diffracted intensities were recorded between 10° and 160° 2θ using Co $K\alpha_{1,2}$ radiation; Kβ radiation was removed via a 10 µm Fe foil placed in front of the detector opening. The obtained powder patterns were analysed by following the Rietveld technique using TOPAS V6 software (Coelho Software, Brisbane, Australia/Bruker-AXS) [30,31]. The Mo/V ratio in the identified BCC solid solution phases was determined from their respective unit cell volume under application of Vegard's law [32]. A calibration curve was calculated from literature data of Mo, V and Mo-V solid solution phases obtained from the Crystallographic Open Database (COD) [33]. Besides the phase composition, the microstrain ε_0 was determined for each phase from the reflection profiles. The contribution of the instrument to the reflection profiles was determined from a measurement of the NIST 660a standard (LaB_6) using the Fundamental Parameter Approach [34,35]. The diffractograms were treated using the Fundamental Parameter Approach (FPA). An instrument function, describing the influence of the diffractometer on reflection shape, was determined from a reference measurement of the NIST 660a material (LaB_6). This instrument function contained parameters describing the emission profile of the X-ray source, slits and axial divergence. Sample-related reflection broadening was treated using macros for size and strain broadening, where applicable.

Microstructures after different milling durations were characterized using an SEM (FEI ESEM XL30 FEG/Philips equipped with EDS, Hillsboro, OR, USA) and Zeiss EVO 15 (equipped with EDS, Carl Zeiss Microscopy GmbH (Jena, Germany) equipped with EDS, Oberkochen, Germany) in SE mode. For this purpose, the samples were first mounted in a cold embedding material (Technovit 4071, Heraeus Kulzer, Wehrheim, Germany) and then wet-ground (600, 1200, 2500 grit SiC paper) and polished (3 µm and 1 µm diamond suspension).

Measurements of particle size and particle size distribution were analysed using laser diffraction analysis (Mastersizer® 2000, Malvern Panalytical, Malvern, UK) with water as the dispersion medium and evaluation of the results according to the Fraunhofer diffraction theory.

Determination of the oxygen concentration of the pure powders and the mechanically alloyed powders was achieved by using the ON/H-mat 286 analyser (G8 GALILEO, Bruker, Viersen, Germany).

Microhardness tests were conducted by using a Micro-Duromat 4000 E device (Reichert-Jung, Depew, NY, USA) on the embedded powder particles. For these tests, it is necessary to have a sufficient distance between the hardness indentation and the boundary of the particles in order to keep the influence of the embedding material on microhardness as low as possible. Since the particles are relatively small, the applied load was

set to 0.1 N, which was applied for 10 s using a load rate of 0.01 N/s. The indentations were measured manually with ImageJ software (Version 1.54p), and the Vickers hardness value was calculated from the mean value of the two diagonals for a minimum of 15 indentations.

The mean centre-to-centre spacing between silicide phases was estimated using a simple stereological relation:

$$\lambda = d \cdot \left(\frac{1-f}{f} \right)^{1/3} \quad (1)$$

where d is the average silicide width and f is the silicide volume fraction.

The theoretical density was calculated based on the phase fractions (ω_i) and densities (ρ_i) obtained from the Rietveld refinement. Subsequently, the overall density of the multi-phase material was determined using the inverse rule of mixtures, as follows:

$$\rho_{theo} = \left(\sum_i \frac{\omega_i}{\rho_i} \right)^{-1} \quad (2)$$

The density of the FAST alloys Mo-40V-9Si-8B and Mo-40V-9Si-8B-5Ti was measured by using Archimedes' method with an analytical balance (Sartorius, Göttingen, Germany) at 20 °C, whereby each specimen was measured three times.

Using the CALPHAD (Calculation of Phase Diagram) method to develop the Mo-Si-B-V database, each phase of the system was modelled with a separate Gibbs energy expression as a function of temperature T and pressure p. These models contain parameters obtained by fitting experimental and theoretical data. A detailed description of the CALPHAD method is given in [36].

For a multicomponent system, thermodynamic data on its constituents (i.e., pure elements) as well as all of the subsystems included are required. In the present case, the quaternary Mo-Si-B-V system contains six binary and four ternary subsystems in addition to pure elements. Available experimental and theoretical literature data were utilized while modelling multicomponent phases. It has to be mentioned that neither experimental nor theoretical data for the two ternary subsystems Mo-Si-V and Mo-B-V are available in the literature. Taking this shortcoming into account, the database in its current state does not provide a full description, especially for the B- and Si-rich alloys within the Mo-Si-B-V system. Since Mo- and V-rich alloys are of primary interest in the present study, the thermodynamic modelling can be considered a first rough estimation of phase equilibria in the quaternary system. FactSage 8.2 software was used for thermodynamic calculations.

3. Results

3.1. X-Ray Diffraction (XRD) Measurements

Since the diffractograms of the investigated alloys are largely similar, Figure 1 provides a representative example, displaying the X-ray diffractograms of the Mo-40V-9Si-8B and Mo-40V-9Si-8B-5Ti alloys at different milling times. As milling time increases, reflection broadening becomes more pronounced due to the high concentrations of V, Si and B, as well as Ti in the case of the Ti-alloyed powders, within the molybdenum lattice. Additionally, the reflections of molybdenum (approx. 47°) and vanadium (approx. 49°) in the lower 2θ range merge within the first hours of mechanical alloying, indicating the progressive dissolution of vanadium into the Mo solid solution (Mo_{ss}). It is noteworthy that Mo and V can be entirely dissolved. However, the addition of small amounts of Ti to Mo-40V-9Si-8B does not noticeably affect the position of the reflections. It can be seen that a supersaturated Mo(V,Si,B) and Mo(V,Si,B,Ti) solid solution formed after 20 h of milling, where Si, B and Ti are dissolved quite quickly in the Mo solid solution during mechanical

alloying. Diffraction patterns of the individual elements disappear even at the beginning of the mechanical alloying process, and the most significant Si pattern cannot be detected after 1 h of milling. These results are in agreement with those of Becker et al. [17] on similarly treated Mo-40V-9Si-8B.

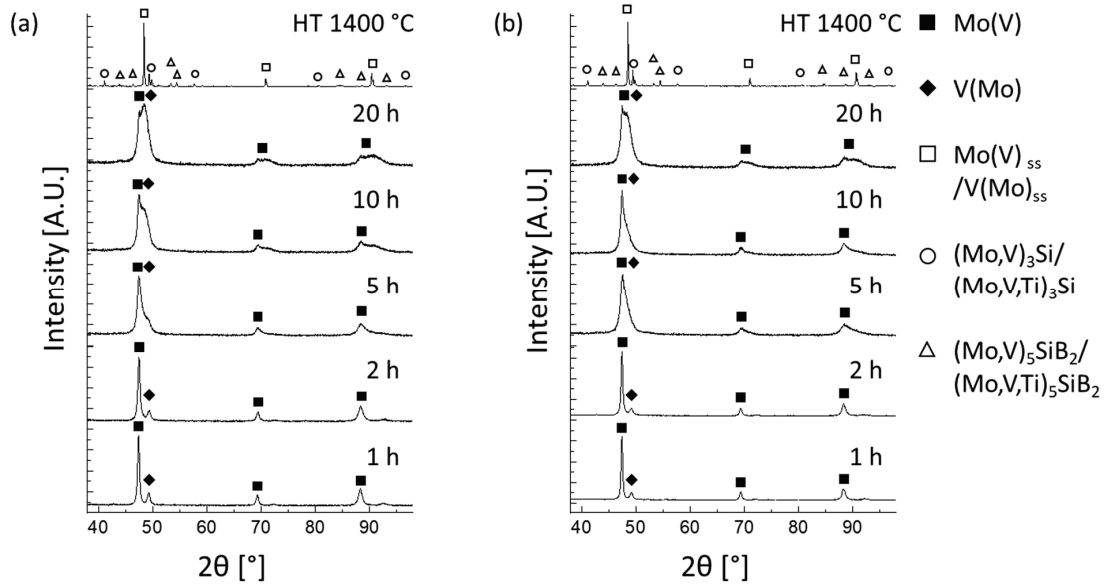


Figure 1. X-ray diffractograms of (**a**) Mo-40V-9Si-8B and (**b**) Mo-40V-9Si-8B-5Ti powders after different milling durations and after heat treatment at 1400 °C for 1 h, showing the progress of mechanical alloying and the phase evolution in the as-milled powders.

Rietveld refinement reveals the existence of two solid solution phases for the milled samples: a V-rich $V(Mo)_{ss}$ solid solution phase in which molybdenum is dissolved and a Mo-rich $Mo(V)_{ss}$ solid solution phase in which V is dissolved. Table 1 presents a comparison of the evolution of the lattice parameter, microstrain (ε_0) and phase fraction of the two solid solutions, with exemplary values shown for 2, 10 and 20 h of milling. With increasing milling time, the lattice parameter of $Mo(V)_{ss}$ decreases, starting from a value of 3.147 Å for pure Mo, while the lattice parameter of $V(Mo)_{ss}$ increases, starting from a value of 3.024 Å for pure V. During mechanical alloying, the values of the lattice parameters converge according to Table 1, but two solid solution phases can still be detected, even after milling for 20 h. The large difference in the lattice parameters of the Ti-doped powders is attributed to this effect, which means that the progress of solid solution formation is slower compared to the Ti-free alloys. This indicates that longer milling durations must be foreseen to entirely homogenize the Ti-containing powders.

The microstrain in $V(Mo)_{ss}$ increases from approximately 3.5×10^{-3} after 2 h up to values ranging between 7×10^{-3} and 13.2×10^{-3} after 20 h of milling. In contrast, the microstrain in $Mo(V)_{ss}$ is slightly higher at 2 h (around 5×10^{-3}) but decreases after 20 h, ranging between 4.88×10^{-3} and 8.9×10^{-3}. The increase in microstrain can be related to the high plastic deformations occurring during mechanical alloying due to the high-energy collision between milling balls and powders. Consequently, the dislocation density increases, leading to a higher degree of lattice defects in the microstructure [8,37,38].

The phase fraction of $Mo(V)_{ss}$ initially increases but then decreases between 10 and 20 h of milling for all investigated alloys. On the other hand, the phase fraction of $V(Mo)_{ss}$ continuously increases over the entire milling time. As expected, the phase fraction of pure Mo decreases, but after 20 h of milling there is still residual Mo left, which is not dissolved during the milling process, and therefore, a complete (Mo,V) solid solution has not yet

formed. This incomplete dissolution, as evidenced by residual Mo reflections in the XRD pattern, may be attributed to the lower energy input of the PM100 planetary mill used in this study. Compared to the PM400 planetary mill used in prior studies [17], the PM100 mill employed here has a smaller sun wheel radius, which leads to reduced kinetic energy transfer during milling, despite the higher rotation speed. As the kinetic energy imparted to the powder is proportional to the square of the radius and rotation speed ($E \propto R^2 \cdot \omega^2$), the total energy input per unit powder mass is significantly lower in the present setup. This reduced energy input likely contributes to the incomplete dissolution of Mo observed after 20 h and indicates that either a higher energy milling setup or prolonged milling duration may be necessary for full alloying.

Previous investigations using the PM400 mill (Becker et al. [17]) reported complete Mo dissolution under similar milling durations. In the present study, the lower energy input of the PM100 mill likely limited the degree of Mo dissolution, despite the relatively long milling time of 20 h. Therefore, increasing the milling energy by using a higher rotational speed is expected to be more effective than merely extending the milling duration. Nevertheless, care must be taken to avoid negative side effects such as powder agglomeration, contamination or excessive work hardening, which may arise under high-energy milling conditions.

The concentration of V in $Mo(V)_{ss}$ and Mo in $V(Mo)_{ss}$ increases during milling, indicating the complete solubility of V in Mo and vice versa. The decrease in Mo concentration in the $V(Mo)_{ss}$ phase between 10 and 20 h in Mo-40V-9Si-8B and Mo-35V-9Si-8B-5Ti, but not in the other alloys, suggests inhomogeneous milling progress in the mechanically alloyed powder batch. Initially, Mo dissolves into $V(Mo)_{ss}$, but extended milling likely induces local supersaturation, promoting partial Mo segregation from the solid solution without distinct phase formation. In Mo-35V-9Si-8B-5Ti, the high Ti concentration may enhance Mo displacement from the $V(Mo)_{ss}$ phase, while in the alloys with 2 at. % Ti, the solubility limit is not exceeded, preventing Mo depletion from $V(Mo)_{ss}$. After 20 h, a steady state is reached, stabilizing the Mo concentration in the V-based solid solution. At this stage, the degrees of Mo and V dissolution in their respective solid solutions are nearly identical, except for the Mo-40V-9Si-8B alloy. This suggests that Mo and V dissolve in their respective lattice to a similar extent, which is more pronounced for the Ti-doped alloys.

After heat treatment of the mechanically alloyed powders at 1400 °C for 1 h under vacuum, the two silicide phases $(Mo,V)_3Si/(Mo,V,Ti)_3Si$ (A15 structure) and $(Mo,V)_5SiB_2/(Mo,V,Ti)_5SiB_2$ ($D8_l$ Structure) are formed and embedded in the $(Mo,V)_{ss}/(Mo,V,Ti)_{ss}$ matrix phase (BCC, A2 structure). It is important to note that the silicide phases $(Mo,V)_3Si$ and $(Mo,V)_5SiB_2$ were only observed after the annealing step and were therefore not included in Rietveld refinement of the as-milled powders. While the main reflections of the matrix and silicide phases are visible after heat treatment, some reflection overlap remains, particularly between the $(Mo,V)_3Si$ and $(Mo,V)_5SiB_2$ phases, due to their partially overlapping diffraction angles and similar scattering intensities. Nevertheless, both were included as separate phases in Rietveld refinement using well-established crystal structures. The formation of these silicides indicates that Si and B are primarily responsible for the precipitation of the A15 and $D8_1$ phases during annealing, while V and Ti remain partially dissolved in all three phases. Finally, no additional phases were detected in Ti-doped samples, suggesting that Ti has no significant influence on the overall phase evolution during post-alloying heat treatment.

The lattice parameter of $(Mo,V)_{ss}$ for the Mo-40V-9Si-8B alloy slightly increases after heat treatment compared to the as-milled state because some of the V and Si diffuse out of the $(Mo,V)_{ss}$ to form the two silicide phases (Table 2). Vanadium (134 pm), being slightly

smaller than Mo (139 pm), may reduce the lattice parameter upon diffusion, leading to a more compact atomic arrangement. In contrast, Si has a significantly smaller atomic radius (111 pm) and a strong tendency to form silicide phases, further depleting the solid solution and potentially causing additional contraction. However, since Mo is larger than both V and Si, its increased concentration in the solid solution is likely to result in moderate expansion of the lattice parameters of $(Mo,V)_{ss}$. In the Ti-doped alloys, the lattice parameter slightly decreases due the slightly larger atomic radius of Ti (147 pm) compared to Mo, which consequently contributes to a higher lattice parameter of $Mo(V)_{ss}$ after mechanical alloying. During heat treatment, some of the Ti diffuses from the supersaturated $Mo(V)_{ss}$ and is dissolved in the respective silicide phases, causing a slight decrease in the lattice parameter.

However, the X-ray diffractograms in Figure 1 appear visually unchanged, as the reflex shift remains below the resolution limit of the XRD analysis. In the Mo-substituted alloys Mo-40V-9Si-8B-2Ti and Mo-40V-9Si-8B-5Ti, the phase fraction of the $(Mo,V)_{ss}$ matrix phase slightly decreases with the addition of Ti, while the phase fraction of the two silicides increases. For the V-substituted alloys Mo-38V-9Si-8B-2Ti and Mo-35V-9Si-8B-5Ti, however, there is no significant change regarding the phase fractions compared to the Mo-40V-9Si-8B alloy.

A comparison of the obtained experimental data with the theoretical results calculated using the self-developed thermodynamic database for a quaternary alloy system Mo-Si-B-V is performed. According to the theoretical assessment, the calculated equilibrium phase composition of the alloy Mo-40V-9Si-8B at 1400 °C yields 60.1, 21.3 and 18.5 wt.% for $(Mo,V)_{ss}$, $(Mo,V)_3Si$ and $(Mo,V)_5SiB_2$, respectively. These results are in good agreement with the experimental values given in Table 2. In order to further confirm the validity of the developed database in a wider concentration range of V, a comparative analysis of the calculated phase composition for Mo-xV-9Si-8B alloys with different V contents (x = 10, 20, 30 and 40 at. %) at 1400 °C and the experimental data [17] is performed (see Figure 2a). A very good agreement is obtained for 10 and 20 at. % V, while a slight deviation (up to 5 wt.%) is observed for 30 and 40 at. % V.

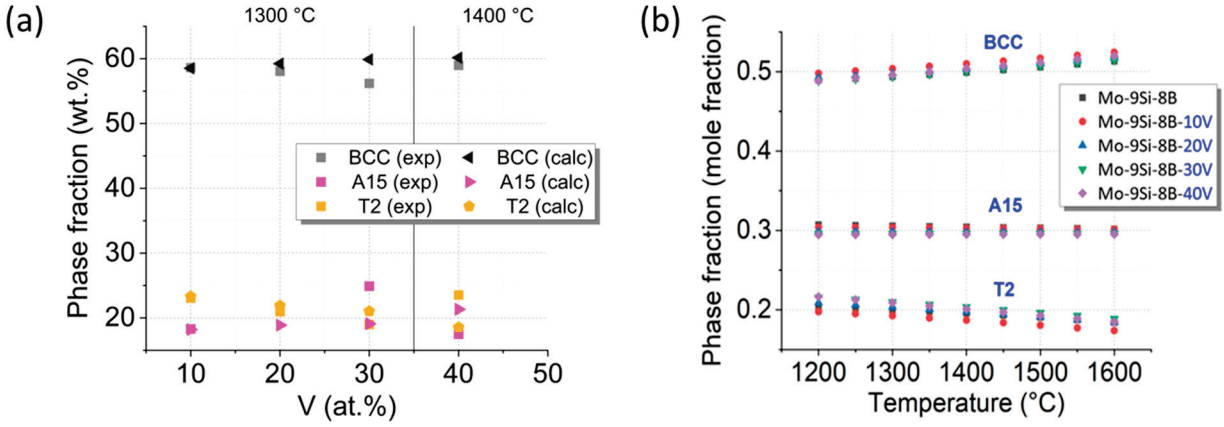


Figure 2. (**a**) The calculated (calc) and experimentally (exp) observed [17] equilibrium phase composition of Mo-xV-9Si-8B (x = 10, 20, 30 and 40 at. %) at 1400 °C. Note: experimental data for 10, 20 and 30 at. % V are taken from Becker et al. [17] and correspond to measurements at 1300 °C, while the 40 at. % V data were obtained in this study at 1400 °C. (**b**) The calculated equilibrium phase composition of Mo-xV-9Si-8B (x = 0, 10, 20, 30 and 40 at. %) in the temperature range 1200–1600 °C. The data for the V-free alloy Mo-9Si-8B comply with the thermodynamic assessment of the Mo-Si-B system presented in [39].

Table 1. The XRD results as a function of milling time for the five alloys investigated.

Alloy	Mo-40V-9Si-8B			Mo-40V-9Si-8B-2Ti			Mo-40V-9Si-8B-5Ti			Mo-38V-9Si-8B-2Ti			Mo-35V-9Si-8B-5Ti		
Milling time [h]	***2***	***10***	***20***	***2***	***10***	***20***	***2***	***10***	***20***	***2***	***10***	***20***	***2***	***10***	***20***
Lattice parameter $Mo(V)_{ss}$ [Å]	3.146	3.105	3.087	3.141	3.119	3.100	3.139	3.111	3.106	3.140	3.107	3.105	3.143	3.106	3.090
Lattice parameter $V(Mo)_{ss}$ [Å]	3.034	3.050	3.079	3.040	3.059	3.085	3.043	3.066	3.069	3.040	3.062	3.072	3.045	3.078	3.072
Microstrain $Mo(V)_{ss}$ [10^{-3}]	5.3	8.2	8.7	4.8	6.8	8.9	5.0	6.1	5.3	4.9	4.9	4.9	4.7	7.3	8.1
Microstrain $V(Mo)_{ss}$ [10^{-3}]	3.4	6.5	13.2	3.2	7.2	10.0	3.4	9.2	7.2	3.5	6.7	7.1	3.9	10.9	8.1
Phase fraction Mo [wt.%]	45.1	12.1	10.1	62.5	22.9	12.0	67.5	33.2	19.5	64.4	35.1	18.8	68.6	15.0	7.9
Phase fraction $Mo(V)_{ss}$ [wt.%]	21.2	55.5	44.3	6.7	32.3	20.1	3.7	26.5	25.8	6.7	20.1	19.0	6.5	32.2	22.2
Phase fraction $V(Mo)_{ss}$ [wt.%]	33.7	32.4	45.6	30.8	44.9	68.0	28.8	40.3	54.7	28.9	44.8	62.2	24.8	52.8	70.0
Concentration of V in $Mo(V)_{ss}$ [wt.%]	2.2	34.4	48.4	4.3	22.6	47.6	6.0	29.4	33.3	5.4	32.8	34.3	3.2	33.8	46.4
Concentration of Mo in $V(Mo)_{ss}$ [wt.%]	7.4	20.8	17.0	11.9	27.5	43.8	14.4	33.7	36.3	12.2	30.3	38.4	15.9	43.8	38.3
Microhardness [GPa]	8 (±3)	10.5 (±2)	11 (±3)	6.5 (±2)	8 (±2)	9.5 (±2)	5 (±1)	10.5 (±3)	11.5 (±2)	8 (±1)	11 (±2)	11.5 (±2)	7.5 (±1)	13 (±2)	14.5 (±2)

Table 2. XRD parameters including lattice parameter, phase concentration and results of microhardness measurements after heat treatment at 1400 °C.

Alloy	Mo-40V-9Si-8B	Mo-40V-9Si-8B-2Ti	Mo-40V-9Si-8B-5Ti	Mo-38V-9Si-8B-2Ti	Mo-35V-9Si-8B-5Ti
Lattice parameter $(Mo,V)_{ss}/(Mo,V,Ti)_{ss}$ [Å]	3.090	3.089	3.084	3.098	3.083
Lattice parameter $(Mo,V)_3Si/(Mo,V,Ti)_3Si$ [Å]	4.798	4.796	4.796	4.799	4.800
Lattice parameter $(Mo,V)_5SiB_2/(Mo,V,Ti)_5SiB_2$ [Å]	5.867 10.883	5.865 10.876	5.876 10.915	5.870 10.885	5.890 10.935
Phase fraction $(Mo,V)_{ss}/(Mo,V,Ti)_{ss}$ [wt.%] BCC	59.0	56.8	54.7	58.7	54.8
Phase fraction $(Mo,V)_3Si/(Mo,V,Ti)_3Si$ [wt.%] A15	17.5	19.1	21.0	18.3	21.9
Phase fraction $(Mo,V)_5SiB_2/(Mo,V,Ti)_5SiB_2$ [wt.%] T2	23.5	24.1	24.3	23.0	23.3
Microhardness [GPa]	12 (±3)	9 (±2)	13 (±2)	12 (±2)	12 (±2)
Theoretical density [g/cm^3]	7.91	7.78	7.79	7.88	7.82
Measured density [g/cm^3]	7.88 *		7.54 *		

* Measured after field-assisted sintering (FAST) of the mechanically alloyed powders.

Figure 2b shows the calculated phase composition of the alloy Mo-xV-9Si-8B (x = 0, 10, 20, 30 and 40 at. %) in the temperature range 1200–1600 °C. Three-phase equilibria over the temperature range 1200–1600 °C are expected for all alloys analysed. The change in the phase composition with increasing temperature follows the same trends: the content of the BCC phase increases, the amount of the A15 phase ($(Mo,V)_3Si$) changes not significantly, and, consequently, the amount of the T2 phase ($(Mo,V)_5SiB_2$) decreases. The essential implication of the diagram shown in Figure 2a is that the V additions—at least up to 40 at. %—do not notably alter the phase equilibria in the given temperature range. It can, therefore, be anticipated that the microstructure of the V-containing alloys resembles the microstructure of the Mo-9Si-8B counterpart, as proposed above. Moreover, the increasing temperature up to 1600 °C exhibits a negligibly small effect on the phase equilibria, suggesting a highly stable microstructure.

While the thermodynamic calculations presented in this study show good agreement with the experimental results, it must be emphasized that the available thermodynamic descriptions for the Mo-Si-B-V quaternary system are still limited due to the lack of comprehensive experimental data, particularly in the Mo-B-V and Mo-Si-V subsystems. As the Mo-Si-B-V alloy system is relatively novel, existing databases do not yet cover the entire compositional space with high fidelity. In the present work, the modelling was therefore focused on the Mo- and V-rich regions, which are of particular relevance for the investigated compositions. The thermodynamic parameters used were based on available literature data as well as new experimental results generated during this study. Further refinement of the database will be possible as more experimental data become available, especially for currently underexplored regions of the quaternary phase diagram.

Density measurements reveal an additional density reduction of Mo-V-Si-B alloys due to Ti doping, which is less pronounced in the V-substituted alloys. This is attributed to the fact that these alloys exhibit a lower V concentration, leading to higher densities compared to the Mo-substituted alloys. The results show that the density of these alloy systems is significantly lower than that of the Mo-9Si-8B alloy (9.4 g/cm^3) [40] and even lower than that of commercial nickel-based superalloys like In 713C (7.95 g/cm^3), In 100 (7.91 g/cm^3) and CMSX-4 (8.7 g/cm^3) [41,42].

3.2. Microstructure Evolution During Mechanical Alloying and Heat Treatment

The progress of milling can be monitored very well by analysing microstructure formation as a function of milling time. The SEM images in Figure 3 show the progress of milling in different states for all alloys. Since the microstructures revealed no significant differences after 1 h and 2 h, nor after 5 h and 10 h of milling, the microstructures after 2 h and 10 h are shown as examples, along with 20 h of milling as the maximum milling time investigated in this study. In the first hours of milling, larger light grey Mo-rich phase and dark grey V-rich phase regions can be observed within the individual powder particles. As the milling time increases up to 10 h, a lamellar structure forms, indicating that repeated comminution and cold-welding processes are the working mechanisms during mechanical alloying. In addition, V is increasingly dissolved in the $(Mo,V)_{ss}$ phase and vice versa, and as a result, the microstructure becomes more homogeneous. However, after 20 h of milling, a completely homogeneous microstructure with only single-phase particles is not yet achieved, since lamellar structures can still be detected in some particles of all alloys, which in turn indicates that the mechanical alloying of the powders is not entirely completed at this point. Compared to previous studies on Mo-9Si-8B [8] and Mo-40V-9Si-8B [17], where a homogeneous microstructure was achieved after 20 h of milling using

the higher energy PM400 mill (200 rpm), the present results indicate that the lower energy PM100 setup may not have provided sufficient energy input for full alloying.

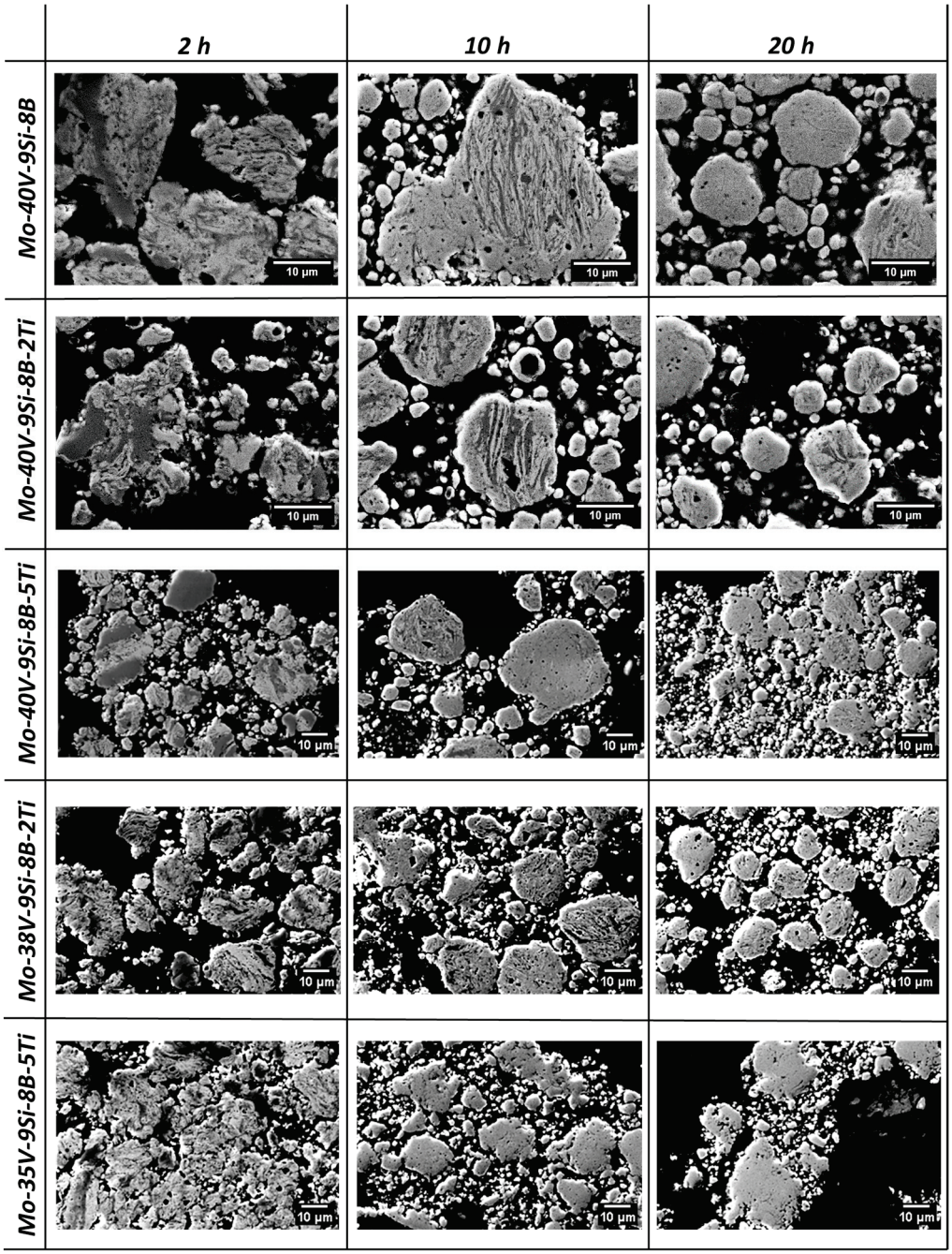


Figure 3. The microstructures of the mechanically alloyed powders after 2 h, 10 h and 20 h of milling. As milling time increases, a characteristic lamellar structure develops, leading to progressive microstructural homogenization.

However, when directly compared to Becker et al. [17], who used the same alloy composition (Mo-40V-9Si-8B) but without Ti and with a higher energy milling setup (PM400, 200 rpm), the present study shows that even with lower energy input, the addition of TiH_2 enables the formation of a supersaturated solid solution and a comparable multiphase microstructure after heat treatment. Notably, the Ti-doped alloys exhibited finer particle sizes, higher microstrain, and in some cases increased microhardness already in

the as-milled state, suggesting an accelerated homogenization effect—possibly due to the fragmentation-promoting nature of TiH_2 and its interaction with oxygen.

During heat treatment of the powders, the two silicide phases $(Mo,V)_3Si/(Mo,V,Ti)_3Si$ and $(Mo,V)_5SiB_2/(Mo,V,Ti)_5SiB_2$ precipitate, which are homogeneously distributed in the continuous $(Mo,V)_{ss}/(Mo,V,Ti)_{ss}$ matrix phase, as can be seen for the two alloys Mo-40V-9Si-8 B and Mo-40V-9Si-8B-5Ti in Figure 4a,b. The microstructures are in agreement with previous studies on similarly treated Mo-9Si-8B and Mo-40V-9Si-8B alloys [6,8,17]. Although a completely homogeneous supersaturated solid solution is not evident after 20 h of mechanical alloying using the aforementioned milling parameters, the desired ultra-fine and homogenous multiphase microstructure has formed after heat treatment. Therefore, it can be concluded that the slight differences between the powder's characteristics milled with the milling aggregates PM100 and those milled with the PM400 [6,8,17] are not significant enough to affect the microstructure after annealing.

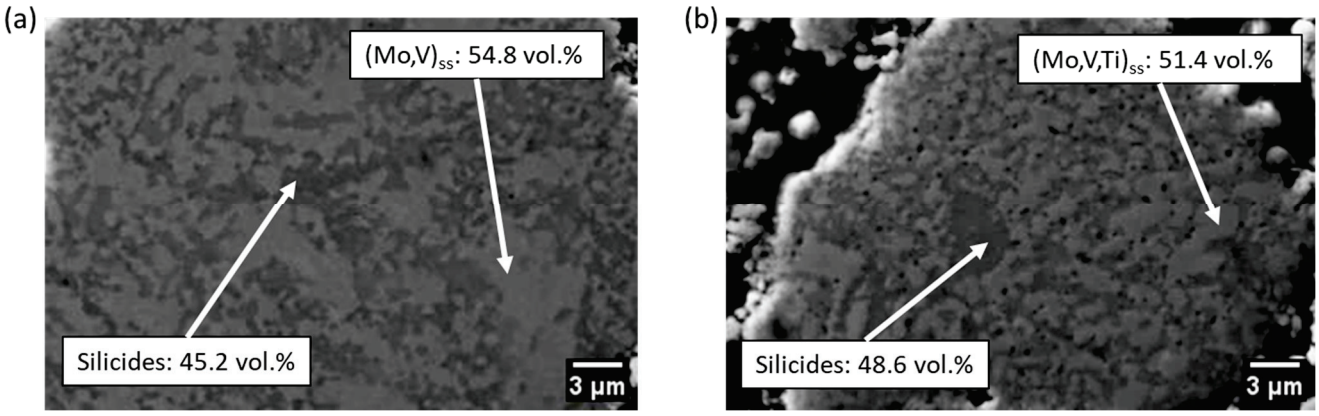


Figure 4. SEM images of the heat-treated (1400 °C for 1 h) powders: (**a**) Mo-40V-9Si-8B and (**b**) Mo-40V-9Si-8B-5Ti. The microstructures reveal a continuous $(Mo,V)_{ss}$ matrix phase (light grey) with homogeneously distributed silicide particles (dark grey).

The volume fractions of the phases were calculated using the density and mass fraction from the Rietveld refinement, with the values given in Table 2. It can be observed that in the Mo-substituted alloys Mo-40V-9Si-8B-2Ti and Mo-40V-9Si-8B-5Ti, the volume fraction of the $(Mo,V)_{ss}$ phase decreases, while the amount of silicide phases increases with higher Ti concentrations. However, in the case of the V-substituted alloys Mo-38V-9Si-8B-2Ti and Mo-35V-9Si-8B-5Ti, the volume fractions of the $(Mo,V)_{ss}$ phase and the silicide phases remain unchanged. In addition, the morphology and distribution of the phases are not affected by the small Ti additions.

It should be noted that the microstructures of the mechanically alloyed powders after heat treatment correspond well to those after sintering via the FAST process (Figure 5a,b), which is consistent with the studies of Becker et al. [17]. In addition, the volume fractions of the $(Mo,V)_{ss}/(Mo,V,Ti)_{ss}$ matrix phase and the silicide phases after heat treatment of the powders and after FAST are almost equal. Therefore, it can be concluded that the phase distribution in both the milled and heat-treated powder and the bulk material (sintered via FAST) are identical. The corresponding X-ray diffractograms in Figure 5c,d exhibit the same reflections as those of the heat-treated powders (Figure 1a,b), confirming that the microstructure consists of the same phases.

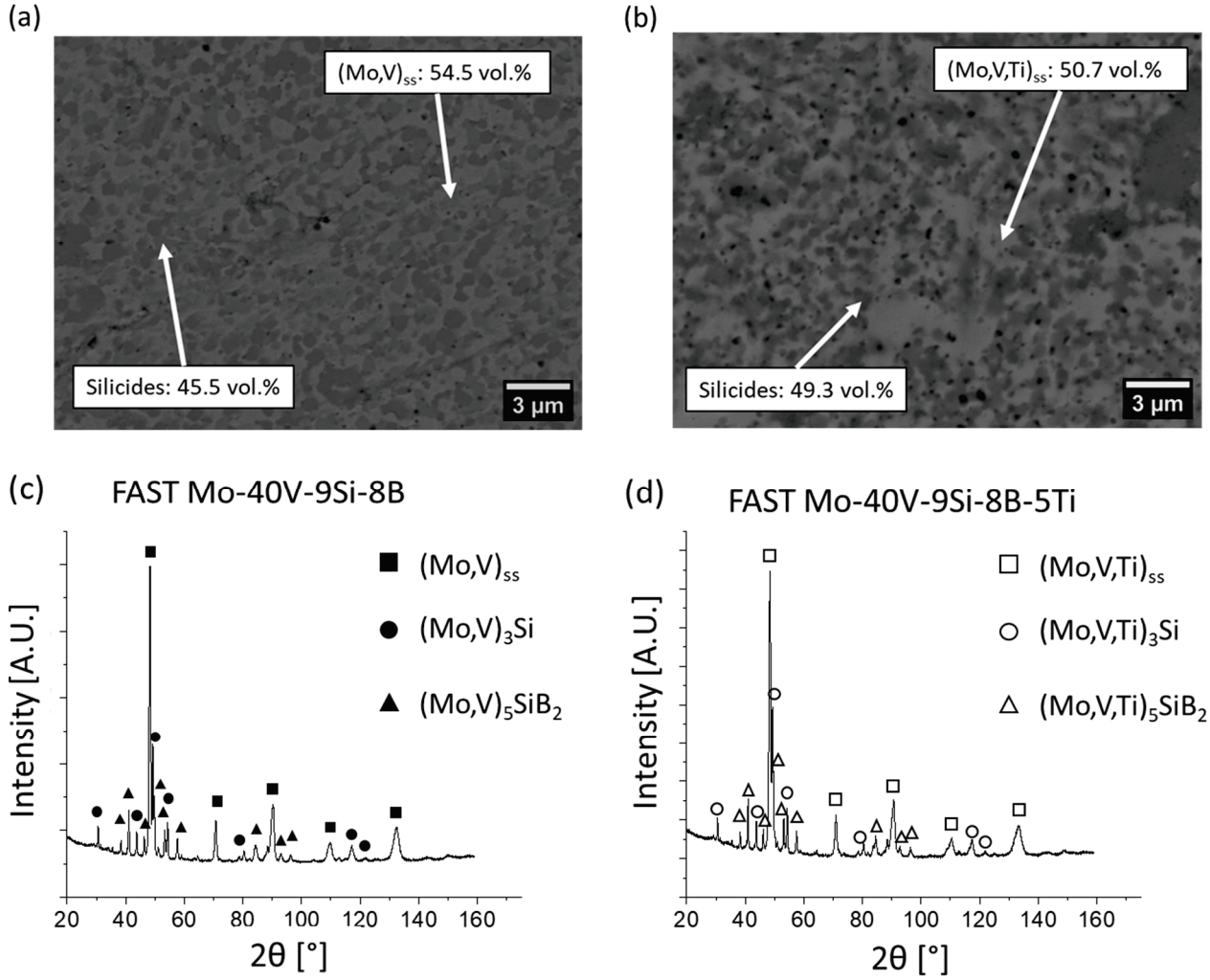


Figure 5. Microstructures after FAST at 1500 °C of (**a**) Mo-40V-9Si-8B and (**b**) Mo-40V-9Si-8B-5Ti, along with their corresponding X-ray diffractograms (**c**,**d**), showing the same phase distribution compared to the heat-treated powders shown in Figure 4.

3.3. Particle Size Evolution During Mechanical Alloying

Figure 6a shows the average particle size of the powders as a function of milling time for all alloys investigated. As milling time increases, the particle size d(0.5), i.e., d_{50} value of the particle size distribution, decreases due to the more pronounced comminution related to the hardening of powders by the formation of a solid solution and the progressive cold working, which corresponds to the increasing microstrain during milling (Table 1). This is due to the fact that the high impact forces of the planetary ball mill not only weld the powder particles but also effectively comminute them, as shown in previous studies [43]. The addition of small amounts of TiH_2 seems to further reduce particle size compared to the Mo-40V-9Si-8B alloy. The TiH_2 powder has a brittle character and is also homogeneously dispersed in the Mo powders during milling. TiH_2 tends to fracture easily under mechanical stress, which contributes to the crushing process. During mechanical alloying, the particle size of the Ti-doped alloys decreases faster due to the easy fragmentation of the hydride [44]. All alloys exhibit a reduction in particle size in the initial stages of milling, which is consistent with Li et al. [11], who investigated Mo-12Si-8.5B nanocomposite powders treated in the planetary ball mill PM100. In the first 5 h of milling, the number of small particles increases and, in contrast to the initial powder particles, they exhibit a rough

and complex shape. At this period of time, fracture and cold-welding processes occur simultaneously. After 20 h of milling, the size of the particles ranges between 4.8 and 7.2 µm, indicating a significant reduction compared to the initial powder. This suggests that steady-state conditions may have been reached, where further size reduction is minimal despite continued milling.

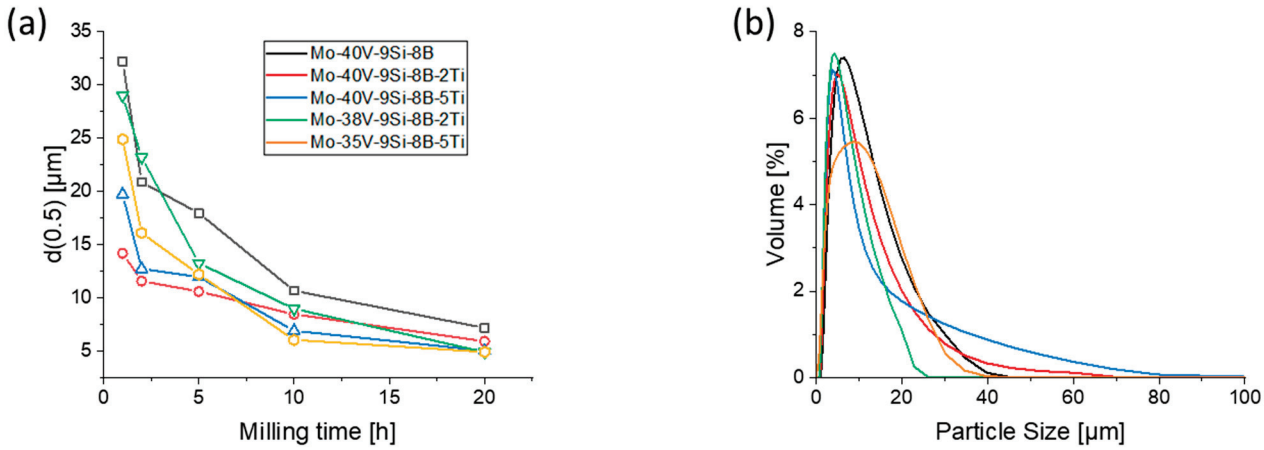


Figure 6. (**a**) Particle size d(0.5) as a function of milling time. The Ti-alloyed powders tend to produce smaller particles. (**b**) Particle size distribution after 20 h of milling reveals a smaller maximum and width of distribution with the addition of Ti.

The particle size distribution after 20 h of milling in Figure 6b shows that with the addition of Ti, the maximum particle size distribution shifts to smaller values (except for alloy Mo-35V-9Si-8B-5Ti), which in general indicates smaller particle sizes for the Ti-alloyed powders. In addition, the width of the distribution becomes smaller with the addition of Ti (only Mo-35V-9Si-8B-5Ti shows almost the same width), which indicates that these alloys exhibit a higher fraction of small particles (smaller scattering in particle size). Therefore, it can be concluded that the addition of the hard and brittle TiH_2 powder is an additional factor of comminution.

3.4. Oxygen Concentration After Mechanical Alloying and Heat Treatment

The oxygen concentration of the elemental powders (Figure 7a) shows that Mo (128 ± 12 wppm, weight parts per million), V (307 ± 69 wppm) and TiH_2 (50 ± 14 wppm) have low oxygen concentrations, while Si (1051 ± 224 wppm) and B (1042 ± 102 wppm) possess higher oxygen concentrations. As visualized in Figure 7b, the oxygen measurements show an oxygen level below 1000 wppm after 20 h for most of the alloys. Specifically, the oxygen concentration in Mo-35V-9Si-8B-5Ti after mechanical alloying was approximately twice as high compared to the other alloys. Since all alloys were processed under the same conditions, this discrepancy indicates that factors such as powder morphology, surface area or batch-to-batch variations in raw material purity influenced the initial oxygen concentration. The markedly elevated oxygen level observed in the Mo-35V-9Si-8B-5Ti alloy may be attributed to a combination of factors, including the high TiH_2 content, which increases the specific surface area during milling due to its brittle behaviour and may locally enhance oxidation. Furthermore, partial oxidation of Ti during decomposition, possibly in the presence of surface-adsorbed moisture or residual air, could contribute to the overall oxygen uptake, even in the absence of detectable oxide phases in XRD or SEM. Although no crystalline oxide phases were detected, the presence of amorphous or nanoscale titanium oxides located on particle surfaces cannot be excluded. Due to the limitations of EDS

in quantifying oxygen and the absence of a thermodynamic database including oxygen-containing phases for this quaternary system, further quantification was not attempted. Nonetheless, no signs of oxide agglomeration were observed in microstructural analysis using SEM.

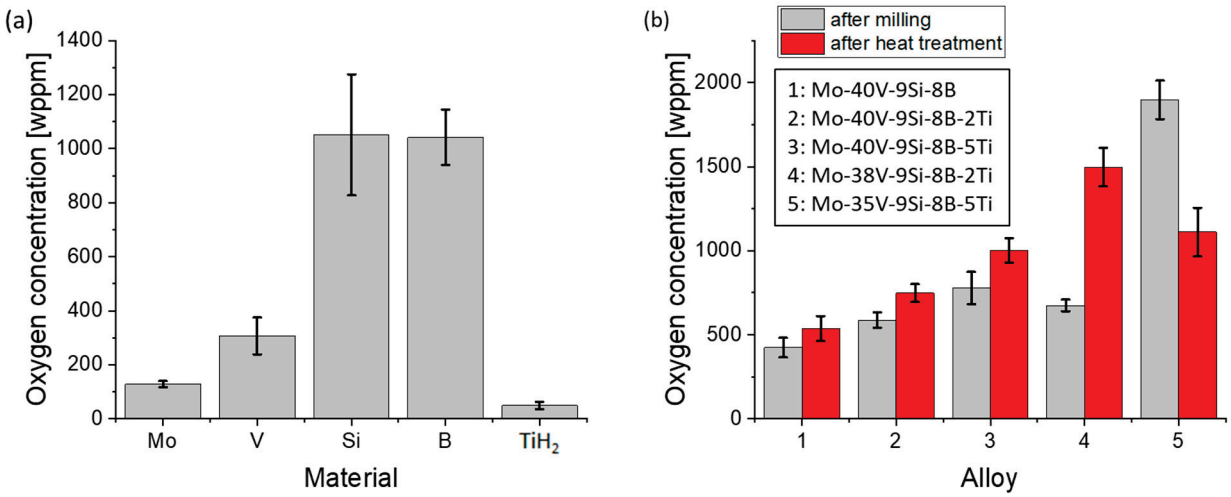


Figure 7. (**a**) The oxygen concentration of the elemental powders and (**b**) after high-energy ball milling and heat treatment.

It should be noted that the oxygen concentration of all alloys slightly increases during mechanical alloying, since the grinding vials are not entirely airtight, and oxygen can penetrate during milling. Consequently, the fresh surfaces, which are formed by breaking during mechanical alloying, can easily pick up residual oxygen from the process atmosphere. With the addition of Ti, the oxygen concentration increases, although the introduced oxygen of the TiH_2 powder is negligible. A possible explanation is the oxidation of Ti to TiO_2, which occurs even in a protective argon atmosphere, leading to the formation of an oxide layer on the TiH_2 powder particles' surface [45].

Figure 7b illustrates the oxygen concentration of the alloys after subsequent heat treatment of the powders. The oxygen concentration of Mo-40V-9Si-8B after heat treatment is 537 $\pm$ 74 wppm, which is less than one tenth of the value measured by Becker et al. (5787 wppm) [17] for the same alloy composition. The reason for this much smaller value is the significantly lower oxygen concentration of the as-received V powder compared with that used by Becker et al. Thus, it can be stated that the oxygen concentration of the as-received powders is crucial for the milling process.

The addition of Ti to Mo-40V-9Si-8B leads to higher oxygen concentrations (except for the Mo-35V-9Si-8B-5Ti alloy). These results are in agreement with those of Hiraoka et al. [46] who showed that the oxygen concentration in Mo-Ti alloys increases due to Ti doping. During heat treatment of the Ti-containing alloys, hydrogen is released as hydrogen gas (H_2), especially at elevated temperatures. The hydrogen reacts with the oxygen available in these alloys to form water vapor, which is evaporated in the atmosphere. Simultaneously, Ti reacts with oxygen, leading to the formation of titanium oxides.

However, no oxides could be found in the X-ray diffractograms (Figure 1) or in the SEM images (Figure 4) for the heat-treated powders of the present studies. Nevertheless, the presence of nano-scaled or amorphous oxides below the detection limits of XRD and SEM cannot be entirely excluded. Such oxides may exist as thin films, grain boundary precipitates or finely dispersed amorphous particles. Despite this uncertainty, the available characterization data suggest that no oxides have a significant impact on the observed phase

formation or overall microstructural homogeneity. The silicide phases form consistently in all samples, and no morphological anomalies or secondary oxide phases are evident.

While the oxygen concentrations in the Ti-containing alloys are slightly elevated compared to the Ti-free reference, they remain significantly lower than those reported by Becker et al. [17] or the same base composition processed without TiH_2 (~5800 wppm). This indicates that the use of TiH_2, despite its inherent reactivity, does not lead to excessive oxidation. On the contrary, it may even contribute to a partial deoxidizing effect during processing, potentially via hydrogen release and subsequent reaction with oxygen-containing species.

However, the oxygen concentration trend observed in Mo-35V-9Si-8B-5Ti differs significantly from that in the other investigated alloys. A possible reason for this discrepancy could be attributed to the initial oxygen concentration present after mechanical alloying. During subsequent heat treatment, the high initial oxygen concentration in Mo-35V-9Si-8B-5Ti may have influenced oxygen redistribution in the alloy. However, phase analysis and microstructural characterization of the heat-treated powder samples did not reveal the presence of volatile oxides or evidence of reduction reactions. In contrast, the alloys with a lower initial oxygen concentration exhibited an increase in oxygen concentration, which may suggest oxygen uptake from residual gas in the vacuum chamber or oxygen redistribution within the material. The measured oxygen concentration for the alloys should therefore be treated with care and seems to represent a kind of trend.

3.5. Microhardness Evolution During Milling and After Heat Treatment

Table 1 shows the evolution of microhardness depending on milling time. At the beginning, the microhardness strongly increases due to the different hardening mechanisms, which occur in the initial stage of mechanical alloying. Firstly, collisions between the powder and the balls lead to plastic deformation of the powder particle and consequently to a higher dislocation density (work hardening) [37]. Secondly, mechanical alloying of similar metallurgically processed Mo-Si-B powder lowers the domain size up to the lower micrometer range due to collisions between balls and between powder and balls (grain refinement) [8]. Thirdly, the addition of V and Ti, which are dissolved in the Mo lattice, further contribute to solid solution strengthening, resulting in an improvement in microhardness [18]. After 20 h, the microhardness of Mo-40V-9Si-8B has reached a value of 11 $\pm$ 3 GPa and the addition of Ti seems to increase the microhardness, except for Mo-40V-9Si-8B-2Ti (9.5 $\pm$ 2 GPa), which has a lower microhardness compared to the Ti-free alloy. On the other hand, the microhardness of Mo-35V-9Si-8B-5Ti has reached a value of 14.5 GPa but has a much smaller standard deviation ($\pm$2 GPa) compared to Mo-40V-9Si-8B. It should be noted that all microhardness measurements were conducted on individual powder particles embedded in cold-mounting resin. Due to the very small particle sizes after 20 h of milling (4.8–7.2 µm, see Figures 3 and 6), it is challenging to place indentations without overlapping phase boundaries or being affected by the softer embedding material.

The results of the measured microhardness after heat treatment are shown in Table 2. For the alloys Mo-40V-9Si-8B, Mo-40V-9Si-8B-5Ti and Mo-38V-9Si-8B-2Ti, there is an increase in microhardness after heat treatment, while the microhardness in Mo-40V-9Si-8B-2Ti and Mo-35V-9Si-8B-5Ti decreases compared to the as-milled state. It should be noted that these measurements were conducted on individual powder particles embedded in cold-mounting resin.

The limited flat surface area per particle and the heterogeneous internal phase distribution further complicates precise positioning, especially when using an optical system with limited spatial resolution. These experimental constraints are compounded by the material-specific characteristics of the heat-treated powders, which exhibit an ultra-fine,

multiphase microstructure with silicides ($(Mo,V)_3Si$ and $(Mo,V)_5SiB_2$) finely dispersed in the $(Mo,V)_{ss}$ matrix. Based on image analysis, the average width of the silicide features is approximately 0.6 μm. Using a simplified model, the mean centre-to-centre spacing of silicide particles was estimated to be ~0.63 μm (assuming 48 vol% silicides), which is significantly smaller than the Vickers indentation size (~10–15 μm). Consequently, each indentation inevitably involves multiple phases, making it difficult to isolate phase-specific mechanical responses and contributing to increased scatter.

In addition, the powders retain a high density of lattice defects introduced during mechanical alloying, as indirectly indicated by the elevated microstrain measured via XRD (Table 1). These lattice defects (mainly point defects and dislocations) locally influence hardness and can either hinder or promote plasticity depending on their interaction with adjacent phases. Since microstrain was only measured in the as-milled state, any interpretation related to internal stresses or defect density applies solely to this condition. Potential recovery processes during subsequent heat treatment cannot be assessed based on the available data. The relatively large standard deviations in microhardness are therefore attributed to the combined effects of measurement limitations, overlapping phase contributions, lattice defects and microstructural inhomogeneities—characteristics that are typical for mechanically alloyed systems and consistent with previous observations [8,17].

It must be noted that the microhardness values given are to be understood as a medium value of the corresponding phases, i.e., a solid solution and the two silicide phases. As can be seen in Figure 4, the dispersed silicide phases are relatively small and close to each other. Due to the limited size of the silicide-free regions, it was not possible to isolate the $(Mo,V)_{ss}$ matrix during indentation. Consequently, the standard deviations are very high, because the silicide phases $(Mo,V)_3Si/(Mo,V,Ti)_3Si$ and $(Mo,V)_5SiB_2/(Mo,V,Ti)_5SiB_2$ exhibit a higher hardness than the $(Mo,V)_{ss}/(Mo,V,Ti)_{ss}$ matrix phase. In this context, Choe et al. [47] investigated the microhardness of Mo-12Si-8.5B and was able to show that the microhardness of Mo_5SiB_2 (18.5 GPa) is slightly higher compared to that of Mo_3Si (15 GPa), which are both significantly higher than that of the Mo_{ss} matrix phase (7 GPa). The addition of 2 at. % Ti to Mo-V-Si-B seems not to affect the microhardness significantly (in the case of Mo-40V-9Si-8B-2Ti, it is even significantly lower), while 5 at. % Ti leads to a noticeable improvement in microhardness. These results are in agreement with those of Becker et al. [18], who showed that the addition of 5 at. % Ti is sufficient to increase the microhardness of pure Mo due to solid solution hardening. However, in the case of Mo-35V-9Si-8B-5Ti, this increase in microhardness is not as pronounced compared to Mo-40V-9Si-8B-5Ti. Therefore, the addition of 5 at. % Ti to Mo-40V-9Si-8B has the highest impact on microhardness in the present study.

4. Conclusions

The present study investigated the effects of small titanium additions (2 and 5 at. %), which were added as TiH_2 powders, on the microstructure, phase evolution, oxygen concentration and microhardness of mechanically alloyed Mo-40V-9Si-8B alloys.

All compositions formed a supersaturated (Mo,V,Ti) solid solution during mechanical alloying, which decomposed into a stable three-phase microstructure consisting of $(Mo,V)_{ss}$, $(Mo,V)_3Si$ and $(Mo,V)_5SiB_2$ or $(Mo,V,Ti)_{ss}$, $(Mo,V,Ti)_3Si$ and $(Mo,V,Ti)_5SiB_2$ after heat treatment. Compared to the Ti-free alloy, the Ti-containing variants showed slightly finer particle sizes, higher microstrain and, in the case of 5 at. % Ti, a modest increase in microhardness. Although the Ti-doped alloys exhibited slightly elevated oxygen concentrations compared to the Ti-free composition, the overall values remained significantly lower

than those reported in earlier studies using conventional powder routes—demonstrating the potential of TiH_2 as a reactive alloying agent and deoxidizing precursor.

The brittleness of TiH_2 affects powder refinement during milling, while its decomposition may support a more homogeneous element distribution. Although the overall oxygen content in the Ti-containing alloys was slightly higher than in the Ti-free reference, it remained significantly lower than in comparable studies using elemental powders—indicating that TiH_2 does not critically promote oxygen uptake and may still offer benefits in oxygen-sensitive processing environments.

Based on the promising results of this study, future research should focus on evaluating the high-temperature performance of these alloys, including their mechanical behaviour in a broad temperature regime (including flexural and tensile deformation, creep and fracture behaviour), as well as their environmental effects (oxidation, corrosion). With their reduced density and complex multiphase architecture, these Ti- and V-modified Mo–Si–B alloys are promising candidates for high-temperature structural applications such as turbine components or thermal barrier systems.

Author Contributions: D.Z., conceptualization, methodology, formal analysis, investigation, writing—original draft preparation, visualization; J.B., methodology, writing—review and editing; U.B., investigation, data curation, writing—original draft preparation; G.H., conceptualization, methodology, writing—review and editing, supervision, project administration; K.K., software, validation, data curation, writing—original draft preparation; B.G., writing—review and editing, supervision; M.K., conceptualization, methodology, writing—review and editing, supervision, project administration. All authors have read and agreed to the published version of the manuscript.

Funding: This work is financially supported by the German Federal Ministry for Economic Affairs and Climate Action within the framework of the "RACe" project (funding no. 20E2112A), part of the "Disruptive Technologies and innovative Systems" program. The support of the DFG, German Research Foundation, as part of the "Major Research Instrumentation Programme", is gratefully acknowledged (grant INST 272/281-1 FUGG; Bruker D8 Discover XRD).

Institutional Review Board Statement: Not applicable.

Informed Consent Statement: Not applicable.

Data Availability Statement: The original contributions presented in this study are included in the article. Further inquiries can be directed to the corresponding author.

Conflicts of Interest: The authors declare no conflict of interest.

References

1. Perepezko, J.H. The hotter the engine, the better. *Science* **2009**, *326*, 1068–1069. [CrossRef] [PubMed]
2. Dimiduk, D.M.; Perepezko, J.H. Mo-Si-B Alloys: Developing a Revolutionary Turbine-Engine Material. *MRS Bull.* **2003**, *28*, 639–645. [CrossRef]
3. Berczik, D.M. Oxidation Resistant Molybdenum Alloy. U.S. Patent 5693156A, 2 December 1997.
4. Berczik, D.M. Method for Enhancing the Oxidation Resistance of a Molybdenum Alloy, and a Method for Making a Molybdenum Alloy. U.S. Patent 5595616A, 21 January 1997.
5. Li, B.; Zhang, G.-J.; Feng, J.; Shuai, R.; Gang, L.; Jun, S. Preparation of fine-grained Mo-12Si-8.5B alloys with improved mechanical properties via a mechanical alloying process. *J. Alloys Compd.* **2014**, *609*, 80–85. [CrossRef]
6. Krüger, M.; Jain, P.; Kumar, K.S.; Heilmaier, M. Correlation between microstructure and properties of fine-grained Mo-Mo3Si-Mo5SiB2 alloys. *Intermetallics* **2014**, *48*, 10–18. [CrossRef]
7. Schneibel, J.H.; Kramer, M.J.; Easton, D.S. A Mo-Si-B intermetallic alloy with a continuous α-Mo matrix. *Scr. Mater.* **2002**, *46*, 217–221. [CrossRef]
8. Krüger, M.; Franz, S.; Saage, H.; Heilmaier, M.; Schneibel, J.H.; Jéhanno, P.; Böning, M.; Kestler, H. Mechanically alloyed Mo-Si-B alloys with a continuous α-Mo matrix and improved mechanical properties. *Intermetallics* **2008**, *16*, 933–941. [CrossRef]

9. Koch, C.C. Materials Synthesis by mechanical alloying. *Annu. Rev. Mater. Sci.* **1989**, *19*, 121–143. [CrossRef]
10. Benjamin, J.S.; Volin, T.E. The Mechanism of Mechanical Alloying. *Metall. Trans.* **1974**, *5*, 1929–1934. [CrossRef]
11. Li, B.; Zhang, G.; Jiang, F.; Ren, S.; Liu, G.; Sun, J. Characterization of Mo-Si-B nanocomposite powders produced using mechanical alloying and powder heat treatment. *J. Mater. Sci. Technol.* **2015**, *31*, 995–1000. [CrossRef]
12. Yang, T.; Guo, X.; Luo, Y. Microstructural evolution of mechanically alloyed Mo-Si-B-Zr-Y powders. *Int. J. Refract. Met. Hard Mater.* **2016**, *56*, 35–43. [CrossRef]
13. Schmelzer, J.; Baumann, T.; Dieck, S.; Krüger, M. Hardening of V-Si alloys during high energy ball milling. *Powder Technol.* **2016**, *294*, 493–497. [CrossRef]
14. Sakidja, R.; Myers, J.; Kim, S.; Perepezko, J.H. The effect of refractory metal substitution on the stability of Moss + T2 two-phase field in the Mo-Si-B system. *Int. J. Refract. Met. Hard Mater.* **2000**, *18*, 193–204. [CrossRef]
15. Yang, Y.; Bei, H.; Chen, S.; George, E.P.; Tiley, J.; Chang, Y.A. Effects of Ti, Zr, and Hf on the phase stability of Moss + Mo3Si + Mo5SiB2 alloys at 1600 °C. *Acta Mater.* **2010**, *58*, 541–548. [CrossRef]
16. Mitra, R.; Srivastava, A.K.; Prasad, N.E.; Kumari, S. Microstructure and mechanical behaviour of reaction hot pressed multiphase Mo-Si-B and Mo-Si-B-Al intermetallic alloys. *Intermetallics* **2006**, *14*, 1461–1471. [CrossRef]
17. Becker, J.; Betke, U.; Hoffmeister, M.; Krüger, M. Density Reduction of Mo-Si-B Alloys by Vanadium Alloying. *JOM* **2018**, *70*, 2574–2581. [CrossRef]
18. Becker, J.; Betke, U.; Wessel, E.; Krüger, M. Alloying effects in Mo-5X (X = Zr, Ti,V)—Microstructural modifications and mechanical properties. *Mater. Today Commun.* **2018**, *15*, 314–321. [CrossRef]
19. Northcott, L. *Metallurgy of the Rarer Metals-5 Molybdenum*; Academic Press INC Pulbishers: New York, NY, USA, 1956.
20. Azim, M.A.; Burk, S.; Gorr, B.; Christ, H.-J.; Schliephake, D.; Heilmaier, M.; Bornemann, R.; Bolívar, P.H. Effect of Ti (Macro-) alloying on the high-temperature oxidation behavior of ternary Mo-Si-B alloys at 820–1300 °C. *Oxid. Met.* **2013**, *80*, 231–242. [CrossRef]
21. Schliephake, D.; Azim, M.; von Klinski-Wetzel, K.; Gorr, B.; Christ, H.-J.; Bei, H.; George, E.P.; Heilmaier, M. High-temperature creep and oxidation behavior of Mo-Si-B alloys with high Ti contents. *Met. Mater. Trans. A* **2014**, *45*, 1102–1111. [CrossRef]
22. Azim, M.A.; Schliephake, D.; Hochmuth, C.; Gorr, B.; Christ, H.-J.; Glatzel, U.; Heilmaier, M. Creep Resistance and Oxidation Behavior of Novel Mo-Si-B-Ti Alloys. *JOM* **2015**, *67*, 2621–2628. [CrossRef]
23. Inoue, T.; Hiraoka, Y.; Sukedai, E.-I.; Nagae, M.; Takada, J. Hardening behavior of dilute Mo-Ti alloys by two-step heat-treatment. *Int. J. Refract. Met. Hard Mater.* **2007**, *25*, 138–143. [CrossRef]
24. Fan, J.; Lu, M.; Cheng, H.; Tian, J.; Huang, B. Effect of alloying elements Ti, Zr on the property and microstructure of molybdenum. *Int. J. Refract. Met. Hard Mater.* **2009**, *27*, 78–82. [CrossRef]
25. Okamoto, H.; Schlesinger, M.E.; Mueller, E.M. *ASM Handbook, Alloy Phase Diagrams*; ASM International Materials Park: Materials Park, OH, USA, 1992; Volume 3.
26. Hu, W.; Ma, Z.; Qian, Z.; Wu, J.; Dong, J.; Wang, H.; Liu, Y. Influence of minor Ti additive on the microstructure and mechanical properties of Mo based alloys. *Int. J. Refract. Met. Hard Mater.* **2021**, *99*, 105599. [CrossRef]
27. Choi, W.J.; Lee, S.Y.; Park, C.W.; Park, J.H.; Byun, J.M.; Kim, Y.D. Effect of titanium addition on mechanical properties of Mo-Si-B alloys. *Int. J. Refract. Met. Hard Mater.* **2019**, *80*, 238–242. [CrossRef]
28. Ivasishin, O.; Moxson, V. Low-cost titanium hydride powder metallurgy. In *Titanium Powder Metallurgy: Science, Technology and Applications, Butterworth-Heinemann*; Elsevier Inc.: Philadelphia, PA, USA, 2015; pp. 117–148. [CrossRef]
29. Stout, V.L.; Gibbons, M.D. Gettering of gas by titanium. *J. Appl. Phys.* **1955**, *26*, 1488–1492. [CrossRef]
30. Coelho, A.A. TOPAS and TOPAS-Academic: An optimization program integrating computer algebra and crystallographic objects written in C++. *J. Appl. Crystallogr.* **2018**, *51*, 210–218. [CrossRef]
31. Rietveld, H.M. A profile refinement method for nuclear and magnetic structures. *J. Appl. Crystallogr.* **1969**, *2*, 65–71. [CrossRef]
32. Vegard, L. Die Konstitution der Mischkristalle und die Raumfüllung der Atome. *Z. Phys.* **1921**, *5*, 17–26. [CrossRef]
33. Gražulis, S.; Chateigner, D.; Downs, R.T.; Yokochi, A.F.T.; Quirós, M.; Lutterotti, L.; Manakova, E.; Butkus, J.; Moeck, P.; Le Bail, A. Crystallography Open Database—An open-access collection of crystal structures. *J. Appl. Crystallogr.* **2009**, *42*, 726–729. [CrossRef]
34. Cheary, R.W.; Coelho, A. A Fundamental parameters approach to x-ray line-profile fitting. *J. Appl. Crystallogr.* **1992**, *25*, 109–121. [CrossRef]
35. Cheary, R.W.; Coelho, A.A.; Cline, J.P. Fundamental parameters line profile fitting in laboratory diffractometers. *J. Res. Natl. Inst. Stand. Technol.* **2004**, *109*, 1–25. [CrossRef]
36. Hans, L.; Fries, S.G.; Sundman, B. *Computational Thermodynamics: The Calphad Method*; Cambridge University Press: Cambridge, UK, 2007.

37. Bäker, M.; Harders, H.; Rösler, J. *Mechanisches Verhalten der Metalle*, 4th ed.; Springer Vieweg: Wiesbaden, Germany, 2012. [CrossRef]
38. Mhadhbi, M.; Khitouni, M.; Escoda, L.; Suñol, J.J. X-ray studies of structure defects in nanostructured FeAl alloy. *Mater. Lett.* **2010**, *64*, 1802–1805. [CrossRef]
39. Yang, Y.; Chang, Y.A. Thermodynamic modeling of the Mo-Si-B system. *Intermetallics* **2005**, *13*, 121–128. [CrossRef]
40. Hochmuth, C.; Schliephake, D.; Völkl, R.; Heilmaier, M.; Glatzel, U. Influence of zirconium content on microstructure and creep properties of Mo-9Si-8B alloys. *Intermetallics* **2014**, *48*, 3–9. [CrossRef]
41. Zagula-Yavorska, M.; Sieniawski, J.; Zieliñska, M.; Yavorska, M.; Porêba, M.; Sieniawski, J. Thermal properties of cast nickel based superalloys. *Arch. Mater. Sci. Eng.* **2010**, *44*, 35–38.
42. Erickson, G.L. The Development and Application of CMSX®-10. *Superalloys* **1996**, *35*, 35–44.
43. Krüger, M.; Schmelzer, J.; Helmecke, M. Similarities and differences in mechanical alloying processes of V-Si-B and Mo-Si-B powders. *Metals* **2016**, *6*, 241. [CrossRef]
44. Bhosle, V.; Baburaj, E.G.; Miranova, M.; Salama, K. Dehydrogenation of TiH2. *Mater. Sci. Eng. A* **2003**, *356*, 190–199. [CrossRef]
45. Park, K.B.; Choi, J.; Na, T.-W.; Kang, J.-W.; Park, K.; Park, H.-K. Oxygen reduction behavior of HDH TiH2 powder during dehydrogenation reaction. *Metals* **2019**, *9*, 1154. [CrossRef]
46. Hiraoka, Y.; Yoshimura, S.; Takebe, K. Low-Temperature Tensile Behavior of Powder-Metallurgy Mo-Ti Alloys. *Int. J. Refract. Met. Hard Mater.* **1993**, *12*, 211–216. [CrossRef]
47. Choe, H.; Chen, D.; Schneibel, J.H.; Ritchie, R.O. Ambient to high temperature fracture toughness and fatigue-crack propagation behavior in a Mo-12Si-8.5B (at. %) intermetallic. *Intermetallics* **2001**, *9*, 319–329. [CrossRef]

Disclaimer/Publisher's Note: The statements, opinions and data contained in all publications are solely those of the individual author(s) and contributor(s) and not of MDPI and/or the editor(s). MDPI and/or the editor(s) disclaim responsibility for any injury to people or property resulting from any ideas, methods, instructions or products referred to in the content.

materials

MDPI

Article

Tailoring Microstructure and Properties of W-Mo-Cu Composites Fabricated via Infiltration Sintering: Effects of Graphene Addition and Skeleton Relative Density

Jinwen Cai [1], Qiaoling Jiang [1], Keqin Feng [1,*] and Hongling Zhou [2,*]

[1] School of Mechanical Engineering, Sichuan University, Chengdu 610065, China; caijinwen@stu.scu.edu.cn (J.C.); jiangqiaoling@stu.scu.edu.cn (Q.J.)
[2] College of Materials Science and Engineering, Chongqing University, Chongqing 400044, China
* Correspondence: kqfeng@scu.edu.cn (K.F.); zhouhongling@cqu.edu.cn (H.Z.)

Abstract: W-Mo-Cu composites show promise for advanced applications, but their properties require optimization. In this study, a novel approach utilizing Cu-coated graphene (Cu@Gr) reinforcement with skeleton relative density adjustment was employed to tailor the microstructure and properties of W-Mo-Cu composites fabricated via infiltration sintering (1300 °C, 1.5 h). The results revealed that Cu@Gr significantly promoted sintering densification, modified the phase composition, and enhanced the properties of the composite. Specifically, the addition of 0.4 wt.% Cu@Gr resulted in a relative density of 98% for the composite, representing an 8% increase compared to the material without Cu@Gr. Furthermore, when higher amounts of Cu@Gr were incorporated, the composite consistently exhibited a high degree of densification. In addition to the primary W, Mo, and Cu phases, molybdenum carbide, Mo_2C, was formed at 0.4 wt.% Cu@Gr, with its content rising proportionally to graphene dosage. Notably, the composite containing 0.6 wt.% Cu@Gr exhibits the highest thermal conductivity and electrical conductivity, showing 64% and 73% increases, respectively, versus Cu@Gr-free samples. Additionally, although W-Mo green compact density variations (73–85%) did not compromise graphene-induced densification, a higher green compact density reduced the thermal/electrical conductivities but increased the hardness. These findings demonstrate that controlled Cu@Gr incorporation and green compact optimization synergistically improve the properties of W-Mo-Cu composites, providing insights into high-performance material design.

Keywords: graphene; infiltration sintering; W-Mo-Cu composites; densification; properties

1. Introduction

Refractory metals, such as tungsten (W) and molybdenum (Mo), possess high melting temperatures, low thermal expansion coefficients, good ablative resistance, and high hardness. These properties make them instrumental in the fabrication of structural materials used in aerospace applications and nuclear reactors [1,2]. In contrast, as a low-melting-point metal, copper (Cu) not only has excellent thermal conductivity and electrical conductivities but also exhibits good toughness [3,4]. Thus, W-Mo-Cu composite, a novel and promising pseudo-alloy with a tailorable composition ratio integrates the advantageous physical properties of metal W, Mo, and Cu, which can be widely applied in various fields, including arcing electrodes, electronic packaging materials, high-voltage electrical contacts, sweating materials, and electromagnetic gun-rail materials [5–7]. Nevertheless,

the fabrication of W-Mo-Cu composites presents challenges due to the significant differences in the melting points of the constituent elements (W: 3410 °C, Mo: 2623 °C, and Cu: 1083 °C), as well as the insolubility of W and Cu, and Mo and Cu [8,9]. Currently, the fabrication of W-Mo-Cu composites predominantly relies on powder metallurgy methods, including liquid-phase sintering, field-assisted sintering techniques, and infiltration sintering [7,10,11]. The liquid-phase sintering method is simple and controllable but requires high temperatures (1100–1400 °C) and long times (3–4 h), which may form Cu melt pools and adversely affect the composite's microstructure. Furthermore, although the pretreatment of powders can enhance the properties of W-Mo-Cu composites, it also increases the preparation time [12]. Field-assisted sintering methods, such as spark plasma sintering, microwave sintering, and large current electric field sintering, utilize external physical fields to activate the sintering process, thereby reducing the temperature (800–1000 °C) and preparation time (5–10 min) for composites. However, the resulting W-Mo-Cu composites exhibit suboptimal ies with a maximum relative density of approximately 94% [10,11,13]. Although it requires similarly high sintering temperatures (1200–1400 °C) and extended durations (4 h) as liquid-phase sintering, the infiltration sintering method produces composites with significantly reduced porosity by effectively filling the W or Mo skeleton with Cu. This enables the preparation of high-density W-Mo-Cu composites without powder pretreatment [14,15]. However, the high temperature and long duration of the infiltration sintering process still pose challenges, such as Cu phase volatilization, weakened interfacial bonding, and grain coarsening during sintering, which may adversely affect the properties of W-Mo-Cu composites. To address these challenges, elements such as Co, Ni, and Fe are frequently added as sintering activators in pseudo-alloys, reducing the activation energy and sintering temperature while enhancing the overall performance [16–18]. However, these elements can negatively affect the electrical conductivity and thermal conductivities of pseudo-alloys, which undoubtedly impacts their practical applications [19]. Therefore, it is essential to select new additives that do not compromise the excellent electrical and thermal conductivities of W-Mo-Cu composites.

Graphene, which is renowned for its exceptional electron mobility (2×10^5 $cm^2/(V{\cdot}S)$), high carrier density (10^{13} cm^{-2}), ultrahigh thermal conductivity (up to 5300 $W/(m{\cdot}K)$), and remarkable mechanical strength (130 GPa), has been successfully integrated into composite materials such as aluminum-, magnesium-, copper-, and titanium-based systems. For instance, Hu et al. [20] fabricated graphene-aluminum matrix composites via electromagnetic stirring and casting processes, achieving optimal performance at 0.2 wt. % graphene content with hardness, electrical conductivity, and thermal conductivity increased by 42%, 5%, and 38%, respectively, compared to pure aluminum. Furthermore, Zhao et al. [21] and Chen et al. [22] demonstrated that graphene incorporation facilitates grain refinement while significantly enhancing the mechanical, electrical, and thermal properties of metal matrices. However, when graphene is incorporated into metal matrix composites, it still encounters challenges such as difficulties in dispersion, a tendency to agglomerate, and susceptibility to reactions with the matrix [23–26]. Consequently, surface pretreatment of graphene is often required, with the electroless deposition of a metal layer onto its surface being a relatively effective modification technique[21,23,27,28].

In this study, surface-modified graphene (Cu@Gr) was fabricated via electroless plating and subsequently incorporated into a W-Mo-Cu composite matrix with varying Cu@Gr contents (0.2–1.0 wt. %) to synthesize Cu@Gr-reinforced W-Mo-Cu (Cu@Gr/W-Mo-Cu) composites through infiltration sintering. The effects of Cu@Gr addition on the microstructure and properties of the composites were systematically investigated. Furthermore, considering the critical role of the relative density in W-Mo green compacts for successful in-

filtration, a complementary study was conducted to evaluate how varying relative densities (73–85%) of the W-Mo skeleton, combined with the optimized Cu@Gr content, influence the final composite performance. This dual-parameter optimization strategy provides insights into both the compositional and structural controls for enhancing W-Mo-Cu composites.

2. Experimental

2.1. Materials

W powders (99.9% purity; average particle size between 1–3 μm), Mo powders (99.9% purity; average particle size between 1–3 μm, Xiamen Golden Egret Special Alloy Co., Ltd. (Xiamen, China)), Cu powders (99.9% purity; average particle size of 5 μm, Zhongye Xindun Co., Ltd. (Xingtai, China)) and Graphene powders with 5–10 layers (99.0% purity; average particle diameter of 5 μm, Shenzhen Suiheng Graphene Technology Co., Ltd. (Shenzhen, China)) were used as raw powders for the experiment. Figure 1 shows the SEM micrographs of the raw powders used for the composite fabrication. The W powder particles exhibited irregular polyhedral morphologies with featureless surfaces, whereas the Mo powder consisted of irregular spherical particles. The Cu powder displayed ellipsoidal irregular shapes, with graphene presenting ultrathin flake-like structures. The auxiliary chemicals employed for graphene surface modification via electroless plating included (except for $C_{10}H_8N_2$ and NaOH, all other raw materials were sourced from Chengdu Kelong Chemical Co., Ltd. (Chengdu, China)): polyvinyl alcohol (PVA), N-methylpyrrolidone (NMP), hydrochloric acid (HCl, 37%), stannous chloride dihydrate ($SnCl_2{\cdot}2H_2O$), palladium chloride ($PdCl_2$), copper sulfate pentahydrate ($CuSO_4{\cdot}5H_2O$), potassium sodium tartrate tetrahydrate ($KNaC_4H_4O_6{\cdot}4H_2O$), ethylenediaminetetraacetic acid disodium salt (Na_2EDTA), sodium carbonate (Na_2CO_3), 2,2′-bipyridine ($C_{10}H_8N_2$) (Chengdu Nuershi Technology Co., Ltd. (Chengdu, China)), sodium hydroxide (NaOH) (Chengdu Kelong Chemical Reagent Factory (Chengdu, China)), and formaldehyde (HCHO, 37%). All reagents were procured as analytical-grade materials and utilized without additional purification. Aqueous solutions were prepared using deionized water (resistivity > 18 MΩ·cm).

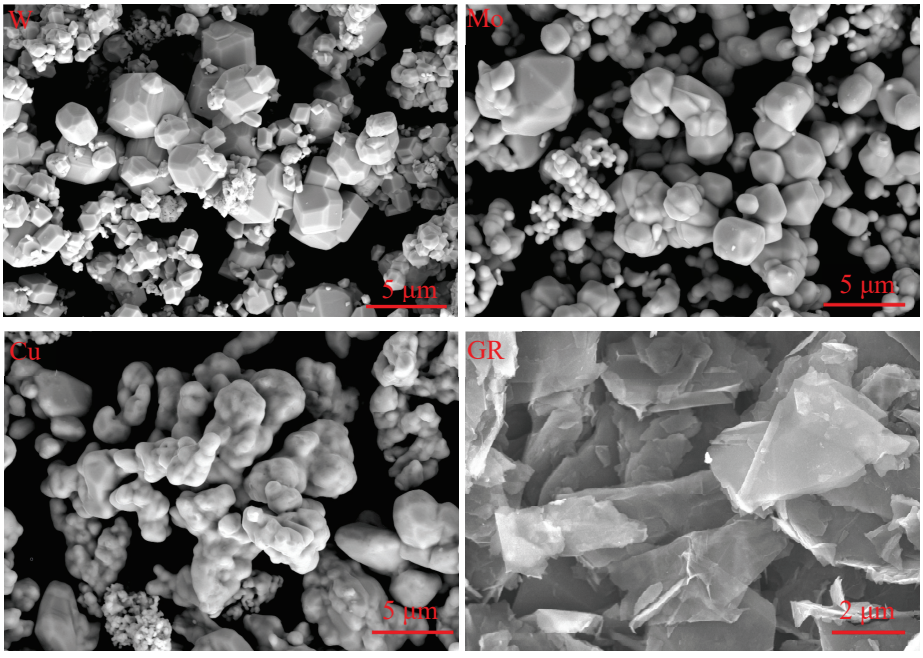


Figure 1. Microstructure of the raw material powders.

2.2. Graphene Surface Modification

Figure 2 illustrates the schematic process of graphene surface modification. Initially, graphene was treated with ultrasonication for 0.5 h and magnetic stirring for 1 h in an NMP solution to eliminate surface contaminants. The sensitization and activation solutions are then prepared by mixing deionized water, HCl, $SnCl_2 \cdot 2H_2O$, and $PdCl_2$ according to the formulation listed in Table 1. The dispersed graphene is immersed in this mixed solution and subjected to ultrasonication for 0.5 h followed by magnetic stirring for 1 h. The resulting material is subjected to vacuum filtration and rinsed with deionized water to yield sensitized and activated graphene. Next, the plating solution is formulated based on the composition specified in Table 2, with a pH adjustment to 12.5 using NaOH. Sensitized and activated graphene are introduced into a pH-controlled plating solution and processed under constant-temperature magnetic stirring in a water bath. The final product is isolated through filtration, thoroughly washed with deionized water, and vacuum-dried at 60 °C for 4 h to obtain Cu@Gr. As revealed by the microstructure analysis in Figure 3, the modified Cu@Gr exhibits a continuous and conformal coating across the majority of graphene surfaces.

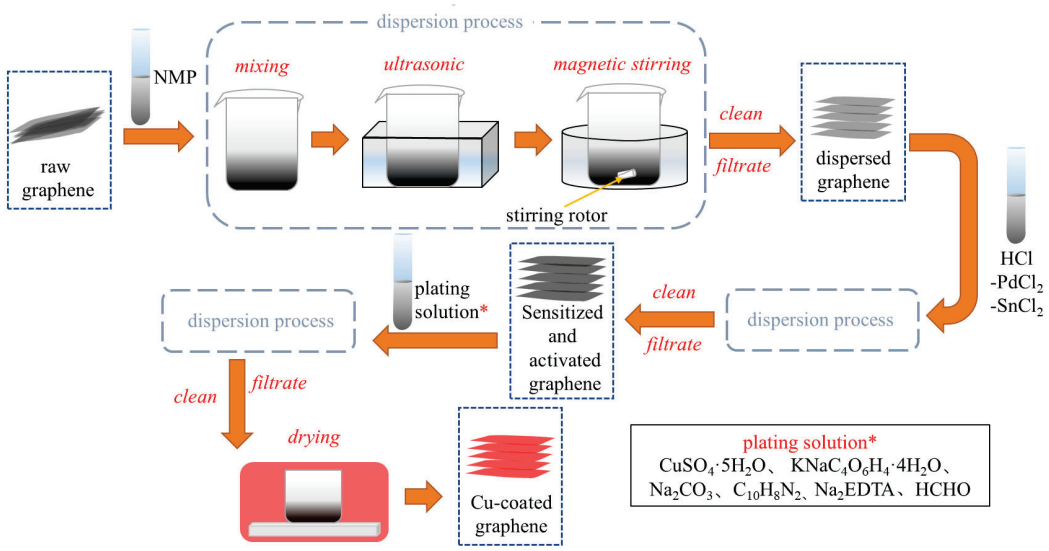


Figure 2. The schematic process of graphene surface modification [29].

Table 1. Formulation of Sensitization and Activation Solution.

Chemical Reagents	Content (g/L)
$SnCl_2 \cdot 2H_2O$	20.0
$PdCl_2$	0.5
HCl	71.4

Table 2. Formulation of electroless plating solution.

Chemical Reagents	Content (g/L)
$CuSO_4 \cdot 5H_2O$	10.0
Na_2CO_3	40.0
Na_2EDTA	20.0
$KNaC_4H_4O_6 \cdot 4H_2O$	40.0
$C_{10}H_8N_2$	4.0
HCHO	17.7

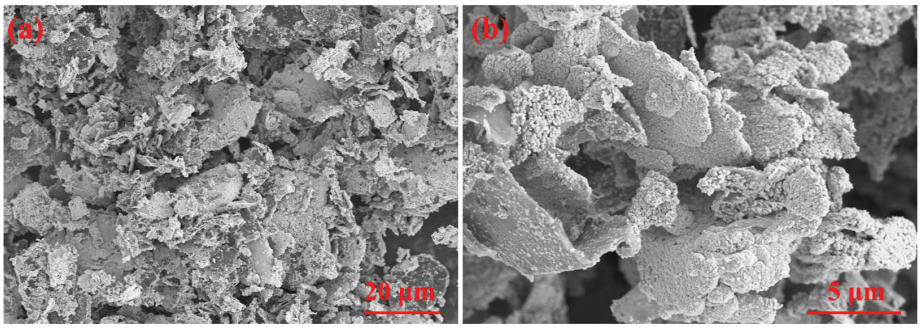


Figure 3. The microstructure of Cu@Gr: (**a**) 1000×, (**b**) 5000×.

2.3. Preparation of Cu@Gr-Reinforced W-Mo-Cu Composites

This study primarily investigated the 40 wt.% W-40 wt.% Mo-20 wt.% Cu system. W and Mo powders were weighed to 2 wt.% pre-added Cu powder to enhance melt infiltration during subsequent sintering. Separately, 0.2 wt.%, 0.4 wt.%, 0.6 wt.%, 0.8 wt.%, and 1.0 wt.% Cu@Gr powder was systematically introduced to the base mixture. The blended powders underwent mechanical alloying in a QM-BP planetary ball mill (ball-to-powder ratio of 3:1, Nanjing Nanda Instrument Co., Ltd., Nanjing, China) at 300 rpm for 3 h. The milled composite powder was then die-compacted using a DHM-YJB6 hydraulic press (Chengdu Dahua Hydraulic Machinery Factory, Chengdu, China) under 400 MPa uniaxial pressure with a 20 s dwell time, forming cylindrical green compacts (Ø13 mm × 11 mm height). The corresponding Cu compacts were pressed similarly for subsequent infiltration.

The W-Mo and Cu compacts were co-sintered in a ZT-40-21Y vacuum furnace (Shanghai Chenhua Science Technology Corp., Ltd., Shanghai, China) using a graphite crucible configuration, with the Cu block positioned above the compact. The furnace pressure was maintained below 2.2×10^{-2} Pa throughout the sintering process, as illustrated in Figure 4, which comprised four distinct phases: (1) rapid heating from ambient temperature to 1000 °C at 10 °C/min, (2) reduced-rate heating to 1300 °C at 6 °C/min, (3) 90-min isothermal holding at 1300 °C to complete Cu infiltration, and (4) furnace cooling to ambient temperature. Post-sintering, excess surface Cu was removed through mechanical machining to obtain the final composites.

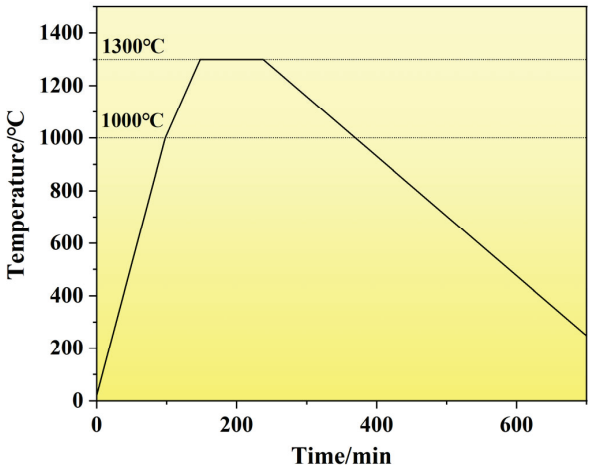


Figure 4. Sintering process of the infiltration sintering.

2.4. Testing and Characterization

After sintering, the phases of Cu@Gr/W-Mo-Cu were analyzed using X-ray diffraction (XRD). The diffraction peaks in the XRD images were identified using the MDI Jade 6.0 soft-

ware. The microstructures were examined using scanning electron microscopy (SEM). The elemental composition was analyzed using energy-dispersive X-ray spectroscopy (EDS). The density of the compact was measured using Archimedes' method. The electrical conductivity, thermal conductivity, and microhardness of the compacts were assessed at room temperature (25 ± 1 °C) using a portable eddy current conductivity meter (FD102, Xiamen Fosite Electronic Technology Co., Ltd., Xiamen, China), laser thermal conductivity meter (LFA 457, NETZSCH–Gerätebau GmbH, Selb, Germany), and digital microhardness tester (HVD-1000AP, Shanghai Jujing Precision Instrument Manufacturing Co., Ltd., Shanghai, China), respectively. All reported data represent the averages of at least five test results.

3. Results and Discussion

3.1. Influence of Cu@Gr Contents on the Microstructure and Properties of Cu@Gr/W-Mo-Cu Composites

3.1.1. Phases and Microstructures of W-Mo-Cu Composites with Different Cu@Gr Contents

Figure 5 shows the XRD patterns of the W-Mo-Cu composites with different Cu@Gr contents. The data indicate that the W-Mo-Cu composite without Cu@Gr primarily consists of W, Mo, and Cu phases. Given that W and Mo belong to the same group of elements, they can form solid solutions with one another in the phase diagram. Consequently, W-Mo solid solutions are expected to form in the composite produced by infiltration sintering. Cao et al. observed W-Mo solid solutions dispersed at the W-Mo interfaces in W-Mo-Cu composites prepared via infiltration sintering at 1500 °C for 4 h, as evidenced by TEM [7,14]. However, the XRD patterns reveal that the diffraction peaks of W and Mo are distinct, indicating that no significant solid solution effect is present. This observation can be attributed to the relatively short sintering duration of only 1.5 h, which restricts the diffusion distance of W and Mo atoms, resulting in a limited degree of solid solution formation between W and Mo. Furthermore, the addition of 0.4 wt.% Cu@Gr, a small quantity of molybdenum carbide, Mo_2C, begins to emerge in the W-Mo-Cu composite. As the Cu@Gr content increases, the intensity of the Mo_2C diffraction peaks gradually increases, although the overall intensity of these peaks remains relatively low. Carbides, being hard phases, can enhance dispersion strengthening when they are uniformly distributed within the composites. However, the comparatively low conductivity of carbides may negatively impact the electrical conductivity of W-Mo-Cu composites. Therefore, to achieve W-Mo-Cu composites with optimal overall performance, the addition of Cu@Gr must be carefully regulated.

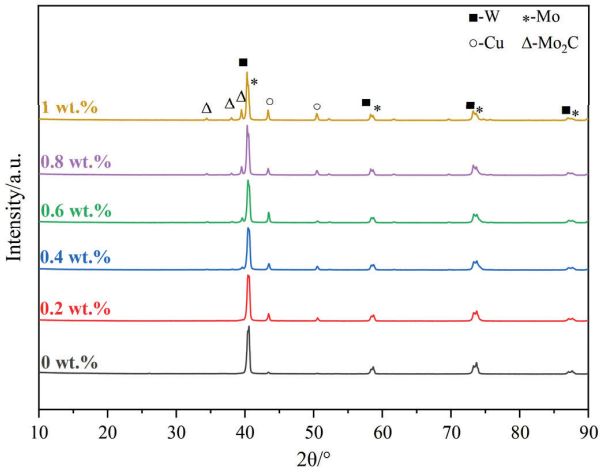


Figure 5. XRD patterns of W-Mo-Cu composites with different contents of Cu@Gr.

Figure 6 shows the SEM images of the infiltration-sintered Cu@Gr/W-Mo-Cu composites. EDS analysis of the 1 wt.% Cu@Gr-added W-Mo-Cu composite was conducted,

with results shown in Figure 7. EDS analysis reveals that the white areas in the SEM image correspond to the W phase, the light gray regions primarily represent the Mo phase, and the dark gray areas were attributed to the Cu phase. The W-Mo-Cu composite without Cu@Gr contains some circular pores of varying sizes, indicating insufficient infiltration of Cu into the W-Mo skeleton during processing, which resulted in incomplete filling of interparticle voids between W and Mo. Furthermore, the distribution of Cu is also not uniform, resulting in the formation of Cu melt pools. The addition of graphene leads to a gradual decrease in porosity and results in a more uniform microstructure, suggesting that graphene facilitates sintering densification. The addition of 0.2 wt.% graphene significantly enhances the density of the composite; however, minor pores remain, and a Cu melt pool is still present. Upon increasing the Cu@Gr addition to 0.4 wt.%, the microstructure of the composite material becomes notably denser and more uniform. The Cu melt pool no longer exists, and a uniform Cu network structure is formed. This improvement is attributed to the superior high-temperature wettability between graphene and Cu compared to that between W/Mo and Cu in the matrix [30,31]. The high wettability of graphene with Cu facilitates the flow of liquid Cu on the matrix surface contained with Cu@Gr. Although the direct wettability between Cu and W/Mo is limited, graphene serves as an intermediate layer, functioning as a "wetting bridge" that directs the liquid Cu to infiltrate the voids of the W-Mo skeleton along the graphene-covered pathway. Thus, Cu@Gr effectively contributes to sintering densification during infiltration.

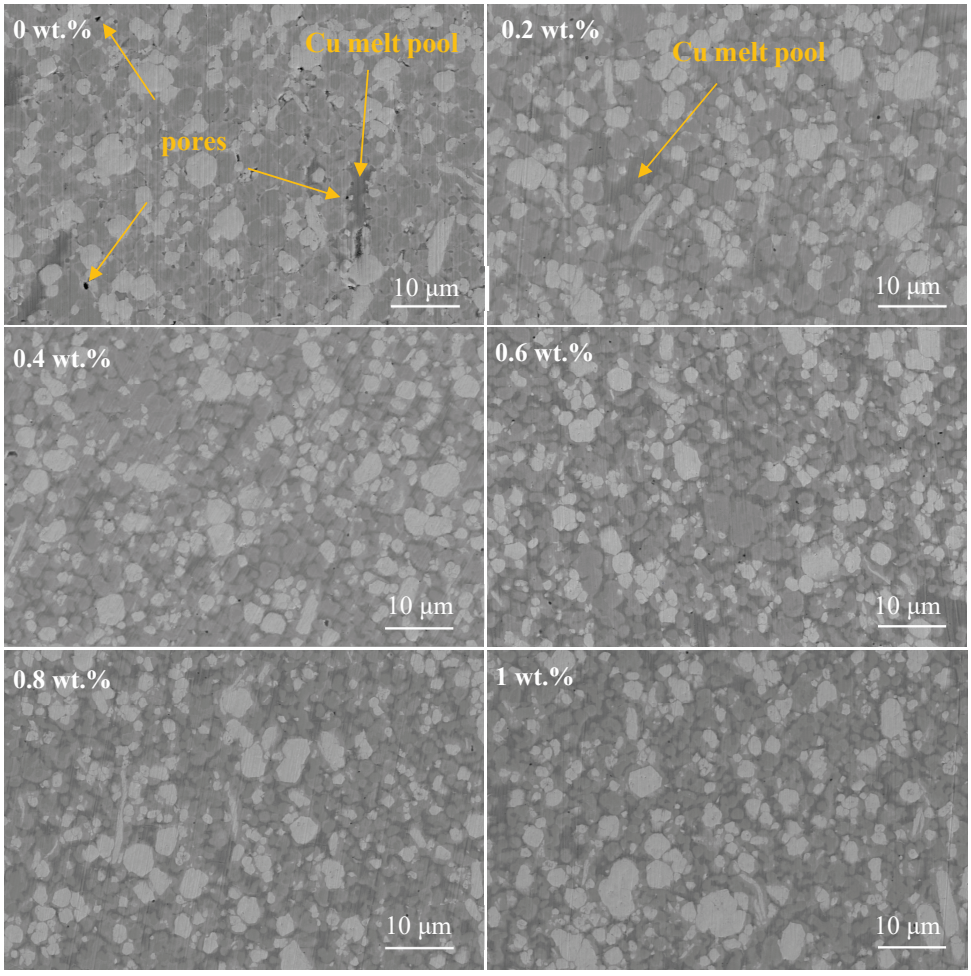


Figure 6. SEM images of W-Mo-Cu composites with different Cu@Gr contents.

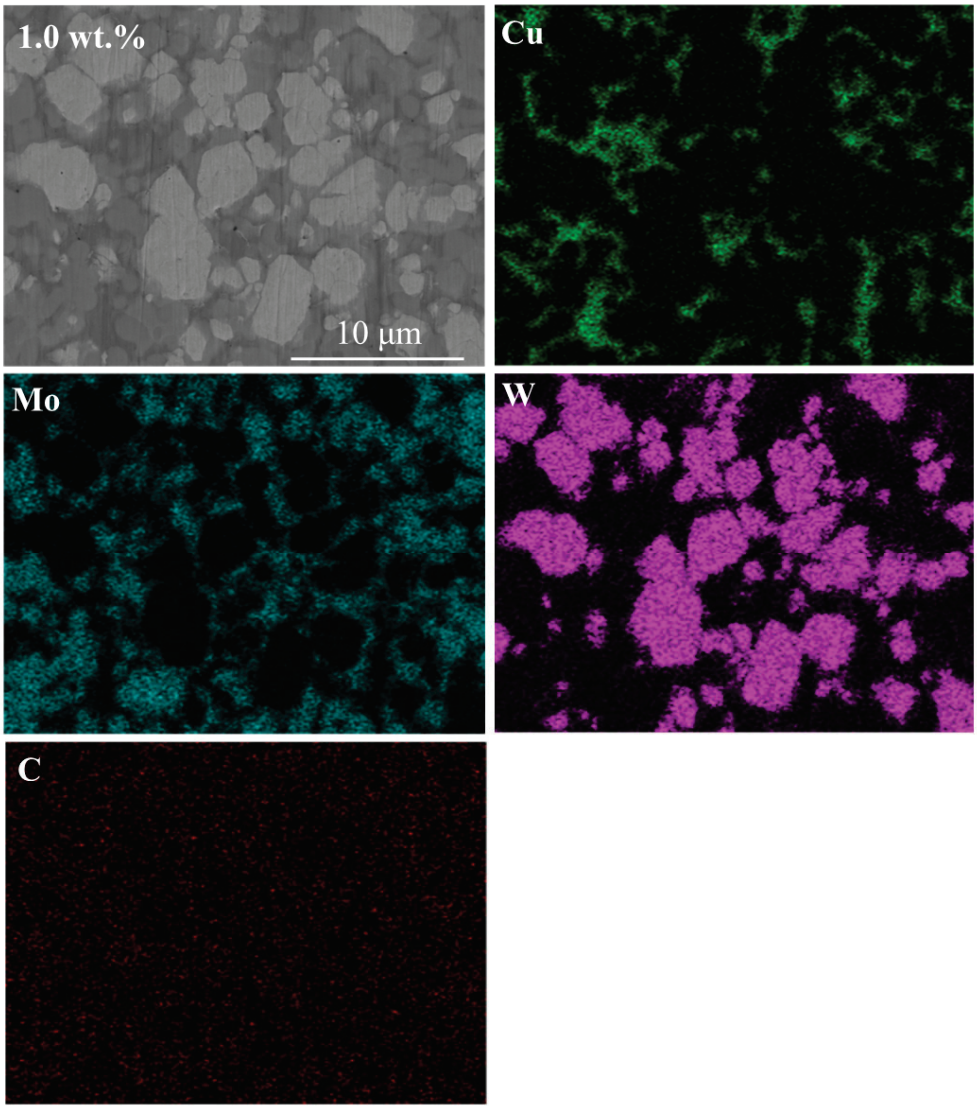


Figure 7. EDS analysis of the 1 wt.% Cu@Gr-added W-Mo-Cu composite.

From the element distribution in the EDS mapping, it can be observed that the distribution of each component is relatively uniform. The Mo phase serves as the matrix surrounding the W phase, while the Cu phase effectively fills the voids between the W and Mo phases, creating a uniform Cu network structure. However, the W phase exhibits slight particle coarsening, primarily due to the non-uniform particle size distribution of the raw W powder, which contains some larger particles. These larger particles hinder the rearrangement of particles during infiltration sintering, leading to the connection and coarsening of certain W phases [32]. Sintering necks are formed between the W, Mo, and Cu phases, tightly bonding them together and ultimately promoting the densification of the composites. Furthermore, the distribution of carbon is relatively uniform and not concentrated around the Mo phase, indicating that not all graphene has reacted to form carbides, and some free graphene still exists within the material.

3.1.2. Properties of W-Mo-Cu Composites with Different Cu@Gr Contents

Figure 8 illustrates the relative density of W-Mo-Cu composites with varying contents of Cu@Gr. The relative density of the composites significantly increases with the incorporation of Cu@Gr. This observation corresponds to the microstructural changes in the

W-Mo-Cu composites depicted in Figure 6, where the addition of Cu@Gr progressively reduces both the number and size of pores within the composites. Notably, when Cu@Gr was not added, the wettability between Cu and W and Mo was poor, and Cu failed to adequately infiltrate into the W-Mo skeleton. The filling effect of copper in the pores between the W and Mo particles was mediocre, resulting in the lowest relative density. When the Cu@Gr content increases from 0 wt.% to 0.4 wt.%, the densification rate of the composites improves considerably; however, further increases in Cu@Gr content do not yield significant changes in the material's densification, with values stabilizing around 98%. At this point, the densification of the composites improved by approximately 8% compared to that of the samples without Cu@Gr. In conclusion, the results indicate that Cu@Gr can effectively promote the sintering densification process of W-Mo-Cu composites during infiltration sintering, and a significant effect can be achieved when the Cu@Gr content reaches or exceeds 0.4 wt.%.

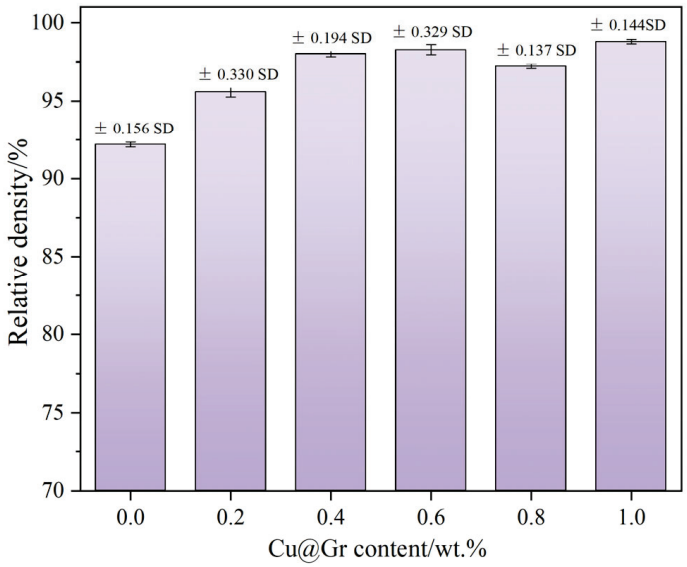


Figure 8. The relative density of W-Mo-Cu composites with varying contents of Cu@Gr.

Figure 9 shows the thermal conductivity, electrical conductivity, and Vickers hardness of W-Mo-Cu composites with varying Cu@Gr contents. As shown in the figure, both the thermal and electrical conductivities of the W-Mo-Cu composites are significantly enhanced, exhibiting similar trends as the Cu@Gr content increases. This is primarily attributed to the fact that the transfer of heat and electricity in metallic materials occurs mainly through the migration of free electrons. The presence of pores within the material can disrupt the continuity of the metal lattice, thereby increasing the resistance to the migration of free electrons. Therefore, the densification degree of the W-Mo-Cu composite is a crucial factor affecting its thermal and electrical conductivities. Furthermore, the thermal and electrical conductivities of W-Mo-Cu composites are influenced by the uniformity and structural integrity of the Cu network within the material, as the electrical and thermal conductivities of Cu are significantly higher than those of W and Mo [33,34]. Without the incorporation of Cu@Gr, Cu cannot sufficiently infiltrate the W-Mo skeleton, leading to a relatively low composite density and an incomplete and non-uniform Cu network, which adversely affects both the electrical and thermal conductivities. Conversely, the addition of Cu@Gr not only significantly enhances the composite's density but also facilitates the formation of a more complete and uniform Cu network. Consequently, as the amount of

Cu@Gr increases, the thermal and electrical conductivities of the W-Mo-Cu composites progressively improve.

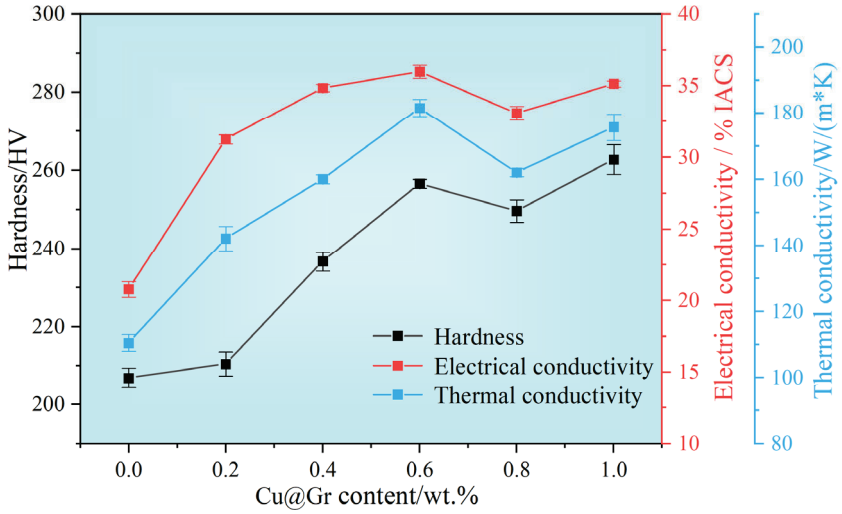


Figure 9. Thermal conductivity, electrical conductivity, and Vickers hardness of W-Mo-Cu composites with different contents of Cu@Gr.

Specifically, the W-Mo-Cu composite without Cu@Gr exhibits thermal and electrical conductivities of 110.61 $W \cdot m^{-1} \cdot K^{-1}$ and 20.81 %IACS, respectively. At a 0.6 wt.% addition of Cu@Gr, these values achieve the highest to 181.54 $W \cdot m^{-1} \cdot K^{-1}$ and 35.99 %IACS, reflecting approximate increases of 64% and 73% compared to the sample without any addition. However, when the Cu@Gr content exceeded 0.6 wt.%, the quantity of carbide produced during the sintering process rose, resulting in a gradual decline in both the thermal and electrical conductivities of the composite. Especially when the addition of Cu@Gr is 0.8 wt.%, the relative density of the composite decreases, resulting in a significant reduction in both the electrical and thermal conductivities of the composite at this composition. Nevertheless, due to the relatively low total content of carbides, this decrease remains relatively small.

Additionally, the hardness of the W-Mo-Cu composites gradually increases with the Cu@Gr contents. In graphene-reinforced composites, graphene serves as an efficient stress-transfer bridge. When a material is subjected to external loads, graphene can absorb and transfer a portion of the load, thereby mitigating the stress concentration within the metal matrix and enhancing the overall load-bearing capacity of the material, thus improving its strength [35,36]. Furthermore, the microstructure of the material is a critical factor influencing the hardness of the W-Mo-Cu composite. A higher relative density and fewer internal pores are conducive to an increase in material hardness. Moreover, the carbides formed during sintering can act as reinforcing phases, providing dispersion strengthening to the material. This reaction also promotes the formation of a strong interfacial bond between graphene and the W phase, effectively facilitating load transfer. Therefore, without the addition of Cu@Gr, the Vickers hardness of the material is 206.87 HV. As the Cu@Gr content in the composite increases to 0.6 wt.%, the hardness significantly improves, reaching 256.57 HV, which represents a 24% increase compared to the absence of Cu@Gr. However, as the Cu@Gr content continues to increase, the change in material hardness becomes marginal, with a slight decrease due to the reduction in the relative density of the composite at a Cu@Gr content of 0.8 wt. % and with a maximum hardness of 262.7 HV achieved at a Cu@Gr content of 1 wt.%.

In conclusion, the addition of 0.6 wt.% Cu@Gr results in the W-Mo-Cu composite exhibiting a higher degree of densification, a highly uniform microstructure, and optimal electrical and thermal conductivities, thereby establishing it as the optimal addition.

3.2. Influence of W-Mo Green Compact Relative Density on the Microstructure and Properties of Cu@Gr/W-Mo-Cu Composites

3.2.1. Phases and Microstructures of W-Mo-Cu Composites with Varying Relative Densities of W-Mo Green Compacts

Given that the relative density of the W-Mo green compact significantly influences the microstructure and properties of the composite fabricated via infiltration sintering, this section maintains a constant Cu@Gr addition of 0.6 wt. % in W-Mo-Cu composites and investigates the effect of the relative density of W-Mo green compact on the microstructure and properties of the composites.

Figure 10 shows the XRD patterns of W-Mo-Cu composites with varying relative densities of W-Mo green compacts. As shown, the phase composition of the W-Mo-Cu composites remains unchanged with variations in the relative density, consisting of the W, Mo, Cu, and Mo_2C phases. The peaks corresponding to the Mo_2C phase remain largely consistent, suggesting that the relative density of the W-Mo green compact had a minimal impact on both the phase composition and carbide formation reaction within the composites.

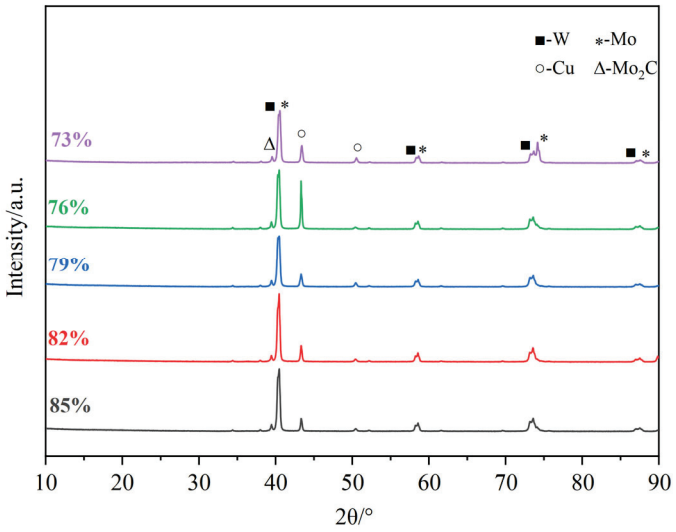


Figure 10. XRD patterns of W-Mo-Cu composites with varying relative densities of W-Mo green compacts.

Figure 11 shows the SEM images of W-Mo-Cu composites with varying relative densities of W-Mo green compacts. As shown, the five groups of samples exhibit relatively uniform and dense structures, with the Cu phase well infiltrating the skeleton. Furthermore, as the relative density of the W-Mo green compacts decreases, the dark gray Cu phase gradually increases. The variation in the relative densities of the W-Mo green compacts does not influence the promoting effect of Cu@Gr on the densification of the composites. Generally, a higher relative density of the W-Mo green compacts correlates with reduced porosity and pore size, which results in a greater capillary force exerted on the Cu melt during sintering, thereby enhancing its infiltration capability. Conversely, the presence of larger pores in the matrix at lower green compact densities can impede the flow and infiltration of the Cu melt. In this study, due to the favorable wettability between graphene

and Cu at elevated temperatures, the densification of the composite remained unaffected by the decrease in the relative density of the W-Mo green compact. Instead, as the porosity of the green compact increased, the volume of Cu that could infiltrate also increased. The greater the amount of liquid Cu, the more it facilitated the rearrangement and redistribution of W-Mo particles, thereby promoting the sintering densification of the composite [37].

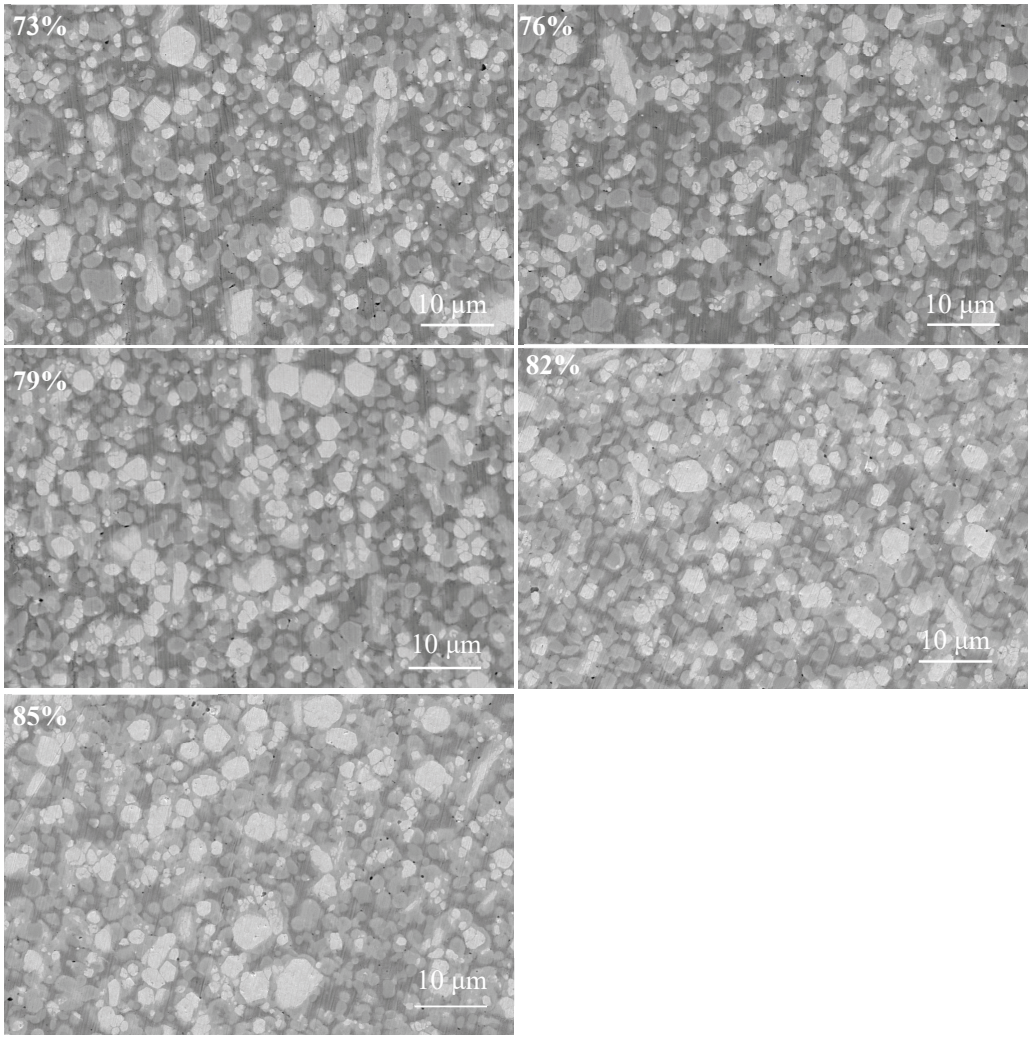


Figure 11. SEM images of W-Mo-Cu composites with varying relative densities of W-Mo green compacts.

3.2.2. Properties of W-Mo-Cu Composites with Varying Relative Densities of W-Mo Green Compacts

Figure 12 illustrates the relative density of W-Mo-Cu composites with varying relative densities of the W-Mo green compacts. It is evident that as the relative density of the W-Mo green compacts decreases, the relative density of the composites gradually increases, reaching a maximum value of 99.2% when the relative density of the green compacts is 73%. Analysis of the SEM images of the W-Mo-Cu composites presented in Figure 11 shows that, despite variations in the relative density of the W-Mo green compacts, the samples consistently exhibit a high degree of densification with minimal differences. Thus, a lower relative density of the W-Mo green compact correlates with a greater variation in the densification of the composites. Specifically, when the relative density of the green compact is 73%, the final density of the sample increases by 35.9%, while at a relative density of 85%,

the final density increases by 15.3%. This indicates that the relative density of the W-Mo green compact significantly influences the densification process of the composite material.

The influence of the relative density of the W-Mo green compacts on the thermal conductivity, electrical conductivity, and Vickers hardness of the W-Mo-Cu composites is illustrated in Figure 13. As shown in the figure, as the relative density of W-Mo green compacts decreases, the thermal and electrical conductivities of the composites gradually increase, reaching maximum values of 203.6 $W \cdot m^{-1} \cdot K^{-1}$ and 44.84 %IACS, respectively, at a relative density of 73%. The minimum values, observed at a relative density of 85%, are 171.36 $W \cdot m^{-1} \cdot K^{-1}$ and 29.87 %IACS, respectively. The relative density of the W-Mo green bodies significantly impacts the thermal and electrical conductivities of the composites. Given that the Cu@Gr content remains constant, the amount of carbides generated during the sintering process is essentially identical, leading to similar effects on the thermal and electrical conductivities of the composites. Therefore, this variation is primarily related to changes in Cu content within the W-Mo-Cu composites. When the relative density of the W-Mo green compact is lower, the Cu content in the composite material is higher, resulting in a complete Cu network structure that facilitates free electron transfer.

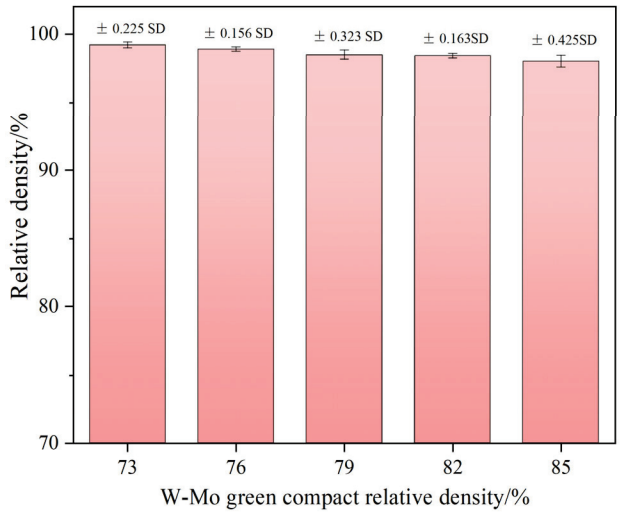


Figure 12. The relative density of W-Mo-Cu composites with varying relative densities of W-Mo green compacts.

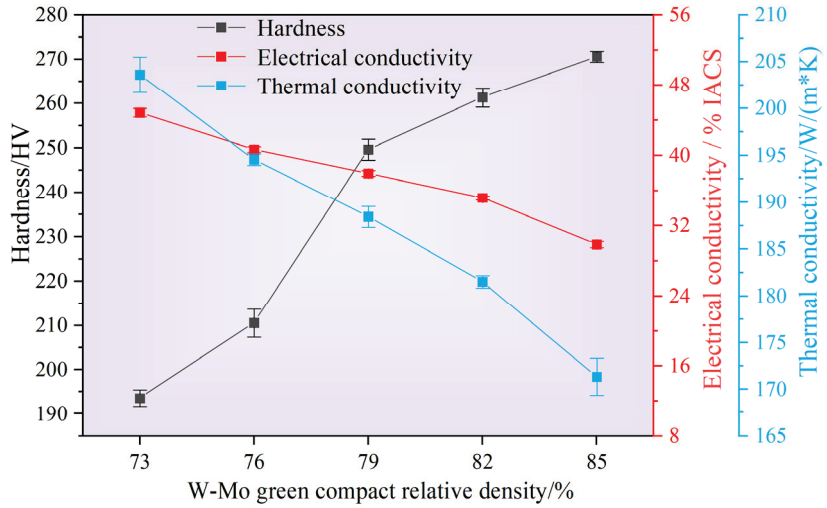


Figure 13. Thermal conductivity, electrical conductivity, and Vickers hardness of W-Mo-Cu composites with varying relative densities of W-Mo green compacts.

The variation in the hardness of the W-Mo-Cu composite primarily exhibits a gradual increase with an increase in the relative density of the W-Mo green compact. The minimum hardness value of 193.6 HV is observed when the relative density of the W-Mo green compact is 73%, while the maximum value of 270.56 HV is achieved at 85%. This result is primarily related to changes in Cu content within the composite material. In the W-Mo-Cu composite, the W and Mo phases possess higher hardness, whereas the Cu phase exhibits lower hardness. As the density of the W-Mo green compact gradually decreases, the composites maintain relative density within a narrow range (98.03–99.20%); however, the content of the W and Mo phases in the composite material diminishes, leading to an increase in the Cu phase content. This shift results in a downward trend in the hardness of the composite material.

In summary, the relative density of W-Mo green compacts significantly influences the densification changes of W-Mo-Cu composites both before and after sintering. Notably, the relative density of the composites remains consistently high across various relative densities of W-Mo green bodies. Furthermore, the relative density of W-Mo green compacts substantially impacts the thermal conductivity, electrical conductivity, and hardness of the composites. As the relative density of W-Mo green bodies increases, the thermal and electrical conductivities of the composites gradually decrease while their hardness increases. In practical applications, it is essential to select an appropriate relative density of W-Mo green bodies based on the specific working conditions. If higher electrical conductivity is required and strength is not a primary concern, a relatively low green compact density may be chosen; conversely, if higher strength is necessary, a relatively high green compact density should be selected.

4. Conclusions

In this study, Cu@Gr/W-Mo-Cu composites were fabricated through vacuum infiltration sintering at 1300 °C with a holding time of 1.5 h. The effects of Cu@Gr content (ranging from 0.2 wt.% to 1.0 wt.%) and the relative density of the W-Mo green compact (from 73% to 85%, in 3% increments) on the microstructure and properties were investigated, yielding the following findings:

(1) Without Cu@Gr, the composite contains W, Mo, and Cu phases. Upon adding 0.4 wt.% Cu@Gr, a small amount of Mo_2C emerges, and its content increases with rising Cu@Gr content. Furthermore, the addition of Cu@Gr significantly enhances densification, reduces pores, enables uniform component distribution, and forms a Cu network between W and Mo. Moreover, composites can still maintain high densification when the Cu@Gr content exceeds 0.4 wt.%.

(2) The addition of Cu@Gr substantially improves the properties of the W-Mo-Cu composites. As the Cu@Gr content increases, both thermal and electrical conductivities and hardness significantly improve. The thermal and electrical conductivities peak at a 0.6 wt.% addition, exhibiting increases of approximately 64% and 73%, respectively, compared to the non-added case. Hardness reaches its maximum at 1 wt.%, showing a roughly 25% increase relative to the non-added state.

(3) Variations in the relative density of the W-Mo green compact have minimal effect on the phases of the composite and do not hinder the pivotal role of Cu@Gr in promoting sintering densification; composites prepared under varying relative densities remain highly dense. However, this parameter significantly influences the properties of the composite. As the relative density of the W-Mo green compact increases, the thermal and electrical conductivities of the composite decrease while its hardness increases.

Author Contributions: J.C.: conceived the project, designed the experiment, and wrote the manuscript. Q.J.: helped in improving the figures and helped in improving the manuscript. K.F.: discussed the results, analyzed the data and helped in improving the manuscript. H.Z.: analyzed the data and helped in improving the manuscript. All authors have read and agreed to the published version of the manuscript.

Funding: This research was funded by the National Natural Science Foundation of China (Grant No. 51674171 and No. 52304380), the Natural Science Foundation Project of Chongqing (Grant No. CSTB2022NSCQ-MSX1496), and the Special Grant for Chongqing Postdoctoral Research Project (Grant No. 2022CQBSHTB3073).

Institutional Review Board Statement: Not applicable.

Informed Consent Statement: Not applicable.

Data Availability Statement: The original contributions presented in the study are included in the article, further inquiries can be directed to the corresponding author.

Acknowledgments: The authors gratefully acknowledge the financial support from the National Natural Science Foundation of China (Grant No. 51674171 and No. 52304380), the Natural Science Foundation Project of Chongqing (Grant No. CSTB2022NSCQ-MSX1496), and the Special Grant for Chongqing Postdoctoral Research Project (Grant No. 2022CQBSHTB3073).

Conflicts of Interest: The authors declare that they have no known competing financial interests or personal relationships that could have appeared to influence the work reported in this paper.

References

1. Sun, G.; Wang, K.; Song, C.; Zhang, G. A low-cost, efficient, and industrially feasible pathway for large scale preparation of tungsten nanopowders. *Int. J. Refract. Met. Hard Mater.* **2019**, *78*, 100–106. [CrossRef]
2. Zhang, H.; Zhang, G. Influence of Ti addition on the microstructure and comprehensive properties of Mo–Cu alloy. *J. Mater. Res. Technol.* **2024**, *30*, 2833–2847. [CrossRef]
3. Cao, L.; Hou, C.; Tang, F.; Liang, S.; Luan, J.; Jiao, Z.; Liu, C.; Song, X.; Nie, Z. Thermal stability and high-temperature mechanical performance of nanostructured W–Cu–Cr–ZrC composite. *Compos. Part B Eng.* **2021**, *208*, 108600. [CrossRef]
4. Guo, W.; Wang, Y.; Liu, K.; Li, S.; Zhang, H. Effect of copper content on the dynamic compressive properties of fine-grained tungsten copper alloys. *Mater. Sci. Eng. A* **2018**, *727*, 140–147. [CrossRef]
5. Zhou, H.; Feng, K.; Liu, Y. Densification, microstructure, and properties of W-Mo-Cu alloys prepared with nano-sized Cu powders via large electric current sintering. *Adv. Powder Technol.* **2022**, *33*, 103703. [CrossRef]
6. Liu, Y.; Feng, K.; Zhou, H.; Chen, S. Microstructure and phases investigations of W-Mo-Cu alloy prepared by large current electric field sintering. *Intermetallics* **2022**, *143*, 107488. [CrossRef]
7. Cao, J.; Liu, J.; Liu, X.; Li, S.; Xue, X. Effect of the distribution state of transition phase on the mechanical properties and failure mechanisms of W-Mo-Cu alloy by tuning elements content. *J. Alloys Compd.* **2020**, *827*, 154333. [CrossRef]
8. Deng, N.; Zhou, Z.; Li, J.; Wu, Y. W–Cu composites with homogenous Cu–network structure prepared by spark plasma sintering using core–shell powders. *Int. J. Refract. Met. Hard Mater.* **2019**, *82*, 310–316. [CrossRef]
9. Li, B.; Jin, H.; Ding, F.; Bai, L.; Yuan, F. Fabrication of homogeneous Mo-Cu composites using spherical molybdenum powders prepared by thermal plasma spheroidization process. *Int. J. Refract. Met. Hard Mater.* **2018**, *73*, 13–21. [CrossRef]
10. Ke, S.; Feng, K.; Zhou, H.; Shui, Y. Phase evolution of Mo-W-Cu alloy rapid prepared by spark plasma sintering. *J. Alloys Compd.* **2019**, *775*, 784–789. [CrossRef]
11. Zhou, H.; Feng, K.; Ke, S.; Liu, Y. Study on the microwave sintering of the novel Mo-W-Cu alloys. *J. Alloys Compd.* **2021**, *881*, 160584. [CrossRef]
12. Li, B.; Chen, Z.; Zhang, Q.; Hu, X.; Kang, W.; Ding, Y.; Liang, S. Preparation and properties of W-Mo-Cu composite using solution combustion synthesized W-Mo solid solution nanopowder. *Int. J. Refract. Met. Hard Mater.* **2023**, *111*, 106064. [CrossRef]
13. Zhou, H.; Feng, K.; Liu, Y. Effects of electro-thermal cycles on the densification and properties of W-Mo-Cu alloys prepared via large current electric field sintering. *Mater. Chem. Phys.* **2022**, *281*, 125887. [CrossRef]
14. Cao, J.; Liu, J.; He, C.; Li, S.; Hao, Z.; Xue, X. Enhanced ductility of W-Mo-Cu alloy through the formation of nanometer-to-micrometer-thick dual-phase transition phase layer. *Mater. Des.* **2019**, *164*, 107536. [CrossRef]

15. Wang, X.; Song, K.; Feng, J.; Xing, J.; Huang, T.; Zhang, Y. Microstructure and mechanical properties of WMoCu alloy doped with different sized Mo particles. *Int. J. Refract. Met. Hard Mater.* **2024**, *119*, 106565. [CrossRef]
16. Ahangarkani, M.; Borji, S.; Abbaszadeh, H.; Rahmani, A.A.; Zangeneh-madar, K. The effect of additive and sintering mechanism on the microstructural characteristics of W-40Cu composites. *Int. J. Refract. Met. Hard Mater.* **2012**, *32*, 39–44. [CrossRef]
17. Zhou, X.; Dong, Y.; Hua, X.; Din, R.U.; Ye, Z. Effect of Fe on the sintering and thermal properties of Mo-Cu composites. *Mater. Des.* **2010**, *31*, 1603–1606. [CrossRef]
18. Hamidi, A.G.; Arabi, H.; Rastegari, S. Tungsten-copper composite production by activated sintering and infiltration. *Int. J. Refract. Met. Hard Mater.* **2011**, *29*, 538–541. [CrossRef]
19. Cai, J.; Feng, K.; Liu, Y. Studies towards activation of cobalt in W-Mo-Cu alloy sintered via large current electric field. *Int. J. Refract. Met. Hard Mater.* **2023**, *117*, 106406. [CrossRef]
20. Hu, Z.; Wu, Z.; Luo, S.; Wang, X.; Nian, Q.; Chen, Y.; Nagaumi, H. Large scale production of graphene aluminum composites by stir casting: Process, microstructure and properties. *J. Mater. Res. Technol.* **2023**, *27*, 681–691. [CrossRef]
21. Zhao, Z.; Zhao, R.; Bai, P.; Du, W.; Guan, R.; Tie, D.; Naik, N.; Huang, M.; Guo, Z. AZ91 alloy nanocomposites reinforced with Mg-coated graphene: Phases distribution, interfacial microstructure, and property analysis. *J. Alloys Compd.* **2022**, *902*, 163484. [CrossRef]
22. Chen, F.; Mei, Q.; Li, J.; Li, C.; Wan, L.; Zhang, G.; Mei, X.; Chen, Z.; Xu, T.; Wang, Y. Fabrication of graphene/copper nanocomposites via in-situ delamination of graphite in copper by accumulative roll-compositing. *Compos. Part B Eng.* **2021**, *216*, 108850. [CrossRef]
23. Zhao, R.; Pei, J.; Du, W.; Zhao, Z.; Zhang, L.; Gao, J.; Bai, P.; Tie, D. Fabrication of magnesium-coated graphene and its effect on the microstructure of reinforced AZ91 magnesium-matrix composites. *Adv. Compos. Hybrid Mater.* **2022**, *5*, 504–512. [CrossRef]
24. Du, X.; Du, W.; Wang, Z.; Liu, K.; Li, S. Ultra-high strengthening efficiency of graphene nanoplatelets reinforced magnesium matrix composites. *Mater. Sci. Eng. A* **2018**, *711*, 633–642. [CrossRef]
25. Bartolucci, S.F.; Paras, J.; Rafiee, M.A.; Rafiee, J.; Lee, S.; Kapoor, D.; Koratkar, N. Graphene–aluminum nanocomposites. *Mater. Sci. Eng. A* **2011**, *528*, 7933–7937. [CrossRef]
26. Wu, P.; Liu, R.; Li, W.; Zhang, W.; Wei, J.; Zhou, Q.; Wei, T.; Kardani, A.; Lin, Z.; Xiao, Y.; et al. Interface optimization by introducing Ti for strengthening graphene network/copper composites: New insight from MD simulations. *Carbon* **2025**, *236*, 120109. [CrossRef]
27. Zhang, D.; Zhan, Z. Preparation of graphene nanoplatelets-copper composites by a modified semi-powder method and their mechanical properties. *J. Alloys Compd.* **2016**, *658*, 663–671. [CrossRef]
28. Peng, Q.; Tan, X.; Venkataraman, M.; Militky, J.; Xiong, W.; Mahendran, A.R.; Lammer, H.; Kejzlar, P. Effects of ultrasonic-assisted nickel pretreatment method on electroless copper plating over graphene. *Sci. Rep.* **2022**, *12*, 21159. [CrossRef]
29. Cai, J.; Liu, Y.; Chen, S.; Feng, K. Effect of Surface-Modified Graphene Addition on In Situ Synthesized Iron-Based Friction Materials. *J. Mater. Eng. Perform.* **2025**, *34*, 2083–2092. [CrossRef]
30. Rafiee, J.; Mi, X.; Gullapalli, H.; Thomas, A.V.; Yavari, F.; Shi, Y.; Ajayan, P.M.; Koratkar, N.A. Wetting transparency of graphene. *Nat. Mater.* **2012**, *11*, 217–222. [CrossRef]
31. Dong, L.; Chen, W.; Zheng, C.; Deng, N. Microstructure and properties characterization of tungsten–copper composite materials doped with graphene. *J. Alloys Compd.* **2017**, *695*, 1637–1646. [CrossRef]
32. Peng, K.; Pan, H.; Zheng, Z.; Yu, J. Compaction behavior and densification mechanisms of Cu-W composite powders. *Powder Technol.* **2021**, *382*, 478–490. [CrossRef]
33. Liu, D.; Meng, L.; Zou, J.; Luo, L.; Wu, Y. Microstructure and properties of silver-added W-Cu prepared by infiltration sintering. *Int. J. Refract. Met. Hard Mater.* **2022**, *108*, 105947. [CrossRef]
34. Chen, P.; Luo, G.; Shen, Q.; Li, M.; Zhang, L. Thermal and electrical properties of W–Cu composite produced by activated sintering. *Mater. Des.* **2013**, *46*, 101–105. [CrossRef]
35. Khanna, V.; Kumar, V.; Bansal, S.A. Mechanical properties of aluminium-graphene/carbon nanotubes (CNTs) metal matrix composites: Advancement, opportunities and perspective. *Mater. Res. Bull.* **2021**, *138*, 111224. [CrossRef]
36. Ghodrati, H.; Ghomashchi, R. Effect of graphene dispersion and interfacial bonding on the mechanical properties of metal matrix composites: An overview. *FlatChem* **2019**, *16*, 100113. [CrossRef]
37. Johnson, J.L.; Brezovsky, J.J.; German, R.M. Effects of tungsten particle size and copper content on densification of liquid-phase-sintered W-Cu. *Metall. Mater. Trans. A* **2005**, *36*, 2807–2814. [CrossRef]

Disclaimer/Publisher's Note: The statements, opinions and data contained in all publications are solely those of the individual author(s) and contributor(s) and not of MDPI and/or the editor(s). MDPI and/or the editor(s) disclaim responsibility for any injury to people or property resulting from any ideas, methods, instructions or products referred to in the content.

materials

MDPI

Article

A Study on Thermally Fatigued Phase Transformation and Bending Fracture Mechanisms of 310S Stainless Steel

Ying-Ting Huang, Yu-Wei Yen and Fei-Yi Hung *

Department of Materials Science and Engineering, National Cheng Kung University, Tainan 701401, Taiwan
* Correspondence: fyhung@mail.ncku.edu.tw

Abstract: This study investigates the microstructural evolution and mechanical degradation mechanisms of cold-drawn 310S stainless steel subjected to repeated thermal cycling between 900 °C and room temperature. The results reveal that thermal cycling induces significant lattice distortion, dislocation accumulation, and recrystallization, leading to grain refinement and increased tensile strength. However, these microstructural changes also initiate subsurface cracks and reduce ductility. TGA analysis confirms thermal weight loss from decarburization, especially under oxidative atmospheres. EPMA analysis and tensile tests after thermal cycling reveal that surface cracks formed during thermal cycling act as origins for transgranular crack propagation under tensile stress, significantly reducing fracture resistance. Bending fatigue tests further demonstrate that thermally fatigued specimens exhibit inferior fatigue life compared to raw material, confirming the deteriorating mechanical properties of 310S stainless steel after thermal cycling. Overall, the combined effects of thermal and mechanical fatigue degrade the structural integrity of 310S stainless steel, revealing that lattice distortion and subsurface cracking are the key factors in its embrittlement and reduced fatigue performance.

Keywords: 310S; thermal cycling; tensile properties; bending; TEM

1. Introduction

Austenitic stainless steels with high Ni and Cr content are the 310S stainless steels in the American Iron and Steel Institute (AISI) nomenclature system. Such composition makes 310S stainless steel a heat-resistant type of stainless steel. It is mainly used in high-temperature environments, possesses excellent mechanical properties, and shows high resistance to oxidation and corrosion [1,2]. Therefore, it is widely applied in furnace tubes or conveyor belts in heat treatment equipment, reaction furnaces or distillers in the chemical industry, gas boilers and flue systems in power engineering, and ovens in the food processing industry [3–5].

Despite its widespread application, the performance of 310S stainless steel in high-temperature environments is significantly influenced by precipitation behavior. In particular, the formation of Cr-rich σ phase and M23C6 carbides at temperatures ranging from 500 °C to 950 °C can lead to embrittlement and reduced corrosion resistance. Studies suggest that the formation of M23C6 carbides facilitates σ phase precipitation, which compromises the mechanical integrity and service life of stainless steel [6,7]. Previous research has investigated these mechanisms using traditional prolonged isothermal or cyclic aging methods, focusing on the impact of various precipitates on the mechanical properties of 310S stainless steel in high-temperature environments.

Another reason for deterioration is the formation of surface substances under various circumstances [8]. Research in this area explores the behavior of austenitic stainless steel under various environmental conditions, including atmospheric conditions, moisture-rich environments, and extreme settings such as supercritical water or supercritical carbon dioxide. Recent studies have shown that high-temperature oxidation and complex corrosive atmospheres can significantly alter the surface composition and structure of 310S stainless steel, leading to selective oxidation and volatile oxide formation [9,10]. These studies focus on the formation of surface substances, including metal oxides, and their mechanisms, aiming to simulate real-world operational scenarios of 310S stainless steel. By correlating surface elemental analyses with the formation of these substances, the studies provide insights into the consumption of key elements from the parent material and its subsequent impact on the deterioration of 310S stainless steel.

For 3XX stainless steels, reliability assessment mainly relies on the extent of loss in their ductility, as indicated by previous studies [11–13]. Under cold working conditions, 310S stainless steel initiates slip systems within the matrix when subjected to an instantaneous external stress, leading to partial lattice shear within the matrix and the formation of twin boundaries in grains. Additionally, these shear behaviors can result in stress-induced martensitic phase transformation, leading to the phenomenon of embrittlement in the mechanical properties of 3XX stainless steels [14,15]. Researchers also focus on changes in microstructure and mechanical properties caused by cold working or investigate the deterioration mechanism of 310S stainless steel through mechanical fatigue. A typical research direction involves utilizing the classic Griffith Law to evaluate the empirical formula for the crack propagation rate under stress in materials and defining the crack propagation rate of stainless steel to assess its service life under different mechanical operating environments [16]. The aforementioned research can simulate the performance of stainless steel in various applications and establish the deterioration mechanism of 310S stainless steel.

Beyond cold work-induced degradation, differences in thermal stability among stainless steels are also critical for understanding material performance under service conditions. Recent studies across various stainless steel grades further emphasize how different heat treatments influence their microstructural evolution and mechanical reliability. Martensitic stainless steels, such as AISI 4140, are typically strengthened through quenching and tempering. However, they tend to exhibit progressive softening under cyclic loading due to the instability of the fine martensitic microstructure [17]. Similarly, the performance of duplex stainless steels is highly sensitive to thermal treatment parameters [18,19]. Insufficient control of heat treatment parameters may lead to the precipitation of brittle intermetallic phases, thereby compromising both toughness and corrosion resistance. In contrast, 310S stainless steel, due to its high Cr and Ni content, exhibits greater thermal stability and retains a single-phase austenitic structure even after thermal cycling.

In high-temperature applications, stainless steel conveyor belts, particularly those made of 310S stainless steel, are widely used due to their excellent mechanical properties and corrosion resistance. However, 310S stainless steel is susceptible to embrittlement and damage when exposed to elevated temperatures [20], especially in environments involving repeated bending and thermal cycling. Among these, bending and fixed strain tensile tests are critical in evaluating its performance under operational conditions. Bending tests simulate the cyclic stress encountered during conveyor operation, while fixed strain tensile tests provide insights into the material's behavior under constant strain at high temperatures, helping to reveal crack initiation and propagation mechanisms.

Although previous studies have extensively examined the high-temperature characteristics of stainless steel, research focusing on short holding times and thermal cycling applications remains limited [21,22]. This study provides a unique perspective by investigating the effect of short-term thermal cycling on crack propagation under subsequent tensile tests and bending fatigue tests [23–26]. By integrating thermogravimetric analysis, subsurface EPMA mapping, and TEM-based lattice distortion characterization, this work provides a more comprehensive understanding of the deterioration mechanisms relevant to thermal cyclic environments commonly encountered in industrial applications such as high-temperature conveyor belts.

2. Experimental Procedures

In this study, 310S stainless steel wires with a diameter of 2 mm were selected as raw materials, labeled as RM. The chemical composition of this material is provided in Table 1 (Walsin Lihwa Co., Ltd., Taipei, Taiwan). The thermal fatigue specimens were prepared using a thermal fatigue test machine (CGTH8-L10-400-BR, TOYO, Tokyo, Japan), depicted in Figure 1, following the conditions: 900 °C (holding for 1 min), air-cooled to room temperature (holding for 1 min), repeated for 100 cycles, and the specimen was denoted as C100. The telescopic rod of the test machine allows for controlling the rate at which specimens enter and exit the high-temperature environment. A thermal gravimetric analyzer (Discovery TGA 55, TA Instruments, New Castle, DE, USA) under different atmospheres was used to investigate possible reasons for the mass loss of stainless steel and short-term oxidation behavior.

Table 1. Chemical composition of the as-received AISI 310S stainless steel (wt.%).

C	Cr	Ni	Mn	Si	P	S	Fe
0.080	25.000	21.000	2.000	1.500	0.045	0.030	Bal.

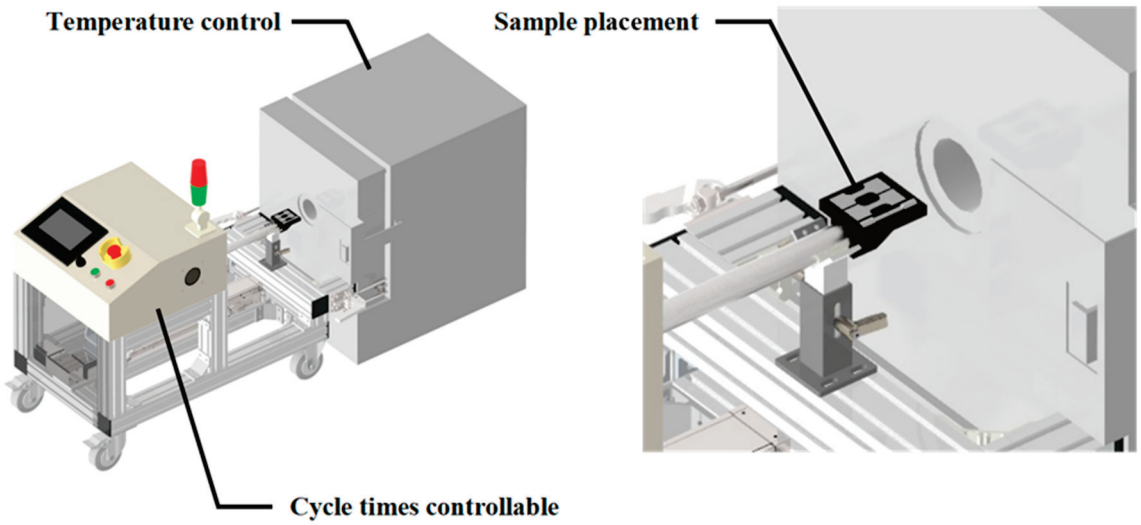


Figure 1. Thermal cycling fatigue equipment schematic [20].

To establish the deterioration mechanism after thermal cycling, two mechanical tests were conducted. Firstly, C100 specimens were subjected to tensile testing on a universal testing machine (AGX-V2, SHIMADZU Corporation, Kyoto, Japan) to the fixed strain levels of 16% and 32%, with the strain rates set at 8.33×10^{-3} s^{-1}. Subsequent sub-surface microstructural analysis was performed to confirm the characteristics of thermal cycling

cracks and tensile crack growth properties. Secondly, both RM and C100 were subjected to mechanical fatigue tolerance tests using a bending fatigue test machine (EJA Vantage, Thwing-Albert, West Berlin, NJ, USA). Figure 2 illustrates the experimental setup for the bending fatigue test employed in this study. The device allows for adjustment of the spacing between fixtures to apply cyclic bending and recovery to the test specimens. The loading was controlled by displacement, with a compression and tension rate ($\dot{\varepsilon}$) set at 50 mm/min. This displacement control was specifically chosen to ensure that the bending deformation was concentrated at the center of the specimen, minimizing unintended stress distribution near the grips. The fatigue test was performed until failure occurred to determine the fatigue life of both RM and C100. Additionally, in order to examine the early-stage microstructural response to bending, the number of cycles was fixed at 20 for a separate set of samples, labeled RM-B20 and C100-B20, and their degradation was subsequently analyzed. RM, C100, RM-B20, and C100-B20 were subjected to grinding and polishing for microstructural analysis using a metallographic microscope (VHX-7000N, KEYENCE, Osaka, Japan).

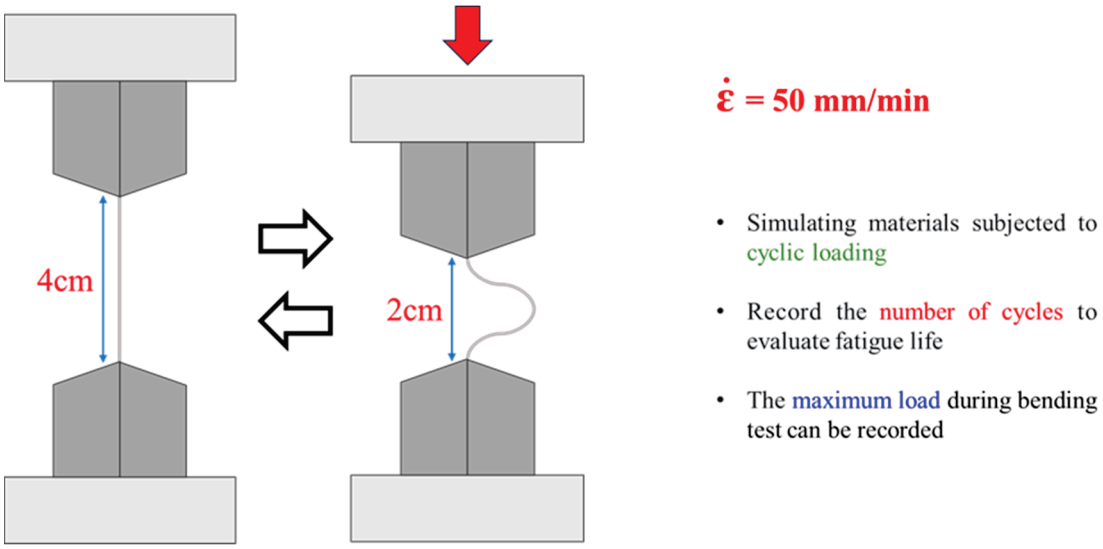


Figure 2. Bend fatigue test schematic.

XRD analysis (ARL EQUINOX 100 X, Thermal Scientific, Waltham, MA, USA) was conducted to analyze the phase composition in the 2θ range of 20° to 95°. Electron microprobe analysis (JXA-8530F Field Emission Electron Probe Microanalyzer, JEOL, Tokyo, Japan) and wavelength dispersive X-ray spectroscopy (JXA-8900R Electron Probe X-ray Microanalyzer, JEOL) were employed to analyze the distribution of elements in the matrix and sub-surface.

Differences in mechanical properties were evaluated using a Vickers hardness testing instrument (HM-101, Mitutoyo, Kawasaki, Japan) with a load of 0.1 kgf and holding time of 1 s; a tensile testing machine (AGX-V2, SHIMADZU Corporation, Japan) was used to conduct the tensile test, and the strain rate was 1×10^{-3} s^{-1}. The most noticeable areas of heating and cooling for C100 specimens were near the surface of the specimens, and to avoid intrusion of oxygen due to surface crack generation, the scanning electron microscope system was used to select a 10 μm depth near the surface of C100 for TEM observation. Each set of data is the average of 5–7 test values.

The selected area was etched down using a focused ion beam (Hydra Bio Plasma-FIB, Thermo Fisher, Waltham, MA, USA), fixed on a C-type ring, and further thinned using

the ion beam until TEM specimens were obtained. The C100 specimens etched using the FIB system were analyzed using a transmission electron microscope (JEM-2100F CS STEM, JEOL, Japan). The analysis included Mapping, SAED, and HR.

3. Results and Discussion

The microstructure and the tensile properties of the raw material are depicted in Figure 3, with a hardness of approximately Hv177 and an average grain size of about 26.2 μm. TGA analysis was conducted for 1 h to investigate the initial oxidation behavior of 310S stainless steel. Considering that low-carbon alloy steels are prone to decarburization in high-temperature environments and atmospheric conditions with a higher O_2 partial pressure, an Ar atmosphere was also established to reduce the gas partial pressure and slow down the rate of decarburization. According to the thermal weight loss analysis results (Figure 4), it was observed that under the condition of holding at 900 °C for 1 h, the weight change was most significant in the first 10 min. After reaching equilibrium, 310S stainless steel continued to undergo decarburization, reflected in the downward trend of the thermal weight loss curve. Compared to the atmospheric atmosphere, 310S stainless steel in an Ar atmosphere still showed weight increase due to oxidation behavior in the first 10 min, as complete oxygen exclusion cannot be achieved inside the TGA instrument. However, after 10 min, the higher O_2 partial pressure in the atmospheric atmosphere made it difficult for C elements to react and form volatile gases. This resulted in a slower increase in the thermal weight loss curve, indicating that the Ar atmosphere provides protection for stainless steel at high temperatures. Simultaneously, decarburization reactions occurred during the 1 h holding time.

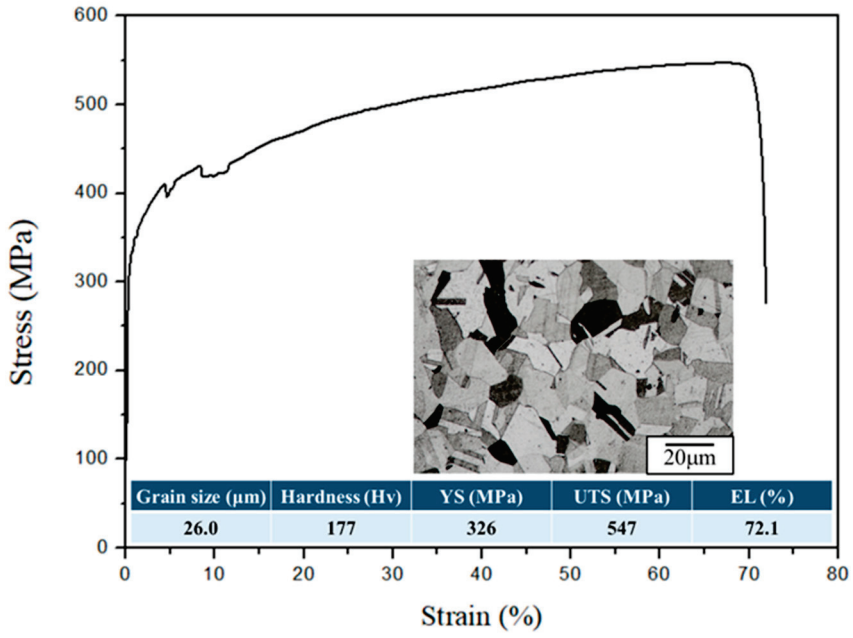


Figure 3. Stress–strain curve and microstructure of raw material (RM).

SEM and EPMA analyses were conducted on the sub-surface of the raw material as a control group, as shown in Figure 5. The sub-surface matrix exhibited a uniform atomic distribution without significant precipitates, while an oxide layer formed on the surface. From the above results, it can be observed that the raw material exhibits a tendency toward a uniform microstructure and elemental distribution, with no surface cracks.

After subjecting the material to 100 cycles of temperature cycling between 900 °C (holding for 1 min) and air cooling to room temperature (holding for 1 min), as depicted in Figure 6, the microstructure exhibits significant changes, primarily characterized by the formation of subgrains due to cyclic thermal stress. While the overall grain size remains mostly unchanged, certain localized regions display smaller grains, suggesting the early stages of recrystallization. This is likely due to the intense temperature fluctuations during the cycling, leading to the continuous generation of defects within the crystal lattice. These defects act as nucleation points for grain recrystallization and refinement. The changes in microstructure are also reflected in the variations in mechanical properties. Investigation of the fatigue material microhardness reveals a significant increase in hardness after the material undergoes severe temperature cycling, consistent with the Hall–Petch relation. The changes in microstructure are also reflected in the variations in tensile properties.

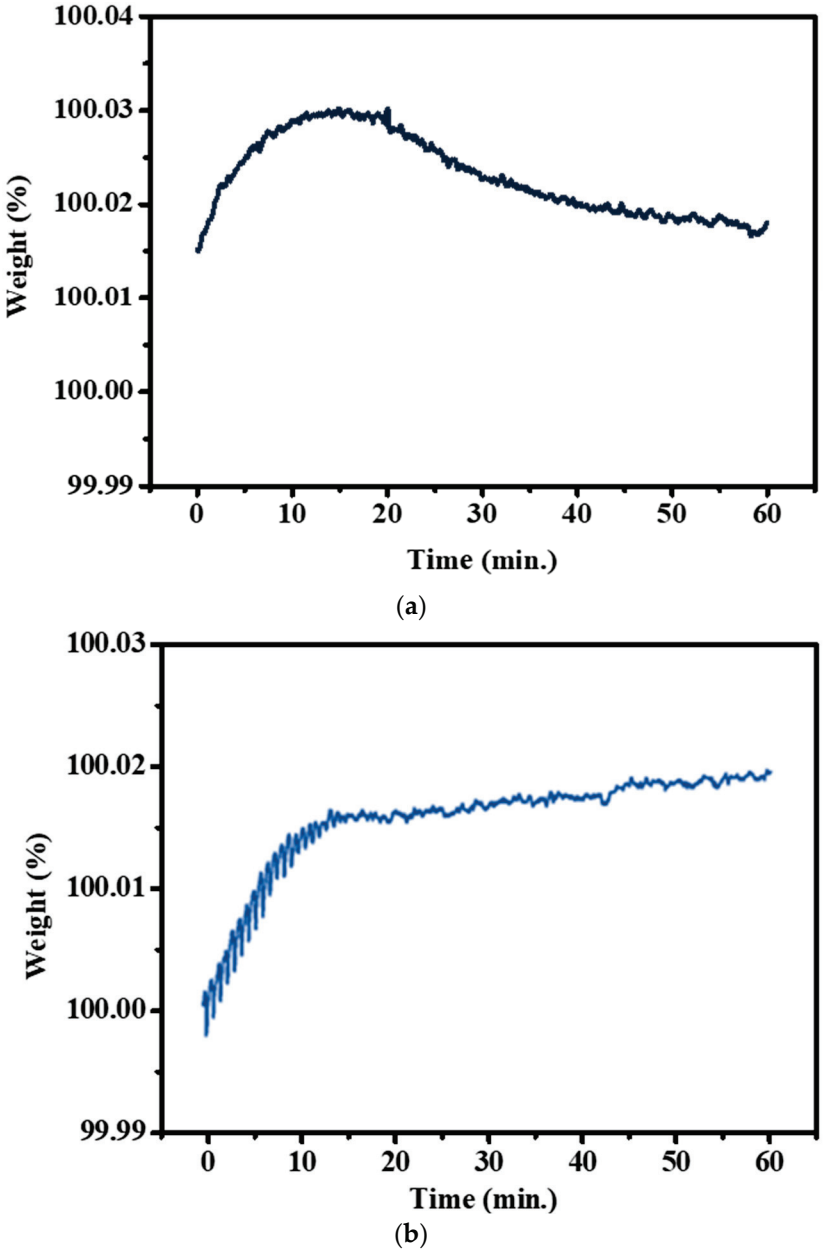


Figure 4. TGA analysis: 900 °C—holding time 1 h. (**a**) Atmospheric atmosphere, (**b**) Ar atmosphere.

The tensile properties of C100 are shown in Figure 7, where an increase in tensile strength is observed after the thermal fatigue test, primarily due to grain refinement. The thermal expansion and contraction caused shear-induced defects in the lattice, leading to grain recrystallization and refinement, thereby increasing the tensile strength. However, the accompanying reduction in ductility after thermal cycling is consistent with findings reported in previous studies on 310S and other high-temperature stainless steels [27–29]. In particular, the grain boundary carbide precipitation and surface embrittlement observed during long-term isothermal aging in these studies are in agreement with the surface crack formation noted in our C100 specimens.

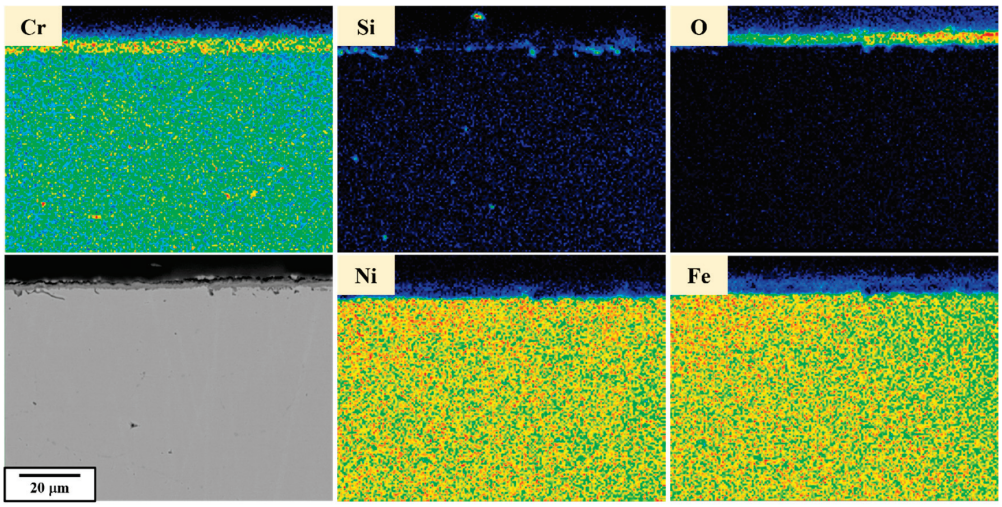


Figure 5. EPMA elemental analysis of raw materials (RM).

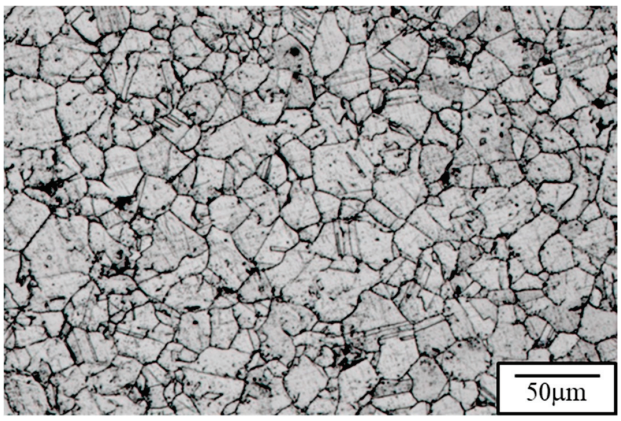


Figure 6. Microstructure of thermal fatigue specimen C100 (grain size: 20.6 μm; hardness: hv 343).

Considering the significant changes in mechanical properties, further analysis of the composition of the raw material and C100 was conducted via XRD analysis to investigate whether the steel was affected by structural effects. The results, as shown in Figure 8, reveal a remarkably high similarity between the XRD diffraction patterns of the raw material and C100. Both exhibit γ-iron peaks, indicating that this condition does not induce phase transformation in 310S. Therefore, the increase in tensile strength of 310S after thermal fatigue can be attributed to the defect-induced grain recrystallization resulting from thermal expansion and contraction.

However, solely from the perspective of grain refinement, it might be challenging to explain the observed decrease in ductility of 310S after the thermal fatigue test. Additionally,

considering that 310S stainless steel may develop cracks or experience element segregation due to uneven heating during cyclic temperature fluctuations, leading to possible crack initiation, FIB and EPMA analyses were performed on the sub-surface of C100. From Figure 9, the FIB image reveals a continuous oxidation film on the surface with a thickness ranging from approximately 1.3 μm to 1.9 μm. Beneath the oxidation layer, cracks are visibly propagating into the subsurface region, suggesting structural degradation due to thermal fatigue. Additionally, the EPMA results shown in Figure 10 further support these observations, highlighting the accumulation of silicon near the surface, which may contribute to the embrittlement and crack formation observed in the FIB image. Considering the possibility of crack generation after the thermal fatigue test, it is reasonable to assume that these cracks may affect the ductility of the material.

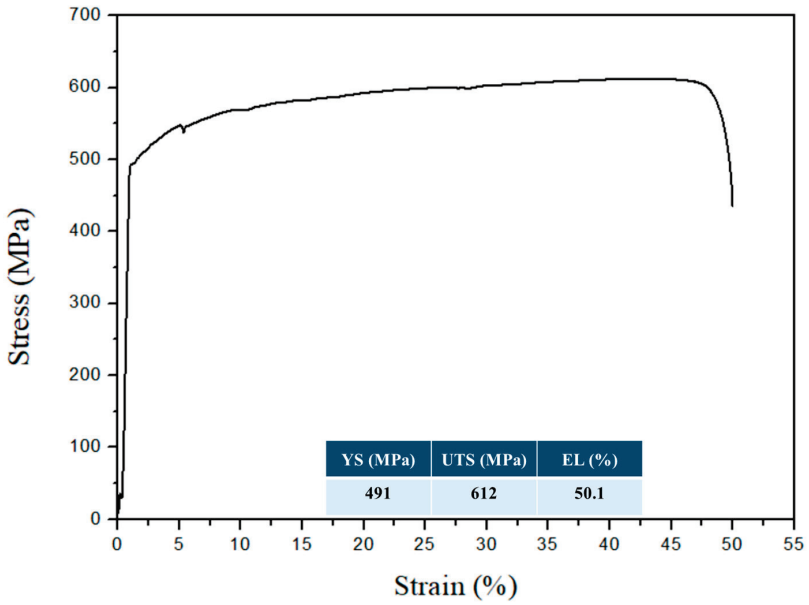


Figure 7. Tensile stress–strain curve of C100.

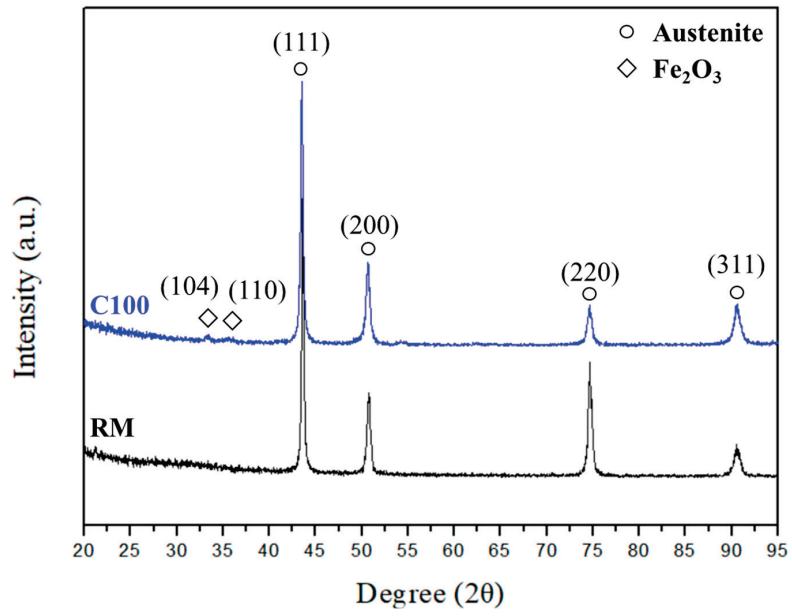


Figure 8. XRD analysis of RM and C100.

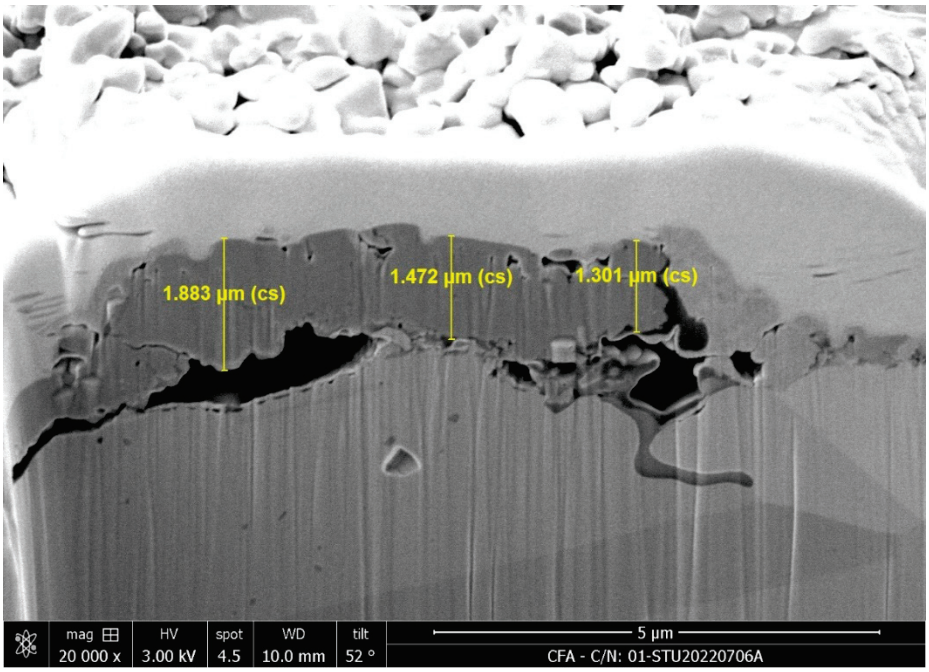


Figure 9. FIB image of C100 cross-section.

Considering that 310S stainless steel, used in this study, is mainly employed in high-temperature conveyor belts that may experience relaxation and subsequent re-tightening during actual operation, it is subjected to external mechanical forces. Therefore, after undergoing thermal fatigue testing, tensile testing was conducted. The elongation was set to 1/3 and 2/3 of the maximum elongation capacity of C100 (approximately 16% and 32%). The microstructural changes in C100 during tensile testing are illustrated in Figure 11. From Figure 11, it can be observed that after experiencing elongations of 16% and 32%, the near-surface cracks in C100 exhibit significant propagation due to tension. At 32% elongation, the depth of the cracks has reached approximately 4–5 times that of C100 material. Therefore, it is inferred that the primary reason for the decreased ductility of 310S stainless steel after thermal fatigue testing is likely due to crack propagation.

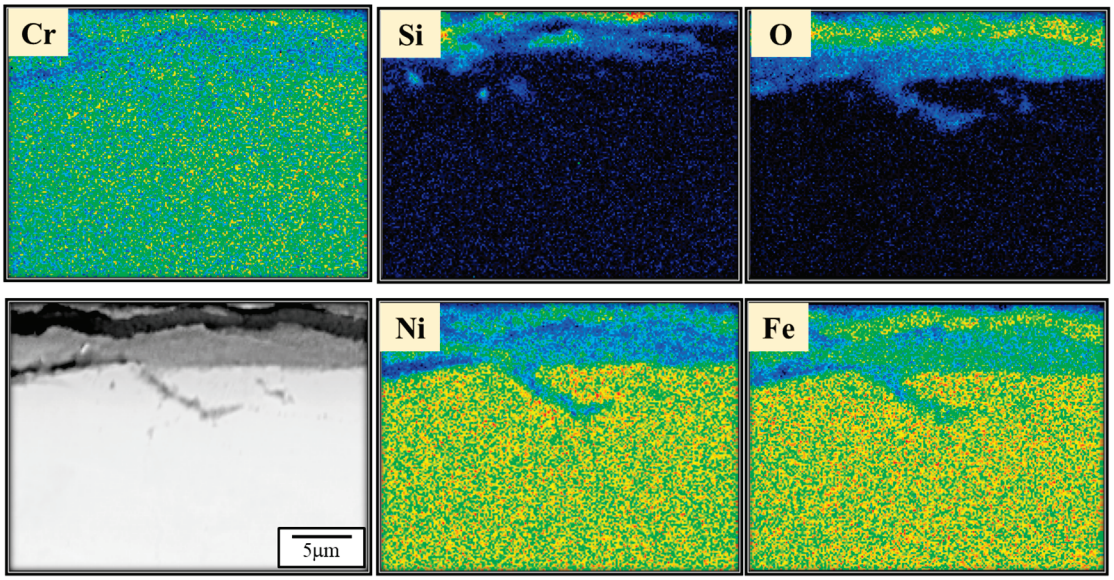


Figure 10. EPMA elemental analysis of near-surface cracks in C100.

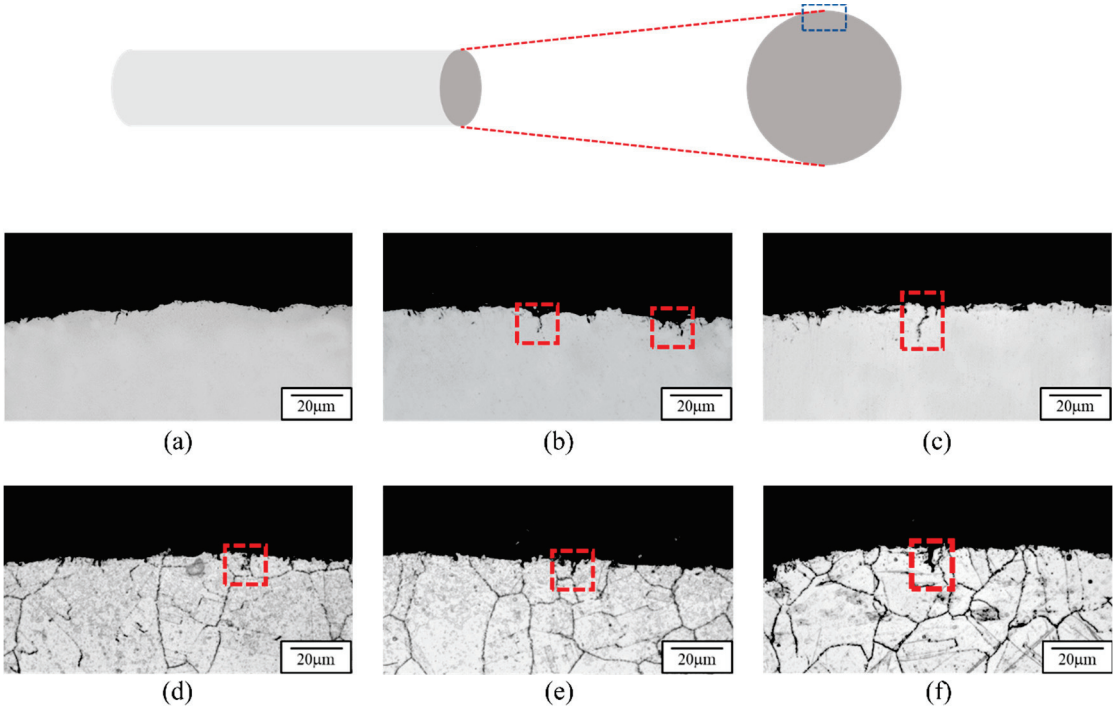


Figure 11. Crack Propagation in 310S Stainless Steel After Thermal Fatigue and Tensile Strain. (**a**) Surface condition after thermal fatigue (100 cycles). (**b**) Thermal fatigue (100 cycles) followed by tensile strain of 16%. (**c**) Thermal fatigue (100 cycles) followed by tensile strain of 32%. (**d**–**f**) Corresponding microstructures with etching, showing crack propagation for (**a**), (**b**), and (**c**), respectively.

Further investigation into the relationship between cracks and grain boundaries, as shown in Figure 11d–f, reveals that the majority of cracks in 310S stainless steel, after undergoing thermal fatigue followed by tension, propagate transgranularly toward the center of the 310S stainless steel. This characteristic is typical of brittle materials and confirms that 310S stainless steel indeed experiences embrittlement after thermal fatigue. This implies that as the strain increases, there is an accelerating trend in crack propagation for the fatigued material. Therefore, it is inferred that in higher strain ranges, cracks dominate the mechanical property effects of the fatigued material more significantly. Consequently, when comparing the ductility of RM and C100 with and without initial cracks, there is a significant discrepancy between the two.

The mechanisms of subsurface initial cracks and their propagation are illustrated in Figure 12. Figure 12a shows the element distribution and crack characteristics of 310S stainless steel after thermal fatigue testing. Due to the severe thermal expansion and contraction cycles near the surface caused by the thermal fatigue test, after 100 fatigue cycles, cracks with an average initial depth of about 5 μm are generated. Subsequent tensile stress after thermal fatigue leads to further propagation of these cracks, as shown in Figure 12b. The crack propagation rate increases with the amount of elongation, resulting in a decrease in the ductility of 310S stainless steel.

To integrate both thermal and mechanical fatigue effects on 310S stainless steel and simulate service conditions in woven high-temperature conveyor belts, RM was used as a control group. Both RM and C100 were subjected to bending fatigue tests. Microstructural observations from Figures 13 and 14 show that after bending fatigue, RM exhibited clear signs of work hardening, with a significant increase in microhardness. The bending fatigue induced the formation of deformation twins within the material, and cracks were primarily observed in the upper region of the specimens, where tensile stress is concen-

trated. In contrast, fewer cracks were found in the lower region under compressive stress. Moreover, in the middle region under minimal stress, microstructural features remained relatively well preserved under similar corrosion conditions. This hardening behavior aligns with previously reported twin-induced strengthening in cold-worked austenitic stainless steels [30–32]. Conversely, the absence of deformation twins in the thermally fatigued specimens (C100) can be attributed to thermally activated recrystallization, which eliminates dislocation structures and suppresses the conditions required for twin formation.

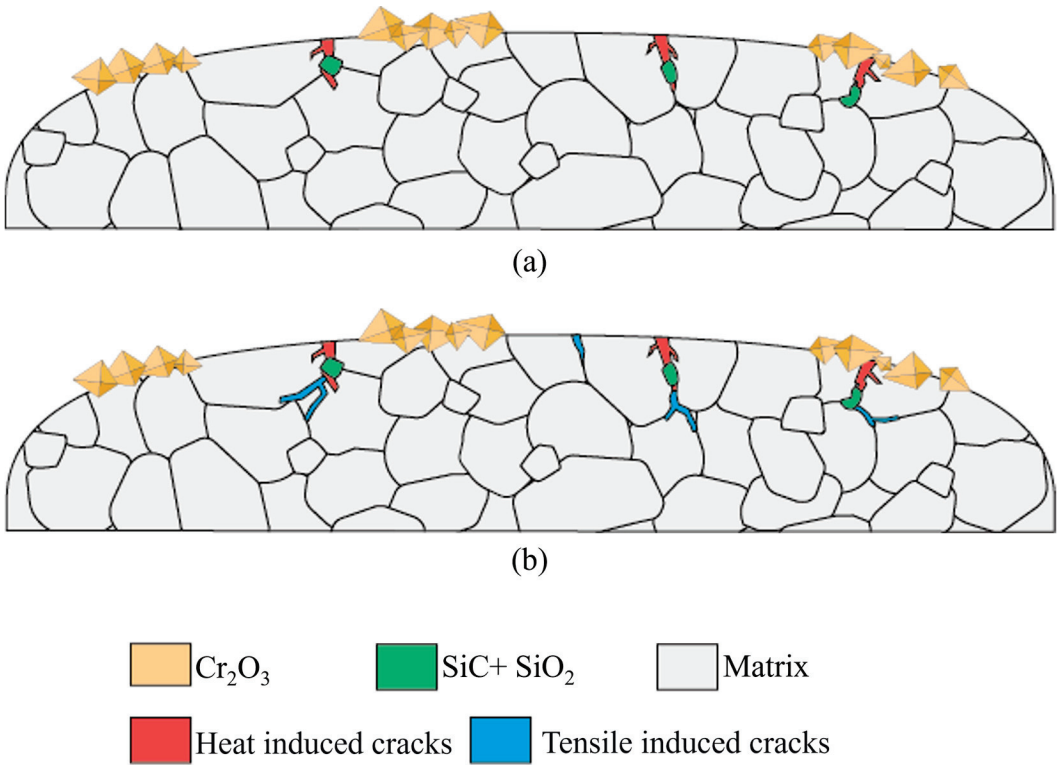


Figure 12. Mechanism of crack propagation after thermal fatigue. (**a**) Initial crack formation after thermal fatigue. (**b**) Propagation of tensile strain-induced cracks.

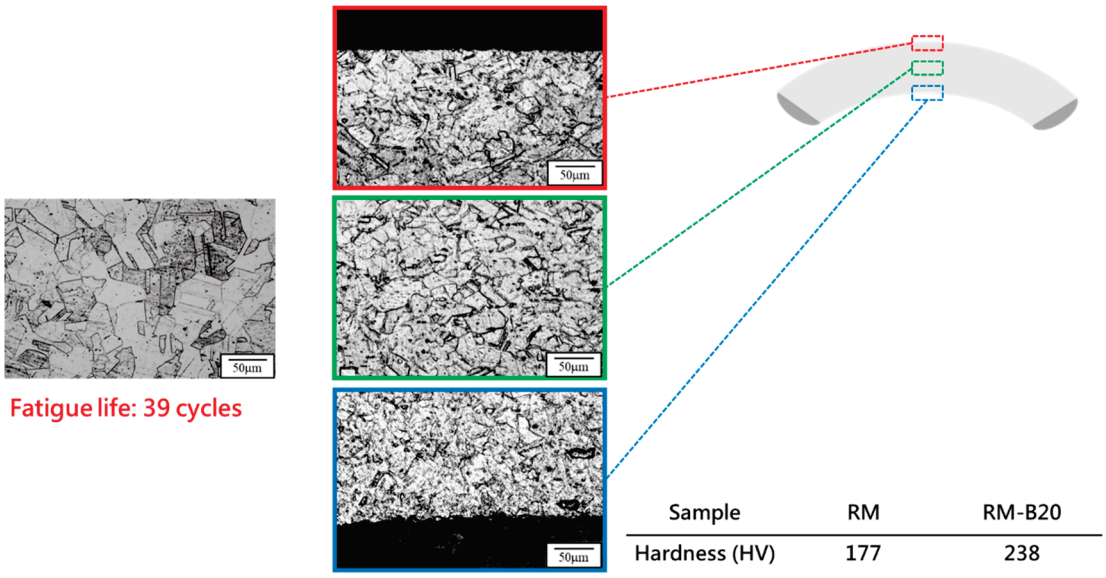


Figure 13. Microstructural characteristics of RM before and after bending: (Before bending: HV177; After bending: HV238; Fatigue life: 39 cycles).

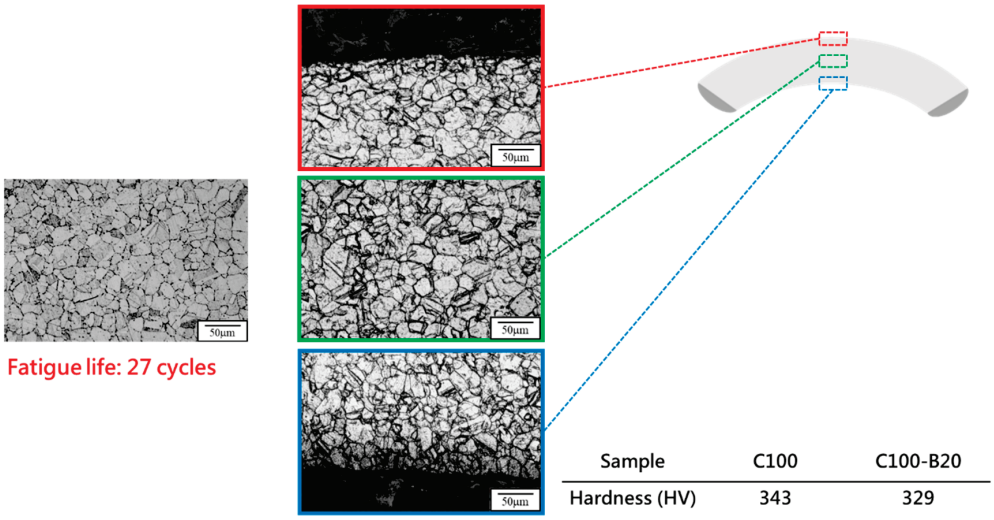


Figure 14. Microstructural characteristics of C100 before and after bending. (Before bending: HV343; After bending: HV329; Fatigue life: 27 cycles).

XRD analysis results from Figure 15 indicate that without stress-induced phase transformations, the hardening observed in RM mainly stems from mechanical fatigue-induced work hardening. In comparison, while RM exhibited a significant increase in hardness, C100 showed no apparent increase after bending fatigue. This outcome may suggest that the extent of work hardening due to the formation of new defects inside 310S stainless steel after thermal fatigue, further contributing to work hardening, has limitations. This indicates that there is a certain limit to the hardening degree due to defects, and after undergoing thermal fatigue followed by bending tests, the material may have reached this limit. The bending fatigue life of RM and C100 also indirectly corroborates this, with C100, having defects formed internally due to thermal expansion and contraction, showing poorer fatigue life.

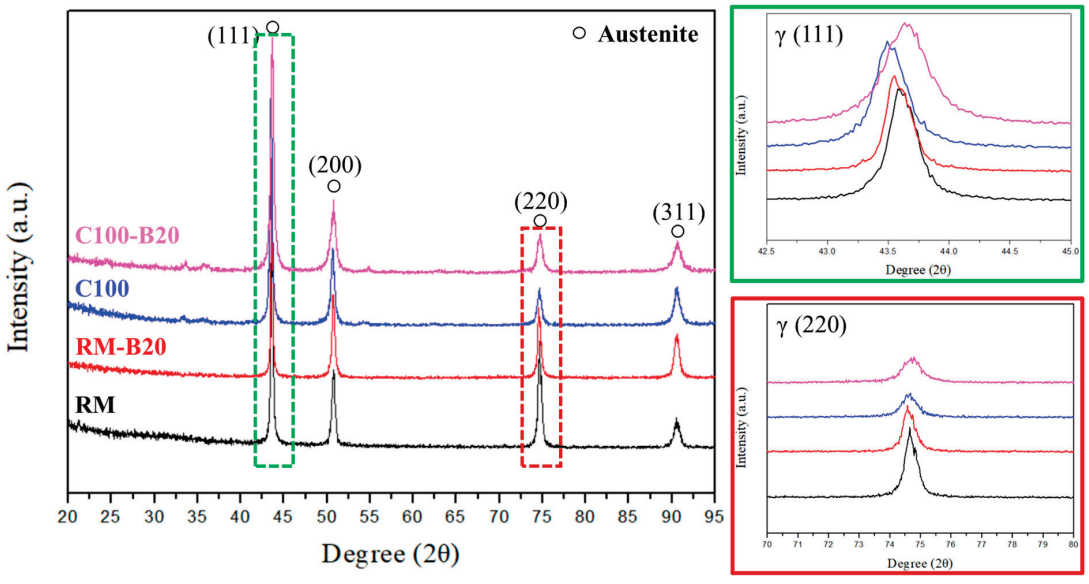


Figure 15. XRD analysis: RM, RM with 20 bending fatigue cycles (RM-B20). C100, C100 with 20 bending fatigue cycles (C100-B20).

The XRD analysis results in Figure 15 show a shift in the main peak (111) after bending tests, indicating changes in the internal lattice constant due to applied external stress. Additionally, a peak was observed in the XRD spectrum at 2θ = 32.5–35°, identified as Fe_2O_3 and Fe_3O_4 after comparison. It is inferred that under short-term thermal fatigue conditions, Fe elements near the surface preferentially form iron oxide. Regardless of thermal or bending fatigue, there were no significant structural differences observed in 310S stainless steel, suggesting that stress-induced phase transformations cannot be observed through XRD analysis under these conditions. While there were no significant changes in peak width and position before and after bending fatigue tests for both RM and C100, the peak shift was more apparent in C100. This suggests that defects formed internally due to thermal expansion and contraction in 310S stainless steel after thermal fatigue, combined with newly formed defects from cold working, create a larger stress field, leading to a more pronounced effect on lattice deformation and peak shifts in XRD.

Figure 16 presents the results of near-surface TEM analysis. The mapping analysis reveals a uniform distribution of elements within the image range. It indicates that under the condition of 900 °C (holding for 1 min) $\rightleftarrows$ room temperature (holding for 1 min) cycling 100 times, all elements exhibit homogeneous distribution. This is likely due to the insufficient total holding time, preventing atoms from having enough time to move at high temperatures. TEM diffraction analysis, as depicted in Figure 17a, shows that the base phase is the γ-Fe lattice. Combined with the bright-field and SAED analysis in Figure 17b, after 100 cycles, there is no apparent phase transformation near the surface of the 310S stainless steel. However, lattice distortion is observed, reflected in the deformation of diffraction spots. Additionally, intense thermal expansion and contraction led to dislocation clustering, corresponding to the XRD diffraction spectrum results for the C100 specimen. It is inferred that thermal cycling causes lattice distortion, potentially satisfying the conditions for stress-induced phase transformation locally. Consequently, the C100 specimen exhibits embrittlement, with thermal cracking on the steel surface and hardening within the base material due to lattice distortion.

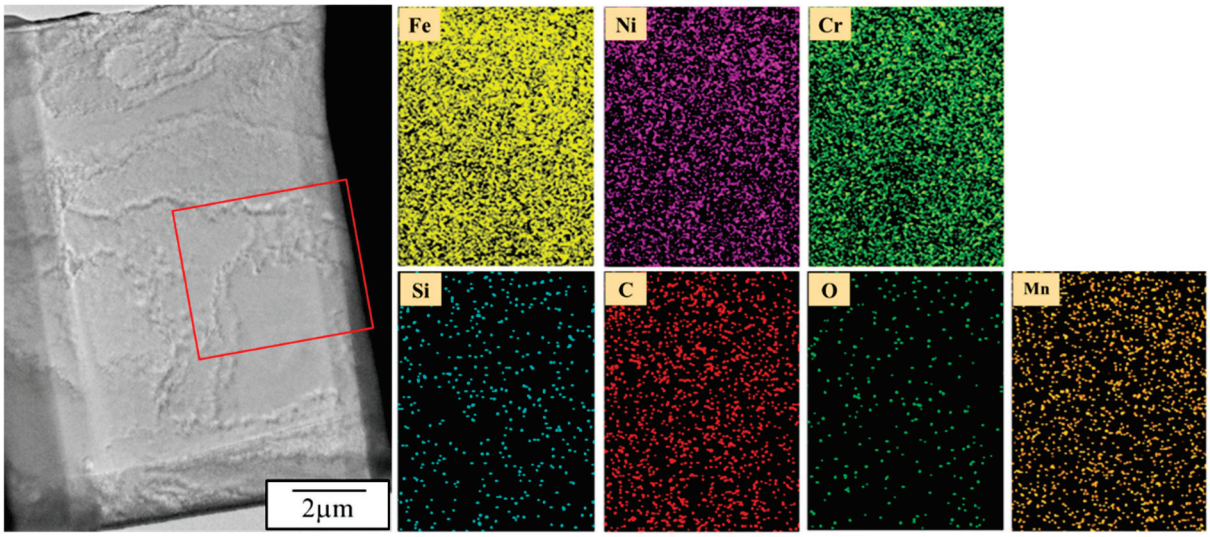


Figure 16. TEM mapping analysis of C100.

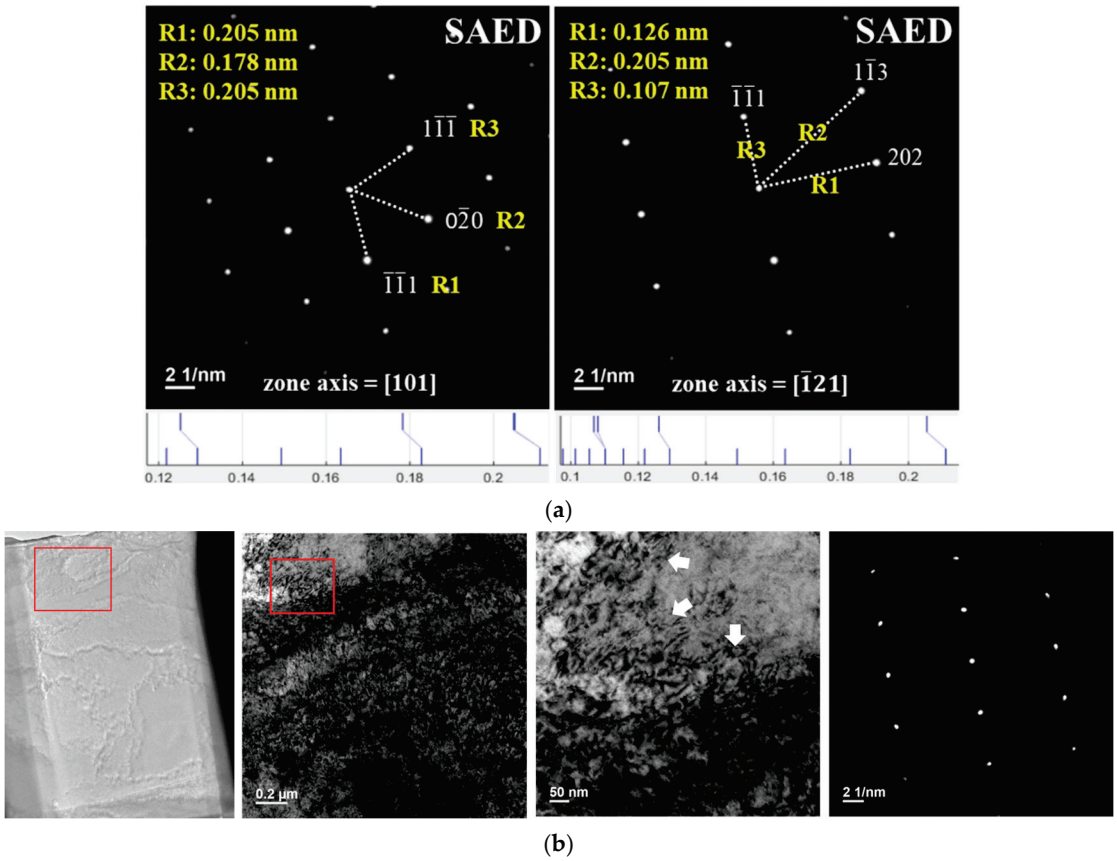


Figure 17. TEM analysis of C100. (**a**) SAED analysis. (**b**) Dislocation accumulation + diffraction patterns.

4. Conclusions

(1) Thermal fatigue testing subjects 310S stainless steel to cyclic thermal stress, inducing lattice distortion, recrystallization, and localized grain refinement. High-temperature cycling (from 900 °C to room temperature) promotes dislocation accumulation and grain boundary movement, facilitating recrystallization. Additionally, atomic stacking faults formed during thermal cycling contribute to the nucleation of annealing twins, a characteristic feature of recrystallized grains.

(2) Subsurface crack formation and propagation reduce the ductility of 310S stainless steel. These cracks act as stress concentrators, leading to premature failure under loading and a marked reduction in the service life of 310S stainless steel. The combined effects of thermal stress and mechanical fatigue testing exacerbate crack growth, making subsurface cracks a critical factor in the degradation of ductility and structural integrity.

(3) The lattice distortion induced by thermal fatigue testing weakens the microstructure of 310S stainless steel, increasing brittleness and reducing resistance to bending. This facilitates the initiation and propagation of subsurface cracks, which expand further during mechanical testing. The combined effects of lattice distortion and crack propagation synergistically degrade the mechanical properties of the material.

(4) The results provide new insight into the deterioration mechanism of 310S stainless steel under realistic thermal and mechanical service conditions, suggesting that even short-term cyclic thermal exposure can accelerate embrittlement. Thus, more conservative design approaches or protective measures may be necessary in industrial applications such as high-temperature conveyor systems.

Author Contributions: Methodology, Y.-W.Y.; Data curation, Y.-T.H.; Writing—original draft, Y.-W.Y.; Writing—review & editing, Y.-T.H.; Supervision, F.-Y.H. All authors have read and agreed to the published version of the manuscript.

Funding: The authors express their gratitude to the Walsin Lihwa Co., Ltd. for their assistance and financial support. They also thank the Instrument Center of National Cheng Kung University of the Ministry of Science and Technology of Taiwan for their assistance in material analysis (NSTC 112-2221-E-006-061-MY2).

Institutional Review Board Statement: Not applicable.

Informed Consent Statement: Not applicable.

Data Availability Statement: The raw data supporting the conclusions of this article will be made available by the authors on request.

Conflicts of Interest: The authors declare no conflict of interest. The authors declare that this study received funding from Walsin Lihwa Co., Ltd. The funder was not involved in the study design, collection, analysis, interpretation of data, the writing of this article or the decision to submit it for publication.

References

1. Lula, R.A. *Stainless Steel*; American Society for Metals: Detroit, MI, USA, 1985.
2. Beddoes, J.; Parr, J.G. *Introduction to Stainless Steels*, 3rd ed.; ASM International: Almere, The Netherlands, 1999.
3. Davis, J.R. (Ed.) *ASM Specialty Handbook: Heat-Resistant Materials*; ASM International: Almere, The Netherlands, 1997.
4. Wu, W.; Hwu, L.Y.; Lin, D.Y.; Lee, J.L. The relationship between alloying elements and retained austenite in martensitic stainless steel welds. *Scr. Mater.* **2000**, *42*, 1071–1076. [CrossRef]
5. Huntz, A.M.; Reckmann, A.; Haut, C.; Sévérac, C.; Herbst, M.; Resende, F.C.T.; Sabioni, A.C.S. Oxidation of AISI 304 and AISI 439 stainless steels. *Mater. Sci. Eng. A* **2007**, *447*, 266–276. [CrossRef]
6. Hall, E.O.; Algie, S.H. The sigma phase. *Metall. Rev.* **1966**, *11*, 61–88. [CrossRef]
7. Perron, A.; Toffolon Masclet, C.; Ledoux, X.; Buy, F.; Guilbert, T.; Urvoy, S.; Suzon, E. Understanding sigma-phase precipitation in a stabilized austenitic stainless steel (316Nb) through complementary CALPHAD-based and experimental investigations. *Acta Mater.* **2014**, *79*, 16–29. [CrossRef]
8. Hsu, H.-W.; Tsai, W.-T. High temperature corrosion behavior of siliconized 310 stainless steel. *Mater. Chem. Phys.* **2000**, *64*, 147–155. [CrossRef]
9. Chen, K.; Zhang, L.; Shen, Z.; Zeng, X. Revealing the oxidation mechanism of 310S stainless steel in supercritical water via high-resolution characterization. *Corros. Sci.* **2022**, *200*, 110212. [CrossRef]
10. Brittan, A.; Mahaffey, J.; Adam, D.; Anderson, M. Mechanical and corrosion response of 316SS in supercritical CO_2. *Oxid. Met.* **2021**, *95*, 409–425. [CrossRef]
11. Parrens, C.; Lacaze, J.; Malard, B.; Dupain, J.L.; Poquillon, D. Isothermal and Cyclic Aging of 310S Austenitic Stainless Steel. *Metall. Mater. Trans. A* **2017**, *48*, 2834–2843. [CrossRef]
12. Garcia, J.M.; Monteiro, A.C.A.; Casanova, A.D.M.B.; Huaman, N.R.C.; Monteiro, S.N.; Brandao, L.P. Microstructural analysis of phase precipitation during high temperature creep in AISI 310 stainless steel. *J. Mater. Res. Technol.* **2023**, *23*, 5953–5966. [CrossRef]
13. Nikulin, I.; Kipelova, A.; Kaibyshev, R. Effect of high-temperature exposure on the mechanical properties of 18Cr–8Ni–W–Nb–V–N stainless steel. *Mater. Sci. Eng. A* **2012**, *554*, 61–66. [CrossRef]
14. Odnobokova, M.; Belyakov, A.; Kaibyshev, R. Grain refinement and strengthening of austenitic stainless steels during large strain cold rolling. *Philos. Mag.* **2019**, *99*, 531–556. [CrossRef]
15. Shen, Y.F.; Li, X.X.; Sun, X.; Wang, Y.D.; Zuo, L. Twinning and martensite in a 304 austenitic stainless steel. *Mater. Sci. Eng. A* **2012**, *552*, 514–522. [CrossRef]
16. Rice, J.R. Thermodynamics of the quasi-static growth of Griffith cracks. *J. Mech. Phys. Solids* **1978**, *26*, 61–78. [CrossRef]
17. Badaruddin, M.; Sugiyanto; Wardono, H.; Andoko; Wang, C.J.; Rivai, A.K. Improvement of low-cycle fatigue resistance in AISI 4140 steel by annealing treatment. *Int. J. Fatigue* **2019**, *123*, 406–417. [CrossRef]
18. Mampuya, M.B.; Umba, M.C.; Mutombo, K.; Olubambi, P.A. Effect of heat treatment on the microstructure of duplex stainless steel 2205. *Mater. Proc.* **2021**, *38*, 1107–1112. [CrossRef]

19. Lakhdari, M.A.; Krajcarz, F.; Mithieux, J.D.; Van Landeghem, H.P.; Veron, M. Strength Enhancement of superduplex stainless steel using thermomechanical processing. *Metals* **2021**, *11*, 1094. [CrossRef]
20. Yen, Y.W.; Hung, F.Y.; Zhao, J.R.; Wu, B.D.; Hsieh, H.Y. A study on thermal-induced phase transformation behavior and deterioration mechanism of 310S stainless steel. *J. Alloys Metall. Syst.* **2024**, *6*, 100069. [CrossRef]
21. Huang, C.T.; Hung, F.Y.; Zhao, J.R.; Hsieh, H.Y. Microstructure and mechanical properties of 631 stainless steel: Study of Yield Slip and Strain Rate Mechanism with Austempering and Martempering. *J. Alloys Metall. Syst.* **2023**, *2*, 100015. [CrossRef]
22. Kuo, Y.A.; Hung, F.Y.; Zhao, J.R.; Wu, B.D.; Huang, B.C.; Chang, K.C.; Chen, K.J.; Ku, C.W.; Huang, C.T.; Hsieh, H.Y. A Study on Structural Characteristics and Metallurgical Mechanism of Carbides for 440 Martensitic Stainless Steel with Different Melt Refining Processes. *J. Alloys Metall. Syst.* **2023**, *3*, 100029. [CrossRef]
23. Kim, J.H.; Kim, D.I.; Suwas, S.; Fleury, E.; Yi, K.W. Grain-size effects on the high-temperature oxidation of modified 304 austenitic stainless steel. *Oxid. Met.* **2013**, *79*, 239–247. [CrossRef]
24. Rout, M.; Pal, S.K.; Singh, S.B. Post-hot-deformation microstructure development in austenitic stainless steel. *Mater. Chem. Phys.* **2023**, *295*, 127064. [CrossRef]
25. Sohrabi, M.J.; Naghizadeh, M.; Mirzadeh, H. Deformation-induced martensite in austenitic stainless steels: A review. *Arch. Civ. Mech. Eng.* **2020**, *20*, 124. [CrossRef]
26. Lo, K.H.; Shek, C.H.; Lai, J.K.L. Recent developments in stainless steels. *Mater. Sci. Eng. R Rep.* **2009**, *65*, 39–104. [CrossRef]
27. Zhong, Y.; Zhou, C.; Chen, S.; Wang, R. Effect of temperature and pressure on stress corrosion cracking behavior of 310s stainless steel in chloride solution. *Chin. J. Mech. Eng.* **2017**, *30*, 200–206. [CrossRef]
28. Tavares, S.S.M.; Moura, V.; Costa, V.C.; Ferreira, M.L.R.; Pardal, J.M. Microstructural changes and corrosion resistance of AISI 310S steel exposed to 600–800 °C. *Mater. Charact.* **2009**, *60*, 573–578. [CrossRef]
29. Lee, J.; Yamashita, S.; Ogura, T.; Saida, K. Effect of cooling rate on solidification cracking behavior in 310S stainless steel. *J. Adv. Join. Process.* **2021**, *3*, 100044. [CrossRef]
30. Maharaja, H.; Das, B.; Singh, A.; Mishra, S. Comparative assessment of strain-controlled fatigue performance of SS 316L at room and low temperatures. *Int. J. Fatigue* **2023**, *166*, 107251. [CrossRef]
31. Smaga, M.; Sorich, A.; Daniel, T.; Beck, T.; Kohler, C.; Soppa, E.; Speicher, M. Nano-twinning and uncommon α'-martensite formation as a result of very high cycle fatigue of metastable austenitic stainless steel at 573 K. *Scr. Mater.* **2023**, *231*, 115457. [CrossRef]
32. Mei, T.; Wang, Q.; Liu, M.; Jiang, Y.; Zou, T.; Cai, Y. The low-cycle fatigue behavior, microstructure evolution, and life prediction of SS304: Influence of temperature. *Materials* **2023**, *16*, 6326. [CrossRef]

Disclaimer/Publisher's Note: The statements, opinions and data contained in all publications are solely those of the individual author(s) and contributor(s) and not of MDPI and/or the editor(s). MDPI and/or the editor(s) disclaim responsibility for any injury to people or property resulting from any ideas, methods, instructions or products referred to in the content.

materials

MDPI

Article

Microstructure Evolution of Ni_3Al-Based Intermetallic Alloy Strips After Hot Rolling

Paweł Jóźwik [1,*], Wojciech Polkowski [2], Andrzej J. Panas [3] and Zbigniew Bojar [1]

[1] Faculty of Advanced Technologies and Chemistry, Institute of Materials Science and Engineering, Military University of Technology, Kaliskiego 2 Str., 00-908 Warsaw, Poland; zbigniew.bojar@wat.edu.pl
[2] Łukasiewicz Research Network—Krakow Institute of Technology, Zakopiańska 73 Str., 30-418 Krakow, Poland; wojciech.polkowski@kit.lukasiewicz.gov.pl
[3] Faculty of Mechatronics, Armament and Aerospace, Institute of Aerospace Technology, Military University of Technology, Kaliskiego 2 Str., 00-908 Warsaw, Poland; andrzej.panas@wat.edu.pl
* Correspondence: pawel.jozwik@wat.edu.pl

Abstract: The effect of the temperature and strain rate during the hot rolling process on the microstructural evolution in fine-grained Ni_3Al intermetallic alloy doped with Zr and B was examined in this work. The hot rolling process was carried out at an initial temperature range of 1000, 1100, and 1280 °C and at a strain rate between 3.9×10^{-1} s^{-1} and 2.5 s^{-1}. The results of the EBSD microstructural analyses revealed that dynamic recrystallization phenomena are initiated at the rolling temperature of 1100 °C, while a fraction of the dynamically recrystallized grains further increases with both the rising temperature and strain rate of the deformation process. Furthermore, to estimate the heat losses during the hot rolling processing, a non-stationary heat transfer model was formulated and then used to evaluate the experimentally received data.

Keywords: Ni_3Al-based intermetallic alloy; hot rolling; dynamic recrystallization; EBSD analysis; heat conduction model

1. Introduction

Ni_3Al-based intermetallic alloys demonstrate superior characteristics compared with conventional heat-resistant nickel-based superalloys, including significantly higher strength at elevated temperatures, relatively lower density, and improved resistance to corrosive environments. An analysis of the properties of these materials and their commercialization potential has been extensively presented by Sikka et al. [1,2], Jozwik et al., [3], Jarosz et al. [4], Sahare et al. [5], Sun and Yuan [6], and Tiwari et al. [7]. Their findings indicate that Ni_3Al intermetallics in bulk form are predominantly utilized in the fabrication of dies and press tool components, equipment for furnaces used in thermochemical treatment, and jet engine components. Considering the aforementioned unique physical and chemical properties of these materials, their potential applications in the form of strips or foils in various advanced components, including electromechanical systems (such as heat exchangers, reactors, actuators, and glucose sensors), solar cells, automotive and aircraft engine components, and thermocatalytic systems, have been proposed.

One possible approach to obtain Ni_3Al strips and foils with enhanced strength and ductility is hot plastic processing. Notably, the literature contains limited information regarding the hot-working of Ni_3Al-based intermetallic alloys. Furthermore, the available studies are limited to only a few research examples related to the hot processing of bulk

materials (i.e., samples with a dimension of at least 8 mm). The studies under consideration include isothermal compression tests (Wang et al. [8], Wu et al. [9], Zhong et al. [10,11], Prasad et al. [12]); hot extrusion (Guo et al. [13], Sheng et al. [14]); compression tests with heated swages; and rotary working tests with localized heating evoked by friction (Schindler et al. [15,16]). The results mentioned in these studies indicate that appropriately selected parameters of the deformation process (temperature, strain rate and degree of deformation, state of the initial structure, and a presence of alloying elements) lead to microstructural changes in Ni_3Al-based alloys as a result of dynamic recrystallization (DRX) or post-dynamic recrystallization. As observed by Bhatia [17] and Ponge et al. [18], the DRX of Ni_3Al-based alloys can result in the presence of a "necklace structure" characterized by fine recrystallized grains surrounding large primary grains of γ' phase. Such a structure can play a pivotal role in achieving the desired combination of high creep and low cycle fatigue resistance. Despite these advances, the impact of specific hot deformation parameters on the microstructural evolution and mechanical properties of Ni_3Al-based alloys remains insufficiently understood, particularly for materials in the form of thin strips or foils. It is worth noting that the hot rolling process used in the presented work has many varieties described in the literature, including rotational hot rolling (RHR) [19], asymmetric rolling (ASR) [20], radial shear rolling (RSR) [21], corrugated rolling [22], etc.

The main objective of this study was to analyze the DRX-induced microstructural changes in Ni_3Al-based intermetallic strips. Because of the significantly limited dimensions (thickness of approximately 1 mm), it should be assumed that the proposed hot plastic processing will occur under conditions of intensive heat exchange between the treated material strips and the working tools (rollers).

An additional aspect of this study is to explore the possibility of obtaining transient strengthening states of Ni_3Al-based alloys with the level of mechanical properties controlled by the occurrence of the necklace structure obtained by hot rolling.

2. Experimental Procedure

The hot rolling process was performed on Ni_3Al-based intermetallic alloy strips with a chemical composition of Ni–22.1Al–0.26Zr–0.1B (at.%), using rolling mill sexto. The material in the initial state (a strip of 150 mm × 30 mm × 1.12 mm) was obtained by consecutive cold rolling and heat treatment (with strictly selected conditions of deformation and recrystallization) to obtain a single-phase fine-grained structure (grain size of d~30 μm) of the γ' phase. Details of the Ni_3Al strip production process were reported previously by Jóźwik et al. [23–25]. The obtained material constituted the "initial" state for the hot rolling. The processing was carried out by pre-heating the Ni_3Al-based strips to 1000 °C, 1100 °C, or 1280 °C. Various strain rate $\dot{\varepsilon}$ values were applied: 3.9×10^{-1} s^{-1}, 9.9×10^{-1} s^{-1}, 1.5 s^{-1}, or 2.5 s^{-1} (the last one was not used for T = 1280 °C). For all hot rolling conditions, the total strain value (i.e., expressed as a relative thickness reduction) was 0.3, and it was set in one pass. To eliminate the possibility of post-dynamic recrystallization in the material, after each hot rolling operation, the samples were immediately (in less than 1 s) cooled in a water bath. Then, an electric discharge machining was used to cut the obtained strips in a plane perpendicular to the rolling direction located in the middle of the length of the rolled material. Metallographic cuts were ground on SiC papers and mechanically polished using diamond suspensions of 3 μm and SiO_2 suspension of 0.1 μm. Microstructural studies were performed by using a Quanta 3D FEG (Thermo Fisher Scientific, Waltham, MA, USA) scanning electron microscope (SEM) equipped with an electron backscattered diffraction detector (EBSD) (Ametek, Berwyn, PA, USA) at an accelerating voltage of 20 kV, a beam current of 8 nA, and analysis step (depending on magnification) from 1 μm to 0.1 μm.

Based on the results of the systematic EBSD mapping of crystallographic orientations, the grain structure of the polycrystalline strips was reconstructed, revealing positions of high- and low-angle grain boundaries, simultaneously. In turn, the maps of the surface distribution of the poles of the mean crystallographic orientation of individual grains inverse pole figure (IPF) maps were the basis for assessing the presence of privileged crystallographic orientation and possible micro-texture. The analysis of structural changes as a result of the performed hot rolling procedures was based on the measurements of the degree of local disorientation of the crystal lattice in the volume of individual grains, presented in the form of grain orientation spread (GOS) parameter maps. In this study, the average GOS parameter, which shows the average value of the disorientation of the particular investigated area, was used. The analysis of the quality of the Kikuchi lines, thereby determining the image quality (IQ) parameter, was also performed. The primary source of imperfections in the measurements of the GOS and IQ parameters is the dependence of the test results on factors related to both the measurement parameters used and the quality of preparation. Therefore, during the sample preparation and testing, special attention was paid to maintaining the repeatability of the applied experimental conditions [26–30].

Finally, hardness measurements were performed in the rolling plane using the Vickers method (HV5), with a load of 5 kg and a 10 s loading time in single measurement (according to the ISO 6507-1:2023 standard [31]), and the average value and standard deviation were determined based on at least ten measurements for each tested material variant.

Additionally, to estimate the temperature changes in the Ni_3Al strips during hot rolling, a model of non-stationary heat conduction in a hot-rolled metal plate was formulated using the Comsol/FEM (finite element method) ver. 6.3 (Comsol, Burlington, MA, USA) calculation package (more details are shown elsewhere [32]).

3. Results and Discussion

The examined Ni_3Al-based intermetallic alloy in the initial stage (before the hot rolling) exhibited a single-phase fine-grained γ' secondary solid solution structure (Figure 1). The results of the EBSD analyses revealed the following features: (i) a dominant (approximately 95%) fraction of high angle grain boundaries (with a disorientation angle greater than 15° between neighboring grains) (Figure 1a), (ii) no visible crystallographic texture (Figure 1b), and (iii) a very low value of the GOS parameter (internal grain orientation spread $\leq 1°$), which is specific for a fully recrystallized material (Figure 1c).

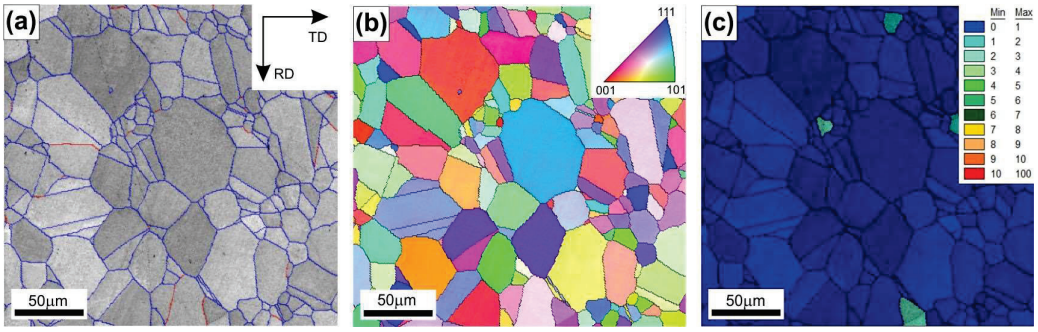


Figure 1. EBSD maps of Ni_3Al-based intermetallic alloy in the initial stage: (**a**) reconstruction of high angle boundaries (blue color) and low angle boundaries (red color), (**b**) IPF map with high angle boundaries ($\geq$15°) marked in black, and (**c**) internal grain orientation spread (GOS).

The GOS parameter (expressed in angular degrees) measures the scattering of the crystal lattice misorientation inside an individual grain. This parameter assumes that

plastic deformation in a metallic polycrystalline material is assisted by local changes in the crystal lattice orientation in the volume of each individual grain. This crystal lattice evolution is necessary to maintain the cohesion along the grain boundaries of a material subjected to a plastic deformation. For thermally activated processes (i.e., recovery and recrystallization), this parameter enables a quantitative assessment of the extent of these processes, as presented by Schwartzer et al. [33], Conde et al. [34], and Esin et al. [35]. In a polycrystalline structure, grains with a very low fraction of structural defects (typically after the recrystallization process, as in the case of the analyzed alloy in the initial state) show negligible differentiation of local crystallographic orientations, and the value of the GOS parameter is $\leq 1^{\circ}$. In turn, deformed grains with a high density of crystal defects show a high value of internal misorientation and, therefore, a high value (GOS > 1°) of this parameter.

The IQ parameter expresses a strong relationship between the degree of crystal structure defects (e.g., as a result of plastic deformation) and the quality (blurring) of the backscattered electron diffraction lines. The electron beam interacting with the surface layer of the sample is dispersed on the crystal lattice's defects, and the crystal planes' curvatures are "bent" due to plastic deformation. Consequently, the diffraction lines obtained from the subareas with a high density of lattice defects are blurred and visible as dark. According to Ku [26] and Alam et al. [36], IQ values can be correlated with the dislocation density, thereby providing a means of quantifying the internal strain energy and residual stress within a material. This correlation can be particularly valuable for understanding the effects of thermal treatments and mechanical processing on material properties [37].

Hot rolling of the Ni_3Al-based alloy to a strain value of 0.3 has a noticeable effect on both the microstructure (Figures 2–7) and hardness (Figure 8) of the tested material, depending on the applied temperature and the strain rate. The results of EBSD analyses (compare Figures 1–3) showed a limited extent of structural reconstruction. A comparative assessment of the GOS parameter for the material after the hot rolling showed a noticeable increase in its value compared to the starting material (the non-deformed one), with the presence of grains exhibiting a GOS >10° (compare Figures 1c, 2a,c,e, and 3a,c,e).

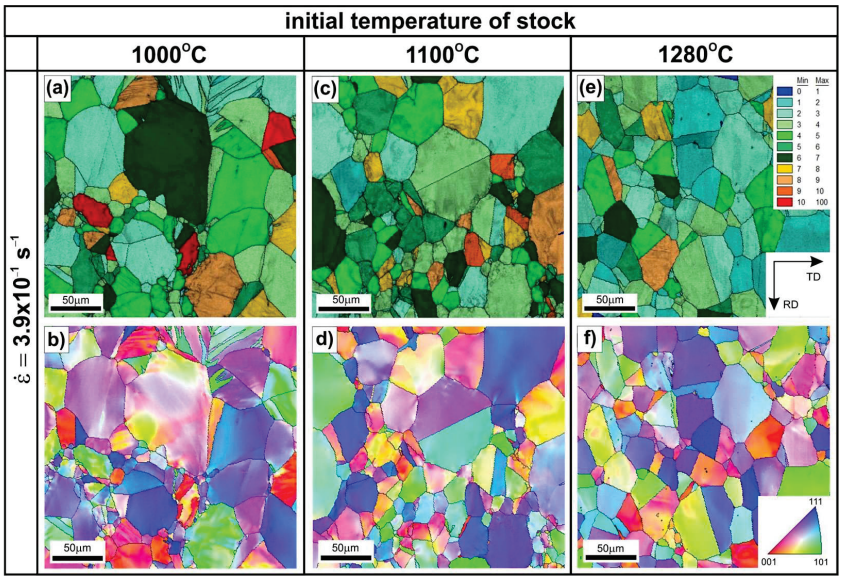


Figure 2. The grain orientation spread (GOS) maps (**a**,**c**,**e**) and IPF maps of with high angle boundaries ($\geq 15^{\circ}$) marked by black lines (**b**,**d**,**f**) of Ni_3Al-based strips after hot rolling up to 0.3 strain, at a strain rate $\dot{\varepsilon} = 3.9 \times 10^{-1}$ s^{-1}, at the initial temperatures of (**a**,**b**) 1000 °C, (**c**,**d**) 1100 °C, and (**e**,**f**) 1280 °C.

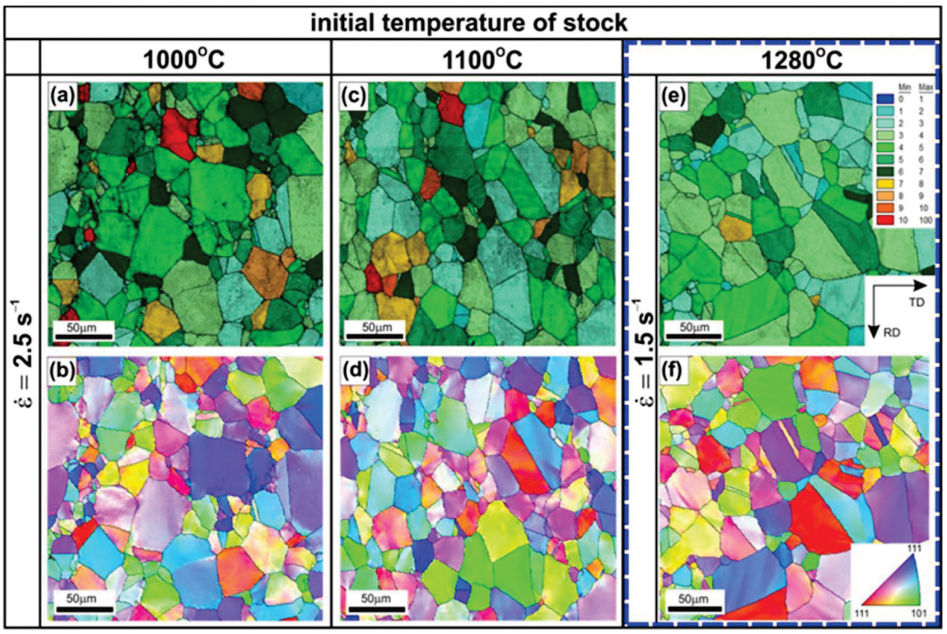


Figure 3. The grain orientation spread (GOS) maps (**a**,**c**,**e**) and the IPF maps with high angle boundaries (≥15°) marked by black lines (**b**,**d**,**f**) of Ni_3Al-based strips after hot rolling up to 0.3 strain, at a strain rate of $\dot{\varepsilon}$ = 2.5 s^{-1}, at the initial temperatures of (**a**,**b**) 1000 °C and (**c**,**d**) 1100 °C, and at a strain rate of $\dot{\varepsilon}$ = 1.5 s^{-1} at a temperature of 1280 °C—(**e**,**f**).

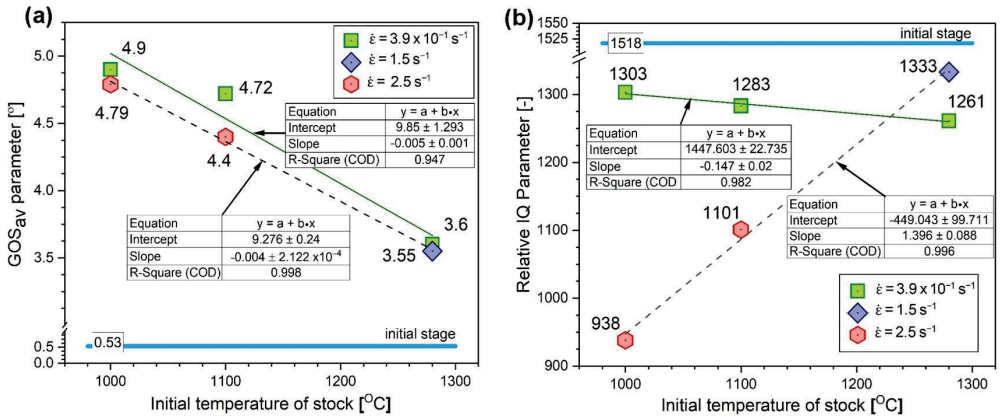


Figure 4. The results of quantitative EBSD analyses obtained for the investigated material: (**a**) average GOS values and (**b**) relative IQ values.

The quantitative evaluation of the averaged GOS parameter values clearly shows the impact of the rolling parameters on the extent of the structural reconstruction (Figure 4a). A much more significant influence of the deformation temperature was observed in relation to the strain rate. For the hot rolling process carried out at the high strain rate ($\dot{\varepsilon} \geq 1.5$ s^{-1}), a similar tendency was observed. An almost linear dependence of the average GOS value on the temperature was obtained (Figure 4a). The influence of a high strain rate on the course of DRX is also indicated by the analysis of the IQ parameter—for the value $\dot{\varepsilon} \geq 1.5$ s^{-1}—increased almost linearly with the deformation temperature (Figure 4b). The IQ parameter value did not show a significant dependence on the temperature due to the hot rolling at a strain rate $\dot{\varepsilon}$ of 3.9×10^{-1} s^{-1}, and the observed changes were insignificant (approximately 3%).

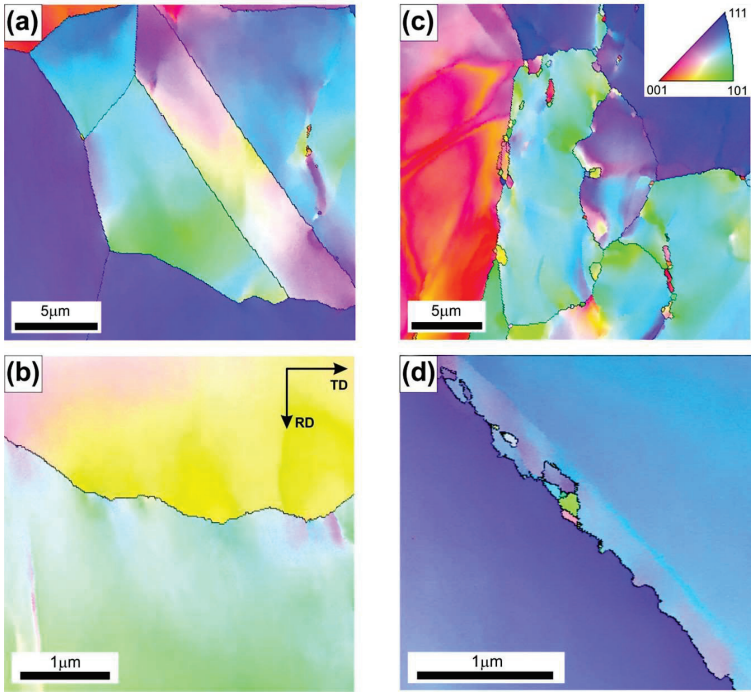


Figure 5. The EBSD IPF maps with high angle boundaries marked by black lines of Ni_3Al-based intermetallic alloy after hot rolling at T = 1000 °C at $\dot{\varepsilon}$ of (**a**,**b**) 3.9 × 10^{-1} s^{-1} and (**c**,**d**) 2.5 s^{-1}.

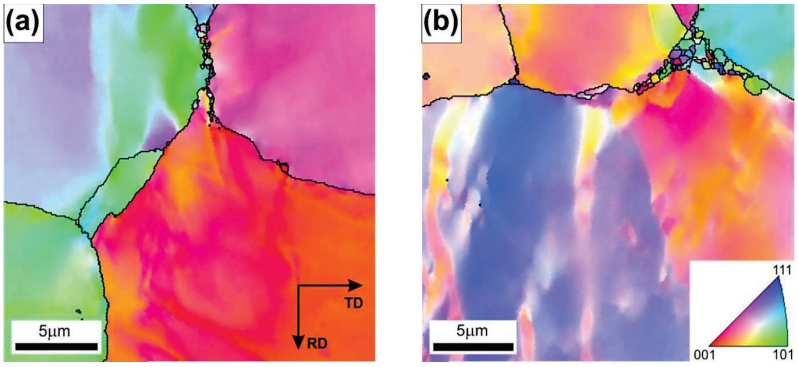


Figure 6. The EBSD IPF maps with high angle boundaries marked by black lines of Ni_3Al-based intermetallic alloy after hot rolling at T = 1100 °C and $\dot{\varepsilon}$ of (**a**) 3.9 × 10^{-1} s^{-1} and (**b**) 2.5 s^{-1}.

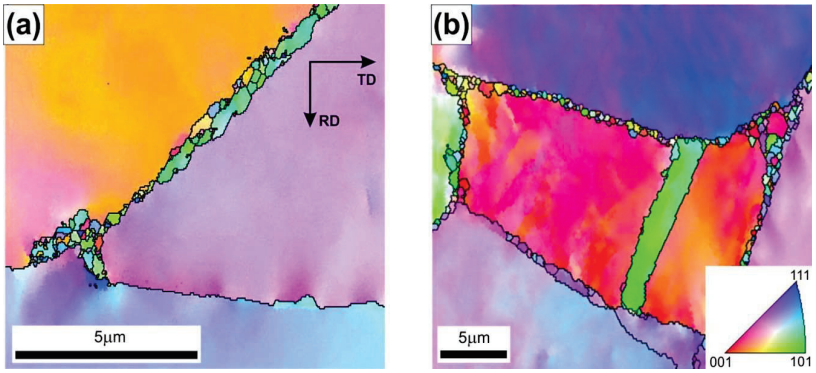


Figure 7. The EBSD IPF maps (high angle boundaries marked by the black lines) of Ni_3Al-based alloy after hot rolling at T = 1280 °C and at $\dot{\varepsilon}$ of (**a**) 3.9 × 10^{-1} s^{-1} and (**b**) 1.5 s^{-1}.

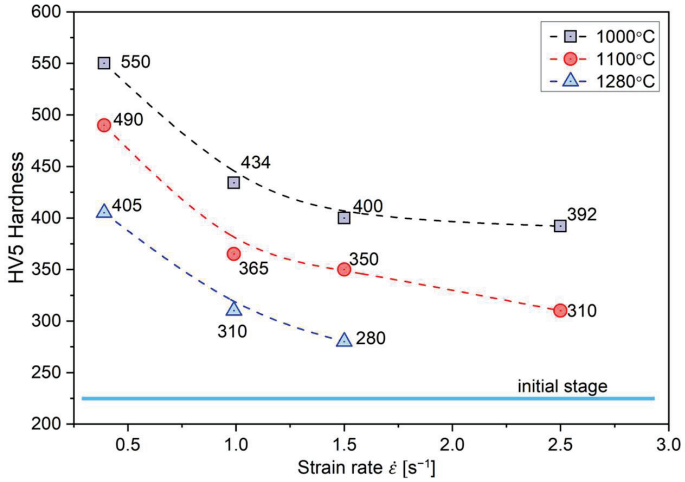


Figure 8. Influence of strain rate $\dot{\varepsilon}$ and initial temperature of stock on Vickers hardness of Ni_3Al-based strips (average values).

The results of more detailed EBSD analyses carried out by using higher magnifications revealed the locally occurring effects of thermally activated processes with intensity dependent on the values of the applied processing parameters (Figures 5–7). The material deformed at T = 1000 °C, with a strain rate of 3.9×10^{-1} s^{-1} (Figure 5a,b), did not show the presence of structural features that are typical for the DRX.

Increasing the strain rate at this temperature resulted in a growing fraction of very fine DRX grains (Figure 5). The serration of primary grain boundaries was observed (Figure 5c,d) in the sample hot-rolled at T = 1000 °C and at a strain rate of 2.5 s^{-1}. Analogous observations were reported by Ponge et al. [18], Sakai et al. [38], and Koundinya et al. [39], according to whom such structural features are specific to a deformation temperature lower than the critical temperature for initiating the dynamic recrystallization process. The serration of grain primary boundaries was also observed after the hot rolling at T = 1100 °C and at a strain rate of 9.9×10^{-1} s^{-1}.

Therefore, an increase in the initial strip temperature (up to 1100 °C) promotes the formation of new grains by the DRX in sites with the highest stress concentration, i.e., the triple-junctions of grain boundaries (Figure 6), as well as along the straight segments of primary grain boundaries. The share of grain boundary segments affected by the DRX increased with an increase in the strain rate, which was also reflected in the observed decrease in the strain strengthening (Figure 8).

After the hot rolling at T = 1280 °C, the material showed the largest share of DRXed grains both in the triple-junction grain boundaries and along the primary grain boundaries (Figure 7b). As reported by Bhatia et al. [17], the tendency to form necklace structures in the Ni_3Al-based alloys is caused by the tendency of planar slip and difficulty of cell formation inside the grains. Karnthaler et al. [40], Kruml et al. [41], and Wang et al. [42] have classified the Ni_3Al-based alloys as high stacking fault energy (SFE of approximately 240 mJ/m^2) materials. However, the results of studies by Jozwik et al. [23,25] and Polkowski et al. [43] indicate that the behavior of materials from this group under plastic deformation conditions and subsequent thermally activated processes is more similar to that of low SFE materials, as they are characterized by intensive strain hardening (resulting from hindered transverse slip of screw dislocations and a tendency to form flat stacking of dislocations on obstacles). Furthermore, as shown by Schindler et al. [15,16], the low SFE of Ni_3Al-based alloys decreases susceptibility to the DRX. Consequently, a higher strain concentration at grain boundaries is obtained leading to the DRX in the necklace structure. Such a microstructure

rebuilding, which is very similar to the model presented by Ponge et al. [18], was observed in the material after the hot rolling at a strain rate $\dot{\varepsilon}$ = 1.5 s^{-1} (Figure 7b).

Regardless of the applied hot rolling process parameters, the deformed material showed a slight increase in hardness as compared with the initial material, resulting from the increased stored deformation energy (Figure 8). Regardless of the applied hot rolling temperature, the increase in the strain rate resulted in a decrease in the strain hardening of the material. It was mostly visible in the case of the process conducted at the highest strain rate (i.e., 2.5 s^{-1}). The obtained results correspond to the discussed changes in the EBSD examined microstructure (Figures 2–7). In other words, the microstructural evolution is dominated by a dynamic recovery process with the DRX limited to some micro-areas. As the dynamic recovery creates low-energy dislocation systems (polygonal walls and subgrains), it effectively contributes to a reduction in the total energy stored.

The obtained results show that under the applied experimental conditions, a higher strain rate favors the microstructure evolution by both the DRX and dynamic recovery. This unusual relationship is probably due to the very low heat storage of the rolled Ni_3Al strips; that is, the initial thickness was 1.12 mm (for comparison, the smallest dimension of the Ni_3Al samples analyzed in the literature is 8 mm), which, in combination with cold work rolls, resulted in greater heat losses, leading to a significant reduction in the actual material temperature during the deformation process. Consequently, a higher strain rate corresponded to a relatively higher process temperature.

To estimate the possible temperature changes in the Ni_3Al strips during the hot rolling, as well as to verify the obtained research results, a non-stationary model of heat conduction in a hot-rolled metal plate was formulated.

Regardless of the applied hot rolling process parameters, the deformed material showed a significant increase in hardness as compared with the initial material, resulting from the increased stored deformation energy (Figure 8). Regardless of the applied hot rolling temperature, the increase in the strain rate resulted in a decrease in the strain hardening of the material. It was mostly visible in the case of the process conducted at the highest strain rate (i.e., 2.5 s^{-1}). The obtained results correspond to the discussed changes in the EBSD examined microstructure (Figures 2–7). In other words, the microstructural evolution is dominated by a dynamic recovery process with the DRX limited to some micro-areas. As the dynamic recovery creates low-energy dislocation systems (polygonal walls and subgrains), it effectively contributes to a reduction in the total energy stored.

3.1. A Non-Stationary Heat Conduction Model in a Strip

The primary purpose of the modeling was to qualitatively determine the temperature changes. For this purpose, the issue was simplified to a model of a heat source moving across the surface of the component. Thus, a contact surface having a linear dimension d was set as the source of heat and, at the same time, the heat receiver (Figure 9).

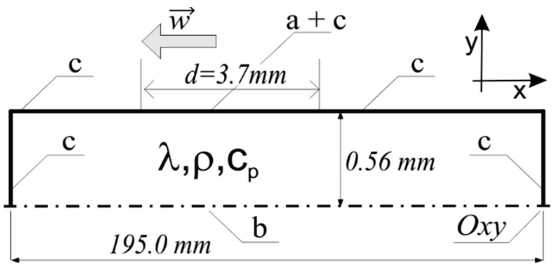


Figure 9. Schematic diagram of the numerical model of heat conduction in a rolled plate (description in the text).

To determine the temperature changes and strain distribution, the presence of the following phenomena were analyzed [44]: (i) the heat conduction in the workpiece to be deformed (i.e., the Ni_3Al strip); (ii) convective and radiative heat losses from the workpiece surface to the environment; (iii) the heat conduction in the machining tool (roller); (iv) the contact heat transfer resistance between the workpiece and the tool; (v) the friction between the workpiece and the roller surface contributing to the surface heat source; (vi) the elastic deformation of the workpiece; (vii) the plastic deformation constituting volumetric heat sources, (viii) the elastic relaxation of the material as it comes off the roller; and (ix) the change in the relative velocity of movement of the workpiece and the roller due to deformation. In the presented simplified model of a moving heat source, only phenomena (i)–(iv) were directly taken into account. A phenomenon that is usually overlooked at this stage of simplification is the volumetric shrinkage caused by thermal expansion.

The relatively large value of the ratio of the wafer width to its thickness provides a justification for adopting a simplified two-dimensional heat conduction model. A geometrical scheme of the model is illustrated in Figure 9.

Thus, the issue was reduced to a two-dimensional model of a non-stationary heat transfer in a plate with dimensions of 195 mm $\times$ 0.56 mm, subjected to a surface moving heat source (surface a in Figure 9) [45]. A symmetric condition in the plane containing the Ox axis was assumed (surface b in Figure 9), while the convection and radiation losses were considered for other surfaces (surface c in Figure 9). Due to the lack of data on the constitutive model, the volumetric heat sources accompanying plastic deformation, as well as the surface frictional heat source, were omitted. An evaluation of the literature data shows that despite the noticeable impact of these effects, they do not play a dominant role in shaping the temperature distribution at a relatively high initial temperature of the hot-machined workpiece (i.e., Ni_3Al strip).

The mathematical equations describing the considered model (in the Oxy coordinate system, Figure 9), are as follows:

- equation for transient heat conduction:

$$\rho c_p \frac{\partial T}{\partial \tau} + \nabla(-\lambda \nabla T) = 0; \tag{1}$$

- initial homogeneous condition:

$$T(x, y, \tau = 0) = T_0; \tag{2}$$

- boundary condition for the adiabatization of the horizontal center symmetry surface of the plate (surface marked as "b" in Figure 9):

$$\left.\frac{\partial T}{\partial y}\right|_S = 0; \tag{3}$$

- boundary conditions of convective and radiative heat loss (surfaces marked "c" in Figure 9, "n" is a normal direction to surfaces c):

$$-\lambda \left.\frac{\partial T}{\partial n}\right|_S = \alpha \cdot (T|_S - T_{amb}) + \varepsilon\, \sigma \left[(T|_S)^4 - {T_{amb}}^4\right]; \tag{4}$$

- the displacement contact zone is modeled by the additional contact loss (surface marked as "a + c" in Figure 9) of the plate surface with the surface of the cylinder at ambient temperature, with the value of the thermal contact resistance r_{cont}:

$$-\lambda \left.\frac{\partial T}{\partial y}\right|_S = h_r \cdot (T|_S - T_{amb}) = \frac{1}{r_{cont}} \cdot (T|_S - T_{amb}) \text{ for } -w \cdot \tau < x < -w \cdot \tau + d \quad (5)$$

The last boundary condition was applied in superposition with Equation (4). The equation describes contact with the cylinder surface excluding radiation losses and convective losses. On the other hand, in the considered case, these losses account for only approximately 2% of the losses caused by a heat transfer through the contact zone. Because determination of the value of thermal contact resistance is subjected to a larger error and because of the need for computational optimization of the numerical model, the arrangement of conditions (4) and (5) remained unchanged.

3.2. Numerical Model

The tools of the Comsol/M FEA (finite element method) calculation package were used to build the numerical model. The temperature dependence of the material parameters of the analyzed alloy was considered (Table 1) by extrapolating data from the studies by Panas et al. [46] and Terpilowski [47]. Table 2 presents the values of the parameters defining the boundary conditions developed based on the analysis of the criterion relations of the heat transfer issue and the data contained in the aforementioned monograph by Lenard et al. [43]. Based on these data, the value of the equivalent heat transfer coefficient in the contact resistance zone was assumed to be 13,000 W $\times$ m^{-2} $\times$ K^{-1}, which corresponds to the value of r_{cont} given in Table 2.

Table 1. Material properties adopted for the calculations based on extrapolation of the results of measurements by Panas [46] and Terpilowski [47] for the Ni-22.1Al-0.26Zr-0.1B (at.%) alloy.

Temperature	Specific Heat	Relative Elongations	Density	Thermal Diffusivity	Thermal Conductivity
t [°C]	c_p [J·kg^{-1}·K^{-1}]	ε [mm·m^{-1}]	ρ [kg·m^{-3}]	a [mm^2·s^{-1}]	λ [W·m^{-1}·K^{-1}]
0	466	−0.31	7592	4.27	15.1
100	482	0.91	7564	4.75	17.3
200	499	2.21	7535	5.24	19.7
300	515	3.58	7504	5.73	22.1
400	532	5.02	7472	6.21	24.7
500	548	6.54	7438	6.70	27.3
600	564	8.13	7403	7.18	30.0
700	581	9.80	7366	7.67	32.8
800	597	11.54	7328	8.16	35.7
900	614	13.35	7289	8.64	38.7
1000	630	15.23	7249	9.13	41.7
1100	647	17.19	7207	9.61	44.8
1200	663	19.22	7164	10.10	48.0
1300	680	21.33	7120	10.59	51.2

Table 2. The values of parameters characterizing the initial and boundary conditions adopted for the calculations.

Temperature		Heat Transfer Coefficient	Thermal Contact Surface Resistance	Surface Emissivity
t [°C]	T [K]	α [W·m^{-2}·K^{-1}]	r_{cont} [m^2·K·W^{-1}]	ε [-]
20	293	10	7.69×10^{-5}	0.7

The analysis considered the realistic conditions of the rolling process, including the thermal exchange between the sample and its environment during the 1 s period from when the sample was removed from the furnace to when it came into contact with the rollers. Consequently, the initial temperature of the stock was reduced, i.e., from 1280 °C of the initial temperature of stock to 1210 °C, from 1100 °C to 1056 °C, and from 1000 °C to 967 °C. Regular rectangular finite elements were used for calculations. A division of eight elements was used in the vertical direction, and 780 elements were used in the horizontal direction. The horizontal division density was set as 1 mm. Numerical simulations of the heat conduction process were performed with a constant time step. For the highest strain rate (i.e., 2.5 s^{-1}), the time step was 0.0015 s, and for the lowest (i.e., 3.9×10^{-1} s^{-1}), it was 0.0075 s.

To visualize the obtained calculation results, control points were defined at the rolled band side surface and core (Figure 10):

- In the plane perpendicular to the rolling direction, core (points A, C, and E) and contact surface of the rollers (points B, D, and F).
- In the plane parallel to the rolling direction, the beginning (points A and B), center (points C and D), and the end of the sample (points E and F).

In terms of the 2D nature of the model, the points represent lines parallel to the roller axis. In the model, it was assumed that points A and B were located 10 mm from the start of the sample, points C and D were positioned at the center of the sample, and points E and F were placed 10 mm before the sample's end.

The results of the modeling showed a significant effect of the strain rate on the change in the material temperature during the rolling process. As expected, the most significant changes in each of the analyzed cases were observed at the surface of the sample directly in contact with the rollers (points: B, D, and F, respectively). After an initial decrease in the temperature of the band, a slight increase was observed because of the heat transmission from the core of the material and the heating of the rollers. Owing to its higher heat capacity, the core point (i.e., points A, C, and E) turned out to be slightly more temperature stable, and the observed changes occurred with significantly lower intensity (Figure 10).

The greatest cooling of the rolled band was observed for the highest initial temperature of stock, i.e., 1280 °C (reduced before contact with the rollers to 1210 °C as a consequence of the heat exchange with the environment) and the lowest strain rate (i.e., $\dot{\varepsilon} = 3.9 \times 10^{-1}$ s^{-1}). Under these conditions, the temperature gradient was the most significant, and the contact time between the rollers and the workpiece material was the longest. Consequently, the temperature in the core of the material decreased by approximately 280 °C at the beginning and 410 °C at the end of the sample. Notably, despite the largest temperature change among the analyzed cases, its value remained above 800 °C throughout the deformation process. The increase in the strain rate for this processing temperature resulted in a significantly higher value of the temperature during deformation (i.e., above 1070 °C for $\dot{\varepsilon} = 1.5$ s^{-1}) owing to the shorter contact time of the rollers with the material. The analyzed temperature changes correspond with the observed microstructural restoration by dynamic recrystallization, the contribution of which increases with the increasing strain rate (Figure 7).

At the initial temperature of the stock to 1100 °C, which was reduced to 1056 °C by losses related to heat exchange with the environment, and the strain rate $\dot{\varepsilon} = 3.9 \times 10^{-1}$ s^{-1}, there was less cooling of the material, by approximately 250 °C at the beginning and 340 °C at the end of rolling, respectively. However, it is worth noting that, in this case, the temperature decreased to approximately 800 °C at the beginning and 720 °C at the end of the band. As shown by the studies of Prasad et al. [12], Schindler et al. [15,16],

and Jóźwik et al. [19,24], this value was not sufficient to initiate recrystallization processes. Consequently, for these rolling conditions (i.e., 1100 °C of the stock and $\dot{\varepsilon} = 3.9 \times 10^{-1}$ s^{-1}), only a slight visible rebuilding effect in the microstructure by dynamic recrystallization was observed (Figure 6), with a simultaneous reduction in the strengthening of the materials under these conditions (Figure 8). Increasing the strain rate $\dot{\varepsilon}$ to 2.5 s^{-1}, with an initial stock temperature of 1100 °C, resulted in a reduced heat transfer with the rollers and consequently a higher material temperature in the core during the deformation process, which was approximately 1010 °C at the beginning and 990 °C at the end of the band. As with the deformation at highest initial temperature of stock (i.e., 1280 °C), dynamic recrystallization processes are most evident for the highest strain rate, which provides the shortest contact time between the rollers and the material (Figure 4).

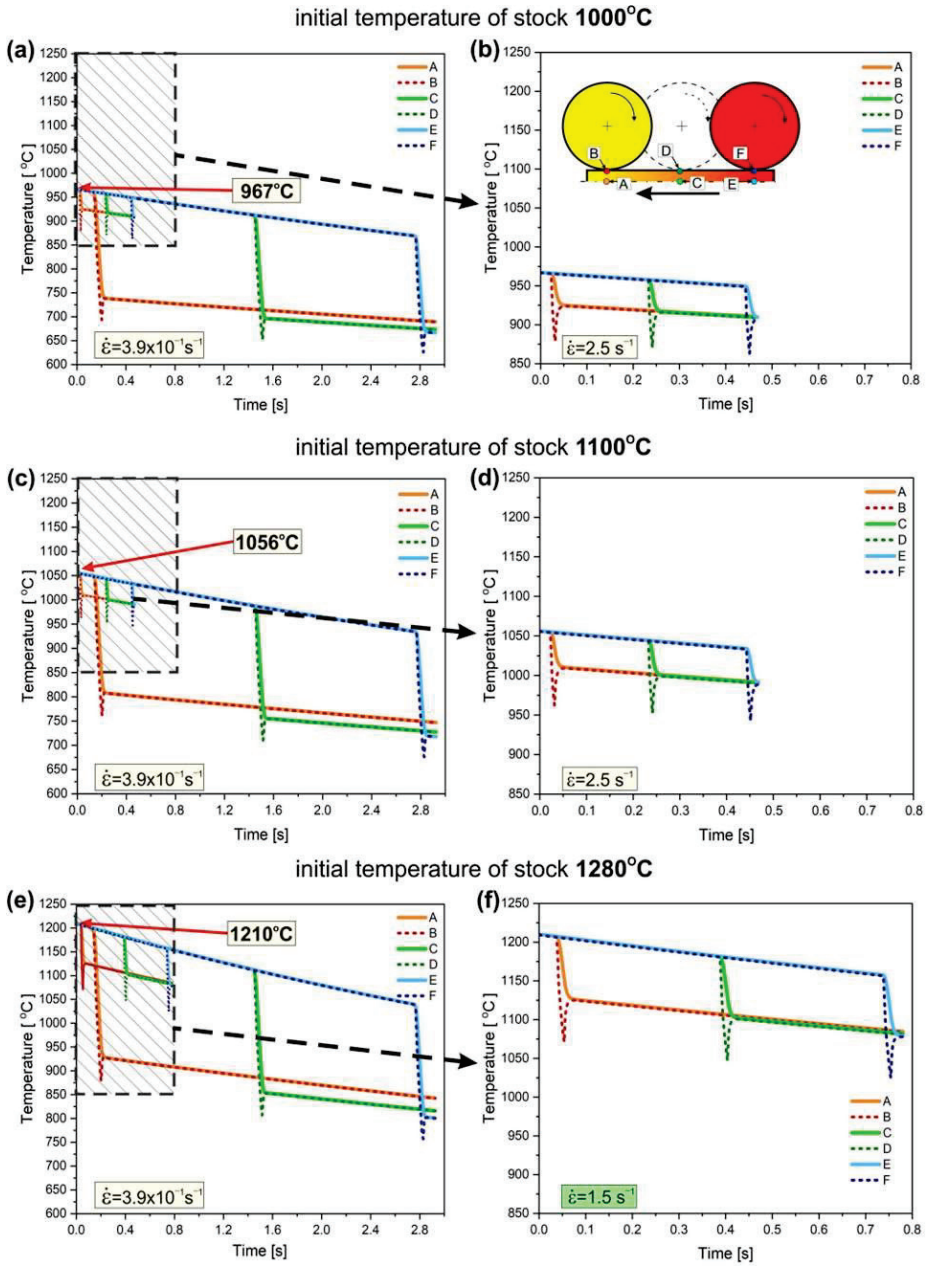


Figure 10. The course of temperature changes obtained from the numerical model at individual points of the rolled strip during hot rolling ((**a**,**c**,**e**)—core, (**b**,**d**,**f**)—surface).

A further decrease in the temperature of the stock down to 1000 °C (reduced to 967 °C by losses related to heat exchange with the environment) and the strain rate $\dot{\varepsilon} = 3.9 \times 10^{-1}$ s^{-1} resulted in a temperature decrease to approximately 740 °C at the beginning and 670 °C at the end of the band. As previously mentioned, this temperature was definitely too low to initiate the dynamic recrystallization process. As a result, no visible effects of the microstructure evolution by dynamic recrystallization were observed under these rolling conditions (Figure 5). Simultaneously, the level of strengthening was the highest among all the analyzed process conditions (Figure 8). Increasing the strain rate $\dot{\varepsilon}$ to 2.5 s^{-1}, with a constant temperature of stock (i.e., 1000 °C), resulted in a higher material temperature in the core during the deformation process: 925 °C at the beginning and 910 °C at the end of the band.

Similar to the deformation processes realized at 1280 °C and 1100 °C, the dynamic recrystallization process was mostly observed for the material processed at the highest strain rate $\dot{\varepsilon}$ because of the lower undercooling and higher rolling temperature (Figure 10).

Finally, considering the corrected temperature in the core of the material (obtained from the model, Figure 10, point C), an almost linear effect on strengthening was observed (Figure 11). It is a macroscopic determinant of the intensity of the heat-activated processes of the structure restoration (recovery and recrystallization), which consequently fully correspond to the analysis of EBSD results presented above (Figures 4–6).

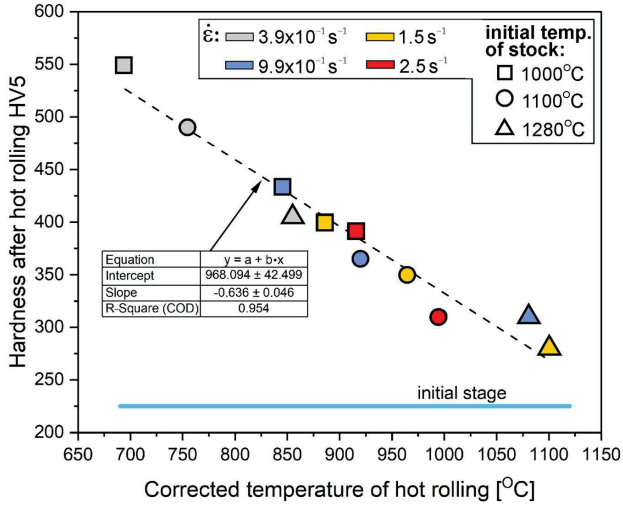


Figure 11. Effect of the numerical modeling-determined temperature in the core of Ni_3Al strips' center (Figure 10, point C) during rolling on HV5 hardness, taking into account the rolling process parameters (average values).

4. Summary and Conclusions

The conditions of the hot rolling process applied in this study noticeably affect the microstructure of Ni_3Al strips by inducing local dynamic recrystallization phenomena. Simultaneously, the hot deformation processing induces an intensive increase in strengthening. The observed behavior suggests the potential for hybrid process development, which warrants further investigation. Such an increase in strength suggests that a significant part of the strain energy was stored in the material during hot forming, which demonstrates the limited extent of the structural evolution through dynamic restoration processes (recovery and recrystallization). The unusual effect of the strain rate on the aforementioned microstructure rebuilding processes was verified using a model of non-stationary heat conduction. Based on the obtained modeling results, a significant effect of the strain rate on the temperature of the material during rolling was found. The low heat capacity of

Ni_3Al strips with an initial thickness of 1.12 mm combined with cold working rolls, caused a significant reduction in the actual temperature of the deformation process. Consequently, a higher strain rate $\dot{\varepsilon}$ corresponds to a higher material temperature during deformation.

Considering some limitations of the model adopted in this study (i.e., no in situ temperature measurement of the material temperature during deformation, the use of estimated thermal contact resistance values, and the assumption of uniform initial conditions across the strip), the authors plan to verify them in real conditions.

Author Contributions: Conceptualization, P.J. and Z.B.; methodology, investigation, and data curation, P.J., W.P., A.J.P., and Z.B.; writing—original draft preparation, P.J., Z.B., and A.J.P.; writing—review and editing, P.J., Z.B., W.P., and A.J.P.; supervision, project administration, funding acquisition, P.J. All authors have read and agreed to the published version of the manuscript.

Funding: This research was funded by the statutory sources of the Department of Structural Materials, Military University of Technology (project no. UGB 531-000032-W900-22).

Institutional Review Board Statement: Not applicable.

Informed Consent Statement: Not applicable.

Data Availability Statement: The data presented in this study are available on request from the corresponding author due to privacy.

Acknowledgments: The authors would like to thank for the opportunity to use the software available at the Air Force Institute of Technology in Warsaw, Poland. The authors also express their gratitude to Ivo Schindler (VSB—Technical University of Ostrava) for his assistance in the research process.

Conflicts of Interest: The authors declare no conflicts of interest.

Abbreviations

The following abbreviations are used in this manuscript:

$\dot{\varepsilon}$	Strain rate
DRX	Dynamic recrystallization
EBSD	Backscattered diffraction detector
IPF	Inverse pole figure
GOS	Grain orientation spread parameter
IQ	Image quality parameter
SFE	Stacking fault energy
ρ	Density
c_p	Specific heat
T	Temperature in Kelvin
t	Temperature in °C
T_{amb}	Ambient temperature
τ	Time
λ	Thermal conductivity
x	Horizontal coordinate
y	Vertical coordinate
α	Heat transfer coefficient
ε	Surface emissivity
σ	Stefan–Boltzmann constant
h_r	Thermal contact heat transfer coefficient
r_{cont}	Thermal contact surface resistance

References

1. Sikka, V.K. Commercialization Status of Ni_3Al-Based Alloys. *MRS Proc.* **1996**, *460*, 15. [CrossRef]
2. Sikka, V.K.; Deevi, S.C.; Viswanathan, S.; Swindeman, R.W.; Santella, M.L. Advances in Processing of Ni_3Al-Based Intermetallics and Applications. *Intermetallics* **2000**, *9–11*, 1329–1337. [CrossRef]
3. Jozwik, P.; Polkowski, W.; Bojar, Z. Applications of Ni_3Al Based Intermetallic Alloys—Current Stage and Potential Perceptivities. *Materials* **2015**, *8*, 2537–2568. [CrossRef]
4. Jarosz, M.; Socha, R.; Jóźwik, P.R.; Sulka, G. Amperometric Glucose Sensor Based on the $Ni(OH)_2/Al(OH)_4-$ Electrode Obtained from a Thin Ni_3Al Foil. *Appl. Surf. Sci.* **2017**, *408*, 96–102. [CrossRef]
5. Sahare, S.; Santhosh, K.A.; Bhave, T.; Abhyankar, A. Novel Cost-Effective and Electrocatalytically Active Intermetallic Nickel Aluminide Counter Electrode for Dye Sensitized Solar Cells. *Nano Express* **2020**, *1*, 030029. [CrossRef]
6. Sun, Y.; Yuan, S. Optimization of Processing Parameter and Mechanical Response Analysis of Advanced Heterogeneous Laminated Composites Using Ni/Al Foils by In Situ Reaction Synthesis. *Materials* **2022**, *15*, 8892. [CrossRef]
7. Tiwari, S.K.; Rao, A.U.; Kharb, A.S.; Chawla, A.K.; Avasthi, D.K. A Review of Mechanical and Tribological Properties of Ni_3Al-Based Coatings-Synthesis and High-Temperature Behavior. *Phys. Scr.* **2023**, *98*, 072001. [CrossRef]
8. Wang, J.; Han, W.; Luo, H.; Li, S. Hot Deformation Behavior of Ni_3Al-Based Alloy MX246A. *J. Iron Steel Res. Int.* **2014**, *21*, 264–268. [CrossRef]
9. Wu, Y.; Liu, Y.; Li, C.; Xia, X.; Wu, J.; Li, H. Effect of Initial Microstructure on the Hot Deformation Behavior of a Ni_3Al-Based Alloy. *Intermetallics* **2019**, *113*, 106584. [CrossRef]
10. Zhong, J.; Xu, Z.; Liu, B.; Xu, Q.; Sun, C.; Wu, J. Deformation Behavior and Constitutive Model for High Temperature Compression of a Newly Type of Ni_3Al-based Superalloy. *Mater. Werkst.* **2019**, *50*, 1094–1105. [CrossRef]
11. Zhong, J.; Sun, C.; Wu, J.; Li, T.; Xu, Q. Study on High Temperature Mechanical Behavior and Microstructure Evolution of Ni_3Al-Based Superalloy JG4246A. *J. Mater. Res. Technol.* **2020**, *9*, 6745–6758. [CrossRef]
12. Prasad, Y.V.R.K.; Sasidhara, S.; Sikka, V.K. Characterization of Mechanisms of Hot Deformation of As-Cast Nickel Aluminide Alloy. *Intermetallics* **2000**, *8*, 987–995. [CrossRef]
13. Guo, J.T.; Sheng, L.Y.; Xie, Y.; Zhang, Z.X.; Ovcharenko, V.E.; Ye, H.Q. Microstructure and Mechanical Properties of Ni_3Al and Ni_3Al–1B Alloys Fabricated by SHS/HE. *Intermetallics* **2011**, *19*, 137–142. [CrossRef]
14. Sheng, L.; Du, B.; Zan, S.; Jiao, J. Characterization of Ni_3Al Alloy Fabricated by Thermal Explosion and Hot Extrusion Process. *Mater. Sci.* **2018**, *24*, 393–398. [CrossRef]
15. Schindler, I.; Macháček, J.; Kliber, J.; Greger, M.; Kursa, M. Hot Deformation Behaviour and Grain Refinement of Intermetallic Compound Ni_3Al. *J. Mater. Process. Technol.* **1996**, *60*, 575–580. [CrossRef]
16. Schindler, I.; Macháček, J.; Spittel, M. Recrystallization in As-Cast Polycrystalline Intermetallic Compound Ni_3Al. *Intermetallics* **1999**, *7*, 83–87. [CrossRef]
17. Bhatia, M.L. Recrystallisation—Some Applied Aspects. *Prog. Mater. Sci.* **1997**, *42*, 59–77. [CrossRef]
18. Ponge, D.; Gottstein, G. Necklace Formation during Dynamic Recrystallization: Mechanisms and Impact on Flow Behavior. *Acta Mater.* **1998**, *46*, 69–80. [CrossRef]
19. Wang, S.; Hu, Z.; Zeng, W.; Huang, J.; Xiao, L.; Zhou, H. Improving ductility of Ti–6Al–4V alloy via rotational hot rolling. *Vacuum* **2021**, *191*, 110404. [CrossRef]
20. Pustovoytov, D.; Pesin, A.; Tandon, P. Asymmetric (Hot, Warm, Cold, Cryo) Rolling of Light Alloys: A Review. *Metals* **2021**, *6*, 956. [CrossRef]
21. Arbuz, A.; Kawalek, A.; Panichkin, A.; Ozhmegov, K.; Popov, F.; Lutchenko, N. Using the Radial Shear Rolling Method for Fast and Deep Processing Technology of a Steel Ingot Cast Structure. *Materials* **2023**, *16*, 7547. [CrossRef] [PubMed]
22. Wang, T.; Liu, W.; Liu, Y.; Wang, Z.; Ignatov, A.V.; Huang, Q. Formation mechanism of dynamic multi-neutral points and cross shear zones in corrugated rolling of Cu/Al laminated composite. *J. Mater. Process. Technol.* **2021**, *295*, 117157. [CrossRef]
23. Jóźwik, P.; Bojar, Z. Analysis of Grain Size Effect on Tensile Properties of Ni_3Al—Based Intermetallic Strips. *Arch. Metall. Mater.* **2007**, *52*, 321–327.
24. Jóźwik, P. Mechanical Properties and Cracking Process of Ni_3Al-Based Intermetallic Alloys. Ph.D Thesis, Military University of Technology, Warsaw, Poland, 2004.
25. Jóźwik, P.; Bojar, Z. Influence of Heat Treatment on the Structure and Mechanical Properties of Ni_3Al—Based Alloys. *Arch. Metall. Mater.* **2010**, *55*, 271–279.
26. Ku, T.-W. Numerical and Experimental Investigations on Residual Stress and Hardness within a Cold Forward Extruded Preform. *Materials* **2023**, *16*, 2448. [CrossRef]
27. Nowak, W.J. The Use of Ion Milling for Surface Preparation for EBSD Analysis. *Materials* **2021**, *14*, 3970. [CrossRef]
28. Suzuki, S. Features of Transmission EBSD and Its Application. *JOM* **2013**, *65*, 1254–1263. [CrossRef]

29. Nowakowski, P.; Schlenker, J.; Ray, M.; Fischione, P. Sample Preparation Using Broad Argon Ion Beam Milling for Electron Backscatter Diffraction (EBSD) Analysis. *Microsc. Microanal.* **2016**, *22*, 12–13. [CrossRef]
30. Nowakowski, P.; Wiezorek, J.; Spinelli, I.; Ray, M.; Fischione, P. Elastic and Plastic Strain Measurement Using Electron Backscatter Diffraction Technique: The Influence of Sample Preparation. *Microsc. Microanal.* **2019**, *25*, 534–535. [CrossRef]
31. *Standard PN-EN ISO 6507-1:2024-04*; Introducing the Standard ISO 6507-1:2023. Polish Committee for Standardization: Warsaw, Poland, 2024.
32. Comsol. Available online: https://www.comsol.com (accessed on 14 March 2025).
33. Schwarzer, R.A.; Field, D.P.; Adams, B.L.; Kumar, M.; Schwartz, A.J. Present State of Electron Backscatter Diffraction and Prospective Developments. In *Electron Backscatter Diffraction in Materials Science*; Schwartz, A.J., Kumar, M., Adams, B.L., Field, D.P., Eds.; Springer: Boston, MA, USA, 2009; pp. 1–20. ISBN 978-0-387-88135-5.
34. Conde, F.F.; Ribamar, G.G.; Escobar, J.D.; Jardini, A.L.; Oliveira, M.F.; Oliveira, J.P.; Avila, J.A. EBSD-Data Analysis of an Additive Manufactured Maraging 300 Steel Submitted to Different Tempering and Aging Treatments. *Mater. Charact.* **2023**, *203*, 113064. [CrossRef]
35. Esin, V.A.; François, M.; Belkacemi, L.T.; Irmer, D.; Briez, L.; Proudhon, H. Effect of Microstructure on Fatigue Crack Deviation in AA2050-T84. *Mater. Sci. Eng. A* **2022**, *858*, 144120. [CrossRef]
36. Alam, M.K.; Mehdi, M.; Urbanic, R.J.; Edrisy, A. Electron Backscatter Diffraction (EBSD) Analysis of Laser-Cladded AISI 420 Martensitic Stainless Steel. *Mater. Charact.* **2020**, *161*, 110138. [CrossRef]
37. Radwański, K. Application of FEG-SEM and EBSD Methods for the Analysis of the Restoration Processes Occurring During Continuous Annealing of Dual-Phase Steel Strips. *Steel Res. Int.* **2015**, *86*, 1379–1390. [CrossRef]
38. Sakai, T.; Belyakov, A.; Kaibyshev, R.; Miura, H.; Jonas, J.J. Dynamic and Post-Dynamic Recrystallization under Hot, Cold and Severe Plastic Deformation Conditions. *Prog. Mater. Sci.* **2014**, *60*, 130–207. [CrossRef]
39. Koundinya, N.T.B.N.; Karnati, A.K.; Sahadevan, A.; Murty, S.V.S.N.; Kottada, R.S. Assessment of the Post-Dynamic Recrystallization Effects on the Overall Dynamic Recrystallization Kinetics in a Ni-Base Superalloy. *J. Alloys Compd.* **2023**, *930*, 167412. [CrossRef]
40. Karnthaler, H.P.; Mühlbacher, E.T.; Rentenberger, C. The Influence of the Fault Energies on the Anomalous Mechanical Behaviour of Ni_3Al Alloys. *Acta Mater.* **1996**, *44*, 547–560. [CrossRef]
41. Kruml, T. From Dislocation Cores to Strength and Work-Hardening: A Study of Binary Ni_3Al. *Acta Mater.* **2002**, *50*, 5091–5101. [CrossRef]
42. Wang, J.; Sehitoglu, H. Dislocation Slip and Twinning in Ni-Based L12 Type Alloys. *Intermetallics* **2014**, *52*, 20–31. [CrossRef]
43. Polkowski, W.; Jóźwik, P.; Karczewski, K.; Bojar, Z. Evolution of Crystallographic Texture and Strain in a Fine-Grained Ni_3Al (Zr, B) Intermetallic Alloy during Cold Rolling. *Arch. Civ. Mech. Eng.* **2014**, *14*, 550–560. [CrossRef]
44. Lenard, J.G.; Pietrzyk, M. Rolling Process Modelling. In *Numerical Modelling of Material Deformation Processes*; Hartley, P., Pillinger, I., Sturgess, C., Eds.; Springer: London, UK, 1992; pp. 274–302. ISBN 978-1-4471-1747-6.
45. Panas, A.J. Moving Heat Sources. In *Encyclopedia of Thermal Stresses*; Hetnarski, R., Ed.; Springer: Berlin/Heidelberg, Germany, 2014.
46. Panas, A.J.; Traczyk, P.; Panas, J.J. *Research on the Thermal and Physical Properties of Alloys Based on the Ni3Al Intermetallic Phase*; MUT: Warsaw, Poland, 2010; *unpublished work*.
47. Terpiłowski, J. *Studies on the Thermal Diffusivity of Ni3Al Nanomaterials*; MUT: Warsaw, Poland, 2010; *unpublished work*.

Disclaimer/Publisher's Note: The statements, opinions and data contained in all publications are solely those of the individual author(s) and contributor(s) and not of MDPI and/or the editor(s). MDPI and/or the editor(s) disclaim responsibility for any injury to people or property resulting from any ideas, methods, instructions or products referred to in the content.

materials

MDPI

Article

Microstructural Stability and High-Temperature Mechanical Behavior of Al–Ni–Zr Alloy Strengthened by $L1_2$-Al_3Zr Precipitates

Jan Šmalc [1], Adam Zaky [2], Boštjan Markoli [2] and Roman Šturm [1,*]

[1] Faculty of Mechanical Engineering, University of Ljubljana, Aškerčeva 6, 1000 Ljubljana, Slovenia; jan.smalc@fs.uni-lj.si
[2] Faculty of Natural Sciences and Engineering, University of Ljubljana, Aškerčeva 12, 1000 Ljubljana, Slovenia; adam.zaky@ntf.uni-lj.si (A.Z.); bostjan.markoli@ntf.uni-lj.si (B.M.)
* Correspondence: roman.sturm@fs.uni-lj.si; Tel.: +386-14771203

Abstract: Aluminum alloys based on the eutectic Al–Ni system are a promising class of lightweight materials for applications at elevated temperatures owing to the thermal stability of the eutectic Al_3Ni phase. In this study, the eutectic Al–Ni alloy was modified by the addition of 0.6 wt.% Zr to enhance the α_{Al} matrix by precipitation strengthening. The alloys were cast and subjected to T5 heat treatment followed by long-term isothermal aging at 350 °C. A comprehensive study was carried out to evaluate the evolution of microstructure, microhardness and mechanical performance over time. The formation of fine, coherent $L1_2$-Al_3Zr precipitates contributed to significant strengthening, as reflected by a ~60% increase in microhardness and an approximately twofold improvement in room temperature (RT) yield strength. A TEM analysis of the $L1_2$-Al_3Zr precipitates showed relatively good thermal stability after 30 days. Despite the improved mechanical properties at room temperature, the alloy did not retain this improvement when tested at 300 °C. Nevertheless, these results provide a comprehensive insight into the aging and thermal stability of Al–Ni–Zr alloys.

Keywords: aluminum–nickel eutectic; precipitation strengthening; $L1_2$-Al_3Zr precipitates; microhardness; accelerated creep test

1. Introduction

In the search for a castable aluminum alloy that can withstand high temperatures (i.e., above 200–300 °C) [1], binary alloys from Al–Ni, Al–Ce and Al–La systems have attracted increasing research interest [2–7]. The Al–Ni binary system has a eutectic composition at 6.1 wt.% Ni, and this eutectic alloy exhibits desirable properties such as good castability and resistance to hot-tearing [8,9]. During solidification, the eutectic alloy from the Al–Ni system forms eutectic colonies consisting of the Al_3Ni eutectic phase, which is characterized by a fibrous or rod-like morphology and is surrounded by an α_{Al} matrix. While the Al_3Ni fibers exhibit good thermal and chemical stability at elevated temperatures [10,11], the α_{Al} matrix remains relatively soft due to the limited solubility of Ni in α_{Al}. Therefore, additional alloying elements are required to increase the strength of the α_{Al} matrix.

Previous studies have shown that the addition of transition metals (TMs) and rare earths (REs) to dilute aluminum alloys promotes precipitate formation upon aging, which significantly improves the properties of the matrix [12,13]. These precipitates predominantly form intermetallic tri-aluminide phases with a general stoichiometry of Al_3X (where X = Zr, Ti, Sc and Er) [14–16]. In particular, Al_3Zr and Al_3Ti precipitates initially form

a metastable cubic $L1_2$ structure, while Al_3Sc and Al_3Er directly form stable cubic $L1_2$ structures [12]. The presence of these intermetallic phases contributes significantly to the high-temperature stability of the alloy [14,17], effectively inhibits recrystallization [18,19] and improves the creep resistance of aluminum alloys [20,21]. Small additions of alloying elements such as Zr and Sc to the eutectic Al–Ni system provide a viable means of introducing additional precipitation hardening to complement the inherent benefits of the eutectic microstructure. Previous studies on Sc and Zr additions in the Al–Ni system indicate positive effects on mechanical properties, including increased microhardness at RT and improved creep resistance [22,23].

This study investigates the feasibility of the widespread production of a castable Al–Ni–Zr alloy that exhibits increased thermal stability above 250 °C. Such an alloy would be well suited to high-temperature applications in the automotive, aerospace and power generation industries, including components such as aluminum pistons and water-jacketed turbine housings. To achieve the desired alloy composition, non-equilibrium solidification conditions must be maintained, as higher cooling rates promote the increased supersaturation of Zr within the α_{Al} matrix [24]. After solidification and subsequent heat treatment (T5), the formation of Zr-rich precipitates occurs, as confirmed by previous studies [23]. Based on the results of our previous research [25], an aging temperature of 350 °C was chosen to optimize the precipitation process and thus maximize the precipitate strength throughout the microstructure without negatively affecting the integrity of the eutectic phases. The objective of this study was to investigate the influence of small Zr addition to the eutectic Al–Ni alloy system and the subsequent aging treatment at 350 °C. The main focus was on characterizing the microstructural evolution and evaluating the changes in microhardness during the aging. In addition, tensile tests and accelerated compressive creep tests were performed to quantitatively evaluate the strengthening effects associated with the precipitation of Al_3Zr precipitates.

2. Materials and Methods

The experimental alloys were produced using an electric resistance furnace from technically pure aluminum (99.7%; Mozal SA, Boane, Mozambique), high-purity nickel (99.99%; F. Bauerstatter GES.M.B.H, Vienna, Austria) and an Al–10 wt.% Zr master alloy (KBM Affilips, Oss, The Netherlands). Two alloy compositions were investigated: Al–6.1Ni (referred to as AN) and Al–6.1Ni–0.6Zr (referred to as ANZ). The materials were melted in a graphite crucible and held at 850 °C for at least 30 min after the addition of the Al–Zr master alloy to ensure the complete dissolution of the alloying elements. Before casting, the melt was mechanically stirred and the oxide film was removed from the surface. The prepared melt was then poured into a copper mold, resulting in a test specimen with a dimension of 24 mm × 12 mm × 130 mm.

The casting alloys were aged in air at 350 °C in a muffle furnace EUP-K 20/1200 (Bosio, Celje, Slovenia) and then immediately quenched in water to ambient temperature. The designation of heat-treated samples follows the format Alloy-x, where x indicates the duration of aging at 350 °C in hours. For example, the designation ANZ-12 refers to the Al–Ni–Zr alloy that has been aged at 350 °C for 12 h. The samples for microstructural characterization by light optical microscopy (LOM) and scanning electron microscopy (SEM) were first ground with emery paper with increasing grain sizes of 600, 800, 1000 and finally 1200. The samples were then polished with 3 μm diamond paste, followed by a final polish with 1 μm diamond paste. The LOM analyses were carried out using Axioscope 5 (Carl Zeiss GmbH, Oberkochen, Germany). The chemical composition of the alloys was determined by energy dispersive X-ray spectroscopy with Ultim Max-EDS (Oxford Instruments, Oxford, UK) using a Quanta 650 (Thermo Fisher Scientific, Waltham, MA, USA) SEM operated at an accelerating voltage of 20

kV over an analyzed area of 2.5 mm × 2.5 mm. At least three measurements were performed per sample at randomly selected positions. An additional analysis of the phase fraction was carried out using SEM micrographs and the open-source software Fiji (ImageJ-version 1.54p). The characterization of the precipitates was carried out using a JEM-2100 transmission electron microscope—TEM (JEOL, Tokyo, Japan)—operated at an accelerating voltage of 200 kV. The TEM samples were first mechanically ground to a thickness of approximately 80 µm and then dimpled to a thickness between 20 and 30 µm. The final thinning was carried out using a precision ion polishing system—PIPS model 691 (Gatan, Ametek, Pleasanton, CA, USA)—with argon ions, starting with an ion energy of 4.5 keV and ending with a low-energy polishing step at 2 keV.

Vickers microhardness measurements were carried out using a Wilson VH 1202 (Buehler, Bühler, Switzerland) hardness tester under the HV 0.1 load scale, with at least ten individual measurements per sample. Electrical conductivity was assessed with a Hocking Phasec 2s (General Electric, Evendale, OH, USA) with a 960 kHz probe, with a minimum of four measurements per sample. The tensile tests were performed using a Z250 (Zwick Roell, Ulm, Germany) universal testing machine equipped with a 50 kN load cell and a HTO-08 (Maytec, Singen, Germany) heating furnace. The tensile specimens were machined and heat-treated according to ASTM E8M-04 [26] to achieve the desired condition. Cylindrical specimens with a diameter of 5 mm and a length of 10 mm were prepared for accelerated compression creep tests. These creep tests were performed with a DIL 805A/D (Ta Instruments, New Castle, DE, USA) dilatometer, applying a constant compressive force at predefined temperatures. The applied forces were selected based on previous compression tests at corresponding temperatures so that the applied stresses were between 0.4 and 0.6 of the $Rp_{0.01}$ value for both alloy types. Accelerated creep tests were carried out at temperatures of 250, 275 and 300 °C on samples that had previously been heat-treated.

3. Results and Discussion

3.1. Chemical Composition

The chemical composition and designation of the alloys produced are provided in Table 1. The chemical compositions were determined using an SEM with an EDS detector. The traces of Fe detected in the alloys (Table 1) originated as impurities from technically pure aluminum and the Al–Zr master alloy.

Table 1. SEM analysis of chemical composition and designation of alloys in wt.%.

Expected Composition	Ni	Zr	Fe	Al	Designation
Al-6.1Ni	6.41 ± 0.14	0.00	0.14 ± 0.02	bal.	AN
Al-6.1Ni-0.6Zr	6.28 ± 0.01	0.56 ± 0.1	0.11 ± 0.05	bal.	ANZ

3.2. Microhardness and Electrical Conductivity

Figure 1 shows the evolution of microhardness and electrical conductivity for the AN and ANZ alloys during aging at 350 °C. As can be seen in Figure 1a, the AN alloy shows a minimal change in microhardness aging from an initial value of 62 HV0.1 to approximately 58 HV0.1. Comparable values for the as-cast microhardness of the Al-6Ni alloy were previously reported by Suwanpreecha et al. [22] and Michi et al. [27]. Furthermore, Suwanpreecha also reported unchanged microhardness after the exposure of Al-6Ni at 350 °C for a duration of two months. In contrast, the ANZ alloy shows considerable precipitation strengthening upon aging. The ANZ alloy initially has a lower microhardness than the AN alloy. Although Zr is added to the solid solution, the strengthening effect of the solid solution is less pronounced than the

microstructural changes induced by the Zr addition. The microhardness behavior of an alloy with a comparable chemical composition has already been described in our earlier work [25]. During the initial 6 h of aging, a modest increase in microhardness is observed, followed by a significant increase after 12 h, indicating a pronounced age-hardening effect. Accordingly, the values of electrical conductivity closely follow the trend of microhardness. The peak value of microhardness is reached after about 48 h of aging with 92 HV0.1, an increase that can be attributed to the formation of fine, coherent Zr-containing precipitates. In comparison, Belov et al. [28] and Michi et al. [27] reported peak-aged microhardness (780 and 850 MPa), although the aging was carried out at a higher temperature (400 °C) and shorter time (24 h and 20 h), respectively.

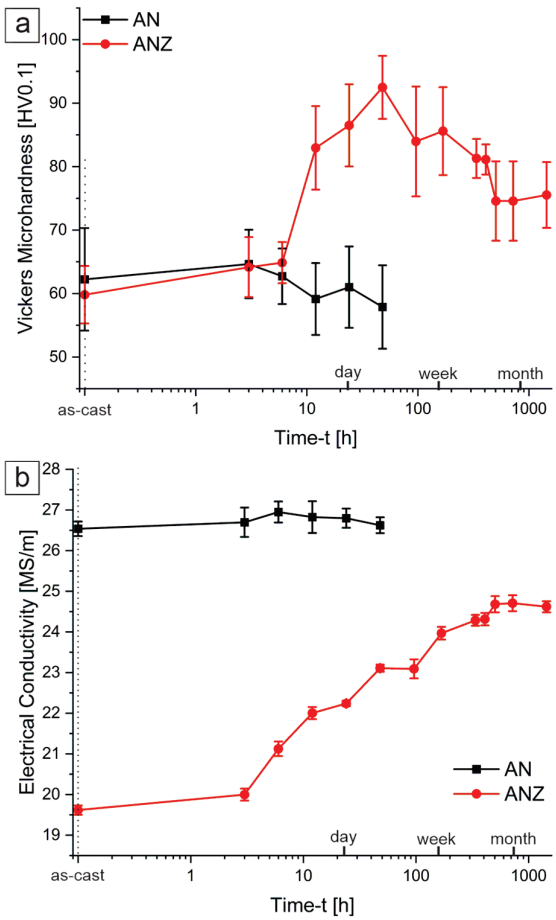


Figure 1. Evolution of Vickers microhardness (**a**) and electrical conductivity (**b**) after aging at 350 °C for alloys AN and ANZ.

Continued aging from 48 to 504 h leads to a gradual decrease in microhardness to around 75 HV0.1, which is due to the coarsening of the precipitates and the associated depletion of Zr from the α_{Al} matrix. During this aging interval, the electrical conductivity increases steadily. It is noteworthy that the microhardness stabilizes at around 75 HV0.1 after 504 h, indicating a balance between the precipitate coarsening of the precipitates and the depletion of Zr in the matrix. This stabilization is accompanied by relatively constant electrical conductivity.

3.3. Microstructure

3.3.1. Optical Microscopy (LOM)

The changes in microstructural constituents are presented in Figure 2, where the alloy AN exhibits a predominantly eutectic microstructure. However, the introduction of Zr

causes an increase in α_{Al} dendrites, which represent ~30% of the microstructure, which was also reported in our previous work [25]. The equiaxed morphology of the α_{Al} dendrites is attributed to the addition of Zr, which promotes solidification through a peritectic reaction with primary Al_3Zr phases, as shown in Figure 3f. The addition of 0.6 wt.% Zr promotes the nucleation of α_{Al} via heterogeneous nucleation initiated by primary Al_3Zr particles.

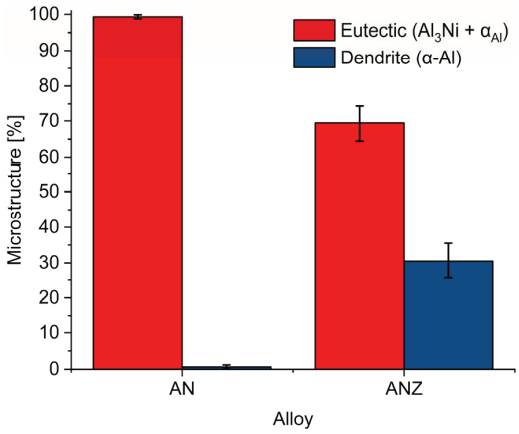


Figure 2. Microstructure fraction for alloys AN and ANZ.

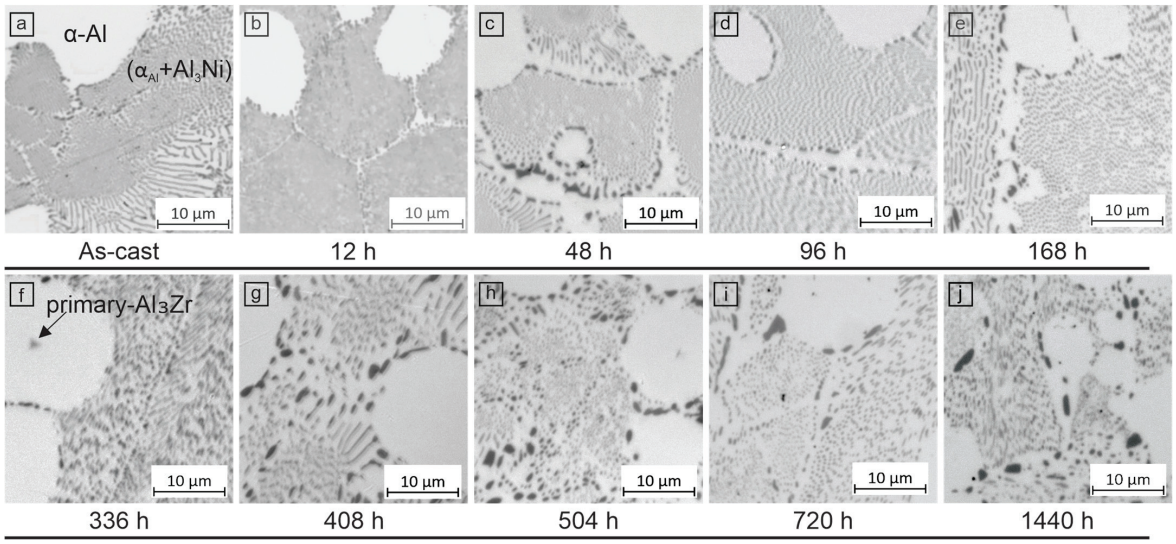


Figure 3. Optical micrographs of microstructural evolution of alloy ANZ after aging at 350 °C: (**a**) As cast; (**b**) 12 h; (**c**) 48 h; (**d**) 96 h; (**e**) 168 h; (**f**) 336 h; (**g**) 408 h; (**h**) 504 h; (**i**) 720 h; and (**j**) 1440 h.

The eutectic Al_3Ni phase mainly exhibits a fibrous morphology, which is embedded in the eutectic α_{Al} phase and jointly forms eutectic colonies. However, a partial transition from the fibrous to the lamellar morphology of Al_3Ni can be observed, especially in the vicinity of α_{Al} dendrites formed during solidification. The relatively pure composition of the dendrites (due to the low solubility of nickel and iron in aluminum) causes impurity atoms to be pushed towards the solidification front. This process inhibits the formation of a fibrous eutectic and promotes the lamellar morphology of Al_3Ni, and this has previously also been observed by Kakitani et al. [29]. Furthermore, the distribution of these eutectic morphologies indicates an influence of latent heat release during solidification. Chemical analyses also indicate a higher iron concentration within the lamellar Al_3Ni phases, which underlines a preferential affinity for Fe (confirmed by SEM).

Aging the ANZ alloy at 350 °C for 12 h shows no significant microstructural changes (Figure 3b). Slight microstructural changes can be observed, with the microhardness of the alloy peaking after 48 h at 350 °C. There is some coarsening of the Al_3Ni phase at the edges of the colonies with a focus on the lamellar phase, while aging has little effect on the morphology of the Al_3Ni fibers. After 168 h (Figure 3e), darker intermetallic phases, probably rich in Fe and/or Ni, form at the colony boundaries and the dendritic edges. The lamellae start to coarsen faster, while the fibrous eutectic shows only minimal coarsening, mainly at the edges of the colonies. After further aging for 408 and 504 h (Figure 3g,h), the lamellar eutectic phases show pronounced segregation and growth, while the fibrous eutectic phases undergo moderate coarsening. At the same time, intermetallic precipitates increasingly accumulate at the colony boundaries. After 720 h of aging, the microstructure approaches a state of relative stability, although the lamellar phases continue to show gradual coarsening and agglomeration into larger intermetallic areas. After prolonged aging (1440 h at 350 °C), the eutectic colony boundaries continue to expand. It is noticeable that the morphology of the dendritic α_{Al} phases changes from globular to spheroidal shape. This development can be attributed to the continued segregation of the elements, especially in regions that were originally dominated by lamellar eutectic phases. The increasing segregation causes these regions to resemble dendritic α_{Al} structures, accompanied by a large, randomly distributed, dark intermetallic Al_3Ni phase (Figure 3j).

3.3.2. Scanning Electron Microscopy (SEM)

Figure 4 shows SEM images with the corresponding EDS analyses summarized in Table 2. Figure 4a highlights the specific regions where EDS measurements were performed on the primary Al_3Zr phase, which appears in two different morphologies. As reported by Khvan et al. [30], the morphology labeled by spot 1 is referred to as a "porous crystal" or "flower crystal". In addition, the second, plate-like morphology corresponding to spot 2 was observed by Michi et al. [27]. According to the SEM-EDS results presented in Table 2, the chemical compositions at spots 1 and 2 are largely similar, with the exception of a higher Ni content in one of the regions, which is most likely due to an analytical deviation. Spots 3 and 4 reflect the chemical composition of the eutectic lamellae. It is noteworthy that the morphology at spot 4 is slightly altered, indicating the instability of the lamellar eutectic phase after one week of aging in the ANZ alloy. The microstructures shown in Figure 4c,d exhibit significant changes, in particular the agglomeration of phases, predominantly at the peripheries of the colonies. In Figure 4c, the lamellar eutectic (α_{Al} + Al_3Ni) morphology appears disrupted and coarsened into larger, irregular phases. The chemical composition of 5–9 spots indicates coarsened regions of the Al_3Ni phase, with a slight enrichment of Fe, a feature more commonly observed at colony boundaries. The coarsening of the Al_3Ni phase has already been documented by Czerwinski [10].

Table 2. Results of SEM-EDS analyses in wt.% from Figure 4.

Spectrum Label	1	2	3	4	5	6	7	8	9
Al	77.4	75.9	91.1	84.0	82.9	68.7	72.3	73.5	83.2
Ni	0.8	7.2	8.5	15.5	15.3	31.2	27.5	26.3	16.6
Fe	-	-	0.1	0.2	1.8	0.1	0.2	0.2	0.2
Zr	21.6	16.4	0.3	0.3	-	-	-	-	-
Si	0.2	0.5	-	-	-	-	-	-	-

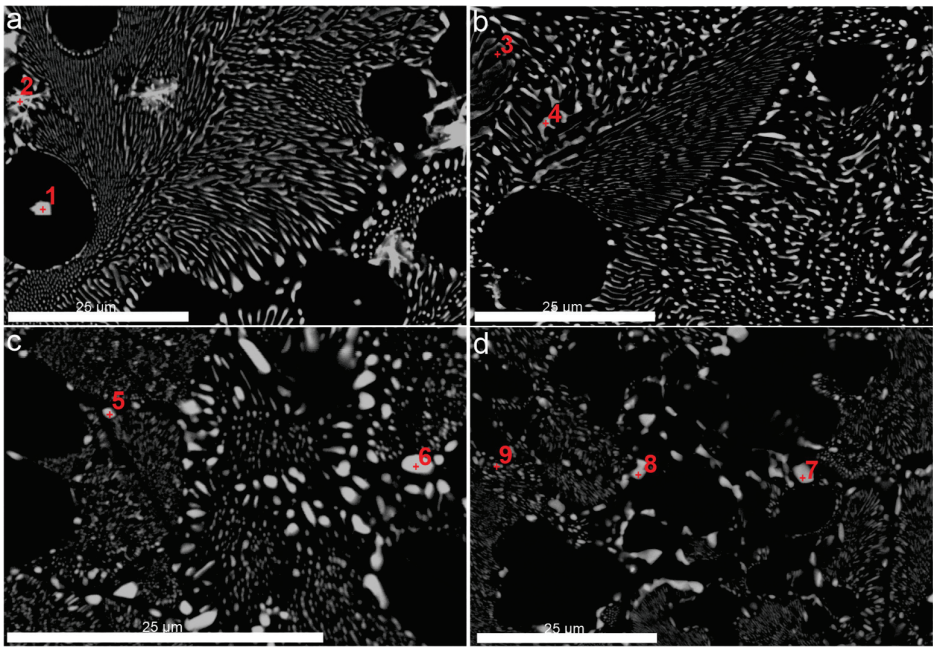


Figure 4. SEM micrographs with EDS analyses (marked red spot): (**a**) Sample ANZ-48; (**b**) Sample ANZ-168; (**c**) Sample ANZ-720; and (**d**) Sample ANZ-1440.

3.3.3. Transmission Electron Microscopy (TEM)

In order to characterize the precipitates on the nanoscale, a detailed TEM analysis was carried out. Figure 5a shows the eutectic microstructure of the alloy ANZ, which was aged at 350 °C for 48 h. Figure 5b,c show magnified images of the areas labeled "1" and "2", respectively. Figure 5b clearly shows the presence of fine Al_3Zr precipitates in close proximity to the eutectic Al_3Ni fibers. Figure 5c also shows areas with $L1_2$-Al_3Zr precipitates, some of which are marked by green circles. Figure 5c shows the darker areas in which strain contrast between matrix and precipitates can be seen. Accordingly, the FFT diffraction pattern in Figure 5c shows the positions of the α_{Al} matrix and the coherent precipitates. The diffraction pattern indicates the positions (yellow circles) of the spots for the ordered f.c.c. $L1_2$ unit cell of the Al_3Zr precipitate. Figure 5d,e show the microstructure of the ANZ-720 alloy and confirm the presence of Al_3Zr precipitates next to eutectic Al_3Ni fibers, confirming that the effective precipitation hardening of the ANZ alloy has taken place. The formation of these fine precipitates during aging predominantly within the eutectic α_{Al} phase contributes significantly to the strengthening of the weaker component of the eutectic microstructure. Figure 5e and the FFT diffraction pattern also show the presence of cubic $L1_2$-Al_3Zr precipitates after 720 h at 350 °C.

Previous studies on Al-based alloys have reported comparable Al_3Zr precipitate sizes under different conditions. For example, Michi et al. [27] observed Al_3Zr precipitates with an average radius of 2.1 ± 0.4 nm after aging at 425 °C for 24 h. Pandey et al. [31] reported Al_3Zr precipitates with an average radius of 2.5 ± 1.0 nm after 10 h and 4.0 ± 1.0 nm after 100 h of aging at 400 °C. In addition, Fan and Makhlouf [15] produced $Al_3(Zr_x,V_{1-x})$ precipitates with an average radius of 2.6 nm after aging at 400 °C for 32 h. Knipling et al. [14] recorded Al_3Zr precipitates with a radius of 5.1 ± 1.7 nm after aging at 425 °C for 400 h in dilute binary Al–Zr alloys. Figure 6 shows the lognormal distributions of precipitate sizes in ANZ alloy samples aged at 350 °C for 48 and 720 h (ANZ-48 and ANZ-720), respectively. The distribution of $L1_2$-Al_3Zr precipitates was assessed using size measurements from TEM images in brightfield and HRTEM modes. The TEM analysis was performed at magnifications from 100,000× to

500,000× and an accelerating voltage of 200 kV. Precipitate size measurements were performed using the open-source software Fiji, analyzing at least 170 precipitates per sample. As can be seen in Figure 6a,b, the average precipitate radius (r) of the $L1_2$-Al_3Zr phase fitted with a lognormal distribution is r = 2.1 ± 1.6 nm for ANZ-48 and r = 3.1 ± 1.6 nm for ANZ-720. With continued aging at a temperature of 350 °C, there is a tendency for small precipitates with higher curvature to dissolve, as can be seen from the changes in the distribution in Figure 6. When small precipitates dissolve, the resulting solute diffuses towards larger precipitates, causing them to grow and hence the total interfacial energy to decrease. Comparing the results obtained in this study with those of the previously cited references, there is good agreement. However, it is important to note that most of these studies were conducted at higher aging temperatures (400–425 °C). Consequently, the larger precipitate sizes are primarily attributed to the increased diffusion rate of Zr in aluminum at higher temperatures, where the diffusivity coefficient is about two orders of magnitude higher than at 350 °C. Furthermore, it is important to emphasize that although the average size of the $L1_2$-Al_3Zr radius increased at aging between 48 h and 720 h, the coherence of the precipitates is maintained.

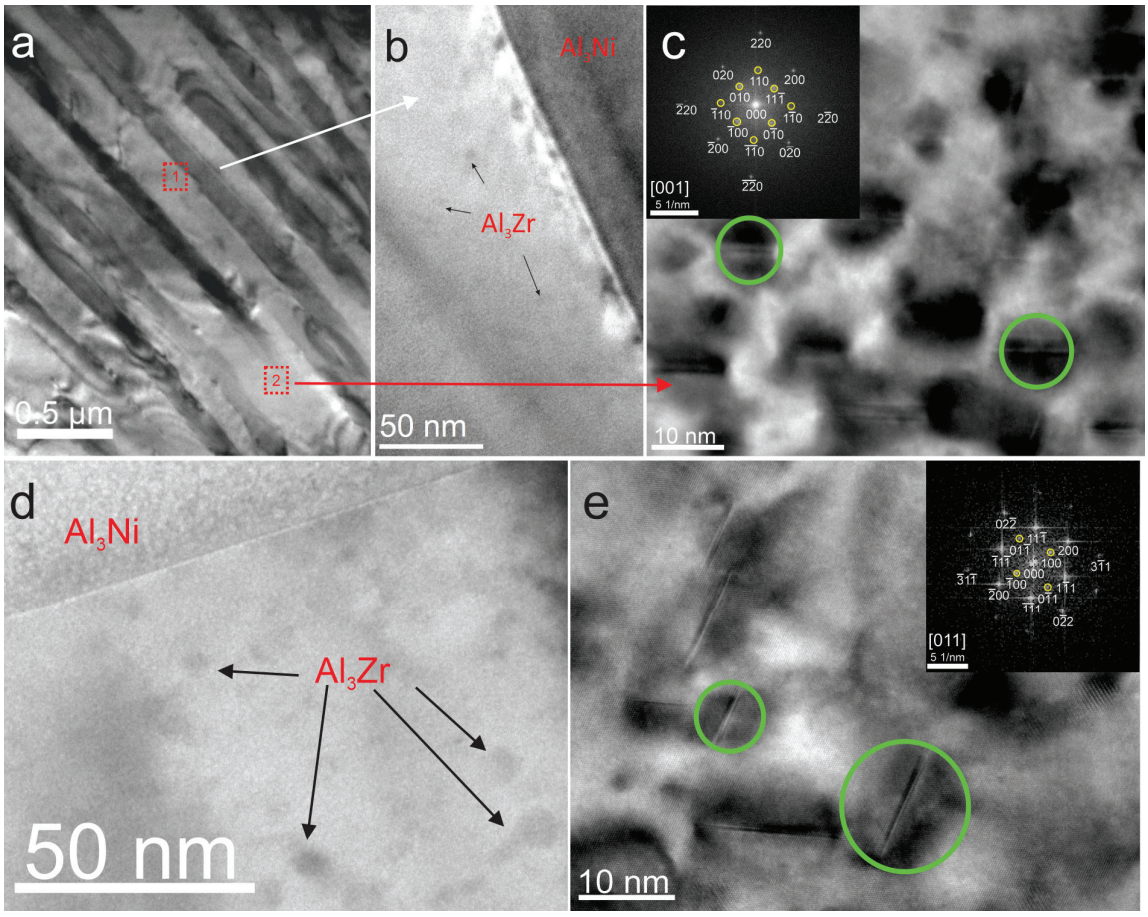


Figure 5. The TEM analysis of the ANZ alloy aged at 350 °C; (**a**) a bright field image of the ANZ-48 sample and (**b**) magnification of the area marked with the dashed square 1, in which the Al_3Zr precipitates marked with arrows can be seen; (**c**) a bright field image of the ANZ-48 sample with green circles indicating the $L1_2$-Al_3Zr precipitates and the FFT pattern in which yellow circles indicate the $L1_2$-Al_3Zr positions; (**d**) a bright field image of the ANZ-720 sample with arrows indicating the Al_3Zr precipitates; and (**e**) a bright field image of the 720 h aged ANZ alloy with green circles indicating the $L1_2$-Al_3Zr precipitates and the FFT pattern of the corresponding diffraction in which yellow circles indicate the $L1_2$ positions.

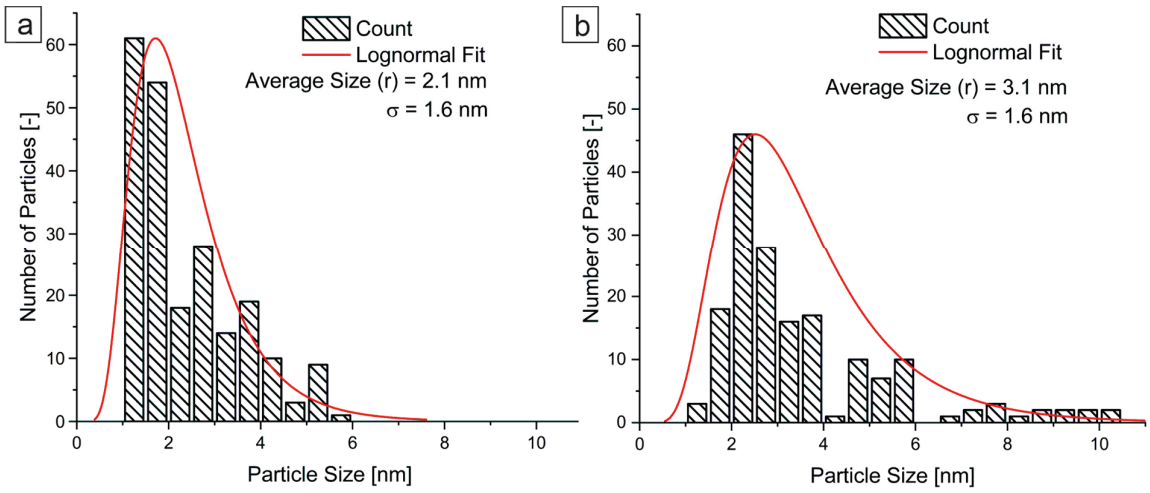


Figure 6. Histogram of average size of precipitates with lognormal distribution for samples: (**a**) ANZ-48; (**b**) ANZ-720.

3.4. Tensile Tests

Tensile test experiments were carried out at RT, 250 °C and 300 °C and the results are presented in Figure 7. Per each tensile test parameter, at least three specimens were measured. The tensile tests performed at room temperature did not reveal any significant differences between the eutectic AN alloy in terms of ultimate tensile strength (UTS) and yield strength (YS), even when exposed to 350 °C for up to 48 h; however, it showed a slight increase in elongation (El), indicating the good thermal stability of the eutectic Al_3Ni fibers. The results for eutectic alloys are in good agreement with those previously reported by Koutsoukis et al. [32]. Similarly, the as-cast ANZ alloy showed similar mechanical properties to the eutectic AN alloy, apart from a slightly lower initial yield strength. In particular, the ANZ-12 alloy showed a 17% improvement in UTS and a 50% increase in YS compared to the as-cast alloy. The highest improvement in mechanical properties was observed with the ANZ-48 alloy, which achieved a remarkable 102% increase in yield strength and a 50.8% improvement in UTS compared to the as-cast alloy.

At an elevated test temperature of 250 °C, the tensile properties of the AN alloy remain similar under the tested conditions. However, the ANZ-48 alloy shows a slight improvement (Figure 7) in mechanical properties, while the ANZ-12 alloy shows a significant increase in YS and UTS. The most significant difference is seen in tensile elongation (El), with the ANZ series alloys exhibiting significantly higher elongation compared to their AN counterpart. Further tensile tests at 300 °C show a significant reduction in mechanical properties, which is particularly noticeable in the Zr-containing alloys. At this temperature, the UTS values of the AN-12, AN-48 and ANZ-12 alloys converge, while ANZ48 has a slightly lower UTS value, indicating the susceptibility of the Zr-strengthened alloys to softening at higher temperatures.

3.5. Accelerated Compressive Creep Test

Figure 8 shows the accelerated compression creep behavior of the investigated ANZ-48 alloy under different test conditions. All experiments shown in Figure 8a exhibit a monotonous creep response. Figure 8b shows the corresponding strain rate curves for the ANZ-48 alloy, where a pronounced primary creep phase is followed by a secondary (steady-state) creep phase. The average minimum creep rates for all investigated alloys were extracted from the secondary phase, where, from average minimum creep rates,

further evaluations were carried out to determine the activation energy for creep (Q_c) and the stress exponent (n), the results of which are summarized in Table 3.

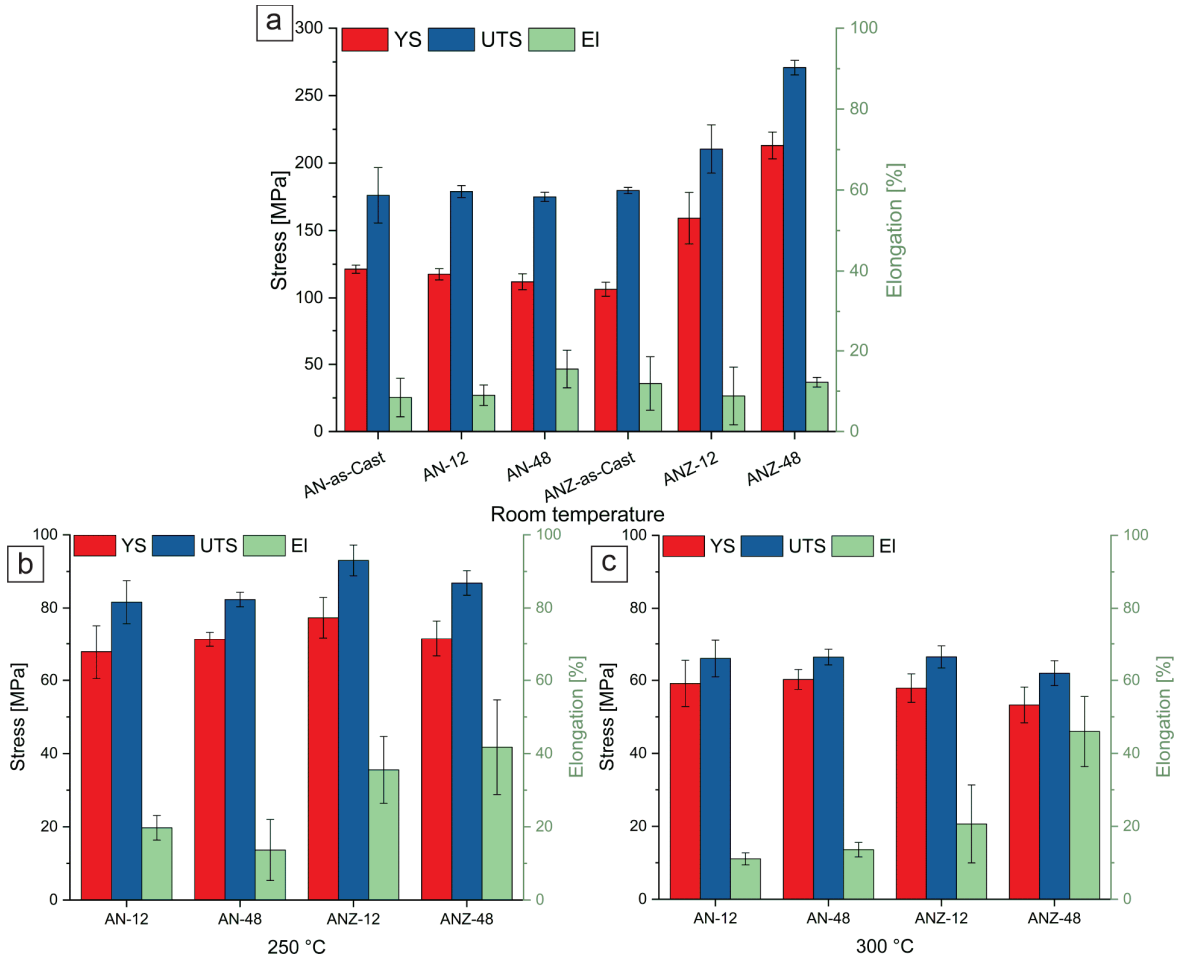


Figure 7. Results of tensile test analysis; (**a**) at room temperature (RT); (**b**) at 250 °C; and (**c**) at 300 °C.

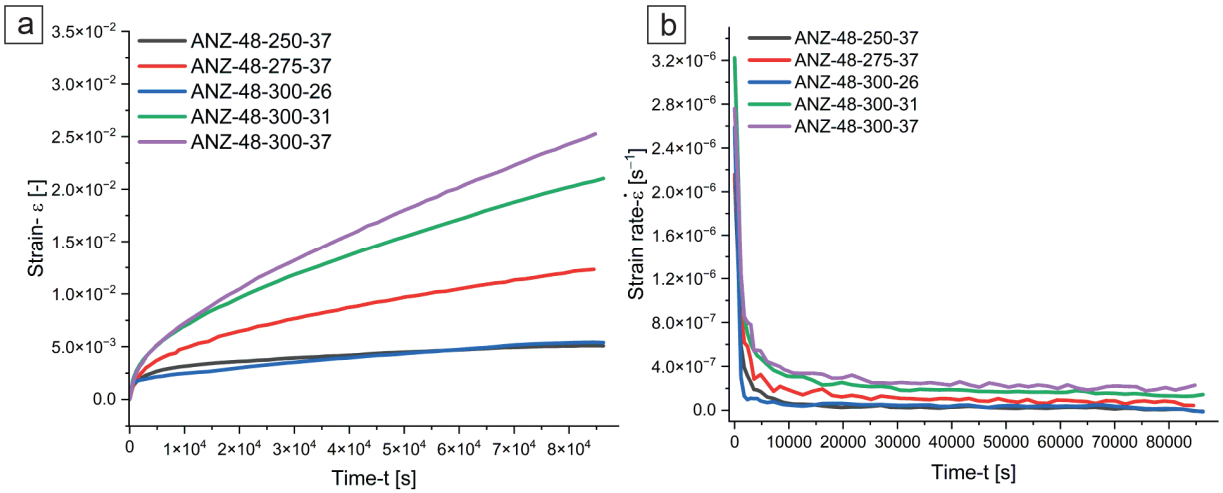


Figure 8. Compressive creep tests curves: strain–time (**a**) and strain rate–time (**b**).

It is evident from Table 3 that the activation energy for creep in the AN alloy is the lowest of the alloys analyzed and closely matches the activation energy for pipe diffusion ($Q \approx 82$ kJ/mol) [33]. In addition, a stress exponent of n = 3 was determined for the AN

alloy, indicating dislocation activity with a dislocation glide mechanism [34]. Taken together, these observations indicate that the dominant creep mechanism in the AN alloy under the applied test conditions is most likely controlled by a combination of pipe diffusion and limited viscous dislocation glide. This is not consistent with previous studies by Michi et al. [27] and Suwanpreecha et al. [22], who investigated eutectic Al–Ni alloys and reported higher stress exponents, suggesting the existence of threshold stress. However, it is important to point out that the creep stresses applied in the present study were lower than those used in previous studies. Table 3 shows that the Q_c for the ANZ-12 and ANZ-48 alloys is close the lattice self-diffusion energy of pure aluminum ($Q \approx 142$ kJ/mol) [33]. This increase, together with the increased stress exponents, indicates a transition to a different creep regime. In particular, the combination of higher Q_c and stress exponent values indicates that the dominant creep mechanism is most likely self-diffusion-driven dislocation climbing, which is usually characterized by the power-law creep regime [35]. These results are in good agreement with the observations of Michi et al. [27], who found a detrimental effect on creep resistance associated with a low volume fraction of α_{Al} dendrites. The shift in the creep mechanism in the ANZ-12 and ANZ-48 alloys correlates with a slight reduction in their creep resistance. This behavior can be attributed to microstructural changes in these alloys, in particular an increased volume fraction of α_{Al} dendrites of up to about 30% (Figure 2), which can disrupt the efficiency of load transfer from the matrix to the Al_3Ni fibers and redirect it towards the α_{Al} dendrites. The results indicate that the increased volume fraction of the α_{Al} dendrites in the microstructure can counteract the strengthening effect of the $L1_2$-Al_3Zr precipitates and thus reduce the overall creep resistance.

Table 3. Results of average minimal strain rates for each condition, activation creep energy and stress exponents of alloys AN, ANZ-12 and ANZ-48.

Temperature T [°C]	Stress σ [MPa]	Strain Rate $\dot{\varepsilon}$ [s^{-1}]		
		AN	ANZ-12	ANZ-48
250	37	6.57×10^{-9}	6.30×10^{-9}	1.15×10^{-8}
275	37	8.21×10^{-9}	3.70×10^{-8}	7.22×10^{-8}
300	26	1.53×10^{-8}	2.34×10^{-8}	1.79×10^{-8}
300	31	1.09×10^{-8}	4.85×10^{-8}	1.39×10^{-7}
300	37	3.79×10^{-8}	2.28×10^{-7}	2.00×10^{-7}
Q_c-Activation creep energy [kJ]		86.2	178.8	142.9
n-stress exponent		3	6	6

4. Conclusions

In this study, eutectic Al–Ni and Al–Ni–Zr cast alloys were investigated, focusing on the development of microstructure, microhardness and electrical conductivity during isothermal aging at 350 °C for a period of two months.

1. The introduction of 0.6 wt.% Zr into the eutectic Al–Ni system leads to an increased proportion of equiaxed α_{Al} dendrites (~30%). Aging alloy at 350 °C leads to a peak in microhardness at 92 HV0.1 after 48 h. Extended aging results in the partial coarsening of the microstructure, with the microhardness stabilizing at 75 HV0.1 after 500 h.
2. Upon aging, coherent $L1_2$-Al_3Zr precipitates with an average radius of r = 2.1 ± 1.6 nm were observed at peak aging conditions (350 °C, 48 h). Their high resistance to coarsening is evident after 30 days of aging, where the average radius of the precipitates increased only slightly to r = 3.1 ± 1.6 nm, while coherence with the matrix was maintained.

3. The tensile tests of the peak-aged ANZ-48 sample revealed a significant increase in yield strength from 106 MPa to 213 MPa at room temperature. However, this increase is not retained at elevated temperatures (300 °C), where the yield strength drops to 53 MPa. The YS value is in a similar range to the alloy without Zr addition.
4. Accelerated compressive creep tests indicated that the AN alloy exhibits a creep-dominated mechanism of pipe diffusion and limited viscous dislocation glide, whereas the ANZ alloy follows a power-law creep regime under the conditions tested.

Author Contributions: Conceptualization, J.Š. and R.Š.; methodology, J.Š. and A.Z.; formal analysis, J.Š., B.M. and R.Š.; investigation, J.Š. and A.Z.; writing—original draft preparation, J.Š.; writing—review and editing, B.M. and R.Š.; supervision, R.Š. All authors have read and agreed to the published version of the manuscript.

Funding: The authors acknowledge the financial support from the Slovenian Research Agency (ARIS) under the research program P2-0270 Production systems, laser technologies and materials welding.

Institutional Review Board Statement: Not applicable.

Informed Consent Statement: Not applicable.

Data Availability Statement: The original contributions presented in this study are included in the article. Further inquiries can be directed to the corresponding author.

Acknowledgments: The authors sincerely thanks Blaž Leskovar (the Faculty of Natural Sciences and Engineering) for his assistance with TEM.

Conflicts of Interest: The authors declare no conflicts of interest.

References

1. Arriaga-Benitez, R.I.; Pekguleryuz, M. Recent Progress in Creep-Resistant Aluminum Alloys for Diesel Engine Applications: A Review. *Materials* **2024**, *17*, 3076. [CrossRef] [PubMed]
2. Fan, Y.; Makhlouf, M.M. The Al-Al_3Ni Eutectic Reaction: Crystallography and Mechanism of Formation. *Metall. Mater. Trans. A Phys. Metall. Mater. Sci.* **2015**, *46*, 3808–3812. [CrossRef]
3. Weiss, D. Improved High-Temperature Aluminum Alloys Containing Cerium. *J. Mater. Eng. Perform.* **2019**, *28*, 1903–1908. [CrossRef]
4. Rogachev, S.O.; Naumova, E.A.; Lukina, E.A.; Zavodov, A.V.; Khatkevich, V.M. High Strength Al–La, Al–Ce, and Al–Ni Eutectic Aluminum Alloys Obtained by High-Pressure Torsion. *Materials* **2021**, *14*, 6404. [CrossRef]
5. Zhang, H.; Li, Z.; Xiao, D.; Wu, M.; Huang, Y.; Liu, W. Enhanced Strength of Al-10Ce-3Mg-5Zn Heat-Resistant Alloy by Combining Extrusion and Heat Treatment. *Materials* **2025**, *18*, 1706. [CrossRef]
6. Kozakevich, J.R.; Sediako, D.; Weiss, D.; Vogel, S.C. A Quantitative Phase Analysis by Neutron Diffraction of Conventional and Advanced Aluminum Alloys Thermally Conditioned for Elevated-Temperature Applications. *Materials* **2024**, *17*, 4311. [CrossRef]
7. Doty, H.W.; El-Hadad, S.; Samuel, E.; Samuel, A.M.; Samuel, F.H. The Influence of Rare Earth Metals on the Microstructure and Mechanical Properties of 220 and 356.1 Alloys for Automotive Industry. *Materials* **2025**, *18*, 941. [CrossRef]
8. Koutsoukis, T.; Makhlouf, M.M. Rendering Wrought Aluminium Alloys Castable by Means of Minimum Composition Adjustments. *Int. J. Cast Met. Res.* **2017**, *30*, 231–243. [CrossRef]
9. Carrara, A.P.; Kakitani, R.; Garcia, A.; Cheung, N. Effect of Cooling Rate on Microstructure and Microhardness of Hypereutectic Al–Ni Alloy. *Arch. Civ. Mech. Eng.* **2021**, *21*, 14. [CrossRef]
10. Czerwinski, F. Thermal Stability of Aluminum-Nickel Binary Alloys Containing the Al-Al_3Ni Eutectic. *Metall. Mater. Trans. A Phys. Metall. Mater. Sci.* **2021**, *52*, 4342–4356. [CrossRef]
11. Tiwary, C.S.; Kashyap, S.; Kim, D.H.; Chattopadhyay, K. Al Based Ultra-Fine Eutectic with High Room Temperature Plasticity and Elevated Temperature Strength. *Mater. Sci. Eng. A* **2015**, *639*, 359–369. [CrossRef]
12. Knipling, K.E.; Dunand, D.C.; Seidman, D.N. Criteria for Developing Castable, Creep-Resistant Aluminum-Based Alloys—A Review. *Int. J. Mater. Res.* **2006**, *97*, 246–265. [CrossRef]

13. Qi, Y.; Wei, F.; Wang, Y.; Jin, Y.; Chang, X.; Chen, G. Microstructure and Mechanical Property of 6082 Aluminum Alloy via Sc and Zr Addition Combined with Squeeze Casting. *Materials* **2025**, *18*, 1988. [CrossRef] [PubMed]
14. Knipling, K.E.; Dunand, D.C.; Seidman, D.N. Precipitation Evolution in Al-Zr and Al-Zr-Ti Alloys during Isothermal Aging at 375–425 °C. *Acta Mater.* **2008**, *56*, 114–127. [CrossRef]
15. Fan, Y.; Makhlouf, M.M. The Effect of Introducing the Al-Ni Eutectic Composition into Al-Zr-V Alloys on Microstructure and Tensile Properties. *Mater. Sci. Eng. A* **2016**, *654*, 228–235. [CrossRef]
16. Marquis, E.A.; Seidman, D.N. Nanoscale Structural Evolution of Al3Sc Precipitates in Al(Sc) Alloys. *Acta Mater.* **2001**, *49*, 1909–1919. [CrossRef]
17. Booth-Morrison, C.; Dunand, D.C.; Seidman, D.N. Coarsening Resistance at 400 °C of Precipitation-Strengthened Al-Zr-Sc-Er Alloys. *Acta Mater.* **2011**, *59*, 7029–7042. [CrossRef]
18. Elasheri, A.; Elgallad, E.M.; Parson, N.; Chen, X.G. Evolution of Zr-Bearing Dispersoids during Homogenization and Their Effects on Hot Deformation and Recrystallization Resistance in Al-0.8%Mg-1.0%Si Alloy. *J. Mater. Eng. Perform.* **2021**, *30*, 7851–7862. [CrossRef]
19. Guo, Z.; Zhao, G.; Chen, X.G. Effects of Two-Step Homogenization on Precipitation Behavior of Al_3Zr Dispersoids and Recrystallization Resistance in 7150 Aluminum Alloy. *Mater. Charact.* **2015**, *102*, 122–130. [CrossRef]
20. Booth-Morrison, C.; Seidman, D.N.; Dunand, D.C. Effect of Er Additions on Ambient and High-Temperature Strength of Precipitation-Strengthened Al-Zr-Sc-Si Alloys. *Acta Mater.* **2012**, *60*, 3643–3654. [CrossRef]
21. Gao, Y.H.; Kuang, J.; Zhang, J.Y.; Liu, G.; Sun, J. Tailoring Precipitation Strategy to Optimize Microstructural Evolution, Aging Hardening and Creep Resistance in an Al–Cu–Sc Alloy by Isochronal Aging. *Mater. Sci. Eng. A* **2020**, *795*, 139943. [CrossRef]
22. Suwanpreecha, C.; Toinin, J.P.; Michi, R.A.; Pandee, P.; Dunand, D.C.; Limmaneevichitr, C. Strengthening Mechanisms in Al–Ni–Sc Alloys Containing Al3Ni Microfibers and Al3Sc Nanoprecipitates. *Acta Mater.* **2019**, *164*, 334–346. [CrossRef]
23. Suwanpreecha, C.; Pandee, P.; Patakham, U.; Dunand, D.C.; Limmaneevichitr, C. Effects of Zr Additions on Structure and Microhardness Evolution of Eutectic Al-6ni Alloy. In *Light Metals 2019*; Minerals, Metals and Materials Series; Springer: Cham, Switzerland, 2019; pp. 373–377.
24. Belov, N.A. Aluminium Casting Alloys with High Content of Zirconium. *Mater. Sci. Forum* **1996**, *217–222*, 293–298. [CrossRef]
25. Šmalc, J.; Zaky, A.; Markoli, B.; Šturm, R. The Impact of Small Zr Addition to Al–Ni Cast Alloy for Elevated Temperature Applications. *J. Mater. Res. Technol.* **2024**, *32*, 1928–1936. [CrossRef]
26. *ASTM E8M-04*; Standard Test Methods for Tension Testing of Metallic Materials [Metric] (Withdrawn 2008). ASTM International: West Conshohocken, PA, USA, 2010.
27. Michi, R.A.; Toinin, J.P.; Seidman, D.N.; Dunand, D.C. Ambient- and Elevated-Temperature Strengthening by Al_3Zr-Nanoprecipitates and Al_3Ni-Microfibers in a Cast Al-2.9Ni-0.11Zr-0.02Si-0.005Er (at.%) Alloy. *Mater. Sci. Eng. A* **2019**, *759*, 78–89. [CrossRef]
28. Belov, N.; Zolotorevskij, V.S.; Goto, S.; Alabin, A.N.; Istomin-kastrovskij, V.V.; Mishin, V.I. Effect of Zirconium on Liquidus and Hardening of Al-6% Ni Casting Alloy. In Proceedings of the Materials Forum, Brisbane, Australia, 2–5 August 2004; Volume 28, pp. 533–538.
29. Kakitani, R.; Reyes, R.V.; Garcia, A.; Spinelli, J.E.; Cheung, N. Relationship between Spacing of Eutectic Colonies and Tensile Properties of Transient Directionally Solidified Al-Ni Eutectic Alloy. *J. Alloys Compd.* **2018**, *733*, 59–68. [CrossRef]
30. Khvan, A.V.; Eskin, D.G.; Starodub, K.F.; Dinsdale, A.T.; Wang, F.; Fang, C.; Cheverikin, V.V.; Gorshenkov, M.V. New Insights into Solidification and Phase Equilibria in the Al-Al_3Zr System: Theoretical and Experimental Investigations. *J. Alloys Compd.* **2018**, *743*, 626–638. [CrossRef]
31. Pandey, P.; Makineni, S.K.; Gault, B.; Chattopadhyay, K. On the Origin of a Remarkable Increase in the Strength and Stability of an Al Rich Al-Ni Eutectic Alloy by Zr Addition. *Acta Mater.* **2019**, *170*, 205–217. [CrossRef]
32. Koutsoukis, T.; Makhlouf, M.M. Alternatives to the Al–Si Eutectic System in Aluminum Casting Alloys. *Int. J. Met.* **2016**, *10*, 342–347. [CrossRef]
33. Frost, H.J.; Ashby, M.F. *Deformation-Mechanism Maps: The Plasticity and Creep of Metals and Ceramics*; Franklin Book Company: Elkins Park, PA, USA, 1982.
34. Himbeault, D.D.; Cahoon, J.R. Creep Regimes for Directionally Solidified Al-Al_3Ni Eutectic Composite. *Metall. Trans. A* **1993**, *24*, 2721–2730. [CrossRef]
35. Kassner, M.E. New Developments in Understanding Harper–Dorn, Five-Power Law Creep and Power-Law Breakdown. *Metals* **2020**, *10*, 1284. [CrossRef]

Disclaimer/Publisher's Note: The statements, opinions and data contained in all publications are solely those of the individual author(s) and contributor(s) and not of MDPI and/or the editor(s). MDPI and/or the editor(s) disclaim responsibility for any injury to people or property resulting from any ideas, methods, instructions or products referred to in the content.

materials

MDPI

Article

Parameter Sensitivity Study of the Johnson–Cook Model in FEM Turning of Ti6Al4V Alloy

Piotr Löschner *, Piotr Niesłonyand Szymon Kołodziej

Faculty of Mechanical Engineering, Opole University of Technology, 76 Proszkowska St., 45-758 Opole, Poland; p.nieslony@po.edu.pl (P.N.); s.kolodziej@po.edu.pl (S.K.)
* Correspondence: p.loschner@po.edu.pl

Abstract: The aim of this study was to analyse in detail the effect of varying the parameters of the Johnson–Cook (JC) material model on the results of a numerical simulation of the orthogonal turning process of the Ti6Al4V titanium alloy. The first step involved an experimental study, including the recording of cutting force components and temperature, as well as the measurement of chip geometry, which was used to validate the FEM simulation. This was followed by a sensitivity analysis of the JC model with respect to five parameters, namely *A*, *B*, *C*, *m*, and *n*, each modified independently by ±20%. The effects of these changes on cutting forces, cutting zone temperature, stresses, and chip geometry were evaluated. The results showed that parameters *A*, *B*, and *m* had the greatest influence on the physical quantities analysed, while *C* and *n* are of secondary importance. The analysis highlighted the need for precise calibration of the JC model parameters, especially when modelling machining processes involving difficult-to-machine materials. The results provided practical guidance for optimising the selection of constitutive parameters in machining simulations.

Keywords: Johnson–Cook model parameters; FEM simulation; Ti6Al4V; orthogonal turning

1. Introduction

Modern machining processes, especially in high-tech sectors such as aerospace, automotive, and biomedical, are becoming increasingly demanding in terms of dimensional accuracy, surface quality, process predictability, and efficiency. The traditional experimental approach, based on numerous physical tests, is time-consuming and costly, especially considering the machining of difficult-to-machine materials such as titanium alloys. Consequently, computer-based modelling methods for machining processes are gaining increasing importance. Numerical simulations based on the finite element method (FEM) play a key role, as they enable the analysis of phenomena occurring in the cutting zone while reducing the number of experiments. Thanks to the development of computational tools and material databases, FEM has become an essential tool for the analysis and optimisation of machining operations. For example, Kandráč et al. [1] demonstrated its application for predicting cutting forces and chip formation during the orthogonal turning of titanium alloys. Lou et al. [2] used FEM for ultra-precision machining, focusing on achieving high surface quality. Song et al. [3] analysed pre-stress multi-step cutting, showing that FEM helps optimise residual stresses and thermal effects in complex machining processes.

The finite element method is widely used in the modelling of machining processes, enabling the detailed analysis of, among other things, stress distribution, displacement, temperature, and chip formation. However, a key aspect of the accuracy of such simulations remains the selection of an appropriate material model, which must adequately represent the behaviour of the material over a wide temperature range and at high strain rates [4,5]. Improperly chosen constitutive parameters can lead to significant errors in predicting cutting forces, chip geometry, or temperature in the cutting zone. This aspect is particularly important for titanium alloys such as Ti6Al4V, which are widely used but very challenging to machine due to their low thermal conductivity, high strength at elevated temperatures, and tendency to cause rapid tool wear. These characteristics make reliable FEM simulation an essential tool for process optimisation and prediction when machining Ti6Al4V. In recent years, there has been growing interest in modern constitutive models that go beyond classical empirical approaches. In addition to simple phenomenological models such as Johnson–Cook, microstructure-based models [6], damage models with fracture criteria [7], and hybrid approaches combining experimental data with inverse modelling [8,9] are increasingly used. In recent years, neural networks have increasingly been used as alternative or hybrid constitutive models. They can act as universal function approximators to predict complex stress–strain relationships directly from the data, or be combined with physical constraints in physics-informed neural networks (PINNs). Such approaches can improve prediction accuracy for materials with complex behaviours, but require extensive datasets for training and careful validation [10].

The Johnson–Cook model is one of the most widely used phenomenological material models for describing the behaviour of a material under high plastic deformation, elevated temperature, and significant strain rates. It accounts for three main mechanisms: strain hardening, strain rate effects, and thermal softening. Mathematically, it is expressed as a multiplicative function of five parameters: A (initial yield stress), B (strain hardening modulus), C (strain rate sensitivity coefficient), m (thermal softening exponent), and n (strain hardening exponent). A key advantage of the model is that it can be calibrated using conventional tensile tests and dynamic Hopkinson bar experiments [11,12]. The JC model is highly effective in representing dynamic processes, but it does not account for microstructural phenomena, dynamic recrystallisation, or strain localisation, which limits its accuracy. Therefore, modified versions of the model are being developed [13].

The parameters of the Johnson–Cook model can be determined through classical uniaxial tests (tension, compression) or by using dynamic Hopkinson bar experiments. However, alternative methods involving the calibration of model parameters based on data from actual cutting processes and the application of various optimisation algorithms are increasingly being adopted [14]. Although these approaches provide a better fit to real-world conditions, they often result in significant discrepancies in the parameter values reported by different authors. Consequently, sensitivity analyses and the evaluation of the influence of each parameter on the final results of FEM simulations are becoming increasingly important [4,15,16].

Numerous research papers attempt to quantify the influence of individual Johnson–Cook model parameters on FEM simulation results. Parameter A is responsible for the initial level of flow stress. Its increase leads directly to higher cutting forces and alters heat distribution in the cutting zone. Shen et al. [15] demonstrated that parameter A has a strong influence on the maximum cutting force. Parameters B and n, on the other hand, describe the effect of material hardening. Their increase leads to greater resistance to plastic deformation, which affects the resulting chip morphology. Shen et al. [15] observed that higher values of parameter n favour chip segmentation, while Zhu et al. [17] confirmed this

effect in the context of high-temperature drilling of Ti6Al4V alloy. Gerstgrasser et al. [11], in turn, showed that changes in B and n significantly affect the accuracy of crack growth predictions in the workpiece material. Parameter C determines the material's sensitivity to strain rate. A study by Zhu et al. [17] showed that a higher value of C results in a local increase in temperature at the tool–material interface and leads to more intensive tool wear. Parameter m, related to thermal softening, controls the extent to which flow stress decreases with increasing temperature. Thornton et al. [18] noted that underestimating this parameter leads to inaccurate chip segmentation modelling and can cause non-linear fluctuations in machining forces. The literature also highlights the existence of non-linear interactions between parameters—for example, simultaneous increases in B and m can produce complex synergistic effects that are difficult to predict without a full sensitivity analysis. Shen et al. [15] and Wang et al. [19] compared multiple sets of JC parameters and concluded that combinations of parameters have a greater effect on cutting forces than variations in individual values. Consequently, modern methods are increasingly used to identify the most influential parameter combinations [5,16,20].

Despite the many papers analysing the JC model, there is still a gap in the literature regarding a systematic and isolated analysis of the effect of each of its parameters on key physical variables in turning simulations of difficult-to-machine alloys such as Ti6Al4V. Previous studies often focused on combined effects or used parameter sets without detailed sensitivity evaluation. This study addresses this gap by providing an individual parameter sensitivity analysis for the orthogonal turning of Ti6Al4V, focusing on the influence of A, B, C, m, and n on cutting forces, temperature distribution, and chip geometry. This new insight can help improve the precision of JC model calibration for machining simulations of titanium alloys.

2. Verification of the Johnson–Cook Material Model

2.1. Experimental Studies

The aim of the experimental study was to compare and numerically validate the Johnson–Cook material model for orthogonal turning of the Ti6Al4V titanium alloy. The validation of the finite element method (FEM) simulations was primarily based on the analysis of cutting force components, the maximum temperature in the cutting zone, and the dimensional and geometric characteristics of the chip.

The experiments were conducted on a multifunctional 3-axis CNC lathe (Okuma Genos L200E-M), equipped with a measurement setup capable of recording the Cartesian components of cutting forces. The cutting forces were measured using a piezoelectric dynamometer (Kistler model 9129AA), while the temperature in the cutting zone was measured using the natural thermocouple method. The calibration of the measurement system and the related accuracy have been described in detail in [21]. A schematic of the measurement setup is shown in Figure 1.

Experimental studies of orthogonal turning were performed using cutting tools manufactured by Tungaloy Corporation (Iwaki, Japan). A carbide insert for orthogonal turning, designated DGG500-0400, was used in the experiments. The insert was clamped in a CTER2020-5T12 toolholder, which allowed the following angles to be obtained in the working system:

- Orthogonal rake angle $\gamma_{\circ} = 20°$;
- Normal clearance angle $\alpha_{\circ} = 7°$.

The experiments were performed under dry cutting conditions, without the use of coolant, at an ambient temperature of approximately 20 °C. The test matrix included six

cutting speeds (v_c = 40, 50, 60, 70, 80, and 90 m/min), three feed rates (f = 0.05, 0.1, and 0.15 mm/rev), and a constant depth of cut a_p = 3 mm.

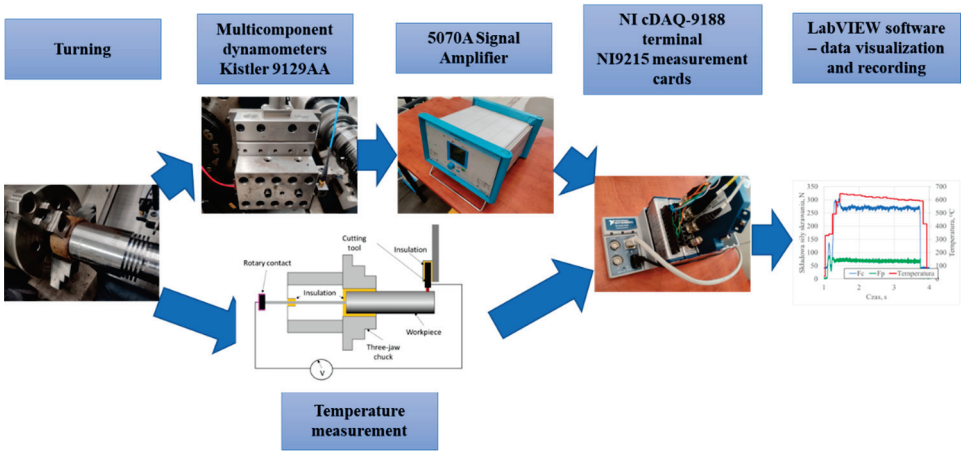


Figure 1. Schematic of the measurement setup for recording cutting force components and temperature using the natural thermocouple method.

2.2. Simulation Studies

Simulation studies of the orthogonal turning process of the Ti6Al4V titanium alloy were conducted using the same technological parameters as in the experimental studies. The aim of the research was to verify the accuracy of the material parameter identification for the Johnson–Cook model. The procedure for determining the individual parameters of the JC model was presented in [21]. Using an analytical method, the following Johnson–Cook parameters were obtained, as listed in Table 1.

Table 1. Material constants of the Johnson–Cook model determined by the analytical method [21].

A	*B*	*C*	*n*	*m*
775.2	440.3	0.01483	0.1668	0.6269

The Design Environment for Forming (DEFORM 2D/3D) engineering simulation system, developed by Scientific Forming Technologies Corporation, was used for the simulation studies. FEM simulations were performed in the DEFORM v12.0.2 environment, using the predefined material parameters of the Johnson–Cook model.

The mechanical, tribological, and thermophysical properties of the workpiece material were defined as temperature-dependent using data from the DEFORM 2D/3D material library. The simulation used an adaptive mesh with quadrilateral elements, with local remeshing in the cutting zone to maintain accuracy. Boundary conditions were set to fully fix the workpiece at the rear side, while the tool was modelled as rigid. Friction at the tool–chip interface was described by the Coulomb friction model with a coefficient of μ = 0.7. The technological parameters in the first stage of the simulation matched the experimental tests, enabling direct comparison.

2.3. Verification of Simulation Studies

After the simulation and experimental studies, a comparative analysis of the obtained results was conducted. Figure 2 presents a comparison between the numerical simulation results and the data obtained from the experimental measurements. Due to catastrophic tool wear during tests with a feed rate of f = 0.15 mm/rev and a cutting speed of v_c = 90 m/min,

it was not possible to obtain repeatable experimental data for this parameter combination. The detailed test procedure and results for this specific case are provided in our previous publication [21].

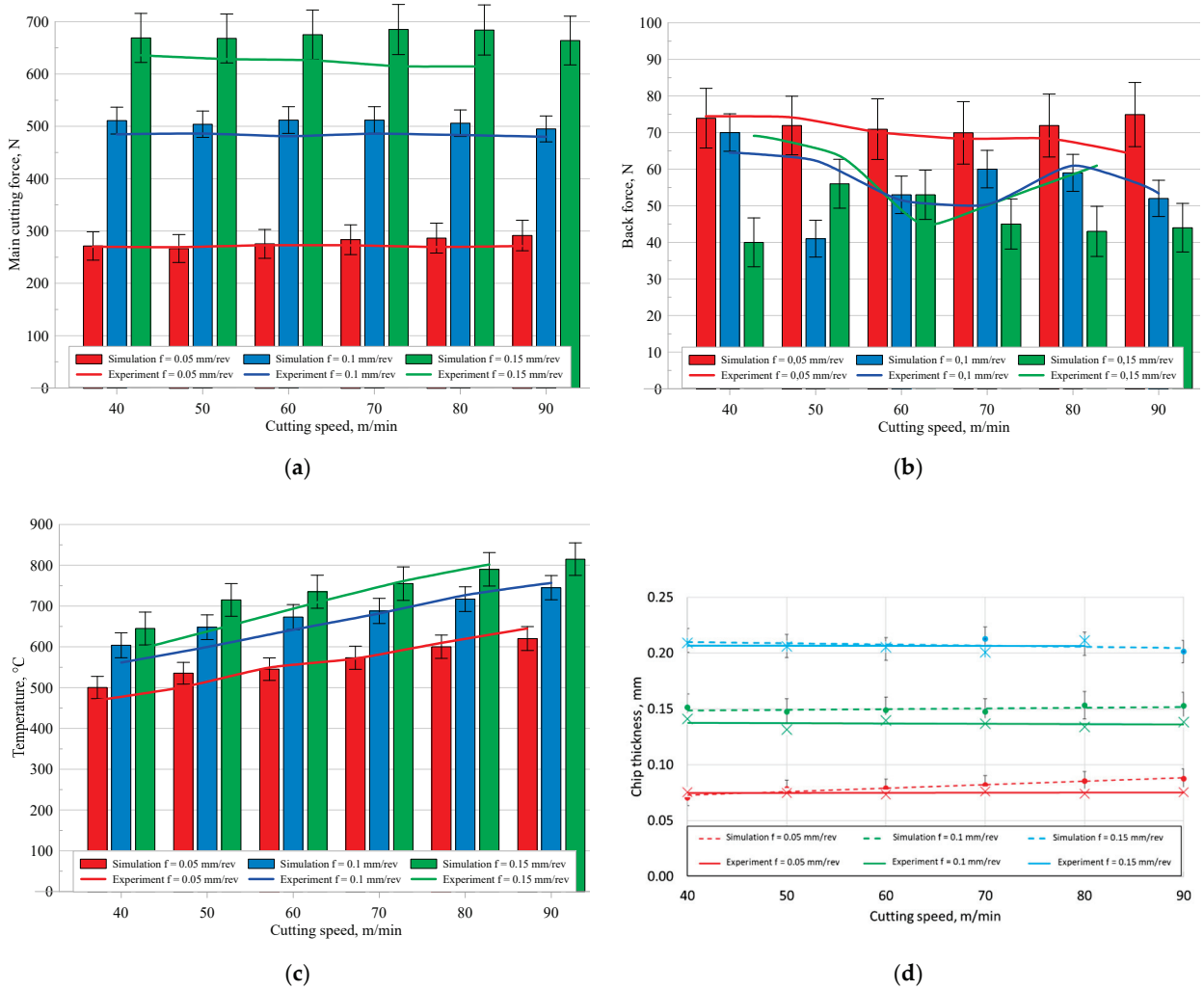


Figure 2. Comparison of simulation and experimental results for (**a**) main cutting force, (**b**) back cutting force, (**c**) cutting zone temperature, and (**d**) chip thickness.

The comparison between the numerical simulation and experimental results focused on three aspects: the cutting force components, the temperature in the cutting zone, and the geometry and thickness of the chip. The main cutting force component F_c was reproduced with high accuracy—the differences between the experimental and simulation results in most cases did not exceed 8%, and were less than 2% at low feed rates. Larger discrepancies were observed for the back force F_p especially at high feed rates, where deviations reached up to 42%. This can be explained by the fact that in orthogonal cutting the back force component is typically very small and highly sensitive to minor tool vibrations, slight misalignments, and local tool wear, which are difficult to reproduce accurately in a 2D simulation. The temperature analysis showed a consistency of 3–4%, regardless of the cutting parameters used, confirming the correct representation of thermal phenomena. The shape and thickness of the chips also showed good agreement—the largest differences in chip thickness did not exceed 14%, with the best fit observed at the highest feed rate. The obtained results confirm that the identified parameters of the JC model enable a reliable representation of the actual course of the Ti6Al4V turning process and can be effectively

used in numerical analyses within the tested range of technological parameters. After finding satisfactory agreement between the FEM simulation results and experimental data, it was concluded that the determined Johnson–Cook model parameters reliably represent the phenomena occurring in the cutting zone during orthogonal turning of the Ti6Al4V alloy. In the next stage of the research, a detailed analysis of the influence of variations in individual JC model parameters on selected physical characteristics of the process was performed. The aim of this analysis was to assess the model's sensitivity to changes in material parameters and to identify the parameters that most significantly influence the cutting process.

3. Evaluation of the Influence of Changes in the Parameters of the Johnson–Cook Constitutive Model on the Physical Characteristics of the Cutting Process

A sensitivity analysis of the Johnson–Cook model was conducted to examine how modifications to individual parameters (A, B, C, m, n) affect physical quantities of the turning process, such as cutting forces (F_c, F_p), temperature in the cutting zone, material stresses, and chip characteristics. Each parameter was independently increased and decreased by 20% relative to the baseline value, while the other model parameters were kept constant. This approach allowed the relative influence of each parameter on the individual variables to be determined and enabled the identification of those with the greatest relevance to the accuracy of cutting process prediction. The model names clearly indicate which parameter was modified and by how much—for example, "A +20%" refers to the model in which parameter A was increased by 20% relative to the baseline. Table 2 presents the values of the material parameters used in the analysis, including both the baseline model and the modified variants.

Table 2. Sets of parameter values for the Johnson–Cook model.

Material Model	*A*	*B*	*C*	*m*	*n*
Base model	775	440	0.01483	0.6269	0.1668
"*A*" +20%	**930**	440	0.01483	0.6269	0.1668
"*A*" -20%	**620**	440	0.01483	0.6269	0.1668
"*B*" +20%	775	**528**	0.01483	0.6269	0.1668
"*B*" −20%	775	**352**	0.01483	0.6269	0.1668
"*C*" +20%	775	440	**0.01780**	0.6269	0.1668
"*C*" −20%	775	440	**0.01186**	0.6269	0.1668
"*m*" +20%	775	440	0.01483	**0.7523**	0.1668
"*m*" −20%	775	440	0.01483	**0.5015**	0.1668
"*n*" +20%	775	440	0.01483	0.6269	**0.2002**
"*n*" −20%	775	440	0.01483	0.6269	**0.1334**

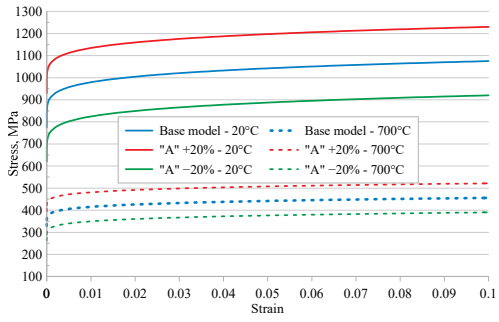
3.1. Stress–Strain Curves

Performing a stress–strain analysis is a key step in assessing the behaviour of a material under real-world cutting process conditions. To determine the influence of individual parameters of the Johnson–Cook constitutive model on the material response, an analysis of the σ–ε curves was performed for different model variants. The analysis was conducted for two representative strain rates: one low and one high. This approach made it possible to capture differences resulting from both strain rate sensitivity and thermal softening, which are incorporated into the structure of the JC model. These temperatures were chosen as they represent the ambient laboratory temperature (20 °C) and the estimated maximum cutting zone temperature (700 °C) for Ti6Al4V during orthogonal turning. The aim of this analysis

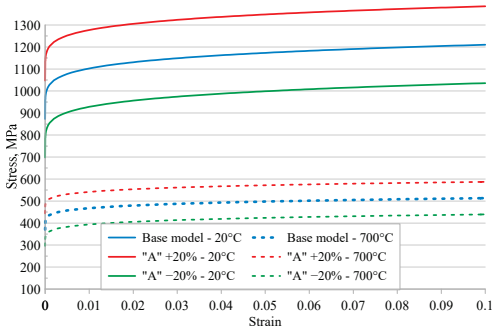
was to identify the parameters that most significantly influence the value and shape of the stress–strain curve. The following section presents the results and a detailed interpretation of the effects of parameter variations on the σ–ε curves. Figure 3 presents the stress–strain curves for the modified Johnson–Cook material models at two strain rates: 0.002604 s^{-1} and 12.5 s^{-1}. The base curve was generated by fitting the experimental tensile and compression test data using the MATLAB R2019b Curve Fitting Tool, as described in [21]. The additional curves illustrate the effect of increasing or decreasing each Johnson–Cook parameter (*A*, *B*, *C*, *m*, *n*) by ±20% to analyse the parameter sensitivity.

When analysing the effect of varying individual Johnson–Cook model parameters on the stress–strain curve, it was noted that the most significant impact on stress values was observed for parameter *A*. Increasing or decreasing the value of *A* by 20% resulted in a change in stress at a given strain of approximately ±155 MPa at 20 °C and ±66 MPa at 700 °C for low strain rates. A similar pattern of variation was observed at higher strain rates, where the stress difference reached ±175 MPa at 20 °C and ±74 MPa at 700 °C. This indicates that parameter *A* plays a key role in determining the level of initial (incipient) stress, and modifying it proportionally shifts the entire stress–strain curve vertically.

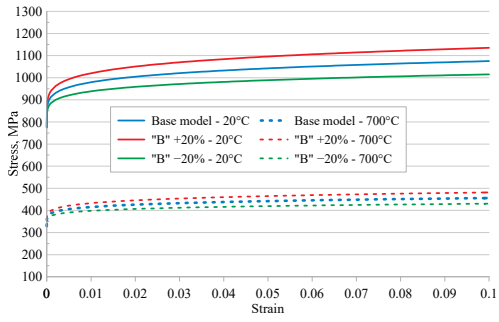
Parameter *B*, which governs strain hardening, exhibited a lesser influence on the stress–strain curve. As the strain increased, the differences between the baseline and modified models became more pronounced. The maximum difference observed within the tested parameter range was ±60 MPa (±5.6%) at a strain of 0.1 and 20 °C, and ±29 MPa (±5.6%) at 700 °C under low-strain-rate conditions. Comparable differences were observed at higher strain rates, where the maximum difference increased to ±68 MPa (±5.6%), while for 700 °C the same level of relative strain change (±5.6%) was maintained. The influence of parameter *B* becomes more pronounced at higher strain rates, where the material undergoes intense hardening.



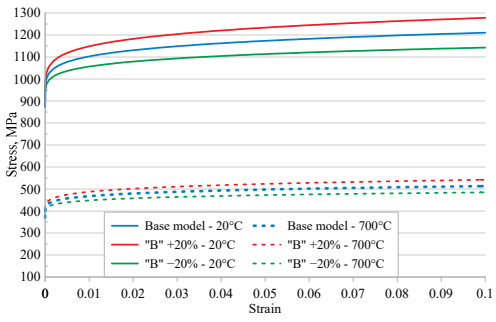
(**a**) *A* ±20%, $\dot{\varepsilon}_p$= 0.002604 s^{-1}



(**b**) *A* ±20%, $\dot{\varepsilon}_p$= 12.5 s^{-1}

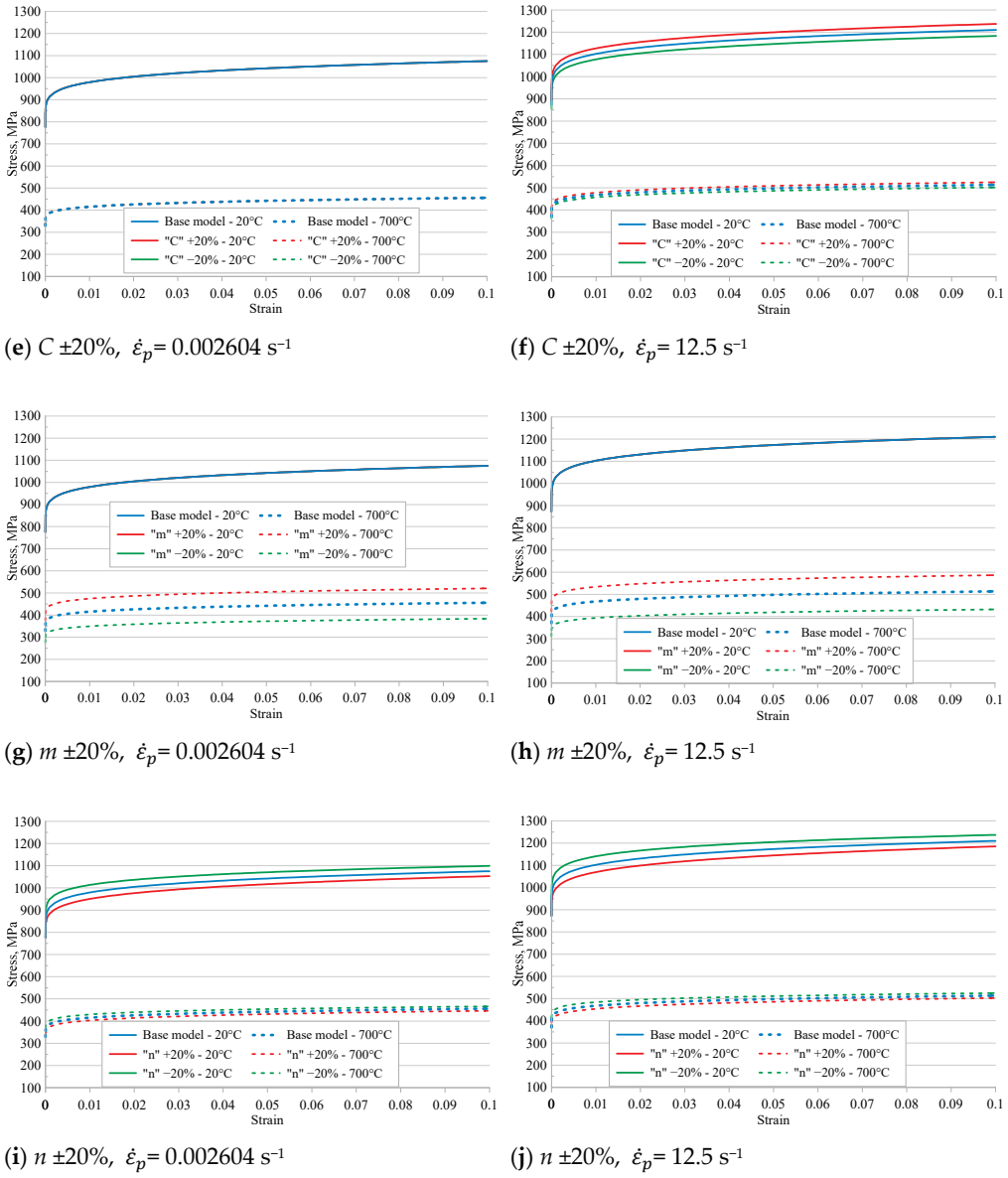


(**c**) *B* ±20%, $\dot{\varepsilon}_p$= 0.002604 s^{-1}



(**d**) *B* ±20%, $\dot{\varepsilon}_p$= 12.5 s^{-1}

Figure 3. *Cont.*



(**e**) C ±20%, $\dot{\varepsilon}_p$= 0.002604 s^{-1} (**f**) C ±20%, $\dot{\varepsilon}_p$= 12.5 s^{-1}

(**g**) m ±20%, $\dot{\varepsilon}_p$= 0.002604 s^{-1} (**h**) m ±20%, $\dot{\varepsilon}_p$= 12.5 s^{-1}

(**i**) n ±20%, $\dot{\varepsilon}_p$= 0.002604 s^{-1} (**j**) n ±20%, $\dot{\varepsilon}_p$= 12.5 s^{-1}

Figure 3. Effect of variations in individual parameters of the Johnson–Cook constitutive model on the stress–strain curve at strain rates of 0.002604 s^{-1} and 12.5 s^{-1}.

Modifying the strain rate sensitivity coefficient C had little effect on the curve under low-strain-rate conditions, since the reference and actual strain rates were equal, resulting in no stress change. As the strain rate increased, larger deviations between the curves of the modified models were observed; however, the overall effect remained relatively small. The maximum difference recorded was ±2%, which confirms the logarithmic nature of strain rate effects in the Johnson–Cook model.

The strongest temperature-dependent influence on stress values was associated with parameter m, which controls thermal softening. At a reference temperature of 20 °C, variations in m had no effect on the stress level, which is consistent with the definition of the Johnson–Cook model. However, as temperature increased, significant deviations from the baseline model were observed. At 700 °C, stress differences ranged from −14.2% to +15.8% under low-strain-rate conditions, indicating that this parameter significantly affects material softening at elevated temperatures. Similar behaviour was observed for higher strain rates.

The final parameter analysed was the strain hardening exponent n, which controls the rate of stress increase as a function of strain. The variation of "A ±20%" in the value of n resulted in stress differences ranging from −4% to +3.1%, confirming its role in defining the intensity of material strengthening. Increasing n led to a decrease in stress relative to the baseline model, whereas decreasing n resulted in a stress increase. This effect was visible across the entire temperature and strain rate range but had little impact on the initial stress values.

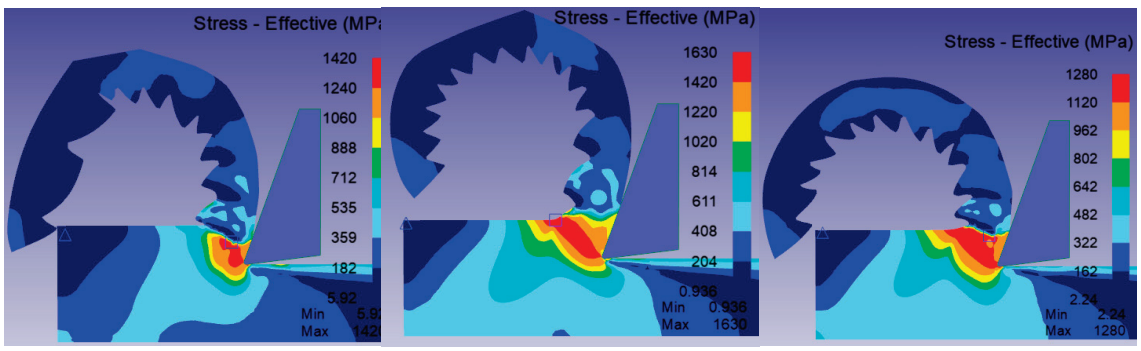
This study confirms that the sensitivity of the Johnson–Cook model to parameter variation depends on the loading conditions. Parameters A and B have the greatest influence on stress–strain behaviour, while C and n exhibit a lesser effect. Parameter m is particularly important when analysing materials subjected to elevated temperatures.

3.2. Chip Characteristics

The first step in evaluating the FEM simulation results was a visual assessment of the chip formed during orthogonal cutting, followed by the measurement of its characteristic dimensions. Figure 4 presents the chip shapes obtained for the baseline model and its parameter modifications. Table 3 presents the characteristic dimensions of the chips.

Table 3. Average values of characteristic chip dimensions for modified parameters of the Johnson–Cook constitutive material model.

Material Model	Chip Thickness on Top, mm	Chip Thickness in the Valley, mm	Chip Tip Distance, mm
Base model	**0.153**	**0.102**	**0.063**
"A" +20%	0.134	0.089	0.058
"A" −20%	0.155	0.106	0.068
"B" +20%	0.140	0.095	0.060
"B" −20%	0.154	0.096	0.178
"C" +20%	0.143	0.098	0.059
"C" -20%	0.150	0.1	0.196
"m" +20%	0.145	0.098	0.063
"m" −20%	0.144	0.111	0.197
"n" +20%	0.149	0.103	0.059
"n" −20%	0.145	0.104	0.139



Base model "A" +20% "A" −20%

Figure 4. *Cont.*

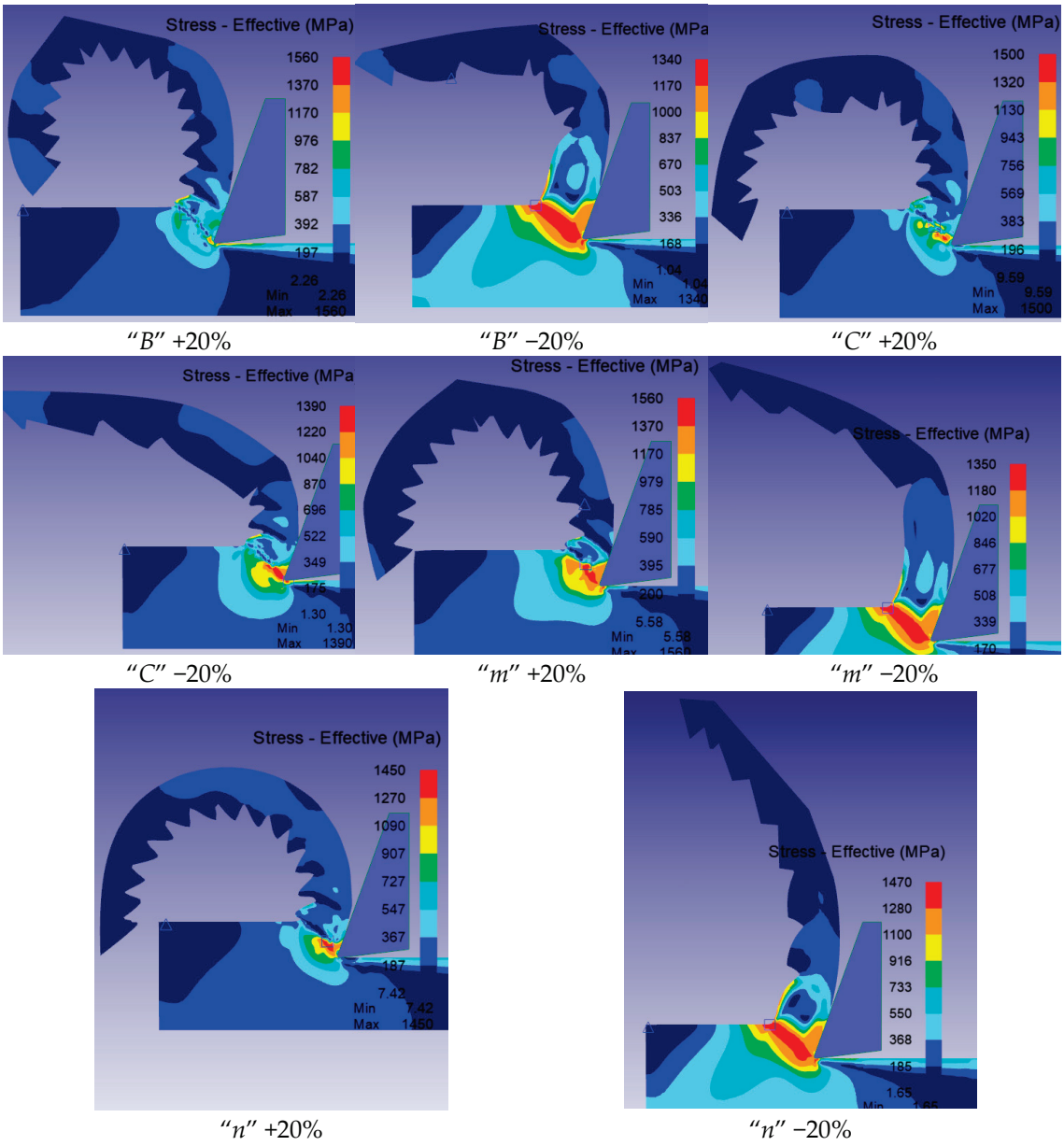


Figure 4. Chip shapes and geometries obtained in simulations using modified parameters of the Johnson–Cook model.

The analysis of the effect of varying individual parameters of the Johnson–Cook constitutive model on the chip characteristics included both a visual assessment of the chip shape and the measurement of its characteristic dimensions. Based on Figure 4 and the data in Table 3, it can be observed that each modification of the model parameters affects the chip geometry and its regularity to varying degrees.

When evaluating the influence of individual Johnson–Cook model parameters on chip shape, it was found that parameter A has the least impact. A 20% decrease in the value of A results in a maximum change of 8% in the characteristic chip dimensions. In contrast, a 20% increase in A causes a 12.5% change in those dimensions.

A further analysis revealed that increasing the remaining parameters by 20% generally results in a sawtooth chip shape, whereas decreasing these parameters causes the loss of the characteristic sawtooth profile. As a consequence, the vertex distance measured on the chip's outer surface increases. When the parameters were decreased by 20%, the vertex

distance increased by 121% to 213% compared to the baseline model, demonstrating a strong influence of these parameters on the chip geometry in FEM simulations. In contrast, increasing the parameters by 20% resulted in a maximum difference of only 8%.

It was also observed that changes in the individual parameters had no significant impact on chip thickness at the tooth tips. For the assumed range of parameter variations, the maximum deviation from the baseline model reached 8.5%. *A* similar trend was noted when analysing the chip thickness at the valleys: parameter changes of ±20% resulted in a maximum variation of ±9% in thickness relative to the baseline model.

3.3. Cutting Forces

In order to compare the effect of changing individual parameters of the Johnson–Cook model, the variations in the main cutting force (F_c) and back force (F_p) were evaluated relative to the base model. Figures 5 and 6 present the results in the form of box plots.

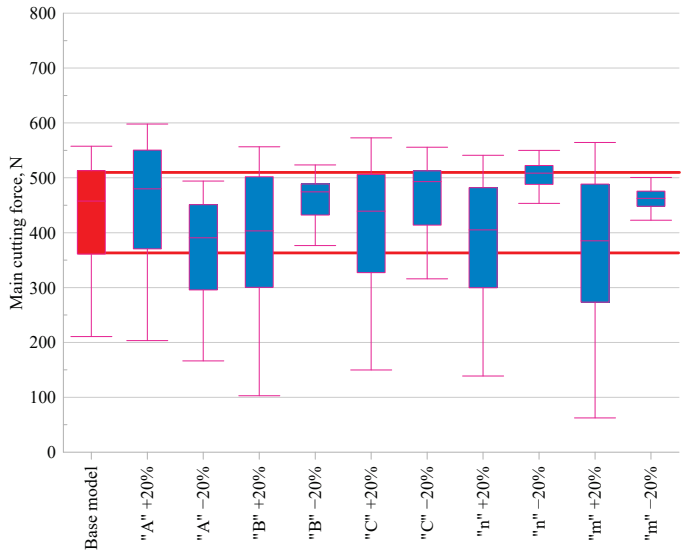


Figure 5. Comparison of main cutting force F_c values for modified Johnson–Cook material models.

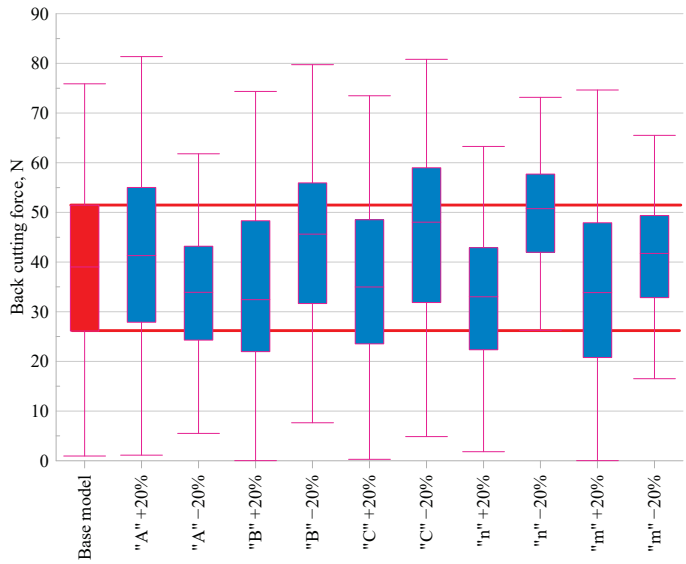


Figure 6. Comparison of back cutting force F_p values for modified Johnson–Cook material models.

An analysis of the effect of varying individual material constants of the Johnson–Cook model on the values of the main cutting force (F_c) and the back force (F_p) is presented based on the data from the graphs. The analysis was conducted relative to the base model, for which the median values were F_c = 458 N and F_p = 39 N.

An analysis of Figure 5, which illustrates the effect of parameter variation on the main cutting force, revealed that modifying the *A* parameter of the Johnson–Cook model by ±20% had a significant impact on F_c. Increasing *A* raised the force to 480 N (+4.8%), whereas decreasing *A* reduced it to 391 N (–14.6%) relative to the base model. This is because parameter *A* directly represents the initial flow stress level, and therefore its increase raises the overall cutting resistance of the material, which increases the cutting forces. Parameter *B* also showed a marked effect: increasing *B* resulted in a reduced force of 403 N (–11.9%), while decreasing *B* raised F_c to 474 N (+3.6%). For parameter *C*, the influence was noticeable but less pronounced. Increasing *C* reduced the cutting force to 439 N (–4.0%), whereas decreasing it increased the force to 493 N (+7.7%), indicating a moderate sensitivity of the force to strain rate effects. The influence of the *n* parameter, associated with strain hardening, showed an asymmetric response, increasing *n* reduced F_c to 405 N (–11.5%), while decreasing it elevated the force to 509 N (+11.1%). Finally, parameter *m*, which accounts for thermal softening, had a moderate effect. Decreasing *m* increased F_c to 463 N (+1.1%), while increasing it led to a more substantial reduction to 385 N (–15.9%). Parameter *m* affects the extent of stress reduction with increasing temperature, which also influences the cutting force level.

An analysis of Figure 6, which illustrates the effect of changing the Johnson–Cook model parameters on the back cutting force (F_p), showed that increasing *A* raised the force to 41.3 N (+5.9%), while decreasing it reduced the force to 34.0 N (–13.0%). For parameter *B*, a significant asymmetry in its influence was observed: increasing *B* decreased F_p to 32.5 N (–16.8%), whereas decreasing *B* increased the force to 45.6 N (+17.0%). Changes in parameter *C* also led to noticeable variations: increasing *C* reduced F_p to 35.0 N (–10.4%), while decreasing it raised the value to 48.0 N (+23.1%). Parameter *n* exhibited the most pronounced influence on the back force. Increasing *n* reduced F_p to 33.0 N (–15.4%), whereas decreasing *n* increased it substantially to 50.8 N (+30.1%), confirming its key role in shaping the material's plastic flow characteristics. As in the case of the main cutting force, parameter *m* had a moderate effect: decreasing *m* led to an increase in F_p to 41.8 N (+7.0%), while increasing it reduced the force to 33.8 N (–13.3%).

3.4. Temperature in the Cutting Zone

In the next stage of the analysis, the effect of changes in the Johnson–Cook model parameters on the temperature in the cutting zone was evaluated. Figure 7 presents the results of the FEM simulations, enabling a comparison of temperature values obtained for the base model and for variants in which the parameter values were altered by ±20%.

When analysing the temperature in the cutting zone (Figure 7), it can be observed that the parameters *A*, *B*, and *m* exert the greatest influence on the temperature value. An increase in the initial flow stress (*A*) leads to a temperature rise of +8.6%, while its decrease results in a −5.5% reduction. A similar effect is noted for parameter *B*, with an increase causing a +5.8% rise and a decrease resulting in a −7.1% drop, indicating its significant contribution to the intensification of thermal effects associated with material hardening. This increase can be explained by the fact that the higher flow stress resulting from larger *A* and *B* values leads to greater plastic deformation work, which is largely converted into heat in the cutting zone. In the case of parameter *m*, which governs thermal softening, variations also lead to noticeable changes: −7.3% for a decrease and +1.8% for

an increase. The strain rate sensitivity coefficient *C* produced relatively minor differences—within ±2%—confirming its limited effect on thermal behaviour in this context. Similarly, modifications of parameter *n* (strain hardening exponent) had only a marginal influence on cutting temperature, with variations of less than ±2.1%.

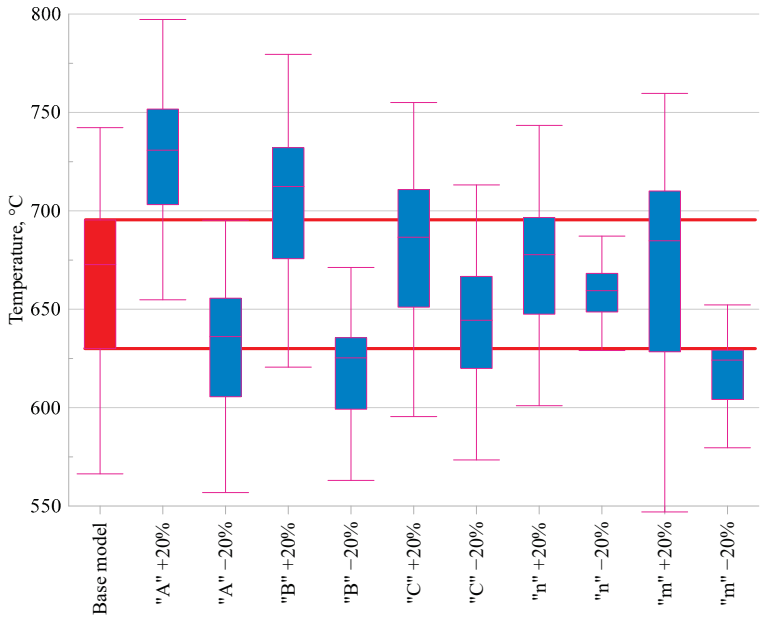


Figure 7. Comparison of the maximum temperature value occurring in the cutting zone for modified Johnson–Cook constitutive models.

3.5. Stress in the Material

The effect of changing the values of the material constants in the Johnson–Cook constitutive model was also assessed in relation to the stresses in the material. Figure 8 showed the impact of modifying individual constants on the stress results obtained.

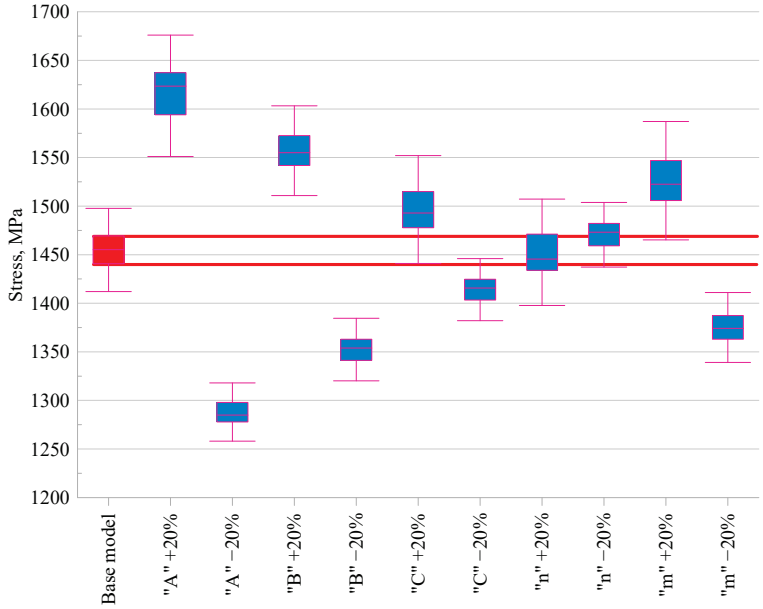


Figure 8. Comparison of the maximum stress occurring in the material for modified Johnson–Cook constitutive models.

Analysing Figure 8, which presents the effect of changing the JC model parameters on the stress in the material, it can be observed that parameter A, representing the yield strength at the reference temperature, has the greatest influence on the stress value. An increase in this parameter led to an 11.6% rise in stress, while a decrease resulted in an 11.7% reduction, clearly indicating that A plays a key role in determining the stress level. Changes in parameter B, responsible for material hardening, showed a similar but slightly less pronounced effect, with an increase in B leading to a 6.9% increase in stress and a decrease resulting in a reduction of the same magnitude. For parameters C, m, and n, the observed changes were less significant. The influence of C and m remained within $\pm$2.7%, which is consistent with their less dominant role in stress development. For parameter n, the differences were minimal, reaching up to $\pm$1.2%, indicating its more subtle effect on material strengthening under the conditions analysed. However, it should be noted that the Johnson–Cook model does not capture microstructural phenomena such as dynamic recrystallisation, which may influence stress predictions at high temperatures. More advanced physically based models exist, but they require extensive microstructural data and calibration, which were beyond the scope of this sensitivity study.

4. Conclusions

In this study, a comprehensive analysis was performed to investigate the influence that the Johnson–Cook constitutive model parameters have on key characteristics of the cutting process of titanium alloy Ti6Al4V, such as cutting forces, temperature in the machining zone, stresses, and chip geometry. As a first step, the numerical model was validated using experimental data obtained from an actual orthogonal turning process. The simulation results showed very good agreement with the experimental measurements, especially in terms of cutting forces and chip thickness, which confirmed the correctness of the material parameters used in the base model.

The remainder of the paper focused on assessing the sensitivity of the JC model to changes in individual parameters: A, B, C, m, and n. The analysis showed that

- the A parameter (plasticising stress) has the greatest influence on the level of cutting forces, temperature, and stresses;
- the B parameter, which is responsible for the strengthening effect of the material, significantly shapes the distribution of stresses and temperatures in the cutting zone and the chip, and its effect on forces is moderate;
- the C parameter has a moderate effect on all the characteristics analysed, which is consistent with the logarithmic nature of its dependence on strain rate;
- the m parameter, which describes thermal softening, is most influenced by temperatures in the cutting zone and stress;
- the n parameter, related to plastic strengthening, mainly affects the components of the cutting force, with a marginal effect on other aspects.

These observations suggest that effective calibration of the Johnson–Cook model parameters requires special attention to the parameters A, B, and m, due to their dominant influence on the thermomechanical phenomena in the cutting process. The use of models based on the literature and unverified parameter values can lead to significant prediction errors in FEM simulations.

Author Contributions: Conceptualisation, P.L. and P.N.; methodology, P.N.; software, P.L.; validation, P.L., P.N. and S.K.; formal analysis, P.L.; investigation, P.L. and P.N.; resources, P.L.; data curation, P.L.; writing—original draft preparation, P.L., P.N. and S.K.; writing—review and editing, P.L. and

S.K.; visualisation, P.L.; supervision, P.N.; project administration, P.L.; funding acquisition, P.L. and S.K. All authors have read and agreed to the published version of the manuscript.

Funding: This work was financially supported by the Opole University of Technology under ALFA project no. 222/24.

Institutional Review Board Statement: Not applicable.

Informed Consent Statement: Not applicable.

Data Availability Statement: The original contributions presented in this study are included in the article. Further inquiries can be directed to the corresponding author.

Acknowledgments: During the preparation of this work, the authors used ChatGPT (OpenAI, GPT-4o model) to check for grammar errors and perform translations. After using this tool/service, the authors reviewed and edited the content as needed and take full responsibility for the content of the publication.

Conflicts of Interest: The authors declare no conflicts of interest.

References

1. Kandráč, L.; Maňková, I.; Vrabe', M.; Beňo, J. Finite element simulation of cutting forces in orthogonal machining of titanium alloy Ti-6Al-4V. *Appl. Mech. Mater.* **2014**, *474*, 192–199. [CrossRef]
2. Lou, Y.; Chen, L.; Wu, H.; To, S. Influence of cutting velocity on surface roughness during the ultra-precision cutting of titanium alloys based on a comparison between simulation and experiment. *PLoS ONE* **2023**, *18*, e0288502. [CrossRef]
3. Song, X.; Li, A.; Lv, M.; Lv, H.; Zhao, J. Finite element simulation study on pre-stress multi-step cutting of Ti-6Al-4V titanium alloy. *Int. J. Adv. Manuf. Technol.* **2019**, *104*, 2761–2771. [CrossRef]
4. Qiu, X.; Cheng, X.; Dong, P.; Peng, H.; Xing, Y.; Zhou, X. Sensitivity analysis of johnson-cook material constants and friction coeffcient influence on finite element simulation of turning inconel 718. *Materials* **2019**, *12*, 3121. [CrossRef]
5. Shokry, A.; Gowid, S.; Mulki, H.; Kharmanda, G. On the Prediction of the Flow Behavior of Metals and Alloys at a Wide Range of Temperatures and Strain Rates Using Johnson–Cook and Modified Johnson–Cook-Based Models: A Review. *Materials* **2023**, *16*, 1574. [CrossRef]
6. Bai, J.; Tong, Z. A novel multiscale material plasticity simulation model for high-performance cutting AISI 4140 steel. *Int. J. Adv. Manuf. Technol.* **2021**, *116*, 3891–3904. [CrossRef]
7. Živković, J.; Dunić, V.; Milovanović, V.; Pavlović, A.; Živković, M. A modified phase-field damage model for metal plasticity at finite strains: Numerical development and experimental validation. *Metals* **2021**, *11*, 47. [CrossRef]
8. Hardt, M.; Bergs, T. Considering multiple process observables to determine material model parameters for FE-cutting simulations. *Int. J. Adv. Manuf. Technol.* **2021**, *113*, 3419–3431. [CrossRef]
9. Ribeiro-Carvalho, S.; Horovistiz, A.; Davim, J.P. Material model assessment in Ti6Al4V machining simulations with FEM. *J. Mech. Eng. Sci.* **2021**, *235*, 5500–5510. [CrossRef]
10. Dornheim, J.; Morand, L.; Nallani, H.J.; Helm, D. Neural Networks for Constitutive Modeling: From Universal Function Approximators to Advanced Models and the Integration of Physics. *Arch. Comput. Methods Eng.* **2024**, *31*, 1097–1127. [CrossRef]
11. Gerstgrasser, M.; Smolenicki, D.; Akbari, M.; Klippel, H.; Roelofs, H.; Cadoni, E.; Wegener, K. Analysis of two parameter identification methods for original and modified Johnson-Cook fracture strains, including numerical comparison and validation of a new blue-brittle dependent fracture model for free-cutting Steel 50SiB8. *Theor. Appl. Fract. Mech.* **2021**, *112*, 102905. [CrossRef]
12. Shahanur Hasan, M.; De Pellegrin, D.; Clegg, R.; Yan, C. Johnson-Cook model parameters determination for 11% and 14% Mn-Steel. *Mater. Sci. Eng. B* **2022**, *283*, 115788. [CrossRef]
13. Zhou, T.; He, L.; Feng, Z.; Tian, P.; Du, F.; Zou, Z.; Zhou, X. Inverse identification of material constitutive parameters based on co-simulation. *J. Mater. Res. Technol.* **2022**, *20*, 221–237. [CrossRef]
14. Zhou, J.; Ren, J.; Jiang, Y. Inverse identification of modified Johnson–Cook model for cutting titanium alloy Ti6Al4V using firefly algorithm. *Proc. Inst. Mech. Eng. B J. Eng. Manuf.* **2020**, *234*, 584–599. [CrossRef]
15. Shen, X.; Zhang, D.; Yao, C.; Tan, L.; Li, X. Research on parameter identification of Johnson–Cook constitutive model for TC17 titanium alloy cutting simulation. *Mater. Today Commun.* **2022**, *31*, 103772. [CrossRef]
16. Wang, C.; Xu, J.; Chen, X.; Han, C.; Wang, W.; Luo, X. A modified Johnson–Cook model for 2A12 aluminum alloys. *Mech. Time-Depend. Mater.* **2024**, *28*, 2085–2104. [CrossRef]

17. Zhu, Z.; Zhu, Y.; Sun, X.; Gao, C.; Lin, Z.; He, B. 3D finite element simulation for tool temperature distribution and chip formation during drilling of Ti6Al4V alloy. *Int. J. Adv. Manuf. Technol.* **2022**, *121*, 5155–5169. [CrossRef]
18. Thornton, E.-L.; Zannoun, H.; Vomero, C.; Caudill, D.; Schoop, J. A Review of Constitutive Models and Thermal Properties for Nickel-Based Superalloys Across Machining-Specific. *J. Manuf. Sci. Eng.* **2023**, *145*, 080801. [CrossRef]
19. Wang, Z.; Cao, Y.; Gorbachev, S.; Kuzin, V.; He, W.; Guo, J. Research on Conventional and High-Speed Machining Cutting Force of 7075-T6 Aluminum Alloy Based on Finite Element Modeling and Simulation. *Metals* **2022**, *12*, 1395. [CrossRef]
20. Shan, C.; Zhang, M.; Zhang, S.; Dang, J. Prediction of machining-induced residual stress in orthogonal cutting of Ti6Al4V. *Int. J. Adv. Manuf. Technol.* **2020**, *107*, 2375–2385. [CrossRef]
21. Löschner, P.; Gupta, M.K.; Niesłony, P.; Korkmaz, M.E.; Jamil, M. Determination and Verification of the Johnson–Cook Constitutive Model Parameters in the Precision Machining of Ti6Al4V Alloy. *Machines* **2024**, *12*, 709. [CrossRef]

Disclaimer/Publisher's Note: The statements, opinions and data contained in all publications are solely those of the individual author(s) and contributor(s) and not of MDPI and/or the editor(s). MDPI and/or the editor(s) disclaim responsibility for any injury to people or property resulting from any ideas, methods, instructions or products referred to in the content.

materials

MDPI

Article

Numerical Simulation Study on Non-Axisymmetric Die-Less Spinning with a Right-Angle Groove in the Tube

Xuesong Ren [1], Zuojun Fan [2], Zhen Jia [1,*], Yongping Shen [1,*] and Huanzhang You [1]

[1] School of Aerospace Engineering, Shenyang Aerospace University, Shenyang 110136, China; 15042172675@163.com (X.R.); 18180848764@163.com (H.Y.)
[2] Prosper Metal Forming Corporation, Xi'an 710089, China; shhybm201@163.com
* Correspondence: jiaz_2006@sina.com (Z.J.); syp0601a@163.com (Y.S.)

Abstract: To address the challenges of non-axisymmetric tube spinning, this study employs finite element simulations to validate a novel spinning method for right-angle groove tubes. Three forming schemes with distinct roller path geometries were designed and analyzed using Simufact Forming, with 6063-O aluminum alloy tubes serving as the research material. The simulation results indicate that multi-pass forming (Schemes I and II) significantly enhances wall thickness uniformity compared to single-pass forming (Scheme III). Scheme I exhibits optimal performance due to the minimized equivalent stress in the final forming pass. The maximum stress is concentrated at the groove bottom, leading to wall thinning and springback, while the maximum strain occurs at the roller exit point, where metal accumulation causes local wall thickening. Experimental observations confirm the consistency with the simulation results, validating the model's reliability. This study deepens the understanding of deformation mechanisms in complex groove forming, highlighting the roller path geometry in controlling stress-strain distribution and final product quality.

Keywords: non-axisymmetric die-less spinning; right-angle groove; finite element simulation

1. Introduction

As an advanced manufacturing technology characterized by high efficiency, precision, and material utilization, spinning has become indispensable across the aerospace, automotive, defense, and medical industries [1–4]. Its ability to produce complex shapes with short production cycles makes it particularly suitable for small-batch manufacturing of special-shaped components, driving extensive research on die-less spinning for asymmetric parts [5].

Asymmetric spinning plays a pivotal role in fabricating plates and cylindrical components [6–10]. Wrinkling and cracking in spinning have received much attention. Chen et al. [11] developed a model for flange wrinkling in conventional spinning (combining energy analysis and real-time geometry updates), finding that elastic strain energy oscillations from circumferential shrinkage cause wrinkling. Wilson and Long [12], via FE simulations, found that roller contact induces large residual stress in the flange due to bending moments. Wrinkling in traditional spinning starts when the roller forms a plastic hinge with the blank edge; these moments make wrinkling energy-favorable (shown by reduced elastic strain energy in the model). He et al. [13] used ECCI and APTRS to study cracks in spun Haynes 230 parts, revealing that grain boundary carbide precipitation

initiates cracking. For asymmetric cylindrical parts, Wilson et al. [14] pioneered offset tube production by adjusting the relative position between the tube axis and rotation axis, thus expanding geometric design possibilities. Arai and Gondo [15] introduced a multi-pass spinning technique to form slanted or curved tubes, enhancing process flexibility for non-axisymmetric profiles. Jia et al. [16] further demonstrated the formation of saddle grooves in tube mid-sections using conventional rollers through optimized roller path derivation, overcoming limitations of traditional symmetric spinning.

The increasing demand for complex geometries has spurred the integration of finite element simulation into spinning research. Huang et al. [17] utilized Abaqus/Explicit to numerically investigate high-temperature neck spinning, analyzing how the friction coefficient, roller speed, and tip radius influence forming quality. Zhao et al. [18] proposed a hybrid spinning-flaring method for uniform-thickness curved workpieces, elucidating deformation mechanisms and failure modes such as compression buckling in transition zones. Xia et al. [19] focused on hot spinning of thin-walled magnesium alloy tubes with internal ribs, revealing defect formation mechanisms such as underfilling and back depression in rib structures. Complementary studies have deepened the understanding of spinning mechanics. Gondo et al. [20] characterized thickness, texture, and crystal orientation changes in aluminum tube spinning, linking microstructural evolution to process parameters. Xu et al. [21,22] identified non-periodic stress distributions caused by uneven roller contact, proposing a three-roller staggered configuration to balance mandrel loads and improve operational stability. Their follow-up work on titanium alloy spinning revealed that only the McClintock model accurately predicts crack reduction under moderate thinning rates, highlighting model specificity in material-dependent processes. Roy et al. [23] validated axisymmetric finite element models' limitations in predicting non-axisymmetric outcomes, while Xiao et al. [24] optimized roller paths for flanged cylindrical components, determining a 21° maximum flange inclination through parametric analysis. Xia et al. [25–27] pioneered non-axisymmetric die-less spinning on tube ends and validated the method via 3D finite element modeling. Subsequently, Jia et al. [17,28] extended this research to the mid-section of the tube, further exploring non-axisymmetric die-less spinning in central regions.

Special-shaped tubular structures exhibit considerable potential application value, and there currently exist typical forms such as saddle-shaped asymmetric structures. However, the special shape of the tube with straight features in the middle has not been thoroughly investigated. This study focused on right-angle groove structures with distinct linear features as the analytical object. Since the stress–strain characteristics of the metal flow field are difficult to obtain directly through experimental means, the finite element simulation method is thus proposed for this research. Through systematic comparative analysis with the experimental results, the reliability of the finite element simulation results is verified. On this basis, by utilizing the simulation results, the distribution characteristics of the stress–strain field under three working conditions are analyzed, and the stress concentration areas and weak parts in the forming process are clarified, which provides a theoretical basis for subsequent actual production.

2. Establishment of the Finite Element Model

2.1. Roller Path Design

To produce a tube with a right-angle groove, the axial and radial movements of the roller are strategically designed. In the radial direction, the roller periodically approaches the tube and retracts according to a specified feed depth. Axially, after completing each radial pass, the roller shifts to the next position at a specified feed rate to prepare for the

subsequent radial pass. As depicted in Figure 1a, the feed depth of the roller is dependent on the angular position of the workpiece, denoted by λ_1, λ_2, and λ_3. When the workpiece rotates 180°, the roller reaches its maximum feed depth, corresponding to the depth λ_2 (represented by the blue line). This depth signifies the maximum depth of the current channel. Concurrently, as illustrated in Figure 1b, once the radial feeding is completed, the roller initiates axial movement. After advancing Δm, the axial motion ceases. When the tube rotates to the designated position, the roller resumes radial movement. This cyclic process is repeated until the forming is completed.

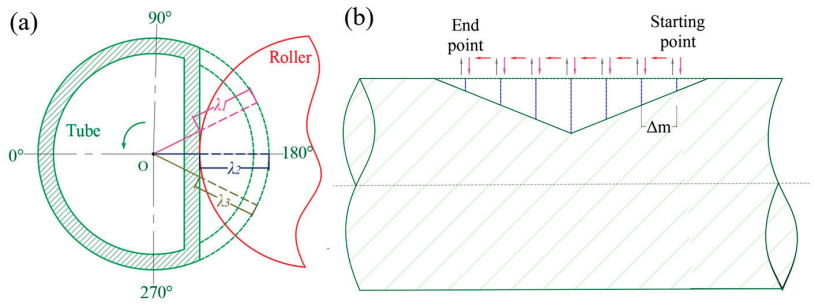


Figure 1. Schematic representation of roller path. (**a**) Radial direction. (**b**) Axial direction.

To optimize the forming process, three distinct forming schemes were designed, comprising two multi-pass forming schemes and one single-pass forming scheme. Scheme I maintains a constant forming width for each pass while gradually increasing the forming depth; Scheme II keeps the forming angle unchanged across passes but progressively increases both the forming width and depth; Scheme III achieves direct forming with the maximum width and depth in a single pass. This systematic design of three schemes investigates the effects of process parameters (width, depth, and wall thickness) on forming quality, providing a theoretical foundation for selecting optimal process routes in practical applications. The specific details of each scheme are illustrated in Figure 2. The final forming depth for all spinning schemes is fixed at 9 mm.

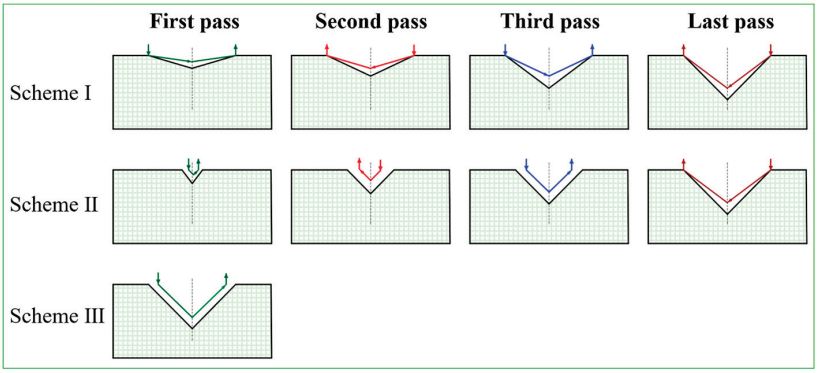


Figure 2. Representations of the axial roller paths for three schemes.

To form a tube with a right-angle groove at its midsection into the target shape, a reasonable roller path is critical. The tube is mounted on a shaft for rotation, and the roller combines axial and radial reciprocating movements; in the radial direction, the roller moves around the tube in the non-deformation region and contacts the tube to initiate deformation. The deformation area path is divided into three stages, with the specific geometric relationship of the radial path illustrated in Figure 3a.

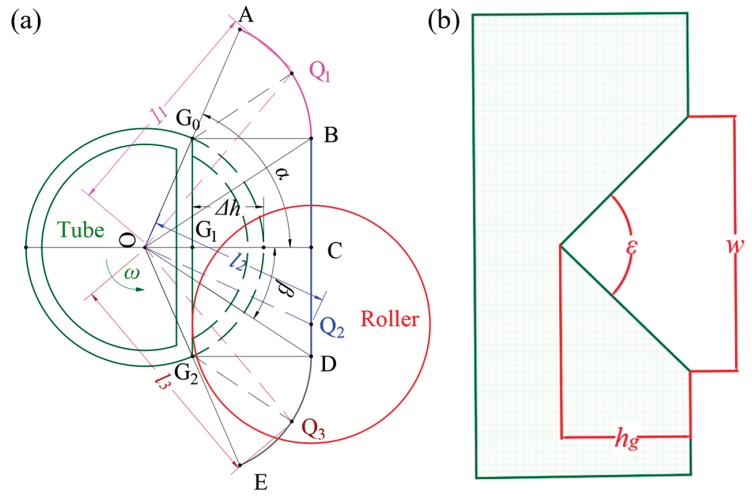


Figure 3. The geometric relationship of the roller path. (**a**) Radial direction. (**b**) Axial direction.

Stage 1 involves the roller center moving from initial point A to boundary point B; Stage 2 involves the roller center moving from B to D at the maximum feed depth, with C (the midpoint of line segment BD) corresponding to the maximum feed depth position; Stage 3 involves the roller center moving from D to the final point E. The critical contact points include G_0 (the first contact point in the current pass), G_1 (the contact point at maximum feed depth), and G_2 (the last contact point before deformation ends), where Q denotes the roller center position and O denotes the tube center position. To determine the rotation angle of each stage, let the angular velocity be Ω and the time be t, where R = roller radius, r = tube radius, and Δh = maximum reduction in the previous pass. In triangle G_0OG_1, $\angle G_0OG_1$ is denoted as α, and its cosine value is given by

$$\alpha = arccos\left(\frac{r-\Delta h}{r}\right) \tag{1}$$

In triangle BOC, $\angle$BOC is denoted as β, and its cosine value is expressed by

$$\beta = \arctan\left(\frac{\sqrt{r^2-(r-\Delta h)^2}}{r+R-\Delta h}\right) \tag{2}$$

The angular ranges of the three stages are as follows:

$$\begin{cases} \pi-\alpha < \Omega t < \pi-\beta \\ \pi-\beta < \Omega t < \pi+\beta \\ \pi+\beta < \Omega t < \pi+\alpha \end{cases} \tag{3}$$

Let the position of the center during Stage 1 be denoted as Q_1. Consider triangle G_0OQ_1, where the length OQ_1 is l_1, and $\angle G_0OQ_1$ is γ_1. Then, γ_1 can be expressed as

$$\gamma_1 = \Omega t - \pi + \alpha \tag{4}$$

Then, according to the cosine theorem, l_1 can be expressed as

$$l_1 = r\left[\cos\gamma_1 + \sqrt{\cos^2\gamma_1 - (R/r)^2 + 1}\right] \tag{5}$$

Let the position of the center during Stage 1 be denoted as Q_2. Consider triangle COQ_2, where the length OQ_2 is l_2, and $\angle COQ_2$ is γ_2. Then, γ_2 can be expressed as

$$\gamma_2 = |\pi - \Omega t| \tag{6}$$

Then, according to the cosine theorem, l_2 can be expressed as

$$l_2 = (R + r - \Delta h)/\cos\gamma_2 \tag{7}$$

Let the position of the center during Stage 3 be denoted as Q_3. Consider triangle G_2OQ_3, where the length OQ_3 is l_3, and $\angle G_2OQ_3$ is γ_3. Then, γ_3 can be expressed as

$$\gamma_3 = \pi + \alpha - \Omega t \tag{8}$$

Then, according to the cosine theorem, l_3 can be expressed as

$$l_3 = r\left[\cos\gamma_3 + \sqrt{\cos^2\gamma_3 - (R/r)^2 + 1}\right] \tag{9}$$

By combining Equations (1)–(10), the complete feed rate δ can be derived as

$$\delta = R + r - \begin{cases} l_1, \pi - \alpha < \Omega t < \pi - \beta \\ l_2, \pi - \beta < \Omega t < \pi + \beta \\ l_3, \pi + \beta < \Omega t < \pi + \alpha \end{cases} \tag{10}$$

As illustrated in Figure 3b, the axial target shape is similar to an isosceles triangle, with a base width of w, a depth of h_g, and a vertex angle of ε, which satisfies the following relationship:

$$\tan\frac{\varepsilon}{2} = \frac{w/2}{h_g} \tag{11}$$

Let the axial feed rate be $z(t)$, the workpiece rotational speed be f_{rot}, and the axial feed rate be f_{ax}; then, $z(t)$ can be expressed as

$$z(t) = f_{ax} f_{rot} t \tag{12}$$

Drawing on Equations (1)–(12), the coordinated control of the roller's axial and radial feed can be effectively achieved. Thus, a comprehensive experimental procedure can be established to meet the specified shape requirements. The radial feed of the roller for forming depths ranging from 1 to 9 mm is detailed in Figure 4. The axial feed can be designed according to three schemes.

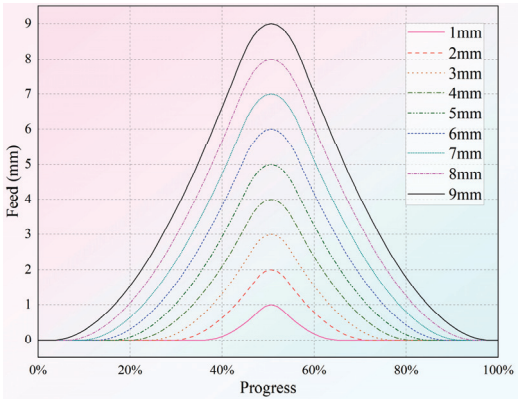


Figure 4. The radial feed of the roller.

2.2. Material Parameters

The tube material selected was 6063-O aluminum alloy. Its detailed chemical composition and mechanical property parameters are listed in Tables 1 and 2 [16,29,30], respectively. The corresponding stress–strain curves are illustrated in Figure 5. The constitutive equation of 6063-O aluminum alloy at room temperature is described by a power-hardening model, expressed as

$$\sigma = \sigma_s + K\varepsilon^n \tag{13}$$

Table 1. Chemical composition of 6063-O aluminum alloy.

Element	Content Range (%)	Typical Value (%)
Aluminum (Al)	Balance	—
Silicon (Si)	0.20–0.60	0.40
Magnesium (Mg)	0.45–0.90	0.65
Iron (Fe)	≤0.35	0.25
Copper (Cu)	≤0.10	—
Manganese (Mn)	≤0.10	—
Zinc (Zn)	≤0.10	—
Titanium (Ti)	≤0.10	—
Other Impurities	Single ≤ 0.05, Total ≤ 0.15	—

Table 2. Mechanical properties (typical values at room temperature) of 6063-O aluminum alloy.

Property	Test Standard [31]	6063-O Aluminum Alloy
Tensile Strength (σ_b)	ASTM B221	≤180.2 MPa
Yield Strength (σ_s)	ASTM B221	≤68 MPa
Relative Elongation (δ_5)	ASTM B221	≤56%
Hardness (HB)	ASTM E18	≤50 HB
Elastic Modulus (E)	—	68–70 GPa
Poisson's Ratio (ν)	—	0.33

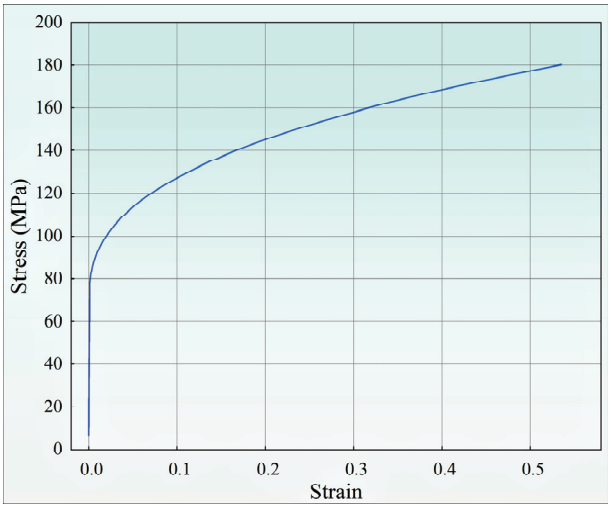


Figure 5. Stress–strain curve of 6063-O aluminum alloy.

In this model, the flow stress σ is defined as the instantaneous stress required to sustain plastic deformation. The plastic strain ε is referenced to the yield point, with ε = 0 corresponding to the onset of yielding. Here, σ_s denotes the yield strength

of the 6063-O alloy, *K* is the strength coefficient, and n is the strain-hardening index. These parameters were determined by fitting experimental stress–strain data, yielding σ_s = 68 MPa, K ≈ 142.35 MPa, and n ≈ 0.38. For regions without plastic deformation (where $\varepsilon = 0$), the material obeys Hooke's law ($\sigma = E\varepsilon$), and the stress remains below the yield strength.

2.3. Settings of the Finite Element Model

In this study, computational models were established using the Simufact Forming 16.0 finite element simulation platform. Three-dimensional geometric models were constructed for key components, including the forming roller, tube, spindle, and tailstock. With the exception of the tube, other components exhibit extremely small and negligible deformation, so they are treated as rigid bodies. Specifically, the mandrel and roller are modeled as rigid bodies due to their significantly higher hardness (45 steel, hardness > 180 HB) compared to the 6063-O tube (annealed, hardness ~55 HB), resulting in negligible tool deformation under actual forming forces (maximum ~0.4 kN). However, minor effects persist—such as a slight overestimation of local contact pressure—though these are negligible for predicting overall trends. Notably, for softer tooling (carbon steel) or extreme forces exceeding the tools' yield limits, the rigid-body assumption may introduce larger errors, though such scenarios lie beyond the scope of this study.

The tube was fixed via two-point fixation using a spindle and a hydraulically driven tailstock; one end was inserted into the spindle, and the other end was secured by the tailstock's conical tip, which extended into the tube and applied a pressure of 2–3 MPa. This ensured coaxial rotation of the tube with the spindle (runout < 0.03 mm) and prevented axial slippage. To simplify the model, the spindle and tailstock were merged into a single model, with corresponding forces applied to simulate their functional roles. Mineral oil containing anti-wear additives was uniformly sprayed onto the tube's outer surface and the roller (flow rate: 5 mL/min), maintaining a Coulomb friction coefficient of 0.12 ± 0.02 (with 0.12 adopted in simulations). The roller and spindle components were calibrated, ensuring dimensional accuracy within ±0.02 mm, and the perpendicularity deviation between the roller axis and the tube axis was controlled to <0.1°. The tube's wall thickness and outer diameter were measured using a digital micrometer and vernier caliper. In the simulation, a table-driven approach was adopted to ensure the accuracy of the roller's axial and radial movements. This means that all movements are time-synchronized, with each time point corresponding to a specific position of the roller.

The radius of the roller is 75 mm. Material properties can be directly simulated by inputting the corresponding data into the software. As depicted in Figure 6, the tube has the following dimensional specifications: an overall length of 120 mm, an outer diameter of 30 mm, and a wall thickness of 2 mm. The tube was firmly mounted between the spindle and tailstock mechanism, with both ends equipped with 40 mm long axle insertions to guarantee precise concentric alignment between the tube, spindle, and tailstock components. The target forming section of the tube remained unconstrained within the central hollow area. The contact surface of the roller featured a small nose radius of 2 mm. The experiment was conducted at room temperature, so the temperature was set to 25 degrees Celsius. Material properties can be simulated by inputting the data from Tables 1 and 2, along with Equation (13), into the software.

The finite element model was constructed using 3D hexahedral elements (Sheetmesh) with reduced integration, which is well suited for handling large plastic deformation and mitigating mesh distortion. To balance computational efficiency and simulation accuracy, a uniform meshing strategy was adopted with a consistent mesh size throughout the

entire model. The consistent mesh size was set to 0.5 mm, determined by the geometric characteristics of the tube (wall thickness 2 mm) and the right-angle groove (minimum radius 2 mm). This size ensures that the deformation zone (e.g., contact area between the roller and tube) is discretized into at least 4 elements along the thickness direction, which is sufficient to resolve local strain gradients while avoiding excessive computational load. This ensures sufficient resolution to capture local strain gradients in deformation zones (contact areas between the tube and roller) while maintaining a manageable computational load. A mesh convergence study was performed for the 6063-O aluminum alloy tubes with a 2 mm wall thickness, focusing on the number of element layers through the thickness (1, 2, and 3 layers). Considering the significant local strain gradients in deformation zones, the three-element layer configuration, despite increasing the computation time by 15% compared to the two-element layer, more accurately captured the stress–strain distribution, especially in stress-concentrated regions such as the groove bottom. Quantitative comparison showed that the one-element layer underestimated the maximum equivalent stress at the groove bottom by 12% compared to the three-element layer, while the two-element layer exhibited a 5% deviation. The three-element layer, despite increasing the computation time from 8 h to 9.2 h (on a 16-core workstation), achieved a convergence error of <2% relative to a finer four-element layer, confirming its optimality. Thus, the three-element layer mesh was selected as optimal for subsequent simulations.

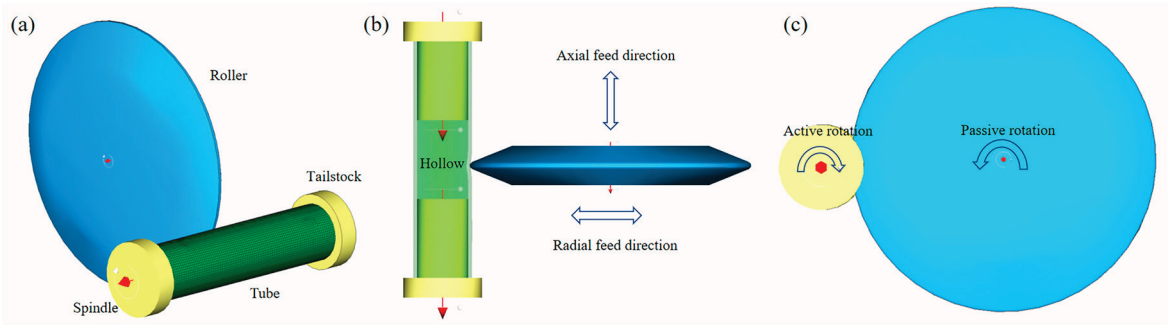


Figure 6. The 3D geometric models of the spinning device. (**a**) Axonometric view. (**b**) Top view. (**c**) Left view.

The nonlinear finite element solver MSC.Mar 11.13 was employed for the simulations, with the key solver parameters configured as follows: the timestep was dynamically adjusted within the range of 1×10^{-6} to 1×10^{-5} s, scaled by the smallest element size in the model to ensure numerical stability. The scaling followed the Courant–Friedrichs–Lewy (CFL) condition with a safety factor of 0.3, i.e., timestep = 0.3 × (smallest element size/maximum material flow velocity). For the 0.5 mm element size, the maximum flow velocity (≈0.1 m/s during peak deformation) yielded the calculated timestep range, ensuring numerical stability in high-strain regions. Convergence criteria were defined as a force residual threshold of $<1 \times 10^{-5}$ N and a displacement tolerance of $<1 \times 10^{-6}$ m, ensuring sufficient accuracy for capturing deformation characteristics. The force residual threshold corresponds to 0.1% of the maximum forming force (≈0.4 kN) measured in experiments, while the displacement tolerance is 0.5% of the minimum wall thickness change (0.2 mm) observed, ensuring that the simulated results match the experimental accuracy.

3. Simulation Results and Verification

To validate the reliability of the simulation results, this study took Scheme II as the comparison object. A comparison of macroscopic appearances between the simulations and

experiments is shown in Figure 7. The shapes from both the simulations and experiments are highly consistent.

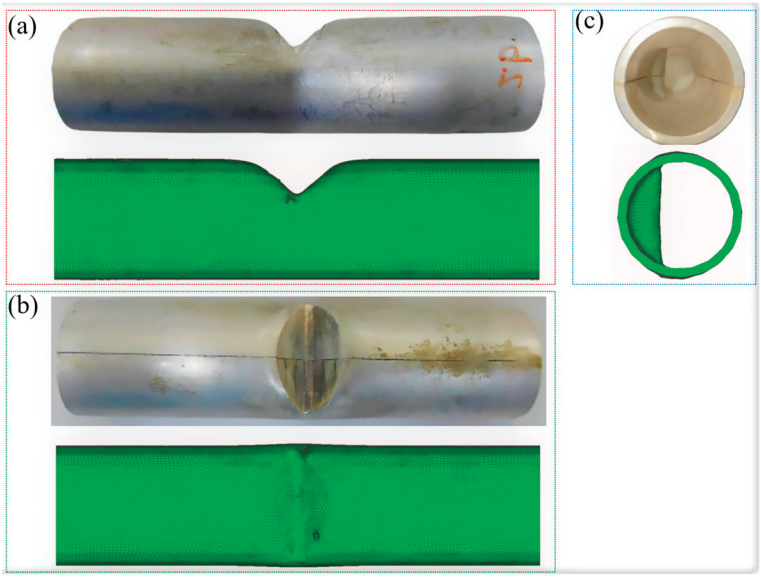


Figure 7. Comparison of the experimental and simulation results. (**a**) Main view. (**b**) Top view. (**c**) Left view.

To accurately measure the wall thickness, the tube is cut along the axial direction (as indicated by the tangent line in Figure 7). To further validate the simulation reliability, the simulated wall thickness was compared with the experimental data. Figure 8 illustrates the wall thickness distribution at 15 positions along the axial section. The maximum wall thickness difference between the simulation and experiment at position 4 is 4.8%. The experimental and simulated wall thickness results are in close agreement.

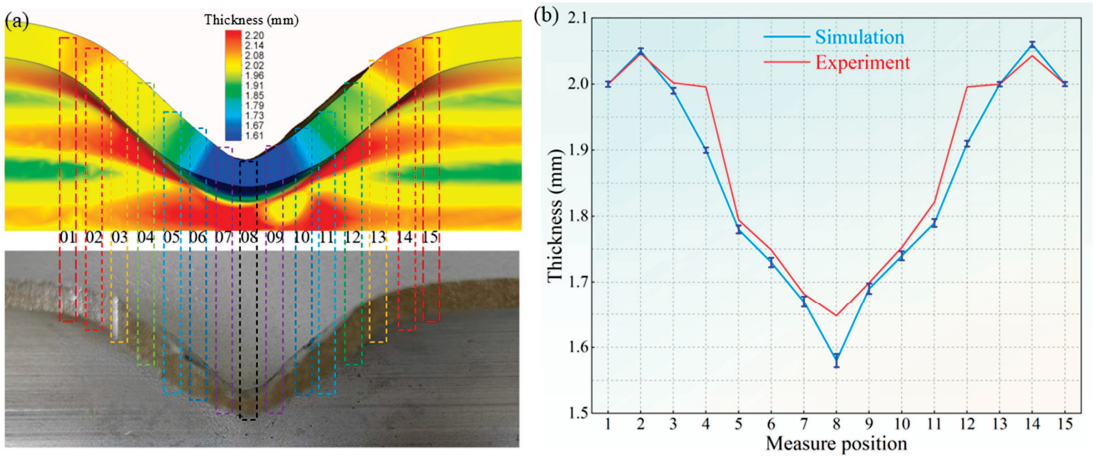


Figure 8. The wall thickness distribution. (**a**) Axial sections of the experimental and simulation results. (**b**) The wall thickness result.

Table 3 presents the forming depth, width, and angle from both the simulation and experiments. All experiments were performed in triplicate, with mean values calculated from repeated measurements. The maximum relative error rates are 12.1% for the forming depth, 7.8% for the forming width, and 5.1% for the forming angle. The measured groove dimensions in both the simulation and experiments were recorded after complete

unloading to account for postforming elastic recovery, which emerges as the dominant factor for depth discrepancies. For 6063-O aluminum, the material exhibits significant springback after spinning; the simulations predict a depth reduction of ≈0.21–0.33 mm due to elastic recovery (from the maximum roller feed to the final dimension), while the experimental measurements show an additional ≈ 1–1.1 mm reduction. This total springback of 1.2–1.4 mm explains why both results fall below the nominal 9 mm target, with the 12.1% maximum discrepancy arising from the slight overestimation of plastic deformation in simulations, and the springback was not fully simulated. Friction variations further contribute to angle deviations (up to 5.1%). The simulations adopted a constant Coulomb friction coefficient (0.12) across the contact interface, whereas experimental lubrication showed localized unevenness. This non-uniform friction altered the plastic flow direction near the apex, causing the experimental angle to be 2–4.5° steeper than the simulated values.

Table 3. The forming depth, width, and angle.

	Scheme	Depth (mm)	Width (mm)	Angle (°)
Experiment	I	7.64	18	95.34
	II	7.60	16	92.93
	III	7.74	17	94.36
Simulation	I	8.73	17.9	91.43
	II	8.67	17.4	90.19
	III	8.79	17.5	89.73

Similar errors also occurred in [28], and they were within an acceptable range. There are acceptable differences between the simulation results and the experimental results, which confirm the accuracy.

4. Discussion

This section explores the forming mechanism of right-angle groove spinning, involving a thorough analysis of the forming process, equivalent stress, and strain distribution. Based on the simulation results, these aspects will be systematically expounded and discussed in the following sections.

4.1. Analysis of the Forming Process

The spinning process is illustrated in Figure 9. Scheme III is single-pass forming. As the roller makes periodic contact with the tube, a local straight slope gradually develops in the middle of the tube until reaching the maximum forming depth of 9 mm. Initially, one slope of the right-angle groove is formed, and the process continues until the other slope is completed, finally forming a fully developed right-angle groove. The forming processes of Schemes I and II are analogous; through multi-pass spinning, small local grooves are generated at the end of each pass, progressively accumulating until a complete 9 mm deep right-angle groove is achieved. This multi-pass deformation mechanism indicates that the spinning device can be effectively modeled with roller paths in a 3D finite element model, capturing the incremental formation of complex geometries via roller–tube interactions.

In order to analyze the wall thickness distribution characteristics in right-angle groove spinning, a key issue arises from non-axisymmetric deformation. Taking Scheme II as an example, each pass forms a partial right-angle groove profile. Focusing on the fourth pass, Figure 10 illustrates the wall thickness measurements at five axial–tangential positions. Notably, the wall thicknesses of the two straight slopes exhibit symmetry at the same forming depth, while a slight thickening occurs in the transition zone between the deformed

and non-deformed regions. This phenomenon is attributed to the resistance from the non-deformed material at the end of each forming pass, which restricts metal flow and causes local accumulation. With the increase in forming depth, wall thinning becomes more significant. When the depth is 3 mm, no obvious thickness change can be observed. As the depth reaches 6 mm, the thinning amount exceeds 0.15 mm. At the final depth of 9 mm, the maximum thinning at the groove bottom approaches 0.42 mm. A larger feed depth leads to higher forming forces, leading to more significant wall thickness thinning.

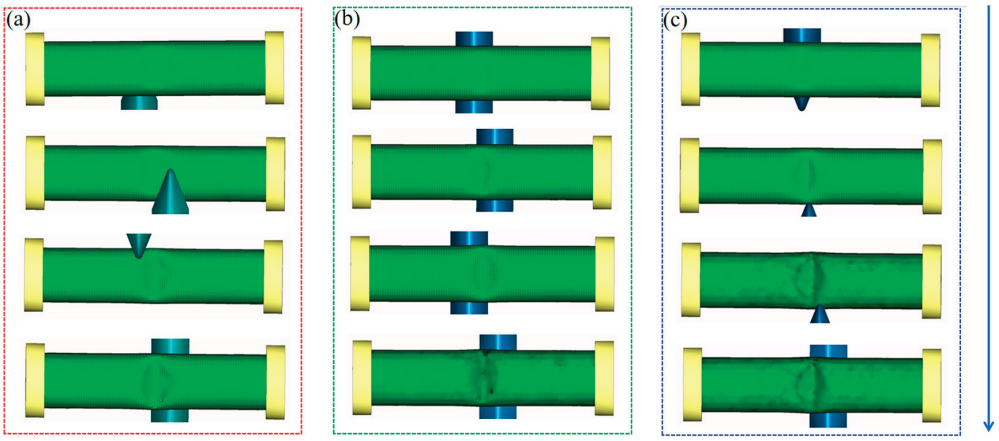


Figure 9. Deformation process of right-angle groove spinning. (**a**) Scheme I. (**b**) Scheme II. (**c**) Scheme III.

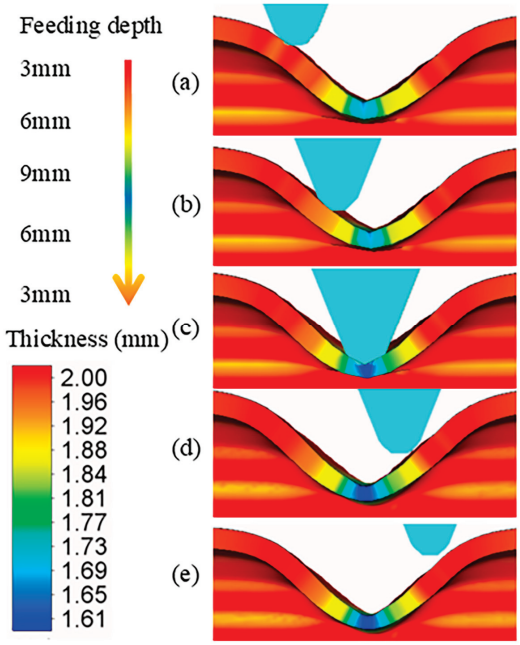


Figure 10. Wall thickness variation in the axial section. (**a**) 3 mm (lower slope). (**b**) 6 mm (lower slope). (**c**) 9 mm (maximum). (**d**) 6 mm (upper slope). (**e**) 3 mm (upper slope).

For the tangential cross-section at a forming depth of 9 mm (as depicted in Figure 11), thinning occurs across the deformed zone, with the most substantial reduction being observed in the central area. The preforming central thinning was approximately 0.25 mm, which increased to nearly 0.4 mm during the forming process, accompanied by minimal post-forming variation. This suggests that wall thinning mainly occurs during the stage of maximum axial feed, when the roller exerts the highest radial force, thereby driving intensive metal flow along the axial direction. The wall thickness change is also evident

between the roller entry and exit sides; the entry side exhibits more pronounced thinning, whereas the exit side accumulates more material due to successive roller passes, which results in higher resistance and localized thickening.

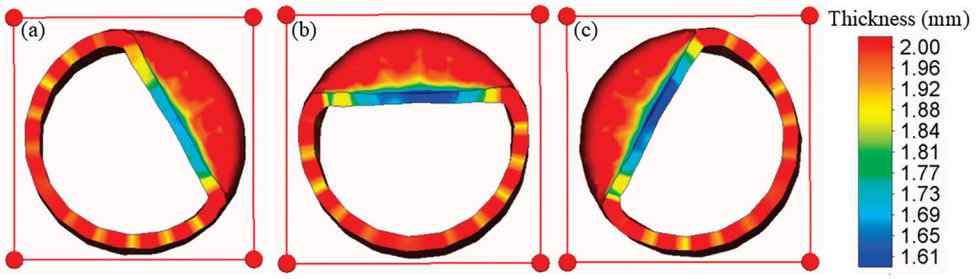


Figure 11. Wall thickness variation in the radial section. (**a**) Before forming. (**b**) During forming. (**c**) After forming.

In summary, non-axisymmetric die-less spinning of right-angle grooves results in a non-uniform wall thickness distribution, characterized by maximum thinning at the right-angle groove vertex and partial thickening at the deformation boundary.

4.2. The Stress Distribution

Figure 12 illustrates the equivalent stress distributions at various stages of the fourth pass with a forming depth of 9 mm for Scheme II. Since the deformation trajectory of the roller is divided into three stages, the stress distribution of each stage is observed as follows: the forming process is divided into the following stages: pre-forming (preparatory setup before deformation), stage 1 (initiation of deformation), stage 2 (application of maximum feed depth (9mm)), stage 3 (transformation nearing completion), and final forming (completion of the process).

The analysis reveals that during pre-forming, stress concentrates on one slope of the groove (the recently processed area), reflecting equivalent stress from previous passes. In Stage 1, stress is concentrated in the roller's contact area, and the feed depth is minimal at this stage. The process then enters Stage 2; as the forming depth increases, the stress magnitude gradually increases, resulting from the cumulative plastic deformation caused by the roller's incremental penetration. When the process enters Stage 3 and the feed depth decreases, the stress decreases accordingly. After the forming is completed, the roller finally separates from the tube. Notably, the maximum stress consistently remains at the bottom of the right-angle groove throughout the entire process. The high equivalent stress in this area is prone to causing springback, thereby affecting forming accuracy.

Different spinning schemes not only directly determine the groove's shape and size but also affect wall thickness and stress–strain distributions, which, in turn, influence the mechanical properties of the spinning component.

The maximum stress occurs at the maximum forming depth. By comparing the equivalent stress after the maximum forming depth in each pass of Scheme I and Scheme II, the forming effects of different schemes can be evaluated. As Scheme III involves single-pass forming, four uniformly selected positions based on the forming sequence are used to observe the forming effect, and T represents the working condition progress, as shown in Figure 13. Single-pass forming in Scheme III leads to unidirectional metal flow, eventually causing stress to concentrate on one side of the groove. Although the target shape can be achieved, excessive wall thickness variation results in an inferior forming effect.

Similar phenomena occur in Scheme I and Scheme II. However, in multi-pass forming, the incremental metal flow in each pass and the reversed flow direction between passes

weaken this effect. In both schemes, equivalent stress concentrates at the bottom of the right-angle groove, with little difference between the schemes. Scheme I exhibits slightly higher equivalent stress in the first three passes than Scheme II but lower equivalent stress in the last pass. Notably, the last pass has the most significant impact on the forming process, as previously processed areas undergo reprocessing. Consequently, Scheme I demonstrates slightly better forming performance than Scheme II.

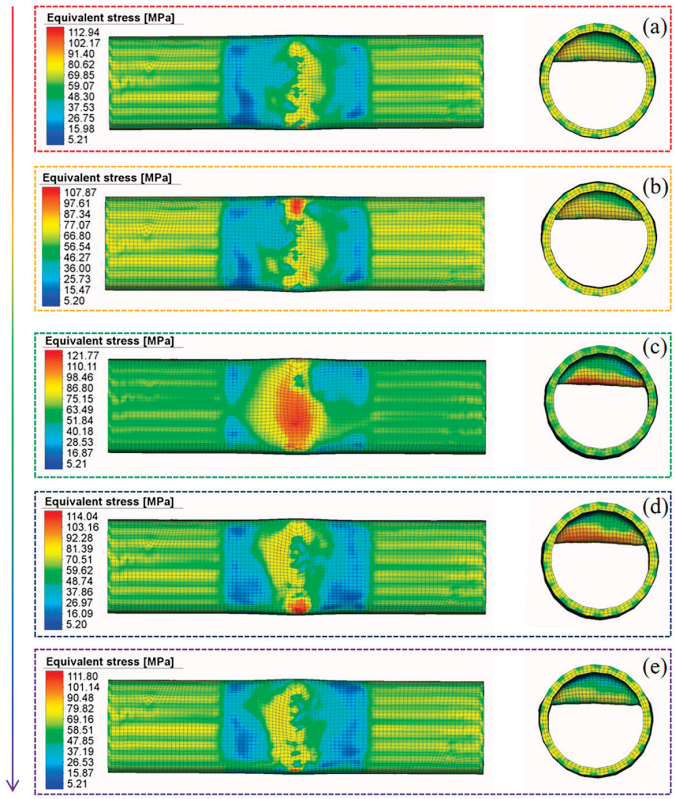


Figure 12. The equivalent stress distribution. (**a**) Pre-forming. (**b**) Stage 1. (**c**) Stage 2. (**d**) Stage 3. (**e**) Final forming.

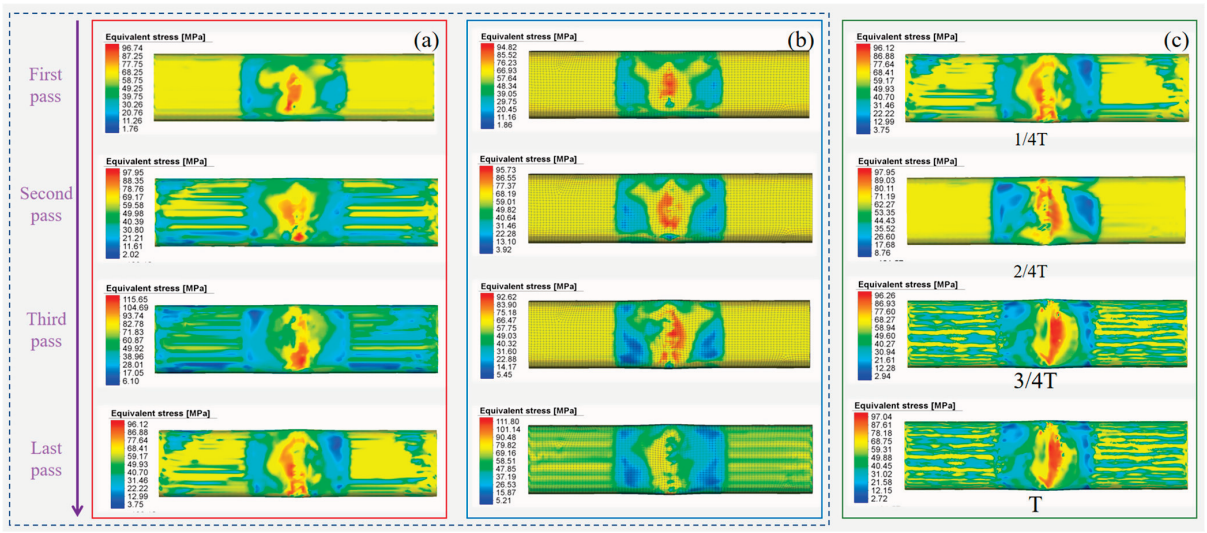


Figure 13. Equivalent stresses of the three schemes. (**a**) Scheme I. (**b**) Scheme II. (**c**) Scheme III.

The multi-directional stress distribution in the post-forming deformed region is presented in Figure 14. For the maximum principal stress (Figure 14a), tension dominates, with a peak value of 106.43 MPa. The high-stress area concentrates on the slope of the roller exit side, forming a band-shaped distribution extending along the roller's pressing direction. This area aligns with the equivalent stress concentration zone at the groove, with both reflecting the core deformation principle of the spinning process. The intermediate principal stress (Figure 14b) exhibits a distinct mixed tension-compression state; a tensile peak of 80.88 MPa and a compressive valley of −85.49 MPa coexist spatially. This duality mirrors the non-uniform circumferential deformation constraints—the stronger constraint on one side of the groove induces compressive stress, while the weaker constraint on the opposite side triggers tension. For the minimum principal stress (Figure 14c), compression is dominant, with a valley value of −125.36 MPa. Its high-magnitude compressive stress zone closely coincides with the bottom of the groove, corresponding to the radial extrusion deformation of the tube wall (where the roller presses the wall, causing radial thickness reduction and compressive stress concentration). The distribution pattern of the three principal stresses intuitively reveals the mechanical field characteristics of "local forced deformation" in spinning: stress concentration with tension-compression coupling in the core contact zone and a gradient decay of stress magnitude toward the non-contact transition zone. These features align well with the experimental observations of deformation uniformity and stress-induced springback.

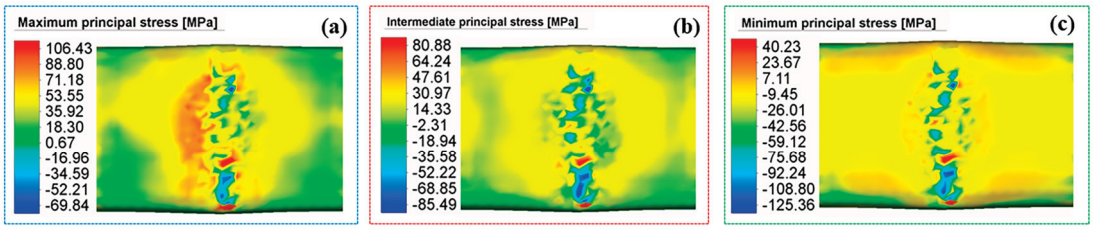


Figure 14. The multidirectional stress distribution in the deformation zone. (**a**) Maximum principal stress. (**b**) Intermediate principal stress. (**c**) Minimum principal stress.

4.3. The Strain Distribution

Similarly to Figure 12, Figure 15 depicts the equivalent strain distribution of the fourth pass with a forming depth of 9 mm for Scheme II. Slight strain variation is observed before and after forming, while the maximum strain occurs in the roller exit area. This is attributed to metal accumulation caused by the roller at this location, where the roller's action leads to increased wall thickness and significant deformation.

Notably, the strain at the bottom of the right-angle groove is significantly higher than in other regions and is directly correlated with the progressive wall thinning as the forming depth increases. The underlying mechanism can be summarized as follows: at the roller exit (specifically at the interface between the deformed and non-deformed zones), tangential stress exceeds that in other regions, causing localized metal accumulation. Here, the metal flow is predominantly tangential, with a minor axial movement component. This phenomenon becomes more pronounced with a deeper forming depth.

To further analyze the deformation, the post-molding deformation area was selected as the observation target. As shown in Figure 16, the major strain, minor strain, and thickness strain in the spinning deformation zone exhibit distinct distribution characteristics: the major strain, dominated by tensile deformation (peak value: 0.41) and concentrated in the bottom of the groove, reflects dominant axial constraints; the minor strain, with a mixed positive and negative distribution (negative peak: −0.23), reveals uneven circumferential

constraints; the thickness strain, centered on radial thinning (peak: −0.26) and strongly coupled with the major strain, aligns with the constant volume assumption in plastic deformation, consistent with the aforementioned content.

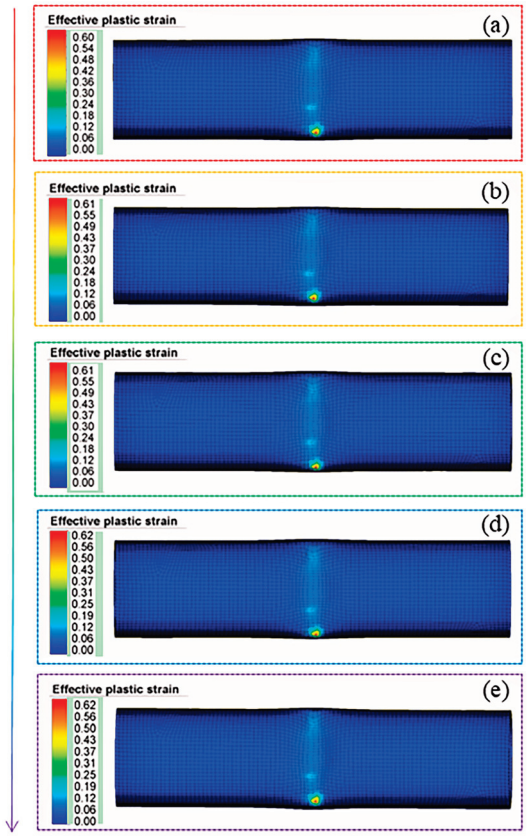


Figure 15. The equivalent strain distribution. (**a**) Pre-forming. (**b**) Stage 1. (**c**) Stage 2. (**d**) Stage 3. (**e**) Final forming.

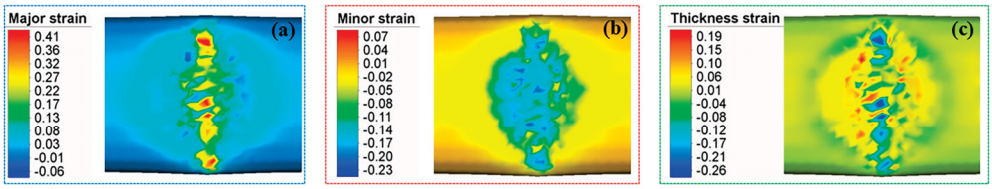


Figure 16. The multidirectional strain distribution in the deformation zone. (**a**) Major strain. (**b**) Minor strain. (**c**) Thickness strain.

5. Conclusions

This study focuses on non-axisymmetric die-less spinning of right-angle grooves in the middle of a tube, verifying the proposed method's credibility via 3D finite element simulation. The core contents are as follows.

(1) The macroscopic shape and wall thickness variations from simulations and experiments are largely consistent, validating the model's accuracy and demonstrating the feasibility of the proposed forming method.

(2) Single-pass forming exhibits severe stress concentration, uneven wall thickness, and unidirectional metal flow, leading to low forming accuracy. Multi-pass forming mitigates stress concentration through staged deformation. Scheme I outperforms

Scheme II because of the lower equivalent stress in the last pass and more uniform wall thickness distribution.

(3) The deformation zone experiences overall wall thickness thinning. The maximum stress localizes at the bottom of the right-angle groove, increasing with the forming depth. Springback causes the actual depth to be slightly less than the ideal value (9 mm). The strain at the groove bottom is higher than in other regions due to the more pronounced wall thickness thinning, while the strain in the roller exit region is significantly elevated by localized thickening due to metal accumulation.

6. Prospects

In future research, the geometric parameters of the roller and roller trajectories can be further optimized to quantitatively investigate their effects on the forming accuracy of right-angle grooves. Additionally, the research scope can be expanded to include high-strength alloys such as titanium alloys and stainless steel, focusing on the stress–strain behavior of these alloys during forming. The integration of artificial intelligence algorithms to optimize multi-pass forming paths is also promising, as it can improve control over wall thickness uniformity. Further improving the accuracy of numerical simulations remains an important research objective. Finally, the development of novel methods for forming more complex geometries will be explored to expand the applicability of this spinning technique.

Author Contributions: Conceptualization, X.R. and Z.J.; methodology, Z.J.; software, X.R. and H.Y.; validation, X.R. and Y.S.; formal analysis, X.R. and Z.F.; investigation, X.R., Y.S. and H.Y.; resources, Z.J.; data curation, Z.F.; writing—original draft preparation, X.R.; writing—review and editing, Z.J. and Z.F.; visualization, Z.F.; supervision, Z.J.; project administration, Z.J. and Z.F.; funding acquisition, Z.J. All authors have read and agreed to the published version of the manuscript.

Funding: This work was supported by the National Natural Science Foundation, China (No. 52275355), Liaoning Provincial Department of Education Fund, China (No. JYTMS20230252), and the fundamental research funds for the universities of liaoning province (No. LJ212410143083, LJ232410143037).

Institutional Review Board Statement: Not applicable.

Informed Consent Statement: Not applicable.

Data Availability Statement: The original contributions presented in this study are included in the article. Further inquiries can be directed to the corresponding authors.

Acknowledgments: This work was supported by the National Natural Science Foundation, China (No. 52275355).

Conflicts of Interest: The author Zuojun Fan was employed by the company "Prosper Metal Forming Corporation". The remaining authors declare that the research was conducted in the absence of any commercial or financial relationships that could be construed as a potential conflict of interest.

References

1. Wong, C.C.; Dean, T.A.; Lin, J. A review of spinning, shear forming and flow forming processes. *Int. J. Mach. Tools Manuf.* **2003**, *43*, 1419–1435. [CrossRef]
2. Music, O.; Allwood, J.M.; Kawai, K. A review of the mechanics of metal spinning. *J. Mater. Process. Technol.* **2010**, *210*, 3–23. [CrossRef]
3. Kang, D.C.; Gao, X.C.; Meng, X.F.; Wang, Z.H. Study on the deformation mode of conventional spinning of plates. *J. Mater. Process. Technol.* **1999**, *91*, 226–230. [CrossRef]
4. Ahmed, K.I.; Gadala, M.S.; El-Sebaie, M.G. Deep spinning of sheet metals. *Int. J. Mach. Tools Manuf.* **2015**, *97*, 72–85. [CrossRef]
5. Xia, Q.; Xiao, G.; Long, H.; Cheng, X.; Sheng, X. A review of process advancement of novel metal spinning. *Int. J. Mach. Tools Manuf.* **2014**, *85*, 100–121. [CrossRef]

6. Jeswiet, J.; Micari, F.; Hirt, G.; Bramley, A.; Duflou, J.; Allwood, J. Asymmetric single point incremental forming of sheet metal. *CIRP Ann.* **2005**, *54*, 88–114. [CrossRef]
7. Music, O.; Allwood, J.M. Flexible asymmetric spinning. *CIRP Ann.* **2011**, *60*, 319–322. [CrossRef]
8. Shimizu, I. Asymmetric forming of aluminum sheets by synchronous spinning. *J. Mater. Process. Technol.* **2010**, *210*, 585–592. [CrossRef]
9. Jianguo, Y.; Makoto, M. An experimental study on spinning of taper shape on tube end. *J. Mater. Process. Technol.* **2005**, *166*, 405–410. [CrossRef]
10. Zhan, M.; Guo, J.; Fu, M.W.; Li, R.; Gao, P.F.; Long, H.; Ma, F. Formation mechanism and control of flaring in forward tube spinning. *Int. J. Adv. Manuf. Technol.* **2018**, *94*, 59–72. [CrossRef]
11. Chen, S.W.; Zhan, M.; Gao, P.F.; Ma, F.; Zhang, H.R. A new robust theoretical prediction model for flange wrinkling in conventional spinning. *J. Mater. Process. Technol.* **2021**, *288*, 116849. [CrossRef]
12. Watson, M.; Long, H. Wrinkling failure mechanics in metal spinning. *Procedia Eng.* **2014**, *81*, 2391–2396. [CrossRef]
13. He, J.; Wang, R.; Li, N.; Xiao, Z.; Gu, J.; Yu, H.; Bi, Z.; Liu, W.; Song, M. Unravelling the origin of multiple cracking in an additively manufactured Haynes 230. *Mater. Res. Lett.* **2023**, *11*, 281–288. [CrossRef]
14. Wilson, S.; Long, H.; Garter, G. Non-axisymmetric tube spinning by offset rotation. *Procedia Manuf.* **2018**, *15*, 1247–1254. [CrossRef]
15. Arai, H.; Gondo, S. Oblique/curved tube necking formed by synchronous multipass spinning. *Metals* **2020**, *10*, 733. [CrossRef]
16. Jia, Z.; Shen, Y.; Gong, X.; Liu, B. Development of a novel approach to middle-tube asymmetric spinning via generic rollers. *J. Mater. Process. Technol.* **2024**, *326*, 118342. [CrossRef]
17. Gondo, S.; Arai, H.; Kajino, S.; Hanada, K. Evolution of texture distribution in thickness direction of aluminum sheet in metal spinning. *Mater. Charact.* **2022**, *188*, 111877. [CrossRef]
18. Xu, W.; Zhao, X.; Ma, H.; Shan, D.; Lin, H. Influence of roller distribution modes on spinning force during tube spinning. *Int. J. Mech. Sci.* **2016**, *113*, 10–25. [CrossRef]
19. Xu, W.; Wu, H.; Ma, H.; Shan, D. Damage evolution and ductile fracture prediction during tube spinning of titanium alloy. *Int. J. Mech. Sci.* **2018**, *135*, 226–239. [CrossRef]
20. Roy, B.K.; Korkolis, Y.P.; Arai, Y.; Araki, W.; Iijima, T.; Kouyama, J. Experimental and numerical investigation of deformation characteristics during tube spinning. *Int. J. Adv. Manuf. Technol.* **2020**, *110*, 1851–1867. [CrossRef]
21. Huang, C.C.; Hung, J.C.; Hung, C.; Lin, C.R. Finite element analysis on neck-spinning process of tube at elevated temperature. *Int. J. Adv. Manuf. Technol.* **2011**, *56*, 1039–1048. [CrossRef]
22. Zhao, X.; Xu, W.; Chen, Y.; Ma, H.; Shan, D.; Lin, H. Fabrication of curved generatrix workpiece of TA15 titanium alloy by variable thickness tube spinning and flaring process. *Int. J. Adv. Manuf. Technol.* **2017**, *88*, 1983–1992. [CrossRef]
23. Xia, Q.; Long, J.; Xiao, G.; Yuan, S.; Qin, Y. Deformation mechanism of ZK61 magnesium alloy cylindrical parts with longitudinal inner ribs during hot backward flow forming. *J. Mater. Process. Technol.* **2021**, *296*, 117197. [CrossRef]
24. Xiao, Y.; Han, Z.; Fan, Z.; Jia, Z. A study of asymmetric multi-pass spinning for angled-flange cylinder. *J. Mater. Process. Technol.* **2018**, *256*, 202–215. [CrossRef]
25. Xia, Q.X.; Cheng, X.Q.; Hu, Y.; Ruan, F. Finite element simulation and experimental investigation on the forming forces of 3D non-axisymmetrical tubes spinning. *Int. J. Mech. Sci.* **2006**, *48*, 726–735. [CrossRef]
26. Xia, Q.X.; Xie, S.W.; Huo, Y.L.; Ruan, F. Numerical simulation and experimental research on the multi-pass neck-spinning of non-axisymmetric offset tube. *J. Mater. Process. Technol.* **2008**, *206*, 500–508. [CrossRef]
27. Xia, Q.; Cheng, X.; Long, H.; Ruan, F. Finite element analysis and experimental investigation on deformation mechanism of non-axisymmetric tube spinning. *Int. J. Adv. Manuf. Technol.* **2012**, *59*, 263–272. [CrossRef]
28. Jia, Z.; Xuan, W.; Shen, Y.; Xie, Y.; Gong, X.; Liu, B. Numerical simulation and experimental study on non-axisymmetric spinning with a groove at the middle of the tube. *Int. J. Adv. Manuf. Technol.* **2022**, *121*, 6271–6284. [CrossRef]
29. Jain, S.; Rai, D.C.; Sahoo, D.R. Postyield cyclic buckling criteria for aluminum shear panels. *ASME J. Appl. Mech. March.* **2008**, *75*, 021015. [CrossRef]
30. Soundararaj, S.; Christopher, T.; Kalaichelvan, K. Process parameter correlation in low pressure hydro forming of 6063-O aluminium tubes. *Mechanics* **2019**, *25*, 64–72. [CrossRef]
31. Misiolek, W.Z.; Kelly, R.M. Extrusion of aluminum alloys. In *Metalworking: Bulk Forming*; Semiatin, S.L., Ed.; ASM International: Novelty, OH, USA, 2005; Volume 14A, pp. 522–527.

Disclaimer/Publisher's Note: The statements, opinions and data contained in all publications are solely those of the individual author(s) and contributor(s) and not of MDPI and/or the editor(s). MDPI and/or the editor(s) disclaim responsibility for any injury to people or property resulting from any ideas, methods, instructions or products referred to in the content.

materials

MDPI

Article

Gleeble-Simulated Ultra-Fast Cooling Unlocks Strength–Ductility Synergy in Fully Martensitic Ti-6Al-4V

Yaohong Xiao [1,2,*], Hongling Zhou [3,*], Pengwei Liu [4] and Lei Chen [1,2]

[1] Department of Mechanical Engineering, University of Michigan, Dearborn, MI 48128, USA
[2] Department of Mechanical Engineering, Mississippi State University, Starkville, MS 39762, USA
[3] College of Materials Science and Engineering, Chongqing University, Chongqing 400044, China
[4] School of Mechanical Engineering, Yanshan University, Qinhuangdao 066004, China
* Correspondence: yaohongx@umich.edu (Y.X.); zhouhongling@cqu.edu.cn (H.Z.)

Abstract: In additively manufactured (AM) Ti-6Al-4V, the role of martensitic α' in governing brittleness versus toughness remains debated, largely because complex thermal histories and other intertwined physical factors complicate interpretation. To isolate and clarify the intrinsic effect of cooling rate, we employed a Gleeble thermal simulator, which enables precisely controllable cooling rates while simultaneously achieving ultra-fast quenching comparable to AM (up to ~7000 °C/s). By varying the cooling rate only, three distinct microstructures were obtained: α/β, α_m/α', and fully α'. Compression tests revealed that the ultra-fast-cooled fully martensitic Ti-6Al-4V attained both higher strength and larger fracture strain, with densely distributed elongated dimples indicative of ductile failure. Three-dimensional microstructures reconstructed from microscopy, analyzed using an EVP-FFT crystal plasticity model, demonstrated that refined α' laths and abundant high-angle boundaries promote more homogeneous strain partitioning and reduce stress triaxiality, thereby delaying fracture. These results provide potential evidence that extreme-rate martensitic transformation can overcome the conventional strength–ductility trade-off in Ti-6Al-4V, offering a new paradigm for processing titanium alloys and AM components with superior performance.

Keywords: elasto-viscoplasticity; misorientation angle; full martensite; Gleeble; elongated dimple

1. Introduction

Ti-6Al-4V (T64) is one of the most widely used titanium alloys in aerospace and biomedical applications due to its excellent fatigue resistance, high strength-to-weight ratio, toughness, corrosion resistance, and biocompatibility. Traditionally, α/β Ti-6Al-4V microstructures have been manufactured by melting, casting, and secondary processes such as hot isostatic pressing (HIP). However, with the rapid advancement of additive manufacturing (AM) techniques such as selective laser melting (SLM) and direct laser deposition (DLD), these conventional methods are increasingly being complemented or replaced. AM offers net-shape fabrication with high design freedom, low material waste, and the ability to produce complex geometries, making it particularly attractive for on-demand and customized Ti-6Al-4V components [1].

In AM, the tiny melt pool generated during layer-wise printing inherently introduces very high cooling rates (on the order of ~10^5 K s^{-1}), which frequently result in the formation of martensitic α' microstructures in as-built Ti64 [2]. Traditionally, α' has been regarded as

intrinsically brittle and thus responsible for reduced ductility, leading to extensive efforts to suppress or decompose it through in situ $\alpha' \rightarrow \alpha + \beta$ transformation by process parameter tuning [3], substrate preheating [4], or post-build heat treatments [5]. However, the blanket assumption that α' is necessarily detrimental to ductility merits careful re-examination. A number of studies [6–9] have reported that Ti64 containing mixed $\alpha + \alpha'$—and even fully α'—can achieve ductility comparable to conventional α/β Ti64. De Formanoir et al. [10] showed that dual-phase α/α' Ti64 produced by sub-transus heat treatment of AM-built material exhibited elongations up to ~22%. Zafari et al. [11] tuned SLM parameters to obtain fully α' Ti64 with yield strength and tensile elongation comparable to the best commercial wrought α/β Ti64. Zou et al. [12] further indicated that refining prior-β grains can simultaneously enhance strength and ductility. Despite these promising results, AM is not ideal for isolating the intrinsic role of cooling rate in martensitic Ti64 because (1) multiple sources of uncertainty hinder precise control of the product uniformity [13]; (2) the complex multi-physical phenomena in AM (including rapid thermal cycles and melt-pool dynamics [2,14,15] confound the interpretation, in particular, the mechanistic interpretation of how ultra-fast cooling rate alone governs martensitic transformation and mechanical response.

To bypass the above limitations and decouple the cooling rate from other AM physics, we employ a Gleeble 3500D thermal simulator (Dynamic Systems Inc., Poestenkill, NY, USA) [16–18]. Unlike AM, the Gleeble platform offers precisely controllable cooling rates in a uniform, well-instrumented environment while still achieving ultra-fast cooling rates comparable to AM (up to ~7000 $^{\circ}$C s^{-1}). Prior work has leveraged Gleeble-mimicked AM thermal cycles to reproduce microstructures otherwise accessible in AM, thereby validating its fidelity to AM-like kinetics [2]. In the present study, Gleeble enables us to produce uniform Ti64 microstructures—lamellar α/β (slow cooling), mixed α_m/α' (intermediate cooling), and fully α' (ultra-fast cooling)—solely by varying the cooling rate, thus isolating its effect on microstructure and properties. Despite this capability, a systematic verification that pure α' Ti64 can exhibit excellent ductility—benchmarked directly against α/β and α_m/α' counterparts obtained under isolated cooling-rate control—has remained lacking.

Concurrently, the development of fast Fourier transform-based elasto-viscoplastic (EVP-FFT) crystal plasticity modeling provides an effective and computationally efficient framework to interrogate local micromechanics in plastically deforming heterogeneous polycrystals using 3D reconstructed microstructures [19,20]. For Ti-alloy systems, Ozturk et al. [21] built synthetic 3D microstructures from experimental images to assess structure–property relations in α/β Ti-6Al-4V, while Liu et al. [22] integrated FEM, phase-field modeling, and EVP-FFT to study AM Ti-6Al-4V with varying lamellar α/β architectures. These advances enable quantitative linkage from microstructure morphology (e.g., phase fractions) to macroscopic yield behavior, strain partitioning, and damage precursors across α/β, α_m/α', and fully α' Ti64.

Herein, we first aim to verify whether an extremely high cooling rate (~7000 $^{\circ}$C s^{-1}) can indeed enable a fully martensitic Ti64 to achieve a superior combination of strength and ductility. To this end, we systematically compare the mechanical response of ultra-fast-cooled α' microstructures with that of α/β and α_m/α' states obtained at lower cooling rates. After establishing this performance advantage, we further investigate the underlying micromechanical mechanisms. Specifically, phases and features are characterized by optical and scanning electron microscopy and a piezo-tribo scanner, enabling reconstruction of three distinct 3D digital microstructures as inputs to an EVP-FFT crystal plasticity model. By calibrating the model against compression experiments, we quantify the effects of morphology on yield behavior, strain partitioning, and stress triaxiality. We demonstrate that a high density of high-angle grain/phase boundaries and refined α' laths facilitates

more homogeneous strain distribution and suppresses localized damage, thereby explaining the enhanced ductility of martensitic Ti64 under extreme cooling. These insights establish a cooling-rate-driven paradigm for engineering martensitic Ti-alloys—and AM components—with simultaneously high strength and ductility.

2. Materials and Experimental Procedures

Commercial Ti-6Al-4V (Ti64) plates (Sigma-Aldrich Inc., St. Louis, MO, USA) were machined into 9.0 × 9.0 × 9.0 mm^3 cubes using a precision diamond saw. Each cube was sandwiched between graphite electrodes and subjected to a constant force of approximately 5.0 kPa to ensure full contact in the Gleeble 3500D thermal simulator, as illustrated in Figure 1, similar to our previous study [2]. Throughout the heating and cooling processes, the chamber was filled with high-purity argon to suppress oxidation. The samples were rapidly heated to 1100 °C by direct electrical resistance, held for 10 min to guarantee complete transformation to the β phase, and subsequently cooled under three distinct conditions: (i) furnace/grip cooling (Case 1), (ii) air quenching (Case 2), and (iii) fast water-flow quenching (Case 3). The corresponding in situ time–temperature curves can be obtained to quantify the cooling rate.

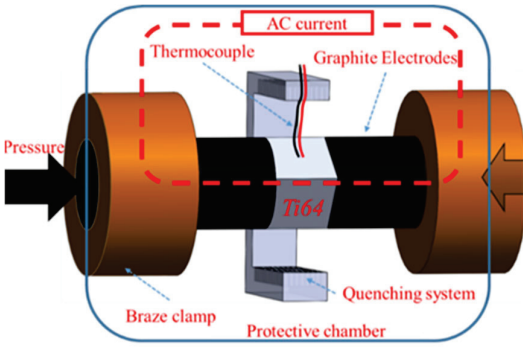


Figure 1. Schematic diagram of the Gleeble 3500D setup with assembled Ti64 sample [2]. The left-pointing arrow on the right side denotes the applied pressure direction during Gleeble thermal simulation.

After cooling, each sample was sectioned to expose a fresh cross-section, which was ground using a Struers Tegrapol-11 polisher (Cleveland, OH, USA) followed by fine polishing with a Buehler VibroMet-2 (Lake Bluff, IL, USA). Phase analysis was performed by X-ray diffraction (XRD). Samples were subsequently etched in Kroll's reagent (2 mL HF, 4 mL HNO_3, 50 mL H_2O; 25 s) and ultrasonically cleaned before microstructural characterization. Optical microscopy (OM) and scanning electron microscopy (SEM) were employed to reveal microstructural morphology. After further vibration polishing, electron backscatter diffraction (EBSD) was performed using a ZEISS SUPRA-40 field emission SEM (Carl Zeiss AG, Oberkochen, Germany) equipped with an EDAX Hikari EBSD camera (AMETEK, Berwyn, PA, USA). Data were analyzed with TSL OIM™ software, version 6.2, with a representative ~1000 × 1000 μm^2 area scanned at a 2 μm step size to obtain grain misorientation statistics. In addition, topographic scanning was performed with the piezo-tribo scanner in a Hysitron Triboindenter (scanning area: 40 × 40 μm^2) (Bruker Hysitron, Billerica, MA, USA), enabling quantitative analysis of phase morphology and lath dimensions. Phase size and grain morphology were further quantified using ImageJ 1.52 software.

Mechanical properties were evaluated by compression testing on an Instron 5882 machine (Instron, Norwood, MA, USA) equipped with a 25 mm extensometer. Tests were conducted at room temperature with a constant strain rate of 0.001 s^{-1}. For each condition, four replicate samples were tested to ensure reproducibility, and average values

are reported. It is noted that the small cubic geometry was intentionally selected to facilitate the achievement of extremely high cooling rates and uniform microstructures, making compression testing more reliable than tensile testing under these conditions.

3. Model Descriptions

3.1. FFT Based Elastic-Viscoplastic Self-Consistent Model

The detailed formulation of the fast Fourier transform (FFT)-based elasto-viscoplastic (EVP-FFT) approach has been reported elsewhere [19]. Here, we briefly summarize the key theoretical framework adopted in this study. The total strain field $\boldsymbol{\varepsilon}(\mathbf{x})$ can be written as follows:

$$\boldsymbol{\varepsilon}(\mathbf{x}) = \mathbf{C}^{-1}(\mathbf{x}) : \boldsymbol{\sigma}(\mathbf{x}) + \boldsymbol{\varepsilon}^{p,t}(\mathbf{x}) + \dot{\boldsymbol{\varepsilon}}^{p}(\mathbf{x})\Delta t \tag{1}$$

where $\mathbf{C}(\mathbf{x})$ is the elastic stiffness tensor, $\boldsymbol{\varepsilon}^{\mathbf{p}}(\mathbf{x})$ is the plastic strain tensor. The plastic strain-rate $\dot{\boldsymbol{\varepsilon}}^{\mathbf{p}}(\mathbf{x})$ is a constitutive relation with stress $\boldsymbol{\sigma}(\mathbf{x})$ at a single crystal material point $\mathbf{x}$ by a sum over the N active slip systems, of the form:

$$\dot{\boldsymbol{\varepsilon}}^{\mathbf{p}}(\mathbf{x}) = \sum_{s=1}^{N} \mathbf{m}^{s}(\mathbf{x})\dot{\gamma}^{s}(\mathbf{x}) = \dot{\gamma}_0 \sum_{s=1}^{N} \mathbf{m}^{s}(\mathbf{x}) \left(\frac{|\mathbf{m}^{s}(\mathbf{x}) : \boldsymbol{\sigma}(\mathbf{x})|}{\tau_0^{s}(\mathbf{x})} \right)^{n} \operatorname{sgn}(\mathbf{m}^{s}(\mathbf{x}) : \boldsymbol{\sigma}(\mathbf{x})) \tag{2}$$

where $\dot{\gamma}^{s}(\mathbf{x})$, $\dot{\gamma}_0$ and $\mathbf{m}^{s}(\mathbf{x})$ are, respectively, the shear rate, normalization factor, and Schmid tensor of slip systems, $\tau_0^{s}(\mathbf{x})$ is the critical resolved shear stress (CRSS), n is a stress exponent, namely, the inverse of the rate-sensitivity exponent.

The stress $\boldsymbol{\sigma}(\mathbf{x})$ can be written as:

$$\sigma_{ij}(\mathbf{x}) = \varphi_{ij}(\mathbf{x}) + C^{0}_{ijkl}(\mathbf{x})u_{k,l}(\mathbf{x}) = \varphi_{ij}(\mathbf{x}) + C^{0}_{ijkl}(\mathbf{x})\varepsilon_{kl}(\mathbf{x}) \tag{3}$$

where $u_{k,l}(\mathbf{x})$ represents the displacement gradient tensor and $\varepsilon_{kl}(\mathbf{x}) = (u_{k,l}(\mathbf{x}) + u_{l,k}(\mathbf{x}))/2$, $\varphi_{ij}(\mathbf{x})$ is the polarization field. Combining Equation (3) with the equilibrium equation ($\sigma_{ij,j}(\mathbf{x}) = 0$):

$$C^{0}_{ijkl}(\mathbf{x})u_{k,lj}(\mathbf{x}) + \varphi_{ij,j}(\mathbf{x}) = 0 \tag{4}$$

The differential Equation (4) for a unit cell with periodic boundary conditions and an initial strain can be solved using the Green function method. As the periodic Green function $G_{km}(\mathbf{x})$ is related to the displacement field $u_k(\mathbf{x})$, the solution of $u_k(\mathbf{x})$ is obtained by the convolution:

$$u_{k,l}(\mathbf{x}) = \int_{R^3} G_{ki,jl}\left(\mathbf{x} - \mathbf{x}'\right)\varphi_{ij}\left(\mathbf{x}'\right)d\mathbf{x}' \tag{5}$$

Further transferring Equation (5) into Fourier space by the convolution theorem, the compatible strain field $\varepsilon_{ij}(\mathbf{x})$ deriving from the solution of Equation (4) is given by:

$$\varepsilon_{ij}(\mathbf{x}) = E_{ij} + \mathrm{FT}^{-1}\left(sym\left(\hat{\Gamma}^{0}_{ijkl}(\boldsymbol{\xi})\right)\hat{\varphi}_{kl}(\boldsymbol{\xi})\right) \tag{6}$$

where the symbol of "$\hat{}$" and "FT^{-1}" indicate the Fourier transform and its inverse transformation, respectively, $\boldsymbol{\xi}$ is a frequency point in Fourier space $\hat{\Gamma}^{0}_{ijkl}(\boldsymbol{\xi}) = -\xi_j\xi_l\hat{G}_{ik}(\boldsymbol{\xi})$, the Green operator in Fourier space is a function of the reference stiffness tensor and frequency, in which $\hat{G}_{ik}(\boldsymbol{\xi}) = \left[C^{0}_{kjil}\xi_l\xi_j\right]^{-1}$.

Equation (6) is a fix-point equation for the strain field that allows solving the constitutive and governing equations iteratively. In practice, for better convergence of our micromechanical model, we use a modified version of the above algorithm, based on the augmented Lagrangian formulation of Michel et al. [23], adapted to the EVP polycrystals (see [19] for details).

3.2. Voce-Type Hardening Law

Considering the strain hardening, the extended Voce Law [24,25] is used to describe the relationship between threshold stress τ^s and total accumulated shear strain Γ, given by:

$$\tau^s(\Gamma) = \tau_0^s + (\tau_1^s + \theta_1^s \Gamma)\left(1 - \exp\left(-\Gamma\left|\frac{\theta_0^s}{\tau_1^s}\right|\right)\right) \quad (7)$$

where θ_0 and θ_1 are the initial and asymptotic hardening rates, respectively, $(\tau_0 + \tau_1)$ refers to the back-extrapolated stress. The elastic constants of β, α, and α′ phases and hardening parameters used for the Voce model are further calibrated in Section 4.2.2, correlating with compression test results.

4. Results

4.1. Experimental Results

4.1.1. Phase and Microstructure Analysis

The real-time heating and cooling histories under the three Gleeble-controlled conditions are presented in Figure 2a, and the corresponding cooling-rate windows between the β-transus and the martensite start temperature are summarized in Figure 2b [26]. Before cooling, all phases in the as-received samples were transformed to β due to 1100 °C > T_β = 994 °C, and the 10 min holding at 1100 °C ensured a complete α + β → β transformation. As illustrated in Figure 2a, subsequent cooling produced three distinct conditions with approximate average cooling rates of 1 °C/s, 145 °C/s, and 7000 °C/s, corresponding to α/β (Case 1), α_m/α' (Case 2), and fully α′ (Case 3) microstructures, respectively, as predicted by the Ti-6Al-4V cooling diagram (Figure 2b). These predictions are verified by XRD (Figure 2c): Case 1 retains both α and β peaks, consistent with a lamellar α/β structure; Case 2 shows weakened β peaks with broadened and shifted α peaks, indicative of coexisting massive α and martensitic α′; Case 3 exhibits only α′, confirming a fully martensitic transformation at the highest cooling rate. Although α and α′ share similar lattice structures, their morphological differences are clarified in etched OM micrographs (Figure 3).

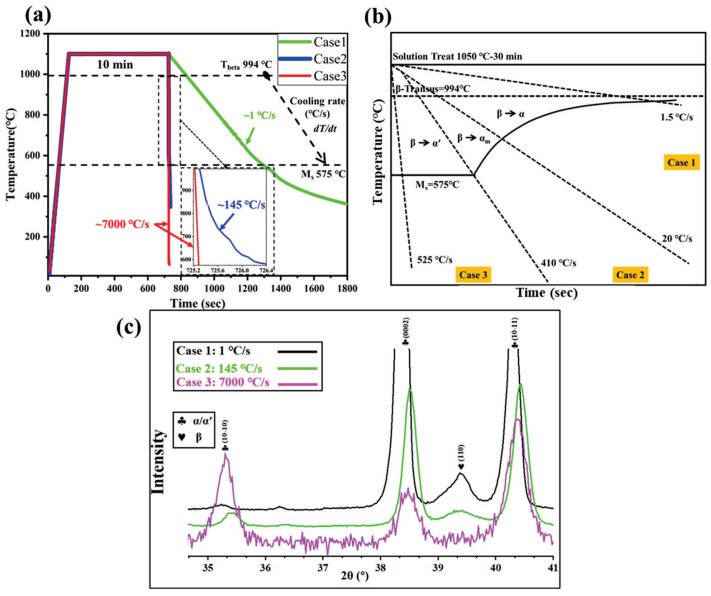


Figure 2. (**a**) In situ time–temperature curves and average cooling rates between β-transus and martensite start temperature; (**b**) Schematic cooling diagram of Ti-6Al-4V [26]; (**c**) XRD patterns of Ti64 under different cooling conditions.

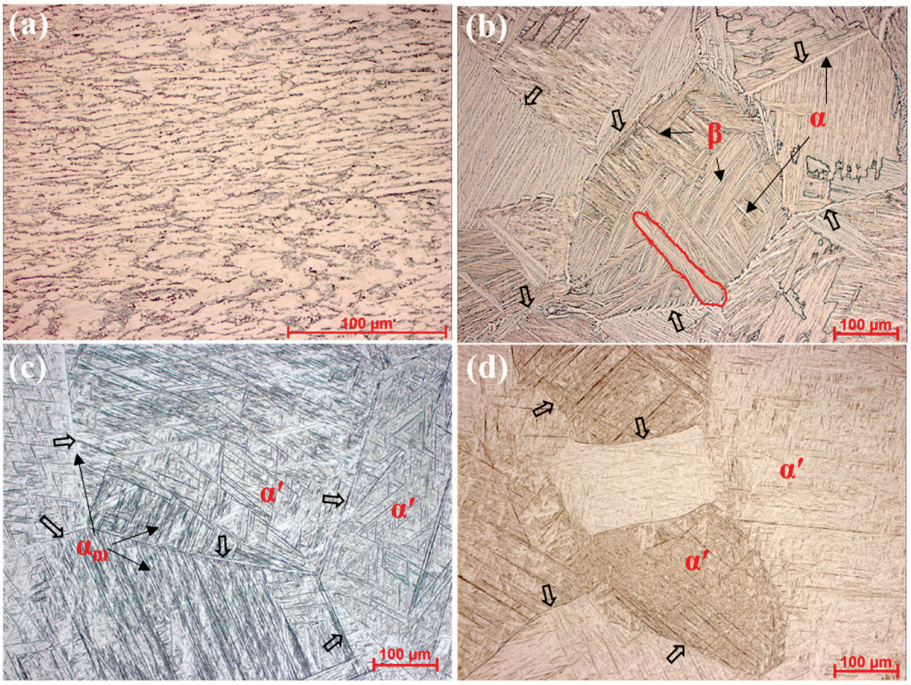


Figure 3. Optical microscopy (OM) images of etched samples with different cooling rates: (**a**) as-received sample, (**b**) Case 1: 1 °C/s, (**c**) Case 2: 145 °C/s, and (**d**) Case 3: 7000 °C/s. Hollow arrows indicate prior-β boundaries, and red outlines highlight colony structures.

Figure 3 further illustrates the morphological differences among cases. The as-received sample (Figure 3a) shows a typical rolled structure consisting of ellipsoidal α plates delineated by thin β films. After Gleeble treatment, prior-β grains coarsened to ~400 μm and changed shape from ellipsoidal to polygonal due to the 10 min holding at 1100 °C. Across all cases, the prior-β grain size remained ~400 μm, reflecting the identical heating schedule. Case 1 (Figure 3b) presents classical lamellar α/β colonies nucleated preferentially at prior-β boundaries (indicated by hollow arrows). In Case 2 (Figure 3c), massive α plates distribute mainly along prior-β boundaries and within some grains, while α′ laths fill the remaining regions, forming an α_m/α' dual microstructure. Case 3 (Figure 3d) shows sharp prior-β interfaces without boundary α films, characteristic of a fully martensitic structure.

In detail, Case 1 exhibits a typical lamellar α/β structure composed of numerous α colonies. As indicated by the hollow arrows in Figure 3b, prior-β grain boundaries serve as preferential nucleation sites for α plates, which subsequently grow inward to form colony structures (outlined by red lines) [27]. The XRD pattern of Case 1 (Figure 2c) also shows pronounced β peaks, confirming a significant β fraction. By contrast, Case 3 (Figure 3d) reveals no α boundary layers; instead, sharp prior-β interfaces are preserved (black arrows), consistent with a fully martensitic transformation and with the absence of β reflections in Figure 2c, Case 3 [28]. Case 2 (Figure 3c) represents an intermediate state where massive transformation and martensitic transformation occur simultaneously, leading to a mixed α_m/α' microstructure. The α_m plates are mainly distributed along prior-β boundaries and partially within grains [26], while α′ laths occupy the same β grains. The residual β fraction in Case 2 is extremely small, reflected by weak β peaks in Figure 2c; this β is typically retained within bulk α, i.e., the α_m phase [2]. Moreover, the presence of α′ broadens and slightly shifts the α/α' reflections, further confirming that both Case 2 and Case 3 contain martensitic α′. To characterize these phase features in detail, topography and SEM imaging were conducted to quantify morphology—including thickness, length, and volume fraction—as summarized in Table 1.

Table 1. Phase dimensions and fractions under different cooling rates.

Sample	Cooling Rate (°C/s)	Phase	Average Thickness (μm)	Average Length (μm)	Average Fraction (%)
Case 1	1	α	2.5 ± 1.0	325 ± 75	87.5 ± 2.5
		β	0.25 ± 0.15	325 ± 75	12.5 ± 2.5
Case 2	145	α_m	8.0 ± 2.0	325 ± 75	35 ± 5
		Primary α′	2.5 ± 0.5	325 ± 75	17.5 ± 2.5
		Secondary α′	4.5 ± 0.5	7.5 ± 0.5	47.5 ± 2.5
Case 3	7000	Primary α′	2.5 ± 0.5	325 ± 75	7.5 ± 2.5
		Secondary α′	0.6 ± 0.2	4.5 ± 1.5	92.5 ± 2.5

To quantify phase features, surface topography, and SEM images (Figure 4) were analyzed. Two α′ morphologies were distinguished: primary α′, coarse parallel-sided needles adjacent to prior-β boundaries, and secondary α′, ultrafine needles distributed within grains. A remarkable primary α′ was captured by piezo-tribo scanning at the prior-β boundary in Case 3 (Figure 4c), confirming its significantly larger thickness and length compared to secondary α′. Comparing Case 2 (Figure 4b) and Case 3 (Figure 4c), both primary and secondary α′ became shorter and finer as the cooling rate increased. With the ImageJ 1.52 software, quantitative thickness, length, and volume fraction of phases are summarized in Table 1, which also served as input data for reconstructing digital microstructures for EVP-FFT modeling (see Section 4.2.1).

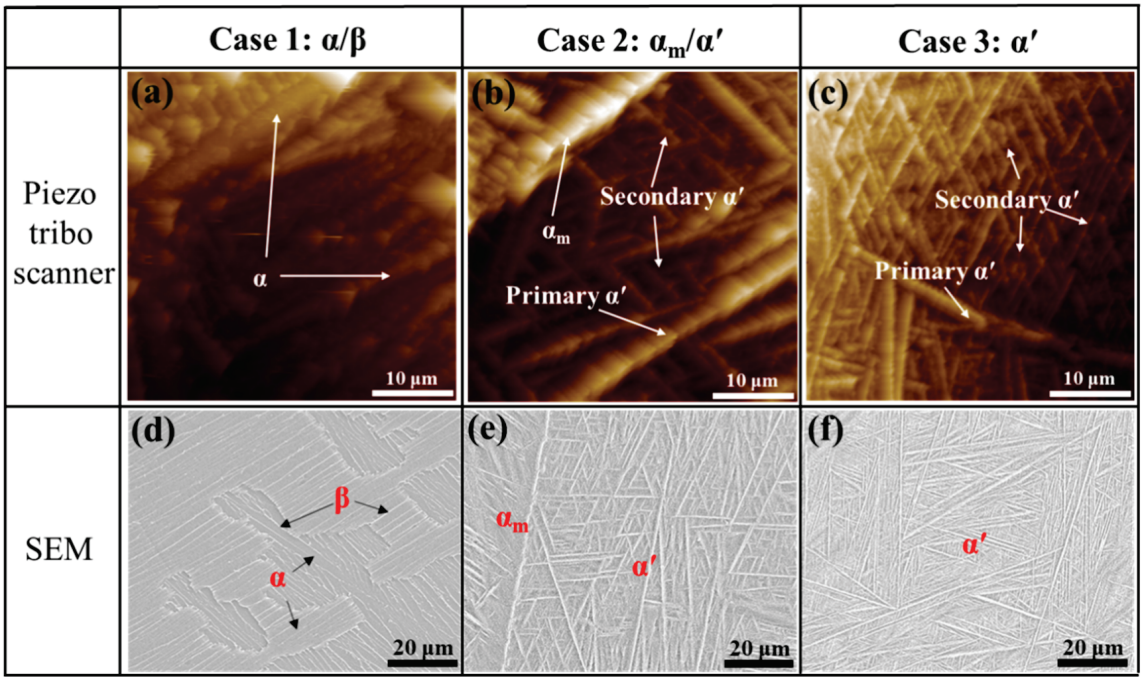


Figure 4. Surface topography images (**a**–**c**) and SEM images (**d**–**f**) of etched samples: (**a**,**d**) Case 1, (**b**,**e**) Case 2, and (**c**,**f**) Case 3.

4.1.2. Compression Testing and Work Hardening Behaviors

The engineering compressive stress–strain curves up to fracture are shown in Figure 5a. Two characteristic points are of primary interest: the yield point and the ultimate compressive point. Because Ti-6Al-4V does not exhibit an obvious yield drop under compression, the 0.2% offset method was applied to define the compressive yield strain ($\varepsilon_{cy0.2}$) and

yield stress ($\sigma_{cy0.2}$). The maximum stress sustained at fracture is reported as the ultimate compressive strength (σ_{cu}), corresponding to the ultimate strain (ε_{cu}).

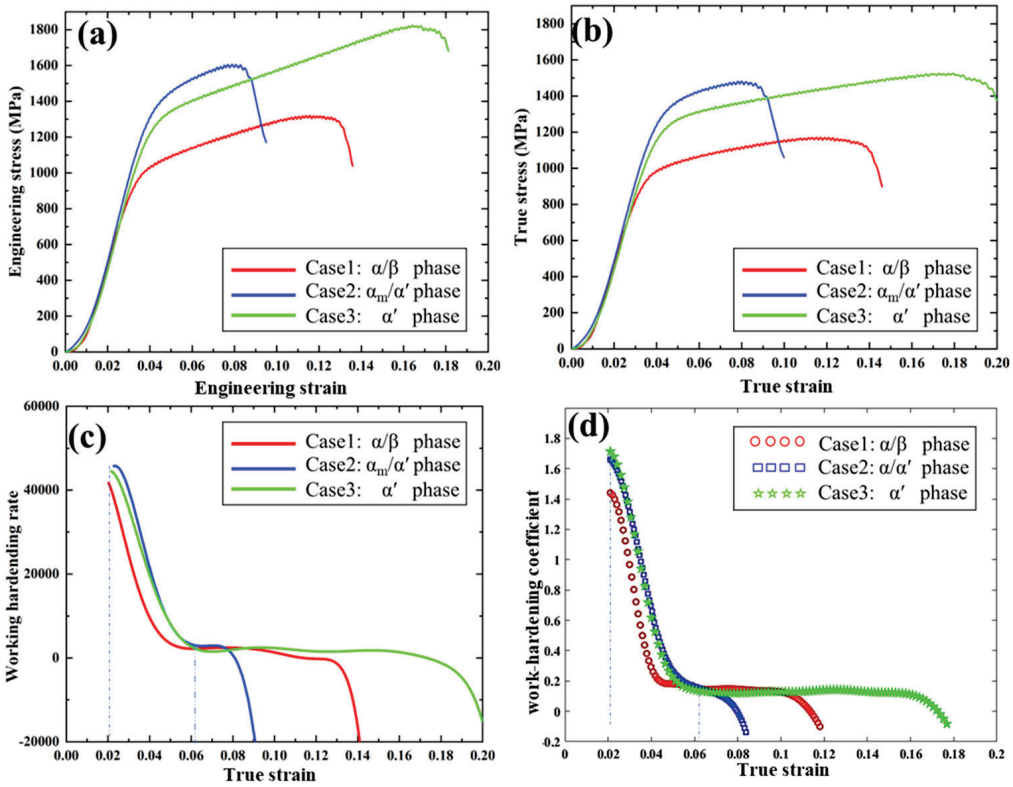


Figure 5. Compression tests of Ti-6Al-4V under different cooling conditions: (**a**) engineering stress–strain curves, (**b**) true stress-strain curves, (**c**) work-hardening rate (θ) as a function of true strain, and (**d**) work-hardening coefficient (*n*) as a function of true strain.

As summarized in Table 2, Case 1 (α/β, 1 °C/s) starts to yield at $\varepsilon_{cy0.2} \approx 0.029$ with $\sigma_{cy0.2} \approx 790$ MPa, close to the value reported in [29]. At $\varepsilon_{cu} \approx 0.12$, shear fracture initiates along a 45° plane with $\sigma_{cu} \approx 1161$ MPa. In Case 2 (α_m/α', 145 °C/s), both $\varepsilon_{cy0.2}$ and $\sigma_{cy0.2}$ increase to ~0.039 and ~1215 MPa, respectively. However, fracture occurs earlier, at $\varepsilon_{cu} \approx 0.08$, although the corresponding σ_{cu} rises to ~1478 MPa, higher than that in Case 1. With further increase in the cooling rate to 7000 °C/s (Case 3, fully α'), the highest $\varepsilon_{cu} \approx 0.17$ and $\sigma_{cu} \approx 1519$ MPa are obtained simultaneously. The yield point of Case 3 is $\varepsilon_{cy0.2} \approx 0.037$ with $\sigma_{cy0.2} \approx 1074$ MPa. These results indicate that full martensitic transformation induced by extremely high cooling rate enables Ti-6Al-4V to achieve both excellent ductility and high compressive strength.

Table 2. Compressive yield strain/stress and ultimate compressive strain/strength for different cases.

Specimens	Compositions (Phase)	Cooling Rate (°C/s)	$\varepsilon_{cy0.2}$	ε_{cu}	$\sigma_{cy0.2}$ (MPa)	σ_{cu} (MPa)
Case 1	α/β	1	0.029	0.12	790.3	1160.5
Case 2	α_m/α'	145	0.039	0.08	1214.7	1478.3
Case 3	α'	7000	0.037	0.17	1074.0	1519.2

The true (logarithmic) stress–strain curves (Figure 5b) were further used for calibration of the EVP-FFT model [30]. The yield behaviors are more clearly reflected in Figure 5c,d, which plot the work-hardening rate ($\theta = \partial\sigma/\partial\varepsilon$) and work-hardening co-

efficient ($n = \partial ln\sigma / \partial ln\varepsilon$), respectively. According to Hollomon's equation [10,31], both curves show a similar trend as reported in [32]: a sharp decrease occurs before $\varepsilon \approx 0.06$, corresponding to the transition from elastic to plastic regimes [33], followed by a relatively stable stage until fracture. During the initial drop, θ and n values for Case 2 and Case 3 remain higher than those of Case 1, consistent with their higher yield strengths as listed in Table 2.

To further understand the micromechanical origins of these trends, the EVP-FFT model was applied to probe strain partitioning and stress triaxiality in the α/β, α_m/α', and fully α' microstructures (Section 4.2).

4.1.3. Fractographic Analyses

To examine fracture features under different cooling conditions, SEM fractographs were captured, as shown in Figure 6. A clear distinction is observed between Case 1 and the other two cases. In Case 1 (α/β, 1 °C/s), fracture surfaces lack obvious dimpled regions, unlike Cases 2 and 3. However, Case 1 does not exhibit a typical brittle fracture, as no transgranular or intergranular cleavage is visible. Instead, failure likely initiates by tearing along weak β regions under compression, consistent with the inherently low strength but high ductility of the β phase. In contrast, dimpled zones are clearly observed in Cases 2 and 3. Moreover, the dimples in Case 3 are larger and more elongated than those in Case 2, which indicates stronger plastic accommodation in the fully martensitic microstructure. Such elongated dimples in Ti64 have also been reported under dynamic compression at a strain rate of ~3900 s^{-1} using a split Hopkinson pressure bar, where they were associated with severe plastic deformation inside adiabatic shear bands [34].

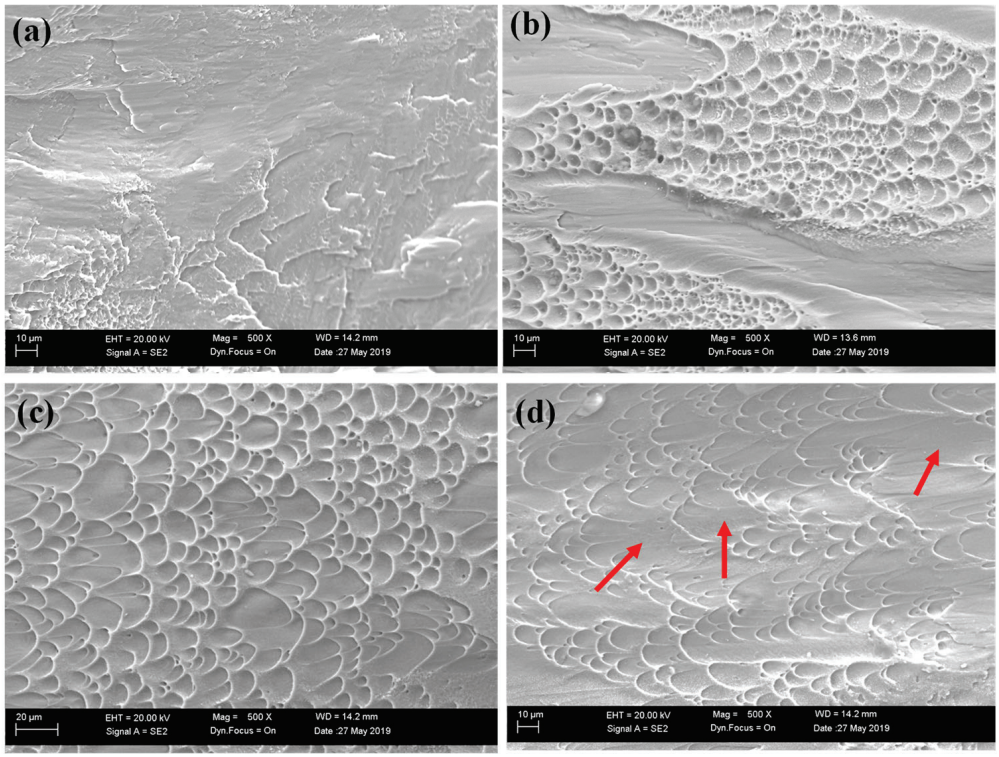


Figure 6. Fractographs of samples compressed under different cooling conditions: (**a**) Case 1 (1 °C/s, α/β), (**b**) Case 2 (145 °C/s, α_m/α'), and (**c**,**d**) Case 3 (7000 °C/s, fully α').

It is well known that spherical dimples correspond to micro-voids that nucleate cracks [35]. In Figure 6b,c, numerous micro-voids are visible at the intersections of dim-

ples. In Case 3 (Figure 6d), elongated dimples coalesce and evolve into smeared surfaces (indicated by red arrows), suggesting that the fully martensitic α' structure can sustain severe plastic deformation even after crack initiation. By contrast, in Case 2, the α_m/α' structure fails to accommodate further deformation once cracking begins, consistent with compression testing results showing that Case 3 exhibits much higher compressive strain to failure than Case 2.

4.2. Modeling the Crystal Plasticity of Different Phase Compositions

4.2.1. Reconstructed 3D Grain Structures

Figure 7 was generated using the MTEX toolbox in Matlab version 9.6 [22,36] based on the morphological information listed in Table 1. The phase distributions of reconstructed 3D microstructures for the three cooling conditions are shown in Figure 7a–c. Specifically, Figure 7a represents the lamellar α/β microstructure, where α plates nucleate preferentially along prior-β boundaries (white lines) and extend into the β matrix. The inner α (blue blocks in Figure 7a) and β (red blocks) form colonies of α/β lamellae following the Burgers orientation relation (BOR) [22]. For simplicity, the competitive colony growth inside individual grains was not considered in the Case 1 model.

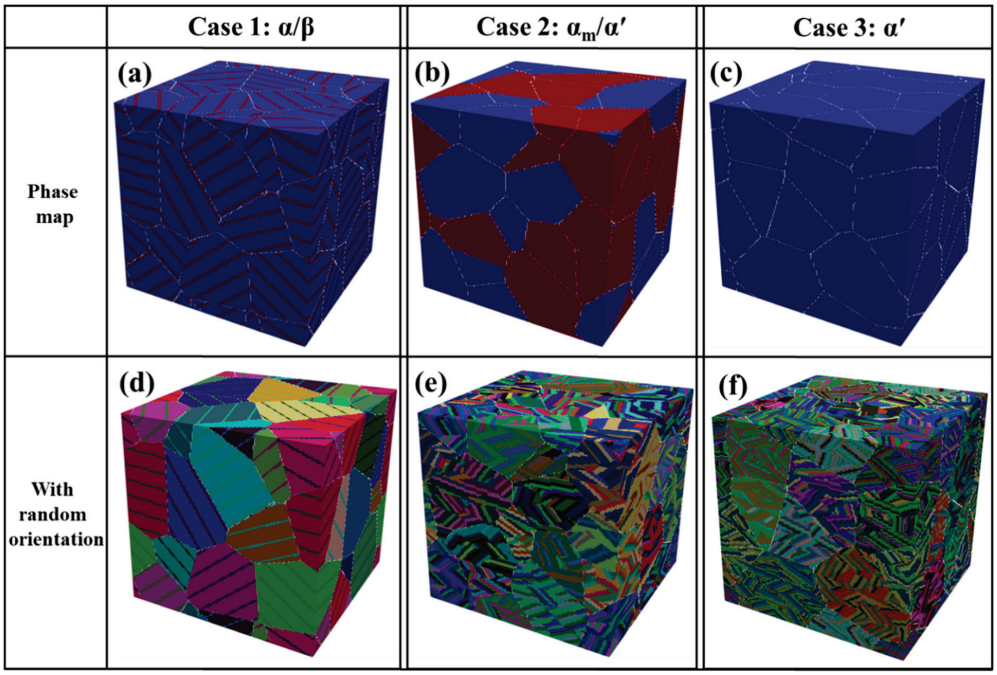


Figure 7. Reconstructed 3D microstructures (64^3 domain size) with different phase compositions. (**a**–**c**) phase maps, and (**d**–**f**) random orientation maps: (**a**,**d**) Case 1 (1 °C/s, α/β), (**b**,**e**) Case 2 (145 °C/s, α_m/α'), and (**c**,**f**) Case 3 (7000 °C/s, primary/secondary α').

Figure 7b shows the α_m/α' microstructure (Case 2). Here, α_m plates (blue blocks) are distributed mainly along prior-β boundaries (white lines) and occupy part of the grains, while the remaining regions are filled with martensitic α' (red blocks). Figure 7c corresponds to the fully martensitic microstructure (Case 3). In this case, a small fraction of long primary α' (white lines) is assigned at prior-β boundaries, whereas the interiors of the grains are occupied by dense secondary α' laths (blue blocks).

It should be noted that crystallographic textures are not emphasized in the present reconstruction; phases are therefore assigned random orientations, as illustrated in Figure 7d–f. This approach approximates the chaotic distribution of needle-like martensite

observed experimentally in Figure 4c,d. To mimic this effect, prior-β grains were subdivided into smaller zones that were filled with randomly oriented secondary α′ needles.

The crystallographic relationship between α and β laths is maintained through the Burgers orientation relation (BOR), namely, $(0001)_\alpha//\{101\}_\beta$ and $<11\bar{2}0>_\alpha/<111>_\beta$ [37]. This was verified by the symmetric rotation tool in TSL OIM Analysis. Figure 8 shows a selected α/β lamellar region in the reconstructed 3D model and the corresponding pole figures obtained after applying the appropriate rotation angles. The result confirms that the reconstructed lamellae preserve the BOR relationship, specifically $(0001)_\alpha//\{101\}_\beta$.

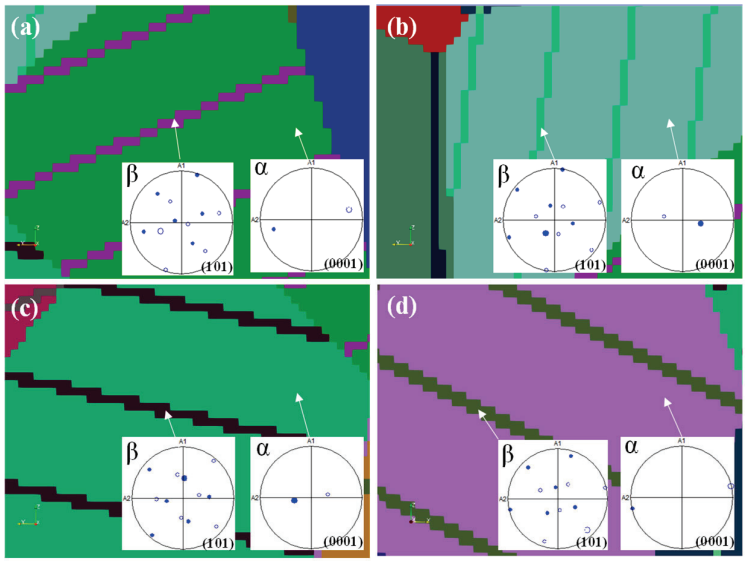


Figure 8. Four randomly selected examples (**a**–**d**) regarding pole-figure verification of the BOR relationship in reconstructed α/β lamellae: (101)β plane aligned with (0001)α plane after simulated rotations.

4.2.2. Calibration of Simulation Compression Curves

Due to the lack of phase-specific elastic constants and hardening parameters measured in compression, the literature values are primarily obtained from tensile tests [21,38] were used as initial priors and then calibrated against the present compression experiments (Figure 5b) for each microstructure. A working hypothesis adopted in the calibration is τ_0 of $\beta \ll \alpha' < \alpha$ as listed in Tables 3 and 4. This ordering is motivated by repeated nanoindentation evidence showing that single-phase α′ is softer than single-phase α [10]. Although this may appear to contradict the popular notion that "α′ is harder than α." The possible reason is that the indentations of general hardness tests like Vikers hardness tests are micro-scale and likely incorporate much α′ phase. Therefore, other factors like dislocations and phase boundaries may contribute to an elevated hardness. Hence, for Case 3, a small τ_0 is reasonably used for calibration. Otherwise, the strain-stress curve of pure martensite is more likely to yield at a higher strain, shown in Figure 9 simulation-α′ (2). It should be noted that the α_m is regarded as the bulk α [2], where the very small amount of β distributed in the bulk α is ignored therein, and the parameters of the bulk α phase are calculated by considering the thickness [22].

Table 3. Calibrated elastic constants of β, α, and α′ phases for Ti-6Al-4V [21].

Elastic Constants (GPa)	C_{11}	C_{12}	C_{13}	C_{33}	C_{44}
β	114	90	90	114	181
α	123	100	69	145	30
α′	120	100	67	125	30

Table 4. Calibrated Voce hardening parameters for different slip systems [21,38].

Hardening Parameters (MPa)	τ	τ_1	θ_0	θ_1
β	41.09	99.62	500	20
α (basal)	253.5	5.0	700	350
α (prismatic)	354.8	5.0	700	350
α (pyramidal)	879.2	5.0	700	350
α′ (basal)	216.7	5.0	750	340
α′ (prismatic)	296.9	5.0	750	340
α′ (pyramidal)	822.3	5.0	750	340

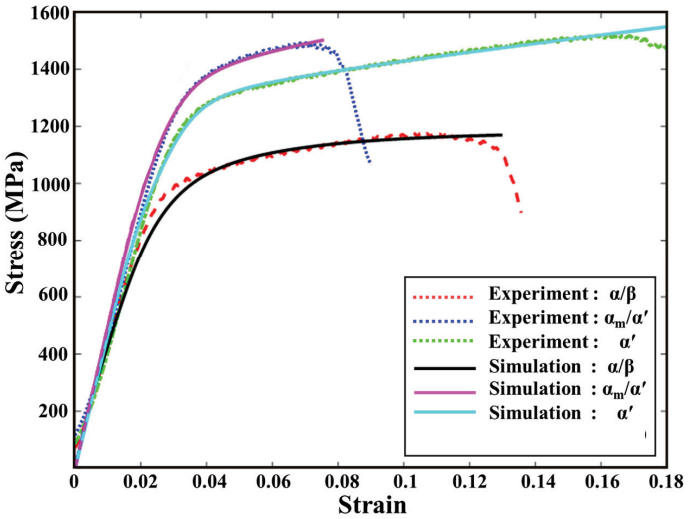


Figure 9. Experimental and EVP-FFT simulated compression stress–strain curves for samples with different phase/microstructure combinations.

Figure 9 compares the computational and experimental stress–strain curves for the three cases. The simulations reproduce both the elastic-to-plastic transition and the relative work-hardening trends across α/β (Case 1), α_m/α' (Case 2), and fully α′ (Case 3). Fracture is not modeled explicitly here due to the absence of a failure criterion; damage precursors and stress-triaxiality analyses are deferred to Section 5.

4.2.3. Overall Compressive Strain Field

Because of the anisotropy of the HCP structure, three <11$\bar{2}$0> (0001) basal, three <11$\bar{2}$0>{10$\bar{1}$0} prismatic, six <11$\bar{2}$0>{10$\bar{1}$1} **<α>** pyramidal slip systems for the HCP phase (α′/α phases) are considered in the crystal plasticity computation. It should be noted that six <11$\bar{2}$3>{10$\bar{1}$1} **<α+c>** pyramidal slip systems are excluded because they are unlikely to be activated [39]. At the same time, twelve <111> {110} slip systems for the BCC phase (β phase) are integrated into this model. Twinning is not considered, as deformation twinning in Ti-6Al-4V is rarely observed at ambient temperature and low strain rates [37,40,41].

Figure 10 shows the simulated 3D elastic and plastic responses after the compression strain of 0.014 (elastic stage) and 0.067 (plastic stage), respectively. It can be observed that the distribution of strain concentration varies in both inter- and intra-grains for different cases. Some of the grains after compression exhibit a strong strain concentration, while some exhibit limited strain concentration. In particular, some extremely high strain concentrations take place locally near the grain boundary, indicated by deep color. The inter- and intra-phases also show a similar trend of strain concentration. However, the strain/stress concentration varies from grain to grain and from phase to phase. Investigation of the plastic behavior of different phases may provide significant insights as to how grain and phase

interactions affect the micromechanics of slip systems, phase species, and morphologies. Because grain and phase boundaries are often the locations where plastic deformation is most pronounced. Moreover, since the reconstructed microstructure does not fully capture the precise morphology and the model does not explicitly include dislocations, the analysis does not account for the role of dislocations in plastic behavior. Instead, the stress and strain concentration coupled with the aforementioned slip systems are used to describe the role of different phases and morphologies on micro-mechanical responses.

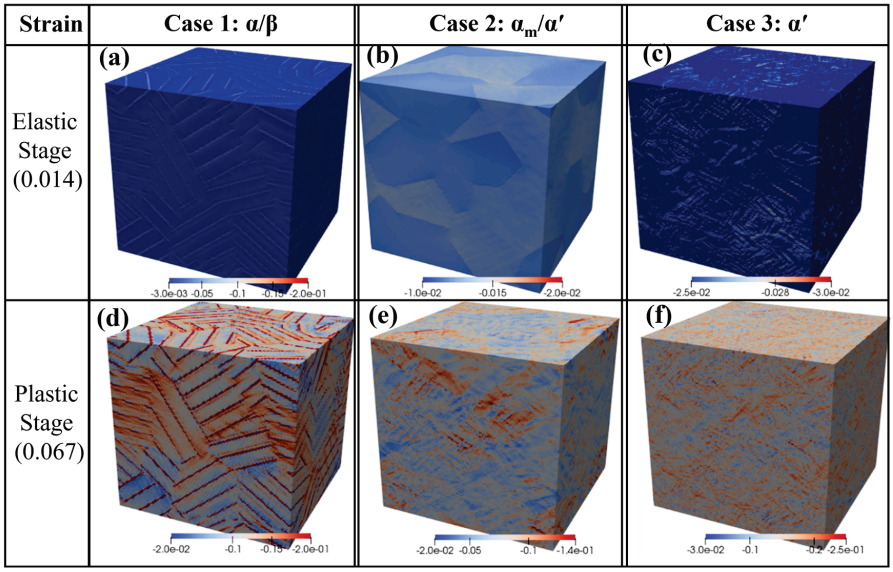


Figure 10. Simulated 3D maps of elastic and plastic strain at true strains of 0.014 (**a**–**c**) and 0.067 (**d**–**f**), respectively: (**a**,**d**) Case 1 (α/β), (**b**,**e**) Case 2 (α_m/α'), and (**c**,**f**) Case 3 (primary/secondary α′). Negative values correspond to compressive strain.

5. Discussion

In this work, Ti64 quenched from above the β-transus at an ultra-high cooling rate of ~7000 °C/s exhibits a concurrent improvement in ductility and strength. This observation challenges the common perception of a strength–ductility trade-off, although several studies have reported excellent performance for fully martensitic Ti64 [11,12] without a systematic mechanistic analysis. Here, we discuss the phase-dependent micromechanics underlying the different behaviors among α/β (Case 1), α_m/α' (Case 2), and fully α′ (Case 3), with emphasis on why the fully martensitic structure obtained under AM-level cooling rate attains enhanced ductility relative to α/β and α_m/α'. These insights suggest a processing paradigm for Ti alloys that achieves high strength and high ductility simultaneously. Methodologically, instead of digital image correlation (DIC), we leverage the EVP-FFT model built on 3D reconstructed microstructures to provide quantitative descriptions of strain partitioning and stress triaxiality—two metrics that capture mechanical contrast among phases and morphologies and link directly to ductile fracture propensity.

5.1. A Quantitative Understanding of the Yield Behaviors for Different Cases

From Table 1, the characteristic phase size in Case 2 is ~7× larger than in Case 1, which would ordinarily reduce yield strength according to Hall–Petch scaling [42]. Yet the measured yield stress increases by ~1.35× (Figure 5c,d), which is credited to two possible reasons. One is that the β phase in Case 2 is nearly replaced by α′ and α_m, both of which are harder-slipping than β due to fewer easy systems and higher CRSS; this is consistent with micro-/nano-scale hardness contrasts reported in [10]. Consequently, the

initial yielding is elevated. Another possible reason is that Case 2 contains a far more intricate network of grain/phase boundaries—especially the disordered distribution of α′ laths (Figure 4e)—than the predominantly lamellar α/β in Case 1. Molecular-dynamics simulations have indicated that disordered grain-boundary structures can significantly raise the yield stress by impeding dislocation motion [43].

For Case 3, the yield strength is slightly lower than Case 2 (with marginally lower initial θ and *n* in Figure 5c,d), even though its martensitic laths are finer. This is consistent with the phase effect: single-phase α′ is intrinsically softer than bulk α (α_m) at the slip-system level [10], so more systems are relatively easier to activate at yielding in Case 3. To quantify these effects, we employed the EVP-FFT model to analyze strain accumulation and partitioning at the yield points of all three cases.

Compared with DIC studies [10], the EVP-FFT approach provides field-resolved strain maps at the yield point along the compression axis, enabling direct comparison of local heterogeneity across phases. The color maps in Figure 11a–c show that microstructural diversity leads to heterogeneous strain accumulation in all cases. In Case 1 (α/β), strain partitions strongly between α and β (Figure 11d) [10], concentrating primarily in β because of its higher symmetry and much lower CRSS, with local values up to ~12.4× the macroscopic yield strain—consistent with fracture surfaces torn along β lamellae. In Case 2 (α_m/α′), localization occurs mainly in α′ (Figure 11e), but the peak is only ~1.5× the yield strain, reflecting smaller CRSS contrasts between α and α′ than between α and β. In Case 3 (fully α′), strain is more uniformly distributed (Figure 11f), and the peak is ~1.2× the yield strain, indicative of reduced partitioning in the refined α′ network.

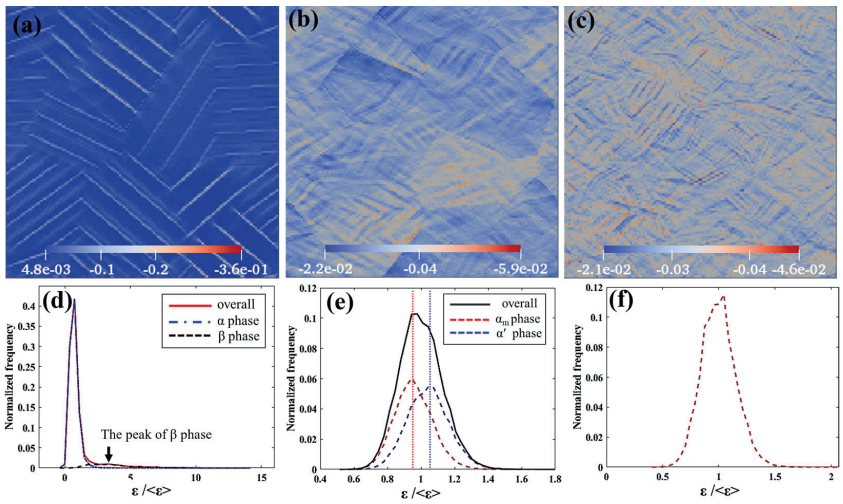


Figure 11. The 2D strain maps sliced from 3D strain models at each yield point for different cases, corresponding to the frequency of strain of each phase normalized by the average strain in the whole domain at the yield point: (**a**,**d**) 0.029 for Case 1; (**b**,**e**) 0.039 for Case 2; (**c**,**f**) 0.037 for Case 3.

Overall, the presence of soft β dominates the pronounced strain partitioning and the lowest yield strain in Case 1. Introducing α′ (Case 2) raises the yield level; switching to fully α′ (Case 3) slightly reduces $\sigma_{cy0.2}$ relative to Case 2 due to α′'s lower CRSS than α, despite finer lath size—consistent with the experimental trends.

5.2. Potential Mechanisms for the Marked Ductility Improvement in Fully Martensitic Structures

5.2.1. High-Angle Interfaces and Ductility

A high density of high-angle interfaces is a plausible contributor to the superior ductility in Case 3. In this study, low-angle grain boundaries (LAGBs) are defined as boundaries with

misorientation angles between 2° and 15°, while high-angle grain boundaries (HAGBs) are defined as those with misorientation angles between 15° and 90° [44]. EBSD misorientation statistics (Figure 12) indicate that increasing the cooling rate raises the fraction of HAGBs: in Case 1, over half of the boundaries are low-angle, whereas in Case 3 ≈70% of boundaries exhibit misorientation even >30%°. Such a population of HAGBs can promote boundary-mediated accommodation—e.g., dislocation absorption and deflection, impeded slip transfer, and crack-tip blunting—thus delaying localization and enhancing macroscopic ductility [5,44].

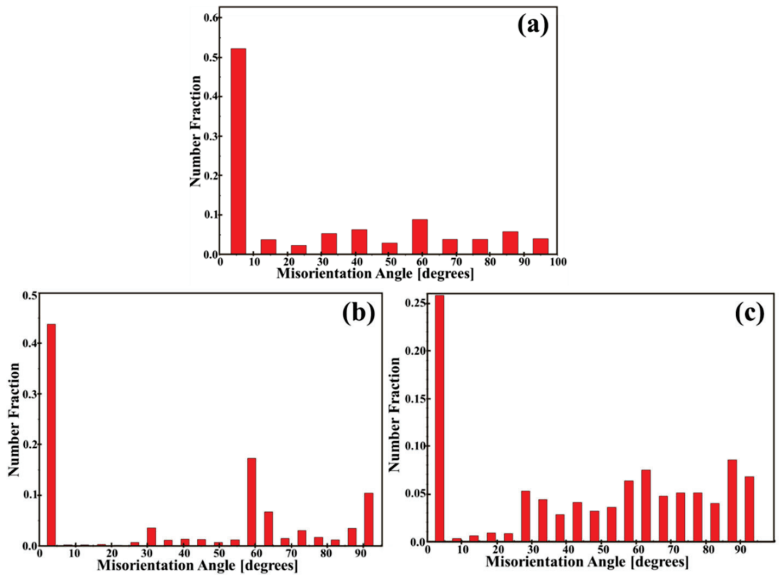


Figure 12. EBSD misorientation distributions: (**a**) Case 1 (α/β), (**b**) Case 2 (α_m/α'), (**c**) Case 3 (α').

Additionally, the ultrafine α' lath network in Case 3 offers a very high density of internal interfaces. Micro-cracks propagating along one α' lath are likely to be deflected or arrested upon encountering another lath with a large misorientation (schematized in Figure 13), delaying crack advance until larger global strains are attained. This interpretation is consistent with our EVP-FFT results that show a narrower strain distribution spread in Case 3 (Figure 11c,f) and with the fractography, where Case 3 exhibits longer wedge-like dimples than Case 2 (Figure 6d vs. Figure 6b). Based on our 3D reconstructions, the interfacial area density in Case 3 is estimated to be several-fold higher (on the order of ~6–10×) than in Cases 1–2, which aligns with the observed enhancement in boundary-mediated plastic accommodation [45,46].

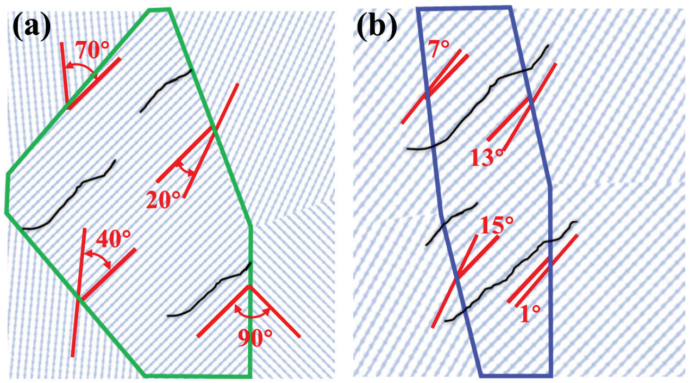


Figure 13. Schematic of boundary effects on crack propagation: (**a**) high-angle misorientation facilitating deflection/blunting; (**b**) low-angle misorientation providing easier crack paths.

5.2.2. Stress Triaxiality Factor

One useful approach to evaluate the stress state during plastic deformation is to track the stress triaxiality factor (TF or η), defined as the ratio of local mean stress (hydrostatic, σ_m) and local equivalent stress (von Mises or effective stress, σ_{vm}) [47,48]. In tensile tests, it is well documented that increased stress triaxiality reduces ductility. Hancock and Mackenzie [49], for example, demonstrated that the ductility of high-strength steels strongly depends on stress state, characterized by σ_m/σ_{vm}, which is also consistent with McClintock's model of ductile failure. Negative values of stress triaxiality indicate compressive stress states [50]. In this study, stress triaxiality was calculated at the fracture point to evaluate potential failure initiation, using EVP-FFT simulations that provide the full stress tensor at every Fourier grid point.

The evolution of average TF as a function of true strain up to fracture is shown in Figure 14a. In Case 1, |TF| first increases and then decreases to ~0.35 at fracture. By contrast, Cases 2 and 3 exhibit the opposite trend, with lower |TF| values throughout. At the fracture point, TF is ~0.26 in Cases 2 and 3, indicating that these microstructures experience less severe stress states and therefore resist fracture initiation more effectively than Case 1. The higher |TF| in Case 1 can be attributed to the presence of the soft β phase, which promotes extreme local stress concentrations.

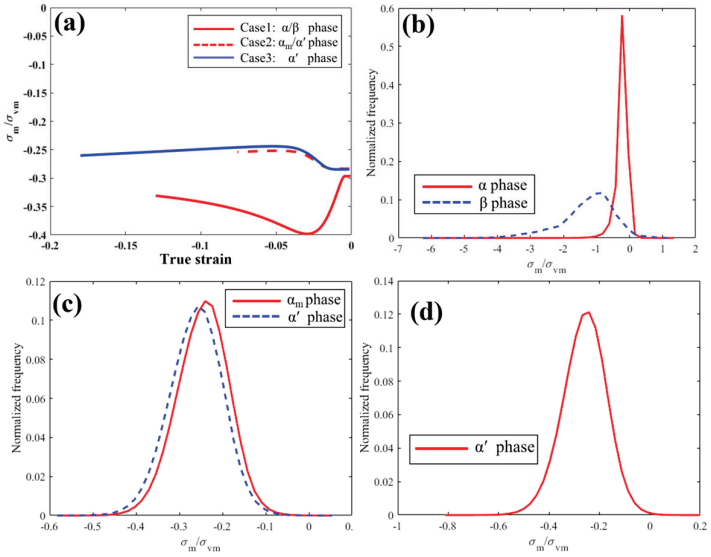


Figure 14. (**a**) The average σ_m/σ_{vm} variation against true strain and σ_m/σ_{vm} distributions for different cases: (**b**) Case 1, (**c**) Case 2, and (**d**) Case 3.

The TF distributions at the fracture point (Figure 14b–d) further illustrate this phase dependence. In Case 1, the β lamellae show the largest |TF|, identifying them as the weakest links, consistent with the fractographic evidence (Figure 6a) where cracks propagate along β. Case 2 shows a similar trend, but with a smaller contrast between α and α′. In contrast, Case 3 exhibits the lowest TF values and the most uniform distribution during compression, correlating with its superior ductility and higher compressive strain to failure.

6. Conclusions

In this study, we demonstrated that Ti-6Al-4V quenched from above the β-transus at an extremely high cooling rate (~7000 °C/s) forms a fully martensitic microstructure that simultaneously achieves enhanced strength and ductility compared with α/β and

α_m/α' microstructures obtained at slower cooling rates. Compression testing confirmed that the fully α' samples exhibit not only higher ultimate compressive strength and larger strain to failure, but also stronger work-hardening, lower stress-triaxiality magnitude, and fracture surfaces dominated by elongated dimples. By contrast, the α/β and α_m/α' conditions display obvious strain partitioning and stress-triaxiality partitioning, as captured quantitatively by EVP-FFT simulations.

Yield behavior was found to depend strongly on phase constitution. The presence of coarse α lamellae and the soft β phase in the α/β microstructure explains its lowest yield strength. With increasing cooling rate, the introduction of α' significantly raises the yield strength in the α_m/α' condition, since β is largely replaced by harder phases. Although the fully martensitic case has the finest lath size, its yield strength is slightly lower than Case 2, because single-phase α' has a lower CRSS than α. Nevertheless, the fully α' structure provides the most favorable combination of strength and ductility.

Two microstructural factors appear to be central to the superior ductility of the martensitic Ti64. First, the high fraction of high-angle grain/phase boundaries—about 70% of boundaries with misorientation > 30° in Case 3—promotes boundary sliding and plastic accommodation. Second, the ultrafine α' lath network produces a very high density of interfaces, which helps deflect and blunt cracks, thereby delaying propagation. These mechanisms, together with possible contributions from dislocation structures formed under rapid cooling, underpin the observed ductility enhancement.

Overall, this work highlights that controlling the cooling rate provides an effective pathway to tailor the phase constitution and interface architecture of titanium alloys. Fully martensitic Ti-6Al-4V produced by ultra-fast cooling challenges the conventional strength–ductility trade-off and offers a new paradigm for designing structural alloys that combine high strength with high ductility.

Author Contributions: Conceptualization, Y.X. and L.C.; methodology, Y.X. and H.Z.; software, Y.X. and P.L.; validation, Y.X., H.Z., and P.L.; formal analysis, P.L.; investigation, Y.X. and H.Z.; writing—original draft, Y.X. and H.Z.; writing—review & editing, Y.X., H.Z., P.L., and L.C.; visualization, Y.X.; supervision, Y.X. and L.C. All authors have read and agreed to the published version of the manuscript.

Funding: This work was financially supported by the National Science Foundation under Grant No. CMMI-1662854. P. Liu acknowledges funding from the Hunan Provincial Innovation Project for Graduate Students (CX2017B081) and the China Scholarship Council.

Institutional Review Board Statement: Not applicable.

Informed Consent Statement: Not applicable.

Data Availability Statement: The original contributions presented in this study are included in the article. Further inquiries can be directed to the corresponding authors.

Acknowledgments: The authors also thank the Center for Advanced Vehicular Systems (CAVS) at Mississippi State University for providing access to the Gleeble 3500D system and related facilities. Special thanks are extended to Matt Cagle for his assistance with Gleeble operations.

Conflicts of Interest: The authors declare no conflict of interest.

References

1. Xiao, Y. Investigations on Microstructure Evolution of Metal Additive Manufacturing by Experiments, Physics-Based and Data-Driven Modeling. Ph.D. Dissertation, University of Michigan, Ann Arbor, MI, USA, 2023. [CrossRef]
2. Xiao, Y.; Cagle, M.; Mujahid, S.; Liu, P.; Wang, Z.; Yang, W.; Chen, L. A Gleeble-Assisted Study of Phase Evolution of Ti-6Al-4V Induced by Thermal Cycles during Additive Manufacturing. *J. Alloys Compd.* **2021**, *860*, 158409. [CrossRef]

3. Rietema, C.J.; Roehling, J.D.; Smith, W.L.; Bertsch, K.M. Microstructural Control of Additively Manufactured Ti6Al4V via In-Situ Large-Area Laser Annealing. *Scr. Mater.* **2024**, *239*, 115823. [CrossRef]
4. Cui, D.; Zhang, Y.; He, F.; Ma, J.; Zhang, K.; Yang, Z.; Li, J.; Wang, Z.; Kai, J.J.; Wang, J.; et al. Heterogeneous Microstructure of the Bonding Zone and Its Dependence on Preheating in Hybrid Manufactured Ti-6Al-4V. *Mater. Res. Lett.* **2021**, *9*, 422–428. [CrossRef]
5. Wang, C.; Lei, Y.; Li, C. Achieving an Excellent Strength and Ductility Balance in Additive Manufactured Ti-6Al-4V Alloy through Multi-Step High-to-Low-Temperature Heat Treatment. *Materials* **2023**, *16*, 6947. [CrossRef] [PubMed]
6. Bertsch, K.M.; Voisin, T.; Forien, J.B.; Tiferet, E.; Ganor, Y.I.; Chonin, M.; Wang, Y.M.; Matthews, M.J. Critical Differences between Electron Beam Melted and Selective Laser Melted Ti-6Al-4 V. *Mater. Des.* **2022**, *216*, 110533. [CrossRef]
7. Murr, L.E.; Quinones, S.A.; Gaytan, S.M.; Lopez, M.I.; Rodela, A.; Martinez, E.Y.; Hernandez, D.H.; Martinez, E.; Medina, F.; Wicker, R.B. Microstructure and Mechanical Behavior of Ti-6Al-4V Produced by Rapid-Layer Manufacturing, for Biomedical Applications. *J. Mech. Behav. Biomed. Mater.* **2009**, *2*, 20–32. [CrossRef]
8. Thijs, L.; Verhaeghe, F.; Craeghs, T.; Van Humbeeck, J.; Kruth, J.P. A Study of the Microstructural Evolution during Selective Laser Melting of Ti-6Al-4V. *Acta Mater.* **2010**, *58*, 3303–3312. [CrossRef]
9. Ricci, S.; Iannitti, G. Mechanical Behavior of Additive Manufacturing (AM) and Wrought Ti6Al4V with a Martensitic Microstructure. *Metals* **2024**, *14*, 1028. [CrossRef]
10. de Formanoir, C.; Martin, G.; Prima, F.; Allain, S.Y.P.; Dessolier, T.; Sun, F.; Vivès, S.; Hary, B.; Bréchet, Y.; Godet, S. Micromechanical Behavior and Thermal Stability of a Dual-Phase A+α' Titanium Alloy Produced by Additive Manufacturing. *Acta Mater.* **2019**, *162*, 149–162. [CrossRef]
11. Zafari, A.; Barati, M.R.; Xia, K. Controlling Martensitic Decomposition during Selective Laser Melting to Achieve Best Ductility in High Strength Ti-6Al-4V. *Mater. Sci. Eng. A* **2019**, *744*, 445–455. [CrossRef]
12. Chong, Y.; Bhattacharjee, T.; Yi, J.; Shibata, A.; Tsuji, N. Mechanical Properties of Fully Martensite Microstructure in Ti-6Al-4V Alloy Transformed from Refined Beta Grains Obtained by Rapid Heat Treatment (RHT). *Scr. Mater.* **2017**, *138*, 66–70. [CrossRef]
13. Wang, Z.; Jiang, C.; Liu, P.; Yang, W.; Zhao, Y.; Horstemeyer, M.F.; Chen, L.Q.; Hu, Z.; Chen, L. Uncertainty Quantification and Reduction in Metal Additive Manufacturing. *npj Comput. Mater.* **2020**, *6*, 175. [CrossRef]
14. Xiao, Y.; Wan, Z.; Liu, P.; Wang, Z.; Li, J.; Chen, L. Quantitative Simulations of Grain Nucleation and Growth at Additively Manufactured Bimetallic Interfaces of SS316L and IN625. *J. Mater. Process. Technol.* **2022**, *302*, 117506. [CrossRef]
15. Xiao, Y.; Wang, X.; Yang, W.; Yao, X.X.; Yang, Z.; Lu, Y.; Wang, Z.; Chen, L. Data-Driven Prediction of Future Melt Pool from Built Parts during Metal Additive Manufacturing. *Addit. Manuf.* **2024**, *93*, 104438. [CrossRef]
16. Zhou, H.; Feng, K.; Xiao, Y.; Liu, Y.; Ke, S. Pressure Effects on a Novel W-Mo-Cu Alloy by Large Current Electric Field Sintering: Sintering Behavior, Microstructure and Properties. *J. Alloys Compd.* **2019**, *785*, 965–971. [CrossRef]
17. Zhou, H.; Feng, K.; Liu, Y. Densification, Microstructure, and Properties of W-Mo-Cu Alloys Prepared with Nano-Sized Cu Powders via Large Electric Current Sintering. *Adv. Powder Technol.* **2022**, *33*, 103703. [CrossRef]
18. Feng, K.; Zhou, H.; Xiao, Y.; Liu, Y. Study on the Electric Current Effects on the Microstructure and Properties of W-Mo-Cu Alloy Under the Action of Electric Field. *JOM* **2023**, *75*, 780–790. [CrossRef]
19. Lebensohn, R.A.; Kanjarla, A.K.; Eisenlohr, P. An Elasto-Viscoplastic Formulation Based on Fast Fourier Transforms for the Prediction of Micromechanical Fields in Polycrystalline Materials. *Int. J. Plast.* **2012**, *32*, 59–69. [CrossRef]
20. Chen, L.; Chen, J.; Lebensohn, R.A.; Ji, Y.Z.; Heo, T.W.; Bhattacharyya, S.; Chang, K.; Mathaudhu, S.; Liu, Z.K.; Chen, L.Q. An Integrated Fast Fourier Transform-Based Phase-Field and Crystal Plasticity Approach to Model Recrystallization of Three Dimensional Polycrystals. *Comput. Methods Appl. Mech. Eng.* **2015**, *285*, 829–848. [CrossRef]
21. Ozturk, T.; Rollett, A.D. Effect of Microstructure on the Elasto-Viscoplastic Deformation of Dual Phase Titanium Structures. *Comput. Mech.* **2018**, *61*, 55–70. [CrossRef]
22. Liu, P.W.; Wang, Z.; Xiao, Y.H.; Lebensohn, R.A.; Liu, Y.C.; Horstemeyer, M.F.; Cui, X.Y.; Chen, L. Integration of Phase-Field Model and Crystal Plasticity for the Prediction of Process-Structure-Property Relation of Additively Manufactured Metallic Materials. *Int. J. Plast.* **2020**, *128*, 102670. [CrossRef]
23. Michel, J.C.; Moulinec, H.; Suquet, P. A Computational Method Based on Augmented Lagrangians and Fast Fourier Transforms for Composites with High Contrast. *Comput. Model. Eng. Sci.* **2000**, *1*, 79. [CrossRef]
24. Tome, C.; Canova, G.R.; Kocks, U.F.; Christodoulou, N.; Jonas, J.J. The Relation between Macroscopic and Microscopic Strain Hardening in F.C.C. Polycrystals. *Acta Metall.* **1984**, *32*, 1637–1653. [CrossRef]
25. Lebensohn, R.A.; Tomé, C.N.; Castañeda, P.P. Self-Consistent Modelling of the Mechanical Behaviour of Viscoplastic Polycrystals Incorporating Intragranular Field Fluctuations. *Philos. Mag.* **2007**, *87*, 4287–4322. [CrossRef]
26. Ahmed, T.; Rack, H.J. Phase Transformations during Cooling in A+β Titanium Alloys. *Mater. Sci. Eng. A* **1998**, *243*, 206–211. [CrossRef]
27. Sieniawski, J.; Ziaja, W.; Kubiak, K.; Motyk, M. Microstructure and Mechanical Properties of High Strength Two-Phase Titanium Alloys. In *Titanium Alloys-Advances in Properties Control*; IntechOpen: London, UK, 2013.

28. Beladi, H.; Chao, Q.; Rohrer, G.S. Variant Selection and Intervariant Crystallographic Planes Distribution in Martensite in a Ti-6Al-4V Alloy. *Acta Mater.* **2014**, *80*, 478–489. [CrossRef]
29. Tuninetti, V.; Gilles, G.; Milis, O.; Pardoen, T.; Habraken, A.M. Anisotropy and Tension-Compression Asymmetry Modeling of the Room Temperature Plastic Response of Ti-6Al-4V. *Int. J. Plast.* **2015**, *67*, 53–68. [CrossRef]
30. Nagra, J.S.; Brahme, A.; Lévesque, J.; Mishra, R.; Lebensohn, R.A.; Inal, K. A New Micromechanics Based Full Field Numerical Framework to Simulate the Effects of Dynamic Recrystallization on the Formability of HCP Metals. *Int. J. Plast.* **2019**, *125*, 210–234. [CrossRef]
31. Ma, X.; Li, F.; Cao, J.; Li, J.; Sun, Z.; Zhu, G.; Zhou, S. Strain Rate Effects on Tensile Deformation Behaviors of Ti-10V-2Fe-3Al Alloy Undergoing Stress-Induced Martensitic Transformation. *Mater. Sci. Eng. A* **2018**, *710*, 1–9. [CrossRef]
32. Hou, X.; Liu, Z.; Wang, B.; Lv, W.; Liang, X.; Hua, Y. Stress-Strain Curves and Modified Material Constitutive Model for Ti-6Al-4V over Thewide Ranges of Strain Rate and Temperature. *Materials* **2018**, *11*, 938. [CrossRef]
33. Ji, X.; Emura, S.; Min, X.; Tsuchiya, K. Strain-Rate Effect on Work-Hardening Behavior in β-Type Ti-10Mo-1Fe Alloy with TWIP Effect. *Mater. Sci. Eng. A* **2017**, *707*, 701–707. [CrossRef]
34. Zhang, J.; Tan, C.W.; Ren, Y.; Yu, X.D.; Ma, H.L.; Wang, F.C.; Cai, H.N. Adiabatic Shear Fracture in Ti-6Al-4V Alloy. *Trans. Nonferrous Met. Soc. China (Engl. Ed.)* **2011**, *21*, 2396–2401. [CrossRef]
35. Liu, X.; Tan, C.; Zhang, J.; Wang, F.; Cai, H. Correlation of Adiabatic Shearing Behavior with Fracture in Ti-6Al-4V Alloys with Different Microstructures. *Int. J. Impact Eng.* **2009**, *36*, 1143–1149. [CrossRef]
36. Mainprice, D.; Hielscher, R.; Schaeben, H. Calculating Anisotropic Physical Properties from Texture Data Using the MTEX Open-Source Package. *Geol. Soc. Spec. Publ.* **2011**, *360*, 175–192. [CrossRef]
37. Mayeur, J.R.; McDowell, D.L. A Three-Dimensional Crystal Plasticity Model for Duplex Ti-6Al-4V. *Int. J. Plast.* **2007**, *23*, 1457–1485. [CrossRef]
38. Tari, V.; Lebensohn, R.A.; Pokharel, R.; Turner, T.J.; Shade, P.A.; Bernier, J.V.; Rollett, A.D. Validation of Micro-Mechanical FFT-Based Simulations Using High Energy Diffraction Microscopy on Ti-7Al. *Acta Mater.* **2018**, *154*, 273–283. [CrossRef]
39. Zhang, M.; Zhang, J.; McDowell, D.L. Microstructure-Based Crystal Plasticity Modeling of Cyclic Deformation of Ti-6Al-4V. *Int. J. Plast.* **2007**, *23*, 1328–1348. [CrossRef]
40. Yapici, G.G.; Karaman, I.; Luo, Z.P. Mechanical Twinning and Texture Evolution in Severely Deformed Ti-6Al-4V at High Temperatures. *Acta Mater.* **2006**, *54*, 3755–3771. [CrossRef]
41. Prakash, D.G.L.; Ding, R.; Moat, R.J.; Jones, I.; Withers, P.J.; da Fonseca, J.Q.; Preuss, M. Deformation Twinning in Ti-6Al-4V during Low Strain Rate Deformation to Moderate Strains at Room Temperature. *Mater. Sci. Eng. A* **2010**, *527*, 5734–5744. [CrossRef]
42. Huang, T.; Shuai, L.; Wakeel, A.; Wu, G.; Hansen, N.; Huang, X. Strengthening Mechanisms and Hall-Petch Stress of Ultrafine Grained Al-0.3%Cu. *Acta Mater.* **2018**, *156*, 369–378. [CrossRef]
43. Borovikov, V.; Mendelev, M.I.; King, A.H. Effects of Grain Boundary Disorder on Dislocation Emission. *Mater. Lett.* **2019**, *237*, 303–305. [CrossRef]
44. Gao, Q.; Li, R.; Wu, H.; Miao, K.; Wu, H.; Liu, C.; Li, X. Revealing the Superior Post-Necking Elongation in the Fine-Grained Ti-6Al-4V ELI at Cryogenic Temperature. *Metals* **2024**, *14*, 600. [CrossRef]
45. Xie, H.; Zhou, S.; Guan, B.; Ren, Y.; Sun, Z.; Dai, G.; Yang, G. Enhanced Strength-Ductility Synergy in Hybrid Additive Manufactured Ti–6Al–4V via Interlayer Friction Stir Processing Assisted Laser-Directed Energy Deposition. *Virtual Phys. Prototyp.* **2025**, *20*, e2499935. [CrossRef]
46. Qiang, F.; Xin, S.; Tu, X.; Wang, H.; Guo, P.; Hou, H.; Lian, Z.; Zhang, L.; Hou, W. Low-Temperature Superplastic Deformation Mechanism of Ultra-Fine Grain Ti–6Al–4V Alloy by Friction Stir Processing. *J. Mater. Res. Technol.* **2024**, *30*, 7413–7419. [CrossRef]
47. Mirone, G. Role of Stress Triaxiality in Elastoplastic Characterization and Ductile Failure Prediction. *Eng. Fract. Mech.* **2007**, *74*, 1203–1221. [CrossRef]
48. El-Magd, E.; Abouridouane, M. Characterization, Modelling and Simulation of Deformation and Fracture Behaviour of the Light-Weight Wrought Alloys under High Strain Rate Loading. *Int. J. Impact Eng.* **2006**, *32*, 741–758. [CrossRef]
49. Hancock, J.W.; Mackenzie, A.C. On the Mechanisms of Ductile Failure in High-Strength Steels Subjected to Multi-Axial Stress-States. *J. Mech. Phys. Solids* **1976**, *24*, 147–160. [CrossRef]
50. Bouchard, P.O.; Bourgeon, L.; Fayolle, S.; Mocellin, K. An Enhanced Lemaitre Model Formulation for Materials Processing Damage Computation. *Int. J. Mater. Form.* **2011**, *4*, 299–315. [CrossRef]

Disclaimer/Publisher's Note: The statements, opinions and data contained in all publications are solely those of the individual author(s) and contributor(s) and not of MDPI and/or the editor(s). MDPI and/or the editor(s) disclaim responsibility for any injury to people or property resulting from any ideas, methods, instructions or products referred to in the content.

MDPI AG
Grosspeteranlage 5
4052 Basel
Switzerland
Tel.: +41 61 683 77 34

Materials Editorial Office
E-mail: materials@mdpi.com
www.mdpi.com/journal/materials



Disclaimer/Publisher's Note: The title and front matter of this reprint are at the discretion of the Guest Editors. The publisher is not responsible for their content or any associated concerns. The statements, opinions and data contained in all individual articles are solely those of the individual Editors and contributors and not of MDPI. MDPI disclaims responsibility for any injury to people or property resulting from any ideas, methods, instructions or products referred to in the content.





Academic Open
Access Publishing

mdpi.com

ISBN 978-3-7258-8716-3